Advances in Materials Science and Engineering

Microstructure, Properties and Tribological Behaviour of Advanced Functional Materials

Lead Guest Editor: Pushpanathan Ganeshan
Guest Editors: Olatunji Oladimeji Ojo, Ali Khorram, and Yahya Bozkurt

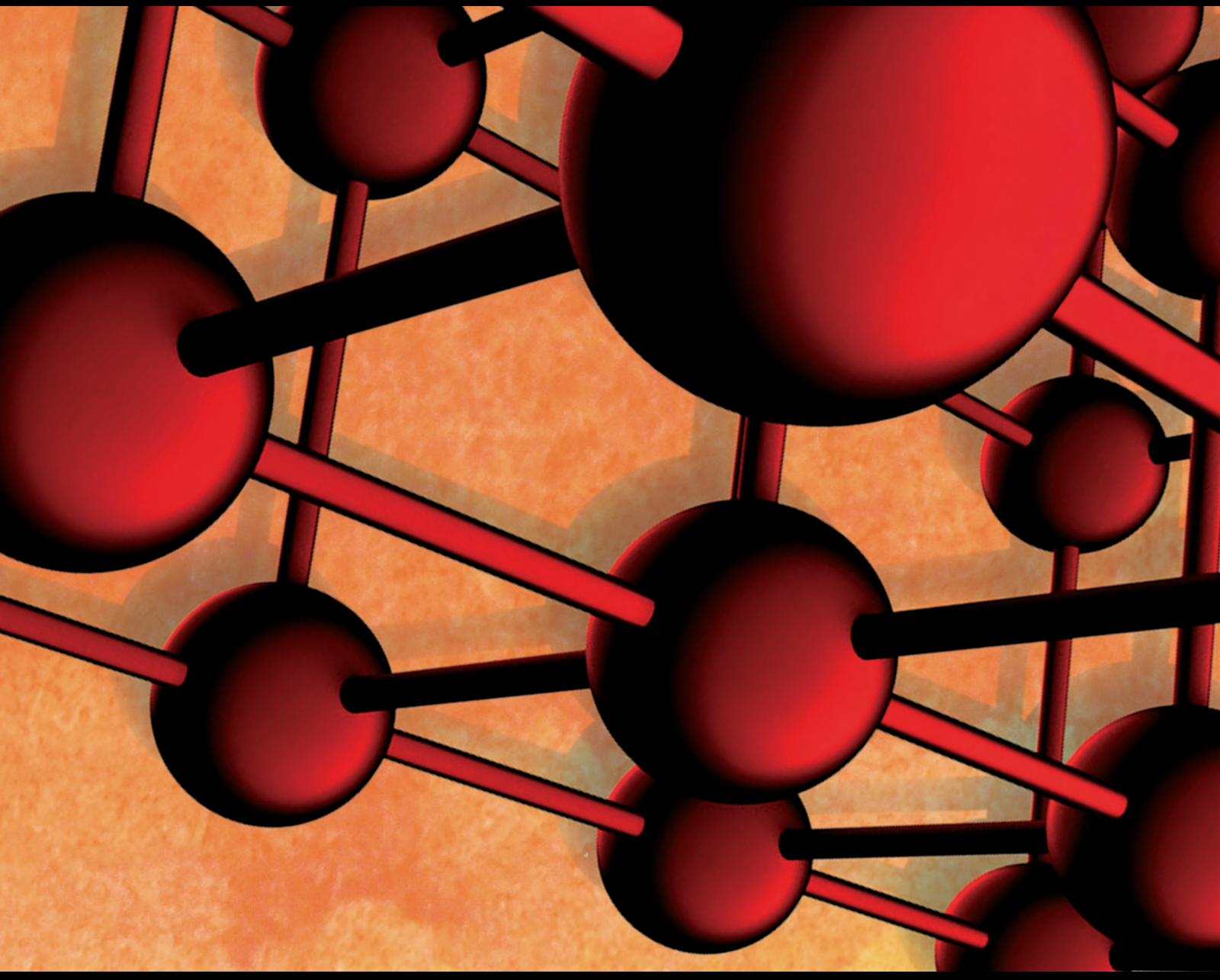

Microstructure, Properties and Tribological Behaviour of Advanced Functional Materials

Advances in Materials Science and Engineering

Microstructure, Properties and Tribological Behaviour of Advanced Functional Materials

Lead Guest Editor: Pushpanathan Ganeshan
Guest Editors: Olatunji Oladimeji Ojo, Ali Khorram, and Yahya Bozkurt

Contents

Natural Fiber Incorporated Polymer Matrix Composites for Electronic Circuit Board Applications
V. S. Chandrika, A. Anamika, C. Jeeva, Bhagavathi Perumal, S. Sanal Kumar, J. Femila Roseline, and Ishwarya Komalnu Raghavan
Research Article (9 pages), Article ID 3035169, Volume 2022 (2022)

Analysis of the Hybrid of Mudar/Snake Grass Fiber-Reinforced Epoxy with Nano-Silica Filler Composite for Structural Application
I. Jenish, A. Felix Sahayaraj, V. Suresh, J. Mani raj, M. Appadurai, E. Fantin Irudaya Raj, Omaima Nasif, Saleh Alfarraj, and Ashok Kumar Kumaravel
Research Article (10 pages), Article ID 7805146, Volume 2022 (2022)

A Cutting-Edge Survey of Tribological Behavior Evaluation Using Artificial and Computational Intelligence Models
Senthil Kumaran Selvaraj, Aditya Raj, Mohit Dharnidharka, Utkarsh Chadha, Isha Sachdeva, Chinmay Kapruan, and Velmurugan Paramasivam
Review Article (17 pages), Article ID 9529199, Volume 2021 (2021)

Mechanical Properties of Titanium Diboride Particles Reinforced Aluminum Alloy Matrix Composites: A Comprehensive Review
V. Mohanavel, M. Ravichandran, V. Anandakrishnan, Alokesh Pramanik, M. Meignanamoorthy, Alagar Karthick, and M. Muhibbullah
Review Article (18 pages), Article ID 7602160, Volume 2021 (2021)

Characterization of TiZrN and TaZrN Nanocomposite Multilayer Coating Deposited via RF/DC Magnetron Sputtering on AISI4140 Steel
R. Hariharan, R. Raja, R. J. Golden Renjith Nimal, Mohamad Reda A. Refaai, S Ravi, and Haiter Lenin Allasi
Research Article (10 pages), Article ID 8273708, Volume 2021 (2021)

3D Printing Manufacturing Techniques, Materials, and Applications: An Overview
D. Srinivasan, M. Meignanamoorthy, M. Ravichandran, V. Mohanavel, S. V. Alagarsamy, C. Chanakyan, S. Sakthivelu, Alagar Karthick, T. Ram Prabhu, and S. Rajkumar
Review Article (10 pages), Article ID 5756563, Volume 2021 (2021)

The Investigation of Mixed Ferrofluids Containing Iron Oxide nanoparticles and Microspheres
Sharanabasava V. Ganachari, Veerabhadragouda B. Patil, Nagaraj R. Banapurmath, Manzoore Elahi M. Soudagar, Kiran Shahapurkar, Ashraf Elfasakhany, Mishal Alsehli, Akshata Yavagal, Pradyumna Mogre, Vijayakumar M Hiremath, and Shankar A. Hallad
Research Article (11 pages), Article ID 7616666, Volume 2021 (2021)

Exploration on Mechanical Behaviours of Hyacinth Fibre Particles Reinforced Polymer Matrix-Based Hybrid Composites for Electronic Applications
Pradeep Kumar Panda, J. Jebastine, Madhialagan Ramarao, Shaik Fairooz, Chirra Kesava Reddy, Omaima Nasif, Saleh Alfarraj, Velu Manikandan, and I. Jenish
Research Article (10 pages), Article ID 4933450, Volume 2021 (2021)

Contents

Hindawi
Advances in Materials Science and Engineering
Volume 2022, Article ID 6328781, 11 pages
https://doi.org/10.1155/2022/6328781

Research Article

Optimization on the Mechanical Properties of Aluminium 8079 Composite Materials Reinforced with PSA

Mohamad Reda A. Refaai,[1] **R. Meenakshi Reddy**,[2] **Jayaprakash Venugopal**,[3] **M. Venkata Rao**,[4] **K. Vaidhegi**,[5] **and Simon Yishak**[6]

[1]*Department of Mechanical Engineering, College of Engineering, Prince Sattam Bin Abdulaziz University, Alkharj 16273, Saudi Arabia*
[2]*Department of Mechanical Engineering, G. Pulla Reddy Engineering College, Kurnool-518007, Andhra Pradesh, India*
[3]*School of Mechanical, Sathyabama Institute of Science and Technology, Chennai, Tamil Nadu 600119, India*
[4]*Department of Civil Engineering, SRKR Engineering College, Bhimavaram, Andhra Pradesh 534204, India*
[5]*Department of Civil Engineering, Sri Sairam Engineering College, Chennai, Tamil Nadu 600044, India*
[6]*College of Engineering and Argo-Industrial Technology, Sawla Campus, Arba Minch University, Arba Minch, Ethiopia*

Correspondence should be addressed to Mohamad Reda A. Refaai; m.rifaee@psau.edu.sa

Received 17 December 2021; Accepted 25 February 2022; Published 22 April 2022

Academic Editor: P. Ganeshan

AA 8079 with variable percentages of peanut shell ash (PSA) was created by stir casting (2.5 percent, 5 percent, 7.5 percent, 10 percent, 12.5 percent, and 15 percent). Compared some of the physical and mechanical properties of the composite material were to the alloy matrix alloy (density; porosity percentage; hardness; wear index; tensile strength; and impact strength). Peanut shell ash reinforcements were found to be distributed uniformly throughout the Aluminum Matrix, with pockets of agglomerated reinforcement particles. The hardness, wear index, and density of the composite were enhanced by adding PSA particles. Compared to the matrix alloy without reinforcement, the composites had lower tensile and impact strengths. Mixture design with Design-Expert (Stat EASY) software package indicated the appropriate matrix and reinforcing combination proportions and how they influenced composites' studied properties. Composites' physical and mechanical properties were predicted and optimized using regression models created and the ideal mixture of matrix and reinforcement wt. According to optimization findings, the components for optimal composite characteristics' responses are 93.48 and 6.52 percent of matrix and reinforcement wt% particles. They can utilize PSA-reinforced AA8079 core materials to make automotive components that need lighter, stackable, and wear-resistant.

1. Introduction

In the recent time, there have been increasing interests in researches on the use of naturally sourced and agro-waste based reinforcements in composite materials due to their ease of fabrication, as well as a growing worldwide effort to conserve the environment and stricter global penalties for noncompliance, flexibility, regenerative, and lower costs are all important factors [1]. The main benefit of aluminum composite materials is the combination of strength and rigidity with light weight. Manufacturers may generate qualities that precisely match the needs for a specific construction for a particular purpose by selecting the right combination of reinforcement and matrix material. Natural fibre and agro-wastes reinforced composites are environmentally benign materials with promising applications in various fields, especially where environmental and energy conservation are of great concern. They are considered as suitable materials to replace the expensive and highly dense Lighter, strong, and energy-saving applications for composite polymers, their related products, and other industrial waste [2, 3]. The real advantages of natural fibre is flexible and light weight. The wide variety of fibre reinforcing elements makes composite materials more versatile and

expands their potential. Composite materials could benefit from the use of natural fibres and agricultural wastes [4]. Because they are biodegradable, renewable, recyclable, and may be found in a wide variety of natural and cultivated forms, natural fibres are superior than synthetic ones. While artificial fibres (like silicon carbide and carbon) are manufactured in advanced developed countries, natural fibres of plant and animal origin are commonly grown in underdeveloped countries as agricultural waste or waste products, [5–8]. A large source of income for the local economies in these underdeveloped countries will be generated by this project. Large amounts of solid wastes, like palm kernel shell, coconut shell and wood charcoal as well as peanut shell, periwinkle husk and rice husk can be generated by the mining of several minerals in India [9, 10]. It is possible to utilize these solid agricultural leftovers individually or in combination to make environmentally-friendly composite materials for diverse uses, including the environment seen in automotive disc brakes [11].

The wide range of applications for aluminium metal matrix composites (AMMCs) in many industries, including aviation, automobile, aviation, maritime, thermal protection, and electrical and electronic engineering, and sporting goods, has made this research area a hotbed of activity [12, 13]. Most commonly, the manufacturing of AMMCs has utilised aluminium alloys from the 2000, 5000, 6000, and 7000 series range as a matrix. AMMCs due to their light weight, they exhibit a high stability ratio [14]. excellent stiffness-to-weight ratio and excellent thermal conductivity. Additionally, AMMCs exhibit superior deformation and creeping resistance [15]. Aluminium alloy AA8079 with the major alloying elements are silicon and magnesium is utilised in the aerospace and automobile industries. When reinforced with properties and low thermal expansion coefficients, high hardness, high tensile strength, and superior durability, composite materials can be tailored to satisfy specific physical and mechanical requirements. AMMCs can be reinforced by continual or intermittent fibres, bristles, or particles [16–19]. These more affordable AMMCs are commonly made by strong (powder metallurgy) or liquid-state techniques (stir casting, infiltration, and in-situ operations). By including minimal and regenerative particulate material fillers such as coconut shell, peanut shell, palm kernel, charcoal, and peanut shell into the alloy matrix, the overall cost of AA8079 and its end products can be decreased. Composites can be used in lightweight, load-bearing, and wear-resistant automotive and aeronautical applications [20, 21]. Figure 1 reveals the schematic diagram of Metal matrix composites advantages and applications.

The Design of Experiment (DOE) tool can be used to run minimal experiments by altering input components between their respective positions, statistically analysing their relevance, creating model equations, and verifying model accuracy and applicability using input-output data [22]. Previously, researchers have employed tools and approaches for Analytical method techniques include response surface analysis (RSA), box Behnken design (BBD), combination testing, factorial design, and the Taguchi approach etc. to optimise and predict composite materials production process factors and attributes [23]. Furthermore, the results showed that it is an excellent tool for the design, composite material simulation and improvement. Factorial, response surface, and mixture designs of the DOE can be used to examine the interplay of MMCs fabrication process factors and their impacts on physical and mechanical properties (response variables) under the conditions of experimentation and predictive modelling [24–26]. For the most part, the factorial design method is used to determine whether or not certain components are critical to the overall process. In certain cases, this can be done by narrowing down the list of elements to just a handful, or by describing how each factor interacts with the others [27]. Components in a mixture, like composite materials, can have different responses based on their respective quantities. Each run sums up to the same amount because all of the mixture components are inputted in the same units of measure. The response surface approach is a quantitative and empirical design technique that involves the examination of how selected dependent variables respond to changes across one or more unbiased or factor variables [28, 29]. These designs enable statistical models and improvement of empirical process factors/variables and response quality. The goal is to optimise the dependent variable's output (output/properties) by altering the implementation of targeted for one or more independent/factor variables (inputs/process parameters) [30].

Natural and agricultural waste materials such as rice husk, sugarcane bagasse, palm kernel shells, and coconut husk have been used to make aluminium alloy-based composites. According to several of these studies, peanut shell ash has the potential to be an effective hybrid reinforcement for composite materials [31–33]. The goal of this study is to construct an aluminium 8079-matrix composite with a single reinforcement of peanut shell ash (PSA). Processing peanut shell particles for use as reinforcement in an aluminium 8079 alloy matrix is the goal of this study. Compared to other synthetic fillers like SiC (3.18 g/cm^3) and Al_2O_3 (3.9 g/cm^3), PSA's low density (1.96 g/cm^3) makes it an ideal companion to hybrid aluminum-based composites, which is why it is being used in this study. In many parts of underdeveloped countries like India, peanut shell is also readily available in big quantities and is frequently distributed [34, 35]. Other impacts on particle-reinforced AA8079 composite physical and mechanical properties (denseness and apparent porosity, hardness and impact strength) were explored when the weight percent of peanut shell ash in the particulate composition was varied [36–38]. The research will also use the mixed design method to model and optimise the properties that have been tested experimentally. Thus the objective is to incorporate the agro-waste peanut shell ash as reinforcement in Metal Matrix Composites in varying percentages and to study the mechanical properties of the produced composites and alleviate some of the environmental concerns associated with this solid agricultural residue [39, 40].

2. Experimental Techniques

The following experimental techniques and procedures were adopted in carrying out this research.

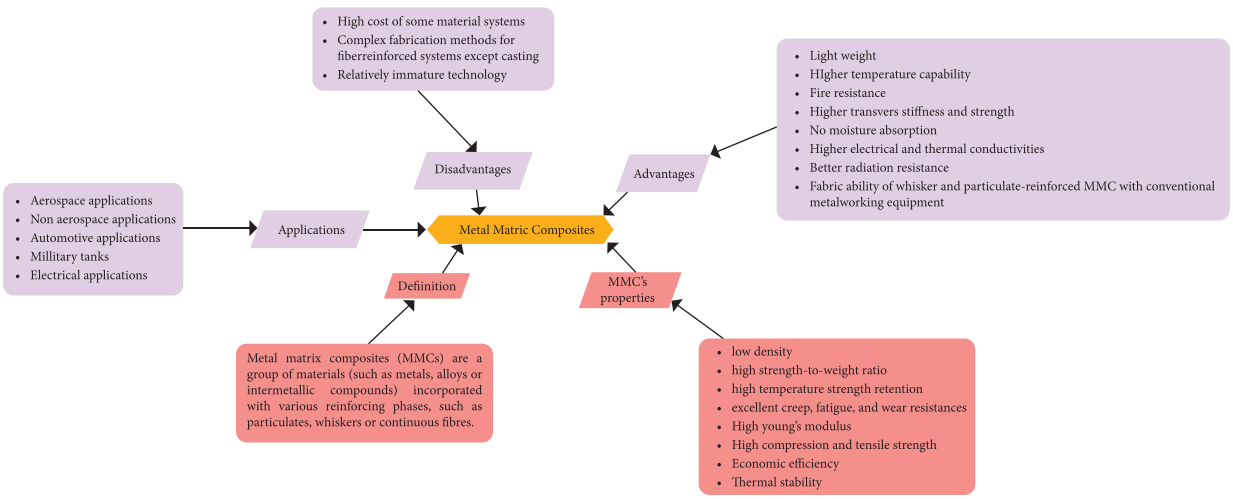

Figure 1: Schematic diagram of Metal matrix composites advantages and applications.

2.1. Materials Preparation

2.1.1. Matrix Material. Aluminum 8079 is a versatile, one-of-a-kind metal that may be brazed, welded, riveted. Most applications do not require a protective coating since aluminium is naturally corrosion resistant. Aluminium based alloy AA8079 with the elemental chemical composition specified in Table 1.

2.1.2. Processing of Reinforcing Material (Peanut Shell Ash). PSA is utilised to create panels, feedlot production, and manufacture activated carbon. Good chemical resistance, economy, improved workability, reduced bleeding and increased impermeability. There were enough dried peanut shells for this study. To ensure total combustion, the peanut shells were placed inside a vertical tube and ignited outdoors. To minimise the ash's volatile components, it was heated to 650°C in a muffle furnace for four hours. Table 2 shows the chemical make-up of peanut shell ash.

2.1.3. Fabrication of Composite. The AA8079 matrix composites were produced following double stir casting technique described elsewhere. To generate cast al-based results observed with peanut shell ash, the melted materials were injected into a readied sand mould and it is shown as a schematic diagram in Figure 2.

2.2. Measurement of Density and Apparent Porosity. Both experimental and theoretical densities of the composition of the unreinforced alloy and the composites formed were determined using the Archimedean principle and pycnometer method respectively. The experimental densities of the composites and the unreinforced AA8079 matrix were compared to the theoretical densities, and this data was used to determine the apparent porosity of the composites. The apparent porosity was calculated using the following relationship.

$$\text{apparent porosity} = \frac{\rho^T - \rho^{EX}}{\rho^T} \times 100, \quad (1)$$

where ρ^T is theoretical density and ρ^{EX} is experimental density.

2.3. Brinell Hardness Test. The Brinell hardness testing equipment is used to appraise the characteristics of toughness of the created metal matrix composite in accordance with the ASTM E10 standard. Each sample was subjected to three hardness tests, with the average value serving as a proxy for the specimen's hardness. The results of the Brinell hardness test was obtained for both the base AA8079 alloy and the composites.

2.4. Charpy Impact Test. Through cutting and grinding of the samples from the material, a test piece of dimension $55 \times 10 \times 10\,\text{mm}^3$ was produced. At half the length of the test piece, a 45-degree notch, 2 mm deep was produced. The specimen is supported as a beam on the pedestal impact testing machine base with the north centrally located and backing the hammer mass of the machine. The specification of the pendulum length of the machine is 0.7486 kg, hammer mass is 22.6 kg. The pendulum with the hammer lifted (swung up backwards) and locked, the nominal energy scale set to a maximum of 320 joules and the specimen north backing the hammer mass, the pendulum released at a velocity of $5.41\,\text{ms}^{-1}$ to load the specimen directly behind the notch. The impact energy of the specimen which reduced the swinging of the pendulum before the fracture is read off the energy scale deflected backwards in a clockwise movement. To compute the impact strength of the material the relation given in equation (2) is used.

$$\text{impact strength} = \frac{\text{impact energy}}{\text{cross sectional area of the material at the notch}}. \quad (2)$$

Table 1: AA8079 aluminum alloy matrix chemical composition.

Element	Al	Si	Mg	Fe	Cu	Mn	Zn	Cr
% Comp	98.61	0.5287	0.4741	0.2214	0.0009	0.0168	<0.0087	<0.0029
Element	Ni	Ti	Sn	Zr	V	Ca	Be	Pb
% Comp	<0.0034	0.0152	<0.0070	0.0028	<0.0056	>0.000	<0.0001	<0.0000

Table 2: Peanut shell ash chemical composition [39].

Compound	SiO_2	Al_2O_3	Fe_2O_3	CaO	MgO	SO_3	Na_2O	K_2O
wt%	66.34	7.48	4.44	11.57	2.06	1.07	0.41	4.92

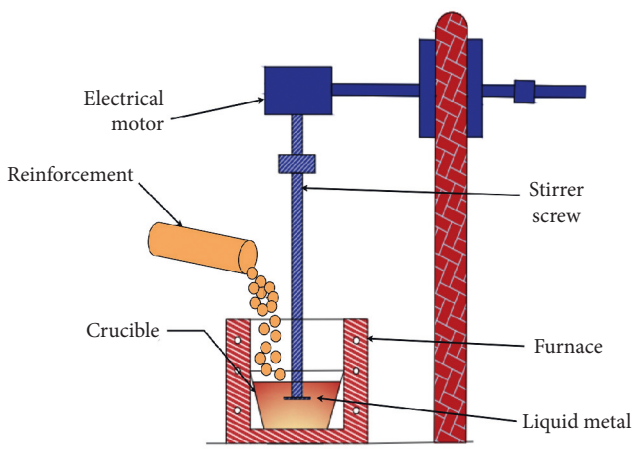

Figure 2: Schematic setup of stir casting.

2.5. Tensile Test. The tensile test was used to measure the material's capacity to developed composite material to withstand loads before elongation. The testing is conducted using digital JPL-100k tensile testing machine. The metal matrix composites were machined to the required dimension for the test. The ultimate tensile strength (UTS) of a material is determined because it is the highest stress that it can withstand when subjected to loading condition.

2.6. Wear Behaviour. The wear behaviour of the composite was determined utilising a Taber Abrasion Machine, a rotational platform abrasion tester. The composite samples were machined in accordance with the wear specification and then put on the wear machine's turntable platform, where they were grabbed continuously two grit rollers descended onto the specimen surface. The spinning platform circles at a constant pace of 1200 revolutions per minute for 15 minutes. The rub action created by the machine's rotational motion between the pattern's surface and the abrasion wheel results in the formation of abraded loose composite dirt on the surface of the sample. The starting and final weights of the sample were obtained using a digital scale, and the wear index was calculated using equation.

$$\text{impact strength} = \frac{\text{impact energy}}{\text{cross sectional area of the material at the notch}}, \quad (3)$$

where the starting and ending weights are in grams and the number of wear test cycles is expressed in revolutions per minute.

An attempt is here made by applying experimental design software packages and mixture design techniques in modelling and optimizing the composites fabrication process variables and predicting the responses of the composites' characteristics. The studied physical and mechanical composites' characteristics were optimized by mixture design tool. Simplex lattice design type, which requires the difference between low and high levels to be the same for all the mixture components, and a quadratic design model was employed in the investigation. Matrix and Reinforcement weight concentrations (%) were chosen to serve as independent variables. (Components 1 & 2), while density, apparent porosity, durometer, compressive strength, fracture toughness, and wear index were the factors that served as the dependent/response variables (Responses 1 to 6). Twelve rounds of investigations were carried out to ascertain the effect of the factor on the qualities tested as well as the dependent variables'/properties' responses.

3. Results and Discussion

3.1. Physical Characteristics. Table 3 summarizes the experimental results for physical parameters (density and porosity). Extracted from the table, it could be observed that both the theoretical and the experimental densities decreased progressively as the reinforcement concentration is increased, while the matrix component is reduced. This decrease in density possibly be attributed to the low density of the reinforcing particles. Reduction in the density of AMMCs reinforced with natural and agro-based fillers have been reported by several investigations. This is a desirable trend, as it motivates their employment in lightweight load-bearing applications.

The apparent porosity is used to estimate the percentage of voids in the fabricated composites. The porosity of the composite as shown in Table 3 increased from 2.218% at 3 wt % PSA to 2.122% at 18 wt% PSA. The maximum porosity of the lightest composite sample is 2.066%, corresponding to the lowest density of 3.428 g/cm^3. Thus, the porosity level of the fabricated composite is below the maximum limit of 4% reported as tolerable for cast AMMC It can further be noted that the composite fabrication route (stir-casting) was necessary and efficient in minimizing to the barest minimum the porosity level of the developed materials.

3.2. Mechanical Properties. AA8079 matrix composite reinforced with Peanut shell ash has lower impact strength

Table 3: Density and apparent porosity of the AA8079/PSA composites and the unreinforced AA8079.

Sample	Theoretical density (ρ^T)[g/cm^3]	Experimental density (ρ^{EX})[g/cm^3]	Apparent porosity (%)
Unreinforced Al	3.48	3.47	1.06
Al – 3 wt% PSA	3.726	3.71	1.91
Al – 6 wt% PSA	3.84	3.86	1.42
Al – 9 wt% PSA	3.76	3.79	1.06
Al – 12 wt% PSA	3.58	3.52	1.76
Al – 15 wt% PSA	3.42	3.41	1.18
Al – 18 wt% PSA	3.38	3.34	2.46

than the base aluminium alloy, the reason as the concentration of PSA increases, the number of hard oxides (SiO_2, CaO, Al_2O_3) and carbon content of the composite is increased [36], the hardness of the composites also increased progressively, thereby resulting in a corresponding impact strength of PSA reinforced composites decreases, as it becomes more brittle. Figures 3–6depicts the effect of reinforcement content on the hardness, abrasion resistance, impact strength, and tensile strength of AA8079-based reinforced materials with Peanut shell ash particles.

Very low impact and tensile strengths were obtained for the 15 and 18 wt% PSA reinforcement content because of the high volume of the dispersed phase (PSA) in the Al-Si-Mg matrix. The entrenching influence weight fraction on the reinforcement particles of the al alloy was determined to be positive. As the amount of peanut shell ash in the composite material rose, the composite material's ability to resist wear improved as well., this is indicated by the progressive decrease in wear index with the addition of the reinforcement particles (Figure 4). This may be explained to be as an outcome of the extraordinary bonding that exists between the aluminium alloy matrix and the reinforcements. There was an abysmal deterioration in the tensile strength, as the amount of PSA in AA8079 matrix increased gradually. This is expected as a trade-off between hardness and strength. Most hard materials are low in tensile and impact strengths. This was why the optimization of the experimental results was carried out to ascertain the optimal composition of the reinforcement and matrix mixture that will yield optimal physical and mechanical properties.

Unreinforced aluminium alloy 8079 is typically composed of an array of $Al1_2Mg_7$, $AlFe_2Mn$, Mg_2Si, and Al-Si-Mg plates in an alpha-aluminum matrix. The structures demonstrate how particle PSA disperses over grain boundaries. Between the peanut Particles of shell ash with the Al-Si-Mg matrix, there was excellent adhesive bonding. The better intermolecular adhesion could be explained by presence of magnesium in the matrix, which contributed to the reinforcement phase's increased wettability in the metal matrix.

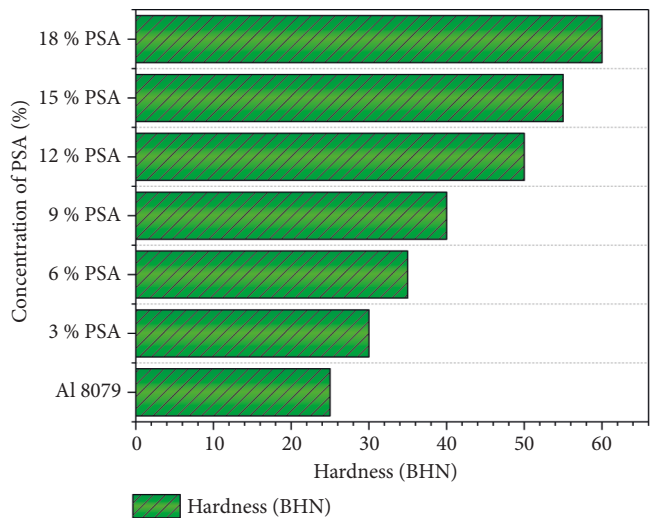

Figure 3: Hardness of the PSA reinforced composites and the unreinforced aluminium AA8079 alloy.

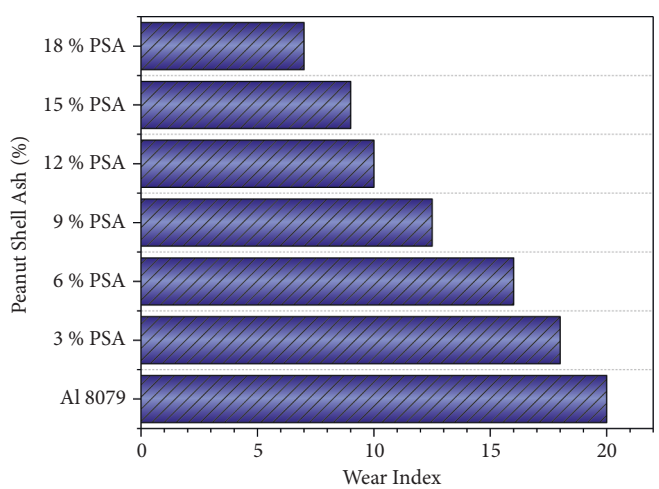

Figure 4: Wear index of the PSA composites with reinforcements and the unreinforced aluminium AA8079 alloy.

3.3. Results of Predictive Modelling and Optimization Using Mixture Design. The results from the mixture design study show that the density, apparent porosity, abrasion resistance, compressive strength, fracture toughness, and wear index are functions of the mixture composition (reinforcement and matrix concentrations). The design summary for the mixture components (matrix and reinforcement) and the responses are given in Tables 4 and 5 respectively. The tables indicate the analysis type, minimum and maximum values for the mixture components and the responses, mean, standard deviation, factor coding and the models, etc.

3.3.1. Analysis of Variance (ANOVA), Fit Statistics, and Model Equations. The detailed results of the polynomial

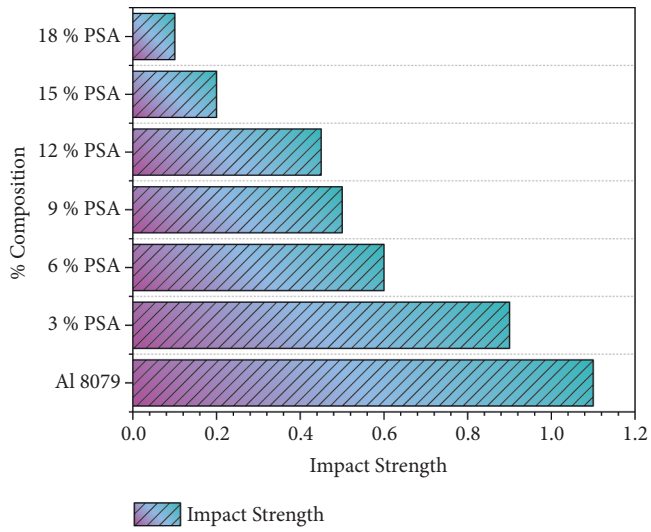

Figure 5: Impact strength of the PSA reinforced composites and the unreinforced aluminium AA8079 alloy.

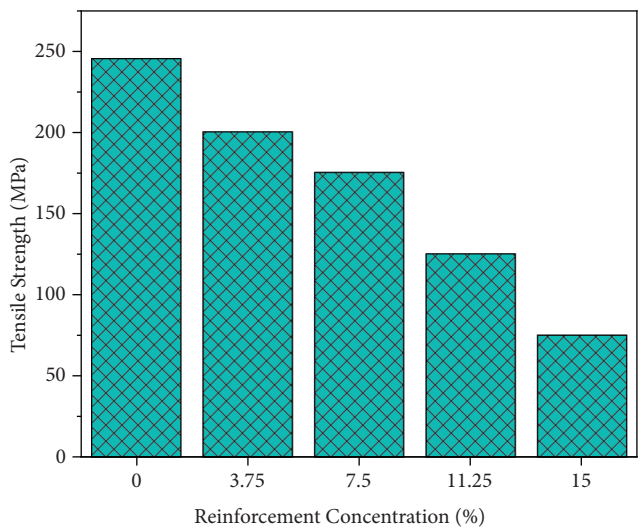

Figure 6: Tensile strength of PSA reinforced composites and the unreinforced aluminium AA8079 alloy.

Table 4: Design summary for mixture components.

Name	Min (%)	Max (%)	Low coded (%)	High coded (%)	% of mean	Std. dev.
Matrix	82	100	+0 ↔ 82	+1 ↔ 100	91	6.21
Reinforcement	0	18	+0 ↔ 0	+1 ↔ 18	9	6.21

Table 5: Design summary for responses.

Response Name	1 Density (g/cm^3)	2 Porosity (%)	3 Impact strength (J/mm^2)	4 Hardness (BHN)	5 Tensile strength (MPa)	6 Wear index
Minimum	3.18	1.12	0.27	28	67.6	8.2
Maximum	3.89	2.34	1.76	62.4	258.16	24
Mean	3.53	1.73	1.015	45.2	162.88	16.1
Std. dev.	0.0961	0.514	0.501	14.56	74.6	6.28
Ratio	1.12	2.9	10.6	2.45	4.18	2.78

analysis of the various factors are discussed in terms of the ANOVA, computational refinement and forecasting. The ANOVA and the displayed on a monitor of fit for the composites response properties are presented in Tables 6–11. The descriptive statistics are used as a check on the models' utility. All responses had probability values (p values) < 0.05,

Table 6: ANOVA and fit statistics for the density of AA8079/PSA composites.

Source	Sum of squares	df	Mean square	F value	p value
Model	0.0921	2	0.0921	1356.4	<0.0001
Linear mixture	0.0921	2	0.0921	1356.4	<0.0001
Residual	0.00061	11	0.0001		
Lack of fit	0.00061	6	0.0001		
Pure error	0	6	0		
Cor total	0.0921	12			
Std. dev.	0.0091		R^2	1.0146	
Mean	2.72		Adjusted R^2	1.1218	
C.V.%	0.4281		Predicted R^2	1.1416	
			Adeq precision	69.82	

Table 7: ANOVA and fit statistics for apparent porosity of AA8079/PSA composites.

Sources	Sum of squares	df	Mean square	F-value	p value
Model	1.28	2	1.28	11.62	0.0091
Linear mixtures	1.28	2	1.28	11.62	0.0091
Residuals	1.42	11	1.42		
Lack of fit	1.42	6	1.58		
Error	0	6	0		
Cor total	2.65	12			
Standard deviation	0.42		R^2	0.61	
Mean	1.56		Adjusted R^2	0.512	
C.V.%	22.8		Predicted R^2	0.4368	
			Adeq precision	6.82	

Table 8: ANOVA and fit statistics for impact strength of AA8079/PSA composites.

Source	Sum of squares	df	Mean square	F value	p value	
Model	1.88	3	0.912	282	<0.0002	Significant
Linear mixture	1.82	2	1.92	541	<0.0002	
AB	0.0312	2	0.0316	8.62	0.0326	
Residual	0.0334	10	0.0034			
Lack of fit	0.0334	5	0.0076			
Pure error	0	6	0			
Cor total	2.1	12				
Std. dev.	0.062		R^2	1.128		
Mean	0.5942	Adjusted R^2	1.21			
C.V.%	10.61	Predicted R^2	1.28			
		Adeq precision	36.53			

Table 9: ANOVA and fit statistics for the hardness of AA8079/PSA composites.

Source	Sum of squares	df	Mean square	F value	p value
Model	2046.5	2	2046.5	401.5	<0.0002
Linear mixture	2.46.5	2	2046.5	401.5	<0.0002
Residual	61.4	11	6.28		
Lack of fit	61.4	6	13.4		
Pure error	0	6	0		
Cor total	85.8	12			
Std. dev.	3.56		R^2	1.46	
Mean	48.4		Adjusted R^2	1.472	
C.V.%	6.21		Predicted R^2	1.52	
			Adeq precision	40.12	

that is a strong indicator that the predictors are genuine. (matrix and reinforcements) had a substantial effect on those response variables. In other words, all replies are meaningful in terms of the model's terms. Additionally, all six replies have a high model F-value. In comparison, all of the models' F-values for lack of fit are non-significant when compared to the pure error, and because the model should fit, a non-significant lack of fit is ideal. Because the difference between R^2 values anticipated and adjusted is less than 0.2, the predicted and adjusted R^2 values for all responses examined

Table 10: ANOVA and fit statistics for tensile strength of AA8079/PSA composites.

Source	Sum of squares	df	Mean square	F value	p value
Model	55281	5	14678	1242.3	<0.0002
Linear mixture	54768	2	55734	4653.74	<0.0002
AB	130.8	2	131.24	11.24	0.0162
AB (A-B)	7.64	2	7.12	0.5807	0.584
Residual	85.18	8	13.2		
Lack of fit	85.18	3	43.4		
Pure error	0	6	0		
Cor total	56467.34	12			
Std. dev.	3.85		R^2	1.212	
Mean	162.86		Adjusted R^2	1.228	
C.V.%	2.37		Predicted R^2	1.12	
		Adeq precision			

Table 11: ANOVA and fit statistics for wear index of AA8079/PSA composites.

Source	Sum of squares	df	Mean square	F value	p value
Model	307.4	5	77.3	7140.61	<0.0002
Linear mixture	301.2	2	301.2	28763.8	<0.0002
AB	3.81	2	3.81	302.6	<0.0002
AB (A-B)	3.06	2	3.06	240.2	<0.0002
Residual	0.0742	8	0.0212		
Lack of fit	0.0791	3	0.0421		
Pure error	0	6	0		
Cor total	311.1	12			
		R^2	1.086		
Std. dev.	0.1176		Adjusted R^2	1.042	
Mean	14.6		Predicted R^2	1.026	
C.V.%	0.821		Adeq precision	197.6	

are in reasonably good agreement. Adeq Precision (adequate precision) is a metric for determining the SNR. A accuracy value > 4 implies that the signals in the model are sufficiently strong and appropriate for optimization. All response ratios are more than four, demonstrating that the signals are appropriate and the models are capable of navigating the entire design area.

Figure 7 shows Model graphs of predicted response values against observed response values of (a) density, (b) apparent porosity, (c) impact strength, (d) hardness, (e) UTS, and (f) wear index. ANOVA for mixture design normally generates three model equations for each response. One for the pseudo model (factor coding) taken from the model coefficient table, one in the real coding scale, and the third one in the actual coding scale. The default analysis computes and tests the pseudo model which is then converted to the real model and finally to the actual model. Density, apparent porosity, hardness, impact strength, tensile strength, and wear index prediction equations for composites as a function of mixture components are supplied in coded form and outlined in equations. The model equations written can be utilised in terms of coding to forecast the composite characteristics' reactions at specified weight concentrations (wt%) of the mixture components (A&B). By default, the combination components' high levels are coded as +1 and their low values as 0. By comparing the factor coefficients, the coded equations May be used to determine the factors' relative importance (mixing components).

3.3.2. Design Numerical Optimization. The DOE's mixed design enables the response values to be optimized by altering the mixture components. The independent variable (mixing components) was optimized to decrease the density, porosity, and wear index of the composites and to enhance their hardness, impact, and tensile strength responses. Target criteria were established for both the constituent materials and the responses during mathematical programming. The matrix and reinforcement concentrations have been set to be within a certain range. Density, apparent porosity, and wear index responses were set to zero, whereas hardness, impact, and tensile strengths were set to their optimum amount. Even though the main objective is not to maximise possibility, The most desired factor settings are those that produce the highest desirability value. suggest that the numerical optimization produced an acceptable result. Table 12 illustrates one numerical optimization approach for the mixture components and responses of PSA reinforced aluminium alloy AA8079 composites with a degree of desire.

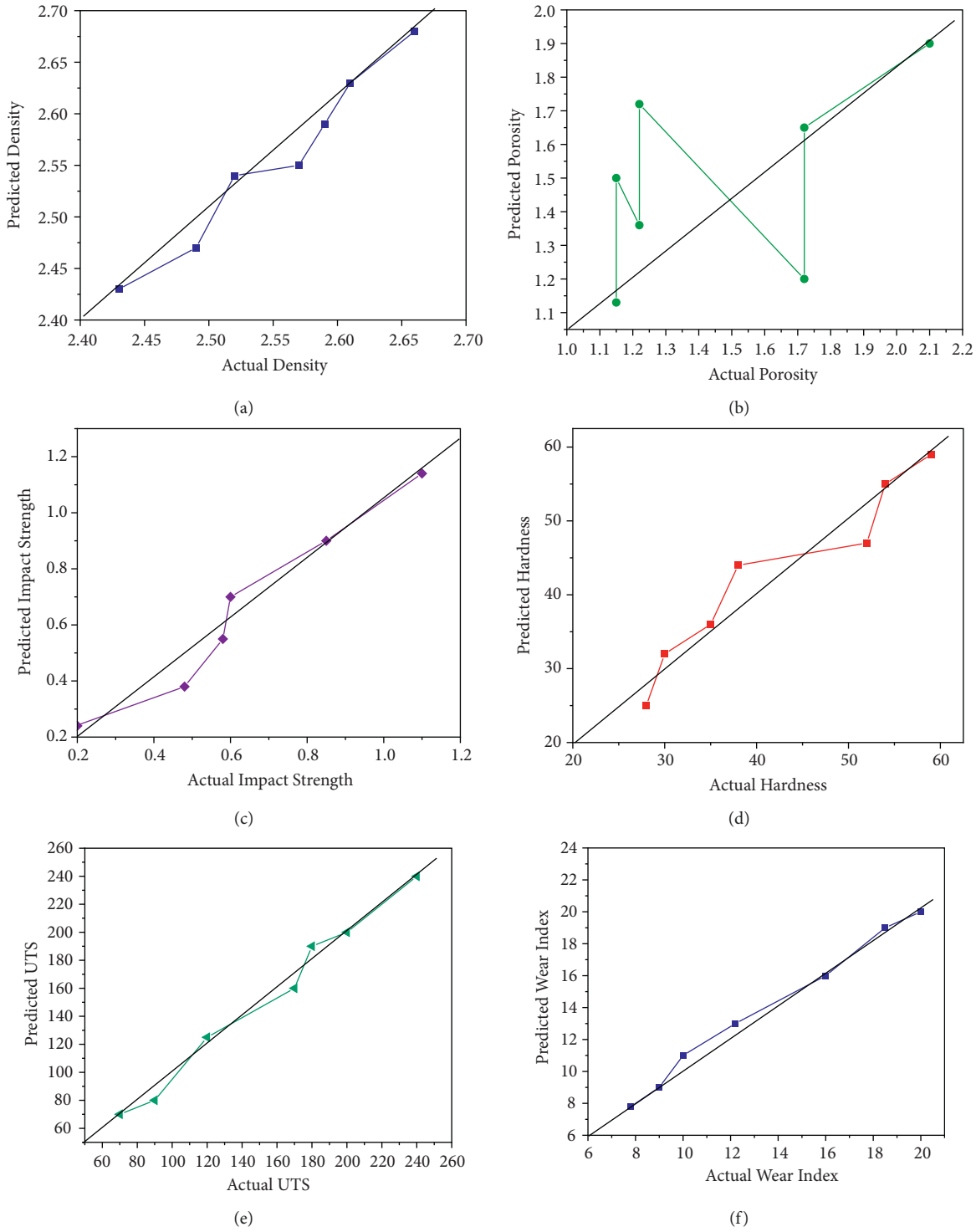

Figure 7: Model graphs of predicted response values against observed response values of (a) Density, (b) Apparent porosity, (c) Impact strength, (d) Hardness, (e) UTS, and (f) Wear index.

Table 12: Optimization solutions.

Matrix	93.48
Reinforcement	6.52
Density	2.64
Porosity	1.520
Impact strength	0.452
Hardness	47.46
Tensile strength	168.05
Wear index	13.18
Desirability	0.608

The results of numerical optimization show that optimal responses for the proposed composite will be attained at matrix and reinforcement concentrations of 93.48 and 6.52 percent, respectively.

4. Conclusion

Stir casting was used to manufacture AA8079/PSA composites successfully.

(i) The composite is more challenging than the pure AA8079 alloy, and its hardness rises as the reinforcing weight percentage rises.

(ii) The porosity of the composite is low and within an acceptable level of 0–4% due to filler matrix compatibility and stir casting process.

(iii) In addition to Peanut, shell ash increases the tendency of the material to resist wear.

(iv) The density of the AA8079/PSA composites formed is lower than that of the AA8079 base alloy. This indicates that peanut shell ash can reinforce lightweight load-bearing Composites.

(v) Mixture design modelling revealed the optimal reinforcement and matrix composition that yield optimal responses of composite mechanical properties.

Data Availability

The data used to support the findings of this study are included within the article. Further data or information are available from the corresponding author upon request.

Conflicts of Interest

The authors declare no conflicts of interest.

Acknowledgments

The authors thank Sri Sai Ram Engineering College, Chennai, Prince Sattam Bin Abdulaziz University, Saudi Arabia, and Sathyabama Institute of Science and Technology, Chennai, for providing technical assistance to complete this experimental work.

References

[1] V. Mohanavel, M. Ravichandran, S. Suresh Kumar, M. Melwin Jagadeesh Sridhar, S. Dineshkumar, and M. M. Pavithra, "Microstructural and tribological characterization of Al/EGG shell ash composites prepared by liquid metallurgy process," *Journal of the Balkan Tribological Association*, vol. 26, no. 2, pp. 319–326, 2020.

[2] S. N. Monteiro, K. G. Satyanarayana, and F. P. D. Lopes, "High strength natural fibers for improved polymer matrix composites," *Materials Science Forum*, vol. 638-642, pp. 961–966, 2010.

[3] U. Shehu, O. Aponbiede, T. Ause, and E. F. Obiodunukwe, "Effect of particle size on the properties of polyester/palm kernel shell (PKS) particulate composites," *Journal of Materials and Environmental Science*, vol. 5, no. 2, pp. 366–373, 2014.

[4] V. R. Rao, J. R. Chowdary, A. Balaji et al., "A review on properties of aluminium based metal matrix composites via stir casting," *International Journal of Scientific Engineering and Research*, vol. 7, no. 2, pp. 742–749, 2016.

[5] R. Dasgupta, "Aluminium alloy-based metal matrix composites: a potential material for wear resistant applications," *International Scholarly Research Notices*, vol. 2012, Article ID 594573, 14 pages, 2012.

[6] P. O. Babalola, C. Bolu, A. O. Inegbenebor, and K. M. Odunfa, "Development of aluminium matrix composites: a review," *International Journal of Engineering Sciences & Research Technology*, vol. 2, pp. 1–11, 2014.

[7] A. V. Muley, S. Aravindan, and I. P. Singh, "Nano and hybrid aluminum based metal matrix composites: an overview," *Manufacturing Review*, vol. 2, no. 15, 2015.

[8] M. Dinesh, D. R. Ravindran, and A. A. Aluminium, "7075 properties enhanced by Zirconium and Chromium nano particle," *International Journal of ChemTech Research*, vol. 9, no. 1, pp. 296–301, 2016.

[9] B. V. Ramnath, C. Elanchezian, R. M. Annamalai et al., "Aluminium metal matrix composites–a review," *Reviews on Advanced Materials Science*, vol. 38, no. 5, pp. 55–60, 2014.

[10] R. O. Akaluzia, F. O. Edoziuno, A. A. Adediran, B. U. Odoni, S. Edibo, and T. M. A. Olayanju, "Evaluation of the effect of reinforcement particle sizes on the impact and hardness properties of hardwood charcoal particulate-polyester resin composites," *Materials Today Proceedings*, vol. 38, pp. 570–577, 2021.

[11] B.-H. Yan and C.-C. Wang, "Machinability of SiC particle reinforced aluminum alloy composite material," *Journal of Japan Institute of Light Metals*, vol. 43, no. 4, pp. 187–192, 1993.

[12] M. Ravichandran, V. Mohanavel, T Sathish, P. Ganeshan, S. Suresh Kumar, and S. Ram, "Mechanical properties of AlN and molybdenum disulfide reinforced aluminium alloy matrix composites," *Journal of Physics: Conference Series*, vol. 2027, Article ID 012010, 2021.

[13] R. Umunakwe, O. C. Okoye, C. I. Madueke, D. O. Komolafe, and I. J. Umunakwe, "Effects of carburization with palm kernel shell/coconut shell mixture on the tensile properties and case hardness of low carbon steel," *FUOYE Journal of Engineering and Technology*, vol. 2, no. 1, p. 83, 2017.

[14] D. Srinivasan, R. S. Kadadeveramath, S. Rajendran, and E. N. Ganesh, "State-of-art review of ceramic reinforced aluminum metal matrix composite and it's machining characteristics," *Journal of Chemical and Pharmaceutical Sciences*, vol. 11, pp. 154–164, 2017.

[15] V. Mohanavel, S. Prasath, K. Yoganandam, T. B. Girma, and S. Suresh Kumar, "Optimization of wear parameters of aluminium composites (AA7150/10 wt% WC) employing Taguchi approach," *Materials Today Proceedings*, vol. 33, no. 7, pp. 4742–4745, 2020.

[16] F. O. Edoziuno, A. A. Adediran, B. U. Odoni, A. D. Akinwekomi, O. S. Adesina, and M. Oki, "Optimization and development of predictive models for the corrosion inhibition of mild steel in sulphuric acid by methyl-5-benzoyl-2-benzimidazole carbamate (mebendazole)," *Cogent Engineering*, vol. 7, no. 1, Article ID 1714100, 2020.

[17] A. James, "The study of wear behaviour of glass/epoxy composites reinforced with titanium dioxide and graphite filler materials," *AIP Conference Proceedings*, vol. 2080, no. 1, Article ID 20011, 2019.

[18] M. I. M. Kandar and H. M. Akil, "Application of design of experiment (DoE) for parameters optimization in compression moulding for flax reinforced biocomposites," *Procedia Chemistry*, vol. 19, pp. 433–440, 2016.

[19] C. Homkhiew, T. Ratanawilai, and W. Thongruang, "The optimal formulation of recycled polypropylene/rubberwood flour composites from experiments with mixture design," *Composites Part B: Engineering*, vol. 56, pp. 350–357, 2014.

[20] C. Homkhiew, T. Ratanawilai, and W. Thongruang, "Optimizing the formulation of polypropylene and rubberwood flour composites for moisture resistance by mixture design," *Journal of Reinforced Plastics and Composites*, vol. 33, no. 9, pp. 810–823, 2014.

[21] P. S. Kumar, S. P. Reddy, and G. Kartheek, "Study of hardness and optimization of wear properties of AL 7075 hybrid composite," *International Journal of Engineering Research and Technology*, vol. 6, no. 6, 2017.

[22] G. Agarwal, A. Patnaik, and R. K. Sharma, "Parametric optimization and three-body abrasive wear behavior of sic filled chopped glass fiber reinforced epoxy composites," *International Journal of Composite Materials*, vol. 3, no. 2, pp. 32–38, 2013.

[23] A. Vedrtnam and A. Kumar, "Fabrication and wear characterization of silicon carbide and copper reinforced aluminium matrix composite," *Materials Discovery*, vol. 9, pp. 16–22, 2017.

[24] Z. Xin-gang, Z. Yuan-feng, and L. Yan-bin, "The spillovers of foreign direct investment and the convergence of energy intensity," *Journal of Cleaner Production*, vol. 206, pp. 611–621, 2019.

[25] C. R. Kothari, *Research Methodology: Methods and Techniques*, New Age International, New Delhi, India, 2004.

[26] R. Umunakwe, D. J. Olaleye, A. Oyetunji, O. C. Okoye, and I. J. Umunakwe, "Assessment of some mechanical properties and microstructure of particulate periwinkle shell-aluminium 6063 metal matrix composite (PPS-ALMMC) produced by two-step casting," *Nigerian Journal of Technology*, vol. 36, no. 2, pp. 421–427, 2017.

[27] A. Yekinni, M. Durowoju, J. Agunsoye, L. Mudashiru, L. Animashaun, and O. Sogunro, "Automotive application of hybrid composites of aluminium alloy matrix: a review of rice husk as based reinforcements," *International Journal of Composite Materials*, vol. 9, pp. 44–52, 2019.

[28] J. E. Hernández-Ruiz, L. Pino-Rivero, and E. Villar-Cociña, "Aluminum matrix composite with sugarcane bagasse ash as reinforcement material," *Revista Cubana de Fisica*, vol. 36, no. 1, pp. 55–59, 2019.

[29] N. Srivastava and S. P. Dwivedi, "Development of green hybrid metal matrix composite using agricultural waste bagasse as reinforcement-A review," *IOP Conference Series: Materials Science and Engineering*, vol. 691, no. 1, Article ID 12051, 2019.

[30] F. O. Edoziuno, B. U. Odoni, F. I. Alo, and C. C. Nwaeju, "Dry sliding wear and surface morphological examination of an aluminium matrix composite reinforced with palm kernel shell," *Acta Metallurgica Slovaca*, vol. 26, no. 2, pp. 54–62, 2020.

[31] F. O. Edoziuno, A. A. Adediran, B. U. Odoni, O. G. Utu, and A. Olayanju, "Physico-chemical and morphological evaluation of palm kernel shell particulate reinforced aluminium matrix composites," *Materials Today Proceedings*, vol. 38, pp. 652–657, 2021.

[32] I. O. Oladele and A. M. Okoro, "The effect of palm kernel shell ash on the mechanical properties of as-cast aluminium alloy matrix composites," *Leonardo Journal of Sciences*, vol. 15, pp. 15–30, 2016.

[33] A. Apasi, D. S. Yawas, S. Abdulkareem, and M. Y. Kolawole, "Improving mechanical properties of aluminium alloy through addition of coconut shell-ash," *Journal of Science and Technology*, vol. 36, no. 3, pp. 34–43, 2016.

[34] O. O. Daramola, A. A. Adediran, and A. T. Fadumiye, "Evaluation of the mechanical properties and corrosion behaviour of coconut shell ash reinforced aluminium (6063) alloy composites," *Leonardo Electronic Journal of Practices and Technologies*, vol. 27, pp. 107–119, 2015.

[35] O. B. Fatile, J. I. Akinruli, and A. A. Amori, "Microstructure and mechanical behaviour of stir-cast Al-Mg-Sl alloy matrix hybrid composite reinforced with corn cob ash and silicon carbide," *International Journal of Engineering and Technology Innovation*, vol. 4, no. 4, p. 251, 2014.

[36] O. O. Joseph and K. O. Babaremu, "Agricultural waste as a reinforcement particulate for aluminum metal matrix composite (AMMCs): a review," *Fibers*, vol. 7, no. 4, p. 33, 2019.

[37] M. N. Nwabufoh, *Development and Characterization of Al-3.7% Cu-1.4% Mg alloy/periwinkle ASH (Turritella Communis) Particulate Composites*, Thesis. Ahmadu Bello University, Zaria, Nigeria, 2015.

[38] K. R. Garadimani, G. Raju, and K. Kodancha, "Study on mechanical properties of corn cob particle and e-glass fiber reinforced hybrid polymer composites," *American Journal of Materials Science*, vol. 5, no. 3C, pp. 86–91, 2015.

[39] F. O. Edoziuno, R. O. Akaluzia, B. U. Odoni, and S. Edibo, "Experimental study on tribological (dry sliding wear) behaviour of polyester matrix hybrid composite reinforced with particulate wood charcoal and periwinkle shell," *Journal of King Saud University-Engineering Sciences*, vol. 33, no. 5, pp. 318–331, 2021.

[40] M. R. Sanjay, G. R. Arpitha, L. L. Naik, K. Gopalakrishna, and B. Yogesha, "Applications of natural fibers and its composites: an overview," *Natural Resources*, vol. 7, no. 3, pp. 108–114, 2016.

Hindawi
Advances in Materials Science and Engineering
Volume 2022, Article ID 3104199, 9 pages
https://doi.org/10.1155/2022/3104199

Research Article

The Influence of Process Parameters on the Mechanical Properties of Friction Stir-Welded Dissimilar Aluminium Alloys AA2219 and AA7068

Mohamad Reda A. Refaai,[1] **R. Meenakshi Reddy**,[2] **A. Radha**,[3] **and David Christopher**[4]

[1]*Department of Mechanical Engineering, College of Engineering, Prince Sattam Bin Abdulaziz University, Alkharj 16273, Saudi Arabia*
[2]*Department of Mechanical Engineering, G. Pulla Reddy Engineering College, Kurnool 518007, Andhra Pradesh, India*
[3]*Department of Mechanical Engineering, Loyola-ICAM College of Engineering and Technology, Chennai, Tamil Nadu 600034, India*
[4]*Department of Mechanical Engineering, College of Engineering, Wolaita Sodo University, Sodo, Ethiopia*

Correspondence should be addressed to Mohamad Reda A. Refaai; m.rifaee@psau.edu.sa

Received 17 December 2021; Accepted 4 February 2022; Published 29 March 2022

Academic Editor: P Ganeshan

A practical solution is friction stir welding (FSW) of heterogeneous alloys in industrial applications. The welded joint's mechanical strength has been improved by combining two different alloys (AA2219 and AA7068). The focus of this study was on friction stir-welded heterogeneous metals' microhardness and material properties. It is possible to work with either hot or cold aluminium alloy, as it is heat treatable. Revitalizing and precipitation hardening follow the heat treatment. The welded joints' hardness was assessed in several locations. Different joints' tensile characteristics are compared. According to the stress-strain curve, the FSW settings' mechanical properties were spread throughout the material flow. In terms of tool profiles, the cylindrical threaded profile is critical. One-third of the efficiency is due to it. A 195 MPa strength was reached in the cylindrical threaded pin profiled tool. In a new study, researchers discovered that cylindrical threads have faster rotary motion, transversal, and D/d speeds. The cylindrical threaded tool provided the highest tensile strength and was superior to other materials. This phase of the material characterization included measurements of tensile strength and hardness.

1. Introduction

Friction stir welding (FSW) was developed in 1991 by the Welding Institute (TWI) in the United Kingdom as a solid-state fusion process. FSW is a cutting-edge technology for permanently connecting materials. FSW involves rotating and gently plunging a cylindrical, shouldered tool with a profiled probe into the joint line between two pieces of sheet or plate material that are butted together. The pieces are held together throughout the welding process to prevent the abutting joint faces from being driven apart [1]. In a wide range of industrial applications, aluminium alloys (AA2219-AA7068) are widely used: for aircraft structures, for maritime applications such as ships and pipelines, for automobiles and shipbuilding, and so on. Due to car body shells' lightweight structures, there are more design requirements than ever before [2, 3]. The wrought aluminium-copper alloy AA2219 belongs to the family of (2000 or 2xxx series). Heat treatment may create tempers with greater strength but poorer ductility. AA7068 alloy is a heat treatable wrought alloy with excellent thermal conductivity, strong fatigue strength, and excellent anodizing reaction. The FSW process is a one-of-a-kind approach to developing lightweight alloy structures. Avoiding manufacturing faults such as approximation permeability, sludge, dispersion, liquid cracks, and heat affected zones (HAZ) is achievable. It is like saying that various alloys of joint technology are used in fabrication because fusion welding has melted numerous

alloys of joint technology while developing secondary phase owing to thermal absences employing base materials as a pin device [4]. It is because of this that the temperature distribution in nugget zones (NZs) has increased more slowly when compared to alloys of different compositions. Collecting rotational and transverse speeds is the ideal approach to this problem. As a result, the instrument is critical in FSW [5]. Using a stirring motion, this tool profile or form is effective at transferring the substance from the base material. Tool profile and various process parameters are not the only factors affecting FSW behaviour [6]. Figure 1 shows an FSW's schematic diagram.

The optical microscope has been used by FSW to identify the four functional zones, including the parent material (PM), NZ, the thermally mechanically impacted zone (TMAZ), and the HAZ. The movement of materials along the route of the welding process generates all of these zones [7, 8]. Plastic deformation has increased on work piece's top surface due to heat generated by rubbing tool. Material flow behaviour refers to the swept volume to pin volume ratio. For a given condition, the swirl revolves at the rotational and transverse speeds specified [9].

In previous studies, AA 2219 and AA 7068 in FSW were extensively examined. Different FSW joints and mechanical characteristics evaluations no longer include quick microstructural investigations [10]. Scientists carried out tensile and microhardness tests on various alloys and used optical microscopy to evaluate FSW elements of the process based on the microstructure of welded joints as part of this investigation [11–18]. This approach's design principles have been described in FSW using multiple tool profiles to combine various alloys. AA 2219 tool profile faults have been analysed and tested which may be found throughout the specification [14]. The interplay between the tool pin profile rotation speed and the heat plastic behaviour on the plate surface caused the heat plasticity [15, 16]. FSW will greatly benefit from this information. It has been determined that process parameter effects on weld zone hardness have been investigated by conducting a hardness survey there. We learned a lot about the connection between microstructure and mechanical properties [17–19].

2. Tool Design

The FSW method includes tool design in some capacity. It examines the properties of the two types of wrought aluminium alloys and compares them. This welder's tool should have dimensions such as height, depth, pin diameter, and width at the shoulder. The FSW technique relies heavily on the pin and shoulder components [20, 21]. The FSW pin forms such as direct cylindrical, taper threaded, and cylindrical have been investigated in this work. FSW pin shapes include the advancing and retracting sides of the rotating pins used to mix the ingredients. To connect the materials, a material deformation will be caused by this pin. The mechanical characteristics and flow characterization were investigated using a variety of tools. During the FSW process, the tool came in with a variety of shapes and sizes, with temperature dispersion as a heat transfer mechanism

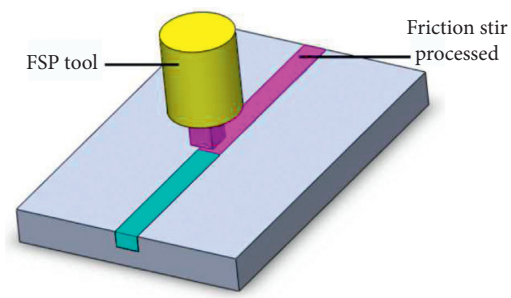

Figure 1: Friction stir welding.

for mixing incompatible alloys. A tool used to spin and add material flow characteristics to the power is sent through it. Tool requirements include things like how much torque is exerted at the pin's end. It would be possible to assess the claimed torque as traction force. Among the welding materials, the temperature normally lived within a specified range is one of the ideal tool parameters' shoulder with heat transmission and flow behaviour. As a flow model, the impact of the tool's shoulder was investigated. We looked at a temperature distribution and material deformation with this thermocouple as part of our FSW process research [22]. The varied tool sizes can adjust the FSW grain size zones. As seen in Figure 2, these tool-end surfaces have a wide range of shapes, including knurling, squared, threaded, scrolls, and ridges.

Certain characteristics, such as product flow behaviour and adequate mechanical toughness under various stress circumstances, should be present on the tool pin surfaces. It is possible that, between an increased shear creation and distortion, there is shoulder and base material which can indicate consistent mixing of incompatible alloys in the material. The probe area mostly controls the material's deformation depth. In terms of maintaining the metals' flow behaviour as well as the various tool pin performance, this is necessary. This is crucial. It compresses the weld centre lines together. The convexity of the material aided a stirring motion known as NZs. The surface probe's primary purpose is to withstand the enormous forces generated while plunging. A very sophisticated and very diverse tool with each movement of material is around the probe.

3. Experimental Setup

FSW was collected in a technical arrangement, as shown in Figure 3. This study looked at the different specimens AA 2219, magnesium, and silicon. AA 2219 is on the leading edge, while AA 7068 is on the reversing edge. The high material flow stability and strong resistance capacity of these AA 2219 alloys make them superior to other materials in terms of design requirements. This FSW method made use of both plates ($120 \times 120 \times 6$). Tables 1 and 2 analyses the AA 2219 and AA7068 alloys' chemical and mechanical properties. To combine dissimilar alloys with different optimal constraints, such as rotatory speed, transversal speed, and different load circumstances, the trail experiments were finished up to this point. Using a vertical milling machine,

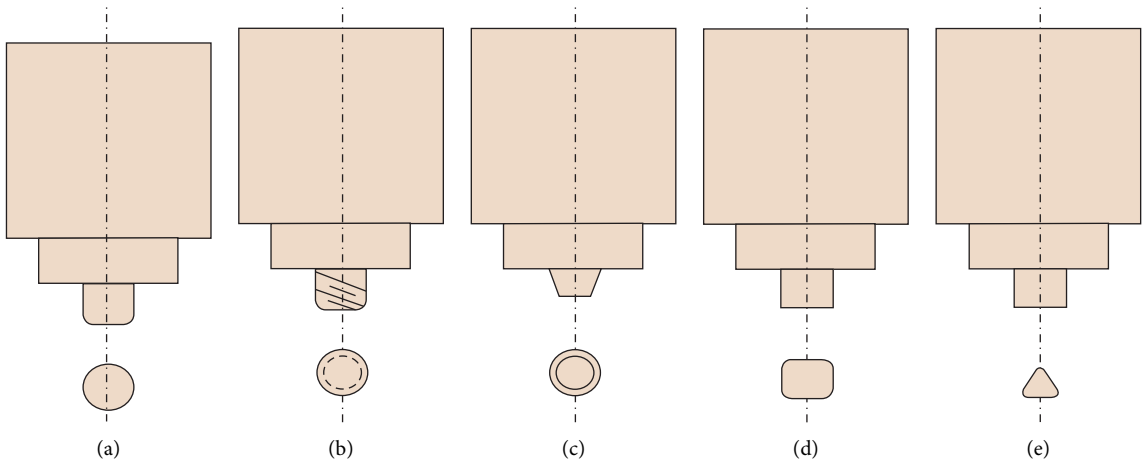

Figure 2: Different tool profiles: (a) straight cylindrical, (b) threaded cylindrical, (c) tapered cylindrical, (d) square, and (e) triangle.

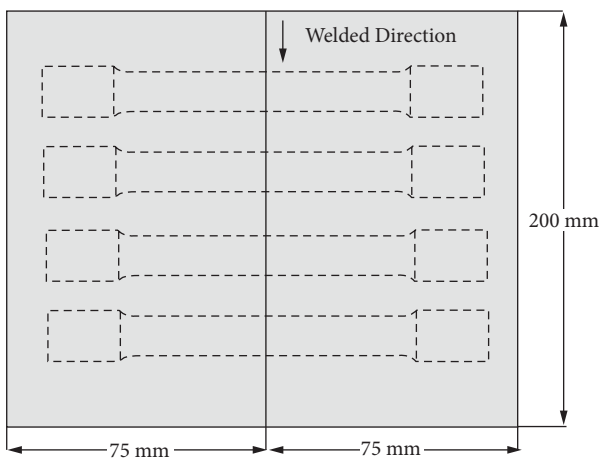

Figure 3: Specimens for tensile testing in the FSW joints.

Table 1: Dissimilar alloys' chemical composition.

Element	Mg	Ni	Si	Fe	Cu	Ti	Al
AA2219-T6	1.60	1.0	0.18	1.1	2.30	0.07	93.7
AA7068-T6	2.7	0.12	5.1	0.35	2.0	0.58	88.1

Table 2: Dissimilar alloys' mechanical composition.

Element	Yield strength (MPa)	Tensile strength (MPa)	Elongation (%)
AA2219-T6	335	363	21
AA7068-T6	495	589	16

FSW is applied. Different pin profiles have the same process limit functions. Pin diameter is 6 millimetres, shoulder diameter and tool pin height are both 18 millimetres, and plate thickness is 6 millimetres. The heat conductivity and resistivity of this tool pin are excellent. The welded plate has a tool pin in the middle of it. Factors of the system such rotating speed, cross-speed, and load capacity were tested on a total of nine samples. Table 3 lists the weld conditions and process parameters.

The UTM machine tested is used for tensile strength. As a welded work piece, precipitated dissimilar alloys are hardened by applying load in the transverse direction. Tensile tests were performed on nine different samples to get the optimal average value.

The nugget region was subjected to a Vickers hardness test as part of the welded zones' transverse load portion. This area has been designated as a TMAZ by the government. The following sections have analysed or plotted the hardness

Table 3: Friction stir-welding criteria.

S. no	Rotatory speed (rpm)	Transformational speed (mm/min)	Pin description
1	900	40	Cylindrical
2	1100	80	Threaded cylindrical
3	1300	120	Taper threaded

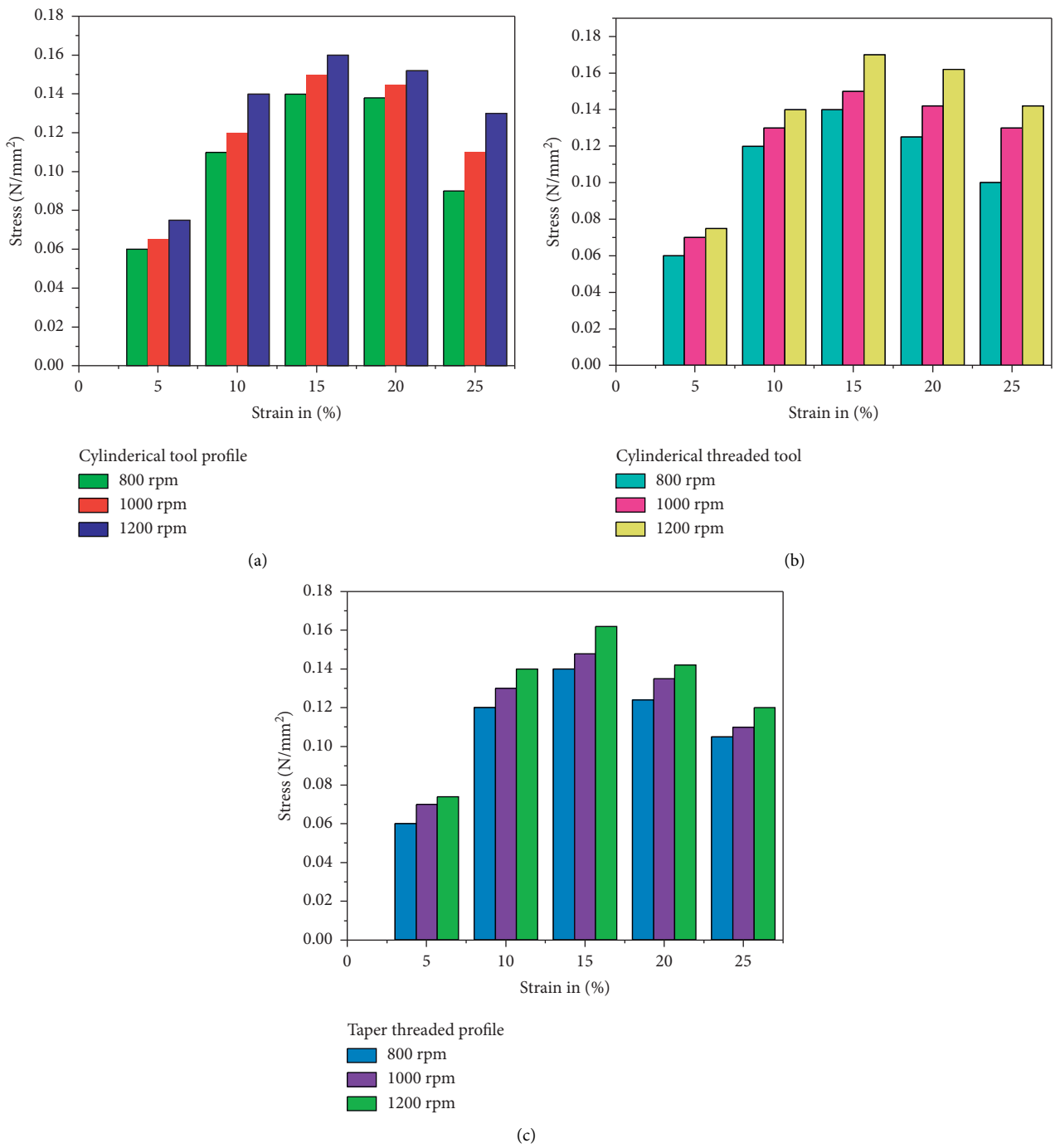

Figure 4: Tensile test: (a) cylindrical contour of the tool, (b) profile of a cylindrical threaded tool, and (c) profile of a tapered tool.

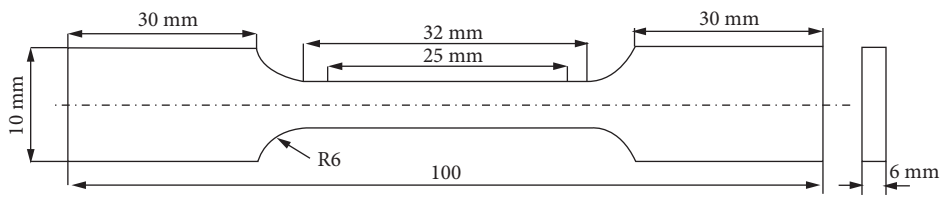

Figure 5: Dimensions of the tensile specimen (ASTM E8M-04).

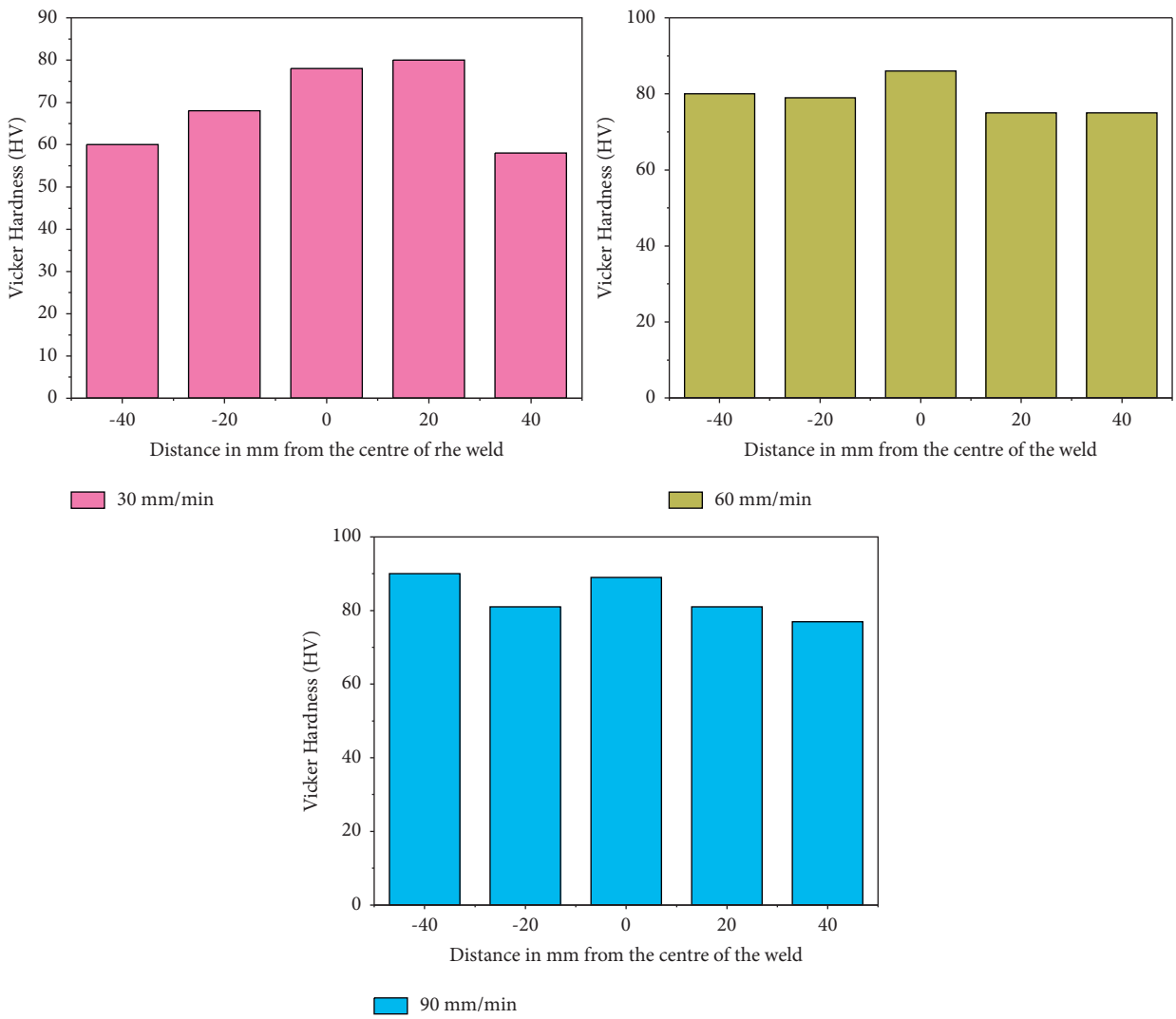

Figure 6: Vickers hardness value for the cylindrical tool.

variation region using various tool profiles. Both dissimilar alloys have their TMAZ zones located in different places. Nevertheless, the variation in hardness values has been detected at diverse locations.

4. Result and Discussion

4.1. Tensile Test. The design guidelines in ASTM standards are followed when performing tensile tests. To ensure welding consistency and testing repeatability, three separate pin profiles were used for the welded junctions. You will see the tallied test results, as well as graphs. Welded work pieces with three different profile examples offer good mechanical properties as seen in the graph of the welded area. In addition to its tensile properties, the material also displays the locations where it is broken. NZs' tool pin profiles have been evaluated on the cracked area.

As the base material's mechanical characteristics and tensile behaviour are increased, the joint welded precipitation hardening portions' tensile properties increase as well. As a result of precipitation hardening dissolving seams that have changed tensile properties, it changes grain boundaries

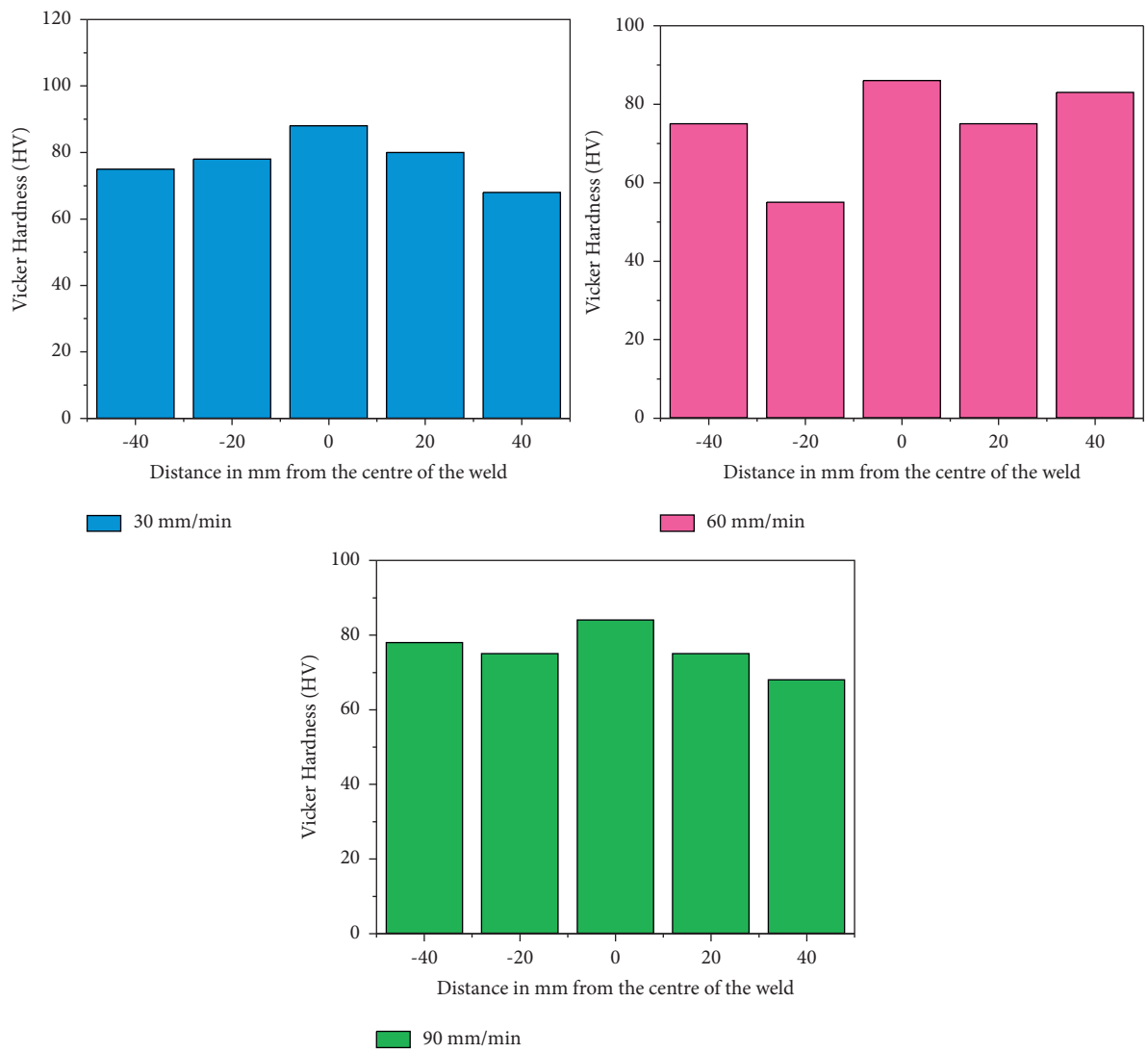

Figure 7: Vickers hardness value for the threaded cylindrical tool.

and grain orientations. All nine samples' joints have low ductility when viewed from above, ensuring the strength of the different alloys, and it is shown in Figure 4.

The specimen's dimensions are depicted in Figure 5. The speed of rotation, spindle speed, and D/d ratios with the best values were determined to be 1300 revolutions per minute, 80 millimetres per minute, and 6. When compared to the other profiles, the cylindrical threaded profile had the best result. It is responsible for 93% of the overall efficiency of the system. The cylindrical threaded tool achieved a maximum strength of 195 MPa. Welded joint tensile behaviour is studied for its impact. Because of this, welded joints have a lower strength rating than those made from other PM materials.

The fracture behaviour occurs in contrast to zones because the agitated zone or NZs are indented. The ductility of the materials was demonstrated by fracturing at a maximum stress condition. Additionally, the TMAZ of the AA 2219 and AA 7068 fractures were affected.

4.2. Hardness Measurements. The graph illustrates the hardness values for various welding speeds, transverse speeds, and ultimate strength. The NZs of hardenability were recognized as a result of their great bonded strength and high hardness values. As the advance side (AA 2219) and the retraction side (AA 7068) have raised consistently, these numbers show a decrease from the beginning. The graph values, as shown in Figures 6–8, also show that the separate zones performing to improve the welding ability of various constructions can be found. TMAZ zones have advanced sides (AA 2219) that are greater than retracted sides (AA 7068) along these values (lowest hardness zone) (minimum hardness zone). A NZ will indicate that the tensile specimen has fractured. The fine grain sizes of the different alloys are depicted as the welding direction of the agitated zone. As AA 2219 materials, it plays an essential part in the character of the mixture. The ideal settings for the taper threaded tool profile were determined to gradually increase the toughness to 92 HV: transverse rate of 60 mm/min and spindle speed of

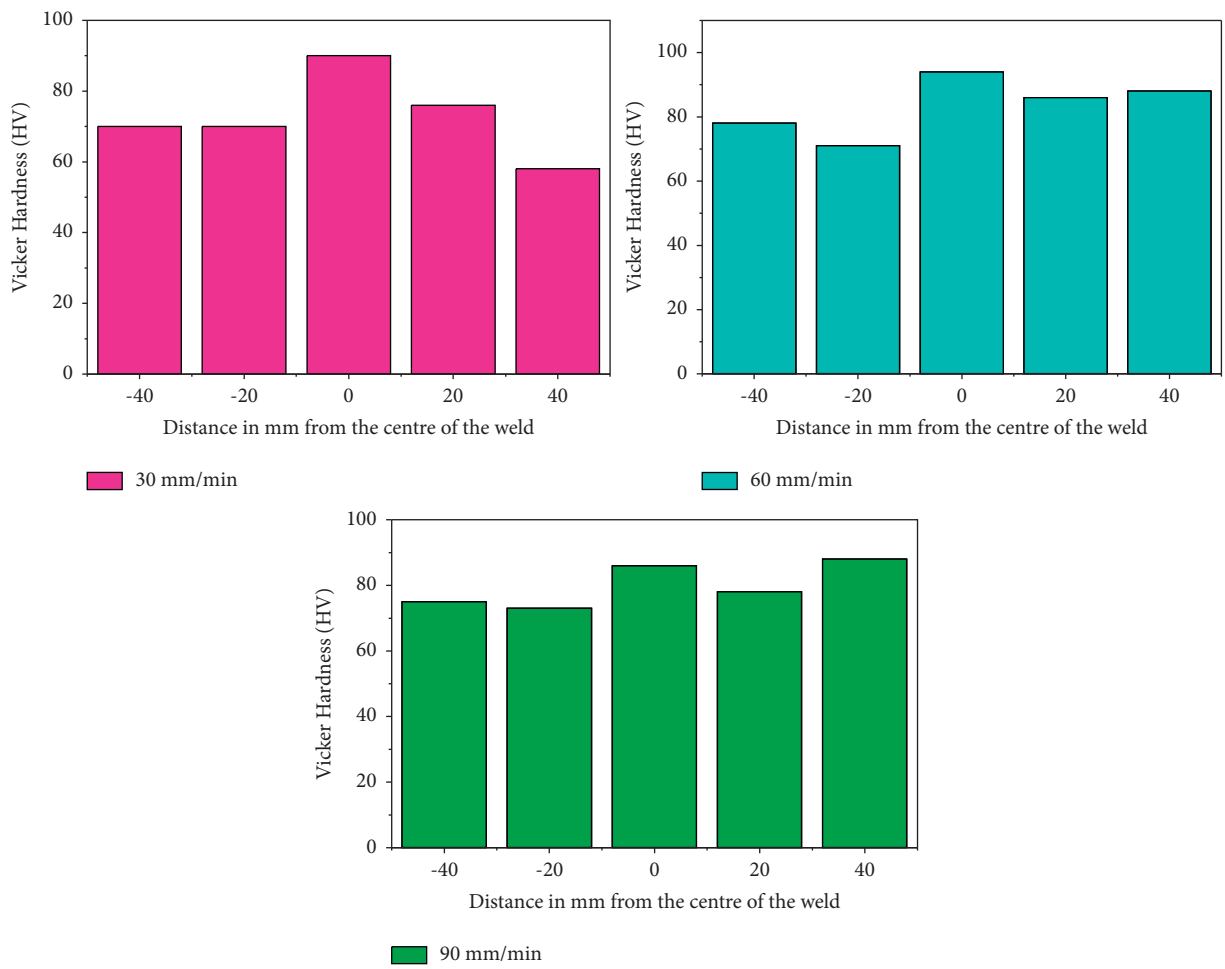

Figure 8: Vickers hardness value for the taper tool.

1000 rpm. Increase speed of rotation further and lower toughness, as with the last tool profile. When the speed is maintained at 1,300 rpm, the toughness decreases. The welded zone had the highest toughness, and mean data were derived for every test. In HAZ, the value of almost hardness increased steadily. The forward-moving side has higher hardness values than the retracting side, which has a lower value. The cylindrical tool profile has higher hardness ratings. Compared to TMAZ zones, NZs appear to have a higher value, while tensile modulus is indicative of the extent of hardness. The toughness rating of the taper threaded profile was greater.

4.2.1. Nugget Zones. The graph illustrates how the hardness values of the tools varied. It is a nonmetallic and thermomechanical influenced zone in which materials combine under a variety of weld connection process settings. The effectiveness of various optimal material flow limitations in the NZ and other recrystallization zones demonstrates the critical nature of tool profiles. There are some test components that do not have enough loading conditions to identify all of the failures. When it comes to FSW, the crystallization effect plays a critical role. It aids in regulating the high degree of softening NZs by lowering the base material's hardness from its centre line and rotational speed.

4.2.2. TMAZ Zones. It was part of the zone that was impacted by thermodynamics and relates to the NZs. The FSW process looked at how weld zones are linked together. The grain sizes control the heat response formed to the midline weld of two alloys, which have a powerful effect on the structures due to the work-hardening state. High temperatures and mechanical pressure were used to join the structure with the two different alloys, resulting in a stronger weld. Some people on the NZ border describe it as having two different alloys in it. The metal matrix has increased hardness due to the fine and homogeneous distribution of strengthening particles. HAZ is located in a very convenient place in relation to New Zealand. This operation's high humidity and temperature accelerated grain growth, which changed the direction of grain flow. On the surface of this NZ, heat and mechanical forces have been applied and have both operated. The eutectics re-emerged from the alumina crystalline phase and fragmented during the heating and chilling phases are formed due to the nugget tool's pin. This part has both the nugget's and the TMT zone's user

interfaces. TMT illustrates larger particles that were not in touch with the instrument but shifted their orientation due to plastic movement, whereas NZ illustrates small eutectic particles.

Shoulder area of the FSW-treated specimen: an advancing zone has grain flow caused by mechanical forces, and this generates heat because of frictional losses. As a result of the pin on the nugget tool spinning throughout the heating and cooling cycles, the eutectics re-emerged and fractured from the aluminium solid solution. The HAZ in the vicinity of the FSW zone has been identified. The eutectics' particle size is increasing.

This is a HAZ, but the grains have not become any bigger because the wind has shifted the direction. HAZ occurs when the eutectics' particles grow in size as a result of the growth, but the particles grow identical to that of the weld bead particles.

5. Conclusions

Good weldability and performance attributes can be produced from dissimilar alloys with FSW. For cylindrical threaded profile pins with a higher D/d ratio, this study concluded that rotational speed, transverse speed, and rotational deflection were more efficient. Cylindrical threaded tools produce maximum tensile strength, which is strong compared to other materials. Compared to the other tool profiles, the cylindrically threaded profile performs the best. The maximum strength of the joint formed with a cylindrical threaded tool rotating at 1,300 rpm and transversely moving at 80 mm/min was 195 MPa. The 110 HV value was attained by using a taper threaded cylindrical shape. Both alloys (AA2219 and AA7068) formed a bond due to the tool's behaviour (AA2219 and AA7068). Vickers hardness tests were used to determine which alloys had the best structural properties. Keller Reagent's effects were used to polish the surface more frequently while also acquiring the functional working zone's FSW. It utilizes advanced mechanical properties and character traits. It was done to determine the weld consistency, and it was done multiple times with different optimization settings. Out of the three-pin profiles, the cylinder-threaded tool has the most gain in strength.

Data Availability

The data used to support the findings of this study are included within the article. Further data or information are available from the corresponding author upon request.

Conflicts of Interest

The authors declare that there are no conflicts of interest regarding the publication of this paper.

Acknowledgments

The authors thank to Loyola-ICAM College of Engineering and Technology, Chennai, and Prince Sattam bin Abdulaziz University, Saudi Arabia, for providing technical assistance to complete this experimental work.

References

[1] K. Mariyappan, K. Praveen, S. Suresh Kumar, K. Kadambanathan, S. Rajamanickam, and R. Vignesh, "Characterization of brass/steel plates joined by friction stir welding," *International Journal of Engineering & Technology*, vol. 7, no. 3, pp. 366–368, 2018.

[2] B. V. Desai, K. P. Desai, and H. K. Raval, "The performance of tool shape on efficiency and quality of forming in incremental sheet-forming process," *International Journal of Rapid Manufacturing*, vol. 6, no. 4, pp. 215–234, 2017.

[3] T. Sathish, S. Tharmalingam, V. Mohanavel et al., "Weldability investigation and optimization of process variables for TIG-welded aluminium alloy (AA 8006)," *Advances in Materials Science and Engineering*, vol. 2021, Article ID 2816338, 17 pages, 2021.

[4] S. Murali, A. Chockalingam, S. Suresh Kumar, and M. Remanan, "Production, characterization and friction stir processing of AA6063-T6/Al3Tip in-situ composites," *International Journal of Mechanical and Production Engineering*, pp. 399–406, 2018.

[5] R. Manikandan and G. Elatharasan, "Effect of process parameters on microstructural and mechanical properties of friction stir welded dissimilar aluminium alloys AA 6061 and AA 7075," *International Journal of Rapid Manufacturing*, vol. 9, no. 1, pp. 1–15, 2020.

[6] K. Elangovan, V. Balasubramanian, and M. Valliappan, "Effect of welding speed and tool pin profile on tensile properties of friction stir welded AA6061 aluminium alloy," *International Journal of Microstructure and Materials Properties*, vol. 4, no. 4, pp. 455–475, 2009.

[7] J. Francis, T. E. Sparks, J. Ruan, and F. Liou, "Multi-axis tool path generation for surface finish machining of a rapid manufacturing process," *International Journal of Rapid Manufacturing*, vol. 4, no. 1, pp. 66–80, 2014.

[8] X. He, F. Gu, and A. Ball, "Recent development in finite element analysis of self-piercing riveted joints," *International Journal of Advanced Manufacturing Technology*, vol. 58, no. 5, pp. 643–649, 2012.

[9] X. He, "Finite element analysis of laser welding: a state of art review," *Materials and Manufacturing Processes*, vol. 27, no. 12, pp. 1354–1365, 2012.

[10] X. He, "Recent development in finite element analysis of clinched joints," *International Journal of Advanced Manufacturing Technology*, vol. 48, no. 5–8, pp. 607–612, 2010.

[11] P. Tasić, I. Hajro, D. Hodžić, and D. Dobraš, "Energy efficient welding technology: Fsw," in *Proceedings of the 11th International Conference on Accomplishments in Electrical and Mechanical Engineering and Information Technology*, Banja Luka, Bosnia and Herzegovina, May 2013.

[12] P. Xue, D. R. Ni, D. Wang, B. L. Xiao, and Z. Y. Ma, "Effect of friction stir welding parameters on the microstructure and mechanical properties of the dissimilar Al–Cu joints," *Materials Science and Engineering A*, vol. 528, no. 13–14, pp. 4683–4689, 2011.

[13] Z. Zhang, Y. L. Liu, and J. T. Chen, "Effect of shoulder size on the temperature rise and the material deformation in friction stir welding," *International Journal of Advanced Manufacturing Technology*, vol. 45, no. 9, pp. 889–895, 2009.

[14] A. Heidarzadeh, H. Khodaverdizadeh, A. Mahmoudi, and E. Nazari, "Tensile behavior of friction stir welded AA 6061-T4 aluminum alloy joints," *Materials & Design*, vol. 37, pp. 166–173, 2012.

[15] M. Jayaraman, R. Sivasubramanian, V. Balasubramanian, and A. K. Lakshminarayanan, "Application of RSM and ANN to predict the tensile strength of Friction Stir Welded A319 cast aluminium alloy," *International Journal of Manufacturing Research*, vol. 4, no. 3, pp. 306–323, 2009.

[16] M. Mehta, A. Arora, A. De, and T. DebRoy, "Tool geometry for friction stir welding-optimum shoulder diameter," *Metallurgical and Materials Transactions A*, vol. 42, no. 9, pp. 2716–2722, 2011.

[17] G. Padmanaban and V. Balasubramanian, "Selection of FSW tool pin profile, shoulder diameter and material for joining AZ31B magnesium alloy - an experimental approach," *Materials & Design*, vol. 30, no. 7, pp. 2647–2656, 2009.

[18] R. Rai, A. De, H. K. D. H. Bhadeshia, and T. DebRoy, "Review: friction stir welding tools," *Science and Technology of Welding & Joining*, vol. 16, no. 4, pp. 325–342, 2011.

[19] C. Chanakyan and S. Sivasankar, "Parametric advancement of numerical model to predict the mechanical properties of friction stir processed AA5052," *International Journal of Rapid Manufacturing*, vol. 8, no. 1–2, pp. 147–160, 2019.

[20] Z. Zhang and H. J. Liu, "Effect of pin shapes on material deformation and temperature field in friction stir welding," *Transactions of the China Welding Institute*, vol. 32, pp. 5–8, 2011.

[21] D. Zhang, N. G. Deen, and J. A. M. Kuipers, "Numerical simulation of the dynamic flow behavior in a bubble column: a study of closures for turbulence and interface forces," *Chemical Engineering Science*, vol. 61, no. 23, pp. 7593–7608, 2006.

[22] A. Arora, A. De, and T. DebRoy, "Toward optimum friction stir welding tool shoulder diameter," *Scripta Materialia*, vol. 64, no. 1, pp. 9–12, 2011.

Hindawi
Advances in Materials Science and Engineering
Volume 2022, Article ID 3982415, 8 pages
https://doi.org/10.1155/2022/3982415

Research Article

Fatigue Failure Analysis of a Gear in Automobile Engine Coolant Pump

Krishnakumar Krishnasamy,[1] **D. Subbulekshmi**,[2] **T. Deepa**,[2] **B. M Gnanasekaran**,[3] **T. Maridurai**,[4] **M. Sriram**,[5] **Srinivasan Suresh Kumar**,[6] **and Mebratu Markos**[7]

[1]*Sr.Manager-Product Development (Engineering), TIDC INDIA, Chennai-600 053, Tamil Nadu, India*
[2]*School of Electrical Engineering, Vellore Institute of Technology, Chennai-600127, Tamil Nadu, India*
[3]*Department of Mechanical Engineering, Fatima Michael College of Engineering and Technology, Madurai – 625020, Tamil Nadu, India*
[4]*Department of Mechanical Engineering, Saveetha School of Engineering, SIMATS, Chennai 602105, Tamil Nadu, India*
[5]*Department of Computer Science Engineering, Bharath Institute of Higher Education and Research, Chennai 600073, Tamil Nadu, India*
[6]*Department of Mechanical Engineering, Panimalar Polytechnic College, Chennai - 600029, Tamilnadu, India*
[7]*Department of Mechanical Engineering, College of Engineering, Wolaita Sodo University, Ethiopia*

Correspondence should be addressed to Krishnakumar Krishnasamy; krishnaksp07@gmail.com

Received 15 December 2021; Accepted 1 February 2022; Published 27 March 2022

Academic Editor: P Ganeshan

Gear is a reliable part of power transmission. This article presents a metallurgical failure analysis of a failed gear used in automobile engine coolant pumps. In gear, the soft microstructure of pearlite and ferrite is witnessed in metallographic analysis. Significant wear is perceived in gear teeth, and significant deformation is observed in the keyway. The crack initiated from the corner radius of the keyway and propagated towards to the root of the teeth, which is evidence of the failure due to fatigue. Recommendations are given to improve the fatigue strength of gear.

1. Introduction

Gear is a reliable power transmission element and is extensively used in automobile and industrial drive applications. There is no intermediate link or connector on the gear, and it transmits the motion by direct contact. Gear is the most frequently failed member in applications. Common failures in gear are pitting, spalling, wear, and fatigue. The failed reducing gear used in the petrochemical industry is carburized, quenched, and tempered. The microstructure of the case is tempered high carbon martensite, and the core is low carbon martensite. The fatigue failure occurred from poorly designed drill holes, which are used for handling large-sized gear [1]. Helical gear in a power generation plant has failed due to fatigue fracture. During microanalysis, inclusions are identified in material with iron oxide surrounded by (FeMo) 3C carbide. The inclusions [2] are formed during the gear blank casting process. The planetary gear failed due to tooth pitting [3] and cracking. The pinion gear crack is originated from small cavities caused by micropitting. In such conditions, the surface is overstressed, and induced plastic deformation by the ridge formation [4] occurs at the bottom of the root fillet. The pinion was loaded heavily near the thrust disc and stress increased in the pinion teeth, which resulted in plastic deformation [5] of the teeth. The author suggested redesigning the pinion assembly to sustain the working load. The failed gear was made up of 20CrNiMo, and surface pitting [6] appeared near the pitch line of the teeth. The gear of the helicopter is rigorously destroyed by spalling [7]. Fractographic analysis confirms the crack originated at the root of the gear. On the other hand, inadequate lubrication, improper mounting, poor

maintenance, unsuitable material selection, and improper heat treatment of drive components result in failure [8–13]. Prior to starting the failure analysis, a literature review is done to realize the various mechanisms of the gear and drive components. Case studies are very useful to understand the causes of drive component failure and the methodology of failure analysis. Most research papers are focussed on failure analysis of helical gear, planetary gear, chains, and drive components used in different applications [14–16]. Limited papers are available on the fatigue failure analysis of gears in automobile applications. Therefore, the motivation behind this investigation is to direct metallurgical examination on a failed engine coolant pump gear and recommend to enhancing the fatigue strength.

2. Materials and Methods

The engine coolant pump gear may fail in function. Analysis of failure detection is conducted using the methods of visual examination, chemical analysis, hardness analysis, scanning electron microscopy (SEM) analysis, and metallographic analysis. The failed gear is made up of EN353 material grade. Experimental tests (ultimate tensile and hardness) are conducted on cylindrical test specimens for performance comparison [33–36]. Test methods are described as follows, and results and discussion are provided. This case study describes the failure analysis of gear that has failed in service [17, 18]. It is reported that the gear is part of the engine coolant pump assembly. Basically, the engine coolant pump consists of the housing, mechanical seal, gear, o-ring, impeller, and integral shaft bearing as shown in Figure 1(a). Integral shaft bearing and mechanical seal are press-fitted with housing. Gear with key is press-fitted at one end of the shaft, and the impeller is press-fitted at the other end of the shaft [25–28].

2.1. Visual Examination. Failed gear has a keyway in the inner diameter and a gear tooth profile in the outer diameter, as shown in Figure 1(c). The gear had failed in a longitudinal mode lengthwise, as shown in Figure 1(b). The longitudinal mode crack occurs up to 65% of the length, and significant wear is perceived in the gear profile [15, 19, 20]. The crack initiated from the corner radius of the keyway and propagated towards the root diameter of the gear.

The gear is cut in a cross-sectional view where the longitudinal mode is ended and cross-sectional keyway of the remaining portion, is shown in Figure 2(a). A close-up view of the remaining part, as shown in Figure 2(b), confirms the enlarged keyway portion. The deep deformation of the keyway is due to the heavy load during application.

2.2. Chemical Analysis. The chemical composition of the failed gear is analysed by optical emission spectroscopy. Table 1 shows the EN353 specifications with the chemical composition of the failed gear. This type of material is typically case-hardened and used in drive components such as bearings, shafts, and spinning tools. The presence of nickel 1.00–1.50% increases the toughness, while molybdenum 0.08–0.15% and chromium 0.75–1.25% contribute to increasing the case harden surface, resulting in an improvement in wear resistance [21–24].

2.3. Hardness Measurement. Hardness measurements are carried out on metallographically polished samples from an area away from the fracture area. A rockwell hardness tester is used to measure the hardness from the cross section of the keyway radius and to the root of the gear radius. The average hardness value is 89 HRB. The hardness indicates the part is not heat-treated. It is in soft condition.

2.4. Scanning Electron Microscopy Analysis. The entirely fractured surfaces are washed by using acetone and diluted HCL. The crack initiated from the keyway edge and propagated towards the root diameter of the gear tooth. The low magnification SEM image (Figure 3(a)) indicates that the top area is the tooth surface and bottom area is the keyway surface. In between the tooth and keyway surface, the crack origin, fatigue propagation zone, and overload zone are presented. Fatigue propagated zone stand up before the overload zone. Figure 3(b) shows the increased magnification SEM view of the fracture surface at the crack origin.

The high magnification shows the fracture origin exposed fatigue striations (beach marks) in Figure 4(a), and the beach marks are concentric rings in a fatigue region which resembles wave marks on a beach. The crack progression is caused by changes in working load and environment. The overload high magnification SEM view in Figure 4(b) revealed a dimpled feature. The dimpled features occurred due to the creation and coalescence of microvoids sideways to the fracture mode. This confirms the ductile overload fracture.

2.5. Metallography. In optical microscopic observation, a minor crack is observed at the corner radius of the keyway shown in Figure 5(a). A considerable grain deformation was also observed in the keyway radius. The fatigue crack initiated from the keyway edge radius and propagated towards the root of the teeth. In the microstructure of the core, soft pearlite and ferrite are perceived, as shown in Figure 5(b). It is confirmed that gear is not heat-treated [29–32].

3. Results and Discussion

The cylindrical test specimens are prepared using a turning center and the dimensions of the specimen are as per the ASTM E8 standard. The specimens are made up of EN353 material. Four specimens are prepared as shown in Figure 6(a). Specimens 1 and 2 are not heat-treated (soft) condition, and specimens 3 and 4 are heat-treated by the case hardening process. Specimens 1 and 3 have undergone hardness testing. Specimens 2 and 4 have been submitted for tensile testing.

3.1. Hardness Test of Specimen. Specimens 3 and 4 are case-hardened by using a mesh belt furnace. The case hardening process cost is approximately 5% of the gear cost. The

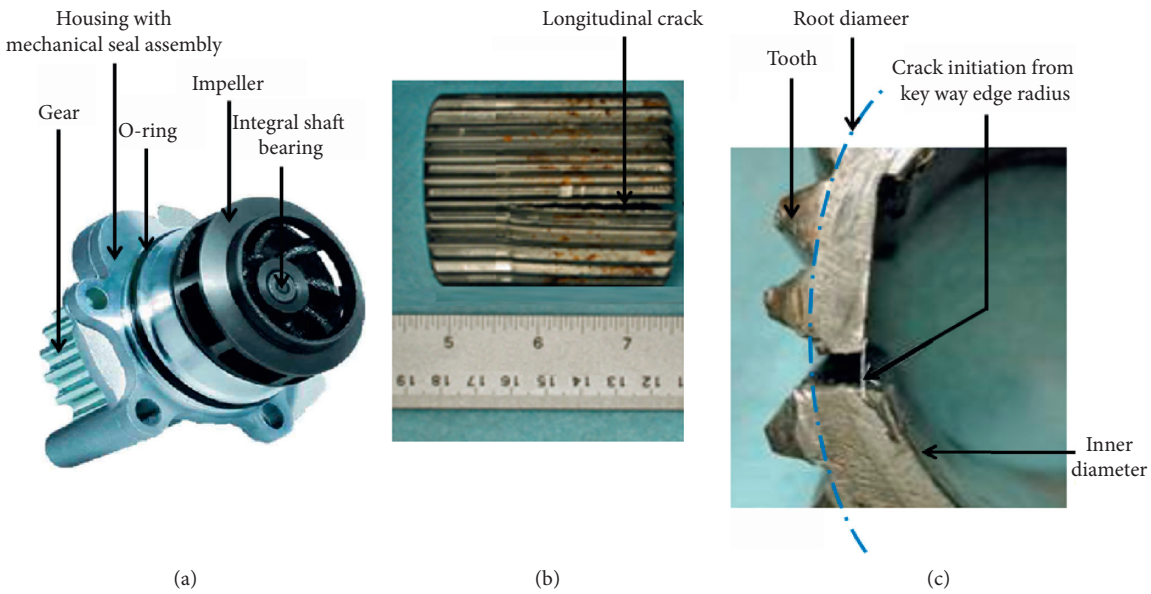

Figure 1: (a) Parts of an engine coolant pump, (b) Crack geometry of the failed gear, (c) Crack initiation.

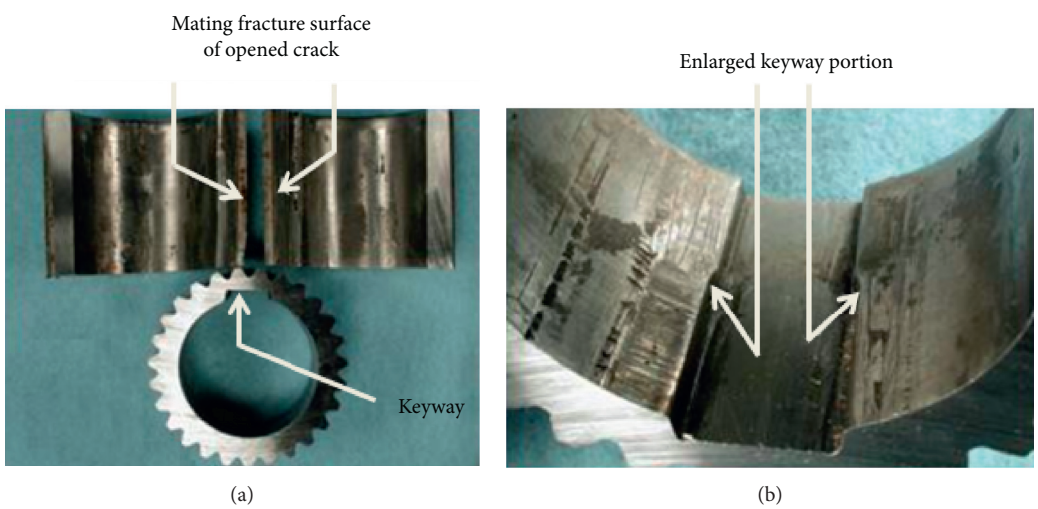

Figure 2: (a) Overview of longitudinal mode crack surface and the cross-sectional view of keyway at the nonfailed portion. (b) Enlarged keyway portion of gear.

Table 1: Failed gear chemical composition compared to the related grade (% wt.).

Sample	C%	Mn%	Si%	S%	P%	Cr%	Mo%	Ni%
Gear #1	0.16	0.99	0.26	0.026	0.005	1.09	0.12	1.15
EN353	0.10–0.20	0.50–1.00	0.10–0.35	0.040 max	0.040 max	0.75–1.25	0.08–0.15	1.00–1.50

microstructure of the specimen is analysed using a Leica DMC2900 microscope. Microstructure is carried out on a metallographically polished specimen 3. Fine-tempered martensite microstructure in the case surface is presented in Figure 7(a), and low carbon martensite microstructure in the core is revealed in Figure 7(b). Readings of hardness are taken in a 15 N : 15 kgf superficial rock well. The surface hardness of specimen 3 is 48.5 HR15 N. The case depth of the outer diameter is 0.35 mm. Core hardness is found to be 415 HV @ 0.20 kgs, as shown in the microhardness traverse survey graph in Figure 7(c). The hardness of the soft specimen 1 is in the range of 180 to 190 HV at 0.20 kgs. (88 to 90 HRB). Rockwell B is shown in the microhardness traverse survey graph in Figure 7(c).

3.2. Tensile Strength Test. The ultimate tensile stress (UTS) of EN353 specimens is tested by using the 1000-ton capacity universal testing machine (UTM). Universal fixtures are designed according to the specimen. In UTM, the upper

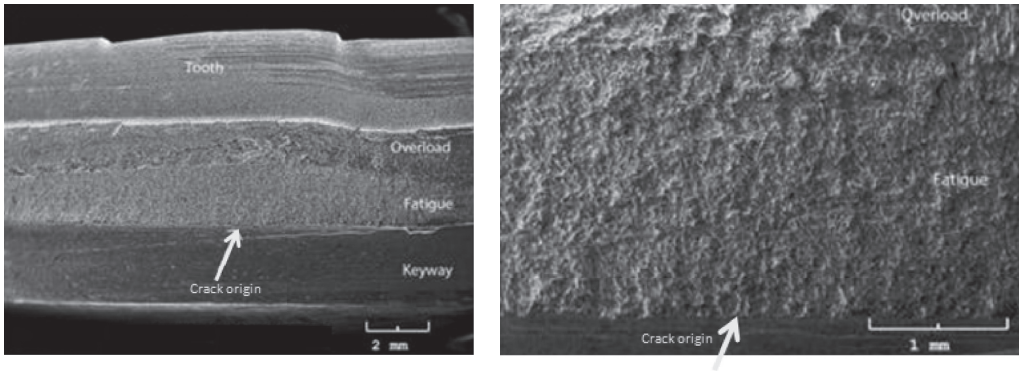

(a) (b)

Figure 3: (a) SEM image of the fractured surface (magnification: 10x). (b) SEM micrograph showing the crack origin, fatigue zone, and overload zone of the fracture surface (magnification: 40x).

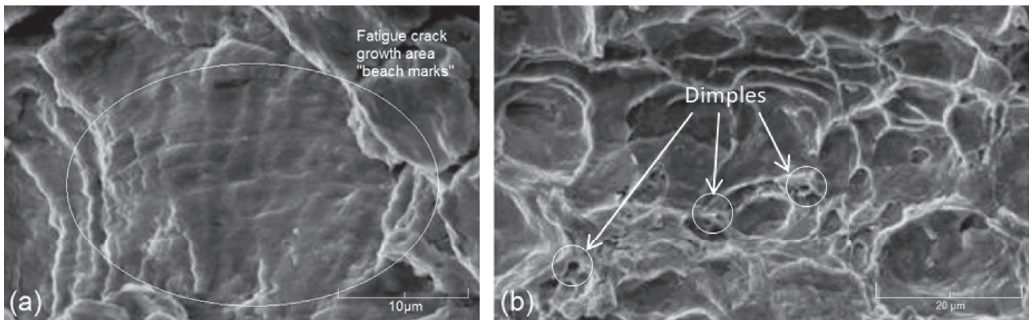

Figure 4: (a) SEM micrograph showing the fatigue (magnification: 4000x). (b) SEM micrograph showing the dimpled surface feature (magnification: 2000x).

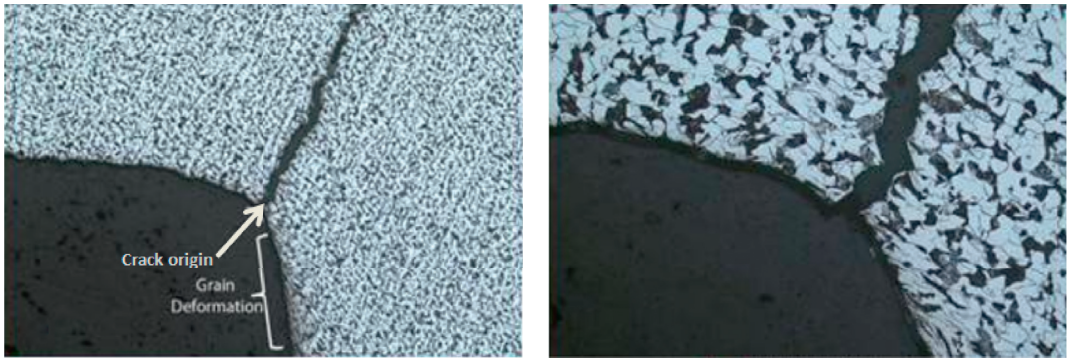

(a) (b)

Figure 5: (a) Optical microscopic view showing the crack origin at the corner radius of keyway (magnification: 50x). (b) Microstructure shows the soft pearlite and ferrite in the core (magnification: 200x).

cross head is the fixed end and the lower is the movable end. The specimen is fixed between two ends as shown in Figure 6(b).

Soft specimen 2 and case-hardened specimen 4 are tested. The stress-strain curve and load-displacement curve of the soft specimen are shown in Figure 8(a) and Figure 8(b), respectively. The stress-strain curve and load-displacement curve of the hardened specimen are shown in Figure 9(a) and Figure 9(b), respectively. The ultimate tensile stress (UTS) of soft specimen 2 is 940 Mpa, whereas hardened specimen 4 is 1495 MPa. Hence, 59% of the ultimate tensile stress (UTS) is higher in hardened specimen 4.

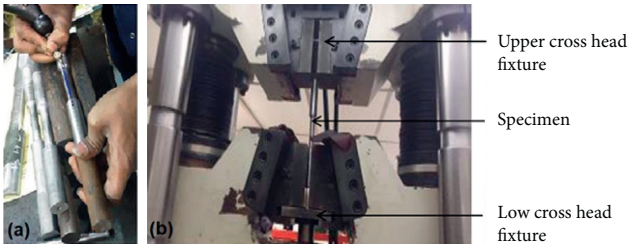

Figure 6: (a) Sample specimens. (b) Tensile test (UTM) machine setup.

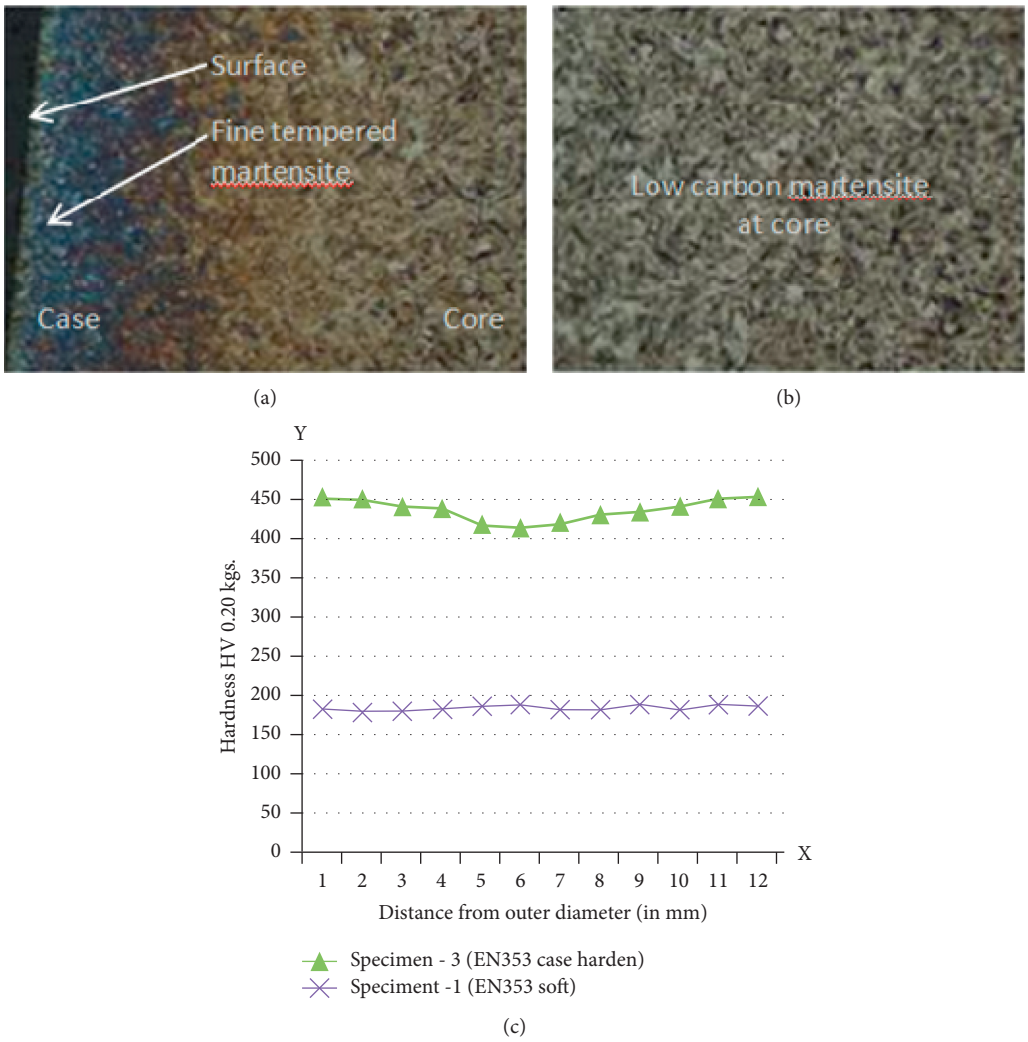

Figure 7: (a) Specimen 3 microstructure shows the finely tempered martensite in the case. (b) Specimen 3 microstructure reveals low carbon martensite in the core. (c) Microhardness traverse survey graph.

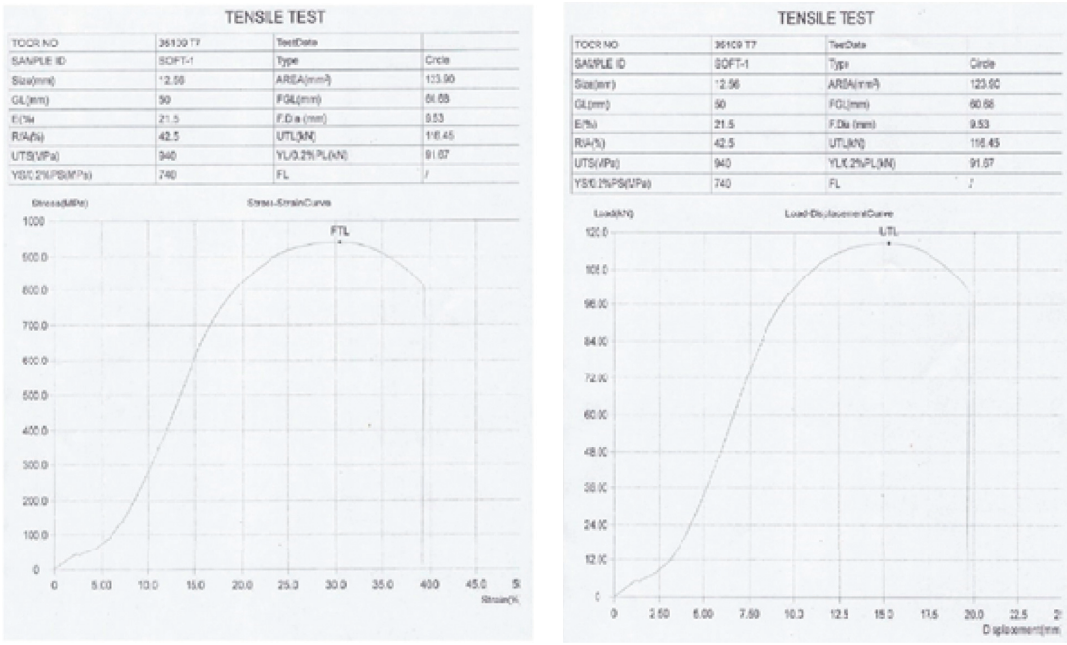

(a) (b)

Figure 8: (a) Stress-strain curve of soft specimen 2. (b) Load-displacement curve of soft specimen 2.

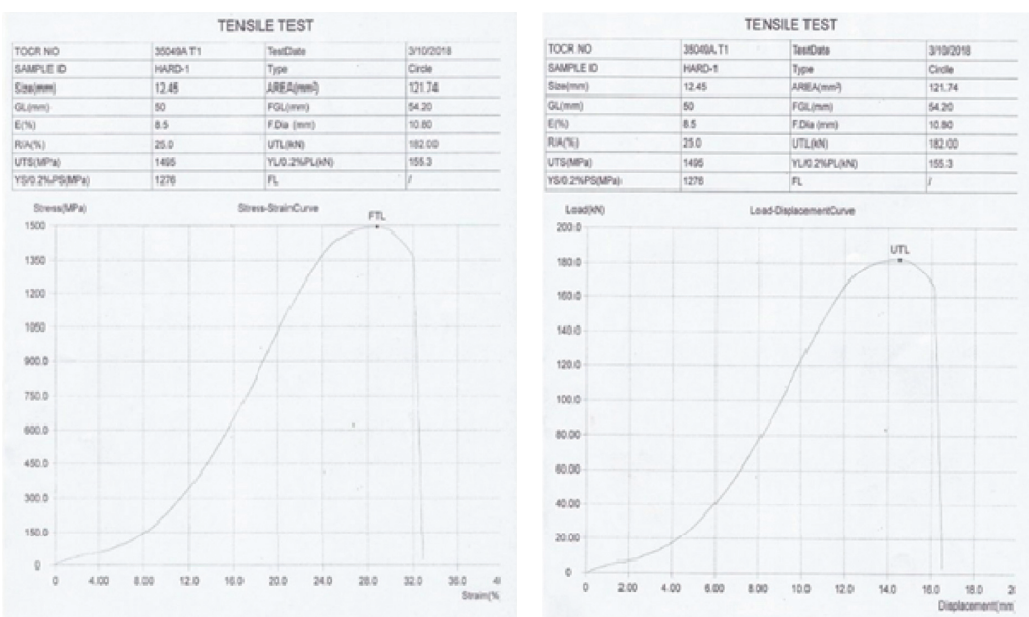

(a) (b)

Figure 9: (a) Stress-strain curve of hardened specimen 4, (b) Load-displacement curve of hardened specimen 4.

4. Conclusion

The crack initiated from the corner radius of the keyway and propagated towards the root of the gear, which confirmed the failure was due to fatigue. Significant wear is observed in gear teeth, and significant deformation is observed in the keyway. A soft microstructure of pearlite and ferrite is observed in metallographic analysis, and an average hardness of 89 HRB confirms that the gear is not heat-treated.

The following measures can be taken to avoid the failure of the gear:

(1) Keyway edge radius to be increased to reduce stress concentrations in the area of fatigue crack origin.

(2) Based on tensile test validation in samples, by the case hardening process, 59% of tensile strength was improved.

(3) The case hardening process followed by quenching and tempering could confidently increase the wear resistance and the fatigue strength of the gear.

Data Availability

The data used to support the findings of this study are included within the article. Further data or information are available from the corresponding author upon request.

Conflicts of Interest

The authors declare that there are no conflicts of interest regarding the publication of this article.

References

[1] S. Griza, A. P. Santos, T. F. Azevedo, C. E. F. Kwietniewski, A. Reguly, and T. R. Strohaecker, "Failure analysis of a petrochemical plant reducing gear," *Engineering Failure Analysis*, vol. 29, pp. 56–61, 2013.

[2] F. Chaari, T. Fakhfakh, and M. Haddar, "Dynamic analysis of a planetary gear failure caused by tooth pitting and cracking," *Journal of Failure Analysis and Prevention*, vol. 6, no. 2, pp. 73–78, 2006.

[3] M. Boniardi, F. D'Errico, and C. Tagliabue, "Influence of carburizing and nitriding on failure of gears - a case study," *Engineering Failure Analysis*, vol. 13, no. 3, pp. 312–339, 2006.

[4] Q. Wang, Y. Zhu, Z. Zhang, C. Fu, C. Dong, and H. Su, "Partial load: a key factor resulting in the failure of gear in the wind turbine gearbox," *Journal of Failure Analysis and Prevention*, vol. 16, no. 1, pp. 109–122, 2016.

[5] S. K. Bhaumik, M. Sujata, M. S. Kumar, M. A. Venkataswamy, and M. A. Parameswara, "Failure of an intermediate gearbox of a helicopter," *Engineering Failure Analysis*, vol. 14, no. 1, pp. 85–100, 2007.

[6] K. Raja, V. S. Chandra Sekar, V. Vignesh Kumar, T. Ramkumar, and P. Ganeshan, "Microstructure characterization and performance evaluation on AA7075 metal matrix composites using RSM technique," *Arabian Journal for Science and Engineering*, vol. 45, no. 11, pp. 9481–9495, 2020.

[7] K. Krishnasamy, "Investigation on metallurgy and material strength enhancement of 20MnCr5 forged link chain in cement mill," *World Review of Science, Technology and Sustainable Development*, vol. 17, pp. 197–210, 2021.

[8] V. V. Kumar, K. Raja, V. S. Chandra Sekar, and T. Ramkumar, "Thrust force evaluation and microstructure characterization of hybrid composites (Al7075/B4C/BN) processed by conventional casting technique," *Journal of the Brazilian Society of Mechanical Sciences and Engineering*, vol. 41, pp. 214–228, 2019.

[9] K. Krishnasamy, "Arockia selvakumar arockia doss, "metallurgical failure analysis and improved core hardness to enhance crushing strength," *Wear Resistance and Fatigue Strength of Chain Bush"*, vol. 20, pp. 967–975, 2020.

[10] M. Rajeshwaran, P. Ganeshan, and K. Raja, "Optimization and biodiesel production from prosopis julifera oil with high free fatty acids," *Journal of Applied Fluid Mechanics*, vol. 11, no. 1, pp. 257–270, 2018.

[11] K. Krishnakumar and A. Arockia Selvakumar, "Enhancement of fatigue strength on SAE 1541 steel link plate with slip ball burnishing technique," *Defence Science Journal*, vol. 70, no. 4, pp. 454–460, 2020.

[12] N. Sivanandham, A. Rajadurai, S. M. Shariff, J. Senthilselvan, and A. Mahalingam, "Microstructure, mechanical properties and corrosion resistance of laser surface melted EN353 low carbon low alloy steel," *International Journal of Surface Science and Engineering*, vol. 11, no. 2, pp. 118–132, 2017.

[13] M. Balu, K. Lingadurai, P. Shanmugam, K. Raja, N. Bhanu Teja, and V. Vijayan, "Biodiesel production from caulerpa racemosa (macroalgae) oil," *International Journal of Mathematics and Statistics*, vol. 49, no. 4, pp. 616–621, 2020.

[14] V. Kumar, K. Raja, K. Chandrasekaran, and T. Ramkumar, "Effect on the behaviour of dynamic mechanical analysis for hybrid epoxy/BN metal matrix composites prepared by conventional casting method," *Materials Research Express*, vol. 6, p. 6, 2019.

[15] V. Yamunadevi, G. Vijayanand, P. Ganeshan, S. Sowmiya, and K. Raja, "Effect on the behaviour of dynamic mechanical analysis for hybrid epoxy nanocomposite," *Materials Today Proceedings*, vol. 37, 2020.

[16] G. Radhaboy, M. Pugazhvadivu, P. Ganeshan, and K. Raja, "Influence of kinetic parameters on calotropis procera by TGA under pyrolytic conditions," *Energy Sources, Part A: Recovery, Utilization, and Environmental Effects*, 2019.

[17] N. Saravanan, P. Ganeshan, B. Prabu, V. Yamunadevi, B. NagarajaGanesh, and K. Raja, "Physical, chemical, thermal and surface characterization of cellulose fibers derived from vachellia nilotica Ssp. indica tree barks," *Journal of Natural Fibers*, 2021.

[18] K. Raja, B. Prabu, P. Ganeshan, V. S. Chandra Sekar, and B. Nagaraja Ganesh, "Characterization studies of natural cellulosic fibers extracted from shwetark stem," *Journal of Natural Fibers*, vol. 18, no. 11, pp. 1934–1945, 2020.

[19] R. Ramkumar, R. Prabu, V. Yamunadevi, P. Saravanan, and P. Ganeshan, "Wear analysis of woven glass/nanofiller fiber reinforced hybrid composites," *Materials Today Proceedings*, Elsevier, 2020.

[20] P. Sainath, F. Mohammed Ajmal Sheriff, and P. Ganeshan, "Fabrication of hybrid polyester composites in various combinations and evaluate the mechanical properties," *Materials Today Proceedings*, Elsevier, 2020.

[21] V. Yamunadevi, K. Palaniradja, A. Thiagarajan, P. Ganeshan, and K. Raja, "Characterization and dynamic mechanical analysis of woven roven glass fiber/cerium- zirconium oxide epoxy nanocomposite materials," *Mater. Res. Express, IOP*, vol. 6, Article ID 095057, 2019.

[22] N. Saravanan, V. Yamunadevi, V. Mohanavel et al., "Effects of the interfacial bonding behavior on the mechanical properties of E-glass fiber/nanographite reinforced hybrid composites," *Advances in Polymer Technology*, vol. 2021, Article ID 6651896, 9 pages, 2021.

[23] V. Mohanavel, S. Suresh Kumar, J. Vairamuthu, P. Ganeshan, and B. NagarajaGanesh, "Influence of stacking sequence and fiber content on the mechanical properties of natural and synthetic fibers reinforced penta-layered hybrid composites," *Journal of Natural Fibers*, Taylor & Francis, 2021.

[24] K. Yoganandam, K. Raja, P. Ganeshan, and V. Mohanavel, "Mechanical properties of calotropis procera/agave fiber

hybrid reinforced polyester composites," *International Journal of Printing, Packaging & Allied Sciences*, vol. 4, no. 5, pp. 3669–3673, 2017.

[25] C. Kandeepan, K. Raja, and P. Ganeshan, "Investigation on the mechanical properties of madar fiber reinforced in polymer matrix composites," *International Conference on Current Research in Engineering Science and Technology*, vol. 4, pp. 110–116, 2016.

[26] B. Ashok Kumar, K. Lingadurai, K. Raja, P. Ganeshan, and S. Vairam, "Prediction effect of fiber content on mechanical properties of banana and madar fiber hybrid polyester composites," *Advances in Natural and Applied Sciences*, vol. 10, no. 7, pp. 180–183, 2016.

[27] P. Ganeshan, K. Raja, K. Lingadurai, and M. Kaliappan, "Analysis of an automobile drive shaft with various composite materials," *International Journal of Applied Engineering Research*, vol. 10, no. 50, pp. 558–594, 2015.

[28] P. Ganeshan, K. Raja, K. Lingadurai, and M. Kaliappan, "Finite element analysis of alternate composite material for an automobile drive shaft," *International Journal of Applied Engineering Research*, vol. 10, no. 49, pp. 447–452, 2015.

[29] K. Yoganandam, K. Raja, and K. Lingadurai, "Mechanical and micro structural characterization of Al6082-TiO," *Indian Journal of Science and Technology*, vol. 9, no. 41, pp. 1–4, 2016.

[30] K. Raja, V. S. Raman, R. Parthasarathi, K. Ranjitkumar, and V. Mohanavel, "Performance analysis of dee-biodiesel blends in diesel engine," *International Journal of Ambient Energy*, 2019.

[31] V. S. Chandrasekar and K. Raja, "Material selection for automobile torsion bar using fuzzy topsis tool," *International Journal of Advances in Engineering & Technology*, vol. 7, no. 2, pp. 343–349, 2016.

[32] B. Babu, K. Raja, S. Dharmalingam, S. Udhayaraj, and V. Vairamani, "Electrochemical micro machining on hybrid metal matrix composites," *International Journal of ChemTech Research*, vol. 8, no. 2, pp. 508–518, 2015.

[33] M. Manikandan, K. Raja, and V. S. Chandrasekar, "Experimental investigation on torsion bar suspension system using e- glass fibre reinforced composite material," *International Journal of Renewable Energy Technology*, vol. 3, no. 11, pp. 2319–2322, 2014.

[34] G. Maruthupandian, R. Saravanan, S. Suresh Kumar, and B. G. Sivakumar, "A study on bamboo reinforced concrete slabs," *Journal of Chemical and Pharmaceutical Sciences*, vol. 9, no. 2, pp. 978–980, 2016.

[35] M. Rajeshwaran, K. Raja, and P. Velmurugan, "Duraimurugan alias saravanan "optimization of soxhlet extraction of prosopis julifera using response surface methodology"," *International Journal of Applied Engineering Research*, vol. 10, no. 49, pp. 552–557, 2015.

[36] G.-Wu Yang, L. Yang, S.-Ne Xiao, S.-L. Jiang, and W. Ma, "Competitive failure of loosening and fatigue of bolts under composite excitation," *Shock and Vibration*, vol. 2021, Article ID 1441122, 13 pages, 2021.

Hindawi
Advances in Materials Science and Engineering
Volume 2022, Article ID 7314694, 13 pages
https://doi.org/10.1155/2022/7314694

Review Article

Waste-Derived Cellulosic Fibers and Their Applications

Antony V. Samrot,[1] Khosa Tariro Ngaakudzwe,[1] D. Rajalakshmi,[2] P. Prakash,[2] S. Suresh Kumar,[3] M. Chandramohan,[1] D. Alex Anand,[4] J. Lilly Mercy,[5] Yishak Simon,[6] and S. Saigeetha[7]

[1]*School of Bioscience, Faculty of Medicine, Bioscience and Nursing, MAHSA University, Jenjarom 42610, Selangor, Malaysia*
[2]*Department of Biotechnology, Sathyabama Institute of Science and Technology, Chennai 600119, Tamil Nadu, India*
[3]*Centre for Materials Engineering and Regenerative Medicine, Bharath Institute of Higher Education and Research, Chennai, Tamil Nadu 600073, India*
[4]*Department of Bioinformatics and the Centre for Molecular Data Science and System Biology, Sathyabama Institute of Science and Technology, Chennai 600119, Tamil Nadu, India*
[5]*School of Mechanical Engineering, Sathyabama Institute of Science and Technology, Chennai 600119, Tamil Nadu, India*
[6]*College of Engineering and Agro—Industrial Technolgy, Sawla Campus, Arba Minch University, Ethiopia*
[7]*Department of Biotechnology, School of Bioscience and Technology, Vellore Institute of Technology, Vellore Campus, Tiruvalam Road, Katpadi, Vellore 632014, Tamil Nadu, India*

Correspondence should be addressed to Antony V. Samrot; antonysamrot@gmail.com and Yishak Simon; simon.yishak@amu.edu.et

Received 18 October 2021; Accepted 3 January 2022; Published 19 March 2022

Academic Editor: Ali Khorram

The use of bio-based materials has become a focus of research nowadays. For the development of new generations of advanced resources, renewable and available resources must be combined with advanced technologies. Researchers have looked into biomass and waste cellulosic materials as sustainable sources for nano-crystalline cellulose extraction. Besides the different treatment methods suitable for various applications, this review aims to provide integrated details on the extraction methods and applications of cellulosic fibers and cellulose nanocrystals derived from wastes of different sources. There are numerous applications including building materials, electronics, furniture, automobiles, medical applications, sports goods, filtrations, water purification, and delivery systems of drugs which have been discussed.

1. Introduction

Food waste can never be defined in one-dimensional terms because the standard of what is edible and inedible varies from individual to individual [1]. Depending on ethnicity and geographical location, dietary habits differ [2]. In the food system, food wastes are placed into four categories: at the postharvest level, during manufacturing, during retail and distribution services, and finally at the household level (Figure 1) [3].

Other important factors that may determine the extent of food waste include pest control efforts, storage, and transportation [4, 5], consumer demand [1], as well as whether or not the country is developed.

The physicochemical properties that usually determine the reutilization of plant-based organic waste are their carbohydrate, lipid, protein and ash content, pH, chemical oxygen demand, and total solids [6]. Fruit and vegetable waste has an abundance of cellulose, carbohydrates, flavors, colorants, minerals, and antioxidants [7]. All these substances are useful and can be used to enhance the quality of other foodstuffs or be added into animal feed [8]. In addition, fruit and vegetable waste contains other extranutritional compounds that can be added to foodstuffs [9]. The most wasted food products are

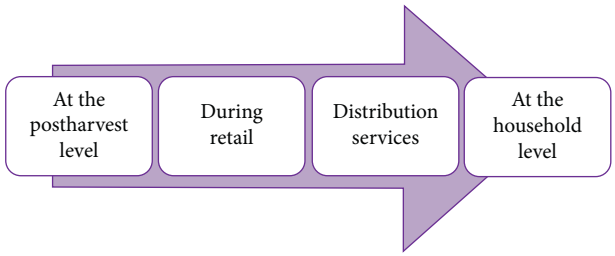

Figure 1: Four categories of food waste: at the postharvest level, during manufacturing, during retail and distribution services, and finally at the household level inspired from [3].

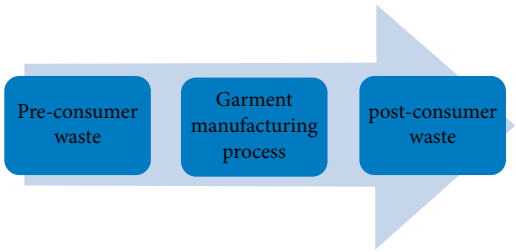

Figure 2: Illustration of the generation of cotton waste.

fruits and vegetables [1]. All these substances are useful and can be used to enhance the quality of other foodstuffs or be added into animal feed [10]. In addition, fruit and vegetable waste contains other extranutritional compounds that can be added to foodstuffs; the most wasted food products are fruits and vegetables. This is usually a consequence of damage to the fruit which renders it unsellable or postprocessing waste such as stalks, peels, leaves, seeds, stems, and husks [1]. In general, discarded cotton fabric has been largely neglected as a potential source of cellulose nanofibers. Recycling textile waste and reusing it in solar steam generation is of tremendous interest [11].

In the previous two years, the amount of cotton consumed in the United States has outpaced production, and the US Department of Agriculture predicts that trend is still continuing. As a result, cotton waste generation increased, wherethere are two types of waste generated: preconsumer waste during the yarn, fabric, and garment manufacturing process and postconsumer waste at the end of the product's life cycle (Figure 2) [12].

Cotton fibers can be reclaimed to make low-grade yarn and nonwoven products for uses in automotive parts, building insulation, and furniture [13]. Approximately, 75% of the preconsumer waste is recycled in this way. Fibers from waste materials to reuse them in future production is commonly referred to as fiber reclamation [14]. As a result of impurities left on used products and their varying tear and wear conditions, postconsumer waste is more difficult to recycle than preconsumer waste. Impurities on fibers are removed by treating with alkali [15]. Cellulose can be converted into useful products rather disposed off or burned [16]. Cotton contains 95% cellulose, and its production is agrochemical and energy-intensive. Regenerating fibers from postconsumer cotton waste is an innovative solution for recycling cotton waste. Cellulose, in particular, has the potential to play a significant role in the replacement of fossil oil-based fibres and cotton with innovative ecological man-made fibres [17]. Despite this, cotton fibers are difficult to dissolve in common solvents as hydrogen bonds between cellulose macromolecules are strong. The viscose process in rayon production uses carbon disulfide (CS_2), and the cuprammonium process employs a complex solution of cuprammonium hydroxide and heavy metals [15]. In a study, the alkali/urea aqueous system was applied for the first time to the recycling of postconsumer cotton products and the regeneration of value-added cellulose fibers through wet spinning [18]. This method is very promising for industry adoption as it uses nontoxic solvents at a low cost. The molecular weight of cotton was reduced by a mild hydrolysis process before dissolution, and impurities were removed [19]. In another work, data were compared between two solvents for dissolving cotton waste and synthesizing cellulose fibers [20]. Some studied on recycling conditions for used white, post-consumer cotton t-shirts [21], where some researchers investigated the possibility of conserving dyes of colorful t-shirts during recycling in order to produce regenerated fibers with intrinsic colors [22].

Plant-based organic waste is comprised of cellulose, which is being used for many applications, including paper and textiles, building, electronics, biomedicine, and many more [23]. Scientists and researchers are currently trying to investigate the potential use of this cellulose derived of waste as a substitute for other environmentally hazardous man-made fibers [24]. Because of its low cost, extensive availability, and low content in non-fibrous components, cellulose is a raw material for fuels, chemicals, paper industry, building board, and food sectors. Not only are these cellulose fibers safe for human intervention but also are also considered a potential source of clean energy [25]. There are many applications for biomass derived from natural fibers: biocomposites, biomedicine, and automotive components. By using waste materials as cellulose fibers, micro and nanoparticles, microfibers, and nanowhiskers can also be produced. Agricultural waste is one of the major sources of cellulosic organic waste. Agricultural waste arises usually as a result of low-quality production and also obtained from post processing of foods [26, 27]. Distribution waste refers to food loss happening in the market, and domestic waste is food loss at the consumer level [3]. Cellulosic waste from food loss and agricultural activities contains approximately 31–60% cellulose, with pentosans accounting for 11–38% and lignin 12–28% [28].

The extent of cellulose polymerization has been a source of debate over the years, with several researchers proposing various structural models [29–31]. Lignins are heterogeneous, branched, three-dimensional structures containing both phenolic and enolic precursors. Hemicellulose on the other hand is a polymer made up of sugars such as cellulitis [32–34]. Fibers are made up of three main components, cellulose, hemicellulose, and lignin, which are arranged in microfibrils. These cellulose fibers are especially important and have many applications in industry owing to their unique properties that include tensile strength, high biodegradability, low weight, and relatively cheap cost [35–38]. Cellulose fibers use get minimized if integrated with other substances such as hemicellulose, lignin, and pectin [39]. Cellulose has a high molecular weight,

making the biopolymer extremely stable and very resistant to degradation by chemicals and enzymes; therefore, to isolate the natural cellulose, intensive pretreatment processes are required [40–44]. These treatment methods varied and range from mechanical, chemical, and chemomechanical [45–49].

2. Pretreatment Methods of Cellulose Extraction

The underlying principle for all cellulose extraction methods is their ability to rid of the noncellulosic parts that are present in the green waste, such as lignin and hemicellulose as previously mentioned (Figure 3). Cellulosic fibers can be extracted from all plant materials, and the choice of cellulosic source is dependent on the availability of the plant source, the application for which the cellulose will be used as well as the associated costs, and they can be used as an alternative to glass fibers [50]. The methods of natural fibers isolation are categorized into chemical, physical, physicochemical, and biological methods.

2.1. Chemical Pretreatment Methods. Chemical pretreatment methods rely on the chemical interactions between cellulosic green waste and the chemical compounds such as acid or alkaline solutions. An acid concentration of 10–30% is effective in degrading both lignin and hemicellulose as well as depolymerizing cellulose. The efficacy of dilute acid of 1- 2% has been proven to be useful in extracting cellulose. It wasmanaged to attain a hemicellulose degradation rate as high as 81% when they treated the perennial grass *Phalaris aquatica*.

Pretreatment with alkaline solutions depends on the process of saponification, and the alkaline compounds cause the lignocellulosic biomass to swell [51–52]. A 4-fold increase was in the total volume of reducing sugars when treated switchgrass with 1% of sodium hydroxide for 12 h at 50°C. In addition to this, it was achieved a delignification rate of up to the maximum lignin reductions were 85.8% at 121°C, 77.8% at 50°C, and 62.9% at 21°C [53].

Organic solvents work by hydrolyzing the internal bonds that compose both lignin and hemicellulose. They also break down the bonds that hold these two structures together [51]. Using organosolvents is a promising pretreatment to solubilize lignin. Coproduction of materials from cellulose fibres and added-value chemicals from hemicelluloses and lignin is an efficient strategy in a biorefinery. Recent researches are focused on employing biphasic systems to fractionate biomass into three separate phases (cellulose, hemicelluloses, and lignin) in a single pot reactor [54].

An alternative to ionic liquids is utilization of deep eutectic solvents (DES). Utilization of DES selectively degrades the biomass, but without damaging any of the carbohydrate structures [55]. As stated, a number of oxidation methods can also be used for biomass delignification; examples include ozonation, cavitation, photocatalysis, and Fenton oxidation [56].

2.2. Physical Pretreatment Methods. The principle goal of physical pretreatment processes is to decrease the size of the cellulosic biomass, thereby increasing its surface area. As surface area increases, the effectiveness of the enzymatic hydrolysis also increases. There is a substantial quantity of literature on the enzymatic hydrolysis of lignocellulosic woods based on the effects of various pretreatment procedures on the enzymatic hydrolysis reaction. Therefore, mechanical disintegration methods such as cutting, grinding, milling, and shredding are usually the methods of choice. The obvious advantage of these kinds of pretreatment methods is that they are environmentally benign, in comparison to chemical pretreatment processes. In contrast, physical disintegration consumes a lot more energy than chemical pretreatment [57–59]. Other than reducing size, physical pretreatment methods also aim to minimize the crystallinity of cellulose, so that it is more accessible for further processing.

2.3. Physicochemical Pretreatment Methods. These pretreatment methods, as the name implies, combine the application of both physical forces and chemical compounds. Using the process of steam explosion, ability is to liberate acetyl residues from cellulosic biomass. The resulting acetic acid facilitated further hydrolysis of the green waste [60]. A process known as ammonia fiber expansion also reduces cellulosic crystallinity while increasing surface area, and this is done by using anhydrous ammonia suspension [59]. In a related procedure known as the ammonia recovery process or ARP, aqueous ammonia is passed through the biomass, allowing for the solubilization and delignification of hemicellulose [61].

In an attempt to determine the extent of degradability of switchgrass, the comparison of two methods such as cellulose solvent and organic solvent-based lignocellulose fractionation (COLSIF) and immersion of the switchgrass in aqueous ammonia was compared. It was found that COLSIF-treated cellulose was 16 times more accessible to cellulase in comparison to the aqueous ammonia immersion method, which mainly got rid of lignin. This led to the conclusion that cellulose accessibility to cellulases is of greater importance than the elimination of lignin [62] which can be done by applying an effective physiochemical method.

Liquid hot water treatment can cause the degradation of hemicellulose, and at temperatures which exceeds 180°C, lignin is also degraded leaving just cellulose [51]. Microwave irradiation is another thermal pretreatment method that works by interfering with the lignocellulosic structures of the green waste. To increase its efficacy, it is often used in combination with chemical methods [63]. Figure 4 shows the pretreatment procedure for lignocellulosic biomass for fermentative utilization.

2.4. Biological Pretreatment Methods. Biological pretreatment is a method which uses microorganisms such as lactic acid bacteria and enzymes to treat the biomass. The two main underlying principles include saccharification and delignification. Variation of microorganisms to pretreat lignocellulosic biomass was used [65]. More specifically, biological delignification uses both fungi and fungal-isolated enzymes. Wood-rot fungi have been proven to degrade both cellulose and lignin [66]. White-rot fungi was used to assess the rate of delignification of Bermuda grass stems which discovered that the white-rot fungi had achieved a 41% removal of all aromatic

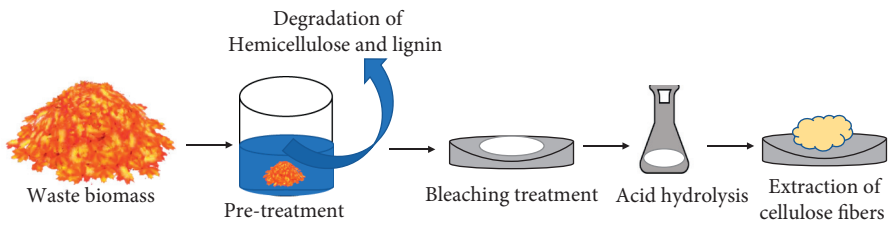

Figure 3: Illustration about methods of extraction of cellulose fiber from waste.

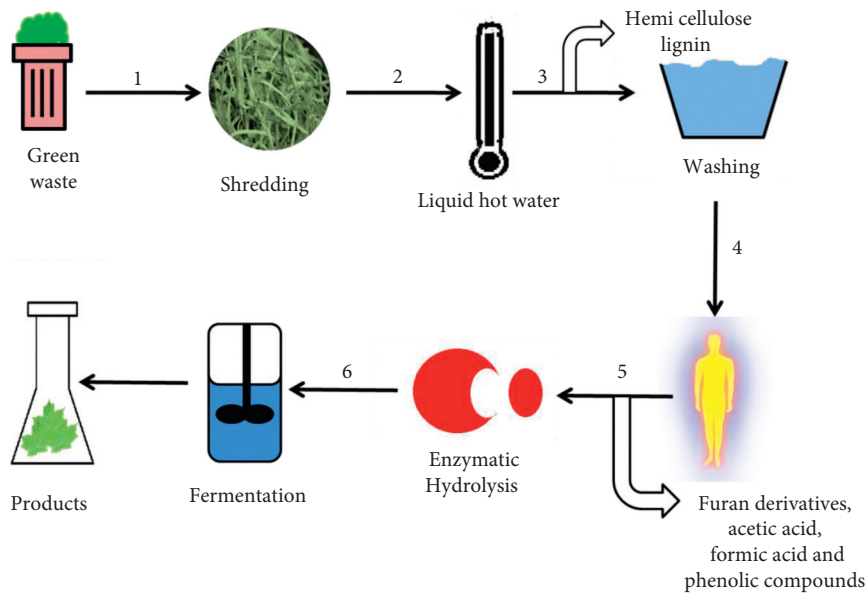

Figure 4: The pretreatment procedure for lignocellulosic biomass for fermentative utilization. (1) Shredding. (2) Use of high temperature and pressure to remove both lignin and hemicellulose. (3) Washing of the hydrolysate. (4) Detoxification. (5) Isolation of the monosaccharides, the samples undergoing enzymatic hydrolysis. (6) Microbial fermentations [64] (Figure 4).

compounds, while also achieving a biodegradability rate of 77%. However, an obvious disadvantage of this method, as with any biological method, is the fact that it is time consuming, and therefore, researchers often have to resort to other more efficient chemical or physical methods. Isolated enzymes offer faster delignification rates in comparison to whole organisms [67]. The phenomenon using the enzyme multicopper oxidase laccase on both eucalyptus and elephant grass [68]. Multicopper oxidase laccase is an enzyme that hydrolyses lignin by altering its three phenolic molecules. Using this enzyme, they achieved delignification rates of 35% for elephant grass and 85% for eucalyptus [68]. *Clostridia* are one of the best-known microorganisms that can undergo biological saccharification. This is made possible because *Clostridia* has a specialized collection of enzymes known as cellulosome which includes chitinases, cellulases, endo and exoglucanases, pectate lyases, xylanases, and hemicellulases. *Clostridium thermocellum* is especially a good candidate because of its ability to tolerate very high temperatures [69]. A disadvantage of utilizing enzymes instead of whole microorganisms is the risk of further metabolizing the generated sugars into unwanted by-products [65]. Another problem arising from the use of enzymes is product inhibition, where after a while, the products made by the enzymes work by negative feedback and bind to the enzyme's active site, thereby, preventing the enzyme from carrying out any further catalytic processes. Prawitwong and their colleagues managed to circumvent the inhibition brought about by *C. thermocellum* with the addition of β-glucosidase, a thermostable enzyme [70]. They coupled this with an alkali pretreatment, and in the end, they were able to achieve saccharification of 72% of all glucan. Another upside of biological pretreatment is the fact that of all the by-products formed, none compromises the success of subsequent enzymatic and microbial hydrolysis reactions [71]. This is not the case with physicochemical methods because there is almost always a detoxification step is required. The overall mechanism of pretreatment is shown in Figure 5.

3. Extraction of Nanocellulosic/ Cellulosic Fibers

Cellulosic fibers can be extracted from cellulosic materials using several techniques either prefers pretreatment or not, it depends on the method preferred by the researcher [72]. There are mainly three categories of isolation methods: mechanical extraction, enzymatic hydrolysis, and acid hydrolysis [73]. In general, there are three main extraction techniques: acid hydrolysis, enzymatic hydrolysis, and mechanical process as mentioned in above pretreatment process. Nanocellulose is most commonly

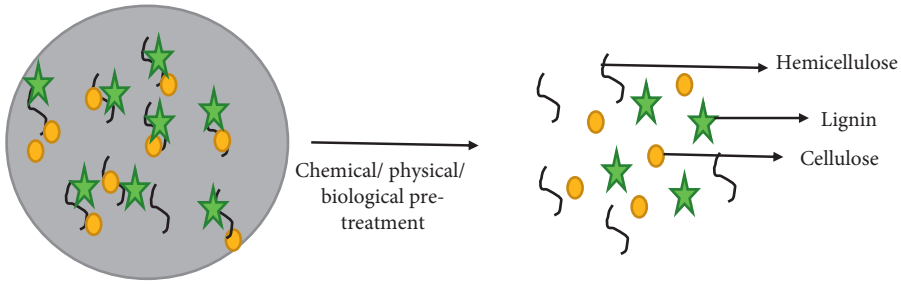

Figure 5: Mechanism of pretreatment.

extracted from biomass fibers by acid hydrolysis [74]. It can be easily hydrolyzed into cellulose as this process uses sulfuric acid for acid hydrolysis. As a result of the esterification of the hydroxyl group by sulfate ions, it is able to isolate nanocrystalline cellulose and disperse it as a stable colloid system [75]. The major problem with acid hydrolysis is the acid wastewater that is generated when the nanocellulose suspension is washed to neutralize the pH value. Usually, cold water is added followed by centrifugation to neutralize the pH of the water [76]. The resulting products can also be washed by washing them in alkaline substance such as sodium hydroxide to neutralize pH levels [77]. The acid hydrolysis of four different types of biomass by Maiti et al. [78] resulted in the extraction of nanocellulose from them. In this reaction, the acid is washed with deionized water and centrifuged, followed by 0.5 N sodium hydroxide for neutralizing the suspension, followed by distilled water for washing again. It is possible to use TEMPO (2,2,6,6-tetramethylpiperidine-1-oxyl radical) as the catalyst to oxidize the carboxylate group of cellulose with the primary oxidant hypochlorite [79]. The process of enzyme hydrolysis refers to the process of digesting or modifying cellulose fibers by enzymes [80]. It was demonstrated by Moniruzzaman et al. [80] that cellulose fibers could be separated from wood chips by pretreatment with ionic liquid for increasing the accessible surface area, followed by enzymatic hydrolysis with laccase. Nanocellulose obtained from wood fibers has a higher crystallinity and thermal stability than native wood fibers. The mechanical process involves applying high shear forces to fibers in longitudinal direction, which cleaves them, resulting in nanofibrillated cellulose [81]. The most prevalent mechanical methods include homogenization under high pressure, ultrasounding, and ball milling. High-pressure homogenization (HPH) involves passing cellulose slurry at high pressure and high velocity through a vessel [82]. Defibrillation of cellulose fibers also done using ultrasonication [83]. The ball milling process is another mechanical method that can defibrillate cellulose fibers. A rotating jar creates shear forces between and among the balls due to its centrifugal force [84]. One of the main disadvantages of mechanical processes is their high energy consumption. In order to decrease energy consumption, the mechanical process is usually combined with other pretreatment methods [85].

4. Applications of Cellulosic Fibers

Natural fiber composites extracted from jute and the fibrous husk of coconuts are used to make building materials (panels, roofing goods, door shutters, door frames, and many other materials) (Figure 6) [86]. In many countries across the world, these cellulosic fibers are used either alone or as composites where they are combined with other materials. Some countries have even used these natural fibers as replacements for wood. In India, agricultural green waste such as bagasse fibers have been used to synthesize insulation boards [87]. In China, the same method has been used to synthesize chipboards [88]. Similar products have also been developed both in Thailand and Japan [89]. In the Philippines, these chipboards were produced mainly from the stalks of bananas and coconut husks [90]. Papua New Guinea, Indonesia, and Malaysia on the other hand have resorted to using fibers isolated from oil palm trees [91–93].

4.1. Furniture. As with all green waste utilization, the use of cellulosic waste fibers in the furniture industry greatly minimizes waste. Fibers isolated from fruit and vegetable waste can be used to create medium density fiber board (MDF) [94]. Similarly, the use of flax fibers in furniture production was described by Van de Velde and Kiekens [95]. Considerable research has been made into the use of cellulosic fibers such as fruit peel waste in manufacturing products such as furniture padding and plastic fencing [96].

4.2. Automobile Industry. For decades now, cellulosic waste fibers have been used in the automobile industry. The use of natural fibers in car manufacture can greatly decrease the car's weight, thereby, also minimizing its fuel consumption. These biocomposite fibers can be used both on the exterior and in the interior of cars. Headliner panel, door panel, dashboard, and seat back are examples of some of the automotive parts that have been created from fiber biocomposites in the past [97]. A study was carried out where the use of palm kernel fibers in the production of brake pads was examined [98]. Popularly known car brands such as Audi, Volvo, Ford, Volkswagen, and many more have all used natural fibers in manufacturing their automotive components [99, 100].

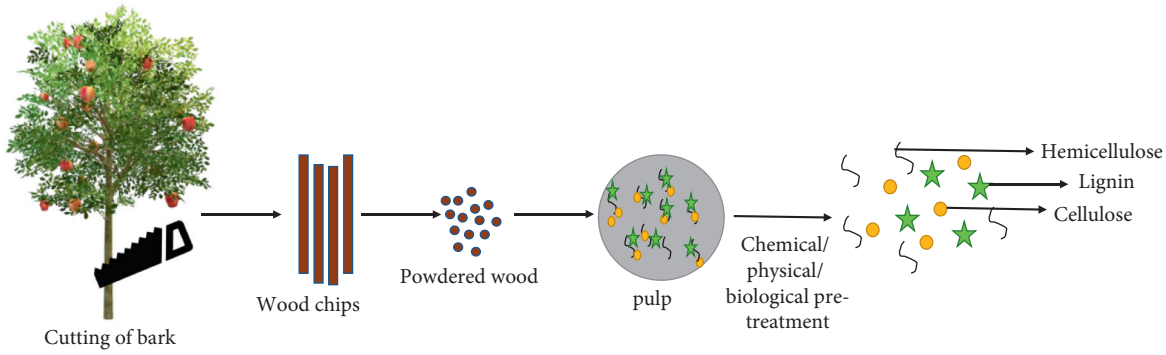

Figure 6: Illustration about the utilization of cellulosic fibres from wood of plant.

4.3. Medical Applications. For natural fibers to be deemed suitable for medical applications, they need to exhibit long-term usage within the body, but without inducing any toxic or allergic reactions [37]. Possible uses of natural fibers in biomedicine include the following: for skin grafting, as drug delivery systems, in dental procedures, bone reconstruction, and as scaffolds for tissue engineering [101–104].

Cellulose nanofibrils have the potencyto enhance cell proliferation additionally as reinforce polymer matrices, making them a great candidate for use in tissue engineering [105]. This includes tissue scaffolding, vascular grafts, and tissue regeneration. A test was carried out about the properties of hydrogels containing modified cellulose nanocrystals (CNC) compared to hydrogels without cellulose nanocrystals [106]; this research proved that the CNC-containing hydrogels were more elastic and showed significant structural stability. The absence of any cytotoxicity made them even more suitable for use in tissue scaffolding. In a study, cellulose nanocrystals were used as fortifying agents for tissue scaffolds in alginate matrices, and though cell proliferation was at the start diminished as a result of the nanocellulose's hydrophobic nature, the CNC's maintained cell growth over a longer period of time, promoting cell proliferation in the long run [107]. The incorporation of the CNCs in the hydrogels also decreased the enzymatic degradation of the hydrogels by the proteolytic enzyme trypsin. The potential use of nanocellulose in bone tissue engineering [108] created hybrid materials that contained both cellulose nanocrystals and hydroxyapatite, where it was examined about the link between hydroxyapatite growth and the surface chemistry of CNC's. A study discovered that the addition of CNCs was an excellent scaffold as they promoted the nucleation of hydroxyapatite. The CNCs also appeared to enhance the viability of fibroblast cells. They studied the efficacy of CNC-coated bioactive glass as a substitute material in the promotion of bone regeneration [25]. The mixture of the two materials would imitate fibrous collagen and hydroxyapatite similar to what is seen in the bone matrix.

In a study, it was observed that the addition of the CNC coating to bioactive glass improved the proliferative and adhesive properties of MC3T3-E1 cells, which can be a useful application in bone implantation. An experiment supporting that nanocellulose can be used in vascular graft therapy [109]. The oxidized cellulose nanocrystals (OCNC) exhibited great tensile strength, likened to that of pig arteries. This showed that the OCNC/fibrin composites are excellent candidates for vascular grafting as their strength and elasticity could be modified.

The utilization of nanocellulose in drug delivery systems is another current area of interest. Drug delivery systems are used to deliver biomolecules including chemical compounds and genes to target tissues or organs. The idea is that once nanocellulose is incorporated, the bioavailability of the drug is enhanced due to slower release rates, which increases the residence time of the drug as well as reducing systemic toxicity.

The use of nanocellulose in drug delivery is by combining curcumin-loaded cellulose nanocrystals with chitosan in alternating layers [110], where thedrug release was sustained at acidic pH which led to the conclusion that if the drug delivery systems can maintain release in acid environments, then the same drug delivery system can be used to treat tumours that thrive in the same acidic surroundings. By integrating cellulose nanocrystals with poly(ethyl ethylene phosphate) , it can be used in delivering antitumor drug doxorubicin to cancer cells. Faster drug release was exhibited at pH 5.0, which demonstrated that at the normal physiological pH of 7.35–7.45, this drug delivery system should be able to successfully evade degradation until it reaches its target site [111].

Incorporation of cellulose nanocrystals and sodium alginate is an attempt to demonstrate the possibility of controlling the release of two separate drugs to the same target site [112]. They created a drug delivery system with an outer membrane that would degenerate to release one drug (ceftazidime), while an inner membrane (consisting of alginate and cellulose nanocrystals) housed an epidermal human growth factor that would later get released at a slower rate. To target folate receptor-positive cancer cells, conjugation of cellulose with folic acid and fluorescein isothiocyanate was obtained. The findings indicated that in

both human and rat brain tumour cells, uptake of the drug was greater in cellulose nanocrystals incorporated drug delivery system than drug delivery systems that did not incorporate cellulose nanocrystals with folic acid [113].

The efficacy of gene delivery was enhanced when cellulose nanocrystals were combined with gold nanoparticles. The same cellulose nanocrystals were grafted with methacrylate derivatives and intertwined with plasmid DNA. CT imagingshowed that the plasmid DNA became condensed and found the interaction with anionic cell membranes to be reduced. Thus, nanocellulose is found to be a promising candidate for potential employment in gene delivery [114]. A multi-layer chitosan-based electrospun mat containing Semellil extract and cross connected by genipin can be used for wound dressing. Due to its better wound healing function, this type of dressing could be an excellent substitute for ANGIPARS™ ointment.[115].

4.4. Sporting Goods. In addition to all these, natural fiber biocomposites may also be used in the production of sporting equipment. The flax-based tennis rackets and bicycles among some of the known sporting goods containing cellulosic fibers were reported. In addition to its high specific stiffness, flax fibre has an inherent vibration absorption property. Hybrid materials, composed of cellulose and other fibers, have already been utilized as replacements for wood and metal in products such as golf clubs, ski equipment, fishing rods, spars, and tennis rackets [116].

4.5. Electronics. In the electrical industry, nanocellulose is used to supplement the conductive power of related composites. Researchers exploit nanocellulose in the production of electrical materials due to its renewability, biodegradability, low cost, light weight, and most importantly because it is environmentally benign [117]. An example of this is the use of nanocellulose-based hybrid materials in the biosensing devices to detect analytes such as pathogens, drugs, gases, and biomarkers that may help in diagnosing various diseases. TEMPO-oxidized cellulose nanocrystals was utilized to determine the presence of the amino acids such as phenylalanine, leucine, and valine. The prevalence of these three amino acids is indicative of type 2 diabetes, and by using this specially designed sensor, it was able to examine the serums of both healthy individuals and those with the disease [118]. Cellulose nanocrystals were conjugated with fluorescent dyes and used as biomarkers in mice. Fluorescent dye conjugated CNCs moved to the bones as a result of electrostatic attraction to the calcium ions that make up the bone matrix. This demonstrated that these modified CNCs could potentially be used in therapy that treats bone-related disorders [119].

4.6. Biodegradable Nutritive Pots. In recent years, many consumers have been searching for greener alternatives to obtain biodegradable, eventually recyclable, and derived from renewable resources with minimal pollution for soils and plants due to reports of the detrimental effects of plastic pots used in agriculture on the environment in recent years.[120]. Plastic pots, containers, trays, and containers are widely used in greenhouses and private gardens. These containers are discarded in landfills, where they degrade very slowly [121]. Accordingly, biodegradable pots are an effective substitute for plastics [122]. Plastic pots tend to be light, inexpensive, and durable, and their walls are relatively impermeable [123]. Biocontainers are considerably more expensive as their prices range from 10% to 40% higher than plastic containers [124]. Cellulose fibers are considered to be the raw materials with the greatest availability among existing plants and renewable resources, offering significant advantages over synthetic, inorganic, or mineral fibers [125]. Cellulose-based biodegradable pots were prepared from peat and cellulose fiber preparations done with wire or vacuum dewatering using special molds [126]. Vegetables, flowers, medicinal plants, ornamental shrubs, or various forest species, nutritive and biodegradable pots are used in seedling manufacture in various ways until vine cuttings are produced [127]. In biodegradable pots, high levels of peat provide an optimal medium for seedling root development and provide a nutritional reserve at the same time. This fibrous component ensures oxygen flow by allowing air and water to circulate. The availability of nutrients from peat is not reliable over the long term. In this regard, the methods for keeping nitrogen from urea or ammonium phosphates, as well as pH, are important [126].

4.7. Separation. Nanofibers can be used as filters to trap particulates [128]. In general, filter effectiveness improves linearly when the thickness of the filter membrane is reduced, and the applied pressure rises. The electrospinning method can reduce filter diameters to less than 0.5 μm, resulting in improved filter efficiency when pressure is increased [129]. An affinity membrane out of regenerated cellulose nanofibers was created. This membrane was functionalized with protein A/G and showed significant immunoglobulin G (IgG) binding capacity, making it suitable for IgG purification [130]. Cellulosic nanofibers have a lot of potential for separation technology in food and beverage plants, but they have not been fully investigated yet [131].

4.8. Water Purification. Cellulose nanofibers (CNFs) of biological origin have been employed to convert waste water into reusable form and for efficient heavy metal cleanup [111]. They are good candidates for application as water purifying biomembranes because of properties such as high specific surface area, nanosize, nontoxicity, hydrophilicity, bioadsorption ability, and so on [132]. Oil and organic pollutants were also separated from water using CNFs. CNFs produced from bacteria were employed as oil adsorbents from water sources was reported by Sai et al. [133]. Incorporation of nanoparticles to the cellulose might also influence the better removal of contaminants (Figure 7).

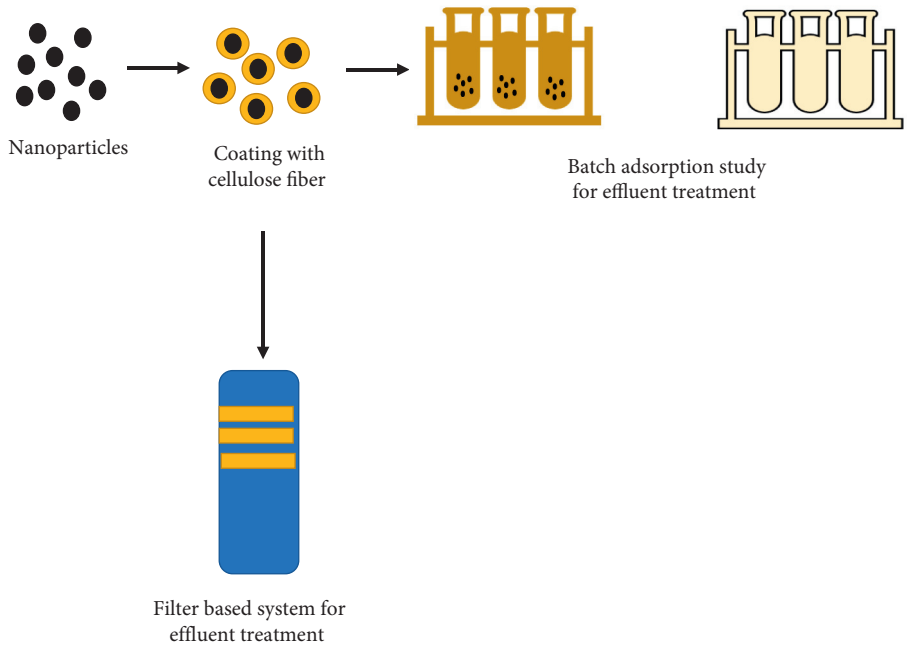

Figure 7: Water purification [134].

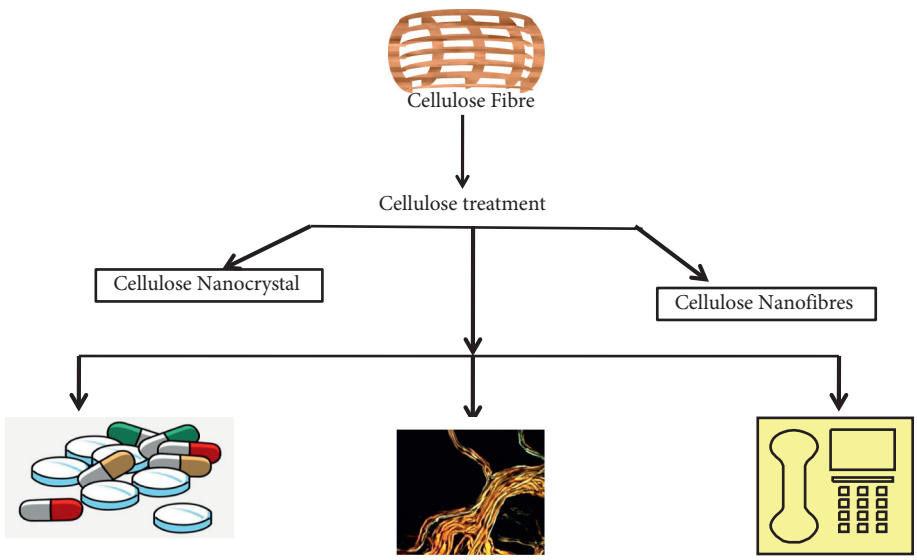

Figure 8: Flowchart of utilization of cellulosic fibres in different fields.

4.9. Food Packaging. Using electrospinning, nanofibers are produced with antimicrobial, antioxidant, oxygen scavenger, moisture absorbent, odor absorbent, and many other bioactive elements embedded [135]. Moreover, nanofibers are highly sensitive to changes in environment and can be modified to contain heat-sensitive molecules [136]. Cellulose offers appealing properties such as hydrophilicity and water insolubility, which can be used as reinforcing agents in packing materials or films [137]. CNFs are utilized as edible coatings on a variety of fruits and vegetables to extend their shelf life. They accomplish this by limiting microbial development, oxidation, and moisture transfer, all of which help to maintain product quality [138]. The presence of cellulose fibers is said to improve the mechanical properties of the fabricated film, such as tensile strength and elastic modulus. The cellulose fibers also lowered water vapor permeability, resulting in a composite edible film with good stability [139].

4.10. Delivery Systems. Nanoencapsulation is a useful technology for disguising unpalatable flavors, protecting nutrients from unfavorable processing and storage conditions, and enhancing the use of low-soluble compounds [140]. Nanolipid carrier (NLC) was used to encapsulate astaxanthin potential application in transparent beverages

[141]. Light, oxygen, and heat are all adversaries of food additives like volatile or unstable flavors and antioxidants. As a result, for the stabilization of functional additives, nanofibers with a greater thermal stability are used [142] (Figure 8). The cellulose can be made into nanoparticle after carboxymethylation and can be used for drug delivery [143–144].

5. Conclusion

Cellulose can be obtained from most plant sources and can also derived from plant-based wastes. It has enormous applications as it is easy to extract, nontoxic, biodegradable, and ecofriendly. Many polyesters and plastics can be replaced by cellulose. In this review, various methods of cellulose extraction and applications of cellulose in various fields like biomedical, environmental, pharmaceuticals, drug delivery, and several nanotechnological applications are discussed. It can be used as a best alternative for commercial products.

Data Availability

No data is used in this review article.

Conflicts of Interest

The authors declare that there are no conflicts of interest.

References

[1] Parfitt, Barthel, and Macnaughton, "Food waste within food supply chains: quantification and potential for change to 2050," *Philosophical Transactions of the Royal Society B: Biological Sciences*, vol. 365, no. 1554, pp. 3065–3081, 2010.

[2] J. C. Buzby and J. Hyman, "Total and per capita value of food loss in the United States," *Food Policy*, vol. 37, no. 5, pp. 561–570, 2012.

[3] S. D. Porter, D. S. Reay, P. Higgins, and E. Bomberg, "A half-century of production-phase greenhouse gas emissions from food loss & waste in the global food supply chain," *The Science of the Total Environment*, vol. 571, no. 1, pp. 721–729, 2016.

[4] C. Mena, B. Adenso-Diaz, and O. Yurt, "The causes of food waste in the supplier-retailer interface: e," *Resources, Conservation and Recycling*, vol. 55, no. 6, pp. 648–658, 2011.

[5] L. S. Kantor, K. Lipton, A. Manchester, and V. Oliveira, "Estimating and addressing America's food losses," *Food Review*, vol. 20, no. 1, pp. 2–12, 1997.

[6] S. Hegde, J. S. Lodge, and T. A. Trabold, "Characteristics of food processing wastes and their use in sustainable alcohol production," *Renewable and Sustainable Energy Reviews*, vol. 81, pp. 510–523, 2018.

[7] T. I. J. Dugmore, J. H. Clark, J. Bustamante, J. A. Houghton, and A. S. Matharu, "Valorisation of biowastes for the production of green materials using chemical methods," *Topics in Current Chemistry*, vol. 375, no. 2, p. 46, 2017.

[8] K. Kumar, A. N. Yadav, and V. Kumar, "Food waste: a potential bioresource for extraction of nutraceuticals and bioactive compounds," *Bioresources and Bioprocessing*, vol. 4, no. 18, 2017.

[9] N. Alok Sagar, S. Pareek, S. Sharma, M. Elhadi, and M. G. Lobo, *Fruit and Vegetable Waste: Bioactive Compounds, Their Extraction, and Possible Utilization*, vol. 17, no. 3, pp. 512–531, 2018.

[10] K. Roesel, *Smallholder Pork: Contributions to Food and Nutrition Security,Encyclopedia of Food Security and Sustainability*, pp. 299–309, Elsevier, Amsterdam, Netherlands, 2019.

[11] M. He, M. K. Alam, H. Liu et al., "Textile waste derived cellulose based composite aerogel for efficient solar steam generation," *Composites Communications*, vol. 28, Article ID 100936, 2021.

[12] V. Pandiyarasan, J. Archana, A. Pavithra et al., "Hydrothermal growth of reduced graphene oxide on cotton fabric for enhanced ultraviolet protection applications," *Materials Letters*, vol. 188, pp. 123–126, 2017.

[13] Y. Wang, Y. Zhang, M. Polk, S. Kumar, and J. Muzzy, *Recycling of Carpet and Textile Fibers in "Plastics and the Environment: A Handbook*, A. L. Andrady, Ed., John Wiley & Sons, Hoboken, NJ, USA, 2003.

[14] S. M. Subramanian, *"Assessing the Environmental Impact of Textiles and the Clothing Supply Chain" Elsevier*, Woodhead Publishing, Sawston, UK, 20140.

[15] T. Budtova and P. Navard, "Cellulose in NaOH-water based solvents: a review," *Cellulose*, vol. 23, no. 1, pp. 5–55, 2016.

[16] H. P. S. Abdul Khalil, A. H. Bhat, and A. F. Ireana Yusra, "Green composites from sustainable cellulose nanofibrils: a review," *Carbohydrate Polymers*, vol. 87, no. 2, pp. 963–979, 2012.

[17] B. Medronho and B. Lindman, "Brief overview on cellulose dissolution/regeneration interactions and mechanisms," *Advances in Colloid and Interface Science*, vol. 222, pp. 502–508, 2015.

[18] W Liu, S. Liu, L. Tian, T. Liu, J. Zhang, and H. Liu, "Eco-friendly post-consumer cotton waste recycling for regenerated cellulose fibers," *Carbohydrate Polymers*, vol. 206, 2018.

[19] S. Asaadi, M. Hummel, S. Hellsten et al., "Renewable high-performance fibers from the chemical recycling of cotton waste utilizing an ionic liquid," *ChemSusChem*, vol. 9, no. 22, pp. 3250–3258, 2016.

[20] H. Bidgoli, A. Zamani, A. Jeihanipour, and M. J. Taherzadeh, "Preparation of carboxymethyl cellulose superabsorbents from waste textiles," *Fibers and Polymers*, vol. 15, no. 3, pp. 431–436, 2014.

[21] J. Cai and L. Zhang, "Rapid dissolution of cellulose in LiOH/urea and NaOH/urea aqueous solutions," *Macromolecular Bioscience*, vol. 5, no. 6, pp. 539–548, 2005.

[22] R. De Silva and N. Byrne, "Utilization of cotton waste for regenerated cellulose fibres: influence of degree of polymerization on mechanical properties," *Carbohydrate Polymers*, vol. 174, pp. 89–94, 2017.

[23] J. Poore and T. Nemecek, "Reducing food's environmental impacts through producers and consumers," *Science*, vol. 360, no. 6392, pp. 987–992, 2018.

[24] S. Huda, N. Reddy, D. Karst, W. Xu, W. Yang, and Y. Yang, "Nontraditional biofibers for A new textile industry," *Journal of Biobased Materials and Bioenergy*, vol. 1, no. 2, pp. 177–190, 2007.

[25] X. Chen, J. Yu, Z. Zhang, and C. Lu, "Study on structure and thermal stability properties of cellulose fibers from rice straw," *Carbohydrate Polymers*, vol. 85, no. 1, pp. 245–250, 2011.

[26] R. Dungani, M. Karina, A. Sulaeman, D. Hermawan, and A Haduyane, "Agricultural waste fibers towards

sustainability and advanced utilization: a review," *Asian Journal of Plant Sciences*, vol. 15, no. 1, pp. 42–55, 2016.

[27] N. Reddy and Y. Yang, "Natural cellulose fibers from soybean straw," *Bioresource Technology*, vol. 100, pp. 3593–3598, 2009.

[28] J. E. McGrath, M. A. Hickner, and R. Höfer, "Introduction," *Polymer Science: A Comprehensive Reference*, Elsevier, Amsterdam, Netherlands, pp. 1–3, 2012.

[29] E. B. Crowling and W. Brown, "Cellulases and their application," in *Advances in Chemistry Series*, R. F. Gould, Ed., American. Chemical. Soc. Publications, Washington, DC, USA, 1969.

[30] G. H. Emert, E. K. Gum, J. A. Lang, T. H. Liu, and R. D. Brown Jr., *Food Related Enzymes Advances in chem. Ser.*American. Chemical. Soc. Publications, Washington, DC, USA, 1974.

[31] H. Sihtola and L. Neimo, *Symposium on Enxymatic Hydrolysis of Cellulose*, Finland: SITRA", Finland, 1975.

[32] J. Pérez, J. Muñoz-Dorado, T. De la Rubia, and J. Martínez, "Biodegradation and biological treatments of cellulose, hemicellulose and lignin: an overview," *International Microbiology: The Official Journal of the Spanish Society for Microbiology*, vol. 5, no. 2, pp. 53–63, 2002.

[33] A. G. Norman, *Noncellulosic Carbohydrates*, Interscience Publishers Inc", 1954.

[34] R. L. Whistler and E. L. Richards, *Hemicelluloses, the Carbohydrates: Chemistry and Biochemistry*, Academic Press, New York, NY, USA, 1970.

[35] M. R. Vignon, L. Heux, M.-E. Malainine, and M. Mahrouz, "Arabinan-cellulose composite in Opuntia ficus-indica prickly pear spines," *Carbohydrate Research*, vol. 339, no. 1, pp. 123–131, 2004.

[36] S. V. Joshi, L. T. Drzal, A. K. Mohanty, and S. Arora, "Are natural fiber composites environmentally superior to glass fiber reinforced composites," *Composites Part A: Applied Science and Manufacturing*, vol. 35, no. 3, pp. 371–376, 2004.

[37] F. Namvar, M. Jawaid, P. Tahir et al., "Potential use of plant fibres and their composites for biomedical applications," *Biores*, vol. 9, no. 3, pp. 5688–5706, 2011.

[38] D. Trache, A. F. Tarchoun, M. Derradji et al., "Nanocellulose: from fundamentals to advanced applications," *Frontiers of Chemistry*, vol. 8, no. 392, 2020.

[39] K. L. Pickering, *Properties and Performance of Natural-Fibre Composites*, Woodhead Publishing Ltd", Swaston, UK, 2008.

[40] M. Mandels, L. Hontz, and J. Nystrom, "Enzymatic hydrolysis of waste cellulose," *Biotechnology and Bioengineering*, vol. 16, no. 11, pp. 1471–1493, 1974.

[41] M. A. Millet, A. J. Baker, and L. D. Satter, "Pretreatments to enhance chemical, enzymatic, and microbiological attack of cellulosic materials," *Biotechnology & Bioengineering Symposium*, vol. 5, no. 1, pp. 193–219, 1975.

[42] C. E. Dunlap, J. Thomson, and L. C. Chang, "Treatment processes to increase cellulose digestibility, aichesymp," *Serif*, vol. 72, no. 158, pp. 58–63, 1976.

[43] T. Tassinari and C. Macy, "Differential speed two roll mill pretreatment of cellulosic materials for enzymatic hydrolysis," *Biotechnology and Bioengineering*, vol. 19, no. 9, pp. 1321–1330, 1977.

[44] M. M. Chang, T. Y. C. Chou, and G. T. Tsao, "Structure, pretreatment and hydrolysis of cellulose," *Bioenergy*, vol. 20, no. 1, pp. 15–42, 1981.

[45] N. Siddiqui, R. H. Mills, D. J. Gardner, and D Bousfield, "Production and characterization of cellulose nanofibers from wood pulp," *Journal of Adhesion Science and Technology*, vol. 25, no. 6-7, pp. 709–721, 2011.

[46] F. Fahma, S. Iwamoto, N. Hori, T. Iwata, and A. Takemura, "Isolation, preparation, and characterization of nanofibers from oil palm empty-fruit-bunch (OPEFB)," *Cellulose*, vol. 17, no. 5, pp. 977–985, 2010.

[47] M. S. Nazir, B. A. Wahjoedi, A. W. Yussof, and M. A. Abdullah, "Eco-friendly extraction and characterization of cellulose from oil palm empty fruit bunches," *Biores"*, vol. 8, no. 2, pp. 2161–2172, 2013.

[48] T. Prakongpan, A. Nitithamyong, and P. Luangpituksa, "Extraction and application of dietary fiber and cellulose from pineapple cores," *Journal of Food Science*, vol. 67, no. 4, pp. 1308–1313, 2002.

[49] E. Abraham, B. Deepa, L. A. Pothan et al., "Extraction of nanocellulose fibrils from lignocellulosic fibres: a novel approach," *Carbohydrate Polymers*, vol. 86, no. 4, pp. 1468–1475, 2011.

[50] M. Jawaid and H. Khalil, "Effect of layering pattern on the dynamic mechanical properties and thermal degradation of oil Palm-Jute Fibers reinforced epoxy hybrid composite," *Bioresources"*, vol. 6, no. 3, pp. 2309–2322, 2011.

[51] K. Kucharska, P. Rybarczyk, I. Hołowacz, R. Łukajtis, M. Glinka, and M. Kamiński, "Pretreatment of lignocellulosic materials as substrates for fermentation processes," *Molecules*, vol. 23, no. 11, p. 2937, 2018.

[52] A. Karapatsia, I. Pappas, G. Penloglou, O. Kotrotsiou, and C. Kiparissides, "Optimization of dilute acid pretreatment and enzymatic hydrolysis of phalaris aquatica L. Lignocellulosic biomass in batch and fed-batch processes," *BioEnergy Research*, vol. 10, no. 1, pp. 225–236, 2017.

[53] J. Xu, J. J. Cheng, R. R. Sharma-Shivappa, and J. C. Burns, "Sodium hydroxide pretreatment of switchgrass for ethanol production," *Energy & Fuels*, vol. 24, no. 3, pp. 2113–2119, 2010.

[54] Q. Schmetz, H. Teramura, K. Morita et al., "Versatility of a dilute acid/butanol pretreatment investigated on various lignocellulosic biomasses to produce lignin, monosaccharides and cellulose in distinct phases," *ACS Sustainable Chemistry & Engineering*, vol. 7, no. 13, pp. 11069–11079, 2019.

[55] Q. Yu, L. Qin, Y. Liu et al., "In situ deep eutectic solvent pretreatment to improve lignin removal from garden wastes and enhance production of bio-methane and microbial lipids," *Bioresource Technology*, vol. 271, pp. 210–217, 2019.

[56] M. M'Arimi, C. Mecha, A. Kiprop, and RamkatR, "Recent trends in applications of advanced oxidation processes (aops) in bioenergy production: Review," *Renewable and Sustainable Energy Reviews*, vol. 121, pp. 109–669, 2020.

[57] R. K DasariR and R. Eric Berson, "The effect of particle size on hydrolysis reaction rates and rheological properties in cellulosic slurries," *Applied Biochemistry and Biotechnology*, vol. 137-140, no. 1-12, pp. 289–299, 2007.

[58] A. Licari, F. Monlau, A. Solhy, P. Buche, and A. Barakat, "Comparison of various milling modes combined to the enzymatic hydrolysis of lignocellulosic biomass for bioenergy production: glucose yield and energy efficiency," *Energy*, vol. 102, pp. 335–342, 2016.

[59] M. T. Holtzapple, J.-H. Jun, G. Ashok, S. L. Patibandla, and B. E. Dale, "The ammonia freeze explosion (AFEX) process," *Applied Biochemistry and Biotechnology*, vol. 28, no. 1, pp. 59–74, 1991.

[60] D Kim, "Physico-chemical conversion of lignocellulose: inhibitor effects and detoxification strategies: a mini review," *Molecules*, vol. 23, no. 2, 2018.

[61] H. H. Yoon, "Pretreatment of lignocellulosic biomass by autohydrolysis and aqueous ammonia percolation," *Korean Journal of Chemical Engineering*, vol. 15, no. 6, pp. 631–636, 1998.

[62] J. A. Rollin, Z. Zhu, N. Sathitsuksanoh, and Y.-H. P Zhang, "Increasing cellulose accessibility is more important than removing lignin: a comparison of cellulose solvent-based lignocellulose fractionation and soaking in aqueous ammonia," *Biotechnology and Bioengineering*, vol. 108, no. 1, pp. 22–30, 2011.

[63] V. Chaturvedi and P. Verma, "An overview of key pretreatment processes employed for bioconversion of lignocellulosic biomass into biofuels and value added products," *3 Biotech*, vol. 3, no. 5, pp. 415–431, 2013.

[64] A. Langsdorf, M. Volkmar, D. Holtmann, and R. Ulber, "Material utilization of green waste: a review on potential valorization methods," *Bioresources and Bioprocessing*, vol. 8, no. 1, p. 19, 2021.

[65] H. Rabemanolontsoa and S. Saka, "Various pretreatments of lignocellulosics," *Bioresource Technology*, vol. 199, pp. 83–91, 2016.

[66] Z. Kerem, D. Friesem, and Y. Hadar, "Lignocellulose degradation during solid-state fermentation: pleurotus ostreatus versus phanerochaete chrysosporium," *Applied and Environmental Microbiology*, vol. 58, no. 4, pp. 1121–1127, 1992.

[67] D. E. Akin, L. L. Rigsby, A. Sethuraman, W. H. Morrison, G. R. Gamble, and K. E. Eriksson, "Alterations in structure, chemistry, and biodegradability of grass lignocellulose treated with the white rot fungi Ceriporiopsis subvermispora and Cyathus stercoreus," *Applied and Environmental Microbiology*, vol. 61, no. 4, pp. 1591–1598, 1995.

[68] A. Gutiérrez, J. Rencoret, E. M. Cadena et al., "Demonstration of laccase-based removal of lignin from wood and non-wood plant feedstocks," *Bioresource Technology*, vol. 119, pp. 114–122, 2012.

[69] E. A. Bayer, J.-P. Belaich, Y. Shoham, and R. Lamed, "The cellulosomes: multienzyme machines for degradation of plant cell wall polysaccharides," *Annual Review of Microbiology*, vol. 58, no. 1, pp. 521–554, 2004.

[70] P. Prawitwong, R. Waeonukul, C. Tachaapaikoon et al., "Direct glucose production from lignocellulose using Clostridium thermocellum cultures supplemented with a thermostable β-glucosidase," *Biotechnology for Biofuels*, vol. 6, no. 1, p. 184, 2013.

[71] R. Sindhu, P. Binod, and A. Pandey, "Biological pretreatment of lignocellulosic biomass—an overview," *Bioresource Technology*, vol. 199, pp. 76–82, 2016.

[72] P.R PatchiyaPhanthong, X. Hao, G. Xu, and G. Guan, "Nanocellulose: extraction and application," *Carbon Resources Conversion*, vol. 1, no. Issue 1, pp. 32–43, 2018.

[73] G Gupta, S Kumar, Lignocellulosic biomass for the synthesis of nanocellulose and its eco-friendly advanced applications," *Frontiers of Chemistry*, vol. 8, p. 1203, 2020.

[74] P. Lu and Y.-L. Hsieh, "Preparation and properties of cellulose nanocrystals: rods, spheres, and network," *Carbohydrate Polymers*, vol. 82, no. 2, pp. 329–336, 2010.

[75] A. Palme, H. Theliander, and H. Brelid, "Acid hydrolysis of cellulosic fibres: comparison of bleached kraft pulp, dissolving pulps and cotton textile cellulose," *Carbohydrate Polymers*, vol. 136, pp. 1281–1287, 2016.

[76] Z. Wang, Z. Yao, J. Zhou, and Y. Zhang, "Reuse of waste cotton cloth for the extraction of cellulose nanocrystals," *Carbohydrate Polymers*, vol. 157, pp. 945–952, 2017.

[77] R. J. Moon, A. Martini, J. Nairn, J. Simonsen, and J. Youngblood, "Cellulose nanomaterials review: structure, properties and nanocomposites," *Chemical Society Reviews*, vol. 40, no. 7, pp. 3941–3994, 2011.

[78] S. Maiti, J. Jayaramudu, K. Das et al., "Preparation and characterization of nano-cellulose with new shape from different precursor," *Carbohydrate Polymers*, vol. 98, no. 1, pp. 562–567, 2013.

[79] O. Nechyporchuk, M. N. Belgacem, and J. Bras, "Production of cellulose nanofibrils: a review of recent advances," *Industrial Crops and Products*, vol. 93, pp. 2–25, 2016.

[80] M. Moniruzzaman and T. Ono, "Separation and characterization of cellulose fibers from cypress wood treated with ionic liquid prior to laccase treatment," *Bioresource Technology*, vol. 127, pp. 132–137, 2013.

[81] H. P. S. Abdul Khalil, Y. Davoudpour, M. N. Islam et al., "Production and modification of nanofibrillated cellulose using various mechanical processes: a review," *Carbohydrate Polymers*, vol. 99, pp. 649–665, 2014.

[82] Y. Wang, X. Wei, J. Li, Q. Wang, F. Wang, and L. Kong, "Homogeneous isolation of nanocellulose from cotton cellulose by high pressure homogenization," *Journal of Materials Science and Chemical Engineering*, vol. 01, no. 05, pp. 49–52, 2013.

[83] L. Tang, B. Huang, Q. Lu et al., "Ultrasonication-assisted manufacture of cellulose nanocrystals esterified with acetic acid," *Bioresource Technology*, vol. 127, pp. 100–105, 2013.

[84] R. Avolio, I. Bonadies, D. Capitani, M. E. Errico, G. Gentile, and M. Avella, "A multitechnique approach to assess the effect of ball milling on cellulose," *Carbohydrate Polymers*, vol. 87, pp. 265–273, 2012.

[85] M. Rajinipriya, M. Nagalakshmaiah, M. Robert, and S. Elkoun, "Importance of agricultural and industrial waste in the field of nanocellulose and recent industrial developments of wood based nanocellulose: a review," *ACS Sustainable Chemistry & Engineering*, vol. 6, no. 3, pp. 2807–2828, 2018.

[86] B. Singh and M. Gupta, "Natural fiber composites for building applications," in *Natural Fibers, Biopolymers and Biocomposites*, A. K. Mohanty, M. Misra, and L. T. Drzal, Eds., CRC Press, Boca Raton, FL, USA, pp. 261–287, 2005.

[87] S. Acharya, P. Mishra, and S Mehar, "Effect of surface treatment on the mechanical properties of bagasse fiber reinforced polymer composite," *Bioresources*, vol. 6, no. 3, pp. 3155–3165, 2011.

[88] D. Verma, P. C. Gope, M. K. Maheshwari, and R. K. Sharma, "Bagasse fiber composites-A review," *Journal of Materials and Environmental Science*, vol. 3, no. 6, pp. 1079–1092, 2012.

[89] S. González-García, G. Feijoo, C. Heathcote, A. Kandelbauer, and M. T. Moreira, "Environmental assessment of green hardboard production coupled with a laccase activated system," *Journal of Cleaner Production*, vol. 19, no. 5, pp. 445–453, 2011.

[90] R. Yevich and J. Logan, "An assessment of biofuel use and burning of agricultural waste in the developing world," *Global Biogeochemical Cycles*, vol. 17, no. 4, p. 1095, 2003.

[91] A. K. Steve and K. E. D. Sumanasiri, "Development of natural fiber composite in Papua New Guinea (PNG)," *Innovation and Technology Transfer*, vol. 2, no. 1, pp. 123–129, 2011.

[92] H. P. S. Abdul Khalil, M. Siti Alwani, R. Ridzuan, H. Kamarudin, and A. Khairul, "Chemical composition,

morphological characteristics, and cell wall structure of Malaysian oil palm fibers," *Polymer - Plastics Technology & Engineering*, vol. 47, no. 3, pp. 273–280, 2008.

[93] A. C. Soh, C. K. Wong, Y. W. Ho, and C. W. Choong, "Oil palm," in *Oil Crops*, pp. 333–367, Springer, New York, NY, USA, 2009.

[94] M. A. N. Izani, M. T. Paridah, A. A. Astimar, M. Y. M. Nor, and U. M. K Anwar, "Mechanical and dimensional stability properties of medium-density fibreboard produced from treated oil palm empty fruit bunch," *Journal of Applied Sciences*, vol. 12, no. 6, pp. 561–567, 2012.

[95] K. Van de Velde and P. Kiekens, "Thermoplastic pultrusion of natural fibre reinforced composites," *Composite Structures*, vol. 54, no. 2-3, pp. 355–360, 2001.

[96] M. A. Azman, M. R. M. Asyraf, A. Khalina et al., "Natural fiber reinforced composite material for product design: a short review," *Polymers*, vol. 13, no. 12, p. 1917, 2021.

[97] J. Holbery and D. Houston, "Natural-fiber-reinforced polymer composites in automotive applications," *Journal of the Minerals Metals & Materials Society*, vol. 58, no. 11, pp. 80–86, 2006.

[98] K. K. Ikpambese, D. Gundu, and L. T. Tuleun, "Evaluation of palm kernel fibers (pkfs) for production of asbestos-free automotive brake pads," *Journal of King Saud University - Engineering Sciences*, vol. 28, no. 1, pp. 110–118, 2016.

[99] B. C. Suddell and W. J. Evans, "Natural fiber composites in automotive applications," in *Natural Fibers, Biopolymers and Biocomposites*, A. K. Mohanty, M. Misra, and L. T. Drzal, Eds., CRC Press, Boca Raton, FL, USA, pp. 231–259, 2005.

[100] A. K. Bledzki, O. Faruk, and V. E Sperber, "Cars from biofibres," *Macromolecular Materials and Engineering*, vol. 291, no. 5, pp. 449–457, 2006.

[101] S.-h. Hsu and Y.-C Kao, "Biocompatibility of poly(carbonate urethane)s with various degrees of nanophase separation," *Macromolecular Bioscience*, vol. 5, no. 3, pp. 246–253, 2005.

[102] L. E. Millon, H. Mohammadi, and W. K. Wan, "Anisotropic polyvinyl alcohol hydrogel for cardiovascular applications," *Journal of Biomedical Materials Research Part B: Applied Biomaterials*, vol. 79B, no. 2, pp. 305–311, 2006.

[103] D. Macocinschi, D. Filip, S. Vlad, M. Cristea, V. Musteata, and S. Ibanescu, "Thermal, dynamic mechanical, and dielectric analyses of some polyurethane biocomposites," *Journal of Biomaterials Applications*, vol. 27, no. 2, pp. 119–129, 2012.

[104] V. Musteata, D. Filip, S. Vlad, and D Macocinschi, "Dielectric relaxation of polyurethane biocomposites," *Optoelectronics and Advanced Materials—Rapid Communications"*, vol. 4, no. 8, pp. 1187–1192, 2010.

[105] N. Grishkewich, N. Mohammed, J. Tang, and K. C. Tam, "Recent advances in the application of cellulose nanocrystals," *Current Opinion in Colloid & Interface Science*, vol. 29, pp. 32–45, 2017.

[106] X. Yang, E. Bakaic, T. Hoare, and E. D. Cranston, "Injectable polysaccharide hydrogels reinforced with cellulose nanocrystals: morphology, rheology, degradation, and cytotoxicity," *Biomacromolecules*, vol. 14, no. 12, pp. 4447–4455, 2013.

[107] K. Wang, K. C. Nune, and R. D. K. Misra, "The functional response of alginate-gelatin-nanocrystalline cellulose injectable hydrogels toward delivery of cells and bioactive molecules," *Acta Biomaterialia*, vol. 36, pp. 143–151, 2016.

[108] E. H. Fragal, T. S. P. Cellet, V. H. Fragal et al., "Hybrid materials for bone tissue engineering from biomimetic growth of hydroxiapatite on cellulose nanowhiskers," *Carbohydrate Polymers*, vol. 152, pp. 734–746, 2016.

[109] E. E. Brown, D. Hu, N. Abu Lail, and X. Zhang, "Potential of nanocrystalline cellulose-fibrin nanocomposites for artificial vascular graft applications," *Biomacromolecules*, vol. 14, no. 4, pp. 1063–1071, 2013.

[110] V. Mohanta, G. Madras, and S. Patil, "Layer-by-Layer assembled thin films and microcapsules of nanocrystalline cellulose for hydrophobic drug delivery," *ACS Applied Materials & Interfaces*, vol. 6, no. 22, pp. 20093–20101, 2014.

[111] Z. Wang, C. Crandall, V. L. Prautzsch, R. Sahadevan, T. J. Menkhaus, and H. Fong, "Electrospun regenerated cellulose nanofiber membranes surface-grafted with water-insoluble poly(HEMA) or water-soluble poly(AAS) chains via the ATRP method for ultrafiltration of water," *ACS Applied Materials & Interfaces*, vol. 9, no. 4, pp. 4272–4278, 2017.

[112] N. Lin, A. Geze, D. Wouessidjewe, J. Huang, and A. Dufresne, "Biocompatible double-mebrane hydrogels from cationic cellulose nanocrystals and anionic alginate as complexing drugs codelivery," *ACS Applied Materials and Interfaces*, vol. 8, no. 11, 2016.

[113] S. Dong, H. J. Cho, Y. W. Lee, and M. Roman, "Synthesis and cellular uptake of folic acid-conjugated cellulose nanocrystals for cancer targeting," *Biomacromolecules*, vol. 15, no. 5, pp. 1560–1567, 2014.

[114] H. Hu, X.-J. Hou, X.-C. Wang, J.-J. Nie, Q. Cai, and F.-J. Xu, "Gold nanoparticle-conjugated heterogeneous polymer brush-wrapped cellulose nanocrystals prepared by combining different controllable polymerization techniques for theranostic applications," *Polymer Chemistry*, vol. 7, no. 18, pp. 3107–3116, 2016.

[115] E BentolhodaAmanzadi, P. M. GholamrezaHassanzadeh, SafiehBoroumand, M. Abdollahi, A. Amir Hossein, and M. Reza Faridi, "Chitosan-based layered nanofibers loaded with herbal extract as wound-dressing materials on wound model studies," vol. 9, pp. 3979–3986, 2019.

[116] M. Z. Rahman, "Mechanical and damping performances of flax fibre composites–a review," *Composites Part C: Open Access*, vol. 4, Article ID 100081, 2021.

[117] S. Naz, J. S. Ali, and M. Zia, "Nanocellulose isolation characterization and applications: a journey from non-remedial to biomedical claims," *Bio-Design and Manufacturing*, vol. 2, no. 3, pp. 187–212, 2019.

[118] H. Golmohammadi, E. Morales-Narváez, T. Naghdi, and A. Merkoçi, "Nanocellulose in sensing and biosensing," *Chemistry of Materials*, vol. 29, no. 13, pp. 5426–5446, 2017.

[119] L. Colombo, L. Zoia, M. B. Violatto et al., "Organ distribution and bone tropism of cellulose nanocrystals in living mice," *Biomacromolecules*, vol. 16, no. 9, pp. 2862–2871, 2015.

[120] C. Carrión, M. Abad, A. Maquieira, R. Puchades, F. Fornes, and V. Noguera, "Leaching of composts from agricultural wastes to prepare nursery potting media," *Acta Horticulturae*, vol. 697, pp. 117–112, 2005.

[121] L. Levitan and A. Barros, "Recycling agricultural plastics in New York state," in *A Research Report Prepared for the Environmental Risk Analysis Program"*Cornell University, Ithaca, NY, USA, 2003.

[122] J. Treinytea, V. Grazulevicienea, D. Bridziuviene, and J. Svediene, "Properties and behaviour of starch and rapeseed cake based composites in horticultural applications," *Estonian Journal of Ecology*, vol. 63, no. 1, pp. 15–27, 2014.

[123] J. C. C. Welleman, "Fytocell, an increasingly popular substrate," *Acta Horticulturae*, vol. 697, no. 697, pp. 195–198, 2005.

[124] T. Robinson, "Containers evolve to satisfy industry, retailer, and consumer needs," *Gmpro*, vol. 28, no. 1, pp. 35–40, 2008.

[125] A. Abaecherli and V. I. Popa, "Lignin in crop cultivations and bioremediation," *Environmental Engineering and Management Journal"*, vol. 4, no. 3, pp. 273–292, 2005.

[126] P. Nechita, "Use of recycled cellulose fibers to obtain sustainable products for bioeconomy applications," in *Generation, Development and Modifications of Natural Fibers*IntechOpen, London, UK, 2019.

[127] M. Maljanen, B. D. Sigurdsson, J. Guðmundsson, H. Óskarsson, J. T. Huttunen, and P. J. Martikainen, "Greenhouse gas balances of managed peatlands in the Nordic countries - present knowledge and gaps," *Biogeosciences*, vol. 7, no. 9, pp. 2711–2738, 2010.

[128] N. Bhardwaj and S. C. Kundu, "Electrospinning: a fascinating fiber fabrication technique," *Biotechnology Advances*, vol. 28, no. 3, pp. 325–347, 2010.

[129] T. Subbiah, G. S. Bhat, R. W. Tock, S. Parameswaran, and S. S. Ramkumar, "Electrospinning of nanofibers," *Journal of Applied Polymer Science*, vol. 96, no. 2, pp. 557–569, 2005.

[130] Z. Ma and S. Ramakrishna, "Electrospun regenerated cellulose nanofiber affinity membrane functionalized with protein A/G for igg purification," *Journal of Membrane Science*, vol. 319, no. 1-2, pp. 23–28, 2008.

[131] H. Ma, C. Burger, B. S. Hsiao, and B. Chu, "Fabrication and characterization of cellulose nanofiber based thin-film nanofibrous composite membranes," *Journal of Membrane Science*, vol. 454, pp. 272–282, 2014.

[132] P. Liu, K. Oksman, and A. P. Mathew, "Surface adsorption and self-assembly of Cu(II) ions on TEMPO-oxidized cellulose nanofibers in aqueous media," *Journal of Colloid and Interface Science*, vol. 464, pp. 175–182, 2016.

[133] H. Sai, L. Xing, J. Xiang et al., "Flexible aerogels based on an interpenetrating network of bacterial cellulose and silica by a non-supercritical drying process," *Journal of Materials Chemistry*, vol. 1, no. 27, pp. 7963–7970, 2013.

[134] S. S. Shekhawat, M. KulshreshthaN, and A. B. Gupta, *1—Tertiary Treatment Technologies for Removal of Antibiotics and Antibiotic Resistance Genes from Wastewater, Removal of Toxic Pollutants through Microbiological and Tertiary Treatment*, Elsevier, Amsterdam, Netherlands, 2020.

[135] J. Anu-Bhushani and C. Anandharamakrishnan, "Electrospinning and electrospraying techniques: potential food based applications," *Trends in Food Science & Technology*, vol. 38, no. 21– 3, 2014.

[136] A. Vega-Lugo and L. Lim, "Controlled release of allyl isothiocyanate using soy protein and poly (lactic acid) electrospun fibers," *Food Research International*, vol. 42, no. – 40, p. 933, 2009.

[137] J. Hosokawa, M. Nishiyama, K. Yoshihara, T. Kubo, and A. Terabe, "Reaction between chitosan and cellulose on biodegradable composite film formation," *Industrial & Engineering Chemistry Research*, vol. 30, no. 4, pp. 788–792, 1991.

[138] R. Andrade, O. Skurtys, and F. Osorio, "Drop impact of gelatin coating formulated with cellulose nanofibers on banana and eggplant epicarps," *Lebensmittel-Wissenschaft und -Technologie- Food Science and Technology*, vol. 61, no. 2, pp. 422–429, 2015.

[139] H. M. C. d. Azeredo, "Nanocomposites for food packaging applications," *Food Research International*, vol. 42, no. 9, pp. 1240–1253, 2009.

[140] F. Tamjidi, M. Shahedi, J. Varshosaz, and A. Nasirpour, "Design and characterization of astaxanthin-loaded nanostructured lipid carriers," *Innovative Food Science & Emerging Technologies*, vol. 26, pp. 366–374, 2014.

[141] M. Fathi, Á. Martín, and D. J. McClements, "Nanoencapsulation of food ingredients using carbohydrate based delivery systems," *Trends in Food Science & Technology*, vol. 39, no. 1, pp. 18–39, 2014.

[142] F. Kayaci and T. Uyar, "Encapsulation of vanillin/cyclodextrin inclusion complex in electrospun polyvinyl alcohol (PVA) nanowebs: prolonged shelf-life and high temperature stability of vanillin," *Food Chemistry*, vol. 133, 2012.

[143] A. V. Samrot, U. Burman, S. A. Philip, N. Shobana, and K. Chandrasekaran, "Synthesis of curcumin loaded polymeric nanoparticles from crab shell derived chitosan for drug delivery," *Informatics in Medicine Unlocked*, vol. 10, pp. 159–182, 2018.

[144] A. V. Samrot, Akanksha, T. Jahnavi et al., "Chelators influenced synthesis of chitosan-carboxymethyl cellulose microparticles for controlled drug delivery," *Applied Nanoscience*, vol. 6, no. 8, pp. 1219–1231, 2016.

Hindawi
Advances in Materials Science and Engineering
Volume 2022, Article ID 8410061, 10 pages
https://doi.org/10.1155/2022/8410061

Research Article

Wire Electrical Discharge Machining Characteristics of Al-4.4 Mg-0.7 Mn-0.15 Cr-12 wt.% MoO_3 Composites Using Taguchi Technique

M. Meignanamoorthy,[1] T. Anandaraj,[2] M. Ravichandran,[1] V. Mohanavel,[3] S. Sathish,[4] S.M. Sivagami,[5] Wadi B Alonazi,[6] Sami Al Obaid,[7] Saleh Alfarraj,[8] Kaliannan Durairaj,[9] and Manikandan Ganesan[10]

[1]*Department of Mechanical Engineering, K. Ramakrishnan College of Engineering, Trichy 621112, Tamilnadu, India*
[2]*Department of Mechanical Engineering, Velalar College of Engineering and Technology, Erode 602105, Tamilnadu, India*
[3]*Centre for Materials Engineering and Regenerative Medicine, Bharath Institute of Higher Education and Research, Chennai 600073, Tamilnadu, India*
[4]*Department of Mechanical Engineering, Sri Ramakrishna Engineering College, Coimbatore 641022, Tamilnadu, India*
[5]*Department of Mechanical Engineering, Alagappa Chettiar Government College of Engineering and Technology, Trichy 630004, Tamilnadu, India*
[6]*Health Administration Department, College of Business Administration, King Saud University, P. O. Box 71115, Riyadh 11587, Saudi Arabia*
[7]*Department of Botany and Microbiology, College of Science, King Saud University, P. O. Box -2455, Riyadh -11451, Saudi Arabia*
[8]*Zoology Department, College of Science, King Saud University, Riyadh 11451, Saudi Arabia*
[9]*Zoonosis Research Center, School of Medicine, Wonkwang University, Republic of Korea*
[10]*Department of Electromechanical Engineering, Faculty of Manufacturing Institute of Technology, Hawassa University, Hawassa, Ethiopia*

Correspondence should be addressed to Manikandan Ganesan; mani301090@hu.edu.et

Received 2 September 2021; Revised 19 January 2022; Accepted 20 January 2022; Published 9 March 2022

Academic Editor: Qian Chen

This research put forth an effort to produce AA5083 (Al-4.4 Mg-0.7 Mn-0.15 Cr)-12 wt.% MoO_3 composite via the stir casting (SC) process, and the effects of process parameters such as pulse on time (T_{ON}), pulse off time (T_{OFF}), and current (I) on the wire electrical discharge machining (WEDM) characteristics such as metal removal rate (MRR) and surface roughness (SR) were investigated using the Taguchi method. Numerous unconventional machining methods are accessible to machine MMCs; among that, WEDM is a significant method. ANOVA was utilized to identify the suitable parameters to obtain maximum MRR and least SR. From the analysis, it is clear that T_{ON} 120 (μs), T_{OFF} 50 (μs), and I 3 (A) are the noteworthy parameters to acquire maximum MRR and T_{ON} 100 (μs), T_{OFF} 40 (μs), and I 3 (A) are the noteworthy parameters to acquire least SR. ANOVA results for MRR showed that T_{OFF} is the extreme inducing factor with the percentage contribution of 27.92% tracked by T_{ON} and I with the percentage contribution of 12.09% and 5.07%, respectively. ANOVA results for SR showed that T_{OFF} is the extreme inducing factor with the percentage contribution of 60.33% tracked by T_{OFF} and I with the percentage contribution of 12.31% and 0.33%, respectively.

1. Introduction

Composite materials exhibit better strength, good toughness, less weight, wear opposition resistance, and less cost. It has already proven its worth as a lighter-weight material for a few years, but the current challenge is to construct it in the cheapest way possible [1]. Metal matrix composites (MMCs) are a collection of materials with perception for a wide range of usages in the structural field. The properties such as lightweight, excellent strength, and opposition to wear are

needed for aeronautics and automotive sectors. MMCs are widely utilized in automotive usages such as brake parts, cylinder liners, pistons, bearing surfaces, and camshafts and aeronautics usages such as aircraft structure (major body), exhaust systems, wing and fuselage, and inner aerospace engine parts [2]. MMCs consist of a matrix as metals with some particulates as reinforcements. Despite its excellent strength, stiffness, and wear opposition, MMCs have gained rising notice in numerous engineering fields [3]. Traditional MMCs strengthened with particulates could attain good strength and improved elastic modulus with higher reinforcement content, when the ductility and toughness fall radically with the rise in the range of reinforcements because of the usual transaction amid strength and ductility [4]. Nowadays, aluminum alloy found numerous applications in Space Shuttle and automotive and aeronautics structures due to its effortlessness of operation and sensibly better mechanical properties. The untainted aluminum alloy properties may be improved by combining the utmost generally utilized particulate reinforcements [5]. Aluminum matrix composites (AMCs) are widely used in the engineering field despite their extraordinary mechanical and tribological behaviour. This leads to the growth of AMCs with each probable aluminum alloy as matrix strengthened with numerous reinforcements to attain the explicitly needed properties [6]. AMCs are lightweight materials accompanied by better electrical and thermal conductivity and good stiffness, hardness, strength, and wear opposition. Because of high fabrication costs, AMCs are deployed solitarily for armour weapons and aeronautics applications. AMCs have additional usages in automotive parts such as engine cylinder liners, disk brakes, drum brakes, and pistons [7]. Molybdenum trioxide (MoO_3) strengthens AMCs which has higher mechanical properties [8]. Concurrently due to bigger self-lubricating contact, MoO_3 improves the composite wear opposition [9]. MoO_3 has arriving widespread deliberation as a potential reinforcement for MMCs to enhance the properties [10]. Stir casting (SC) is an inexpensive method for the production of AMCs [11]. Through the SC process, fine dispersal of reinforcement with matrix could be possible [12]. SC method was extremely concerned to improve the mechanical behaviour and reinforcement of various alloy materials for strengthening of harder particles [13]. Traditional machining methods such as turning and milling are not appropriate for machining composite materials. The presence of hard abrasive and ceramic materials causes tool wear and breakage [14]. Therefore, nontraditional machining process such as WEDM is utilized to machine the composite material [15]. Machining of the smallest hole is not possible in all the nontraditional machining, but it is possible in WEDM [16]. WEDM is a feasible choice for cutting all kinds of materials, which are impossible to cut and somewhat their proposed usages need the shape of complicated profiles [17]. Furthermore, fewer burr arrangements and no residual stresses amid WEDM are the additional merits that extra emphasize its pre-eminence. With reverence to the machine utilized for performing WEDM, two variants are accessible: (i) less speed and (ii) rapid cutting machine [18]. In WEDM, the outside layer of the work material is eradicated by means of a series of sparks created amid the workpiece and electrode. The workpiece and electrode are set aside individually and are completely engrossed in dielectric fluid [19]. When machining via WEDM, electrical conductivity is the main issue for machining materials [20]. Titus et al. [21] studied the influence of WEDM process parameter on Cu-BN composites, found the optimal parameters by Taguchi grey relational analysis, and concluded that pulse $_{ON}$ and BN volume fraction were the major noteworthy parameters to acquire maximum MRR and pulse $_{ON}$ and pulse $_{OFF}$ were the major noteworthy parameters to acquire least SR. Padhi et al. [22] studied the suitable parameters for WEDM of EN-31 using a weighted sum genetic algorithm process to achieve optimum results. Agarwal et al. [23] explored the WEDM characteristics of Ni-27 Cu-3.15 Al-2 Fe-1.5 Mn super alloy and stated that pulse on time has a direct influence on CR while the pulse off time has an opposite influence. Rakesh et al. [24] analyzed the WEDM behavior of MWCNTs and concluded that the inclusion of MWCNTs significantly enhances the machining performance by increasing MRR and concurrently reducing the SR.

From the detailed literature, it has been understood that very few research work has been done by using MoO_3 as reinforcement with aluminum matrix. Hence, this research work made an effort to develop and study the WEDM behavior of Al-4.4 Mg-0.7 Mn-0.15 Cr-12 wt.% MoO_3.

2. Materials and Method

The matrix material utilized was AA5083 and MoO_3 was used as reinforcement. The percentage of alloying elements in AA5083 is Si: 0.4, Fe: 0.4, Cu: 0.1 wt, Mn: 1.0, Mg: 4.9, Zn: 0.25, Ti: 0.15, Cr: 0.25, and Al balance. The essential amount of AA5083 and MoO_3 powders was dignified by an automatic weigh measurement device. By utilizing a crucible furnace, AA5083 was liquefied at 800°C [25]. MoO_3 powders were heated at 400°C. Then, to attain the liquid stage, 12 wt.%, MoO_3 powder was included in the AA5083 matrix. The mixing was done at 30,000 rps speed for 300 seconds [26]. Amid mixing, least amount of Mg was included to increase wettability. In the end, the liquid metal was bestowed into a die to attain required sizes. The dimensions of the workpiece are $8 \times 8 \times 30$ mm. The WEDM procedure was conducted on AA5083-12 wt.% MoO_3 composite via ECOCUT WEDM. Figure 1 displays the machined sample image. The three-level process parameters, namely, T_{ON}, T_{OFF}, and I were selected as variables to investigate their influences on MRR and SR. The dimension of samples to carry out the WEDM process was $8 \times 8 \times 30$ mm. The WEDM performance standards chosen for this investigation were MRR and SR. MRR was calculated via weight difference of workpiece before and after the WEDM process by using the following formula: MRR = $(Wa - Wb)/t$, where Wa and Wb are the weights of the workpiece before and after the WEDM process and "t" is the machining time in minutes. The SR measurement on the machined surface was done via Mitutoyo surftest SJ-210.

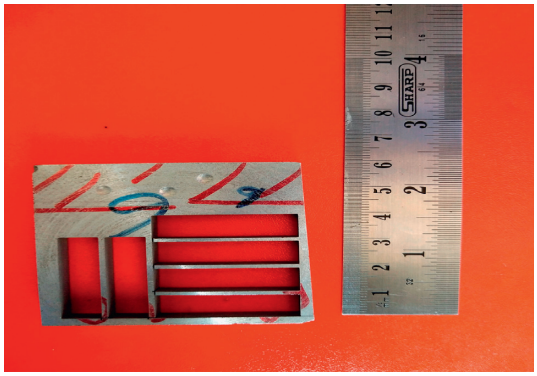

Figure 1: Wire electrical discharge machined AA5083-MoO_3 sample.

3. Results and Discussion

The effect of EDM parameters on SR and MRR was studied via the Taguchi method. The T_{ON}, T_{OFF}, and I were selected as parameters, and MRR and SR were considered as output. The parameters and levels are enumerated in Table 1 and experimental trials performed via L9 orthogonal array are enumerated in Table 2. Table 3 displays the responses and the calculated SN ratio of designed experiments. More ANOVA tests were utilized to predict the appropriate parameters.

3.1. SN Ratio Analysis for MRR and SR. The appropriate process parameter is needed to attain maximum MRR and SR. SN ratio was designed for enlargement quality characteristics of output responses. The mean SN ratios for MRR and SR are displayed in Table 3. Figures 2 and 3 display the main effect plot for SN ratios for MRR and SR. The higher MRR is achieved at T_{ON} 120 μs, T_{OFF} 50 μs, and I 3 A. From the results, it is clear that T_{OFF} is the noteworthy parameter to attain maximum MRR. The least SR is achieved at T_{ON} 100 μs, T_{OFF} 50 μs, and I 3 A. From the results, it is clear that T_{OFF} is the noteworthy parameter to attain the least SR. Current is the most influencing parameter for MRR, and for SR, it does not have much impact.

3.2. Contour Plot Analysis for MRR. Figure 4 displays the contour plots for the MRR with respect to (a) pulse off time vs. pulse on time, (b) current vs. pulse on time, and (c) current vs. pulse off time. Contour plots were generated to analyze the influence of process parameters. These contour plots can also provide more evaluation of the association amid the process parameters and response. The contour plots for MRR with respect to selected input machining parameters are displayed in Figures 4 and 5. In Figure 4(a), the dotted zone displays the MRR rate while the pulse off time and pulse on time interrelate each other. It can be understood that the pulse off time is higher for entire values of pulse on time and the higher MRR could be attained. Figure 4(b) displays the contact of current with pulse on time for the MRR. It can be clear that the current is less and the pulse on time is in maximum. Unless current is maximum, least pulse on time is adequate to attain maximum MRR.

Table 1: Parameters and levels.

S. no	T_{ON} (μs)	T_{OFF} (μs)	I (A)
1	100	40	3
2	120	50	6
3	140	60	9

Table 2: L16 orthogonal array experimental results.

Trial no.	T_{ON} (μs)	T_{OFF} (μs)	I (A)	MRR (g/min)	SR (μm)
1	100	40	3	0.043	1.364
2	100	50	6	0.169	3.621
3	100	60	9	0.075	3.373
4	100	70	12	0.104	3.81
5	120	40	6	0.028	2.447
6	120	50	3	0.194	3.614
7	120	60	12	0.178	3.468
8	120	70	9	0.135	2.268
9	140	40	9	0.162	1.908
10	140	50	12	0.069	2.669
11	140	60	3	0.129	3.224
12	140	70	6	0.019	1.916
13	160	40	12	0.042	1.853
14	160	50	9	0.107	3.831
15	160	60	6	0.126	3.434
16	160	70	3	0.055	3.518

Table 3: Mean of SN ratios for the MRR and SR.

MRR			
Level	T_{ON} (μs)	T_{OFF} (μs)	I (A)
1	−21.23	−25.43	−21.14
2	−19.42	−18.08	−24.73
3	−22.81	−18.32	−18.78
4	−22.53	−24.17	−21.35
Delta	3.39	7.35	5.95
Rank	3	1	2
SR			
Level	T_{ON} (μs)	T_{OFF} (μs)	I (A)
1	−9.013	−5.360	−8.737
2	−9.212	−10.632	−8.828
3	−7.489	−10.561	−8.738
4	−9.666	−8.826	−9.076
Delta	2.178	5.273	0.339
Rank	2	1	3

Figure 4(c) displays the contact of current and pulse off time for the MRR. Although considering the pulse off time and current, the maximum pulse off time is vital to obtain higher MRR.

The contour plot for the SR is displayed in Figure 5 with respect to (a) I vs. T_{OFF}, (b) I vs. T_{ON}, and (c) T_{OFF} vs. T_{ON}. Figure 5(a) displays the least SR while the current is in low level. Figure 5(b) displays the interface of current with pulse on time for the SR. It can be clear that if the pulse on time is less, the least SR could be attained. Figure 5(c) displays the contact of pulse off time and pulse on time for the SR. The least pulse off time and pulse on time resulted in the least SR.

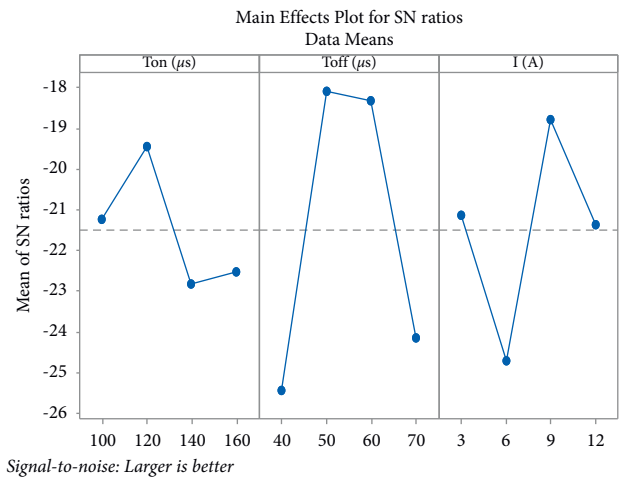

Figure 2: Means of SN ratio for MRR.

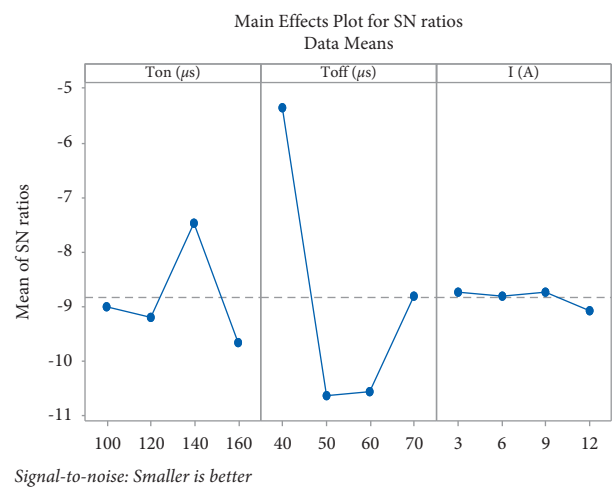

Figure 3: Means of SN ratio for SR.

3.3. ANOVA for MRR and SR. In this investigation, ANOVA was utilized to find the percentage contribution of parameters T_{ON}, T_{OFF}, and I on MRR of AA5083-MoO_3 composites. Table 4 displays the ANOVA result of MRR. It could be clearly understood that T_{OFF} is the utmost impelling factor with the percentage contribution of 27.92% tracked by T_{ON} and I with the percentage contribution of 12.09% and 5.07%, respectively. I is the insignificant parameter with the percentage contribution of 5.07%. The R^2 value for the material removal rate is 45.10%. Figure 6(a) displays the normal probability plot of MRR and it was obvious that all the residuals were found to be normally distributed beside the straight line at 95% confidence level.

In this investigation, ANOVA was utilized to find the percentage contribution of parameters T_{ON}, T_{OFF}, and I on SR of AA5083-MoO_3 composites. Table 5 displays the ANOVA result of SR. It could be clearly understood that T_{OFF} is the utmost impelling factor with the percentage contribution of 60.33% tracked by T_{OFF} and I with the percentage contribution of 12.31% and 0.33%, respectively. I is the insignificant parameter with the percentage contribution of 0.33%. The R^2 value for the material removal rate is 72.98%. Figure 6(b) displays the normal probability plot of SR and it was obvious that all the residuals were found to be normally distributed beside the straight line at 95% confidence level.

3.4. Interaction Plot Analysis for MRR and SR. Figures 7(a) and 7(b) display the interaction plots for the MRR and SR. The interaction amid T_{ON}, T_{OFF}, and I with MRR is displayed in Figure 7(a). From the graph, it could be understood that when T_{OFF} enhances, MRR also increases. The maximum MRR was observed for T_{OFF}. The maximum MRR was obtained for the parameters T_{ON} 120 (μs), T_{OFF} 50 (μs), and I 3 (A). When T_{ON} and I interact, the increase of these parameters enhances the MRR, and T_{OFF} plays a major role in influencing the MRR. The interaction of T_{ON} with I obviously shows this. T_{ON} does not have significance in MRR. The interaction amid T_{ON}, T_{OFF}, and I reveals that T_{ON} is an unimportant factor for MRR.

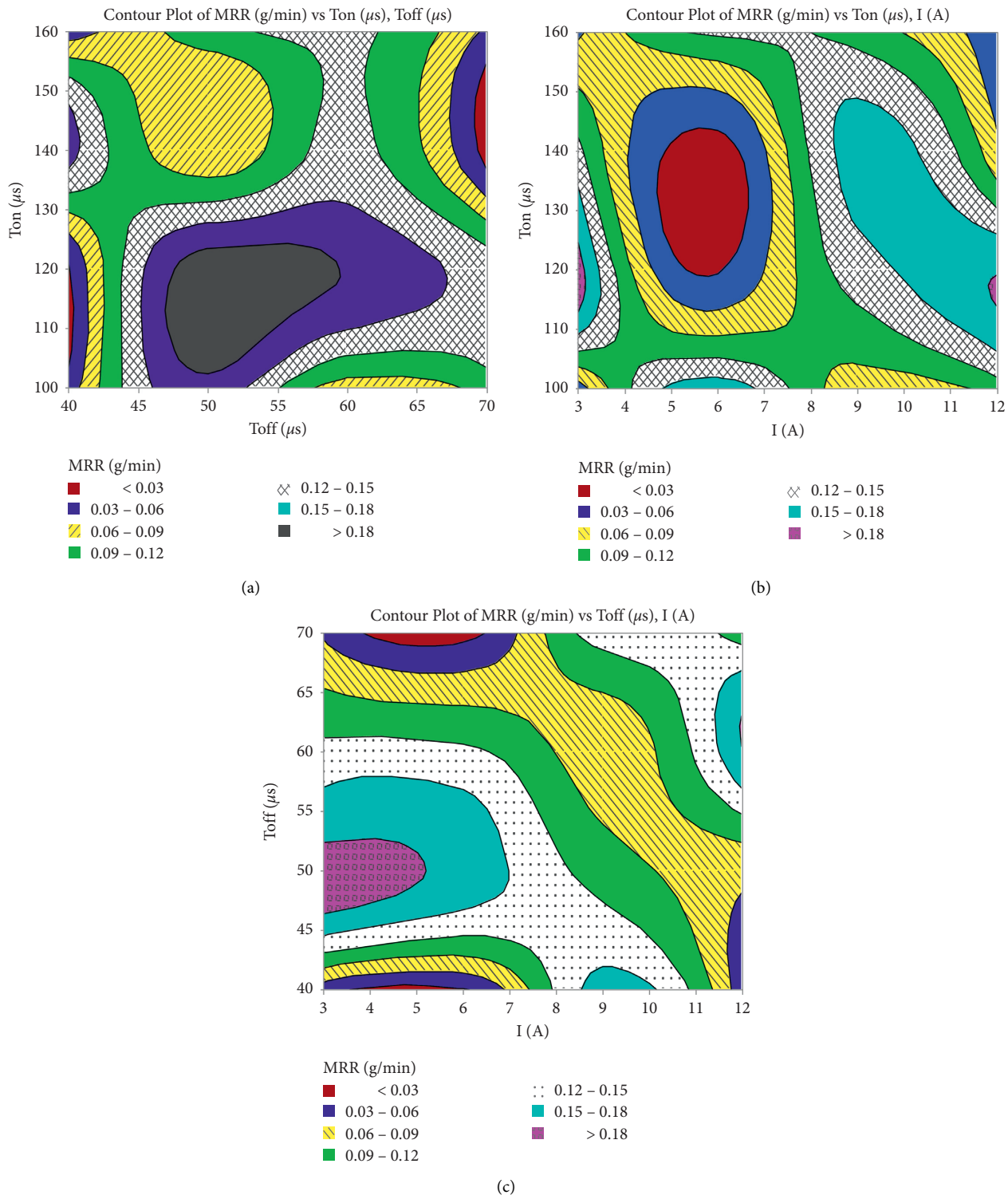

Figure 4: (a). Contour plot for MRR T_{OFF} vs. T_{ON}. (b) Contour plot for MRR I vs. T_{ON}. (c) Contour plot for MRR I vs. T_{OFF}.

The interaction amid T_{ON}, T_{OFF}, and I with SR is displayed in Figure 7(b). From the graph, it could be understood that when T_{OFF} increases, SR reduces. The least SR was observed for T_{OFF}. T_{ON} 100 (μs), T_{OFF} 40 (μs), and I 3 (A) are the noteworthy parameters to acquire the least SR. When T_{ON} and I interact, the increase of these parameters reduces the SR, and T_{OFF} plays a major role in influencing the SR. The interaction of T_{ON} with I obviously shows this. I does

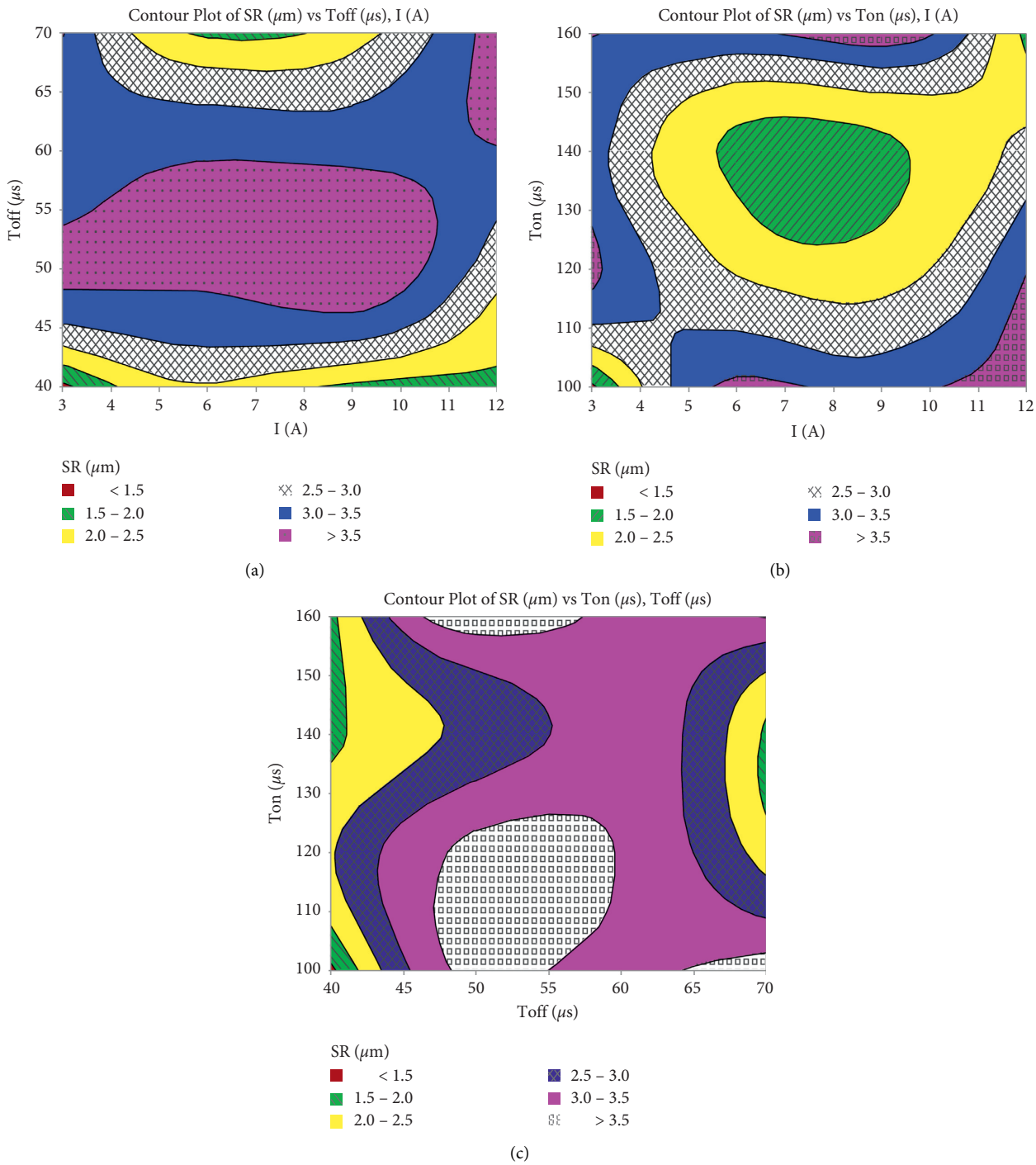

Figure 5: (a) Contour plot for SR I vs. T_{OFF}. (b) Contour plot for SR I vs. T_{ON}. (c) Contour plot for SR T_{OFF} vs. T_{ON}.

Table 4: Results of ANOVA for MRR.

Source	DF	Adj SS	Adj MS	F-value	P value	Percentage contribution
T_{ON} (μs)	2	0.005835	0.001945	0.44	0.732	12.09
T_{OFF} (μs)	2	0.013468	0.004489	1.02	0.448	27.92
I (A)	2	0.002447	0.000816	0.18	0.903	5.07
Error	2	0.026474	0.004412			
Total	8	0.048224				

$S = 0.0664252$; R-Sq = 45.10%; R-Sq(adj) = 0.00%.

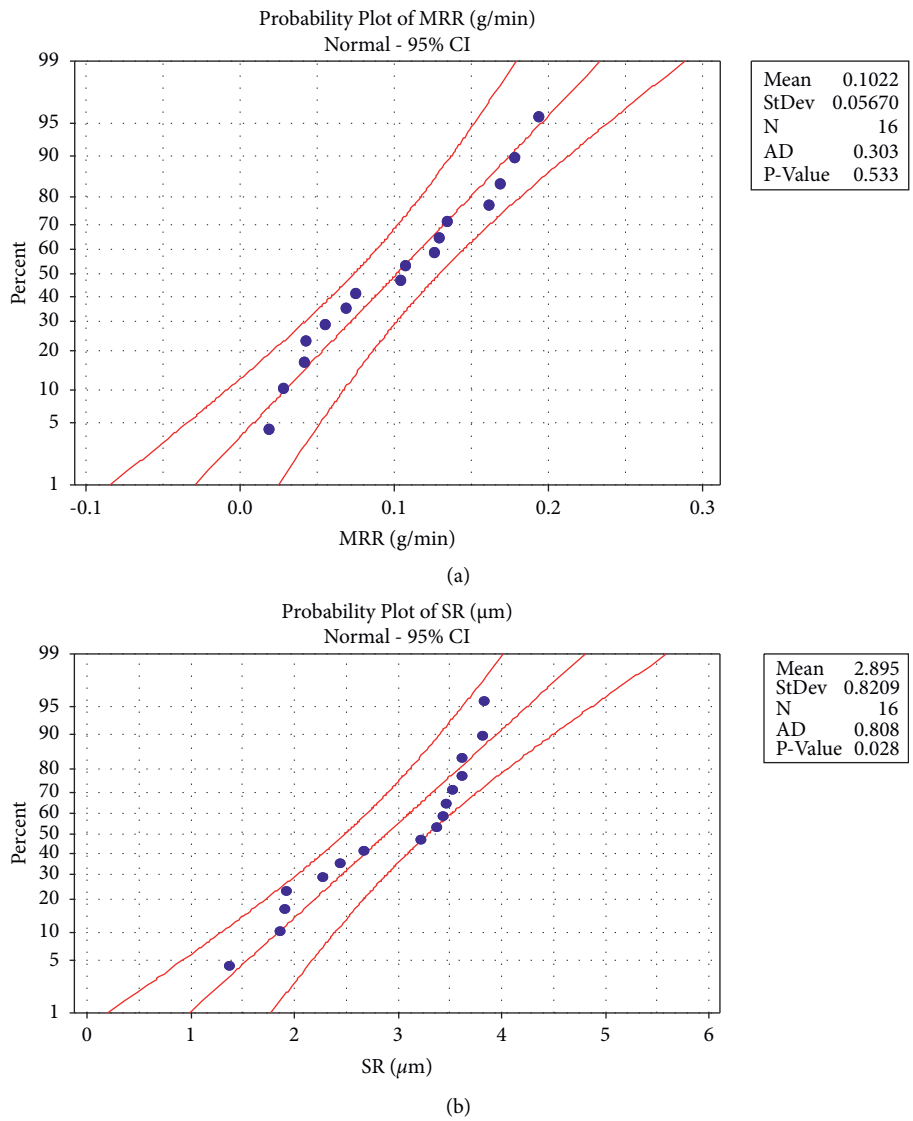

Figure 6: (a) Probability plot for MRR. (b) Probability plot for SR.

Table 5: Results of ANOVA for SR.

Source	DF	Adj SS	Adj MS	F-value	P value	Percentage contribution
T_{ON} (μs)	3	1.2447	0.4149	0.91	0.489	12.31
T_{OFF} (μs)	3	6.0988	2.0329	4.47	0.057	60.33
I (A)	3	0.0336	0.0112	0.02	0.994	0.33
Error	6	2.7312	0.4552			
Total	15	10.1083				

$S = 0.674690$; R-Sq = 72.98%; R-Sq(adj) = 32.45%.

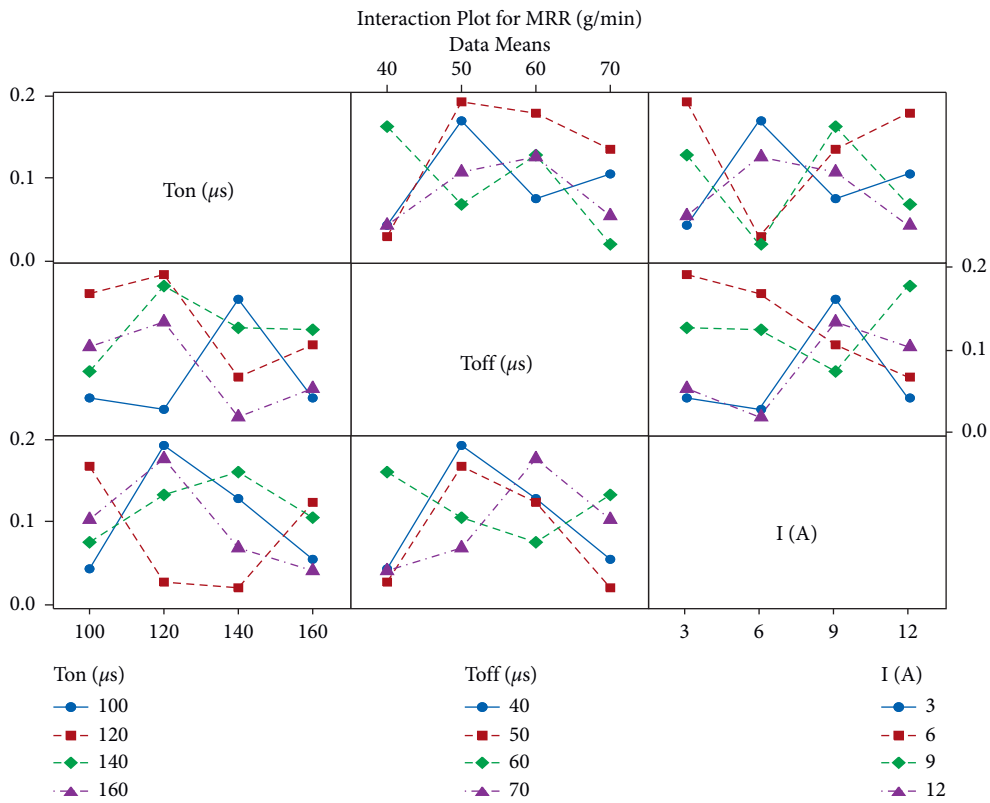

(a)

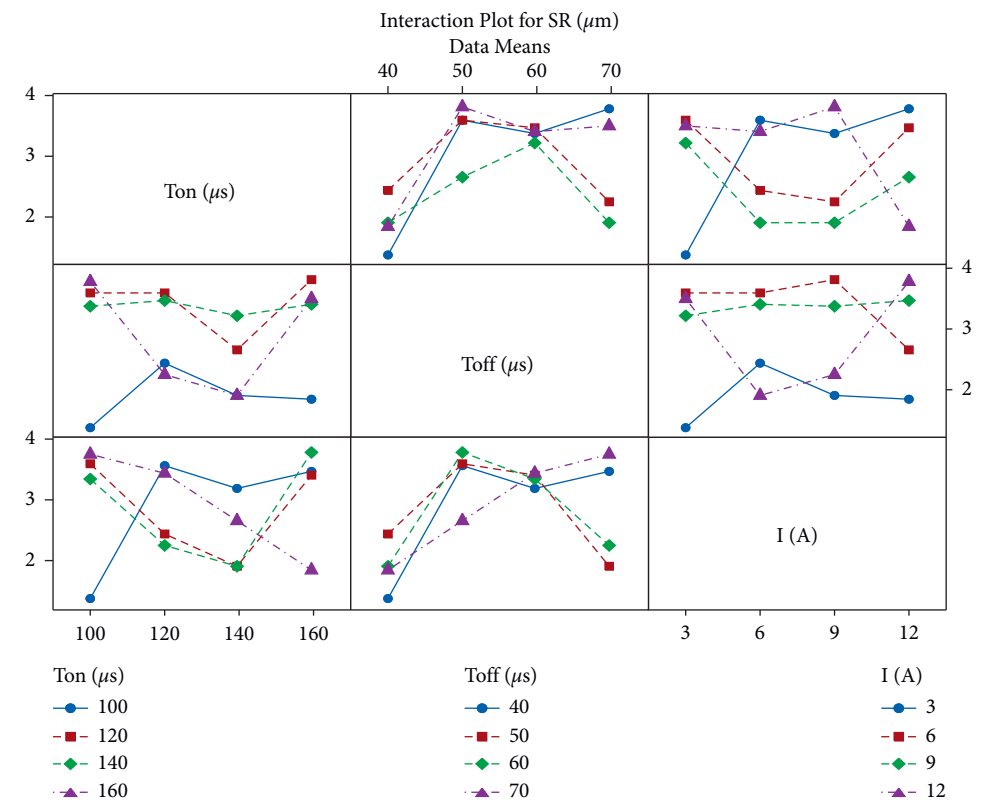

(b)

Figure 7: (a) Interaction plot for MRR. (b) Interaction plot for SR.

not have significance in SR. The interaction amid T_{ON}, T_{OFF}, and I reveals that I is an unimportant factor for SR.

4. Conclusion

(i) AA5083-12 wt.% MoO_3 composites were produced via SC process and the influence of process parameters on WEDM characteristics was investigated using the Taguchi method

(ii) Taguchi method is a suitable tool to identify the optimal process parameters to attain maximum MRR and SR in the WEDM process

(iii) The higher MRR was acquired for the parameters T_{ON} 120 (μs), T_{OFF} 50 (μs), and I 3 (A)

(iv) The least SR was acquired for the parameters T_{ON} 100 (μs), T_{OFF} 40 (μs), and I 3 (A)

(v) For MRR, the ANOVA results exposed that T_{OFF} is the utmost impelling factor with the percentage contribution of 27.92% tracked by T_{ON} and I with the percentage contribution of 12.09% and 5.07%, respectively

(vi) For SR, the T_{OFF} is the utmost impelling factor with the percentage contribution of 60.33% tracked by T_{OFF} and I with the percentage contribution of 12.31% and 0.33%, respectively

(vii) From the obtained results, it is clearly understood that the developed AA5083-12 wt.% MoO_3 composites can replace the existing material in the field of aerospace and automobile sectors

Data Availability

The data used to support the findings of this study are included within the article.

Conflicts of Interest

The authors declare that there are no conflicts of interest regarding the publication of this article.

Acknowledgments

The authors thank K. Ramakrishnan College of Engineering, Trichy and Bharath Institute of Higher Education and Research, Chennai, for providing facilities support to complete this research work. This project was supported by Researchers Supporting Project number (RSP-2021/315) King Saud University, Riyadh, Saudi Arabia.

References

[1] S. Vijayakumar and L. Karunamoorthy, "Wear characterization of aluminium metal matrix composites," *Advanced Composites Letters*, vol. 22, pp. 69–75, 2013.

[2] A. M. Rajesh, M. Kaleemulla, S. Doddamani, and K. N. Bharath, "Material characterization of SiC and Al_2O_3–reinforced hybrid aluminum metal matrix composites on wear behavior," *Advanced Composites Letters*, vol. 28, no. 1–10, 2019.

[3] D. Lee, J. Kim, S.-K. Lee, Y. Kim, S.-B. Lee, and S. Cho, "Experimental and thermodynamic study on interfacial reaction of B4C-Al6061 composites fabricated by stir casting process," *Journal of Alloys and Compounds*, vol. 859, Article ID 157813, 2021.

[4] M. Y. Zhou, L. B. Ren, L. L. Fan et al., "Progress in research on hybrid metal matrix composites," *Journal of Alloys and Compounds*, vol. 838, Article ID 155274, 2020.

[5] V. Mahesh Kumar and C. V. Venkatesh, "A comprehensive review on material selection, processing, characterization and applications of aluminium metal matrix composites," *Materials Research Express*, vol. 6, Article ID 72001, 2019.

[6] A. Kareem and J. Abu Qudeiri, "Asarudheen abdudeen. Thanveer ahammed and aiman ziout. "A review on AA 6061 metal matrix composites produced by stir casting"," *Materials*, vol. 14, pp. 1–22, 2021.

[7] K. S. A. Ali, V. Mohanavel, S. A. Vendan et al., "Mechanical and microstructural characterization of friction stir welded SiC and B_4C reinforced aluminium alloy AA6061 metal matrix composites," *Materials*, vol. 14, pp. 1–16, 2021.

[8] B. Stalin, G. T. Sudha, and M. Ravichandran, "Investigations on characterization and properties of Al-MoO3 composites synthesized using powder metallurgy technique," *Silicon*, vol. 10, no. 6, pp. 2663–2670, 2018.

[9] Y. He, D. Wu, M. Zhou et al., "Effect of MoO3/carbon nanotubes on friction and wear performance of glass fabric-reinforced epoxy composites under dry sliding," *Applied Surface Science*, vol. 506, Article ID 144946, 2020.

[10] T. Anadaraj, P. P. Sethusundaram, M. Meignanamoorthy, and M. Ravichandran, "Investigations on properties and tribological behavior of AlMg4.5Mn0.7(AA5083)-MoO_3 composites prepared by stir casting method," *Surface Topography: Metrology and Properties*, vol. 9, Article ID 25011, 2021.

[11] S. Nanjan and G. Murali Janakiram, "Characteristics of A6061/(Glass Fibre+ Al_2O_3+SiC+B_4C) reinforced hybrid composite prepared through stir casting," *Advances in Materials Science and Engineering*, vol. 2019, Article ID 6104049, 12 pages, 2019.

[12] P. Shanmughasundaram and R. Subramanian, "Wear behaviour of eutectic Al-Si alloy-graphite composites fabricated by combined modified two-stage stir casting and squeeze casting methods," *Advances in Materials Science and Engineering*, vol. 2013, Article ID 216536, 8 pages, 2013.

[13] G. Jegan, P. Kavipriya, T. Sathish, S. Dinesh Kumar, T. Samraj Lawrence, and T. Vino, "Synthesis, mechanical, and tribological performance analysis of stir-casted AA7079: ZrO_2+Si_3N_4 hybrid composites by taguchi route," *Advances in Materials Science and Engineering*, vol. 2021, Article ID 7722370, 15 pages, 2021.

[14] J. Arun Prakash, R. Masilamani, and M. Sujith, "Multi-objective optimization in WEDM process of aluminium-bagassegraphite composite through grey relation analysis," *Journal of Critical Reviews*, vol. 7, pp. 190–193, 2020.

[15] V. Kavimani, K. S. Prakash, T. Thankachan, S. Nagaraja, A. K. Jeevanantham, and J. P. Jhon, "WEDM parameter optimization for silicon@ r-GO/magneisum composite using taguchi based gra coupled PCA," *Silicon*, vol. 12, pp. 1–15, 2019.

[16] C. Wang and Q. Zhang, "Comparison of Micro-EDM characteristics of Inconel 706 between EDM oil and an Al powder-mixed dielectric," *Advances in Materials Science and Engineering*, vol. 2019, Article ID 5625360, 11 pages, 2019.

[17] K. Ishfaq, S. Anwar, M. A. Ali et al., "Pruncu, Mustafa Saleh and Bashir Salah. "Optimization of WEDM for precise

machining of novel developed Al6061-7.5% SiC squeeze-casted composite"," *International Journal of Advanced Manufacturing Technology*, vol. 111, pp. 2031–2049, 2020.

[18] S. Das and S. N. Joshi, "Estimation of wire strength based on residual stresses induced during wire electric discharge machining," *Journal of Manufacturing Processes*, vol. 53, pp. 406–419, 2020.

[19] H. Singh and R. Garg, "Effects of process parameters on material removal rate in WEDM," *Journal of Achievements in Materials and Manufacturing Engineering*, vol. 32, pp. 70–74, 2009.

[20] L. Nagarajan, S. Mahalingam, S. Gurusamy et al., "Optimization of process control parameters for WEDM of Al-LM25/Fly Ash/B_4c hybrid composites using evolutionary algorithms: a comparative study," *Metals*, vol. 11, pp. 1–17, 2021.

[21] T. Titus, K. S. Prakash, and M. Loganathan, "WEDM process parameter optimization of FSPed copper-BN composites," *Materials and Manufacturing Processes*, vol. 33, pp. 350–358, 2018.

[22] P. C. Padhi, S. S. Mahapatra, S. N. Yadav, and D. K. Tripathy, "Multi-objective optimization of wire electrical discharge machining (WEDM) process parameters using weighted sum genetic algorithm approach," *Journal of Advanced Manufacturing Systems*, vol. 15, no. 2, pp. 85–100, 2016.

[23] V. Aggarwal, C. I. Pruncu, J. Singh, S. Sharma, and D. Y. Pimenov, "Empirical investigations during WEDM of Ni-27Cu-3.15Al-2Fe-1.5Mn based superalloy for high temperature corrosion resistance applications," *Materials*, vol. 13, no. 16, p. 3470, 2020.

[24] R. Chaudhari, S. Khanna, J. Vora et al., "Experimental investigations and optimization of MWCNTs-mixed WEDM process parameters of nitinol shape memory alloy," *Journal of Materials Research and Technology*, vol. 15, pp. 2152–2169, 2021.

[25] P. Samal, P. R. Vundavilli, A. Meher, and M. M. Mahapatra, "Influence of TiC on dry sliding wear and mechanical properties of in situ synthesized AA5052 metal matrix composites," *Journal of Composite Materials*, vol. 53, no. 28–30, pp. 4323–4336, 2019.

[26] A. Baradeswaran and A. Elaya Perumal, "Influence of B4C on the tribological and mechanical properties of Al 7075-B4C composites," *Composites Part B: Engineering*, vol. 54, pp. 146–152, 2013.

Hindawi
Advances in Materials Science and Engineering
Volume 2022, Article ID 2203717, 9 pages
https://doi.org/10.1155/2022/2203717

Research Article

Investigation of Various Coating Resins for Optimal Anticorrosion and Mechanical Properties of Mild Steel Surface in NaCl Solution

Sandeep V. Gujjar,[1] Nandini Nadar,[2] Kanaram Choudhary,[3] Anand M. Hunashyal,[4] Kiran Shahapurkar,[5] M. A. Mujtaba,[6] Mohammed Asadullah,[7] Manzoore Elahi M. Soudagar,[6,8] T. M. Yunus Khan,[9] Khadiga Ahmed Ismail,[10] and Ashraf Elfasakhany[11]

[1]*Department of Civil Engineering, Pillai HOC College of Engineering and Technology, Dist. Raigad, Rasayani 410207, Maharashtra, India*
[2]*Department of Mechanical Engineering, B.M.S.Institute of Technology and Management, Bangalore 64, Karnataka, India*
[3]*Rustomjee Academy for Global Careers, Dahanu Road (E), 401602 Mumbai, Maharashtra, India*
[4]*Department of Civil Engineering, BVB College of Engineering and Technology, KLE Technological University, Hubli 580021, India*
[5]*School of Mechanical, Chemical and Materials Engineering, Adama Science and Technology University, Adama 1888, Ethiopia*
[6]*Department of Mechanical Engineering, Faculty of Engineering, University of Malaya, Kuala Lumpur 50603, Malaysia*
[7]*Mechanical Engineering Department, Faculty of Engineering, Lords Institute of Engineering and Technology, Hyderabad, India*
[8]*Department of Mechanical Engineering, School of Technology, Glocal University, Delhi-Yamunotri Marg, SH-57, Mirzapur Pole, Saharanpur District, Uttar Pradesh 247121, India*
[9]*Department of Mechanical Engineering, College of Engineering, King Khalid University, Abha 61421, Saudi Arabia*
[10]*Department of Clinical Laboratory Sciences, College of Applied Medical Sciences, Taif University, P.O. Box 11099, Taif 21944, Saudi Arabia*
[11]*Mechanical Engineering Department, College of Engineering, Taif University, P.O. Box 11099, Taif 21944, Saudi Arabia*

Correspondence should be addressed to Kiran Shahapurkar; kiranhs1588@astu.edu.et

Received 29 September 2021; Revised 21 January 2022; Accepted 29 January 2022; Published 28 February 2022

Academic Editor: P Ganeshan

The primary objective of the research was to investigate the ideal resin coating on the mild steel surface among various resin coatings which are in use. These resin coatings are used as an anti-corrosive material for mild steel surfaces with enhanced mechanical properties. The resins (epoxy, polyurethane, polyester, and phenolic) on mild steel surface were applied by the pneumatic spray coating method. In addition, immersion test and salt spray test methods were followed using sodium chloride (NaCl) solution. Furthermore, the rate of corrosion and mechanical properties of mild steel coated with different resins was evaluated by conducting various experiments (immersion test, salt spray test, tensile strength test, and scratch hardness test) and was compared with a bare mild steel surface. The results of the current research showed that the mild steel surface coated with epoxy resin was found to be the most effective corrosion resistance material with better mechanical properties compared to other tested mild steel resin-coated surfaces.

1. Introduction

Mild steel plays a vital role in the lifespan of a civil engineering structure, and usually, the performance of carbon steels is hampered by its surface features such as surface texture and surface energy due to corrosion [1, 2]. It is causing a serious issue in the field of the construction industry due to loss of structural strength, reduced bond strength, ductility, and shear capacity [3, 4]. To avoid the corrosion problem and increase the tensile strength of mild

steel, many attempts have been made so far by surface coating using inorganic coating, paints, resins, alloying additions, and many others. Different types of resins have been studied individually in the literature and found to be very effective in controlling the corrosion of civil structures. Many researchers have evaluated the anticorrosion properties of various types of resin coatings on mild steel surfaces. Epoxy-silane hybrid coatings have coating ratios between 1 to 3wt.% on galvanized steel which has improved the adhesion and corrosion behavior of the surface, whereas a further add up to 5wt.% resulted in reducing its corrosion/adhesion performance [5]. The cathodic delamination of polyurethane/multiwalled carbon nanotube composite coatings up to 0.5 wt.% on steel substrate has increased the corrosion protective performance in the NaCl solution proved by the scanning Kelvin probe (SKP) results [6]. Corrosion-performance evaluation studies in a 3.5wt.% NaCl electrolyte conducted via EIS and potentiodynamic polarization tests have shown that the MWCNT in polypyrrole (PPY) coating has considerably reduced the corrosion rate. Interestingly, PPY/MWCNT-COO-functionalized nanocomposite provided a higher corrosion resistance coating than PPY/MWCNT alone [7]. Mild steel coated with MWCNT/epoxy nanocomposite (0.75 wt.%) revealed a decrease in the corrosion rate up to 2.5×10^3 MPY and the protection efficiency increased up to 99.99% [8]. From the electrochemical measurements, it was found that the corrosion resistance of carbon steel has significantly improved by the hybrid coating in a 0.75% saline solution [9]. From another experimental study, it was observed that about 0.1 wt.% graphene oxide (GO) was the appropriate GO content to prepare nanocomposites of GO-epoxy with an optimum corrosion resistance [10].

It was found that MWCNTs were dispersed uniformly in the PU matrix from 4 to 6 wt. %, no aggregation and precipitation phenomena were observed in the fast spraying process [11]. B. Ramezanzadeh et al. [12] proved a coating of 0.1wt.% GO and PI-GO nanosheets to the polyurethane resin have enhanced its corrosion protection properties. Figure 1 shows the synthesis of waterborne epoxy resin (WEP) coating and fluorinated graphene (FG)-modified WEP coatings [13].

Research studies on individual resins coatings for mild steel surfaces have targeted better mechanical, physical, water, heat, resistance, and antimicrobial activity. However, very few research works were focused on identifying the optimum resin that produced the best anticorrosion and mechanical properties on the mild steel surface. Hence, the objective of the present study was to determine the ideal resin with anticorrosion and enhanced mechanical properties for a mild steel substrate. The resins (polyester, epoxy, polyurethane, and phenolic) were prepared by using the respective accelerator, hardener, and thinners. The prepared resins were used as coatings on the fabricated mild steel surface. Furthermore, the surface was subjected to corrosion analysis by performing an immersion and salt spray test. In addition, the tensile strength and scratch hardness tests were performed to evaluate the mechanical properties of the mild steel surface. The degree of anticorrosion performance and morphological characteristics of epoxy [5, 8–10, 14–24], polyurethane [6, 11, 12, 25, 26], phenolic [25, 27, 28], and polyester resins [29] as surface coatings for mild steel were compared and discussed.

2. Experimental Procedure

2.1. Materials. Polyurethane resin (FINESTER-1100) is a two-component polyurethane composition based on acrylic polyol and isocyanate. Epoxy resin (FINE COAT-EP 200A & B) is a two-component epoxy clear lacquer, cured with polyamide hardener. It cures at room temperature (above 10°C). Polyester Resin (PS) (FINESTER – 1100) is a medium viscosity modified ISO polyester resin. Phenolic Resin (PH) INSUFINE-VI 610 is an impregnating varnish based on alkyd and phenolic resins. The epoxy, polyurethane, polyester, and phenolic resins were purchased from the Fine Finish Organics Pvt. Ltd., Navi Mumbai, India. Mild steel panels were purchased from Shubh M L Shah and Sons Steel Pvt. Ltd., Mumbai, India. A pneumatic spray gun was purchased from Burhani hardware, Dahanurd, India. The technical specifications of epoxy resin, polyurethane resin, polyester resin, and phenolic resins are listed in Table 1.

2.2. Preparation of Resins and Mild Steel Surface. The polyester resin coating was prepared by adding 10 gm of polyester resin (PS) (FINESTER-1100) with accelerator-1100 and catalyst-1100 in the ratio of 100 : 1 : 1 by weight, and further, 20 mL of the thinner 643 was added for curing purposes (Figure 1). The curing was performed at room temperature between 25 and 40°C. The epoxy resin coating was prepared by first adding 10 gm of FINE COAT (EP 200 A) with EP 200 B hardener in the ratio of 2 : 1 and then the thinner of grade 643 was added (20 ml) (Figure 1). Polyurethane coating was prepared by first adding 10 gm of polyurethane resin (PU) (PU 500 A) with PU 500 B hardener (1 : 1) ratio (Figure 2). Furthermore, for phenolic resin coating, 10 gm of phenolic resin (INSUFINE-VI610) was taken for the coating purpose (Figure 2).

The surface of mild steel sheets was blasted with emery paper 80 grit size and washed with acetone to clean and remove the oxides present on the surface of mild steel. Furthermore, the specimens were dried at room temperature for 1 hour and were coated with resin. The prepared epoxy, polyurethane, polyester, and phenolic resins were sprayed on the surface of mild steel through a pneumatic spray gun. Finally, the coated mild steel specimens were dried at room temperature for 48 hours and annealed at 150°C for 1 hour in a hot-air oven. The distance maintained between the spraying gun and the specimen was about 100–150 mm to obtain the required thickness (160–180 μm) of the coating layer. Mild steel specimens coated with the different resin of 12 mm diameter were cut to a length of 300 mm for performing a tensile test. Furthermore, a flat mild steel specimen of size $125 \times 60 \times 6\,\text{mm}^3$ was used for the scratch hardness test.

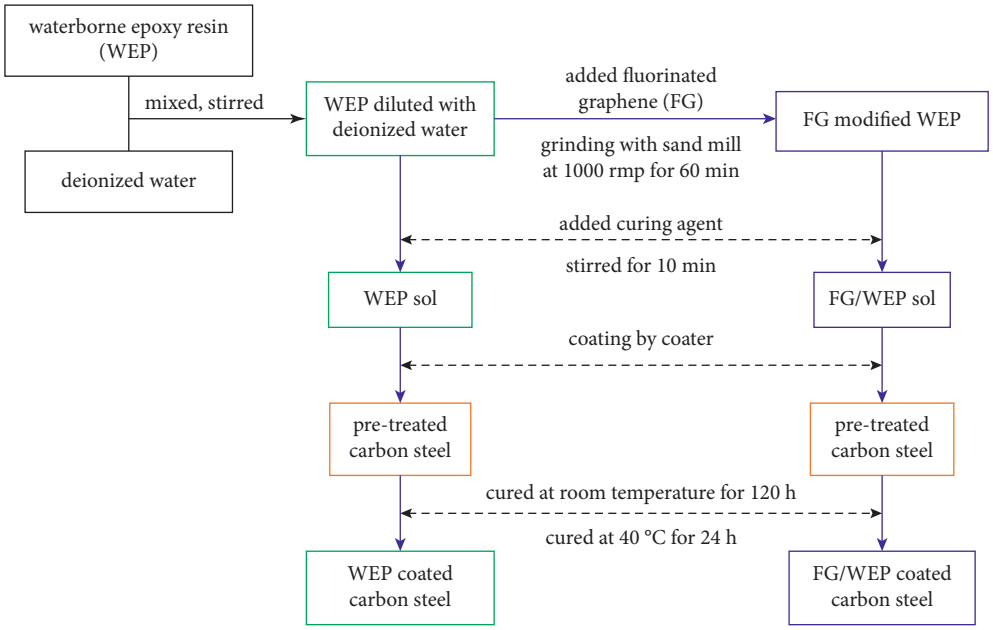

Figure 1: Synthesis of waterborne epoxy resin (WEP) coating and fluorinated graphene (FG)-modified WEP coatings [13].

Table 1: Technical specifications of resin.

Sl. No.	Resin specifications			
	Epoxy	Polyurethane	Polyester	Phenolic
1	Color: clear and can be dyed as per the requirement	Color: colorless (PU500/A and PU500/B)	Viscosity range, MPa.s.@30°C: 300–500	Color: yellow
2	Finish: glossy	Finish: glossy	Acid value, mg of KOH/g: 10–20	Viscosity @25°C (B4 flow cup): 30–40 sec
3	Mixing ratio Base : hardener = 2 : 1 (by volume)	Mixing ratio (PU500A : PU500B) 1 : 1 (by weight)	Color, gardener: <1	Finish: glossy
4	Pot life 14–16 hours @30°C	Viscosity at 25°C: 15 ± 5 MPa·s	Specific gravity: 1.10–1.12	Bond strength, at 30°C: 25
5	Theoretical covering capacity: 12 sq.m./lit @25 microns dft.	Solid content: 60 ± 2%	Volatile content (max.): 40	Volume resistivity at 30°C: $1–1.5 \times 10^{16}$ cm after immersion
6	Application method: air-assisted/airless spray/brush	Application method: brush/Spray	—	—
7	—	Continuous operating temperature: 155°C	—	—

*denotes as supplied by the manufacturer.

2.3. Morphological Studies. The corrosion behavior on the surface of mild steel specimens coated with different resins was evaluated by morphological studies using a field emission scanning electron microscope (FESEM). The corroded surface was gold coated by a sputtering unit and FESEM was operated at an accelerating voltage of 20 kV.

2.4. Corrosion Studies by Immersion Test. The corrosion resistance properties of epoxy, polyurethane, polyester, and phenolic resins coated on mild steel surface were subjected to immersion method. The resin-coated samples were immersed in the aqueous 3.5% NaCl solution for 336 hours, and the corrosion rate was determined by the weighing

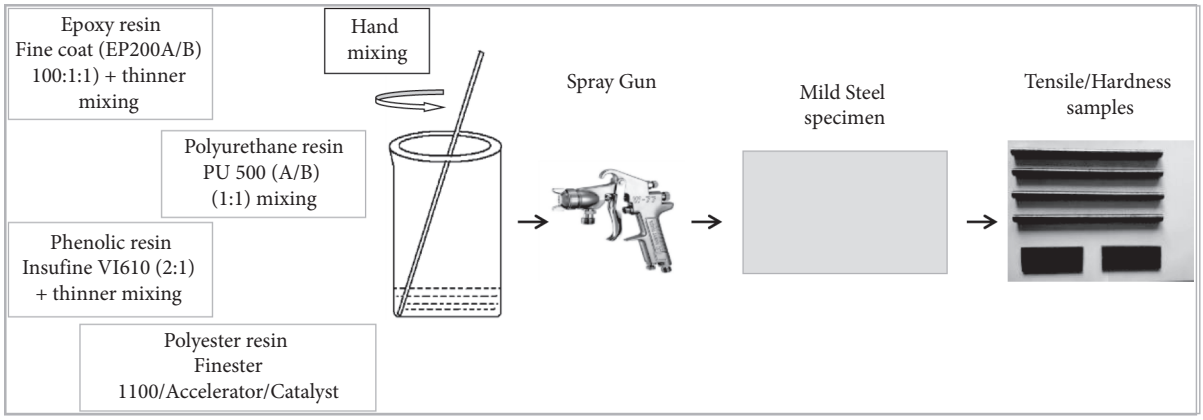

Figure 2: Schematic representation of the coating process of mild steel specimen.

method. The weight of the steel sample coated with a resin was measured before and after immersion to determine the corrosion rate. A minimum of three samples per composition were tested for obtaining an averaged corrosion response. The corrosion resistance properties obtained for bare and resin-coated mild steel samples are listed in Table 2.

2.5. Mechanical Properties

2.5.1. Tensile Strength Test (A370 : 2017). The effects of epoxy, polyurethane, polyester, and phenolic resins coated on mild steel surfaces were studied to determine their tensile strength properties. The tensile test was carried out by using a universal testing setup (A370 : 2017) to determine its ultimate tensile strength, yield load, and yield stress. For ensuring repeatability of the results, three samples were tested for each category of the resin-coated mild steel specimens. The ultimate tensile strength of plain mild steel and samples coated with different resins are presented in Table 2.

2.5.2. Scratch Hardness Test. The flat mild steel sample of a dimension of $120 \times 60\,\text{mm}^2$ was subjected to scratch hardness testing according to IS 101 (Part-5, Sec.2):1988. The minimum load required to cause the failure was noted as the hardness of the resin-coated mild steel surface. All the resin-coated specimens were tested in a batch of 3 samples to obtain accurate results, which are recorded and reported in Table 2.

3. Results and Discussion

The cumulative result of the obtained average values of corrosion resistance, ultimate tensile strength, toughness, and scratch hardness test of the bare and resin-coated mild steel specimens are listed in Table 2.

3.1. Corrosion Properties of Resin Coating. The average value of the corrosion resistive properties obtained from the immersion test for all the types of resin-coated mild steel samples is plotted as shown in Figure 3. The epoxy resin-coated mild steel sample exhibited the maximum corrosion resistivity of 4102.29 mil, followed by phenolic resin (1414.97 mil), polyester resin (1233.38 mil), and polyurethane resin (635.85 mil) coated samples in comparison to the uncoated mild steel surface, as shown in Figure 3. It was observed also that the epoxy resin-coated samples have yielded the maximum corrosion resistance property, which can be accounted for its chemical structure that induces high chemical resistivity and good adhesion properties under a wide range of corrosive conditions. This enables the mild steel specimen to remain intact even in highly humid and corrosive conditions.

3.2. Mechanical Properties

3.2.1. Stress-Strain Curve (A370 : 2017). Figure 4 depicts the stress-strain curve for different resins coated mild steel specimens. This curve is utilized for evaluating the tensile strength and toughness of the resin-coated samples. It can be observed that the ratio of stress and strain was proportional for all the types of resin-coated mild steel samples under small applied tensile force. A straight line between zero to stress value around 300 MPa can be also observed. When the force applied is greater, the samples experience elastic deformation as seen from curves. Further loading induces plastic deformation in the samples and results in a fracture. It is observed that the epoxy-coated mild steel specimen has yielded higher ultimate strength in comparison to other samples due to the difference in the elastic modulus between the two materials that make the best microstructure design in handling the applied load gradually.

3.2.2. Tensile Strength Test (A370 : 2017). The average value of ultimate tensile strength obtained from UTM for all the types of resin-coated samples in comparison to plain mild steel specimen is plotted, as shown in Figure 4(a). The samples coated with epoxy resin showed a maximum ultimate tensile strength of $505.82\,\text{N/mm}^2$, followed by phenolic resin ($491.47\,\text{N/mm}^2$), polyurethane resin ($485.63\,\text{N/mm}^2$), and polyester resin ($474.54\,\text{N/mm}^2$) in comparison with mild steel surface, as shown in Figure 5(a). The samples

Table 2: Anticorrosion and mechanical test results.

Sl. No.	Specimen	Corrosion resistance by resin (mils)	Ultimate tensile strength (N/mm^2)	Toughness (N/mm)	Scratch hardness (mg)
1	Plain mild steel	—	456.23 ± 9.12	—	150.00 ± 3
2	Polyurethane resin	635.85 ± 12.71	485.63 ± 9.71	5893.224	800.00 ± 16
3	Epoxy resin	4102.29 ± 82.04	505.82 ± 10.12	7057.32	700.00 ± 14
4	Polyester resin	1233.38 ± 24.66	474.54 ± 9.49	6738.417	300.00 ± 6
5	Phenolic resin	1414.97 ± 28.29	491.47 ± 9.82	5394.345	300.00 ± 6

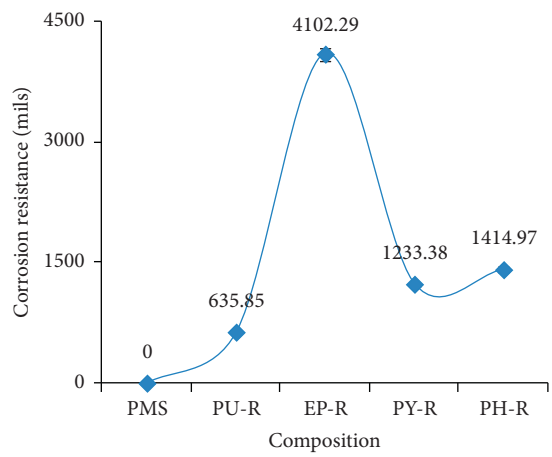

Figure 3: The corrosion resistance of the samples.

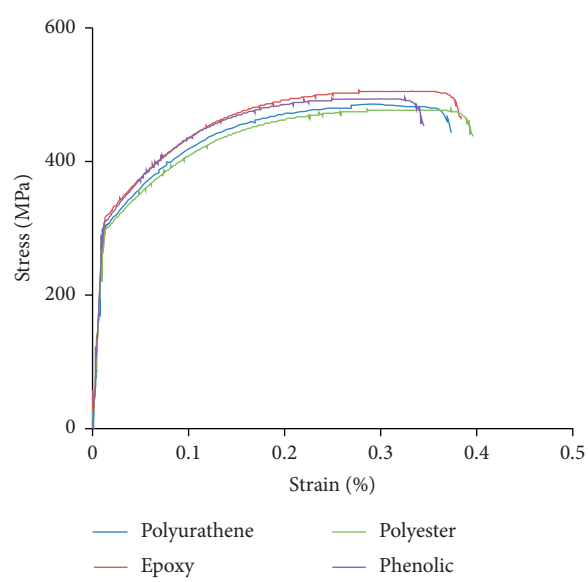

Figure 4: Representative stress-strain curves of samples coated with different polymer resins.

coated with epoxy resin showed the maximum percentage of increase in ultimate tensile strength in comparison to mild steel samples by 9.80%. It is because of the multi-coordination sites formed by the hydroxyl and amine groups that form a 3D cross-linked polymeric network for metals [30]. The good physical properties of epoxy resin such as toughness, flexibility, and abrasion resistance are superior to almost all thermoplastics in elevated temperature performance, whereas phenolic resin showed 7.72%, polyurethane showed 6.05%, and polyester resin revealed the least increase of 3.85% w.r.t the mild steel samples without coating.

3.2.3. Toughness Test of Mild Steel Samples. The toughness of resin-coated mild steel specimens is illustrated in

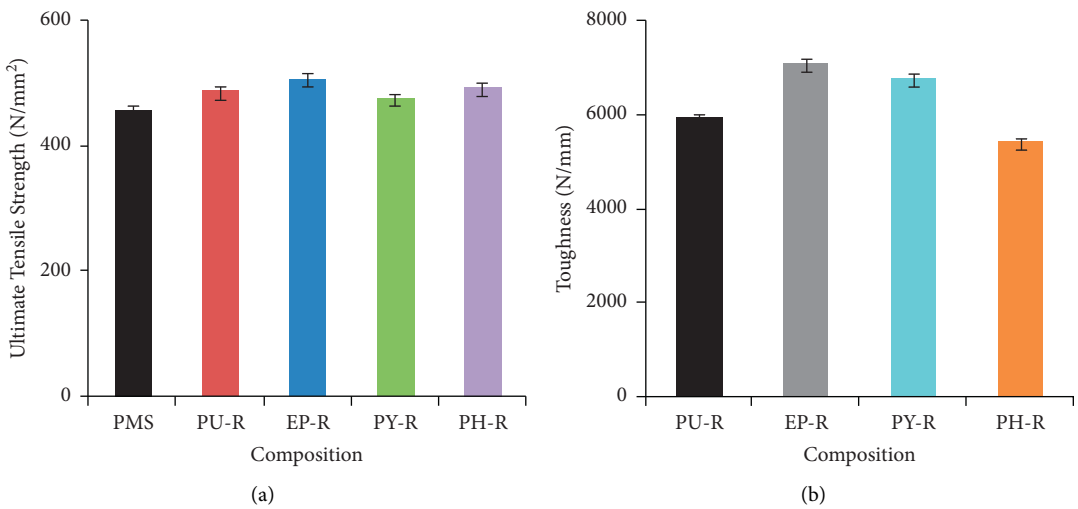

Figure 5: Experimentally calculated (a) ultimate tensile strength and (b) toughness of samples.

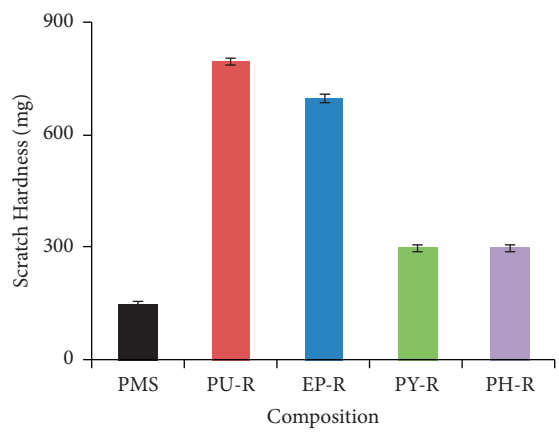

Figure 6: Scratch hardness of samples.

Figure 5(b). It can be observed that the toughness value of the resin-coated mild steel specimens was comparatively higher than the bare mild steel sample. The epoxy resin-coated sample exhibited the highest toughness index with 7057.32 N/mm compared to the phenolic resin-coated sample with 5394.345 N/mm, polyurethane resin-coated sample with 5893.224 N/mm, and polyester resin-coated sample with 6738.417 N/mm. The enhancement in the toughness result for the epoxy-coated samples is due to the two-component epoxy clear lacquer, cured with polyamide hardener and good comparative tracking index > 500 V. This is due to the extension of the 3D polymeric network by the hydroxyl and amine group present in the epoxy matrix [30]. In addition, the physical properties of epoxy resin are comparatively better than polyurethane, polyester, and phenolic resins.

3.2.4. Scratch Hardness Test. The hardness test results of bare mild steel and various types of resin-coated samples are shown in Figure 6. The scratch hardness of the polyurethane resin-coated sample revealed the maximum hardness (800mg), followed by an epoxy resin-coated sample with 700 mg. Polyester and phenolic resin-coated samples showed the least increase of hardness (300 mg) in comparison to pure mild steel samples. The scratch hardness of polyurethane resin-coated samples yielded the highest because the layer of polymer used here can protect the base material from corrosion, weathering, abrasion, and other processes that would protect the material from degradation over time.

3.3. Morphology. The morphology of various types of resin-coated mild steel samples before and after corrosion areas is depicted in Figure 7. Figures 7(a) and 7(b) show the images of FESEM of the polyurethane resin before and after the mild steel samples were exposed to corrosion. Figure 6(b) depicts the corrosion developed on the surface. Figures 7(c) and 7(d) show the images of epoxy resin-coated samples. Figure 7(d) indicates that epoxy resin has successfully protected the mild steel surface with minimum rust on its surface. Figures 7(e) and 7(f) show polyester resin-coated samples before and after oxidization, and Figure 7(f) indicates a high level of

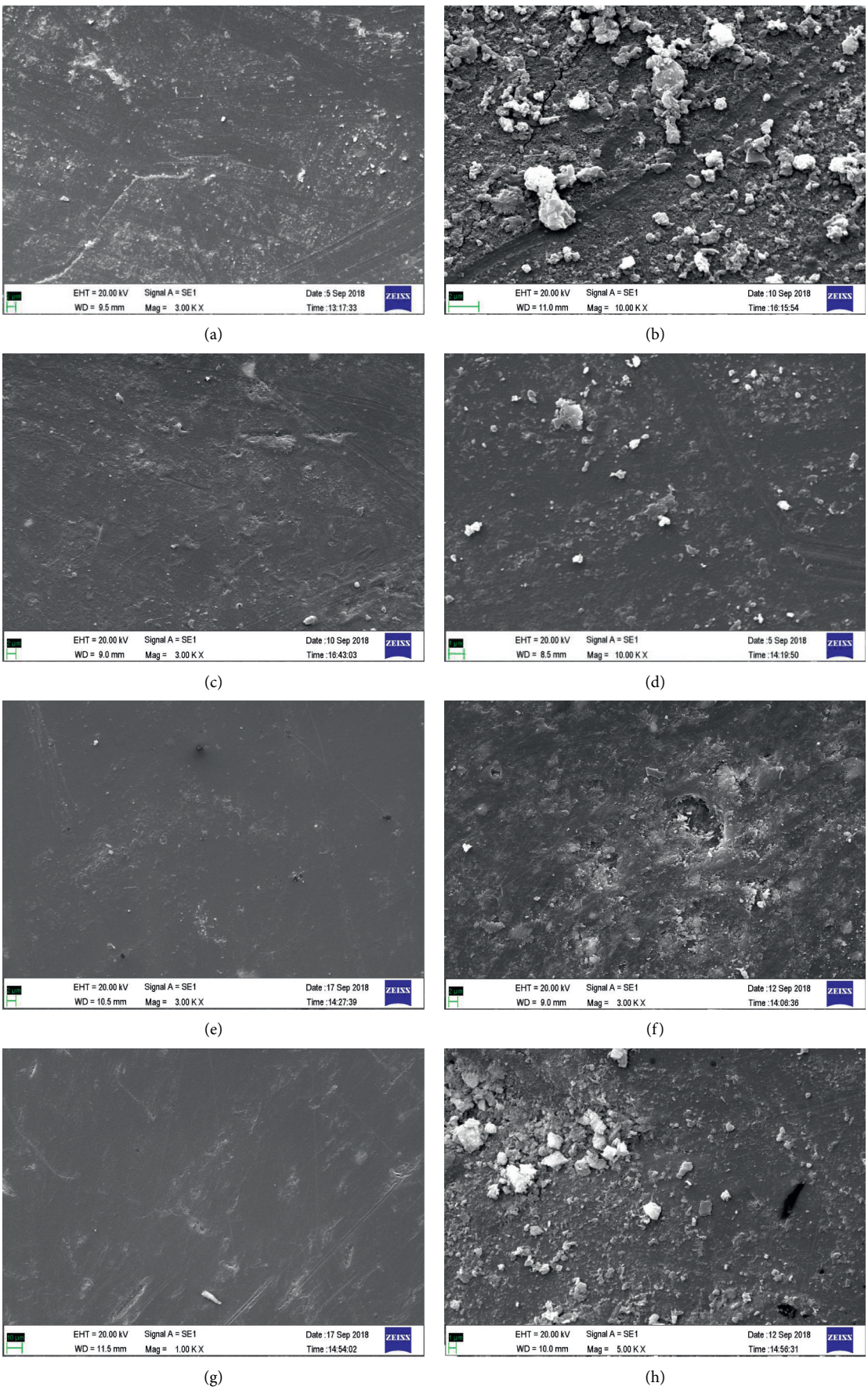

Figure 7: FESEM images of samples coated with polyurethane resin (a) before corrosion and (b) after corrosion, epoxy resin (c) before corrosion and (d) after corrosion, polyester resin (e) before corrosion and (f) after corrosion, and phenolic resin (g) before corrosion and (h) after corrosion.

corrosion. It is also worthy to notice the rusted surface (Figure 7(h)) on the mild steel sample coated with phenolic resin earlier after exposure to corrosion in comparison to before exposure (Figure 7(g)). It can be observed that the mild steel samples coated with the epoxy resin (Figure 7(d)) showed the lowest corrosion in comparison to polyurethane, polyester, and phenolic resins. The morphology results are in agreement with the results of the ultimate tensile strength and corrosion resistive in which the epoxy resin-coated mild steel specimens yielded the best performing results.

4. Conclusions

In summary, the outcomes of this study are as follows:

(i) Mild steel samples coated with epoxy resin exhibited very good resistance to corrosion. There was a remarkable increase in the rate of tensile strength of mild steel specimens coated with the epoxy resin.

(ii) It was found that the surface morphology of mild steel specimens with epoxy resin coating exhibits minute rust particles compared with other resins and plain mild steel.

(iii) Scratch hardness of polyurethane resin-coated mild steel specimen yielded better hardness in comparison to other mild steel specimens due to the presence of acrylic polyol and isocyanate. This induces better hardness to the coating surface. However, the corrosion resistance and tensile property are less than the epoxy coated samples.

(iv) FESEM analysis shows the samples coated with epoxy resin observed to have the least corroded surface compared with the other resin-coated surfaces.

(v) Since epoxy resin FINECOAT-EP 200 is a two-component epoxy clear lacquer, cured with polyamide hardener, coated samples showed superior results in comparison with the polyurethane, phenolic, and polyester resins. Epoxy resin is the most suitable resin for surface coating of mild steel to shield from corrosion and also to enhance mechanical properties.

Data Availability

The data used to support the findings of this study are included within the article.

Conflicts of Interest

The authors declare that they have no conflicts of interest.

Acknowledgments

The authors extends his appreciation to the Deanship of Scientific Research at King Khalid University for funding this work through research groups program under grant number (R.G.P 1/221/41). This study was supported by Taif University Researchers Supporting Project Number (TURSP-2020/40), Taif University, Taif, Saudi Arabia.

References

[1] R. K. Gupta, M. Malviya, C. Verma, and M. A. Quraishi, "Aminoazobenzene and diaminoazobenzene functionalized graphene oxides as novel class of corrosion inhibitors for mild steel: experimental and DFT studies," *Materials Chemistry and Physics*, vol. 198, pp. 360–373, 2017.

[2] H. Eivaz Mohammadloo, S. M. Mirabedini, and H. Pezeshk-Fallah, "Microencapsulation of quinoline and cerium based inhibitors for smart coating application: anti-corrosion, morphology and adhesion study," *Progress in Organic Coatings*, vol. 137, Article ID 105339, 2019.

[3] A. Khorram, "Microstructural evolution of laser clad Stellite 31 powder on Inconel 713 LC superalloy," *Surface and Coatings Technology*, vol. 423, Article ID 127633, 2021.

[4] M. Taheri, J. E. Jam, M. H. Beni, A. Khorram, S. F. Kashani-Bozorg, and M. J. Torkamany, "The effect of service temperature on the impact strength and fracture toughness of GTD-111 superalloy," *Engineering Failure Analysis*, vol. 127, Article ID 105507, 2021.

[5] S. Bera, T. K. Rout, G. Udayabhanu, and R. Narayan, "Water-based & eco-friendly epoxy-silane hybrid coating for enhanced corrosion protection & adhesion on galvanized steel," *Progress in Organic Coatings*, vol. 101, pp. 24–44, 2016.

[6] N. W. Khun and G. S. Frankel, "Cathodic delamination of polyurethane/multiwalled carbon nanotube composite coatings from steel substrates," *Progress in Organic Coatings*, vol. 99, pp. 55–60, 2016.

[7] A. Davoodi, S. Honarbakhsh, and G. A. Farzi, "Evaluation of corrosion resistance of polypyrrole/functionalized multiwalled carbon nanotubes composite coatings on 60Cu-40Zn brass alloy," *Progress in Organic Coatings*, vol. 88, pp. 106–115, 2015.

[8] A. Kumar, P. K. Ghosh, K. L. Yadav, and K. Kumar, "Thermomechanical and anti-corrosive properties of MWCNT/epoxy nanocomposite fabricated by innovative dispersion technique," *Composites Part B: Engineering*, vol. 113, pp. 291–299, 2017.

[9] W. Shen, L. Feng, X. Liu et al., "Multiwall carbon nanotubes-reinforced epoxy hybrid coatings with high electrical conductivity and corrosion resistance prepared via electrostatic spraying," *Progress in Organic Coatings*, vol. 90, pp. 139–146, 2016.

[10] S. Pourhashem, M. R. Vaezi, A. Rashidi, and M. R. Bagherzadeh, "Exploring corrosion protection properties of solvent based epoxy-graphene oxide nanocomposite coatings on mild steel," *Corrosion Science*, vol. 115, pp. 78–92, 2017.

[11] G. Li, L. Feng, P. Tong, and Z. Zhai, "The properties of MWCNT/polyurethane conductive composite coating prepared by electrostatic spraying," *Progress in Organic Coatings*, vol. 90, pp. 284–290, 2016.

[12] B. Ramezanzadeh, E. Ghasemi, M. Mahdavian, E. Changizi, and M. H. Mohamadzadeh Moghadam, "Covalently-grafted graphene oxide nanosheets to improve barrier and corrosion protection properties of polyurethane coatings," *Carbon*, vol. 93, pp. 555–573, 2015.

[13] B. Dou, H. Xiao, X. Lin et al., "Investigation of the anti-corrosion properties of fluorinated graphene-modified waterborne epoxy coatings for carbon steel," *Coatings*, vol. 11, no. 2, p. 254, 2021.

[14] V. K. Srivastava, "Enhancement of elastic modulus of epoxy resin with carbon nanotubes," *World Journal of Nano Science and Engineering*, vol. 01, no. 1, pp. 1–6, 2011.

[15] S. Ammar, K. Ramesh, B. Vengadaesvaran, S. Ramesh, and A. K. Arof, "Amelioration of anticorrosion and hydrophobic properties of epoxy/PDMS composite coatings containing nano ZnO particles," *Progress in Organic Coatings*, vol. 92, pp. 54–65, 2016.

[16] S. Park and M. Shon, "Effects of multi-walled carbon nano tubes on corrosion protection of zinc rich epoxy resin coating," *Journal of Industrial and Engineering Chemistry*, vol. 21, pp. 1258–1264, 2015.

[17] M. Rostami, S. Rasouli, B. Ramezanzadeh, and A. Askari, "Electrochemical investigation of the properties of Co doped ZnO nanoparticle as a corrosion inhibitive pigment for modifying corrosion resistance of the epoxy coating," *Corrosion Science*, vol. 88, pp. 387–399, 2014.

[18] W. Xia, H. Xue, J. Wang et al., "Functionlized graphene serving as free radical scavenger and corrosion protection in gamma-irradiated epoxy composites," *Carbon*, vol. 101, pp. 315–323, 2016.

[19] Z. Yu, H. Di, Y. Ma et al., "Preparation of graphene oxide modified by titanium dioxide to enhance the anti-corrosion performance of epoxy coatings," *Surface and Coatings Technology*, vol. 276, pp. 471–478, 2015.

[20] A. Talo, P. Passiniemi, O. Forsén, and S. Yläsaari, "Polyaniline/epoxy coatings with good anti-corrosion properties," *Synthetic Metals*, vol. 85, no. 1, pp. 1333-1334, 1997.

[21] K. Shahapurkar, C. D. Garcia, M. Doddamani, G. C. Mohan Kumar, and P. Prabhakar, "Compressive behavior of cenosphere/epoxy syntactic foams in arctic conditions," *Composites Part B: Engineering*, vol. 135, pp. 253–262, 2018.

[22] K. Shahapurkar, V. B. Chavan, M. Doddamani, and G. C. M. Kumar, "Influence of surface modification on wear behavior of fly ash cenosphere/epoxy syntactic foam," *Wear*, vol. 414-415, pp. 327–340, 2018.

[23] K. Shahapurkar, M. Doddamani, G. C. Mohan Kumar, and N. Gupta, "Effect of cenosphere filler surface treatment on the erosion behavior of epoxy matrix syntactic foams," *Polymer Composites*, vol. 40, no. 6, pp. 2109–2118, 2019.

[24] C. D. Garcia, K. Shahapurkar, M. Doddamani, G. C. M. Kumar, and P. Prabhakar, "Effect of arctic environment on flexural behavior of fly ash cenosphere reinforced epoxy syntactic foams," *Composites Part B: Engineering*, vol. 151, pp. 265–273, 2018.

[25] G. Yang, Y. Wang, H. Xu, S. Zhou, S. Jia, and J. Zang, "Preparation and properties of three dimensional graphene/phenolic resin composites via in-situ polymerization in graphene hydrogels," *Applied Surface Science*, vol. 447, pp. 837–844, 2018.

[26] G. Christopher, M. Anbu Kulandainathan, and G. Harichandran, "Comparative study of effect of corrosion on mild steel with waterborne polyurethane dispersion containing graphene oxide versus carbon black nanocomposites," *Progress in Organic Coatings*, vol. 89, pp. 199–211, 2015.

[27] L. Liu and Z. Ye, "Effects of modified multi-walled carbon nanotubes on the curing behavior and thermal stability of boron phenolic resin," *Polymer Degradation and Stability*, vol. 94, no. 11, pp. 1972–1978, 2009.

[28] S. A. Song, Y. S. Chung, and S. S. Kim, "The mechanical and thermal characteristics of phenolic foams reinforced with carbon nanoparticles," *Composites Science and Technology*, vol. 103, pp. 85–93, 2014.

[29] G. Bahlakeh, B. Ramezanzadeh, and M. Ramezanzadeh, "Cerium oxide nanoparticles influences on the binding and corrosion protection characteristics of a melamine-cured polyester resin on mild steel: an experimental, density functional theory and molecular dynamics simulation study," *Corrosion Science*, vol. 118, pp. 69–83, 2017.

[30] O. Dagdag, A. El Harfi, A. Essamri et al., "Phosphorous-based epoxy resin composition as an effective anticorrosive coating for steel," *International Journal of Integrated Care*, vol. 9, no. 3, pp. 231–240, 2018.

Hindawi
Advances in Materials Science and Engineering
Volume 2022, Article ID 4883764, 7 pages
https://doi.org/10.1155/2022/4883764

Research Article

Experimental Investigations on Mechanical Properties of AZ31/Eggshell Particle-Based Magnesium Composites

N. Ramanujam,[1] S. Muthukumaran,[2] B. Nagesawara Rao,[3] M. Ramarao,[4] Amol L. Mangrulkar,[5] K. S. Ashraff Ali,[6] L. Pugazhendhi,[7] and Mebratu Markos[8]

[1]*Department of Mechanical Engineering, E.G.S. Pillay Engineering College, Nagapattinam 611002, Tamilnadu, India*
[2]*Department of Mechanical Engineering, University College of Engineering Panruti, Panruti, Tamil Nadu, India*
[3]*Department of Mechanical Engineering, VFSTR, Vadlamudi, Guntur 52213, Andhra Pradesh, India*
[4]*Department of Mechanical Engineering, Bharath Institute of Higher Education and Research, Chennai 600073, Tamilnadu, India*
[5]*Department of Mechanical Engineering, Rajiv Gandhi Institute of Technology, Mumbai 400053, India*
[6]*Department of Mechanical Engineering, C. Abdul Hakeem College of Engineering & Technology, Vellore 632509, Tamil Nadu, India*
[7]*Department of Mechanical Engineering, Chennai Institute of Technology, Chennai 600059, Tamilnadu, India*
[8]*Department of Mechanical Engineering, College of Engineering, Wolaita Sodo University, Ethiopia*

Correspondence should be addressed to Mebratu Markos; mebratumarkos@wsu.edu.et

Received 1 October 2021; Accepted 15 December 2021; Published 30 January 2022

Academic Editor: P. Ganeshan

Magnesium (AZ31) is an excellent choice for a bionic implant. To enhance biocompatibility, the hardest graphene nanoparticles were reinforced with biocompatible materials. In this paper, biocompatibility composite material is produced by stir-casting nanoshell particles reinforced with various weight percentages (0, 1, 2, 3, and 4 wt. percent) of AZ31 magnesium alloy. To understand the mechanical properties of the composite material, results of which are compared to the base alloy (AZ31) are used. The study mentioned how AZ31 magnesium alloy, reinforced with reinforcing particles, may be used to create implant-related human bone materials. Magnesium alloy reinforced with reinforcing particles is described in the study.

1. Introduction

Magnesium has excellent biocompatibility and modulus of elasticity in line with the human bone. Inorganic-stage calcium-containing crystals are embedded in the bone, increasing the tissue's sensitivity to normal stresses. Due to pathology and desorption, bone tissue breaks. Metals utilized for clinical purposes are found in the manufacturing process of bone fixation devices [1]. Magnesium is in high demand in every sector involved in the design and manufacture of automobiles, aircraft, and diverse engineering to meet those industry's needs. However, further advancement will be necessary if this technological evolution is to continue. MMC is a possible solution. Fibres or particulate of a ceramic material, i.e., silicon carbide or graphite, are usually present in metal matrix composites to reinforce the low-density material, i.e., aluminium or magnesium. Specifically, higher stiffness, operating temperature, wear resistance, and customizable properties can be found in these materials. AZ31 magnesium alloys have the opportunity to explore as light alloys for replacing some conventional structural materials in cars and trucks, locomotives, and general aviation. Using particulate magnesium matrix composites to make isotropic materials with improved mechanical properties is a favourable fabrication process (MMCs). Each of these variables is beneficial in increasing the mechanical properties of MMCs. Mg alloy in the AZ series has properties of cost effectiveness, density friendliness, and good mechanical properties, as well as cast ability [2]. The resulting thermomechanical processed precipitates of Mg17Al12

improve the mechanical properties. In addition, AZ Mg alloy incorporates particle reinforcements (which causes a higher strengthening efficiency) and thus incorporates reinforcements [3, 4]. The AZ Mg alloy has a significant increase in the amount of aluminium in its semisolid region, making it appropriate for semisolid casting. Developing new lightweight materials from recycled materials will be critical to sustainable development [5–7]. When there are Ti and SS alloys limiting the supply, magnesium can be a suitable alternative. Magnesium is exceptional in having a high level of strength, load-bearing capacity, biocompatibility, toxicity, and wide abundance in the earth's crust, water, and the human body and a modulus of elasticity that matches the bone [8, 9]. This is why the bone is more elastic than normal; thus, it protects the implant and bone better.

Additionally, Mg-based materials reduce the trauma the host patient experiences while also benefiting the host [10–14]. This is significant because even though it is possible for Mg to be absorbed into the human body and excreted without triggering an inflammatory response, this does not occur if Mg is consumed or injected. To make magnesium an attractive temporary implant, it is necessary to use conventional materials with these two features [15–19]. There are various requirements for materials that use Mg; they must meet them all to function as an equivalent replacement for the materials they replace. The importance of having important properties such as biocompatibility and low toxicity and other undesirable side effects over the service life cannot be stressed enough [20]. To obtain novel Mg-based materials with enhanced mechanical and corrosion responses, biocompatible alloying elements/reinforcements are required [21, 22]. Magnesium, in its original form, has few disadvantages, such as flexibility and corrosion resistance, in aqueous environments [23, 24]. Ball milling is a mechanical method for grinding particles into small particulates. Conventionally, the particles are usually cracked apart by solvent molecules; however, the reactants are separated apart by mechanical stresses in ball milling.

Methods used in the past have included the use of Al_2O_3, Y_2O_3, SiC, and CNT nanoparticles in various Mg-based composites (also known as carbon nanotubes). Also, recent studies [25–29] show that increasing magnesium's strength and ductility at the nanoscale by using ceramic reinforcements is possible. Because AZ31 alloy is so widely used in engineering applications, it has been paid a lot of attention [30]. From a survey of the relevant literature, the researchers found that very little research has been conducted to study the mechanical behaviour of nanometer-sized particulate or fibre hybrid-reinforced metal matrix composites. Results obtained from experiments with AZ31 magnesium matrix composites reinforced with submicron-SiC particulates showed that the mechanical properties were improved significantly. Xiang et al. [4] proceeded with the stir casting of AZ31 and discussion of mechanical characterization of the SiC particles included. The studies found that increasing the reinforcing particle from titanium dioxide, also called titanium(III) oxide, increases ultimate tensile strength, yield strength, and elastic modulus, along with a decrease in grain size [31]. Eggshell is a low-cost, abundant source of calcium, one of the best reinforcement options, which can be derived from chicken aviculture. Bone flours and oyster shells contain toxic elements such as Cd, Al, and Hg, and these toxins cause diseases in people, making bone flours and oyster shells less useful for medical use. The role of calcium in promoting bone mineralization aids in bone remodelling [32]. Eggshell having a lower density and greater stability has been superior to calcium carbonate, industrially prepared. It has recently been discovered that eggshells enhance the refining and strengthening of grain size and strength in the Al and Mg matrix. Magnesium alloy AZ31 was synthesized by stirring in water, and this solution was applied to small eggshell-sized nanoeggshell particles [32–34]. Researchers are conducting a series of experiments in order to determine the effect of nanoeggshell particles on the mechanical properties of magnesium alloy AZ31 in which the particles are also incorporated.

2. Materials and Methods

Magnesium is an important metal used in numerous industries, including electronics, automobiles, and aerospace. The composition of magnesium alloy AZ31 is listed in Table 1. Ball milling was used to reduce the average size of the eggshell powder (15–35 nm) to a finer nanosize that is just above the sub-nanosize range. The particle size of the product dropped dramatically after ball milling. The powder was ball-milled for 15 hours and then refined for 20 hours, which refined the powder to an average particle size of less than 75 nm and a range of 15–35 nm. The overall size of the ball mill did not change as the 40-hour ball milling time remained constant. This is why the synthesis of the composite materials required a total of 20 hours of eggshell powder that had been ball-milled. Powdered eggshells did not have detectable peaks other than calcium carbonate after the milling process. After ball milling, no impurities or additional secondary phases were found. Magnesium's biocompatible feature is increased by utilizing nanoeggshell particles (15–35 nm size), which improve the material's mechanical properties. Magnesium alloy AZ31's distinct composition details are shown in Table 2.

The density data from the samples that were developed are documented in Table 3. To obtain theoretical density, the rule of mixtures method was used.

The experimental density of magnesium alloy AZ31 used in the experiment is 2.231 g/cc. In order to measure experimental densities, the nanoeggshell particles (wt. percentages of 1, 2, 3, and 4) were added. This increased the measured densities to 2.568, 2.765, 2.963, and 3.123 g/cc, respectively. A study following up on this led to a later discovery of rising porosity levels in the samples. Near-dense materials are acceptable under certain porosity limits, which is what makes this trend in porosities acceptable. The lower porosity levels primarily attributed to our control of extrusion parameters and avoidance of air entrapment in the molten slurry during the stirring process occur because of our advanced control techniques. Promotion of nanoeggshell particle reinforcement is made easier because the molten slurry in the steel mould is rendered incapable of

Table 1: Various chemical elements available in magnesium alloy AZ31.

Elements	Aluminium	Zinc	Manganese	Silicon	Ferrous	Calcium	Magnesium
Contribution (%)	3.3	0.83	0.31	0.03	0.002	0.0023	Ball

Table 2: Composition details of the composite specimens.

Specimen identification	Wt. % of magnesium alloy AZ31	Wt. % of nanoeggshell particles
MG0	100	0
MG1	99	1
MG2	98	2
MG3	97	3
MG4	96	4

Table 3: Density and porosity values of the samples.

Composition	Theoretical density (g/cc)	Measured density (g/cc)	Porosity
MG0	2.231	2.228	0.1346
MG1	2.568	2.561	0.2733
MG2	2.765	2.757	0.2902
MG3	2.963	2.951	0.4066
MG4	3.123	3.101	0.7094

supporting itself before the slurry is applied, so the particles are more uniformly distributed, and the occurrence of porosity is avoided.

3. Experimental Procedure

Stir casting (Figure 1) was used to make the AZ31 magnesium metal matrix composite. Once the furnace was hot enough, the ingot of magnesium was put in. Because magnesium is highly flammable, a gas that is both nonflammable and safe to breathe was continuously supplied to the furnace as an atmosphere. To prevent the egg white from becoming sticky, the nanoeggshell particles are preheated to 350°C before the addition of magnesium alloys. Magnesium must be heated to 750°C in the crucible before it is used to raise the temperature of the heating element to 450°C. The procedure involves mixing the eggshell particles with molten magnesium in the crucible furnace and then stirring the mixture for 15 minutes using an electric stirrer. The metal has reached a solidified state when it is naturally heated by convection and then poured into a fixed, large iron die, 150 mm × 150 mm × 25 mm in size. Figure 2 reveals the impact tester. The impact sample prepared by the ASTM standard is shown in Figure 3.

4. Results and Discussion

4.1. Tensile Strength. In order to investigate the elasticity and ultimate strength of the material, the tensile test was performed according to ASTM-E32 standards. Every time the materials were reinforced, a specified amount was cut and machined at three different locations according to ASTM standards. The reinforced composite was built to an approximate 34% construction, and the calculated and graphed averages were compared to the testing on a UTM machine. As reinforcement was added, tensile strength increased gradually, as illustrated in Figure 4. Strength increases

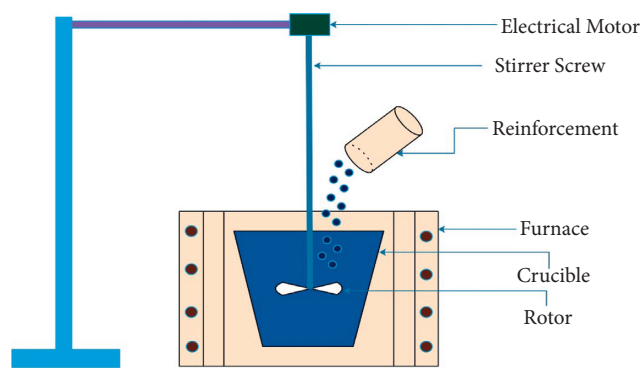

Figure 1: Experimental setup of the stir-casting technique.

gradually with the increasing base magnesium alloy content to 80.73 percent. A pie chart displaying the percentage elongation of the composite is shown in Figure 5. The elongation increased at a much higher rate than the AZ31 alloy.

4.2. Young's Modulus. Figure 6 shows the variation in Young's modulus for all composite specimens. With nanoeggshell particles' content, Young's modulus of the MG0 composite sample is around 71 GPa, but it slightly increased to 83 GPa for MG4 composite specimens (4 wt. percent nanoeggshell particles).

Young's modulus depends on the orientation of nanoeggshell particles when being loaded. When nanoeggshell particles are positioned parallel to the loading direction, Young's modulus variation will be high. Conversely, when they are positioned perpendicular to the loading direction, the variation will be low. To get a medium value, roll a random number to find the orientation. As reported by this study, the milling and stir-casting techniques used in the current investigation could have caused nanoeggshell

Figure 2: Impact tester.

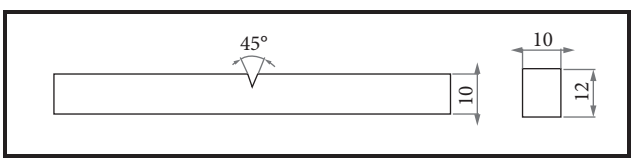

Figure 3: Schematic image of the impact sample.

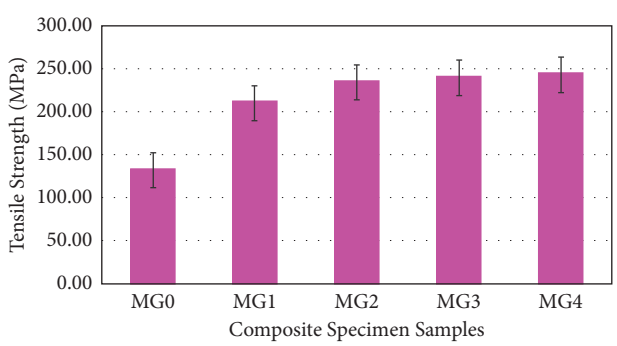

Figure 4: Tensile strength variation of composite specimens.

particles to align in a random orientation, which did not change in response to the applied tensile loads. Additional investigation is required to better understand the variation in Young's modulus in the peak loading condition with nanoeggshell particles' content. Since there is a greater amount of nanoeggshell particles in the composition, the ductility of the Mg alloy/nanoeggshell particle composite is drastically increased, and it still fits within the elongation limits for many applications. Ductility may have improved because there are more void nucleation sites due to the inclusion of nanoeggshell particles, resulting in a lower fracture strain.

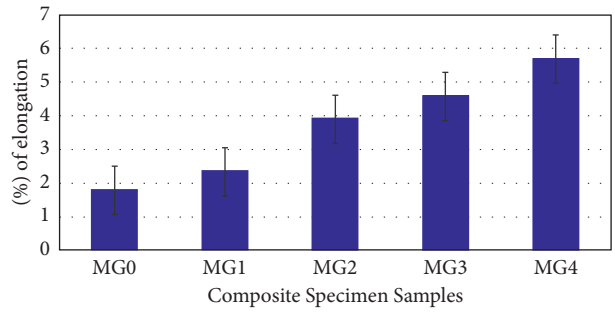

Figure 5: Variation on elongation percentage of composite specimens.

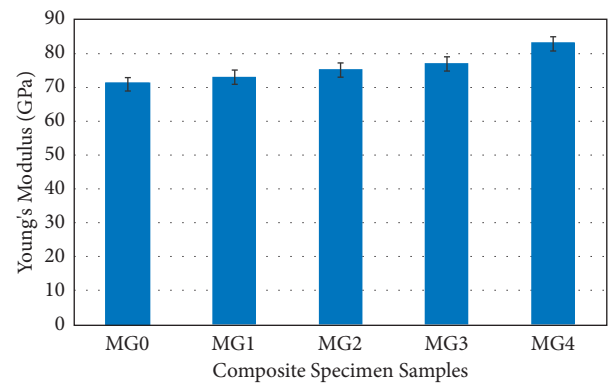

Figure 6: Variation on Young's modulus of composite specimens.

4.3. Yield Strength. Figure 7 shows how variations in yield tensile strengths are affected by Mg alloy and nanoeggshell particles' content. The MG1, MG2, MG3, and MG4 samples that contain nanoeggshell particle-reinforced composite specimens have the highest yield strength (MG0).

This boost from 93 MPa (with no nanoeggshell particles) to 131 MPa represents a boost in tensile strength (Mg alloy with 4 wt. percent of nanoeggshell particles). While improvements in yield strength (29% better) were due to the reinforcement effect of nanoeggshell particles, the strengthening of strengths (yield) was caused by the reinforcement effect of eggshell particles. Based on the findings of the present study, it can be inferred that the mechanical strength of Mg alloy, reinforced with nanoeggshell particles, gets stronger when compared to the studies conducted by other researchers. Concerning the yield strength of the magnesium alloy AZ31, the contributions of different reinforcements are considered, which include the addition of the nanoeggshell particle-reinforced composites.

4.4. Compressive Strength. A compression test was carried out using ASTM standards to understand the material's compressive properties. Every time the materials were reinforced, a specified amount was cut and machined at three different locations according to ASTM standards. Compression test results were recorded and plotted against the composite's reinforcement percentage. It can be concluded from Figure 8 that the compressive strength of the composite material increases with reinforcement and

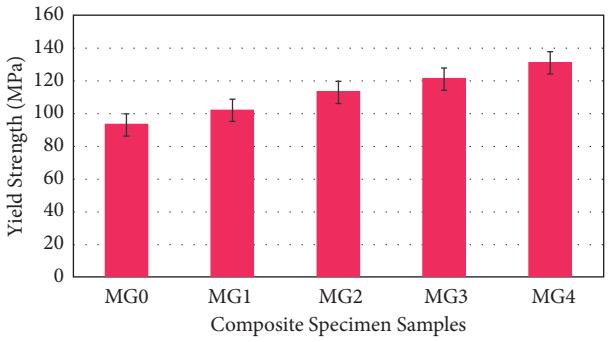

Figure 7: Variation on the yield strength of composite specimens.

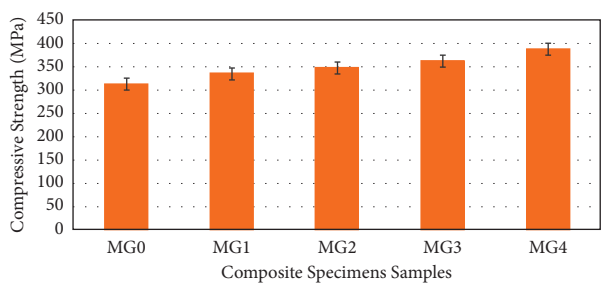

Figure 8: Variation on compressive strength of composite specimens.

increases quickly for a moderate amount of reinforcement. Using base magnesium alloy as a baseline, the strength of the composites gradually improves to 24.36%.

4.5. Microhardness. AZ31 magnesium alloy and composite materials were both tested in the hardness test, ASTM E384-99, to understand the effect of nanoeggshell particles in the magnesium matrix. Micro Vickers hardness test results show that the composite material was impacted by a 400 g load for 50 seconds with an 8 mm steel ball indenter. Five locations on the material were tested, and the results were plotted and represented as the composite's overall hardness. The hardness of the composite, which is shown in Figure 9, increases to 29.63 as opposed to the magnesium matrix.

The microhardness test results are shown in Figure 9. A pure AZ31 alloy composite specimen (MG0) was found to have a microhardness of 76 HV. Monolithic magnesium traditionally has microhardness in the range of 35–55 HV. Significant improvement in the properties of the magnesium alloy can be attributed to the solid solution strengthening of zinc in the melt in the presence of zinc as an alloying element. A monotonically increasing effect was observed after the addition of nanoeggshell particles. While all four composites show 88, 96, 108, and 114 HV in microhardness, MG1 has 1 wt.% nanoeggshell percentage, MG2 has 2 wt.% nanoeggshell percentage, MG3 has 3 wt.% nanoeggshell percentage, and MG4 has 4 wt.% nanoeggshell percentage. Using this enhancement, you can now see the difference between soft nanoeggshell particles and hard nanoeggshell particles, which results in improved grain size and resistance to localized deformation. Tribo measurements should not be confused with materials' hardness as an indicator of tribological response.

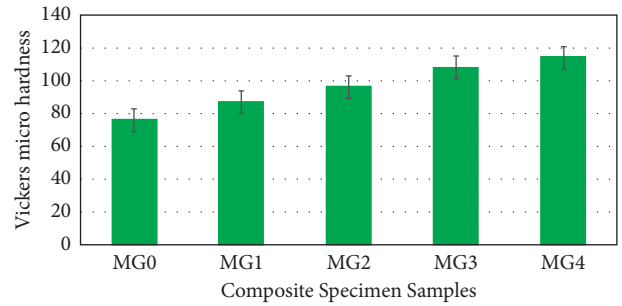

Figure 9: Variation on Vickers microhardness of composite specimens.

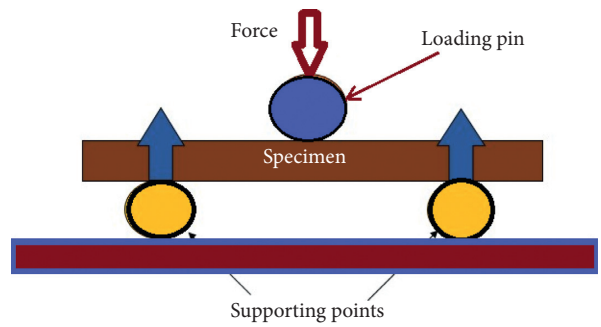

Figure 10: Schematic image of the flexural test setup.

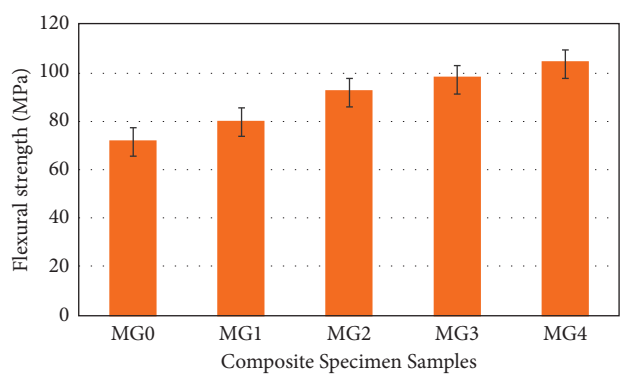

Figure 11: Variation on flexural strength of composite specimens.

4.6. Flexural Strength. The three-point bend test was developed to study the material's bending behaviour according to ASTM standards. With each reinforcment, the prescribed amount was divided into three portions, which were then milled and machined at three separate locations according to ASTM standards. Flexural test arrangement is shown in Figure 10. After the value was plotted versus the percentage of reinforcement from the three-point flexural testing machine, the values were recorded. The composite's flexural strength will increase when the reinforcement intensity increases, as shown in Figure 11. Composites' strength was found to improve gradually to 30.89% when compared to the base magnesium alloy.

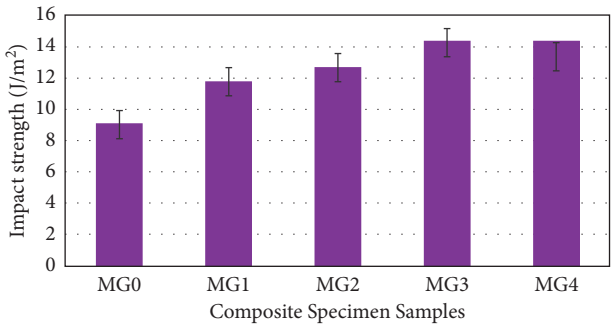

Figure 12: Variation on impact strength of composite specimens.

4.7. Impact Strength. To comply with ASTM standards, Charpy impact testing was required. The size we used for the test was $55 \times 10 \times 10$ mm, with a 2 mm depth and the standard angle. The composites were divided into three groups, and the impact toughness of each was then investigated. In Figure 12, it was discovered that impact strength increases steadily with the percentage of nanoeggshell particles, then plateaus, and declines at levels of 1 to 3 percent of composite oxidation.

5. Conclusions

Based on the experimental studies, the following findings were drawn: the pure magnesium alloy AZ31 (0, 1, 2, 3, and 4 wt.% of nanoeggshell particle-reinforced composite specimens) was found to have the following properties: after developing an AZ31 magnesium alloy with nanoeggshell particle-reinforced composites, the particles were dispersed evenly throughout the alloy. When compared to AZ31 magnesium alloy, which was interesting, reinforced material had better results. A few early findings of the experimental phase indicated that the metal matrix composite did not include any intermetallic phase. AZ31 alloy was changed by the addition of nanoeggshell particles. The composite is typically stronger because of the more intricate texture. There is a positive correlation between the nanoeggshell particle hybrid ratio and overall strengthening (96 : 04). Hybrid ratios that are large produce the most robust hybrid composites. The new model agrees with the experimental data very well.

Data Availability

The data used to support the findings of this study are included within the article. Further data or information is available from the corresponding author upon request.

Conflicts of Interest

The authors declare that there are no conflicts of interest regarding the publication of this article.

Acknowledgments

The authors appreciate the support from Wolaita Sodo University, Ethopia. The authors thank the Bharath Institute of Higher Education and Research, Chennai, and E.G.S. Pillay Engineering College, Nagapattinam, for providing technical assistance to complete this experimental work.

References

[1] S. Raja, U. M. Kumar, S. Mathivanan et al., "Mechanical and microstructural properties of graphene reinforced magnesium composite," *Materials Today Proceedings*, vol. 44, pp. 3571–3574, 2021.

[2] W.-J. Li, K.-K. Deng, X. Zhang et al., "Microstructures, tensile properties and work hardening behavior of SiCp/Mg-Zn-Ca composites," *Journal of Alloys and Compounds*, vol. 695, pp. 2215–2223, 2017.

[3] S.-J. Huang and A. N. Ali, "Effects of heat treatment on the microstructure and microplastic deformation behavior of SiC particles reinforced AZ61 magnesium metal matrix composite," *Materials Science and Engineering: A*, vol. 711, pp. 670–682, 2018.

[4] S. L. Xiang, M. Gupta, X. J. Wang, L. D. Wang, X. S. Hu, and K. Wu, "Enhanced overall strength and ductility of magnesium matrix composites by low content of graphene nanoplatelets," *Composites Part A: Applied Science and Manufacturing*, vol. 100, pp. 183–193, 2017.

[5] M. Torabi Parizi, H. R. Ezatpour, and G. R. Ebrahimi, "High mechanical efficiency, microstructure evaluation and texture of rheo-casted and extruded AZ80-Ca alloy reinforced with processed Al2O3/GNPs hybrid reinforcement," *Materials Chemistry and Physics*, vol. 218, pp. 246–255, 2018.

[6] X.-F. Sun, C.-J. Wang, K.-K. Deng, K.-B. Nie, X.-C. Zhang, and X.-Y. Xiao, "High strength SiCp/AZ91 composite assisted by dynamic precipitated Mg17Al12 phase," *Journal of Alloys and Compounds*, vol. 732, pp. 328–335, 2018.

[7] F. Guo, D. Zhang, X. Yang, L. Jiang, and F. Pan, "Strain-induced dynamic precipitation of Mg17Al12 phases in Mg-8Al alloys sheets rolled at 748 K," *Materials Science and Engineering: A*, vol. 636, pp. 516–521, 2015.

[8] M. Torabi Parizi, A. Habibolahzadeh, and G. R. Ebrahimi, "Optimizing and investigating influence of manufacturing techniques on the microstructure and mechanical properties of AZ80-0.5Ca-1.5Al2O3 nanocomposite," *Materials Chemistry and Physics*, vol. 199, pp. 485–496, 2017.

[9] S. A. Sajjadi, H. R. Ezatpour, and M. Torabi Parizi, "Comparison of microstructure and mechanical properties of A356 aluminum alloy/Al2O3 composites fabricated by stir and compo-casting processes," *Materials & Design*, vol. 34, pp. 106–111, 2012.

[10] M. R. Doddamani, S. M. Kulkarni, and Kishore, "Behavior of sandwich beams with functionally graded rubber core in three point bending," *Polymer Composites*, vol. 32, no. 10, pp. 1541–1551, 2011.

[11] M. L. Jayavardhan and M. Doddamani, "Quasi-static compressive response of compression molded glass microballoon/HDPE syntactic foam," *Composites Part B: Engineering*, vol. 149, pp. 165–177, 2018.

[12] C. D. Garcia, K. Shahapurkar, M. Doddamani, G. C. M. Kumar, and P. Prabhakar, "Effect of arctic environment on flexural behavior of fly ash cenosphere reinforced epoxy syntactic foams," *Composites Part B: Engineering*, vol. 151, pp. 265–273, 2018.

[13] V. Manakari, G. Parande, M. Doddamani, and M. Gupta, "Evaluation of wear resistance of magnesium/glass microballoon syntactic foams for engineering/biomedical applications," *Ceramics International*, vol. 45, no. 7, pp. 9302–9305, 2019.

[14] B. Patil, B. R. Bharath Kumar, S. Bontha et al., "Eco-friendly lightweight filament synthesis and mechanical characterization of additively manufactured closed cell foams,"

Composites Science and Technology, vol. 183, Article ID 107816, 2019.

[15] G. Parande, V. Manakari, G. K. Meenashisundaram, and M. Gupta, "Enhancing the hardness/compression/damping response of magnesium by reinforcing with biocompatible silica nanoparticulates," *International Journal of Materials Research*, vol. 107, no. 12, pp. 1031–1099, 2016.

[16] R. Swaminathan, "Magnesium metabolism and its disorders," *Clinical Biochemist Reviews*, vol. 24, no. 2, pp. 47–66, 2003.

[17] A. Atrens, G.-L. Song, M. Liu, Z. Shi, F. Cao, and M. S. Dargusch, "Review of recent developments in the field of magnesium corrosion," *Advanced Engineering Materials*, vol. 17, no. 4, pp. 400–453, 2015.

[18] M. Gupta and W. L. E. Wong, "Magnesium-based nanocomposites: lightweight materials of the future," *Materials Characterization*, vol. 105, pp. 30–46, 2015.

[19] M. S. Kujur, A. Mallick, V. Manakari, G. Parande, K. S. Tun, and M. Gupta, "Significantly enhancing the ignition/compression/damping response of monolithic magnesium by addition of Sm2O3 nanoparticles," *Metals*, vol. 7, no. 9, p. 357, 2017.

[20] J. Walker, S. Shadanbaz, T. B. F. Woodfield, M. P. Staiger, and G. J. Dias, "Magnesium biomaterials for orthopedic application: a review from a biological perspective," *Journal of Biomedical Materials Research Part B: Applied Biomaterials*, vol. 102, no. 6, pp. 1316–1331, 2014.

[21] G. Kumar Meenashisundaram, T. Hou Damien Ong, G. Parande, V. Manakari, S. Xiang, and M. Gupta, "Using lanthanum to enhance the overall ignition, hardness, tensile and compressive strengths of Mg-0.5Zr alloy," *Journal of Rare Earths*, vol. 35, no. 7, pp. 723–732, 2017.

[22] A. Atrens, G.-L. Song, F. Cao, Z. Shi, and P. K. Bowen, "Advances in Mg corrosion and research suggestions," *Journal of Magnesium and Alloys*, vol. 1, no. 3, pp. 177–200, 2013.

[23] J. Lan, Y. Yang, and X. Li, "Microstructure and microhardness of SiC nanoparticles reinforced magnesium composites fabricated by ultrasonic method," *Materials Science and Engineering: A*, vol. 386, no. 1–2, pp. 284–290, 2004.

[24] G. Cao, H. Choi, J. Oportus, H. Konishi, and X. Li, "Study on tensile properties and microstructure of cast AZ31D/AlN nanocomposites," *Materials Science and Engineering: A*, vol. 494, no. 1–2, pp. 127–131, 2008.

[25] S. F. Hassan and M. Gupta, "Development of high performance magnesium nanocomposites using solidification processing route," *Materials Science and Technology*, vol. 20, no. 11, pp. 1383–1388, 2004.

[26] W. L. E Wong and M. Gupta, "Simultaneously improving strength and ductility of magnesium using nano-size SiC particulates and microwaves," *Advanced Engineering Materials*, vol. 8, no. 8, pp. 735–740, 2006.

[27] C. Goh, J. Wei, L. Lee, and M. Gupta, "Properties and deformation behaviour of Mg-Y2O3 nanocomposites," *Acta Materialia*, vol. 55, no. 15, pp. 5115–5121, 2007.

[28] S. F. Hassan and M. Gupta, "Development and characterization of ductile Mg/Y 2 O 3 nanocomposites," *Journal of Engineering Materials and Technology, Transactions of the ASME*, vol. 129, no. 3, pp. 462–467, 2007.

[29] K. S. Tun and M. Gupta, "Improving mechanical properties of magnesium using nano-yttria reinforcement and microwave assisted powder metallurgy method," *Composites Science and Technology*, vol. 67, no. 13, pp. 2657–2664, 2007.

[30] K. K. Deng, K. Wu, Y. W. Wu, K. B. Nie, and M. Y. Zheng, "Effect of submicron size SiC particulates on microstructure and mechanical properties of AZ91 magnesium matrix composites," *Journal of Alloys and Compounds*, vol. 504, no. 2, pp. 542–547, 2010.

[31] G. Parande, V. Manakari, S. D. S. Kopparthy, and M. Gupta, "Utilizing low-cost eggshell particles to enhance the mechanical response of Mg–2.5 Zn magnesium alloy matrix," *Advanced Engineering Materials*, vol. 20, no. 5, Article ID 1700319, 2018.

[32] S.-Y. He, Y. Sun, M.-F. Chen, D.-B. Liu, and X.-Y. Ye, "Microstructure and properties of biodegradable β-TCP reinforced Mg-Zn-Zr composites," *Transactions of Nonferrous Metals Society of China*, vol. 21, no. 4, pp. 814–819, 2011.

[33] A. Chaithanyasai, P. R. Vakchore, and V. Umasankar, "The micro structural and mechanical property study of effects of EGG SHELL particles on the Aluminum 6061," *Procedia Engineering*, vol. 97, pp. 961–967, 2014.

[34] S. B. Hassan and V. S. Aigbodion, "Effects of eggshell on the microstructures and properties of Al-Cu-Mg/eggshell particulate composites," *Journal of King Saud University - Engineering Sciences*, vol. 27, no. 1, pp. 49–56, 2015.

Hindawi
Advances in Materials Science and Engineering
Volume 2022, Article ID 8761865, 8 pages
https://doi.org/10.1155/2022/8761865

Research Article

Characterization of the Aluminium Matrix Composite Reinforced with Silicon Nitride (AA6061/Si_3N_4) Synthesized by the Stir Casting Route

B. Ashok Kumar,[1] **M. Muthu Krishnan**,[2] **A. Felix Sahayaraj**,[2] **Mohamad Reda A. Refaai**,[3] **G. Yuvaraj**,[4] **D. Madhesh**,[5] **and Haiter Lenin Allasi**[6]

[1]*Department of Mechanical Engineering, Nandha Engineering College, Vaikkaal Medu, Erode 638052, Tamil Nadu, India*
[2]*Department of Mechanical Engineering, Kalaignar Karunanidhi Institute of Technology, Coimbatore 641402, Tamil Nadu, India*
[3]*Prince Sattam bin Abdulaziz University, College of Engineering, Department of Mechanical Engineering, Alkharj 16273, Saudi Arabia*
[4]*Department of Mechanical Engineering, Easwari Engineering College, Chennai 600089, Tamil Nadu, India*
[5]*Department of Mechanical Engineering, Academy of Maritime Education and Training (AMET), Chennai 603112, Tamil Nadu, India*
[6]*Department of Mechanical Engineering, Wollo University, Kombolcha Institute of Technology, Kombolcha, Ethiopia*

Correspondence should be addressed to Haiter Lenin Allasi; drahlenin@kiot.edu.et

Received 25 October 2021; Accepted 4 January 2022; Published 29 January 2022

Academic Editor: P. Ganeshan

The current work is concerned with the synthesis of aluminium (AA6061-T6) matrix composites (AMCs) reinforced with 15 and 20 weight percentages of silicon nitride (Si_3N_4) particulates using the indigenously fabricated electric stir casting furnace with bottom discharge arrangement. The major concern in the synthesis of AMCs of ceramic particles with the aluminium matrix is wettability in the casting route, and it was overcome by adding 2% of magnesium in the melt, proper incorporation time, and appropriate stirring speed. The microstructure and mechanical characteristics of the synthesized AMC were analyzed. Si_3N_4 particles in the matrix are uniformly dispersed in the optical and scanning electron micrographs (SEM). Adding reinforcement particles of Si_3N_4 to the AA6061 matrix increased microhardness, macrohardness, and ultimate tensile strength significantly. Microhardness and macrohardness of the AA6161/20 wt.% Si_3N_4 composite were 98 VHN and 91 BHN, respectively, which were 117.8% and 111.63% higher than those of the AA6061 matrix alloy, respectively. Ultimate tensile strength (UTS) of AA6061 was 159.82 MPa which was increased to 249.12 MPa in the AA6061/20 wt.% Si_3N_4 composite. Percent elongation of the AA6061/Si_3N_4 composite was reduced with the addition of Si_3N_4 reinforcement.

1. Introduction

Industry 4.0 demands novel materials, and the demand for monolithic alloys is decreasing as they could not meet the requirements of the modern structural applications. Advanced materials such as aluminium metal matrix composites (AMCs) are a new generation of materials and find a wider scope in aeronautical, automobile, and electronics parts' and turbine blades' applications owing to their attractive mechanical and structural properties of lightweight and high strength, better wear and fatigue resistance, greater stiffness, and highly effective electrical and thermal conductivities [1, 2]. They also exhibit high stability at elevated temperatures. Even though many processes such as squeeze casting technique, powder metallurgy, in situ reaction, and powder injection moulding are employed to synthesize AMCs, stir casting route is commonly employed commercially as it has many advantages over other processing methods.

Stir casting is one form of casting process where a mechanical stirrer is used to mix the reinforcement with the

matrix base material such as aluminium by forming a vortex. Stir casting is one of the most effective methods for mass fabrication of AMCs because it is simple, flexible, economical, and suitable for mass production and production of complex profiled composite components without damaging the reinforcement particles [3, 4]. A typical stir casting machine comprises a mechanical feeder, reinforcement stirrer, and furnace that withstands high temperature and is used for melting of aluminium matrix materials.

The stir casting process involves various steps such as the following: (a) melting of the matrix aluminium materials; (b) stirring of molten matrix materials by using a mechanical stirrer; (c) feeding of reinforcement materials that have higher melting point than matrix materials. Generally, reinforcements are preheated before using in the matrix solution; (d) continuous stirring of the mixture of reinforcement and matrix; (e) pouring of the mixture in the mould after ensuring proper distribution of reinforcement throughout the matrix; (f) solidification of the mixture for further processing and testing. Mechanical properties of the AMCs depend on the effective distribution of the reinforcements in the matrix which in turn depends on the proper stirring of the mixture. These dispersions depend on the stirring parameters such as stirring speed, stirring time, position of the stirrer, stirrer size, and the feed rate of the reinforcements [5].

Kalaiselvan et al. [6] fabricated the AMC reinforced with various (viz., 4, 6, 8, 10, and 12) wt.% of B_4C by using the stir casting process and studied its metallurgical and mechanical properties. The K_2TiF_6 flux added to improve the wettability was reacted with B_4C particles and produced K and F compounds which contributed for removing the oxide film from the Al surface. Macrohardness, microhardness, and UTS of the AMC reinforced with 12% of B_4C were 58%, 70%, and 16% higher than those of 4% of B_4C particles, respectively. Wahab et al. [7] fabricated the Al-Si alloy reinforced with the AlN composite by the stir casting process. No porosity was observed in the microstructure which might be due to optimum stirring speed of the slurry and good bonding. Pazhouhanfar and Eghbali [8] fabricated the AA2024 matrix composite reinforced with Al_2O_3 particles of various sizes viz., 16, 32, and 66 μm by the stir casting route. The dispersion of the coarser size (66 μm) was more uniform, while the finer particles (16 and 32 μm) were led to agglomeration and segregation of the particles and porosity. It was justified that the Al dendrites solidified first during solidification of the composite, and the particles were rejected by the solid-liquid interface and, hence, were segregated to the interdendritic region. This event occurred more easily with the finer particles. Both hardness and tensile strength increased with the amount of Al_2O_3 particles present and decreasing particle size.

Several studies have shown an incremental value in the mechanical properties such as hardness and tensile properties with an increase in reinforcement weight percentage in AMCs [9–11]. Also, studies on AA6082/Si_3N_4 are found to increase in wear resistance and hardness properties [12, 13]. In this study, silicon nitride (Si_3N_4) was reinforced in AA6061 alloy, and its mechanical and metallurgical characterizations were analyzed.

2. Experimental Procedure

Wolfram-coated stainless steel crucibles of the electric furnace were used to heat a predetermined quantity of heat-treatable aluminium alloy AA6061-T6 (Mg-0.9, Si-0.64, Fe-0.26, Cu-0.21, Mn-0.1, Cr-0.05, Zn-0.04, Ni-0.02, Ti-0.01, and Al-balance by wt.%) rods which are shown in Figure 1. Wolfram coating prevents the contamination of melt at higher temperature. Crucible temperature was set to 1000°C. When the crucible attained 600°C, it was supplied with a constant volumetric flow of argon gas of 2 liters per min which is applied to prevent the aluminium alloy from reacting chemically with oxygen and nitrogen in the atmosphere. When the crucible attained 1000°C, the wettability of the alloy was enhanced by adding magnesium (2%) with the metal between Si_3N_4 and AA6061 alloy. The melt was stirred at 400 rpm using a Wolfram-coated stainless steel stirrer and an electric motor. It is imperative that stirring of the molten alloy aids the incorporation of the reinforcement particles Si_3N_4 in the AA6061 alloy and facilitates homogeneous dispersion. Appropriate stirring speed must be maintained to avoid entrapment of the gas in the molten alloy which may form because of overagitation of the melt and lead to poor quality of the cast. A predetermined amount (15% of weight of the composite to be produced) of Si_3N_4 particles of size 5 to 6 μm and purity of more than 99.6% was preheated to 750°C in a separate electric furnace which is shown in Figure 2. Preheating of Si_3N_4 was done (i) to remove all the moisture and trapped air between the reinforcement particles, (ii) to reduce the temperature gradient between the molten alloy and reinforcement particle which would increase the viscosity of the slurry as the result of difficulties in eliminating the trapped gases, and (iii) to remove the impurities from the surface of the particles. Preheated Si_3N_4 was added into the molten matrix, and the slurry was stirred for 1200 s. Without stopping the stirring and supply of the argon gas, the slurry was poured through the bottom pouring attachment into the cavity of the preheated permanent die at 300° C. Figure 2 shows the permanent die and electric preheater. The composites were solidified in the ambient condition. Similarly, AA6061 matrix containing 20 wt.% of Si_3N_4 and AA6061 alloy were fabricated. The fabricated AA6061 alloy and AA6061/15 and 20 wt.% Si_3N_4 composite castings are presented in Figure 3.

To perform the metallurgical characterization, specimens of size 25 mm × 25 mm × 6 mm were taken out from the cast alloy and composite containing 15 and 20 wt.% of Si_3N_4. As per the standard metallographic techniques, all the specimens were prepared. The specimens have been polished with emery sheets from 280 to 1200 grit and further polished using a disc polishing machine by diamond pastes of sizes 6, 3, and 0.5 m. Acetone and purified water were used to clean the polished specimens completely. The cleaned specimens were etched for microstructural analysis by means of a colour etchant solution of 1 g of sodium hydroxide (NaOH) and 4 g of potassium permanganate ($KMnO_4$) in 100 ml of distilled water. Optical microscope (Olympus BX51M) and scanning electron microscope (SEM) were used to observe the microstructural analysis of the etched specimens. Brinell

Figure 1: Modified electric stir casting furnace with the bottom pouring attachment and the electric furnace used to preheat Si_3N_4.

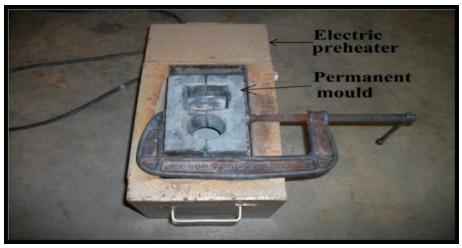

Figure 2: Preheater of the permanent mould.

hardness tester (model 7KB3000) with an axial load of 500 kg operated for 15 seconds at ten separate sites was used to determine the macrohardness of the AA6061 alloy and AA6061/15 and 20 wt.% Si_3N_4. With a microhardness tester (Mitutoyo MVK-H1), the specimens were tested by placing a 500 g load for 15 seconds on 25 different spots. From each cast composite and AA60601 alloy, 2 tensile specimens were cut as per the American Society of Testing and Materials (ASTM: E8/E8 M-11) standard [14]. The tensile specimen dimensions according to the ASTM standard are presented in Figure 4. The fabricated tensile specimens as per the ASTM standard are shown in Figure 5. A computerized universal testing machine (HI-TECH TUE-C-1000) was used for determining the ultimate tensile strength (UTS) and percent elongation (PE) at ambient temperature, and the standard values were recorded.

3. Results and Discussion

The matrices of the AA6061 alloy reinforced with 15 and 20 wt.% of Si_3N_4 composites were successfully manufactured through the stir casting route with optimized process parameters. The metallurgical and mechanical characterization studies of the AA6061/Si_3N_4 fabricated composites are discussed below.

3.1. Microstructure of AA6061/Si_3N_4 Composites. The optical microstructures of the AA6061 alloy and AA6061 alloy-fabricated matrix composites reinforced with 15 and 20 wt.% of Si_3N_4 are shown in Figure 6. The optical microstructure of the cast AA6061 alloy can be observed in Figure 6(a). Alpha-aluminium dendritic network structures were found in the microstructure. Formation of the alpha-aluminium dendritic network structure is attributed to the rapid cooling of the AA6061 alloy during solidification. In the microstructure, precipitation of the inorganic compound magnesium silicate (Mg_2Si) is observed. Figure 6(b) reveals the micrographs of AA6061/15 and 20 wt.% Si_3N_4 composites, respectively. There are no signs of porosity or other casting defects in these micrographs, and the Si_3N_4 reinforcement particles are more uniformly dispersed in the aluminium alloy matrix. These indicate that proper casting procedure was employed to cast composites. The causes for refinement of alpha-aluminium grains are as follows: (i) during the solidification of the AA6061/Si_3N_4 composite, Si_3N_4 particles are pushed in the direction of refined alpha-aluminium grains and (ii) alpha-aluminium grains settle on Si_3N_4 particles, which act as a nucleus [15].

Figure 6(a) depicts the precipitation of Mg_2Si in the matrix. Magnesium silicide is formed from a variety of sources: (i) Si and Mg are the major constituents in the AA6061 alloy and (ii) the incorporation of magnesium into a molten alloy (for increasing the wettability between the AA6061 alloy and Si_3N_4 particles). Oxide layer inclusions and intermetallic compounds were not seen in the microstructure of composites. It may be due to the continuous supply of inert argon gas into the crucible. Figure 7 shows the SEM image of AA6061/15 and 20 wt.% Si_3N_4 composites. It is obvious from the SEM micrographs that dispersion of Si_3N_4 reinforcement particles in the matrix alloy is more homogeneous.

3.2. Assessment of Mechanical Properties. The microhardness values of the AA6061 alloy and AA6061/15 and 20 wt.% Si_3N_4 composites are shown in Figure 8. Both hardness of the composites increases linearly with the increase of hard Si_3N_4 reinforcement particles in the AA6061 alloy matrix. Microhardness of AA6061/15 and 20 wt.% Si_3N_4 composites is 86 VHN and 98 VHN, respectively, and these are 91.11% and 117.78% higher than those of the AA6061 matrix alloy, respectively. Microhardness of the AA661 alloy is 45 VHN. Similarly, macrohardness of AA6061/15 and 20 wt.% Si_3N_4 composites is 79 BHN and 91 BHN, respectively, and these are 83.72% and 111.63% greater than those of the AA6061 matrix alloy, respectively. Macrohardness of the AA6061 alloy is 43 BHN. Average UTS and elongation percentage of the AA6061 matrix and AA6061 matrix composites containing 15 and 20 wt.% of Si_3N_4 reinforcement particles are shown in Figure 9. UTS of AA6061/15 and 20 wt.% of Si_3N_4 was 229.48 and 249.12 MPa, respectively. The addition of Si_3N_4 particles (which are having a lower coefficient of thermal expansion of 3.7×10^{-6}/K) in the aluminium alloy (which is having a higher coefficient of thermal expansion of 24×10^{-6}/K) alters the microstructural changes in the matrix which enhances the strength of the composites. When the amount of Si_3N_4 ceramic particles in an aluminium matrix alloy is increased, the grain size and substructure of the matrix are reduced, while the dislocation density surrounding the Si_3N_4 particles increases during solidification [16].

Figure 3: Fabricated AA6061/Si_3N_4 composite castings.

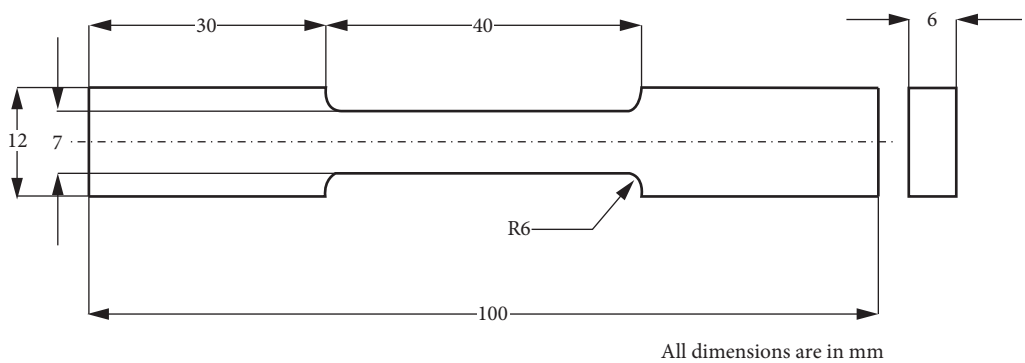

Figure 4: Dimensions of the tensile specimen as per the ASTM: E8/E8 M-11 standard.

During solidification, hard ceramic Si_3N_4 particles in the molten aluminium alloy provide additional heterogeneous nucleating sites. As a result, further decrease in grain size of the AA6061 matrix alloy is observed. All these microstructural changes increase the resisting force against the macroscopic- and microscopic-level dislocations under the action of a far-field stress [17]. As a result, an increase of Si_3N_4 in the matrix increases the hardness and UTS of the composites. The effect of reinforcement of Si_3N_4 on percent elongation (PE) of the composite is presented in Figure 9(b). The ductility of the aluminium matrix is reduced due to the following: (i) an increasing amount of hard Si_3N_4 in the AA6061 matrix which reduced the plastic flow of the matrix, (ii) more grain boundaries per unit area due to the grain refinement as the incorporation of reinforcement particles increases the number of turns of the dislocation path, and (iii) increased weight percentage of Si_3N_4 reinforcement particles in the composite reduces the volume fraction of the ductile aluminium alloy matrix. As a result of all these effects, PE of the composite is decreased with the addition of Si_3N_4-reinforced particles.

3.3. Fracture Morphology. AA6061 alloy and AA6061/20 wt. percent Si_3N_4 composite fracture surface is shown in Figure 10. The fracture surface of the AA6061 alloy is shown in Figure 10(a). The figure clearly indicates that aluminium alloys undergo a plastic flow during tensile loading. Many dimples are also visible. All these marks indicate that fracture occurred in the ductile mode. Figure 10(b) shows the fracture surface of the AA6061 composite containing 20 wt.% of Si_3N_4 particles. Size of the dimples in the fracture surface of the composite is less than that of the aluminium alloy. Degree of flatness of the surface is also increased in the fracture surface of the composite. It is apparent that ductility is reduced in the composite, and the failure mode of the

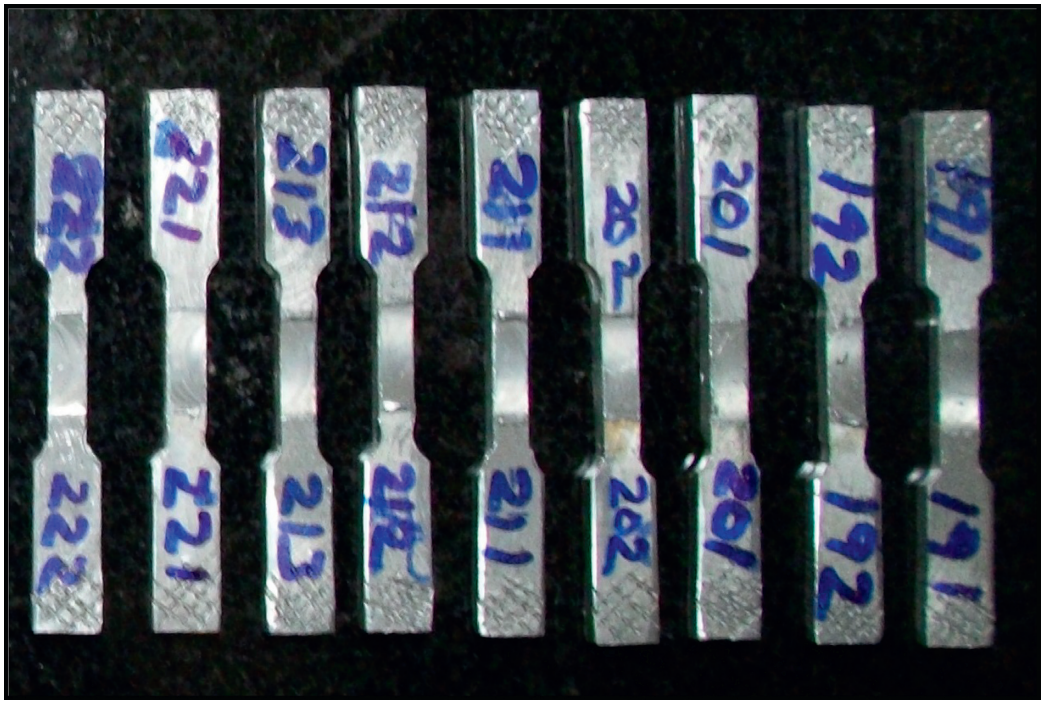

Figure 5: Fabricated tensile specimens as per the ASTM: E8/E8 M-11 standard.

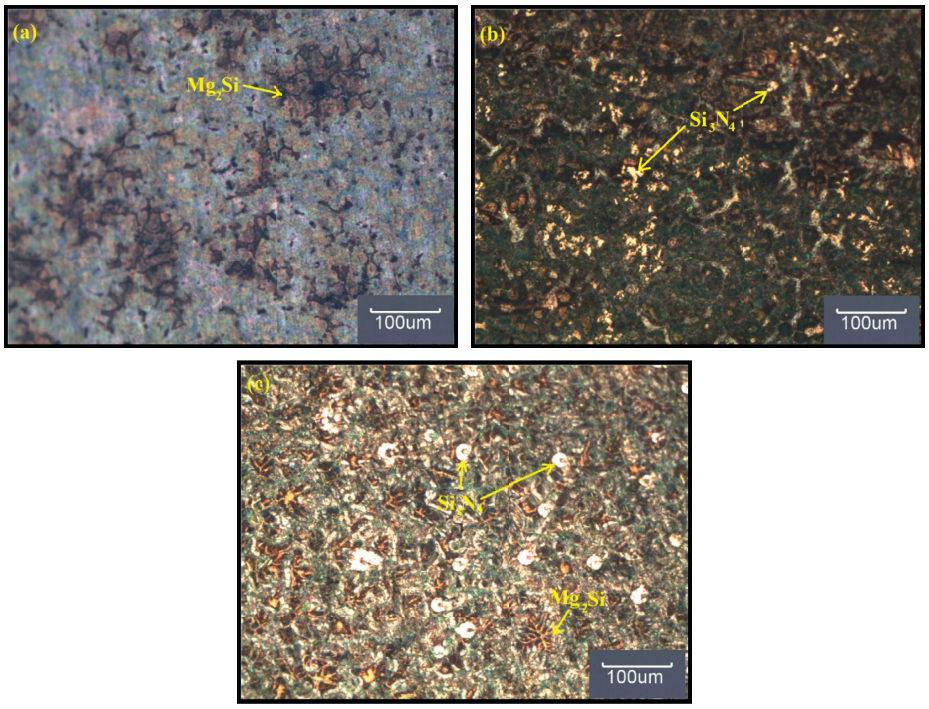

Figure 6: Optical photomicrograph of the (a) as-cast AA6061 alloy, (b) AA6061/15 wt.% Si_3N_4 composite, and (c) AA6061/20 wt.% Si_3N_4 composite.

composite is brittle. As the addition of reinforcement particles reduced the grain size, dislocations during tensile loading have less space before they hit a grain boundary. As dislocation is restricted by the grain boundary, plastic deformation is decreased, and the fracture mode becomes brittle [18].

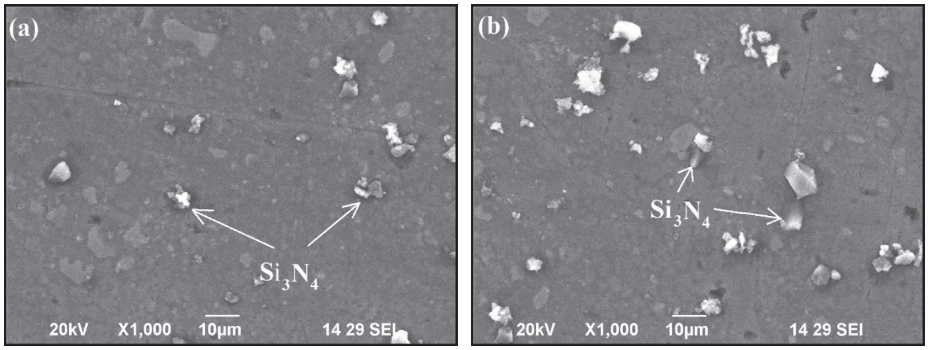

Figure 7: SEM micrograph of the (a) AA6061/15 wt.% Si_3N_4 composite and (b) AA6061/20 wt.% Si_3N_4 composite.

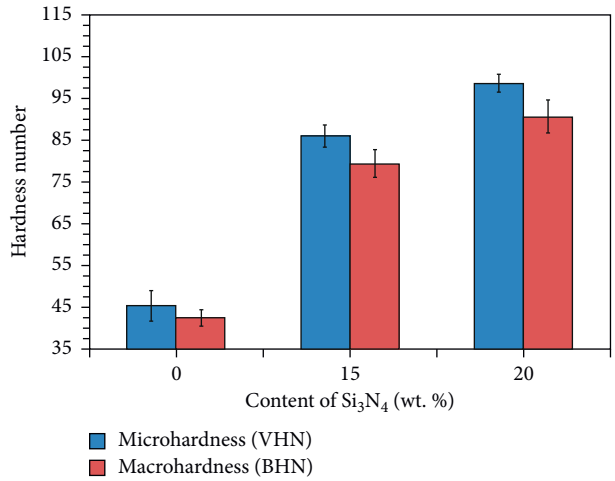

Figure 8: Effect of weight percentage of Si_3N_4 on microhardness and macrohardness of the Al/Si_3N_4 composite.

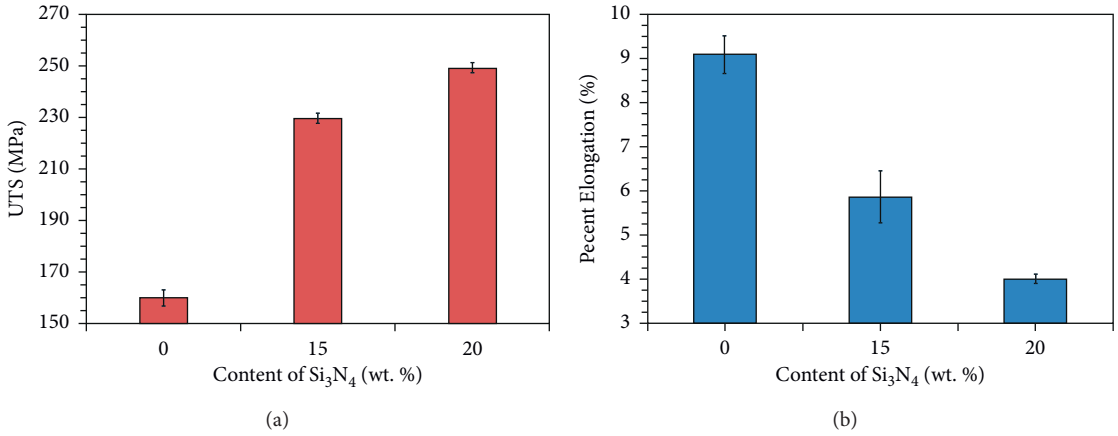

Figure 9: Effect of weight percentage of Si_3N_4 on (a) UTS and (b) PE of the AA6061/Si_3N_4 composite.

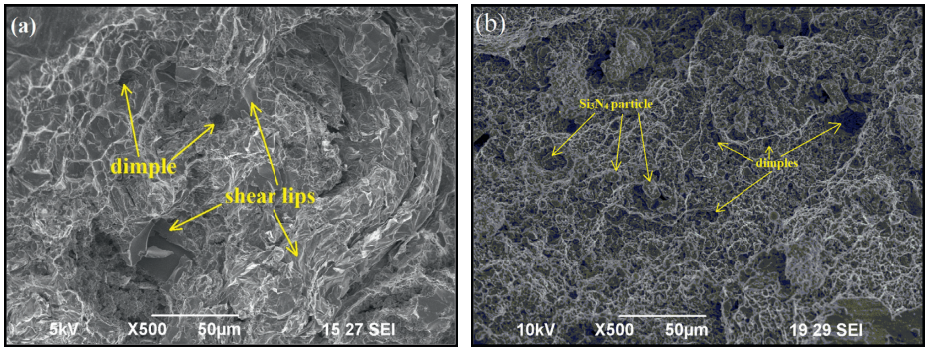

Figure 10: SEM micrographs of the fracture surface of the tensile specimen of (a) AA6061 alloy and (b) AA6061/20 wt.% Si_3N_4 composite.

4. Conclusions

(i) AA6061 alloy and AA6061 alloy matrix composite containing 15 and 20 weight percentage of Si_3N_4 reinforcement were successfully synthesized by the indigenously developed modified stir casting furnace with the bottom discharging attachment.

(ii) Si_3N_4 reinforcement particles were more uniformly dispersed in the AA6061 matrix.

(iii) Hardness and UTS of the AA6061/Si_3N_4 composite increased with the addition of Si_3N_4 particles. Microhardness and macrohardness of the AA6161/20 wt.% Si_3N_4 composite were 98 VHN and 91 BHN, respectively, which were 117.8% and 111.63% higher than those of the AA6061 matrix alloy, respectively. UTS of AA6061 was 159.82 MPa which was increased to 249.12 MPa in the AA6061/20 wt.% Si_3N_4 composite, but percent elongation of the composite reduced with the increase in the amount of particles. Percent elongation of the AA6061 alloy was 9 which was reduced to 4 in the AA6061/20 wt.% Si_3N_4 composite.

(iv) Failure mode of AA6061 and AA6061/20 wt.% Si_3N_4 composite was found to be ductile and brittle, respectively.

Data Availability

The data used to support the findings of this study are included within the article.

Conflicts of Interest

The authors declare that there are no conflicts of interest regarding the publication of this article.

Acknowledgments

The authors wish to place their sincere thanks to the Management and Department of Mechanical Engineering, Coimbatore Institute of Technology, Coimbatore, India, for extending the facilities of Welding Research Laboratory to carry out this investigation. They also wish to thank Karunya University, Coimbatore, India, for providing SEM and UTM testing facilities. They are also thankful to Mr. A. Raja for his assistance offered to execute the above work.

References

[1] J. Hemanth, "Quartz (SiO2p) reinforced chilled metal matrix composite (CMMC) for automotive applications," *Materials & Design*, vol. 30, no. 2, pp. 323–329, 2009.

[2] G. Naveen Kumar, R. Narayanasamy, S. Natarajan, S. P. Kumaresh Babu, K. Sivaprasad, and S. Sivasankaran, "Dry sliding wear behaviour of AA 6351-ZrB2 in situ composite at room temperature," *Materials & Design*, vol. 31, no. 3, pp. 1526–1532, 2010.

[3] S. Soltani, R. Azari Khosroshahi, R. Taherzadeh Mousavian, Z.-Y. Jiang, A. F. Boostani, and D. Brabazon, "Stir casting process for manufacture of Al–SiC composites," *Rare Metals*, vol. 36, pp. 581–590, 205.

[4] J. Jebeen Moses, I. Dinaharan, and S. Joseph Sekhar, "Prediction of influence of process parameters on tensile strength of AA6061/TiC aluminium matrix composites produced using stir casting," *Transactions of Nonferrous Metals Society of China*, vol. 26, no. 6, pp. 1948–1511, 2016.

[5] J. Hashim, L. Looney, and M. S. J. Hashmi, "Particle distribution in cast metal matrix composites-Part I," *Journal of Materials Processing Technology*, vol. 123, no. 2, pp. 251–257, 2002.

[6] K. Kalaiselvan, N. Murugan, and S. Parameswaran, "Production and characterization of AA6061-B4C stir cast composite," *Materials & Design*, vol. 32, no. 7, pp. 4004–4009, 2011.

[7] M. N. Wahab, A. R. Daud, and M. J. Ghazali, "Preparation and characterization of stir cast-aluminium nitride reinforced aluminium metal matrix composites," *International Journal of Mechanical and Materials Engineering*, vol. 4, no. 2, pp. 115–117, 2009.

[8] Y. Pazhouhanfar and B. Eghbali, "Microstructural characterization and mechanical properties of TiB_2 reinforced Al6061 matrix composites produced using stir casting process," *Materials Science and Engineering: A*, vol. 710, pp. 172–180, 2018.

[9] V. Bharath, M. Nagaral, V. Auradi, and S. A. Kori, "Preparation of 6061Al-Al 2 O 3 MMC's by stir casting and evaluation of mechanical and wear properties," *Procedia Materials Science*, vol. 6, pp. 1658–1667, 2014.

[10] V. Mohanavel, K. Rajan, and M. Ravichandran, "Synthesis, characterization and properties of stir cast AA6351-Aluminium Nitride (AlN) composites," *Journal of Materials Research*, vol. 31, no. 24, pp. 3824–3831, 2016.

[11] V. Mohanavel and M. Ravichandran, "Experimental investigation on mechanical properties of AA7075-AlN composites," *Materials Testing*, vol. 61, no. 6, pp. 554–558, 2019.

[12] K. Shirvanimoghaddam, H. Khayyam, and H. Abdizadeh, "Effect of B_4C, TiB_2 and $ZrSiO_4$ ceramic particles on mechanical properties of aluminium matrix composites Experimental investigation and predictive modelling," *Ceramics International*, vol. 42, no. 5, pp. 6206–6220, 2016.

[13] R. Kumar Arya and T. Amit, "Silicon nitride as a reinforcement for aluminium metal matrix composites to enhance microstructural, mechanical and tribological behavior," *International Journal of Engineering and Advanced Technology*, vol. 9, no. 3, pp. 3366–3374, 2020.

[14] ASTM Standard E8, *Standard Test Method for Tension Testing of Metallic Materials*, ASTM, International, West Conshohocken (USA), 2004.

[15] I. Dinaharan, N. Murugan, and S. Parameswaran, "Influence of in situ formed ZrB_2 particles on microstructure and mechanical properties of AA6061 metal matrix composites," *Materials Science and Engineering A*, vol. 528, pp. 5733–5740, 2011.

[16] B. Ashok Kumar and N. Murugan, "Metallurgical and mechanical characterization of stir cast AA6061-T6-AlN_p composite," *Materials and Design*, vol. 40, pp. 52–58, 2012.

[17] M. Gupta and TS. Srivatsan, "Interrelationship between matrix microhardness and ultimate tensile strength of discontinuous particulate-reinforced aluminium alloy composites," *Materials Letters*, vol. 51, pp. 255–261, 2001.

[18] B. Ashok Kumar, I. Dinaharan, and M. N. Microstructural, "Mechanical and wear properties of friction stir welded AA6061/AlN_p composite joints," *Journal of Materials Engineering and Performance*, vol. 31, no. 1, pp. 651–666, 2021.

Hindawi
Advances in Materials Science and Engineering
Volume 2022, Article ID 3035169, 9 pages
https://doi.org/10.1155/2022/3035169

Research Article

Natural Fiber Incorporated Polymer Matrix Composites for Electronic Circuit Board Applications

V. S. Chandrika,[1] A. Anamika,[2] C. Jeeva,[3] Bhagavathi Perumal,[4] S. Sanal Kumar,[5] J. Femila Roseline,[6] and Ishwarya Komalnu Raghavan[7]

[1]*Department of Electrical and Electronics Engineering, KPR Institute of Engineering and Technology, Coimabatore 641407, Tamil Nadu, India*
[2]*Department of Electrical and Electronics Engineering, Galgotias College of Engineering and Technology, Greater Noida 201310, India*
[3]*Department of Electrical and Electronics Engineering, Sri Sairam Engineering College, Chennai 600044, Tamil Nadu, India*
[4]*Department of Civil Engineering, Sri Sairam Engineering College, Chennai - 600044, Tamil Nadu, India*
[5]*Department of Instrumentation, NSS College Nemmara, Palakkad, India*
[6]*Department of Electronics and Communication Engineering, Saveetha School of Engineering,SIMTAS,Saveetha University, Chennai, Tamil Nadu, India*
[7]*Department of ElectroMechanical Engineering, Faculty of Manufacturing, Institute of Technology, Hawassa University, Ethiopia*

Correspondence should be addressed to Ishwarya Komalnu Raghavan; ishwarya138@hu.edu.et

Received 19 September 2021; Accepted 16 December 2021; Published 29 January 2022

Academic Editor: P Ganeshan

There are many more applications for fibre-reinforced epoxy composites than there are for metals and alloys today. For example, sustainable, recyclable, and biodegradable reinforcements have been used in numerous studies to improve the mechanical and thermal properties of composite materials. It was discovered that the properties of epoxy-based composites could be improved by combining biosolid waste sugarcane bagasse ash fillers, madar fibre, and epoxy resin. Conventional compression molding techniques were used to prepare the sugarcane bagasse ash (SBA) particles and madar fibre-reinforced epoxy resin-based composites (PMCs), which were loaded with varying amounts of fibre and fillers. Hybrid biocomposites were evaluated for mechanical (tensile, flexural, impact, and hardness) and water absorption characteristics. Epoxy matrix composites containing 28 wt.% madar fibre and 7 wt.% sugarcane bagasse ash fillers had tensile, flexural, hardness, and impact values of 61 MPa, 147 MPa, and 54 kJ/m^2, respectively.

1. Introduction

In recent years, researchers all over the world have been studying to incorporate the inorganic nanoparticles or fillers into the polymer matrix. This work has attracted the increasing interest of the researchers because of the improved mechanical, thermal stability, electrical, optical, and wear resistance properties of several filler-based composites when compared with various neat polymers [1–3]. Usually, PMCs are exploited in aircraft, automotive, and electronic applications. The fabrication of printed circuit boards (PCBs) mainly based on woven glass fibre cloths and other reinforcements, including paper, glass fibre matte, nonwoven glass fibres, nonwoven aramid fibres, and other fillers, is the most widely utilized for PCB materials. Figure 1 shows the schematic illustration of PCBs. Generally, the PCB base materials come in various shapes and sizes. They all contain resin systems, reinforcements, and conductors. Epoxy, cyanate ester, polyimide, polyester, and polytetrafluoroethylene are among the resins used.

A variety of technical applications have proven that natural fillers and fiber-reinforced thermoplastic composites

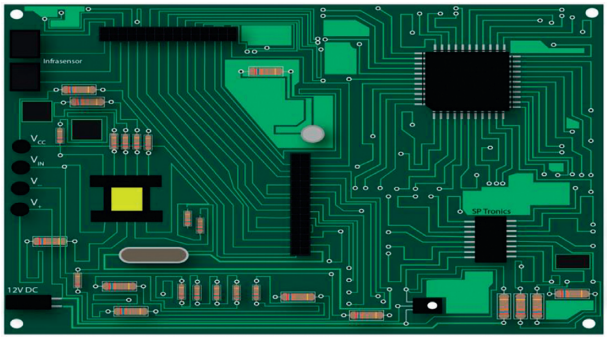

Figure 1: Printed circuit board schematic diagram.

have excellent properties. Due to their low density, good thermal insulation, mechanical properties, reduced tool wear, unlimited availability, low cost, and hassle-free disposal, thermoplastic fibres such as aramid and glass are increasingly used as thermoplastic reinforcement materials. The strength and cost of wood fibre/particle cannot be matched with synthetic or mineral-filled thermoplastics. Artificial and mineral fibres cause more wear on processing equipment than wood filler does. Wood reduces fibre damage during processing, allowing for the recycling of production waste without compromising quality. Available, renewable, and low density make them an attractive eco-alternative to current composite materials made of glass, carbon, and man-made fibres. They are also mechanically sound. Due to their environmental friendliness, natural fibre composites are used in transportation, military, construction, packaging, consumer products, etc. [4]. Most of the research studies have focused on the naturally available fillers such as sawdust, rice husk, coconut shell powder, sugarcane bagasse ash, eggshell powder, wood flour, fly ash, and red mud because of their cost-effectiveness and abundance. Carbon nanotubes, nanoclay, silicon carbide, talc, and calcium carbonate are some of the inorganic fillers that are mostly or widely used reinforcements for polymer matrices. For a variety of rubber applications, fillers have also been used to improve the properties of various composites [5, 6]. The tensile strength of biocomposites decreases slightly as the filler content increases, but their strength remains adequate. Increased filler loading resulted in lower composite tensile strengths and Izod impact strengths due to poor interfacial bonding between the matrix polymer and filler [7]. Study of nonwood and kenaf natural fibres with high stiffness and strength values was conducted [8]. A higher aspect ratio makes them an ideal material for the fibrous phase, according to their research. Additional measurements are required to interpret the mechanical properties of a composite system when its relative volume, properties, or fabrication process changes. As a result, experiments may take a long time and be expensive. Moisture absorption increased as fibre loading increased, according to findings [9]. The pineapple leaf fibre reinforced with a low-density polyethylene matrix was being studied for its moisture absorption properties at the same time, he explained. With fibre loading, moisture absorption increases almost linearly. George et al. [10] studied a number of polymers and concluded that when submerged in water, their composites absorbed moisture from the humid atmosphere. Composites with natural fibres have a lower mechanical strength because they absorb more moisture than synthetic fibres. It is stated in [11] that "Composite material with a 45 wt% fibre content and 5 mm fibre length performs optimally". A study of banana fibre-reinforced composites using a variety of banana fibre lengths and banana fibre weight percentages was conducted by Athijayamani et al. [12]. Composites with banana fibre lengths of 30 to 40 mm and banana fibre content of 40 wt percent exhibited the best mechanical properties. For example, polyester resin composites reinforced with Sansevieria cylindrica fibres were proposed [13]. Researchers studied storage modulus, damping factor, and loss modulus of biodegradable Sansevieria cylindrica fibre-reinforced polyester matrix composites. There was a significant effect on properties due to changes in fibre length, content, and chemical treatment under transient temperatures. Basalt fibres and their adhesion to polypropylene matrix were investigated in a study by Sreenivasan et al. [14]. Maleic anhydride grafted PP was also used to achieve different fibre lengths and matrix modification. Experimentally determined basalt fibre mechanical properties by tensile tests on a single filament of basalt were studied. Study of mechanical properties, including tensile strength and flexural strength, of composite materials with 20 percent fibre content in HDPE was conducted. Polymers are reinforced with fibres derived from natural sources, such as animal fibres [15]. Epoxy resin is the most common structural adhesive and engineering adhesive used in human life applications, and it has a high bonding strength. An epoxy resin matrix with madar fibre reinforcement and sugarcane bagasse ash filler is used in the present work to fabricate a composite. In a hand layup technique, different weight fractions of fibre and filler were used. Impact, hardness, and water absorption were among the other properties tested on the composites, in addition to tensile and flexural strength [16–18]. This study examined the effects of adding sugarcane bagasse ash particles to a madar fibre/epoxy resin matrix on various mechanical properties.

2. Materials and Methods

The Apocynaceae family produces the madar fibre. Fibres are extracted from the madar plant's stem. An abundance of madar fibre (MF) is found in the agricultural lands of the southern region of India. Figure 2 shows the madar plant. Madar fibre contains mucilaginous substances in the primary wall, while cell lumen is found in the secondary wall. This is due to the fact that it contains more lignin than existing bast fibres. We can use it in lightweight applications such as textiles and automobiles because of its lower density. A natural bast fibre with lower elongation, higher strength, and better tensile property is known as MF. Fibres such as glass and carbon can be substituted for it in polymer matrices. In this current work, six different biocomposites were produced by using the biowastes, i.e., madar fibre, sugarcane bagasse ash filler, and epoxy resin through the conventional

Figure 2: Madar plant.

compression molding technique. Compression molding is a composite manufacturing approach generally utilized to make high-volume composite components, such as automobile components. Cold compression and hot compression moldings are the two compression molding processes. Figure 3 shows the schematic image of the compression molding technique.

Different percentages of fibre (35, 34, 32, 30, 28, and 26 wt. %) and filler loadings (0, 1, 3, 5 7, and 9 wt. %) with a mould of dimension of about 250 mm long, 250 mm width, and 5 mm thick were used for the fabrication of specimens. The cavity surface of the mould was waxed in order to facilitate the removal of the composite plate. It was then mixed for 45 minutes with measured vinyl ester resin to achieve homogeneity and reduce air bubble generation. The supplier also recommended adding 1.5 percent dimethylaniline accelerator, 1.5 percent methyl ethyl ketone peroxide catalyst, and 1.5 percent cobalt naphthenate promoter to the mixture. Once the mould cavity was completely filled, a die was used to seal it. In order to cure properly, it is compressed for 30 hours at room temperature with a constant pressure of 125 kPa. They were then removed from the mould cavity. A similar procedure has been adopted to prepare the other five biocomposite plate preparations with different percentages of fibre and filler loadings.

2.1. Mechanical Testing. A saw cutter was used to cut the fabricated composite plates to the desired shapes for different test specimens. Using a UTM, tensile and flexural tests were performed at room temperature. For each weight percentage, three specimens were tested to ensure that the results could be repeated. The ASTM D638 standard specifies a crosshead speed of two millimetres per second (mm/sec) for testing tensile strength. The ASTM D790-10 standard was followed, and the crosshead speed was set at 2 mm/sec. When a reinforced epoxy resin composite is able to absorb energy from an impact load without breaking, it is said to have impact resistance. The interfacial adhesions between the filler and matrix, the presence of voids, the filler's influence, and the testing environment all have an impact on the impact strength of a composite. The Charpy test method evaluated impact strength according to ASTM D256. Also, the hardness was measured using the Barcol Hardness tester, according to the ASTM 2583 standard.

2.2. Water Absorption Behaviour. This was performed in accordance with the ASTM D570-99 standard. Initially, they were baked at 80°C until they reached a uniform weight. Five replicas of each specimen were immersed in normal water for 48 hours. A known weight (W_1) of each specimen was immersed in water for 48 hours one after the other. Moisture on the specimen surface was removed with absorbent paper afterward. Immediately, the weight of the specimen was measured. The water absorption percentage was determined by finding the weight difference between the dry specimens and specimens immersed in water by the following equation:

$$\text{percentage of water absorption} = \left(\frac{W_2 - W_1}{W_1}\right), \quad (1)$$

where W_2 is the weight of the specimen after test and W_1 is the weight of the specimen before test.

3. Results and Discussions

3.1. Tensile Strength. In order to determine the tensile strength of biocomposites, different percentages of fibre and filler were used in the fabrication process. Figure 4 shows the tensile strength results as a function of fibre and filler loading weight percentages for biocomposites.

The ultimate tensile strengths of 0, 1, 3, 5, 7, and 9 wt. % of sugarcane bagasse ash-filled composites were in the range of 34, 39, 45, 52, 61, and 41 MPa, respectively. According to the researchers, 7 wt. % filler improved tensile strength by 44 percent over pure epoxy resin/madar fibre-reinforced composite specimens. After increasing it from zero to seven weight percent, the tensile strength increased dramatically from 34 MPa to 61 MPa. Tensile strength improved by 44 percent when filler weights of 7 weight percent were added to epoxy resin/madar fibre-reinforced composite specimens. The tensile strength dropped suddenly from 61 to 41 MPa at 9 percent filler weight. This was due to the filler and a matrix having distorted bonding properties, as well as the presence of voids. Increase in biocomposite tensile strength of 34 to 61 MPa was observed with variations in filler weight percentage. 61 MPa tensile strength was achieved by the biocomposite at 7% weight. As a result of this, it was 44.26 percent higher than that of the pure epoxy resin/madar fibre-reinforced composite samples. Figure 5 depicts the tensile stress-strain curves for various filler weight

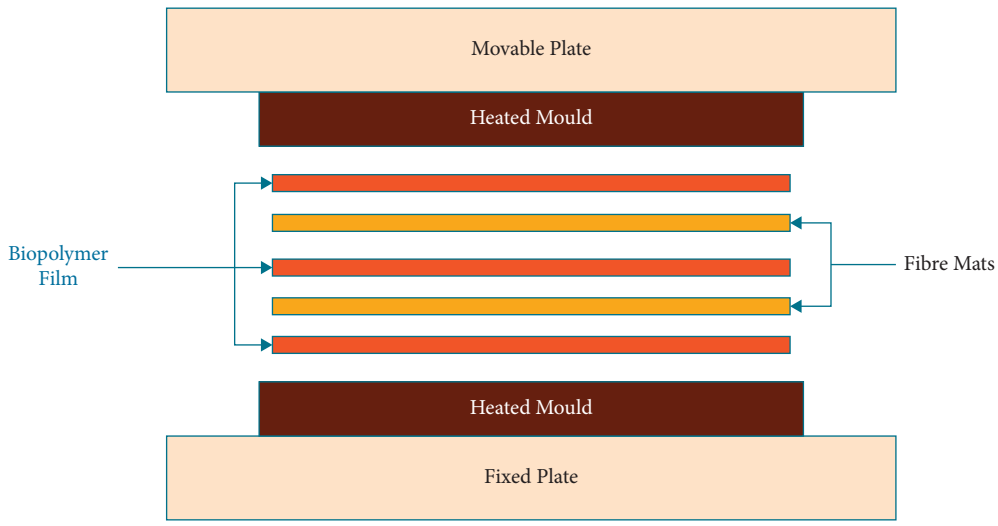

Figure 3: Schematic image of the compression molding technique.

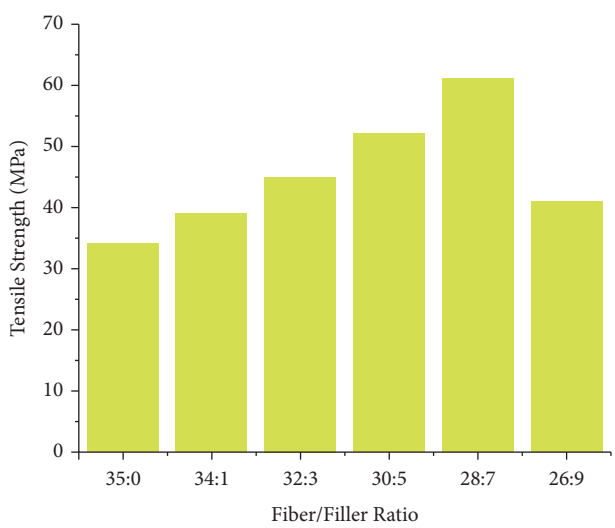

Figure 4: Epoxy resin/madar fibre/sugarcane bagasse ash composites: effect of fibre/filler loading on tensile strength.

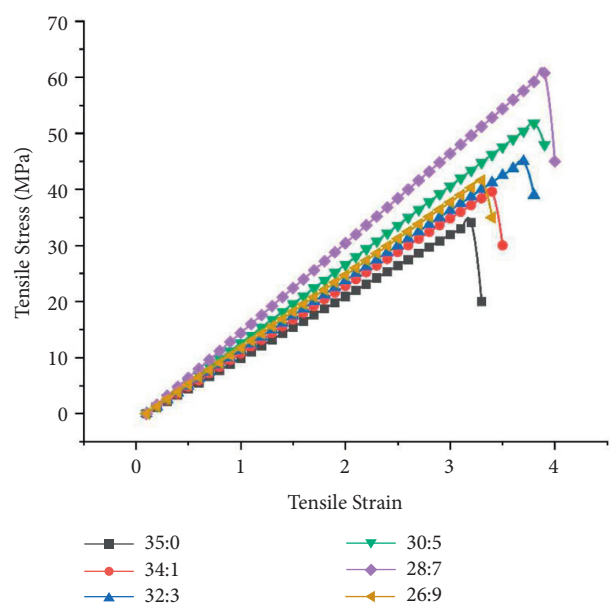

Figure 5: Tensile strain vs. tensile stress curves for epoxy resin/madar fibre/sugarcane bagasse ash composites.

percentages. Moreover, biocomposites showed an increasing trend in the fibre and filler weight percentage up to 28 wt. % and 7 wt. %.

Fiber and filler reinforcement carried the tensile load more effectively than the matrix, which caused the matrix to break. It has higher stiffness and strength. Hence, it was observed that when fibre and filler weight percentage was increased beyond 28 wt. % and 7 wt. %, the strength of biocomposites decreased. The increase in filler weight percentage continued in a sinusoidal pattern. It has been found that the epoxy matrix and filler do not adhere well to each other when the filler percentage is high enough. While being tested for tensile strength, the material developed holes and showed reduced strength.

Figure 6 depicts the tensile load-displacement curves for the various fibre and filler weight percentages. The percentage of elongation between 0 wt. % and 9 wt. % ranged from 1.25 to 3.4%, correspondingly.

An elastic material's tensile modulus is a measure of stiffness. The effect of different weight percentage addition of the filler material into the fibre and epoxy resin combination is illustrated in Figure 7.

Moreover, the addition of filler weight from 0 wt% to 9 wt% increased or enhanced the modulus value from 1.4 GPa to 2.6 GPa. Optimum tensile strength of 61 MPa of sugarcane bagasse ash filler/madar fibre/epoxy resin composites was close to that of coconut shell powder-reinforced epoxy, oil palm shell powder-reinforced polyester, oil palm shell powder and kenaf-coconut-kenaf fibre-reinforced polyester composites. Composites made from groundnut powder and vinyl ester reinforcement were tested at 27.3 MPa, tamarind seed filler composites were tested at 33.21 MPa, and composites made from date palm wood flour

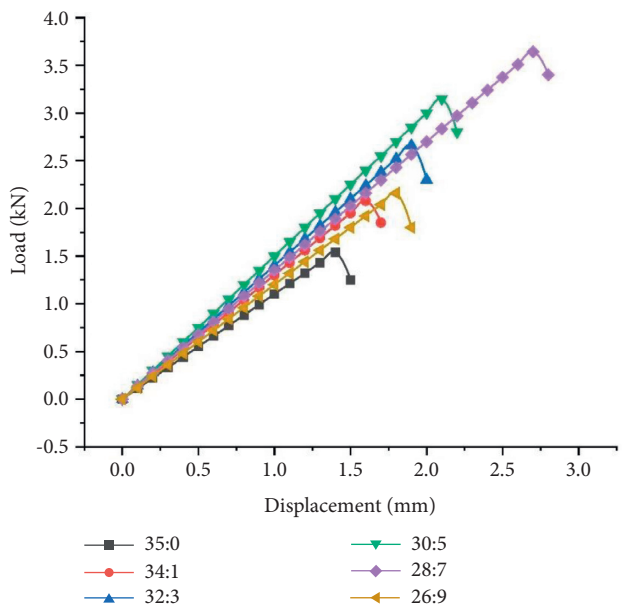

Figure 6: Displacement vs. load curves for epoxy resin/madar fibre/sugarcane bagasse ash composites.

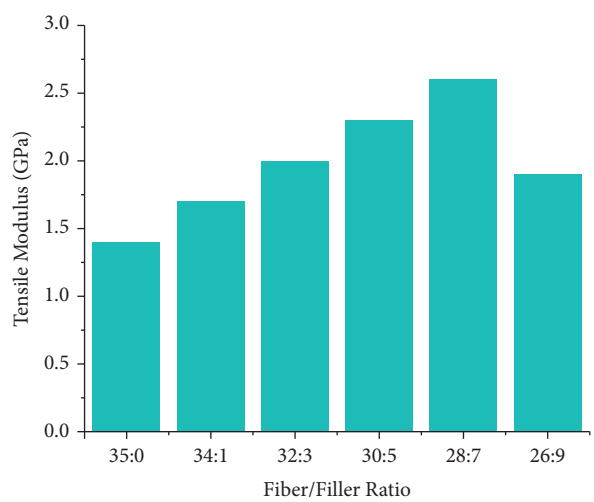

Figure 7: Effect of fibre/filler loading on tensile modulus for epoxy resin/madar fibre/sugarcane bagasse ash composites.

and glass fibre-reinforced polypropylene were tested at 24.89 MPa. Composites made from boiled eggshell powder and vinyl ester reinforcement were tested at 23.6 MPa [6, 12, 13]. This comparative analysis on mechanical behavior (tensile and other properties) of the sugarcane bagasse ash filler/madar fibre/epoxy resin composite shows that the sugarcane bagasse ash filler/madar fibre/epoxy resin is a promising material for engineering structures.

3.2. Flexural Strength. Figure 8 shows the bending test results obtained on variations in the flexural characteristics obtained for the sugarcane bagasse ash/madar fibre/epoxy resin composites with the effect of fibre/filler loadings.

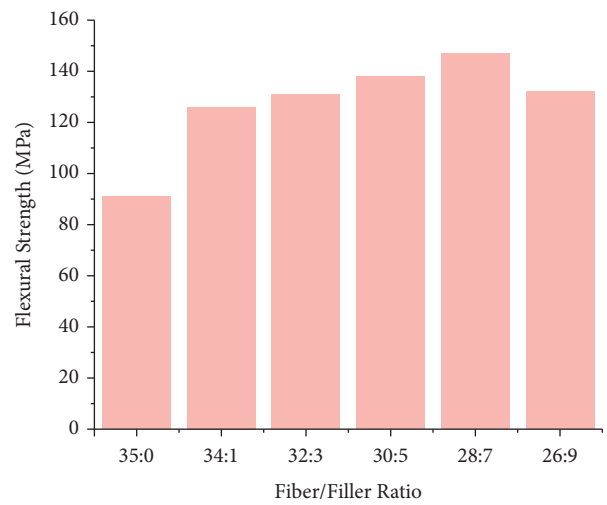

Figure 8: Epoxy resin/madar fibre/sugarcane bagasse ash composites: effect of fibre/filler loading on flexural strength.

The flexural strength and flexural modulus of the epoxy resin/madar fibre composite specimen were 91 MPa and 5.8 GPa, respectively. Figure 9 shows the variation of flexural modulus for all composites. The flexural strength of the composites increased with filler loadings of 1, 3, 5, and 7 wt.% when compared to pure epoxy resin/madar fibre specimens. Also, the flexural modulus increased as the sugarcane bagasse ash filler content increased. Comparing sugarcane bagasse ash/madar fibre/epoxy resin composite specimens with pure epoxy resin/madar fibre composite specimens, the average flexural strength increased as the filler loading increased. Composites with sugarcane bagasse ash/madar fibre loadings of 28 and 7 weight percent, respectively, showed increased flexural strength of 38 and 57 percent over pure epoxy resin/madar fibre composite specimens. Then, a decreased trend was evident from the test results obtained beyond the 7 wt. % filler loadings. The flexural modulus remained almost constant with the sugarcane bagasse ash/epoxy resin/madar fibre composite specimen composites manufactured with filler loading of 1 and 3 wt. %. Sugarcane bagasse ash loading of 7 wt. % increased flexural strength dramatically. When the filler was omitted, the flexural strength was 38 percent higher than that of pure resin/madar fibre composites.

Sugarcane bagasse ash/madar fibre-reinforced composites with a 7 weight percent sugarcane bagasse ash content had a flexural strength of 147 MPa, which was 38 percent higher than that of pure resin/madar fibre-reinforced composites. Admittedly, the flexural modulus was observed to be highest for 7 wt. % filler loading. There was a sinusoidal decrease in flexural strength with filler loadings higher than 7 wt. %, due to the agglomeration and incompatibility between a higher quantity of sugarcane bagasse ash filler and epoxy resin. Furthermore, it can be significantly observed that the trend of the flexural strength of sugarcane bagasse ash/madar fibre-reinforced composites was similar to the tensile strength for various filler loadings. As shown in Figure 10, sugarcane bagasse ash/madar fibre/epoxy resin

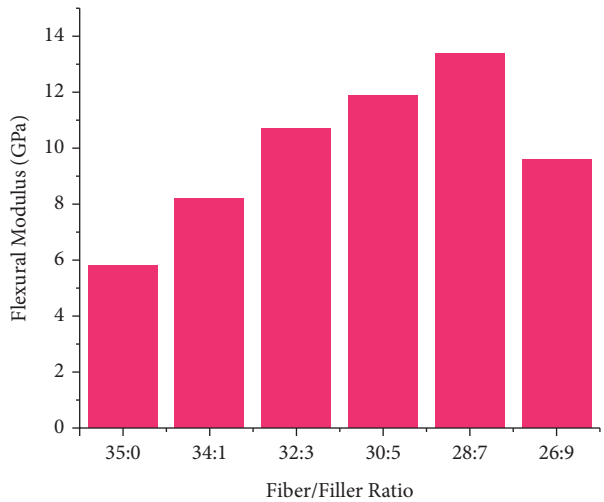

Figure 9: Equivalent flexural modulus of epoxy resin/madar fibre and sugarcane bagasse ash composites with different percentages of fibre/filler loadings.

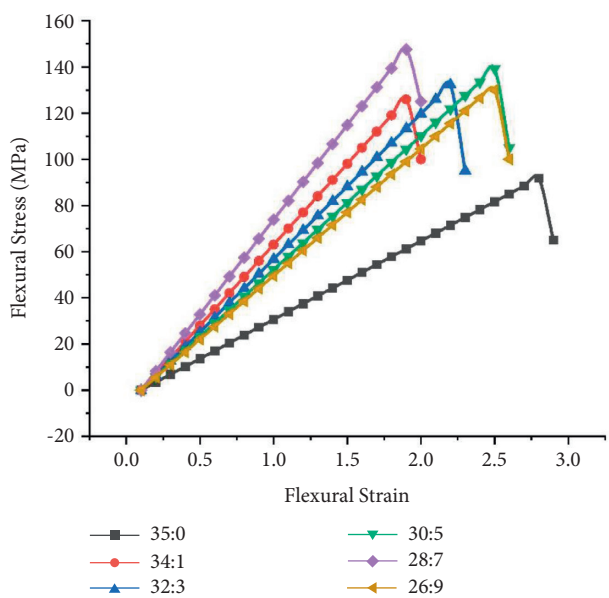

Figure 10: Flexural strain vs. flexural stress curves for epoxy resin/madar fibre/sugarcane bagasse ash composites.

composites with varying filler loadings exhibit different flexural stress and strain curves.

147 MPa was the maximum flexural strength of the sugarcane bagasse ash and madar fibre-reinforced epoxy resin composites, compared to 122 MPa for tamarind seed filler/vinyl ester composites, 91 MPa for Arundo donax fillers/epoxy composites, and 82 MPa for wood apple shell/epoxy composites.

3.3. Impact Strength. Unnotched sugarcane bagasse ash/madar fibre/epoxy resin composites were held in an Izod Charpy instrument and broken by a pendulum. It is shown in Figure 11 that the composites with different filler loadings had different average impact energy values. Experimentally, sugarcane bagasse ash-madar fiber-epoxy resin composites showed increased impact strength with increase in filler loading. When filler content was increased by 7 weight percent, impact energy increased by 22.28 percent. Importantly, the sugarcane bagasse ash/madar fibre/epoxy resin composites exhibited a maximum impact strength of 17.5 kJ/m^2 at 7 wt. % of filler loading, and it was 22.28% higher than the madar fibre/epoxy resin composites. When compared with neat madar fibre/epoxy resin composites, the sugarcane bagasse ash/madar fibre/epoxy resin composites were capable of absorbing high energy to stop crack propagation.

The higher impact strength of sugarcane bagasse ash/madar fibre/epoxy resin composites was due to the filler's excellent homogeneous dispersion in the matrix, which produced excellent interfacial adhesion. Impact strength was decreased as a result of crack prevention and easy energy absorption. On the other hand, poor dispersion of filler increased the tendency to agglomerate the particle, thus minimizing their surface areas. Therefore, the crack propagation was increased, and the energy absorption was also less. The phenomenon has explained the decrease in impact strength of 9% weight loadings of the composites. Filler loading up to 7 wt. % increased impact strength more pronouncedly.

3.4. Barcol Hardness. Figure 12 depicts the Barcol hardness values of the sugarcane bagasse ash/madar fibre/epoxy resin composites with respect to different filler loadings. It was inferred that the sugarcane bagasse ash filler was well dispersed all over the matrix and produced an excellent surface roughness. Up to 7 wt. % increase in filler loading resulted in an increase in hardness. It had a hardness of 32. In particular, the hardness for 7 wt. % addition of sugarcane bagasse ash increased by 41 percentage than that of the madar fibre/epoxy resin composites. A similar trend of results was followed by many researchers, as reported on rice husk reinforced with polyester and epoxy.

Admittedly, increasing values of hardness property were produced by increasing the filler loadings, especially between 0% (neat epoxy resin with no filler) and 7 wt. %.

3.5. Water Absorption Behaviour. Figure 13 shows the percentage of water absorption curves for the sugarcane bagasse ash/madar fibre/epoxy resin composites with average data of three specimens of different filler loadings after immersing the composite specimens in normal water. The hydrophilic nature of the filler material led to an increase in the water absorption percentage. A similar trend was observed in different natural filler/fibre-reinforced composites. Hydrophobicity of epoxy resin prevented water absorption in the four environments mentioned above.

Due to the presence of microvoids in composites, sugarcane bagasse ash/madar fibre/epoxy resin composites absorbed more water than the other five fibre/filler combinations. With higher filler loadings, the sugarcane bagasse ash/madar fibre/epoxy resin composites contained less matrix, which resulted in an

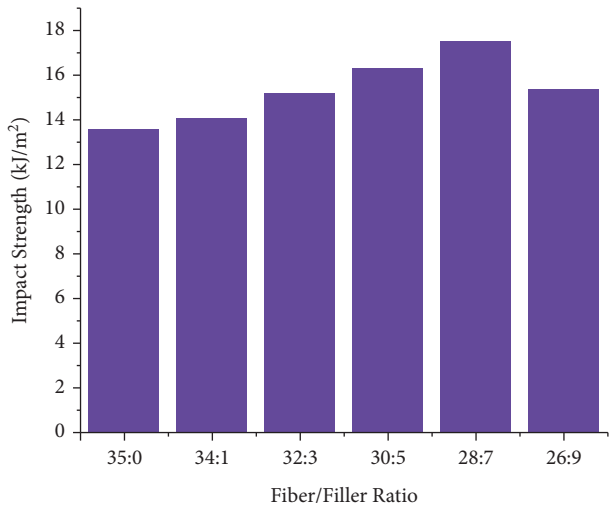

Figure 11: Effect of fibre/filler loading on impact strength for epoxy resin/madar fibre/sugarcane bagasse ash composites.

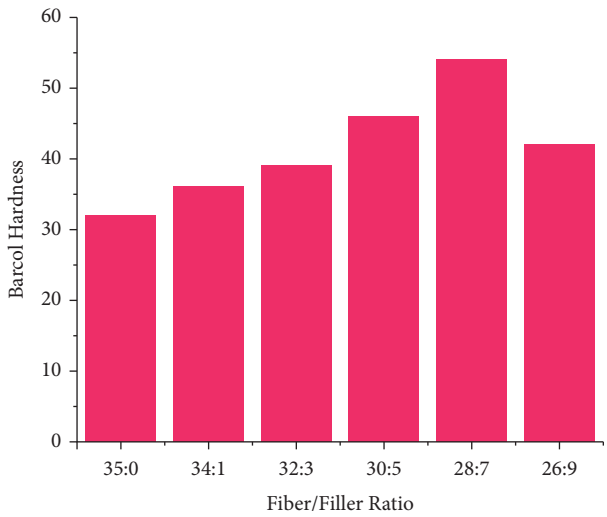

Figure 12: Effect of fibre/filler loading on Barcol hardness for epoxy resin/madar fibre/sugarcane bagasse ash composites.

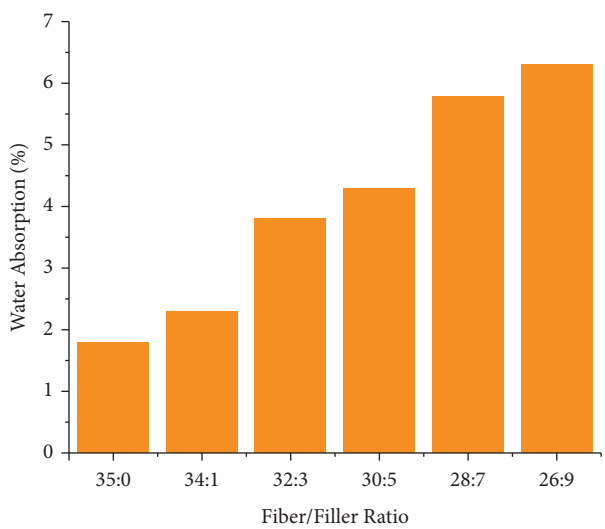

Figure 13: Variation of water absorption properties for epoxy resin/madar fibre/sugarcane bagasse ash composites.

increase in voids. However, the lowest water absorption was recorded with pure epoxy resin/madar fibre when compared with the other five combinations because of the absence of sugarcane bagasse ash molecules in the particular composite specimens. The slow penetration of large molecules into the composites produced a smallest moisture absorption percentage.

4. Conclusions

Efforts have been made to determine how filler loading affects the mechanical and thermal properties of date palm seed-reinforced vinyl ester composites. The following conclusions are drawn from this study's promising results:

(i) In terms of mechanical and water absorption properties, the fibre/filler weight percentages of epoxy resin/madar fibre/sugarcane bagasse ash composites were found to be critical, with 28 and 7 percent being optimal.

(ii) 61 MPa and 2.6 GPa were the maximum tensile and modulus values for epoxy resin/madar fibre/SBA composites.

(iii) In addition, the flexural and impact tests performed on the epoxy resin/madar fibre/sugarcane bagasse ash composites with a filler loading of 7 wt. % exhibited a maximum strength of 147 MPa and 17.5 kJ/m^2, respectively. The Barcol hardness of the epoxy resin/madar fibre composites was 32, and the addition of sugarcane bagasse ash loading of 7 wt. % increased it by 41% than that of the epoxy resin/madar fibre composites.

(iv) Furthermore, the water absorption test showed that the lowest and highest percentages of water absorptions were recorded in 0 wt.% and 9 wt. % of sugarcane bagasse ash filler weight percentage, respectively. Also, as filler loadings increased, so did the percentages of water absorption.

(v) Epoxy resin/madar fibre/sugarcane bagasse ash composites with a 7 wt. % filler content had significantly higher tensile, flexural, impact, and hardness values compared to epoxy resin/madar fibre composites.

Data Availability

The data used to support the findings of this study are included within the article. Further data or information is available from the corresponding author upon request.

Conflicts of Interest

The authors declare that there are no conflicts of interest regarding the publication of this article.

References

[1] H. Alamri and I. M. Low, "Effect of water absorption on the mechanical properties of nano-filler reinforced epoxy nanocompositesfiller reinforced epoxy nanocomposites," *Materials & Design*, vol. 42, pp. 214–222, 2012.

[2] T. Raja, V. Mohanavel, T. Sathish et al., "Thermal and flame retardant behavior of neem and banyan fibers when reinforced with a bran particulate epoxy hybrid composite," *Polymers*, vol. 13, no. 22, p. 3859, 2021.

[3] H. Essabir, E. Hilali, A. Elgharad et al., "Mechanical and thermal properties of bio-composites based on polypropylene reinforced with Nut-shells of Argan particles," *Materials & Design*, vol. 49, pp. 442–448, 2013.

[4] V. Mohanavel, S. Suresh Kumar, J. Vairamuthu, P. Ganeshan, and B. NagarajaGanesh, "Influence of stacking sequence and fiber content on the mechanical properties of natural and synthetic fibers reinforced penta-layered hybrid composites," *Journal of Natural Fibers*, vol. 2021, Article ID 1875368, 13 pages, 2021.

[5] V. Mohanavel, T. Raja, A. Yadav, M. Ravichandran, and J. Winczek, "Evaluation of mechanical and thermal properties of jute and ramie reinforced epoxy-based hybrid composites," *Journal of Natural Fibers*, vol. 2021, Article ID 1958432, 11 pages, 2021.

[6] P. Vimalanathan, N. Venkateshwaran, and V. Santhanam, "Mechanical, dynamic mechanical, and thermal analysis ofShorea robusta-dispersed polyester composite," *International Journal of Polymer Analysis and Characterization*, vol. 21, no. 4, pp. 314–326, 2016.

[7] H. Ismail, N. Othman, and M. Komethi, "Curing characteristics and mechanical properties of rattan-powder-filled natural rubber composites as a function of filler loading and silane coupling agentfilled natural rubber composites as a function of filler loading and silane coupling agent," *Journal of Applied Polymer Science*, vol. 123, no. 5, pp. 2805–2811, 2012.

[8] Han-Seung Yang, H.-joong Kim, H.-J. Park, Bum-Jae Lee, and T.-S. Hwang, "Water absorption behavior and mechanical properties of lignocellulosic filler-polyolefi bio-composites," *Elsevier, composite structures*, vol. 72, pp. 429–437, 2006.

[9] A. R. Sanadi, D. F. Caulfield, R. E. Jacobson, and R. M. Rowell, "Renewable agricultural fibers as reinforcing fillers in plastics: mechanical properties of kenaf fiber-polypropylene composites," *Industrial & Engineering Chemistry Research*, vol. 34, no. 5, pp. 1889–1896, 1995.

[10] J. George, S. S. Bhagawan, and S. Thomas, "Effects of environment on the properties of low-density polyethylene composites reinforced with pineapple-leaf fibre," *Composites Science and Technology*, vol. 58, no. 9, pp. 1471–1485, 1998.

[11] T. A. Collings, "Moisture absorption fickian diffusion kinetics and moisture profiles," *Handbook of Polymer Fiber Composites*, Longman Scientific and Technical, Essex, UK, 1994.

[12] M. T. Athijayamani, S. S. Winowlin, and A. Alavudeen, "Effect of fiber content on mechanical properties of short roselle and sisal fiber hybrid polyester composite," *International Journal of Computer Aided Engineering and Technology*, vol. 1, pp. 58–62, 2008.

[13] L. A. Pothan, S. Thomas, and N. R. Neelakantan, "Short banana fiber reinforced polyester composites: mechanical, failure and aging characteristics," *Journal of Reinforced Plastics and Composites*, vol. 16, no. 8, pp. 744–765, 1997.

[14] V. S. Sreenivasan, N. Rajini, A. Alavudeen, and V. Arumugaprabu, "Dynamic mechanical and thermogravimetric analysis of Sansevieria cylindrica/polyester composite: effect of fiber length, fiber loading and chemical treatment," *Composites Part B: Engineering*, vol. 69, pp. 76–86, 2015.

[15] G. Antonio, M. Alfonso, C. Giovanni, and C. Flavio, "Mechanical properties of basalt Fibers and their adhesion to polypropylene matrices," *Comp Part B*, vol. 67, pp. 233–238, 2014.

[16] P. J. Herrera-Franco and A. Valadez Gonzalez, "A study of the mechanical properties of short natural-fiber reinforced composites," *Composites Part B*, vol. 36, pp. 597–608, 2007.

[17] V. Yamunadevi, K. Palaniradja, A. Thiagarajan, P. Ganeshan, and K. Raja, "Characterization and dynamic mechanical analysis of woven roven glass fiber/cerium-zirconium oxide epoxy nanocomposite materials," *Materials Research Express*, vol. 6, no. 9, Article ID 095057, 2019.

[18] B. N. Ganesh and B. Rekha, "A comparative study on tensile behaviour of plant and animal fiber reinforced composites," *International Journal of Innovation and Applied Studies*, vol. 2, pp. 645–648, 2013.

Hindawi
Advances in Materials Science and Engineering
Volume 2022, Article ID 7805146, 10 pages
https://doi.org/10.1155/2022/7805146

Research Article

Analysis of the Hybrid of Mudar/Snake Grass Fiber-Reinforced Epoxy with Nano-Silica Filler Composite for Structural Application

I. Jenish,[1] A. Felix Sahayaraj,[2] V. Suresh,[3] J. Mani raj,[2] M. Appadurai,[4] E. Fantin Irudaya Raj,[5] Omaima Nasif,[6] Saleh Alfarraj,[7] and Ashok Kumar Kumaravel[8]

[1]*Department of Applied Mechanics, Seenu Atoll School, Hulhu-medhoo, Addu City Postal Code 19060, Maldives*
[2]*Department of Mechanical Engineering, Kalaignar Karunanidhi Institute of Technology, Coimbatore 641402, Tamilnadu, India*
[3]*Department of Biotechnology, Sharafuddin School, Hithadhoo 19020, Maldives*
[4]*Department of Mechanical Engineering, Dr. Sivanthi Aditanar College of Engineering, Tuticorin 628215, Tamilnadu, India*
[5]*Department of Electrical and Electronics Engineering, Dr. Sivanthi Aditanar College of Engineering, Tuticorin 628215, Tamilnadu, India*
[6]*Department of Physiology, College of Medicine and King Khalid University Hospital, King Saud University, Medical City, PO Box-2925, Riyadh 11461, Saudi Arabia*
[7]*Zoology Department, College of Science, King Saud University, Riyadh 11451, Saudi Arabia*
[8]*School of Chemical Engineering & Bio-Engineering University of Ulsan, Ulsan 680749, Republic of Korea*

Correspondence should be addressed to V. Suresh; suresh.velse@sharafuddin.edu.mv

Received 29 September 2021; Accepted 2 November 2021; Published 5 January 2022

Academic Editor: P Ganeshan

Natural fiber composite materials are competent materials that may replace conventional synthetic materials where the strength to weight ratio is essential. In this paper, the mechanical characteristics of composites made up of randomly oriented natural fibers (mudar fiber and snake grass fiber) with nano-silica filler are detailed for the first time. From the various literature surveys, the critical length of mudar and snake grass fiber is chosen as 40 mm and 30 mm, respectively. The test samples were prepared with a fiber content of 10%, 20%, 30%, and 40% with an equal amount of mudar and snake grass fiber. The percentage of nano-filler is maintained as constant as 3% with all the compositions. The composites showed that the highest mechanical properties were found at 30% fiber volume. The maximum tensile strength is 45 MPa, and the flexural strength is 51 MPa. The maximum impact strength is 4.5 J. Sample ID 3 provided the best results compared to other proportions. The fiber/matrix adhesion was investigated using a scanning electron microscope (SEM). These predominant mechanical properties make it easier for the implementation of the prepared composite material in structural and automotive applications.

1. Introduction

The mechanical properties of the natural fiber polymer composites depend on several factors, such as single fiber strength, average fiber length, and fiber-matrix adhesion. Strong interfacial bonding is necessary for optimal stress transmission between fiber and matrix [1–3]. The resistance to moisture-induced deterioration of the matrix-fiber adhesion was improved by surface treatment of fiber [4]. The mechanical properties of natural fiber-reinforced polymer composites are significantly influenced by certain manufacturing processes [5]. Natural fibers, particularly jute, hemp, flax, and kenaf, have excellent mechanical characteristics and may be able to compete with glass fiber in terms of specific strength and modulus [6]. Several kinds of research were done on the variety of natural fibers, including jute, hemp, sisal, and kenaf, to see

how they affect the mechanical characteristics of composite materials [7]. Bast fibers are derived from the outer cell layers of diverse plant stems and account for one-third of the total weight. Bast fibers are a collection of fiber bundles. To improve finer fiber extraction, these bundles are physically or chemically broken down. The filaments are comprised of cellulose and hemicellulose and are held together by a lignin or pectin matrix. Purely natural bast fibers come from the vascular tissue or outer bark of jute, kenaf, flax, and hemp plants and are strong cellulosic fibers [8]. The flax fibers were extracted from the bast or skin of the plant. Flax fibers are smooth, less dense, and flexible, and bundles of fiber resemble blonde hair, thus the term "flaxen" [9–12]. The banana fiber composite is ductile, requiring little plastic deformation [13]. Pandanus plant fiber is easily accessible and has higher fiber content [14]. Incorporation of nano-silica increased the mechanical properties without increasing the density of the composite materials [15]. The stiffness of the matrix is increased by adding nano-silica which leads to transferring the load easily from matrix to fiber, so automatically, the properties of the composite material are improved [16]. The tensile (tensile strength/modulus) and flexural (tensile strength/modulus) properties are increased by adding 3 wt.% of nano-silica with epoxy hybrid composite [17]. Natural fiber characteristics are determined by their chemical components [18], which are determined by the geological conditions in which they were found. The amount of cellulose in natural fiber determines its strength [19]. Characteristics like fiber selection and the matrix used during processing influence the characteristics of natural fiber-reinforced composites [20]. The bonding between the fiber and the matrix determines the strength of the processed natural fiber composite, which is affected by surface shape [21]. Kevlar and Napier grass fibers are bonded with epoxy matrix to create a novel composite utilizing a traditional hand layup fabrication method, and five different sequences are fabricated to measure the mechanical properties of this hybrid composite laminate [22]. Thus, natural fibers are regarded as the suitable reinforcement in material industries for better development. In this article, hybrid of mudar/snake grass fiber-reinforced epoxy composite particulate-filled with silica nano-powder has been fabricated, and the mechanical properties of the fabricated samples are discussed. As it has a substantial load carrying capacity, obligating a preferable structural application would give the value of this material.

2. Materials and Methods

The raw materials used in the fabrication of hybrid composites are mudar fiber (*Calotropis gigantea*), snake grass (*Sansevieria ehrenbergii*), nano-silica, epoxy resin (LY 556), and hardener (HY 951). The epoxy resin has the density of 1.11 g/cm3 and Young's modulus of 3400 MPa. Moreover, it has the failure stress and strain value of 95 MPa and 3%. The composite fabrication process is shown in Figure 1. The properties of the fibers are given in Table 1.

2.1. Mudar Fiber. The fibers were collected from the Kanyakumari region, Tamil Nadu, India. The fine, robust fibers that predominate throughout the plant make it useful. The scientific name of the plant is *Calotropis gigantea*. To get them, the straightest branches are cut and left to wither for at least twenty four hours; the skin is then peeled and the stringy part between the bark and the inner layer is removed on the second and third days. They are then exposed to the sun to dry. This method is time-consuming and costly, but soaking the bark in water causes it to decompose the layers, and cutting it will ruin it. The fiber may be separated as finest fiber for the useful work. It can withstand water for a long period. Then, it is dried at 70°C in an oven. The plant is illustrated in Figure 2, and extracted fiber is shown in Figure 3.

2.2. Snake Grass Fiber. Snake grass fibers were extracted from leaves of the *Sansevieria ehrenbergii* plant from local parts of Kannampalayam village, Coimbatore, India. Snake grass has several physical characteristics that make it more ideal for spinning finer counts, including length, strength, and uniformity. The fiber has been extracted through the microbial degradation technique. Figures 4 and 5 show the plants and fiber images.

2.3. Nano-Silica. The nano-silica is not very expensive and easily available in most of the shops and also easy to transport. But, it must be neatly packed during transport because the size is in nano-scale. The nano-silica was bought from Astrra Chemicals, Chennai. The size of the powder is 15–80 nm. The colour is pure white. Special care was taken during material preparation time because it easily spreads over the air. The normal and SEM images of the nano-silica are given in Figures 6(a) and 6(b).

2.4. Epoxy Resin. Epoxy (LY 556) was obtained from Covai Seenu Chemicals, Coimbatore, Tamil Nadu, India. The epoxy resin is coupled with catalyzing ingredients to form polyepoxide which is in the form of polymers and cross-links. The viscosity of the mixture and its shrinking properties are influenced by epoxy resin and additives. The number of fillers and diluents used will affect the resin system's physical and handling qualities.

2.5. Hardener. The hardener (HY 951) is being utilized was supplied by Covai Seenu Chemicals, Coimbatore, Tamil Nadu, India. These hardeners react with the epoxy resins and have a significant impact on the ultimate properties of the cured epoxy resin system. Epoxy with hardener blending provides significant properties of gel time, combined viscosity, and demold time. Epoxy hardeners have an impact on the physical characteristics of epoxy resin systems, such as tensile, compression, and flexural qualities.

2.6. Mold Design for Specimen Preparation. The composite plates with mudar and snake grass hybrid fibers as reinforcement were prepared with the dimension of 300 mm × 150 mm × 3 mm, as shown in Figure 7. Steel plates were used to create the mold. For non-sticking purposes, Teflon

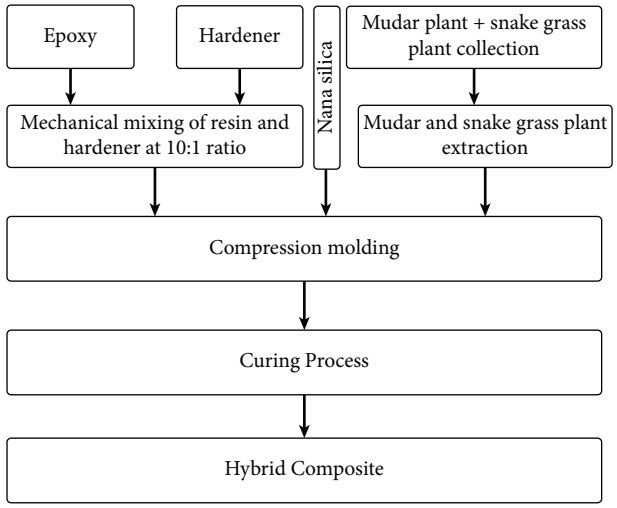

Figure 1: Composite fabrication process.

Table 1: Properties of the fibers.

Fiber name	Density (g/cm^3)	Diameter (μm)	Gage length (mm)	Tensile strength (MPa)	Tensile modulus (GPa)	Elongation (%)
Calotropis gigantea [23]	0.56	125	50	382	9.7	2.1
Sansevieria ehrenbergii [24]	0.887	20–250	10–50	50–585	1.5–7.67	2.8–21.7

Figure 2: *Calotropis gigantea*.

sheets were placed at the top and bottom. A spacer frame was employed to lay the fiber on the mold. The different combinations of fabricated samples are shown in Table 2.

3. Experimental Procedure

3.1. Chopped Fiber-Reinforced Nano-Silica Composite Material Preparation. The samples were fabricated with 10%, 20%, 30%, and 40% volume fractions of fibers with 3% of nano-silica. The compression molding technique was employed to fabricate the samples. The fibers were cut into 5 mm to 8 mm lengths. Extracted fibers were kept in the oven at 70°C for 6 hours to remove the moisture content. The matrix solution was formed by mixing the epoxy and hardener in the ratio of 10 : 1. 3% of nano-silica was mixed with matrix and hardener for better propagation. The mixer was poured into the fiber and then the mold was closed. Pressure was applied to the mold to get the sample compacted. The remaining mixture was applied to the unfinished parts. Meanwhile, the composite plate was squeezed and compacted with a hand to remove the bubbles from the plate. The composite plate was left to cure for 20–24 hours until it was completely dry. A determined quantity of epoxy resin and hardener was employed for varying volume fractions of fibers.

Figure 3: Extracted mudar fiber.

Figure 4: *Sansevieria ehrenbergii*.

Figure 5: Extracted snake grass fiber.

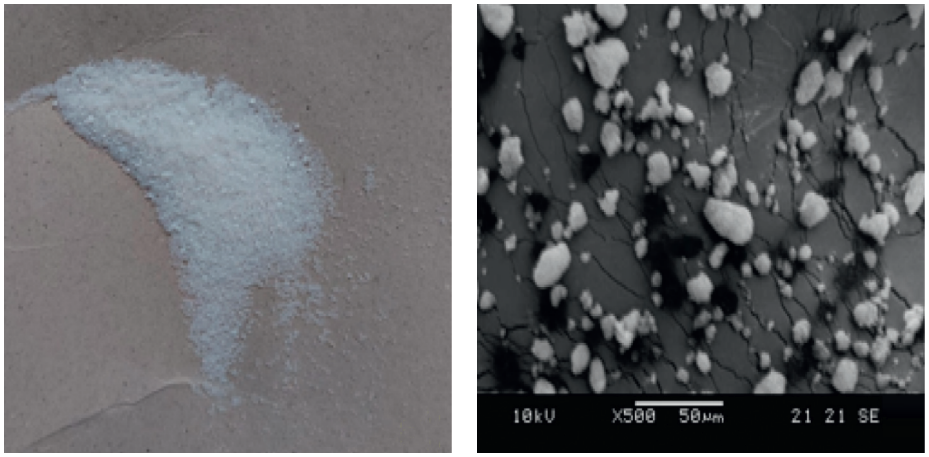

(a) (b)

Figure 6: (a) Image of nano-silica. (b) SEM image of nano-silica.

Figure 7: Steel die mold.

3.2. Specimen for Testing. The mechanical properties were analyzed after preparing the samples. The composite boards were cut into the standard test specimens (5 specimens were prepared for each testing to get an average value). Handsaws and other tools were used in the cutting process. All specimens tested were conditioned according to ASTM standards. The test specimens were kept in a room with a temperature of 23°C ± 2°C with 50% of relative humidity for 40 hours before starting the test. All of the tests were carried out in a typical laboratory environment with a temperature of 23°C and relative humidity of 50%.

3.3. Mechanical Testing. Following manufacture, the test specimens were put through a series of ASTM-required mechanical testing. Tensile, impact, and flexural test specimens with ASTM standard and dimensions are listed in Table 3.

3.4. Tensile Test (ASTM D3039). Once the curing process was done on the developed composite, a wire cutting instrument was employed to make the specimens into the required dimensions. The tensile test specimen was made as per ASTM D3039 (Figure 8); the testing specimen has a length of 250 mm and width of 25 mm. The item was held in the grips of an Instron universal tester with a gage length of 100 millimeters. The ultimate tensile strength and tensile modulus of the composite were determined from the stress-strain diagram.

3.5. Flexural Test (ASTM D790). After the fiber-reinforced composite was cured, the specimens were cut into the required dimension with the aid of a wire cutting machine. The flexural test specimen was made following ASTM D790 (Figure 9); the composite was cut into the required dimension of 154 mm in length and 13 mm in width. The

Table 2: Composition of fabricated samples.

Sample ID	Composition		
	Epoxy (%)	Fiber (MF + SGF) (%)	Nano-silica (%)
Sample 1	87	10	3
Sample 2	77	20	3
Sample 3	67	30	3
Sample 4	57	40	3

Table 3: Test specimen standards with dimension.

S. No	Type of testing	Standard used	Specimen dimension
1	Tensile testing	ASTM D3039	250 mm × 25 mm × 2.5 mm
2	Flexural testing	ASTM D790	154 mm × 13 mm × 3 mm
3	Impact testing (Izod)	ASTM D4812	64 mm × 12.7 mm × 3.2 mm

Figure 8: Specimen for tensile test.

specimen was fixed tightly with the Instron testing machine for measurement. The ultimate flexural strength of the specimens was measured from the stress-strain graph.

3.6. Impact Test (ASTM D4812). This test was done to measure the impact resistance of the developed composite. The amount of energy required to initiate the crack and keep it up to fracture is called impact. This test may be used to assess whether a material fulfills specified impact qualities or to compare materials for overall toughness. The specimens were prepared according to ASTM D4812 standard. The test sample is shown in Figure 10.

4. Results and Discussion

Previous sections covered the preparation of these composites as well as the tests that were undertaken on them. Here are the findings of several characterization tests. Tensile strength, flexural strength, and impact strength have all been investigated and analyzed.

4.1. Tensile Test. Table 4 shows the tensile properties of epoxy/SGF/MF with nano-silica hybrid composite. From the table, it was clear that sample 3 (67% epoxy with 30% fiber volume fraction with 3% nano-silica) produces maximum tensile properties (45 N/mm^2) compared with other volume fractions. Hence, fiber volume fractions and nano-silica influenced the tensile strength of the developed composite. It was observed that the addition of fiber with the epoxy matrix improves the mechanical properties to the certain level. Fiber percentage more than 30% decreases the matrix-fiber adhesion, leading to the decrease in mechanical properties. Also, increased fiber content beyond 30% will increase the void percentage in the developed composite materials.

4.2. Flexural Test. Flexural strength also called as bending strength can be measured using a 3-point flexural testing procedure. Flexural strength of the developed composites is listed in Table 5. The samples start to crack when the load exceeds the strength of developed samples. The flexural strength (51 N/mm^2) of sample 3 is more compared to the remaining developed samples. The presence of mudar fiber, snake grass fiber, and nano-silica increases the flexural strength. The higher flexural strength enhances the load-bearing capacity of samples. Flexural strength variation is very similar to tensile strength results. Adhesion between matrix and fiber reduces when the fiber percentage is more than 30%. It does not allow a significant improvement for further addition of fiber in the sample.

4.3. Impact Test. The impact test determines the material's capacity to sustain abrupt shock loads. This test is carried out using an XJJU-50 impact testing machine. The mechanism comprises a loaded striker with set kinetic energy when released. The load will be removed once the specimen manufactured according to the specifications is retained in the machine. The amount of energy absorbed would be shown on display.

The impact strength of developed samples is listed in Table 6. From Table 6, sample 3 (67% resin +30% fiber + 3% nano-silica) produces the highest impact strength compared to other developed composites. Hence, sample 3 could be the suitable material for high damping and vibration-related applications.

Figure 9: Specimen for flexural test.

Figure 10: Specimen for impact test.

Table 4: Tensile test result.

Sample ID	Breaking load (N)	Ultimate stress (N/mm^2)	Max. displacement (mm)
Sample 1	1315	28	3.5
Sample 2	1610	36	3.7
Sample 3	2760	45	3.4
Sample 4	1448	38	3.2

4.4. SEM Investigation. The surface characteristics of developed samples were analyzed by using a scanning electron microscope (SEM). Samples were prepared with gold sputter coating for conducting purposes. A fractured tensile sample is shown in Figure 9. Sample 3 produces better mechanical properties that show proper bonding between matrix and fiber, resulting in improved tensile, flexural, and impact properties. The crack content and void content are less compared with other samples. Nano-silica increased the flexibility of the matrix, which led to the movement of the mixture inside the fiber wall and around the surface of the fiber. This phenomenon increases the mechanical properties.

Figure 11(a) shows the fractured surface of the sample, which indicates that the surface has matrix fracture, fiber fracture, and fiber pullout. Fiber pullout happens due to the poor adhesive of fiber and matrix. The fiber carries the load until it gets fractured which improves the mechanical properties. Figure 11 (b) depicts the matrix penetration inside the fiber walls, which increases the fiber-matrix attachment.

Table 5: Flexural test result.

Sample ID	Breaking load (N)	Ultimate stress (N/mm^2)	Max. displacement (mm)
Sample 1	198	31	10.5
Sample 2	182	35	11.5
Sample 3	455	51	7.1
Sample 4	204	39	3.2

Table 6: Impact test results.

Sample ID	Impact strength (J)
Sample 1	2.94
Sample 2	3.33
Sample 3	4.50
Sample 4	2.80

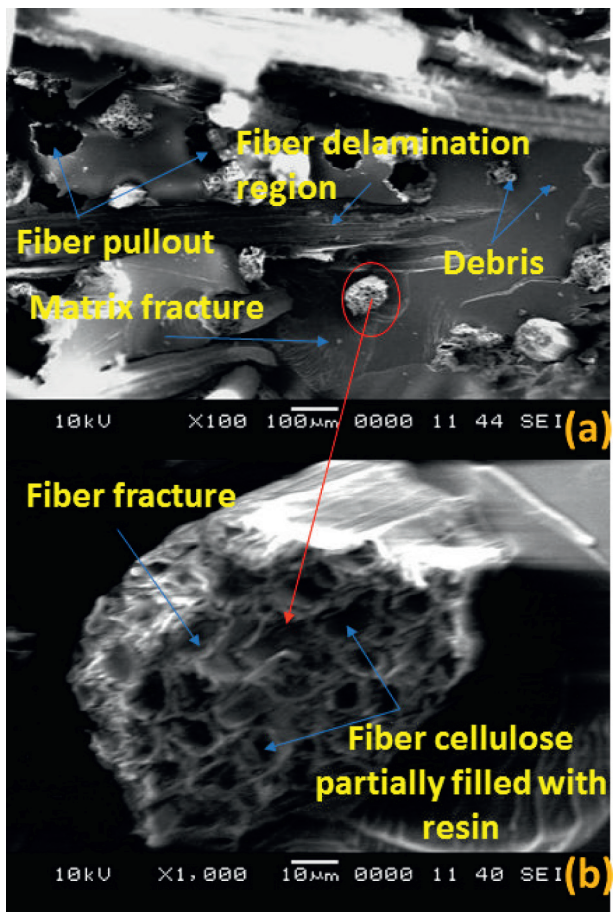

Figure 11: (a, b) Tensile fractured surface morphology of sample 3.

5. Conclusion

The following are the results derived from the experimental research of snake grass fiber and mudar fiber-reinforced epoxy with nano-silica filler composites.

This study demonstrates the successful fabrication of nano-silica incorporation with natural fiber-reinforced epoxy composites with varying fiber percentages using the hand layup technique. It has been discovered that differing volume fractions of fiber significantly affect the mechanical characteristics of composites, such as tensile, flexural, and impact strength. For varying breaking loads of fiber, tensile testing of composites is also strongly impacted. The strength of the fiber content at 30% is superior than the fiber content at 10%, 20%, and 40%. The incorporation of nano-silica (3%) provided additional support to improve the properties of the prepared composite materials. The fiber content of 30% has a strong impact strength, which is followed by a reduction.

The major ruptured mechanisms are matrix fracture, fiber fracture, and fiber pullout, which were substantiated by SEM images.

Fiber filled with resin increased the bonding strength between fiber and matrix. Moreover, incorporation of silica nanofiller increased the cohesive strength of the interlaminar structure. These behavioural changes strengthen the material at the optimum level of 30% hybrid fibers and 3% nano-silica. The prepared sample 3 provides the maximum tensile strength of 45 MPa and the flexural strength of 51 MPa. This result is more significant for fabricating products such as partition board, roof ceiling, circuit board, and roof gutter.

Data Availability

The data used to support the findings of this study are included within the article. Further data or information is available from the corresponding author upon request.

Conflicts of Interest

The authors declare that there are no conflicts of interest regarding the publication of this article.

Acknowledgments

The authors appreciate the support from Sharafuddin School, Hithadhoo, Maldives. The authors also thank Dr. Sivanthi Aditanar College of Engineering, Tuticorin, and this project was supported by Researchers Supporting Project number (RSP-2021/257), King Saud University, Riyadh, Saudi Arabia.

References

[1] M. Ramesh, C. Deepa, L. Rajeshkumar, M. Tamil Selvan, and D. Balaji, "Influence of fiber surface treatment on the tribological properties of Calotropis gigantea plant fiber reinforced polymer composites," *Polymer Composites*, 2021.

[2] S. Sathish, K. Kumaresan, L. Prabhu, and N. Vigneshkumar, "Experimental investigation on volume fraction of mechanical and physical properties of flax and bamboo fibers reinforced hybrid epoxy composites," *Polymers and Polymer Composites*, vol. 25, no. 3, pp. 229–236, 2017.

[3] S. Sathish, L. Prabhu, S. Gokulkumar, N. Karthi, D. Balaji, and N. Vigneshkumar, "Extraction, treatment and applications of natural fibers for bio-composites–a critical review," *International Polymer Processing. Walter de Gruyter GmbH*, vol. 36, 2021.

[4] C. Dash, A. Das, and D. Kumar Bisoyi, "Influence of pretreatment on mechanical and dielectric properties of short sunn hemp fiber-reinforced polymer composite in correlation with fine structure of the fiber," *Journal of Composite Materials*, vol. 54, no. 23, pp. 3313–3327, 2020.

[5] A. Felix Sahayaraj, M. Muthukrishnan, R. Prem Kumar, M. Ramesh, and M. Kannan, "–Review," *IOP Conference Series: Materials Science and Engineering*, vol. 1145, no. 1, Article ID 012069, 2021.

[6] P. Raveendran, S. V. Alagarsamy, C. Chanakyan, M. Meignanamoorthy, M. Ravichandran, and S. Sakthivelu, "A hybrid approach for predition of machining performances of glass fiber reinforced plastic (epoxy) composites," *Surface Topography: Metrology and Properties*, 2021.

[7] P. Wambua, J. Ivens, and I. Verpoest, "Natural fibres: can they replace glass in fibre reinforced plastics?" *Composites Science and Technology*, vol. 63, no. 9, pp. 1259–1264, 2003.

[8] A. V. Ratna Prasad and K. Mohana Rao, "Mechanical properties of natural fibre reinforced polyester composites: jowar, sisal and bamboo," *Materials & Design*, vol. 32, no. 8–9, pp. 4658–4663, 2011.

[9] ASTM, *International A. ASTM D638-14, Standard Test Method for Tensile Properties of Plastics*, ASTM International, West Conshohocken, PA, US, 2015.

[10] K. M. M. Rao, A. V. R. Prasad, M. N. V. R. Babu, K. M. Rao, and A. V. S. S. K. S. Gupta, "Tensile properties of elephant grass fiber reinforced polyester composites," *Journal of Materials Science*, vol. 42, no. 9, pp. 3266–3272, 2007.

[11] ASTM I, *Standard test methods for flexural properties of unreinforced and reinforced plastics and electrical insulating materials*, ASTM D790-07, 2007.

[12] S. Jayabal and U. Natarajan, "Influence of fiber parameters on tensile, flexural, and impact properties of nonwoven coir-polyester composites," *International Journal of Advanced Manufacturing Technology*, vol. 54, no. 5–8, pp. 639–648, 2011, [Internet].

[13] G. Kalaprasad, K. Joseph, S. Thomas, and C. Pavithran, "Theoretical modelling of tensile properties of short sisal fibre-reinforced low-density polyethylene composites," *Journal of Materials Science*, vol. 32, no. 16, pp. 4261–4267, 1997.

[14] G. V. Vigneshwaran, I. Jenish, and R. Sivasubramanian, "Design, fabrication and experimental analysis of pandanus fibre reinforced polyester composite," in *Advanced Materials Research*vol. 984-985, , pp. 253–256, Trans Tech Publ, 2014.

[15] G. L. Devnani and S. Sinha, "Effect of nanofillers on the properties of natural fiber reinforced polymer composites," *Materials Today: Proceedings*, vol. 18, pp. 647–654, 2019.

[16] N. Sapiai, A. Jumahat, M. Jawaid, M. Midani, and A. Khan, "Tensile and flexural properties of silica nanoparticles modified unidirectional kenaf and hybrid glass/kenaf epoxy composites," *Polymers*, vol. 12, no. 11, Article ID 2733, 2020.

[17] B. Suresha, G. S. Divya, G. Hemanth, and H. M. Somashekar, "Physico-mechanical properties of nano silica-filled epoxy-based mono and hybrid composites for structural applications," *Siliconindia*, vol. 13, pp. 2319–2335, 2021.

[18] P. Madhu, M. R. Sanjay, P. Senthamaraikannan, S. Pradeep, S. S. Saravanakumar, and B. Yogesha, "A review on synthesis and characterization of commercially available natural fibers: part-I," *Journal of Natural Fibers*, vol. 16, no. 8, pp. 1132–1144, 2019a.

[19] V. K. Thakur and A. S. Singha, "Natural fibres-based polymers: part I-mechanical analysis of Pine needles reinforced biocomposites," *Bulletin of Materials Science*, vol. 33, no. 3, pp. 257–264, 2010.

[20] R. Vijay, D. Lenin Singaravelu, A. Vinod et al., "Characterization of raw and alkali treated new natural cellulosic fibers from Tridax procumbens," *International Journal of Biological Macromolecules*, vol. 125, pp. 99–108, 2019a.

[21] S. M.R., S. Siengchin, J. Parameswaranpillai, M. Jawaid, C. I. Pruncu, and A. Khan, "A comprehensive review of techniques for natural fibers as reinforcement in composites: preparation, processing and characterization," *Carbohydrate Polymers*, vol. 207, pp. 108–121, 2019.

[22] R. Ganesamoorthy, R. Meenakshi Reddy, T. Raja et al., "Studies on mechanical properties of kevlar/napier grass fibers reinforced with polymer matrix hybrid composite," *Advances*

in Materials Science and Engineering, vol. 2021, Article ID 6907631, 2021.

[23] A. Ashori and Z. Bahreini, "Evaluation of Calotropis gigantea as a promising raw material for fiber-reinforced composite," *Journal of Composite Materials*, vol. 43, no. 11, pp. 1297–1304, 2009.

[24] T. P. Sathishkumar, P. Navaneethakrishnan, and S. Shankar, "Tensile and flexural properties of snake grass natural fiber reinforced isophthallic polyester composites," *Composites Science and Technology*, vol. 72, no. 10, pp. 1183–1190, 2012.

Hindawi
Advances in Materials Science and Engineering
Volume 2021, Article ID 9529199, 17 pages
https://doi.org/10.1155/2021/9529199

Review Article

A Cutting-Edge Survey of Tribological Behavior Evaluation Using Artificial and Computational Intelligence Models

Senthil Kumaran Selvaraj,[1] **Aditya Raj**,[2] **Mohit Dharnidharka**,[1] **Utkarsh Chadha**,[1] **Isha Sachdeva**,[2] **Chinmay Kapruan**,[1] **and Velmurugan Paramasivam**[3]

[1]*Department of Manufacturing Engineering, School of Mechanical Engineering (SMEC), Vellore Institute of Technology (VIT), Vellore, Tamilnadu 632014, India*
[2]*School of Information Technology and Engineering (SITE), Vellore Institute of Technology (VIT), Vellore, Tamilnadu 632014, India*
[3]*School of Mechanical and Automotive Engineering, College of Engineering and Technology, Dilla University, P.O. Box 419, Dilla, Ethiopia*

Correspondence should be addressed to Senthil Kumaran Selvaraj; senthilkumaran.s@vit.ac.in and Velmurugan Paramasivam; drvelmuruganp@du.edu.et

Received 28 October 2021; Revised 14 December 2021; Accepted 16 December 2021; Published 29 December 2021

Academic Editor: Ali Khorram

Any metal surface's usefulness is essential in various applications such as machining and welding and aerospace and aerodynamic applications. There is a great deal of wear in metals, used widely in machines and appliances. The gradual loss of the upper metal layers in all metal parts is inevitable over the machine or component's lifetime. Artificial intelligence implementations and computational models are being studied to evaluate different metals' tribological behavior, as technological progress has been made in this field. Different neural networks were used for different metals. They are classified in this paper, together with a description of their benefits and inconveniences and an overview and use of the different types of wear. Artificial intelligence is a relatively new term that uses mechanical engineering. There is still no scientific progress to examine various metal wear cases and compare AI and computational models' accuracy in wear behavior.

1. Introduction

Given the potential and technological developments we have experienced in an industrial revolution, we have a long path to cover as engineers. The wear behavior varies from metal to metal, mainly depending on its properties or the method used, and AI has helped companies better understand metals' wearing behavior and deploy them in processes or machinery because the speed with precision is more critical in the industry, helping companies increase their response speed. Artificial intelligence is a computer science field dealing with the simulation of computer systems to imitate human intelligence. AI is a large field in computers and other areas such as economics, theory of control, probability, optimization, and bilingualism. AI is such a phenomenon that it can model and find patterns in complex inputs and outputs on the given data. It has been made an essential element of our lives without even realizing weather prediction, mechanical wear and tear, the probability of different diseases, and many more, as recommended by Netflix and YouTube. An AI process consists of data acquisition and correction to enhance its earlier forecasts over time. Mechanical engineering, as technology helps mechanical design or engineering works, is AI's biggest consumer. All sections of mechanical engineering benefiting highly from AI are robotics, automation, and sensor technology.

Wear means that the substance is consistently removed from or deformed from a solid surface while moving about another substance or fluid. Wear is a natural phenomenon when two bodies are rubbed or slipped. Mechanical and

chemical behavior and combinations of these factors, such as corrosion, erosion, and abrasion, cause wear on the solid surface of the material. Tribology is the wear science involving friction, lubrication, and wear applications and concepts. Wear is an essential characteristic of products that must be carefully examined before producing a product. Other processes such as fatigue, material failure, and loss of functionality cause surface degradation. In the manufacturing industry, wear is a constant inconvenience, and it is expensive because it is causing loss of part and wear deterioration. The wear of the active surfaces, near-surface compositions, and fragmentation leads to wear debris caused by the plastic deformation of metals. The wear waste produced varies between nanometers and thousands. Wear can be correlated with the help of the wear rate. The material mass or volume removed by the sliding distance of each unit is the ratio. The wear volume per unit is usually expressed as a dimensionless entity called the wear coefficient on the unit's sliding distance (K). The wear mechanism is generally considered a negative feature and is unwanted in most practical contexts, but it has many applications. Wear, for example, is affected by processes such as filing, lapping, sanding, and polishing used to create finished surfaces.

They also collected datasets, if provided, software used, benefits, and drawbacks, and all studies referred to for that survey were fully applicable to explain the subject matter of the case studies cited beforehand and cover artificial intelligence and calculation models as shown in Figure 1.

2. Types of Wear

We must first understand the various types of wear before applying artificial intelligence principles to evaluate wear behavior. Wear can occur due to a single mechanism or a complex combination of mechanisms. To solve a wear problem, we must first understand the various wear mechanisms at work. Abrasion or surface deterioration occurs when the force acting on the surface is caused by load stress or friction. When chemical reactions alter a material body's outer layer, the wear mechanisms responsible are adhesion and tribo-oxidation. The sections that follow describe the various types of clothing.

The most common wear process encountered in the industry is abrasive wear. According to reports, abrasion is to blame for 50% of all wear issues. Abrasive wear is the substance loss caused by hard particles being forced against and moved along a solid surface [1]. The wear mechanism that causes abrasive wear is referred to as abrasion (scraping off). Abrasion occurs when a solid body with a rough surface collides with a coupling part with a soft surface. Abrasive wear is classified into two types based on the type of contact and the contact environment.

(a) Three-body abrasion: A third dimension is included in sliding two surfaces (as shown in Figure 2), hence blaming the third body for material removal from both surfaces (particles are usually assumed the third body).

(b) Two-body abrasion: This occurs when the hard material on one surface absorbs material from the opposite surface. Two-body abrasion is always possible because the asperities that cause removal on a hard surface can never be removed entirely, even with the most advanced polishing. As a result, wear debris forms between the two sliding surfaces. Long-term two-body abrasive wear causes three-body abrasion, which causes more wear than two-body abrasion.

Three mechanisms commonly cause abrasive wear:

(1) Ploughing: The displacement of particles away from the wear particles causes the formation of grooves. Ridges form on the edges of the grooves and are removed by abrasive materials moving through them.

(2) Cutting is the removal of material from a solid surface in the form of primary debris or microchips. This method is similar to traditional machining.

(3) Fragmentation occurs when the indenting material is removed from the surface, resulting in a localized fracture.

Adhesive wear: This occurs due to the interaction of asperities between two surfaces [2]. Formalized paraphrase adhesion is the wear mechanism that causes adhesive wear (stickiness). It occurs when the compositions of the two metals are incredibly similar. A bond can form because of this compatibility, allowing parts to seize or become cold-welded together (as seen in Figure 3). Because of these bonded sections' swaying and sliding motion, abrasion occurs on the bordering surfaces. Adhesive wear is classified into two types:

(a) Classifying wear due to relative motion/direct contact between two surfaces along with plastic deformation, leading to transfer of metal debris onto the other metal's surface during wear.

(b) Cohesive-adhesive forces hold two faces together even when a significant distance separates them. The actual transition could occur.

Surface fatigue: This occurs when the surface of a material is stressed. As a result of this phenomenon, which thermal or mechanical forces can cause, surfaces crack. The fatigue wear caused due to particle detachment is mainly because of cyclic increase of metal surface microcracks (as shown in Figure 4). Each period increases the crack by a small amount until a surface microcrack develops. As a result, large surface cracks develop over time, posing a direct threat to the components.

Corrosive wear/oxidation wear: This material deterioration combines corrosion and wear. It is defined as a wear phase in which materials slide against each other in a corrosive environment. It is a type of material degradation that combines corrosion and wear. It is defined as a corrosive wear process in which materials slide against each other. When there is no sliding, corrosion on the surfaces forms a micrometer-thick film layer, reducing or even preventing further corrosion. This film is chipped away during the sliding application, exposing the metal surface to further corrosion (as shown in Figure 5). This process of wear occurs in the presence of harmful or

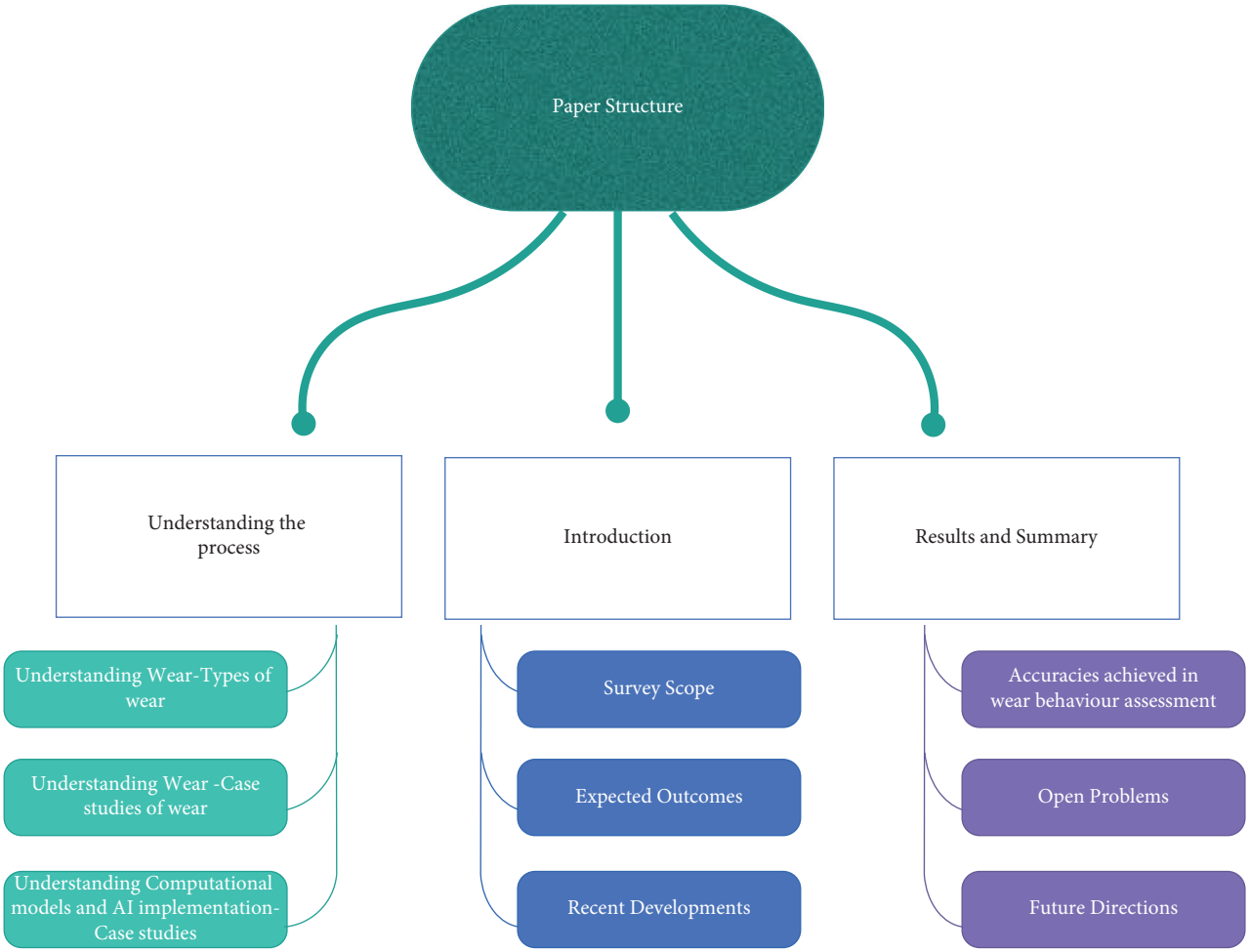

Figure 1: Structure of the survey paper.

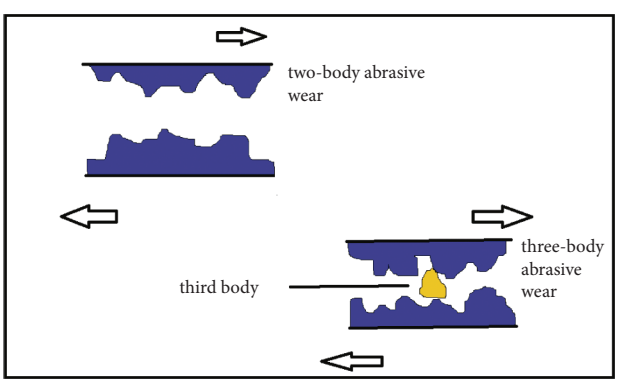

Figure 2: Two-body and three-body abrasive wear.

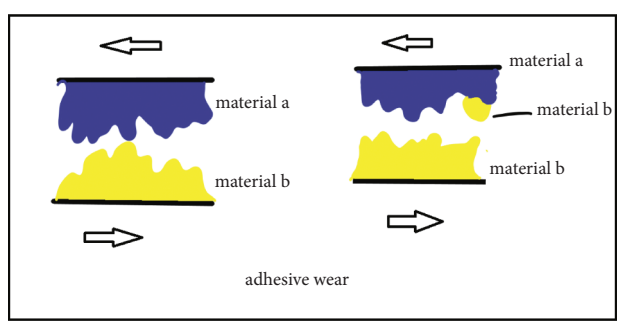

Figure 3: Adhesive wear.

oxidizing metals. Oxidation, also known as rust, is a severe form of corrosive wear. Oxides create a decrease in the equilibrium of friction between surfaces or are often a more significant challenge to work with than the materials involved and can be used as excellent abrasives.

Cavitation wear: A liquid medium causes cavitation wear on metal surfaces. It happens when cavities in a liquid flowing near the material are nucleated, developed, and violently collapsed repeatedly. Because of the rapid changes in liquid pressure, small vapor-filled craters with low vapor pressure form. Cyclic stress occurs when these craters or voids collapse near a metal surface. It causes surface fatigue, which contributes to the wear of the base material over time.

3. Wear Tests

The wear rate is defined as the volume loss per unit sliding distance. It is a dimensionless quantity (K) that can assess wear damage. The wear rate is defined as the body's height adjustment ratio to the relative sliding distance duration.

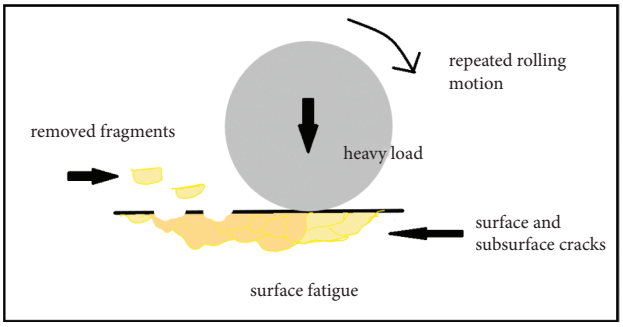

Figure 4: Surface fatigue.

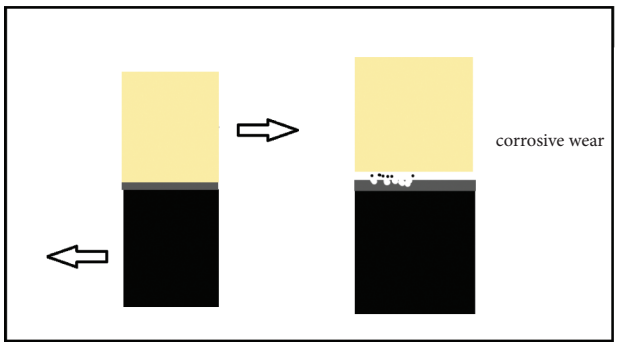

Figure 5: Corrosive wear.

Under normal conditions, wear progresses through three stages, the first of which is the primary stage, during which the surfaces involved adjust to one another, and the wear rate can be high or low. The second level, also known as the mid-age process, follows the first and is distinguished by a consistent wear rate. This process consumes the majority of the component's operating life. Finally, the component reaches the tertiary level, also known as the "old-age phase." The surfaces involved experience rapid wear, resulting in the component's premature failure [3–11].

Wear tests are classified as follows:

(1) *Pin-on-Disc Wear Test*. This is one of the most common ways to test wear rates and wear resistance. It is popular due to its ability to simulate various wear modes including omnidirectional, bidirectional, unidirectional, and quasi-rotational wear. Many different materials can be tested for wear. A test of wear resistance between PTFE (polytetrafluoroethylene) and its composites [12] was done using a pin-on-disc wear test, and it was observed that as the load increased, the coefficient of friction decreased. Pure PTFE experienced maximum wear followed by PTFE with 17% GFR, PTFE with 25% bronze, and PTFE with 35% carbon which experienced minimum wear.

(2) *Block-on-Ring Wear Test*. This is widely used to evaluate the sliding wear behavior of materials in various simulated conditions. It also helps in ranking material couples for specific tribological applications. A test of woven glass fibers is conducted on a block-on-ring wear testing machine [13], and it was found that aramid fiber-reinforced composites are less prone to wear than simple glass fabrics. Also, weaved 300 glass fabrics displayed better wear resistance than woven 500 glass fabrics.

(3) *Abrasion Wear Test*. This is used to test the abrasive resistance of materials such as metals, composites, ceramics, thick thermal spray, and weld overlay coatings.

(4) *Cavitation Erosion Vibratory Test*. The surface of the test sample is immersed in liquid, and the cavitation process is induced by vibrational erosion. Ultrasonic waves consisting of alternate expansions and compressions are transmitted into the liquid, which causes erosion (material loss) of the surface of the sample. This method is used to determine the relative wear resistance of test samples to cavitation erosion. In a test between HN steel and AISI 304 steel [14], the samples' cavitation wear increased with the decrease in the pH value of the water. Also, AISI 304 steel was more resistant to wear than HN steel.

(5) *Ball-on-Flat Wear Test*. This allows observing the wear tracks' dynamic load, friction force, and depth. Three different teeth from three different young males were tested using this apparatus [15], and it was observed that, for all the three teeth, three different wear scars were observed. The enamel layer displayed better wear resistance and had a lower friction coefficient than the dentin region.

4. Wear Testing Case Studies

Tables 1 to 5 discuss various case studies that involve various wear tests, briefly discussing the test and the implementations or additions in the metal workpiece chosen along with the observed outcomes.

5. Computational and Artificial Intelligence Models to Detect Wear Behavior

Artificial neural networks are a subset of AI widely used in mechanical engineering. ANNs are modelled after the biological neural system like an animal brain and are made up of neurons linked to each other that perform complex computations in the same way that the brain does. Dr. Robert Hecht–Nielson defined ANNs as "***a computing system composed of several simple, highly interconnected processing elements that process information through their dynamic state response to external inputs.***" The networks are widely applicable in solving classification and optimization problems, predictions, pattern recognition, etc. Because ANNs are adaptable, they can imitate linear and nonlinear relationships since the data are divided into various layers, making them well generalizable. These are trained using the datasets defined for training and then further used to predict the output values with the help of different algorithms (Figure 6) [4, 5].

Table 1: Comparison of materials with the pin-on-disc wear test and the results observed.

Materials used	Tests performed	Results observed	Ref.
The unreinforced portion was made of aluminum alloy (Al-2014). Various SiC particles were added to the Al alloy as a reinforcing substance.	Pin-on-disc wear test	With the increase in grain size, weight loss was observed to increase. It was discovered that composites with larger particle sizes had better wear resistance.	[16]
AZ91D alloy	Pin-on-disc	Due to the relative motion of AZ91D and stainless steel, frictional heat is generated, which affects the rate of wear.	[17]
1. Nylon gears 2. Acetal gear pairs	Pin-on-disc	The acetal gear pair has a higher wear rate than the nylon gear pair. Each acetal gear pair has a sliding speed threshold above which the wear rate dramatically increases.	[18]
A substrate made of BBS: LM 11 alloys was used, which was reinforced with (a) SiC particles and (b) SiC fibers for producing composites.	Pin-on-disc	The wear rate of the base alloy with no reinforcements was the highest, while the composites had the lowest wear rate. Because of a solid particle-matrix interface, the alloy reinforced with SiC particles had a low wear rate, whereas the alloy reinforced with SiC fibers had a higher wear rate due to a weak fiber-matrix interface.	[19]
Glass fiber-reinforced polyphenylene sulfide polymers APK polymer POM polymer UHMWPE polymer PA66 polymer	Pin-on-disc	A constant rate of steady-state wear was observed. POM polymer observed the highest wear out of all. It had the highest wear rate across all sliding distances.	[20]
147 Al alloy matrix composite containing the following: 1. 10% B4C 2. 15% B4C 3. 20% B4C 4. 4147 Al/SiC composite	Pin-on-disc	Due to stronger SiC particle binding to the alloy matrix, Al/SiC matrix alloys outperformed AL/B4C alloys in terms of wear resistance.	[21]
Aluminum syntactic foam	Pin-on-disc	The wear rate decreased as the sliding velocity increased. Despite its porous nature, this material showed strong wear resistance.	[22]
Untreated G3500 cast iron and S0050A cast steel Treated G4TG3500 cast iron and TS0050A cast steel	Pin-on-disc	Untreated and treated cast iron outperformed untreated cast steel in wear resistance. Both EPN-treated substrates outperformed untreated substrates in terms of wear resistance.	[23]
1. AA6061 alloy 2. AA6061 + 20 vol.% Saffil 3. AA6061 + 20 vol.% SiCp 4. AA6061 + 11 vol.% Saffil + 20% SiCp 5. AA6061 + 60 vol.% SiCp	Pin-on-disc test	Weight loss was found to decrease as the volume percent of the reinforcement was increased. Wear resistance was highest in the 60 percent SiCp composite.	[24]
1. PEEK 2. PEK 3. PEKK	1. Pin-on-disc test 2. Abrasion test on rubber wheels	A linear increment in wear volume was observed with sliding distance and sliding load increase.	[25]
1. Alloy 2014 2. Alloy 2024 3. Cast alloy 201 containing Al2O3 and SiC	Pin-on-disc	Wear resistance was higher in aluminum matrices with a high weight percent with no metallic component. SiC-containing alloys showed a substantial change.	[26]
1. Grey cast iron 2. A356/25SiCp aluminum metal matrix composite	Pin-on-disc	MMCs have a slightly lower wear rate than grey cast iron.	[27]
1. Al 2. Al + 10 SiC 3. Al + 20 SiC 4. Al + 30 SiC 5. Al + 40 SiC	Pin-on-disc	Resistance to wear for Al-SiC MMC is reported to be more significant than that to Al; with an increase in reinforcement volume, wear resistance reportedly increased.	[28]
Ti-6Al-4V alloy without thermal oxidation and Ti-6Al-4V alloy with thermal oxidation	Pin-on-disc	The handled specimen has shallower and thinner wear tracks than the untreated alloy.	[29]
1. Al-SiC-Gr composites 2. Al-SiC composites	Pin-on-disc	Al-SiC composites displayed lower resistance to wear than Al-SiC-Gr hybrid composites.	[30]
Commercially available pure Al and aluminum-scandium alloy	Pin-on-disc	The aluminum-scandium alloy outperformed the pure industrial alloy in terms of wear resistance.	[31]

Table 1: Continued.

Materials used	Tests performed	Results observed	Ref.
1. PEEK 2. 20 wt.% GF-PEEK 3. 30 wt.% GF-PEEK 4. 30 wt.% CF-PEEK	Pin-on-disc	According to the pin-on-ring sliding test, PEEK has a higher wear resistance than other thermoplastics. Carbon fibers outperformed glass fibers in terms of wear resistance.	[32]
Al-7Si alloy reinforced with the following: 1. 0 wt.% 2. 5 wt.% 3. 10 wt.% TiB2	Pin-on-disc	The wear rate decreased with an increase in TiB2 content in the alloy.	[33]
1. Mg-9Al 2. Mg-9Al with SiC-reinforced composite	Pin-on-disc	Due to high load-bearing capacity, the composite displayed significant wear resistance.	[34]
Brushes made of copper and graphite	Wear test with a pin-on-slip ring	Under 30 kPa BSP, arc erosion wear was the dominant wear process; abrasion wear was dominant above 120 kPa BSP.	[35]
18 polymers were examined	Pin-on-disc	PA 66-PTFE, POM-PTFE, PETP-PTFE, and PEEK-PTFE may be used in dry air. PA 66, PA 66-PTFE, and POM are the best materials for use in water.	[36]

Table 2: Comparison of materials with the block-on-ring wear test and the results observed.

Materials used	Tests performed	Results observed	Ref.
In one experiment, the NiCrBSi castellan PE 3309 alloy was flame sprayed onto prism-shaped grey cast iron, and in another, the alloy was laser remelted.	Block-on-ring test	The laser remelted coating wore out faster. The most common wear mechanism discovered is adhesion.	[42]
The substrate is grey cast iron, and the coating material is NiCrBSi alloy powder.	Block-on-ring test	Sliding speed had little to no effect on the wear rate as observed during the sliding test. Adhesive wear was observed at the highest loads.	[43]
Al coated with a polyetheretherketone (PEEK) composite and Al coated with a polyetheretherketone/SiC (PEEK/SiC) composite	Block-on-ring test	Compared to aluminum substrates, both polymer coatings showed a substantial improvement in wear resistance. In most sliding conditions, the addition of SiC to polymer coatings improved wear resistance even further.	[44]
WC-Co cemented carbides	Block-on-ring test	As the binder content of the WC-Co alloys increased, the wear rate caused by slipping increased.	[45]

Table 3: Comparison of materials with abrasive wear tests and the results observed.

Materials used	Tests performed	Results observed	Ref.
By compressing commercially available jute with the polypropylene thermoplastic matrix, composites were produced. Half of the composites were incorporated with maleic anhydride-grafted polypropylene, dissolved in toluene solution. The other half was left untreated.	Abrasion experiments were carried out using an SUGA abrasion tester.	Compared to the treated jute fiber, the untreated jute fiber showed more substantial volume loss.	[46]
1. Cold-formed steel, hot rolled 2. Wear-resistant steel with a low carbon content that has been hot rolled 3. Cold-rolled martensitic wear-resistant steel 4. Wear-resistant martensitic steel that has been tempered and quenched 5. Wear-resistant steel, bainitic, hot rolled	Impact/abrasion tester with impeller tumbler	The most weight was lost in hot-rolled cold-formed steel, then by tempered and quenched wear-resistant steel.	[47]
1. Commercially pure aluminum 2. Aluminum-magnesium alloys	1. Sliding wear tests 2. Abrasive wear tests	The Mg content in the matrix increased as metal-metal wear resistance and metal-abrasive wear resistance increased.	[48]
Grey cast iron plate	Abrasion test	Wear resistance is improved with hard-facing electrodes that contain more chromium and carbon.	[49]

Table 3: Continued.

Materials used	Tests performed	Results observed	Ref.
WC-Co powders used were as follows: 1. 17 wt.% Co and 83 wt.% WC 2. 15 wt.% Co and 85 wt.% WC	Abrasion test	Traditional powder-sprayed coating has a lower wear rate than HVOF-sprayed WC-Co coating.	[50]
Composites used were as follows: 1. Carbon/epoxy 2. Glass/epoxy 3. Aramid/epoxy 4. Aramid/polyetheretherketone 5. Carbon/polyetheretherketone	Abrasion test	A polyetheretherketone matrix is reinforced by oriented aramid and carbon fibers parallel to the surface. The composite was stated as a low-wear composite material.	[51]
Three plasma-sprayed coatings: 1. Al2O3 2. Al2O3-13% TiO2 3. Cr2O3 (with NiCoCrAlY bond coat) Two HVOF-sprayed cermet coatings: 1. WC-17% Co 2. WC-10% Co-4% Cr	1. Dry sliding experiments with a ball on a disc 2. Test on a dry sand-steel wheel	Plasma-sprayed ceramics displayed better results than HVOF coatings in dry particle abrasion conditions. The plasma-sprayed Cr2O3 and HVOF-coated ceramics displayed the best results in the pin-on-disc test.	[52]

Table 4: Comparison of materials with the corrosion wear test and the results observed.

Materials used	Tests performed	Results observed	Ref.
1. AISI 1045 steel with HVOF cermet coating 2. AISI 1045 steel with a hard chromium coating	Tribocorrosion tests	HVOF-coated materials outperformed hard chromium-coated steel in terms of wear resistance.	[37]

Table 5: Comparison of materials with other types of wear tests and the results observed.

Materials used	Tests performed	Results observed	Ref.
Epoxy resin Carbon nanotubes	Ball-on-prism tribometer	Wear resistance was improved when CNTs were combined with an EP matrix.	[38]
Cemented carbide tools	Disc turning test	The most prevalent wear mechanisms observed were built-up edge, adherent layer, and diffusion.	[39]
Nylon gears and acetal gears	Back-to-back test configuration	The wear characteristics of nylon gears vary significantly from those of acetal gears.	[40]
Ni-SiC composites	Ring-on-disc test	With the increase in the percentage of SiC, the wear resistance of the deposited layer increases.	[41]

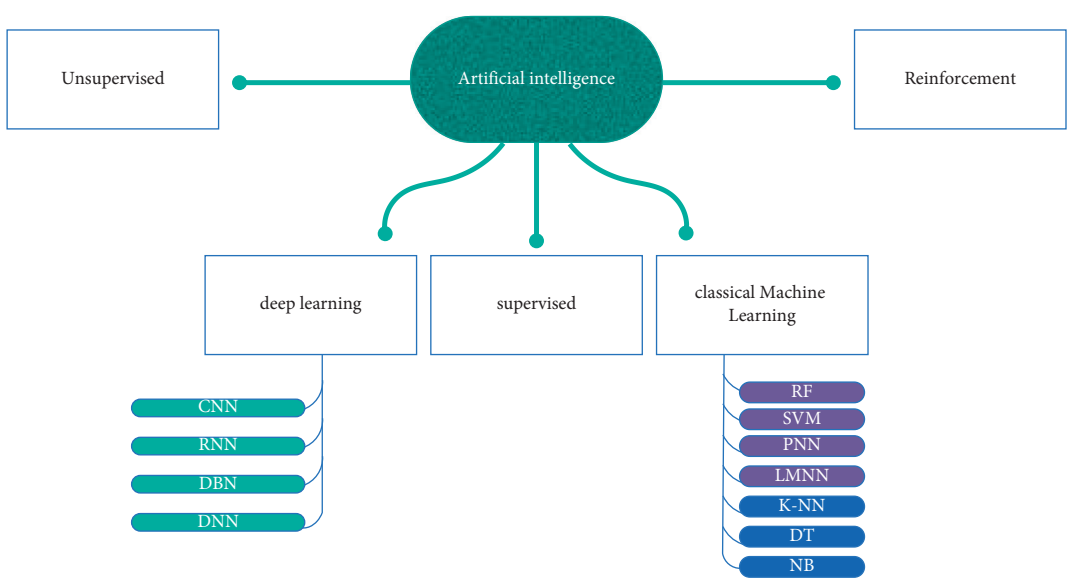

Figure 6: AI models: taxonomy.

Table 6: Algorithms used for evaluation of wear behavior in different metals.

Algorithm used	AI model taxonomy	Depth, layer sizes, training time, testing time	Dataset	Framework, core language, interface	Ref.
The backpropagation algorithm trains the weights of feedforward NNs consisting of multiple layers to predict the mass loss quantities of A390 aluminum alloy.	Supervised learning	An NN has a first layer containing three neurons and a second layer containing two neurons; overall, a two-hidden-layer network was used.	Data were normalized in the middle of [**0, 1**].	No data	[53]
An NN containing two hidden layers was used. The standard load, environment, and time are the three input variables. The amount of wear loss and microhardness are the two output variables. The LMA was used to train the ANN along with BP.	Supervised learning method: BP	Three layers, 3-2-2 topology	No data	No data	[54]
trainlm (network training function) was used to train a multilayer ANN. Two outputs were recorded. The LMA was applicable in adjusting the biases and weights.	Feedforward NN with BP	The ANN with three inputs and two hidden layers has the first layer containing 20 and 30 neurons. The data used for training were 70% and 15% each for validation and testing.	No data	MATLAB 2016a for the ANN Minitab 16 for visualizing the linear regression model	[55]
The NNs were diversified and tested to discover the most acceptable results possible. Thrust, cutting speed, and force were the inputs, and tool wear was the output. In contrast, the second is for predicting the surface roughness.	Feedforward NN using BP	NN topologies 3-5-1 and 3-4-1 were tested for tool wear, and 4-6-1 and 4-6-4-1 were tested for predicting surface roughness.	Laboratoire Génie de Production, ENIT Tarbes, France	No data	[56]
SVR (support vector regression) was applied to solve the regression problem, and here the least square error is also used; therefore, it is known as LSSVM.	LSSVM	The kernel chosen was the radial basis function.	No data	MATLAB 2013	[57]
A model having a three-layer Taguchi coupled ANN was proposed. The input nodes were sliding distance, load, sliding velocity, and weight percentage. The hidden layer had seven neurons, whereas the output layer had a single neuron. The LMA was used to train this model.	Supervised learning	3-7-1 architecture ANN	No data	MATLAB 2013	[58]
The network consists of three layers and four PCA-declared input nodes, whereas the hidden layer has three nodes, and the output layer having a single node was best out of all the networks. The first two layers used the neural transfer function tansig, whereas the last layer used purelin.	Supervised learning	4-3-1 architecture with the three-layer feedforward ANN	No data	A commercial Neural Network Toolbox	[59]

Table 6: Continued.

Algorithm used	AI model taxonomy	Depth, layer sizes, training time, testing time	Dataset	Framework, core language, interface	Ref.
Adaptive neuro-fuzzy inference system combines the "Takagi–Sugeno fuzzy inference system" and the principles of ANN.	Supervised learning	Five layers in ANFIS	No data	MATLAB	[60]
Taguchi technique has been used here. A weight-loss model to make predictions was made using regression. Nonlinear regression was used to correlate control factors and weight loss.	Supervised learning	No data	No data	Minitab 15.1	[61]
The AI algorithms used here are random forests, regression trees, MLP, and RBF.	Supervised learning: MLP, RBF, and random forests	RBF has one layer, and MLP has one hidden layer.	The experimental data were collected to provide a broad number of wear conditions and processing times while acquiring data on the power drive for a fixed machining process—the face milling of carbon-quality structural steel 45.	No data	[62]
"Kohonen's self-organizing map" was used to evaluate the tool's working status. Also, a triangular membership function applied neuro-fuzzy and fuzzy logic. The "centroid method of defuzzification" was used to obtain the flank wear.	Supervised learning: backpropagation NN	2-3-1 architecture	The training data for the networks were collected through experimental studies.	No data	[63]
One neuron represents each input parameter distinctively related to the coefficient of friction. The input variables include applied load, sliding velocity, sliding distance, and material type, whereas the output is the coefficient of friction. It has 4-6-4-1 architecture. An MLP model was applied here because of its feedforward nature.	Supervised learning: MLP	4-6-4-1 architecture	No data	No data	[64]
For evaluating the tool wear, a developed configuration system was applied. Also, using an expert system at different wear states helped clarify the output values of ANN.	Unsupervised learning: ART2	Number of input neurons in SOM: 15, and number of neurons in an SOM layer: 36	No data	No data	[65]
The network used in this study was a generalized feedforward network. Input parameters were sliding time, sliding speed, load, and Al-Si%, whereas the output parameter was specific wear rate. The network consisted of three hidden layers with 16, 8, and 5 neurons. The first two layers used the TanhAxon function, whereas the last layer applied the BiasAxon function.	Supervised learning	4-11-5-1 architecture and two hidden layers with four inputs and one output layer were applied.	No data	No data	[66]

Table 6: Continued.

Algorithm used	AI model taxonomy	Depth, layer sizes, training time, testing time	Dataset	Framework, core language, interface	Ref.
The LMA along with BP was applied in this study. Load and speed are the two nodes of the input layer, whereas the friction and mass loss coefficient are the two nodes of the output layer. The minimal fault was observed in the output due to ten neurons in the hidden layer.	Supervised learning	Two output and ten hidden neurons	No data	MATLAB	[67]
The proposed reduction model here is a combination of POD and RBF.	Supervised learning	The network consists of two layers, one with RBF neurons and the other with output neurons.	No data	MATLAB	[68]
The ANN was trained with the Levenberg–Marquardt algorithm (LMA), Bayesian regulation (BR), resilient backpropagation (RP), scaled conjugate gradient (SCG), and gradient descent (GD).	Supervised learning	Five distinct training algorithms were used, along with eighteen different architectures. The Bayesian algorithm trained in a two-layered neural network has reached the best results (26 10 5 1).	Training data were obtained by 360 randomly distributed data collected from testing of four friction materials. Training data were acquired by testing eight different friction materials, only predicting fade performance.	No data	[69]
The ANN and Sugeno FIS have been applied, and BP having 4-3-1 architecture and LMA is adopted here.	Supervised learning: backpropagation	The network has 4-3-1 architecture and one hidden layer.	No data	MATLAB R2015a using NN Toolbox	[70]
FZM and ANN, along with a neuro-fuzzy ANFIS, are adopted here.	Supervised learning: backpropagation for ANN Unsupervised learning for fuzzy c-means clustering	The ANN having 4-3-1 architecture and ninety-cluster C-mean clustering gave the best performance.	No data	No data	[71]
The Elman-inspired RNN was applied. The sensor uses the relationship between the variables to be measured and the power consumption.	Bayesian regularization	The best model HU55 implies five hidden units and a delay of 5.	A Training and Test Data Set (TTDS) is generated with a specific combination of the grinding experiments collected.	MATLAB	[72]
RF, MLP, RBF, etc., were used in this study to predict surface roughness and mass loss.	Supervised learning: regression trees, MLP BP	A network having a three-layer architecture and a hidden layer consisting of RBF was used.	No data	No data	[73]
Output, i.e., tool wear, is predicted with the help of residual errors as the basis of decision-making.	Supervised learning: MLP	MLP has 6-12-1 architecture, and one hidden layer was used here.	No data	MATLAB	[74]
Volume loss is predicted using LR, SVM, ANN, and other extreme learning methods.	Supervised learning: ANN, SVR, and LR	The ANN has a 3-4-1 architecture and a quadratic function as the SVR kernel, whereas ELM used here is a feedforward NN having a single hidden layer.	Experimentally obtained data	MATLAB	[75]

Table 6: Continued.

Algorithm used	AI model taxonomy	Depth, layer sizes, training time, testing time	Dataset	Framework, core language, interface	Ref.
Supervised learning methods such as SVR, RF regression, decision tree regression, GBR, GPR, MLP, and KNN are used.	Supervised learning	SVR uses an RBF for the kernel. MLP having five hidden layers and ten neurons in each layer with ReLU activation was used here.	Collected from 13 references of 316L SS parts processed by SLM	Python TensorFlow, scikit-learn, Google Colab	[76]
The ANN with BP is applied along with ANOVA to decide the potential parameters to predict the specific wear rate reduction.	Supervised learning	The ANN has the 2 : 5:1 architecture with sigmoid activation.	No data	Python, Minitab 19	[77]
Analysis of the erosion process is done using the ANN model along with LMA.	Supervised learning	The network having three layers and 2-6-3 architecture is used here.	No data	MATLAB 2017a Neural Network Toolbox	[78]
ANN and RSM models were compared based on their predictive capacity of wear behavior of fabricated composites.	Supervised learning	Three inputs, ten hidden layers, and two outputs	No data	MATLAB	[79]

Table 7: Advantages and disadvantages of the above-discussed algorithms (Table 6) used to evaluate wear behavior in different metals.

Advantages	Disadvantages	Ref.
NNs are quite endurable as the parameter (weight) values are changed according to the performance. The modifications are made according to an ML algorithm called gradient descent (GD).	Other algorithms like SVM in [56] could be implemented and compared for better performance and results. For example, the LMA (Levenberg–Marquardt algorithm) could improve the model instead of GD.	[53]
The model was concluded to be excellent and fast because of the little prediction time, and the results of the ANN model, along with the experimental study, indicated the same. Also, the LMA was faster than GD or GN.	The LMA gives us only the local optimum instead of the global optimum. Because the derivatives of the flat functions do not exist after a certain point in time, the algorithm might be a failure.	[54]
The experiment helped perceive the most influential factors affecting the friction coefficient and the wear rate. Therefore, the ANN is very much capable of predicting the same.	The LMA might not be a potential choice if the beginning point does not have the right quality, i.e., distant from the actual required values.	[55]
NNs can take in linear and nonlinear relationships, generating and performing well to show good results.	Sigmoid (the activation function) was not zero-centered that could give undesired results and implications during the implementation of GD. An alternative for it could be tanh, and where priority is speed, ReLU would be suitable.	[56]
LSSVM could eliminate local minima. Also, comparing the relative error of RSM and LSSVM, the graph depicts LSSVM as a suitable model since it has fewer relative errors.	SVM underperforms if the number of characteristics for a data point exceeds the number of training data samples. Therefore, a considerable amount of data are required to be enforced.	[57]
To obtain an optimal value of the input parameter and achieve an output value with the minor target, Taguchi coupled ANN was applied.	The effects of a parameter on the resultant value were not precise. Also, the method did not provide any absolute results; therefore, it was stated unsuitable for a constantly changing process.	[58]
The ANN was better than a statistical approach since it has three times lower relative mean error and higher stability for all studied conditions.	A model without units makes the equations incomprehensible physically; therefore, it is necessary to include units to make sense in the world.	[59]
The aim behind ANFIS is to connect inputs and outputs accurately. It could help set up a model with uncertainties and composite data distribution.	The limitations of ANFIS are the computational expense, and it is hard to compute large input values. Therefore, it cannot be used in a big data paradigm.	[60]
To determine parameters having minimum variations, Taguchi methods were helpful. Also, ANOVA was used to check the quality of features affected by design parameters.	The effects of a parameter on the resultant value were not precise. Also, the method did not provide any absolute results; therefore, it was stated unsuitable for a constantly changing process.	[61]
RF showed the highest precision. Due to its ability to get tuned and give visual information, RF can be directly used by product engineers.	The RF creates many trees and needs a lot of computational power and colossal training time. Overfitting of noisy data may lead to unfavorable outputs.	[62]
To improve user-friendliness, linguistic rules were applied. Also, for fuzzy logic, they act as an advantage.	To achieve a stable mapping with the help of Kohonen's SOM, the nearby data point needs to behave similarly.	[63]

Table 7: Continued.

Advantages	Disadvantages	Ref.
The ANN aids in estimating the coefficient of friction for parameter values more significant than those included in POD experiments.	Increasing the total number of parameters in an MLP might lead to more time. It is inefficient as such high dimensions might be redundant.	[64]
An ANN and expert systems were used to find the worn-out tools. A blend of inference results and complex sensor outputs helped achieve a positive result.	Expert systems collapse without a proper output from the ANN; therefore, they will face issues classifying the tool's wear.	[65]
GFs usually take in more compound, nonlinear, and unpredictable relationships since their connections can skip several layers.	A network of this kind could overfit due to its inability to deduce the latest data when applied to simple tasks.	[66]
ANN's characteristics like adaptability and fault tolerance are beneficial here.	The beginning point is far off the desired value; the LMA might not perform well here.	[67]
The unknown parameters can be found through this technique if the outputs are already known.	Massive space for inputs is required when using RBF though it is not favorable to waste inputs while having other essential tasks.	[68]
Less period is required for training the Bayes, and its application is effortless.	The nature of the attributes is presumed to be mutually independent in the Bayesian algorithm, but that seems impossible as the predictors cannot be fully independent.	[69]
Results were in order with the experimental values; therefore, the neuro-fuzzy approach is good.	Sugeno FIS provided no output membership function, and chances of loss of interpretability are high.	[70]
A framework based on the Takagi–Sugeno neuro-fuzzy network has proven to be the best of both worlds.	Massive inputs and computational expenses are some of the limitations of ANFIS. Therefore, it is not applicable for a "big data paradigm."	[71]
The RNN can mimic the dynamic nature of the problem here as the old network values are reused, in turn, giving the ANN memory.	There can be problems with the gradient not converging. It is a complex task while working with tanh or ReLU activation functions.	[72]
RF is concluded to be best for industry purposes as no parameter tuning was required for it. Also, its predictions are equally good as MLPs.	The RF creates several trees; therefore, it requires more computational power and more training time. Chances of noisy overfitting data having unfavorable outputs as results are there.	[73]
This model practices a high-powered working nature, whereas a supervision system cannot.	A neuro-FIS might be applicable in such a dynamic environment.	[74]
An R2 error value of 0.989 was obtained using the ELM method, and a reduced number of tests, testing time, and cost were also observed here.	More training cases could lead to the loss of the essence of the problem as the ELM consists of only one hidden layer. This was not observed here since the number of cases is only 40.	[75]
GBR was concluded as the best out of the seven ML algorithms compared here since it resulted in the slightest standard deviation and good accuracy.	KNN, STR, and GPR will not be recommended as they are considered the worst-performing algorithms here.	[76]
Minimum error artificial data were generated for processing, and the method used here is flexible and considered best for evaluating the tribo-parameters.	The work is limited to the general behavior of distinct reinforcement particles due to the variable metallurgical properties.	[77]
The ANN investigated the impact on the APS process parameters well.	Future work includes the optimum coating properties dependent on the APS process parameters.	[78]
A regression coefficient value of 0.99996 using the ANN was the best of all the other proposed models.	Different algorithms could be used for training the ANN along with GBR and SVR, and it can be used to compare the results.	[79]

(1) ANNs typically have three main layers. Input layer: The layer to which input data and patterns are fed is always a single input layer.

(2) Hidden layers: There could be several of these layers. Behind the scenes, processing occurs, and the output is calculated based on "weights," which determine the significance of a specific characteristic. These layers also remove inessential data from the input data before sending them to the hidden layer, next in line for processing.

(3) The endmost hidden layer is linked to the output layer, which provides the final output value(s).

The center of NNs is backpropagation. It is an algorithm through which the neural network corrects itself with each iteration that relies on weights.

6. Summary and Conclusions

The research works discussed briefly in this review propose various systems for supervising the machining process, tool wear monitoring, determination of wear state for a tool, and many more. Significant research has been done involving ANNs with the LVM (as shown in Tables 6 and 7) algorithm training the models, resulting in highly generalized and fault-tolerant models; however, LVM can only provide a local optimum and may not respond to flat functions, producing unwanted results, and the starting point is way far from the optimal.

Some studies consider the ANFIS, adaptive neuro-fuzzy interface system, method that combines ANN and fluidic logic, specifically the "Takagi–Sugeno fuzzy interference system," which can capture neural networks fumigating logic

in one. However, this model may not perform well for many inputs, i.e., this model fails in a big data paradigm. The surface roughness and wear were predicted using RNNs, i.e., ANNs having memory; hence, they are more suitable for a constantly developing environment of such wear behavior of tools. Surface wear was detected using random forests and multilayer perceptrons based on surface isotropy levels. Random forests are superior because MLPs require parameter tuning, and their output is nearly identical to that of RFs. These methods for various processes are also discussed in some research that encompasses most of the approaches [80–92].

6.1. Accuracies Achieved in Recent Research Works. Using a two-hidden-layer neural network, Kumar and Singh [53] obtained a normalized standard error of 0.00085. At the same time, Çetinel et al. [54], who also used a two-hidden-layer network but with the addition of the Levenberg–Marquardt algorithm, found an average error of 2.461% for wear (in micrometers) and 0.245% error for microhardness (in HV). A least square support vector machine to predict wear behavior in [56] yielded an average of 1.2 percent better results on 52 runs than the RSM model. Kolodziejczyk [58] used PCA preprocessing and the LVM algorithm to achieve a mean relative error of 1.8 percent, three times lower than that in previous studies. A multilayer perceptron model was used in [64], which yielded 0.0186 and 0.0180 training and testing residual errors, respectively. The SOM model had a higher correlation coefficient than the ART2 model in [65], with 0.964 and 0.946 for the training and test sets. The ANN was combined with the Taguchi method in [55], and a 99.5 percent confidence level was observed between predicted and actual wear rates and coefficients of friction. In [93], the ANN with one hidden layer had a more significant sum of squares error (SSE) of 0.025 and 0.25 for training and testing, respectively, whereas the ANN with two hidden layers had 0.008 and 0.46 SSEs for training and testing. As a result of the lower SSE, the two-hidden-layer networks were chosen, with an RMSE of 2.64 percent on average. The ANFIS models—sigmoidal, triangular, Gaussian, and bell-shaped MFs—were used [59]. The most accurate model was sigmoidal MF, which had a regression coefficient of 0.96775. RFs and MLPs were used in [62], with RFs having a better accuracy of 33 to 44 percent and an error of 0.2457 micrometers than the MLP's 0.4139. An ANFIS was used for various membership functions [70]. The RMSE was in the order of E-11, which was 0.557 for the ANN. The Sugeno-type ANFIS model had the best correlation coefficient of 97.74 percent with gbellmf membership. Nagaraj and Gopalakrishnan [66] reported an MSE of 0.0904 and an MAE of 0.1257. In [73], various ML techniques model various parameters, with MLPs better in 3/4 of them and RFs taking one of the parameters. MLPs were found to have a 52 percent accuracy rate. The ANFISs appear to have the least amount of error.

6.2. Open Issues. Multiple systems have been proposed in recent research to address the supervision process in machining, tool wear monitoring, tool wear detection, and so on. More researchers use ANNs with the LVM algorithm to train fault-tolerant and well-generalized models, but the LVM only provides a local optimum and may not work for flat functions. If the starting point is too far from the optimal, it may also produce undesirable results. The ANFIS, adaptive neuro-fuzzy interface system, is a combination of ANN and fuzzy logic used in a few papers, specifically the Takagi–Sugeno fuzzy interference system, which can capture the essence of both neural nets and fuzzy logic in one [94–102]. However, this model may not work well for many inputs, i.e., this model fails in a big data paradigm. RNNs, which are technically ANNs with memory and thus more suited for such ever-changing dynamic environments as tool wear, were also used to predict wear and surface roughness [103–106]. Surface wear was also predicted using random forests and multilayer perceptrons and surface isotropy levels. MLPs require parameter tuning, and their output is nearly identical to that of RFs, so random forests are preferable. These various processes are also discussed in [107], which encompasses most approaches.

6.3. Future Directions. Wear analysis using artificial intelligence is a relatively new concept. Formal result: Accordingly, it was discovered that there is less work on AI than aluminum (e.g., FGP grey-coated or NiCrBSi-coated aluminum) writable composites (e.g., polymer-reinforced glass), which indicates that it is to be expected since less work has been done on AI (e.g., plastic/FGP-NiCr alloyed glass) to grasp fully [80, 108].Further study is required to understand the full capabilities of using AI. This state-of-the-art technology for analyzing artificial neural networks is now being utilized for efficient and economical wear-resistant materials. Tool wear is one of the most common aspects of the machining process that needs to be analyzed. Research can be done on the tool metal's wear behavior in the future, and the metal can be modified and tested for wear. New research opportunities can be found to find an ideal metal for machining processes. Artificial neural networks for wear analysis can help identify the most efficient coating materials for various substrates to increase the substrate's wear resistance with accurate predictions, which is inefficient and time-consuming when identified using traditional methods. Artificial intelligence is currently limited to analyzing wear for various materials used in manufacturing and production. Still, the main benefit of using AI is studying a wide range of data and making accurate predictions. More experimentation is needed to make the most of this technology, which will allow industries to predict the time and type of wear that will occur on a material ahead of time, allowing them to continue operating without interruption [108–114].

Abbreviation

ANN: Artificial neural network
NN: Neural network
ML: Machine learning
GD: Gradient descent
LMA: Levenberg–Marquardt algorithm

BP: Backpropagation
GN: Gaussian network
SVR: Support vector regression
LSSVM: Least square support vector machine
RSM: Response surface methodology
RBF: Radial basis function
MLP: Multilayer perceptron
SOM: Self-organizing map
GF: Generalized feedforward
POD: Proper orthogonal decomposition
BR: Bayesian regulation
RP: Resilient backpropagation
SCG: Scaled conjugate gradient
FIS: Fuzzy inference system
FZM: Fuzzy clustering method
LR: Linear regression
ELM: Extreme learning method
RF: Random forest
GBR: Gradient boosting regression
GPR: Gaussian process regression.

Conflicts of Interest

The authors declare no conflicts of interest.

Authors' Contributions

Senthil Kumaran Selvaraj and Aditya Raj have Contributed Equally AR and SKS conceptualized the research idea and ran the software. SKS performed the methodology, validated the data, and administered the project. AR, MD, UC, IS, and CK were involved in formal analysis and wrote the original draft. AR, MD, and UC investigated the data and obtained the resources. AR, MD, UC, and IS curated the data. UC and CK visualized the data and reviewed and edited the paper. SKS and UC supervised the study. All the authors have read and agreed to the published version of the manuscript.

References

[1] "Standard terminology relating to wear and erosion," *Annual Book of Standards*, vol. 03.02, pp. 243–250, 1987.
[2] G. W. Stachowiak and A. W. Batchelor, *Engineering Tribology*, Elsevier Applied Science, Amsterdam, Netherland, 2014.
[3] F. Kara, M. Karabatak, M. Ayyıldız, and E. Nas, "Effect of machinability, microstructure and hardness of deep cryogenic treatment in hard turning of AISI D2 steel with ceramic cutting," *Journal of Materials Research and Technology*, vol. 9, no. 1, pp. 969–983, 2020.
[4] R. M. C. Karthik, R. L. Malghan, F. Kara, A. Shettigar, S. S. Rao, and M. A. Herbert, "Influence of support vector regression (SVR) on cryogenic face milling," *Advances in Materials Science and Engineering*, vol. 2021, Article ID 9984369, 18 pages, 2021.
[5] A. Eser, E. A. Ayyıldız, M. Ayyıldız, and F. Kara, "Artificial intelligence-based surface roughness estimation modelling for milling of AA6061 alloy," *Advances in Materials Science and Engineering*, vol. 2021, Article ID 5576600, 10 pages, 2021.
[6] P. Ganeshan, S. S. Kumaran, K. Raja, and D. Venkateswarlu, "An investigation of mechanical properties of madar fiber reinforced polyester composites for various fiber length and fiber content," *Materials Research Express*, vol. 6, 2019.
[7] S. Kannan, S. S. Kumaran, and L. A. Kumaraswamidhas, "Optimization of friction welding by taguchi and ANOVA method on commercial aluminium tube to Al 2025 tube plate with backing block using an external tool," *Journal of Mechanical Science and Technology*, vol. 30, pp. 2225–2235, 2016.
[8] S. K. Senthil, S. Muthukumaran, and C. R. Chandrasekhar, "Effect of tube preparations on joint strength in friction welding of tube-to-tube plate using an external tool process," *Experimental Techniques*, vol. 37, pp. 24–32, 2013.
[9] V. V. Kumar and S. S. Kumaran, "Friction material composite: types of brake friction material formulations and effects of various ingredients on brake performance-a review," *Materials Research Express*, vol. 6, 2019.
[10] S. K. Senthil, S. Muthukumaran, D. Venkateswarlu, G. K. Balaji, and S. Vinodh, "Eco-friendly aspects associated with friction welding of tube-to-tube plate using an external tool process," *Int J Sustain Eng*, vol. 5, pp. 120–127, 2012.
[11] S. K. Senthil and A. D. Daniel, "Friction welding joints of SA 213 tube to SA 387 tube plate boiler grade materials by using clearance and interference fit method," *Materials Today Proceedings*, vol. 5, pp. 8557–8566, 2018.
[12] H. Unal, A. Mimaroglu, U. Kadıoglu, and H. Ekiz, "Sliding friction and wear behaviour of polytetrafluoroethylene and its composites under dry conditions," *Materials & Design*, vol. 25, no. 3, pp. 239–245, 2004.
[13] H. Pıhtılı and N. Tosun, "Effect of load and speed on the wear behavior of woven glass fabrics and aramid fiber-reinforced composites," *Wear*, vol. 252, no. 11-12, pp. 979–984, 2002.
[14] G. Bregliozzi, A. Di Schino, S. U. Ahmed, J. M. Kenny, and H. Haefke, "Cavitation wear behavior of austenitic stainless steels with different grain sizes," *Wear*, vol. 258, no. 1-4, pp. 503–510, 2005.
[15] J. Zheng, Z. R. Zhou, J. Zhang, H. Li, and H. Y. Yu, "On the friction and wear behavior of human tooth enamel and dentin," *Wear*, vol. 255, no. 7-12, pp. 967–974, 2003.
[16] Y. Şahin, "Abrasive wear behavior of SiC/2014 aluminium composite," *Tribology International*, vol. 43, no. 5-6, pp. 939–943, 2010.
[17] N. N. Aung, W. Zhou, and L. E. Lim, "Wear behavior of AZ91D alloy at low sliding speeds," *Wear*, vol. 265, no. 5-6, pp. 780–786, 2008.
[18] A. R. Breeds, S. N. Kukureka, K. Mao, D. Walton, and C. J. Hooke, "Wear behaviour of acetal gear pairs," *Wear*, vol. 166, no. 1, pp. 85–91, 1993.
[19] O. P. Modi, B. K. Prasad, A. H. Yegneswaran, and M. L. Vaidya, "Dry sliding wear behaviour of squeeze cast aluminium alloy-silicon carbide composites," *Materials Science and Engineering: A*, vol. 151, no. 2, pp. 235–245, 1992.
[20] H. Unal, U. Sen, and A. Mimaroglu, "Abrasive wear behaviour of polymeric materials," *Materials & Design*, vol. 26, no. 8, pp. 705–710, 2005.
[21] R. Ipek, "Adhesive wear behaviour of B4C and SiC reinforced 4147 Al matrix composites (Al/B4C-Al/SiC)," *Journal of Materials Processing Technology*, vol. 162-163, pp. 71–75, 2005.
[22] D. P. Mondal, S. Das, and N. Jha, "Dry sliding wear behaviour of aluminum syntactic foam," *Materials & Design*, vol. 30, no. 7, pp. 2563–2568, 2009.
[23] X. Nie, L. Wang, Z. C. Yao, L. Zhang, and F. Cheng, "Sliding wear behavior of electrolytic plasma nitrided cast iron and steel," *Surface and Coatings Technology*, vol. 200, no. 5-6, pp. 1745–1750, 2005.

[24] A. B. Gurcan and T. N. Baker, "Wear behavior of AA6061 aluminium alloy and its composites," *Wear*, vol. 188, no. 1-2, pp. 185–191, 1995.
[25] A. P. Harsha and U. S. Tewari, "Two-body and three-body abrasive wear behaviour of polyaryletherketone composites," *Polymer Testing*, vol. 22, no. 4, pp. 403–418, 2003.
[26] F. M. Hosking, F. F. Portillo, R. Wunderlin, and R. Mehrabian, "Composites of aluminium alloys: fabrication and wear behaviour," *Journal of Materials Science*, vol. 17, no. 2, pp. 477–498, 1982.
[27] N. Natarajan, S. Vijayarangan, and I. Rajendran, "Wear behavior of A356/25SiCp aluminium matrix composites sliding against automobile friction material," *Wear*, vol. 261, no. 7-8, pp. 812–822, 2006.
[28] B. Venkataraman and G. Sundararajan, "The sliding wear behaviour of AlSiC particulate composites-I. Macro-behaviour," *Acta Materialia*, vol. 44, no. 2, pp. 451–460, 1996.
[29] H. Güleryüz and H. Çimenoğlu, "Effect of thermal oxidation on corrosion and corrosion–wear behavior of a Ti–6Al–4V alloy," *Biomaterials*, vol. 25, no. 16, pp. 3325–3333, 2004.
[30] S. Suresha and B. K. Sridhara, "Effect of addition of graphite particulates on the wear behaviour in aluminium-silicon carbide-graphite composites," *Materials & Design*, vol. 31, no. 4, pp. 1804–1812, 2010.
[31] K. Venkateswarlu, L. C. Pathak, A. K. Ray et al., "Microstructure, tensile strength and wear behaviour of Al-Sc alloy," *Materials Science and Engineering: A*, vol. 383, no. 2, pp. 374–380, 2004.
[32] H. Voss and K. Friedrich, "On the wear behaviour of short-fibre-reinforced peek composites," *Wear*, vol. 116, no. 1, pp. 1–18, 1987.
[33] S. Kumar, M. Chakraborty, V. S. Sarma, and B. S. Murty, "Tensile and wear behavior of in situ Al–7Si/TiB2 particulate composites," *Wear*, vol. 265, no. 1-2, pp. 134–142, 2008.
[34] C. Y. H. Lim, S. C. Lim, and M. Gupta, "Wear behavior of SiCp-reinforced magnesium matrix composites," *Wear*, vol. 255, no. 1-6, pp. 629–637, 2003.
[35] I. Yasar, A. Canakci, and F. Arslan, "The effect of brush spring pressure on the wear behaviour of copper-graphite brushes with electrical current," *Tribology International*, vol. 40, no. 9, pp. 1381–1386, 2007.
[36] J. W. M. Mens and A. W. J. D. Gee, "Friction and wear behavior of 18 polymers in contact with steel in environments of air and water," *Wear*, vol. 149, no. 1-2, pp. 255–268, 1991.
[37] L. Fedrizzi, S. Rossi, R. Cristel, and P. L. Bonora, "Corrosion and wear behavior of HVOF cermet coatings used to replace hard chromium," *Electrochimica Acta*, vol. 49, no. 17-18, pp. 2803–2814, 2004.
[38] O. Jacobs, W. Xu, B. Schädel, and W. Wu, "Wear behaviour of carbon nanotube reinforced epoxy resin composites," *Tribology Letters*, vol. 23, no. 1, pp. 65–75, 2006.
[39] G. List, M. Nouari, D. Géhin et al., "Wear behavior of cemented carbide tools in dry machining of aluminium alloy," *Wear*, vol. 259, no. 7-12, pp. 1177–1189, 2005.
[40] K. Mao, W. Li, C. J. Hooke, and D. Walton, "Friction and wear behavior of acetal and nylon gears," *Wear*, vol. 267, no. 1-4, pp. 639–645, 2009.
[41] K. H. Hou, M. D. Ger, L. M. Wang, and S. T. Ke, "The wear behavior of electro-codeposited Ni–SiC composites," *Wear*, vol. 253, no. 9-10, pp. 994–1003, 2002.
[42] R. Gonzalez, M. Cadenas, R. Fernandez, J. L. Cortizo, and E. Rodríguez, "Wear behavior of flame sprayed NiCrBSi coating remelted by flame or by laser," *Wear*, vol. 262, no. 3-4, pp. 301–307, 2007.
[43] E. Fernández, M. Cadenas, R. González, C. Navas, R. Fernández, and J. D. Damborenea, "Wear behavior of laser clad NiCrBSi coating," *Wear*, vol. 259, no. 7-12, pp. 870–875, 2005.
[44] G. Zhang, H. Liao, H. Li, C. Mateus, J.-M. Bordes, and C. Coddet, "On dry sliding friction and wear behaviour of PEEK and PEEK/SiC-composite coatings," *Wear*, vol. 260, no. 6, pp. 594–600, 2006.
[45] J. Pirso, S. Letunovitš, and M. Viljus, "Friction and wear behavior of cemented carbides," *Wear*, vol. 257, no. 3-4, pp. 257–265, 2004.
[46] N. Chand and U. K. Dwivedi, "Effect of coupling agent on abrasive wear behaviour of chopped jute fibre-reinforced polypropylene composites," *Wear*, vol. 261, no. 10, pp. 1057–1063, 2006.
[47] A. Sundström, J. Rendón, and M. Olsson, "Wear behavior of some low alloyed steels under combined impact/abrasion contact conditions," *Wear*, vol. 250, no. 1-12, pp. 744–754, 2001.
[48] A. Hayrettin, K. Tolga, C. Ercan, and C. Huseyin, "Wear behavior of Al/(Al2O3p/SiCp) hybrid composites," *Tribology International*, vol. 39, pp. 213–220, 2006.
[49] S. Chatterjee and T. K. Pal, "Wear behavior of hardfacing deposits on cast iron," *Wear*, vol. 255, no. 1-6, pp. 417–425, 2003.
[50] D. A. Stewart, P. H. Shipway, and D. G. McCartney, "Abrasive wear behaviour of conventional and nano-composite HVOF-sprayed WC-Co coatings," *Wear*, vol. 225-229, pp. 789–798, 1999.
[51] M. Cirino, R. B. Pipes, and K. Friedrich, "The abrasive wear behaviour of continuous fibre polymer composites," *Journal of Materials Science*, vol. 22, no. 7, pp. 2481–2492, 1987.
[52] G. Bolelli, V. Cannillo, L. Lusvarghi, and T. Manfredini, "Wear behavior of thermally sprayed ceramic oxide coatings," *Wear*, vol. 261, no. 11-12, pp. 1298–1315, 2006.
[53] A. Kumar and D. Singh, "Artificial neural network-based wear loss prediction for A390 aluminium alloy," *Journal of Theoretical and Applied Information Technology*, vol. 4, no. 10, 2008.
[54] H. Çetinel, H. Öztürk, E. Çelik, and B. Karlık, "Artificial neural network-based prediction technique for wear loss quantities in Mo coatings," *Wear*, vol. 261, no. 10, pp. 1064–1068, 2006.
[55] B. Stojanović, A. Vencl, I. Bobić, S. Miladinović, and J. Skerlić, "Experimental optimisation of the tribological behaviour of Al/SiC/Gr hybrid composites based on Taguchi's method and artificial neural network," *Journal of the Brazilian Society of Mechanical Sciences and Engineering*, vol. 40, no. 6, 2018.
[56] S. B. Mishra, R. Pattnaik, and S. S. Mahapatra, "Parametric analysis of wear behaviour on fused deposition modelling build parts," *International Journal of Productivity and Quality Management*, vol. 21, no. 3, pp. 375–391, 2017.
[57] V. Kavimani and K. S. Prakash, "Tribological behaviour predictions of r-GO reinforced Mg composite using ANN coupled Taguchi approach," *Journal of Physics and Chemistry of Solids*, vol. 110, pp. 409–419, 2017.
[58] T. Kolodziejczyk, R. Toscano, S. Fouvry, and G. E. Morales, "Artificial intelligence as efficient technique for ball bearing fretting wear damage prediction," *Wear*, vol. 268, no. 1-2, pp. 309–315, 2010.
[59] M. Marani, M. Zeinali, J. Kouam, V. Songmene, and C. K. Mechefske, "Prediction of cutting tool wear during a turning process using artificial intelligence techniques,"

International Journal of Advanced Manufacturing Technology, vol. 111, no. 1-2, pp. 505–515, 2020.

[60] L. Monostori, "AI and machine learning techniques for managing complexity, changes and uncertainties in manufacturing," *Engineering Applications of Artificial Intelligence*, vol. 16, no. 4, pp. 277–291, 2003.

[61] P. Padmanabhan, A. Arulbrittoraj, R. Srinivasan, and G. Ebenezer, "Study the influence of case hardening and sliding wear parameters on carburised AISI 1211 steel," *International Journal of Surface Science and Engineering*, vol. 10, no. 5, p. 415, 2016.

[62] D. Y. Pimenov, A. Bustillo, and T. Mikolajczyk, "Artificial intelligence for automatic prediction of required surface roughness by monitoring wear on face mill teeth," *Journal of Intelligent Manufacturing*, vol. 29, no. 5, pp. 1045–1061, 2017.

[63] C. S. Rao and R. R. Srikant, "Tool wear monitoring-an intelligent approach," *Proceedings of the Institution of Mechanical Engineers - Part B: Journal of Engineering Manufacture*, vol. 218, no. 8, pp. 905–912, 2004.

[64] T. Sahraoui, S. Guessasma, N. E. Fenineche, G. Montavon, and C. Coddet, "Friction and wear behaviour prediction of HVOF coatings and electroplated hard chromium using neural computation," *Materials Letters*, vol. 58, no. 5, pp. 654–660, 2004.

[65] R. G. Silva, S. J. Wilcox, and R. L. Reuben, "Development of a system for monitoring tool wear using artificial intelligence techniques," *Proceedings of the Institution of Mechanical Engineers - Part B: Journal of Engineering Manufacture*, vol. 220, no. 8, pp. 1333–1346, 2006.

[66] A. Nagaraj and S. Gopalakrishnan, "Modelling wear behavior of aluminium-silicon alloys using generalized feed forward neural network," *Tierärztliche Praxis*, vol. 40, 2020.

[67] D. Vijay and T. K. Kandavel, "Application of artificial neural network on wear properties of sinter-forged Fe-C-Mo low alloy steel," *International Journal of Advanced Intelligence Paradigms*, vol. 7, no. 3/4, 2015.

[68] S. Wang, S. Khatir, and M. Abdel Wahab, "Proper Orthogonal Decomposition for the prediction of fretting wear characteristics," *Tribology International*, vol. 152, Article ID 106545, 2020.

[69] D. Aleksendrić and Č. Duboka, "Fade performance prediction of automotive friction materials by means of artificial neural networks," *Wear*, vol. 262, no. 7-8, pp. 778–790, 2007.

[70] A. A. Sosimi, O. P. Gbenebor, O. Oyerinde, O. O. Bakare, S. O. Adeosun, and S. A. Olaleye, "Analysing wear behaviour of Al-CaCO3 composites using ANN and Sugeno-type fuzzy inference systems," *Neural Computing & Applications*, 2020.

[71] F. Alambeigi, S. M. Khadem, H. Khorsand, and E. S. H. Mirza, "A comparison of performance of artificial intelligence methods in prediction of dry sliding wear behavior," *International Journal of Advanced Manufacturing Technology*, vol. 84, no. 9-12, pp. 1981–1994, 2015.

[72] A. ArriandiagaLaresgoiti, E. P. Portillo, J. A. G. Sánchez, I. A. Cabanes, and I. R. Pombo, "Virtual sensors for on-line wheel wear and part roughness measurement in the grinding process," *Sensors*, vol. 14, no. 5, 2014.

[73] A. Bustillo, D. Y. Pimenov, M. Matuszewski, and T. Mikolajczyk, "Using artificial intelligence models for the prediction of surface wear based on surface isotropy levels," *Robotics and Computer-Integrated Manufacturing*, vol. 53, pp. 215–227, 2018.

[74] R. E. Haber and A. Alique, "Intelligent process supervision for predicting tool wear in machining processes," *Mechatronics*, vol. 13, no. 8-9, pp. 825–849, 2003.

[75] F. Aydin, "The investigation of the effect of particle size on wear performance of aa7075/al2o3 composites using statistical analysis and different machine learning methods," *Advanced Powder Technology*, vol. 32, no. 2, 2021.

[76] G. O. Barrionuevo, J. A. Ramos-Grez, M. Walczak, and A. B. Carlos, "Comparative evaluation of supervised machine learning algorithms in the prediction of the relative density of 316L stainless steel fabricated by selective laser melting," *International Journal of Advanced Manufacturing Technology*, vol. 113, no. 8, 2021.

[77] M. Agarwal, M. Kumar Singh, R. Srivastava, and R. K. Gautam, "Microstructural measurement and artificial neural network analysis for adhesion of tribolayer during sliding wear of powder-chip reinforcement based composites," *Measurement*, vol. 168, Article ID 108417, 2021.

[78] M. Szala, M. Awtoniuk, L. Łatka, W. Macek, and R. Branco, "Artificial neural network model of hardness, porosity and cavitation erosion wear of APS deposited Al2O3-13 wt% TiO2 coatings," *Journal of Physics: conference Series*, vol. 1736, no. 1, Article ID 012033, 2021.

[79] L. Tyagi, R. Butola, L. Kem, and M. S. Ranganath, "Comparative analysis of response surface methodology and artificial neural network on the wear properties of surface composite fabricated by friction stir processing," *Journal of Bio- and Tribo-Corrosion*, vol. 7, 2021.

[80] S. Basavarajappa, G. Chandramohan, and J. P. Davim, "Application of Taguchi techniques to study dry sliding wear behavior of metal matrix composites," *Materials & Design*, vol. 28, no. 4, pp. 1393–1398, 2007.

[81] Y. Sahin, "Optimization of testing parameters on the wear behavior of metal matrix composites based on the Taguchi method," *Materials Science and Engineering: A*, vol. 408, no. 1-2, pp. 1–8, 2005.

[82] V. E. Buchanan, P. H. Shipway, and D. G. McCartney, "Microstructure and abrasive wear behavior of shielded metal arc welding hardfacings used in the sugarcane industry," *Wear*, vol. 263, no. 1-6, pp. 99–110, 2007.

[83] C. S. Ramesh and A. Ahamed, "Friction and wear behavior of cast Al 6063 based in situ metal matrix composites," *Wear*, vol. 271, no. 9-10, pp. 1928–1939, 2011.

[84] H. Ahlatci, T. Koçer, E. Candan, and H. Çimenoğlu, "Wear behavior of Al/(Al2O3p+SiCp) hybrid composites," *Tribology International*, vol. 39, no. 3, pp. 213–220, 2006.

[85] Y. Sahin and K. Özdin, "A model for the abrasive wear behavior of aluminium based composites," *Materials & Design*, vol. 29, no. 3, pp. 728–733, 2008.

[86] S. Basavarajappa, G. Chandramohan, A. Mahadevan, M. Thangavelu, R. Subramanian, and P. Gopalakrishnan, "Influence of sliding speed on the dry sliding wear behavior and the subsurface deformation on hybrid metal matrix composite," *Wear*, vol. 262, no. 7-8, pp. 1007–1012, 2007.

[87] K. Umanath, K. Palanikumar, and S. T. Selvamani, "Analysis of dry sliding wear behavior of Al6061/SiC/Al2O3 hybrid metal matrix composites," *Composites Part B: Engineering*, vol. 53, pp. 159–168, 2013.

[88] J. M. Durand, M. Vardavoulias, and M. Jeandin, "Role of reinforcing ceramic particles in the wear behavior of polymer-based model composites," *Wear*, vol. 181-183, pp. 833–839, 1995.

[89] J. Kondratiuk and P. Kuhn, "Tribological investigation on friction and wear behavior of coatings for hot sheet metal forming," *Wear*, vol. 270, no. 11-12, pp. 839–849, 2011.

[90] T. Sathish and S. Karthick, "Wear behavior analysis on aluminium alloy 7050 with reinforced SiC through taguchi

approach," *Journal of Materials Research and Technology*, vol. 9, no. 3, 2020.

[91] P. Sharma, K. Paliwal, R. K. Garg, S. Sharma, and D. Khanduja, "A study on wear behavior of Al/6101/graphite composites," *Journal of Asian Ceramic Societies*, vol. 5, no. 1, pp. 42–48, 2017.

[92] S. A. Alidokht, A. Abdollah-zadeh, and H. Assadi, "Effect of applied load on the dry sliding wear behavior and the subsurface deformation on hybrid metal matrix composite," *Wear*, vol. 305, no. 1-2, pp. 291–298, 2013.

[93] M. Vrabeľ, I. Mankova, J. Beno, and J. Tuharský, "Surface roughness prediction using artificial neural networks when drilling udimet 720," *Procedia Engineering*, vol. 48, pp. 693–700, 2012.

[94] A. Leyland and A. Matthews, "On the significance of the H/E ratio in wear control: a nanocomposite coating approach to optimised tribological behavior," *Wear*, vol. 246, no. 1-2, pp. 1–11, 2000.

[95] F. Aydin and R. Durgut, "Estimation of wear performance of AZ91 alloy under dry sliding conditions using machine learning methods," *Transactions of Nonferrous Metals Society of China*, vol. 31, no. 1, pp. 125–137, 2021.

[96] P. Ramkumar, *Trends in Mechanical and Biomedical Design*, E. T. Akinlabi, P. Ramkumar, and M. Selvaraj, Eds., Springer, Singapore, 2021.

[97] L. Provezza, I. Bodini, C. Petrogalli, M. Lancini, L. Solazzi, and M. Faccoli, "Monitoring the damage evolution in rolling contact fatigue tests using machine learning and vibrations," *Metals*, vol. 11, 2021.

[98] S. K. Pattnaik, A. Nayak, A. Parida, and S. S. Kumar, "The study of surface roughness and tool wear analysis in turning of aluminum using different advanced cutting tools (january 16, 2021)," in *Proceedings of the International Conference on Artificial Intelligence in Manufacturing & Renewable Energy (ICAIMRE)*, Bhubaneswar, India, October 2019.

[99] C. S. Lee, Y. H. Kim, K. S. Han, and T. Lim, "Wear behavior of aluminium matrix composite materials," *Journal of Materials Science*, vol. 27, no. 3, pp. 793–800, 1992.

[100] B. Gülenç and N. Kahraman, "Wear behavior of bulldozer rollers welded using a submerged arc welding process," *Materials and Design*, vol. 24, no. 7, pp. 537–542, 2003.

[101] M. Semlitsch and H. G. Willert, "Clinical wear behavior of ultra-high molecular weight polyethylene cups paired with metal and ceramic ball heads in comparison to metal-on-metal pairings of hip joint replacements," *Proceedings of the Institution of Mechanical Engineers - Part H: Journal of Engineering in Medicine*, vol. 211, no. 1, pp. 73–88, 1997.

[102] K. Sivaprasad, S. K. Babu, S. Natarajan, R. Narayanasamy, B. A. Kumar, and G. Dinesh, "Study on abrasive and erosive wear behavior of Al 6063/TiB2 in situ composites," *Materials Science and Engineering: A*, vol. 498, no. 1-2, pp. 495–500, 2008.

[103] L. Natrayan and M. K. Senthil, "Optimization of wear behavior on AA6061/Al2O3/SiC metal matrix composite using squeeze casting technique – statistical analysis," *Materials Today Proceedings*, vol. 27, 2019.

[104] J. U. Prakash, T. V. Moorthy, and S. Ananth, "Fabrication and sliding wear behavior of metal matrix composites," *Applied Mechanics and Materials*, vol. 612, pp. 157–162, 2014.

[105] C. S. Ramesh, C. K. Srinivas, and B. H. Channabasappa, "Abrasive wear behavior of laser sintered iron–SiC composites," *Wear*, vol. 267, no. 11, pp. 1777–1783, 2009.

[106] A. Raj, S. R. Kishore, L. Jose et al., "A survey of electromagnetic metal casting computation designs, present approaches, future possibilities, and practical issues," *Eur. Phys. J. Plus*, vol. 136, 2021.

[107] G. Hermann, "Artificial intelligence in monitoring and the mechanics of machining," *Computers in Industry*, vol. 14, no. 1-3, pp. 131–135, 1990.

[108] S. K. Selvaraj, K. Srinivasan, U. Chadha et al., "ContemporaryProgresses in ultrasonic weldingof aluminum metal MatrixComposites," *Frontiers in Materials*, vol. 8, Article ID 647112, 2021.

[109] A. Sharma, A. Chouhan, L. Pavithran, U. Chadha, and S. K. Selvaraj, "Implementation of LSS framework in automotive component manufacturing: a review, current scenario and future directions," *Materials Today Proceedings*, vol. 46, 2021.

[110] R. Sivasubramani, A. Verma, G. Rithvik, U. Chadha, and K. S. Senthil, "Influence on nonhomogeneous microstructure formation and its role on tensile and fatigue performance of duplex stainless steel by a solid-state welding process," *Materials Today Proceedings*, vol. 46, no. 5, 2021.

[111] K. Virmani, C. Deepak, S. Sharma et al., "Nanomaterials for automotive outer panel components: a review," *Eur. Phys. J. Plus*, vol. 136, 2021.

[112] K. S. Senthil, R. Ramesh, M. Tharun et al., "New developments in carbon-based nanomaterials for automotive brake pad applications and future challenges," *Journal of Nanomaterials*, vol. 2021, Article ID 6787435, 24 pages, 2021.

[113] M. Dharnidharka, U. Chadha, L. M. Dasari et al., "Optical tomography in additive manufacturing: a review, processes, open problems, and new opportunities," *Eur. Phys. J. Plus*, vol. 136, 2021.

[114] T. Ghimire, A. Joshi, S. Sen, K. Chinmay, U. Chadha, and K. S. Senthil, "Blockchain in additive manufacturing processes: recent trends & its future possibilities," *Materials Today Proceedings*, in Press, 2021.

[115] S. D. Mamdiwar and Z. Shakruwala, "Recent advances on IoT-assisted wearable sensor systems for healthcare monitoring," *Biosensors*, vol. 11, no. 11, p. 372, 2021.

[116] T.. Pati, P. H. Kabra, and U. Chadha, "Statistical quality study of the parts produced in an automobile industry: a Daimler India case study," *In IOP Conference Series: Materials Science and Engineering*, vol. 1206, no. 1, Article ID 012022, 2021.

[117] H. Unal and A. Mimaroglu, "Friction and wear behaviour of unfilled engineering thermoplastics," *Materials & Design*, vol. 24, no. 3, pp. 183–187, 2003.

Hindawi
Advances in Materials Science and Engineering
Volume 2021, Article ID 7602160, 18 pages
https://doi.org/10.1155/2021/7602160

Review Article

Mechanical Properties of Titanium Diboride Particles Reinforced Aluminum Alloy Matrix Composites: A Comprehensive Review

V. Mohanavel,[1] M. Ravichandran,[2] V. Anandakrishnan,[3] Alokesh Pramanik,[4] M. Meignanamoorthy,[2] Alagar Karthick,[5] and M. Muhibbullah[6]

[1]*Centre for Materials Engineering and Regenerative Medicine, Bharath Institute of Higher Education and Research, Chennai 600073, Tamil Nadu, India*
[2]*Department of Mechanical Engineering, K. Ramakrishnan College of Engineering, Trichy 621 112, Tamil Nadu, India*
[3]*Department of Production Engineering, National Institute of Technology, Trichy 620015, Tamil Nadu, India*
[4]*School of Civil and Mechanical Engineering, Curtin University, Perth, Australia*
[5]*Renewable Energy Lab, Department of Electrical and Electronics Engineering, KPR Institute of Engineering and Technology, Arasur, Coimbatore 641407, Tamil Nadu, India*
[6]*Department of Electrical and Electronic Engineering, Bangladesh University, Dhaka 1207, Bangladesh*

Correspondence should be addressed to V. Mohanavel; mohanavel2k16@gmail.com

Received 5 August 2021; Accepted 22 November 2021; Published 23 December 2021

Academic Editor: Ivan Giorgio

Aluminum alloys with silicon, magnesium, and copper were extensively used alloying elements in various applications because of their excellent properties. In recent decades, aluminum matrix composites (AMCs) are an advanced engineering material widely utilized in diverse engineering applications, including aircraft, automobile, marine, and shipbuilding, owing to their low density, lightweight, good stiffness, superior strength, and good tribological properties. Aluminum is abundant and its use is as vast as the ocean. It is also the most used matrix material in the composite arena. Therefore, incorporating a ceramic particle into a relatively soft aluminum matrix improves hardness, strength, stiffness, creep, fatigue, and wear properties instead of the conventional materials. This article is an assay to review and spotlight some recent works on the mechanical behaviors of aluminum-based titanium diboride reinforced metal matrix composite. This review article concentrates on the mechanical properties and the fabrication processes of Al-TiB_2 composites to provide a valuable reference to nurture future research precisely.

1. Introduction

In the past few decades, aluminum matrix composite has acted an essential role in material science, especially in aircraft, marine, automobile, transportation, and defense sectors [1]. Several investigations have reported that the inclusion of ceramic filler contents to the matrix improves the mechanical, physical, and tribological properties [2]. Aluminum matrices that are incorporated with hard ceramic filler contents expose the augmented mechanical properties as compared to the plain alloy materials [3]. Figure 1 exhibits the list of wrought aluminum alloy. Due to their high strength-to-weight ratio, high thermal conductivity, good corrosion resistance, and improved mechanical properties, aluminum metal matrix composites (AMCs) are increasingly used as structural materials. Composite materials are becoming more popular due to their unique properties and high strength-to-weight ratio. Ceramic particles provide exceptional strength and wear resistance to AMCs [4–6]. Figure 2 reveals the classification of aluminum composites fabrication process. A large range of filler particles such as SiC, Si_3N_4, ZrN, TiN, TiB_2, Al_2O_3, BN, WC, and SiO_2 has used the reinforcements for the manufacture of composites. Amid the other filler materials, titanium diboride (TiB_2) is a promising candidate filler material for aluminum-based composites. It exhibits an enticing combination of mechanical and physical properties, superior

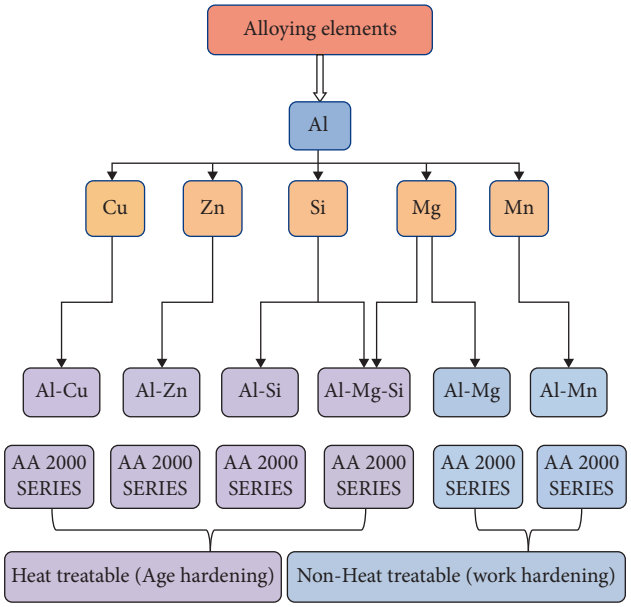

Figure 1: List of wrought aluminum alloy.

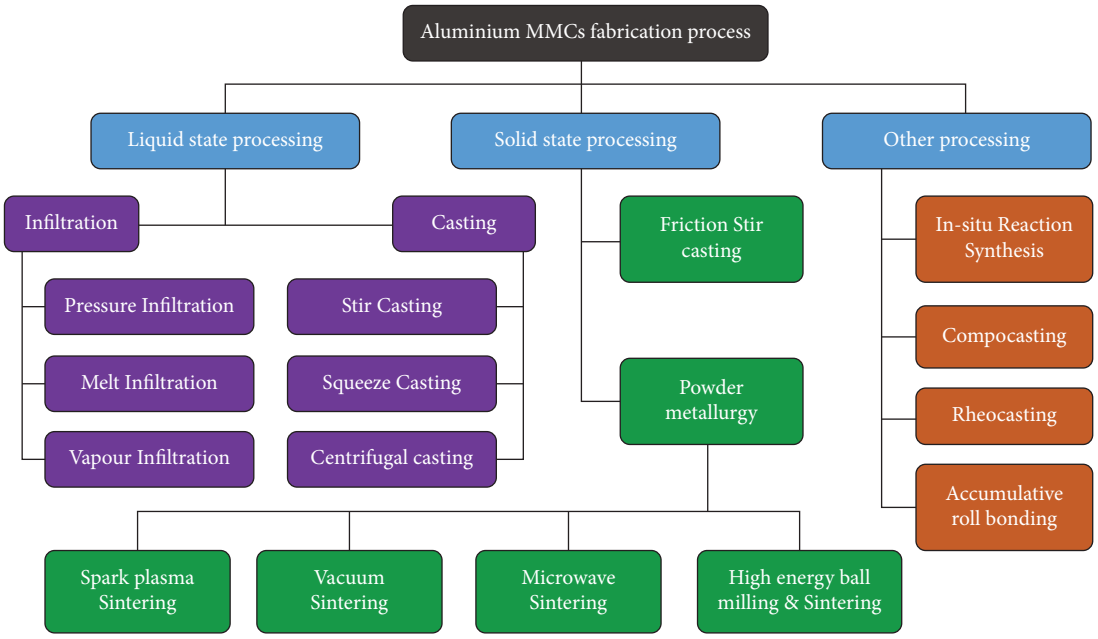

Figure 2: Classification of aluminum composites fabrication process.

strength, perfect hardness, high melting point, excellent corrosion resistance, and excellent wear protection [7–10]. Figure 3 illustrates the advantages and disadvantages of different techniques for composites.

Titanium diboride (TiB_2) particle does not react with molten aluminum and cannot form reaction products at the intergap between matrix and reinforcement [11]. Compared with the other filler contents, TiB_2 is a desirable strengthening agent for aluminum-based metal matrix composites [12]. Titanium diboride based aluminum matrix composites were recently employed in the manufacturing of automobile piston, vehicle drive shaft, cylinder liners, cutting tools, crank shaft, brake drum, and bicycle frames and were also employed in aerospace, marine, and automotive industries because of their good stiffness, superior strength, high temperature stability, and lightweight [13]. AMCs have been fabricated using a variety of methods like compocasting, melt stirring casting, powder metallurgy, in situ casting, squeeze casting, and spray forming and mechanical alloying methods. Figures 4(a)–4(c) reveal the schematic diagram of stir casting, powder metallurgy, and hot extrusion process.

Liquid state processing method contains incorporation of ceramic particles externally or formed inside the molten metal. The former is known as ex situ (stir casting technique)

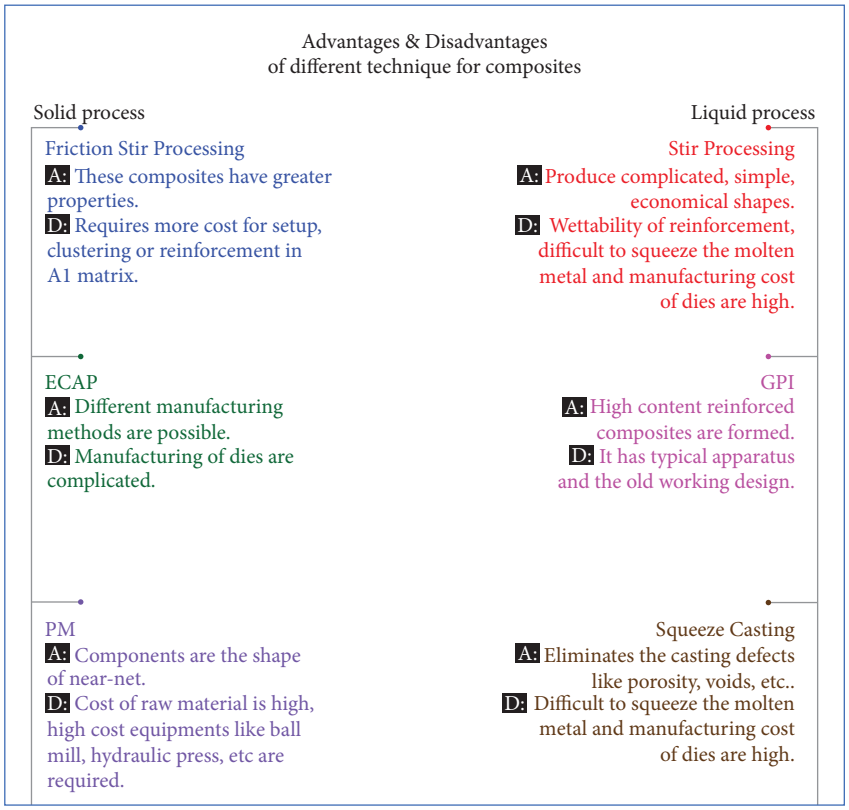

Figure 3: Advantages and disadvantages of different techniques for composites.

while the latter is called as in situ (direct melt reaction technique or exothermic salt-metal reaction technique) fabrication. Liquid state casting techniques have shown some incomparable benefits like constant dissemination of filler particles in the matrix and strong interfacial attachment between the matrix and the filler particle [14]. Figure 5 reveals the classification of fabrication method of AMCs.

Figure 6 exhibits the influence of various parameters on hardness. A number of researchers have produced titanium diboride reinforced AMCs using various techniques. This scientific review article provides an aerial view of research efforts that are focused on mechanical properties and synthesizing techniques of aluminum-based titanium diboride composites. Table 1 reveals the physical and mechanical properties of several ceramics reinforcements. The SEM image of the TiB_2 particles is depicted in Figure 7.

2. Fabrication Techniques of Al-TiB_2 Composites

Among the several manufacturing techniques, the two techniques that are being used quite often are in situ casting and stir casting. Figure 8 reveals the process parameters influence the production of composites through the melt stirring route.

2.1. Stir Casting. The processing route is the most significant consideration in the fabrication of AMCs. In 1968, S. Ray dispersed alumina (Al_2O_3) ceramic filler materials into the Al melt, and in this process the incorporated filler material is blended with a molten state alloy by means of mechanical stirring [15]. For the processing of discontinuous rein-forced AMCs, several researchers prefer to employ stir casting route. The foremost objective of melt stirring is that it is trouble-free, flexible, unproblematic, reasonable, and appropriate for bulk production [16, 17]. Mohanavel et al. [18] utilized melt stirring to manufacture AA6351/SiC AMCs. SEM images of the resultant AA6351/SiC AMCs comprising 4%, 8%, and 12% SiC, respectively, are revealed in Figures 9(a)–9(c). The SEM images demonstrate a nearly homogeneous dispersion of the SiC in the AA6351 alloy. Moreover, the stir casting is affordable and provides an efficient stirring movement in the melts due to the sound particle-matrix association in the filler material. The cast-on route for the development of inhomogeneous filler in integrated MMCs is the most widely used liquid state casting process. Figure 10 reveals the experimental structure for the fabrication of composites through melt stirring route.

2.2. In Situ Casting. The in situ technique has been an attractive processing route for producing AMCs. In situ synthesizing technique was started in the early 1990s. In this process in situ reaction between the halide salts and molten metal takes place to form reinforcement particles. Exothermic method is more effective than the stir casting process [19, 20]. In situ formed reinforcement exhibits homogeneous dissemination of fine sized filler materials. It

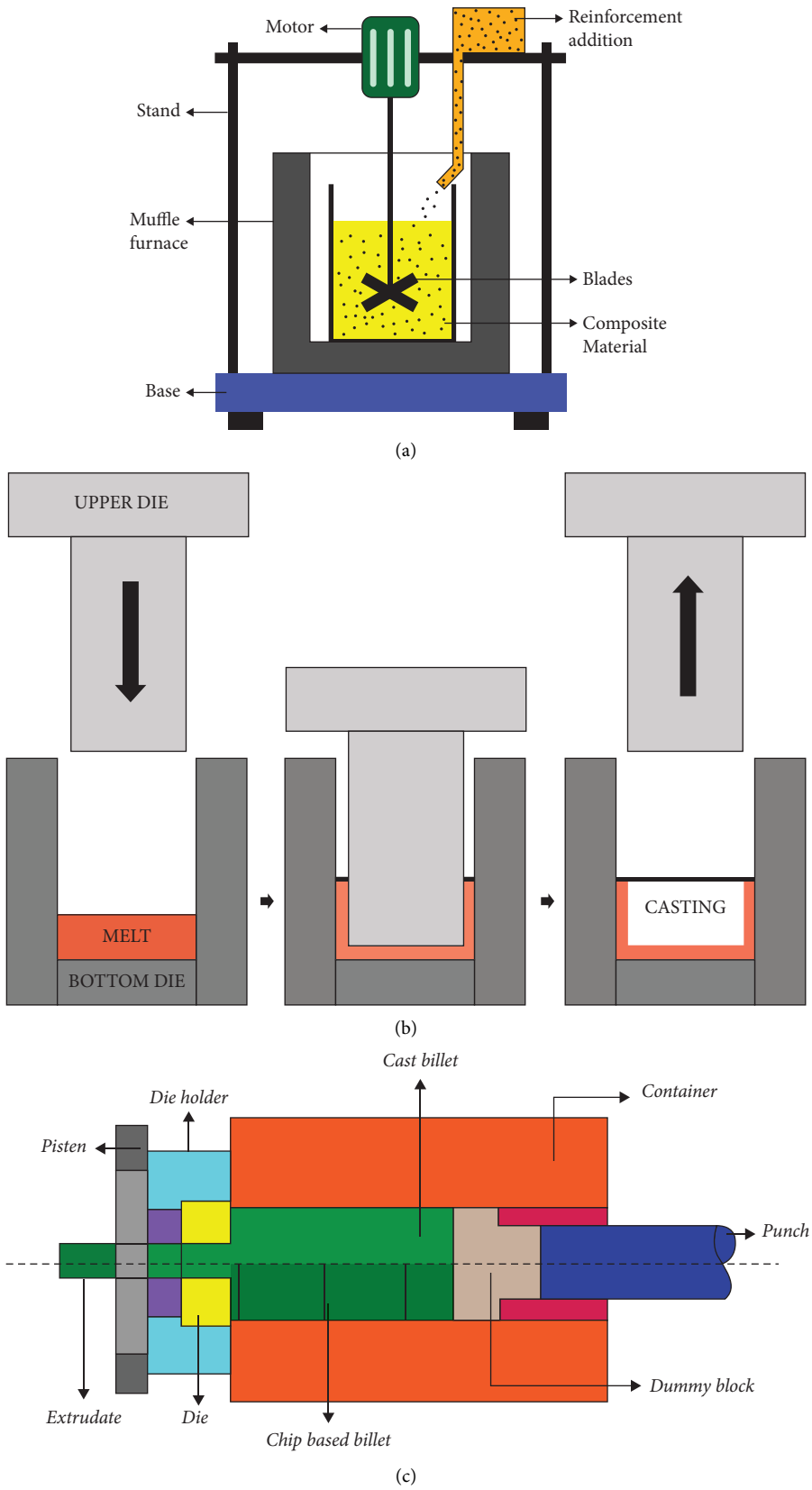

Figure 4: Schematic diagram of fabrication process: (a) stir casting, (b) powder metallurgy, and (c) hot extrusion.

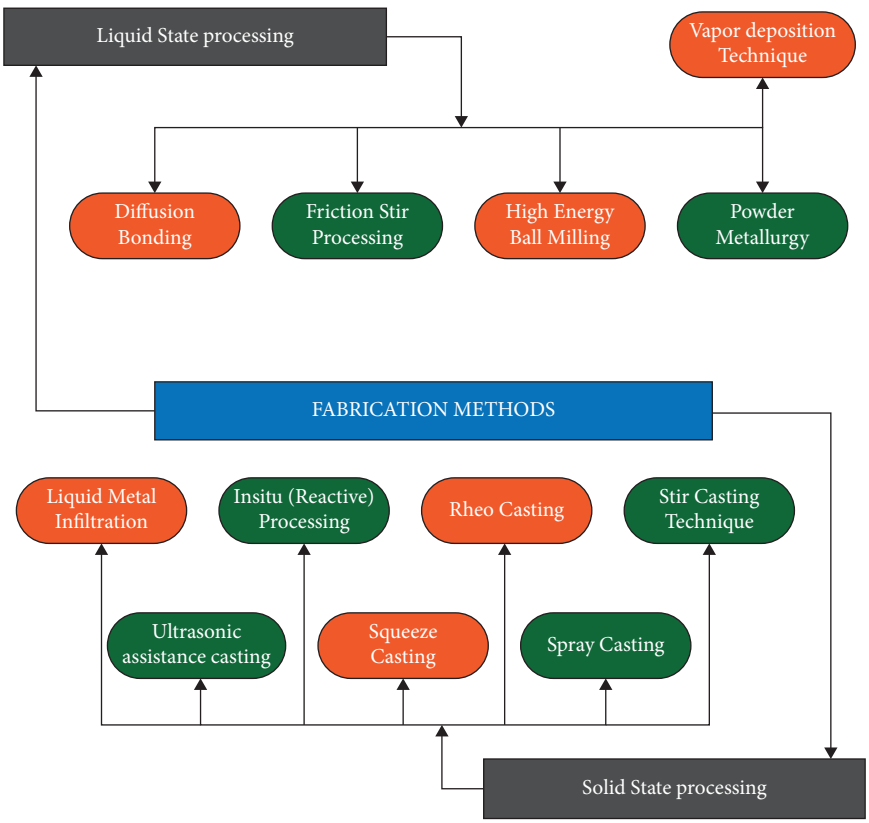

Figure 5: Classification of fabrication method of AMCs.

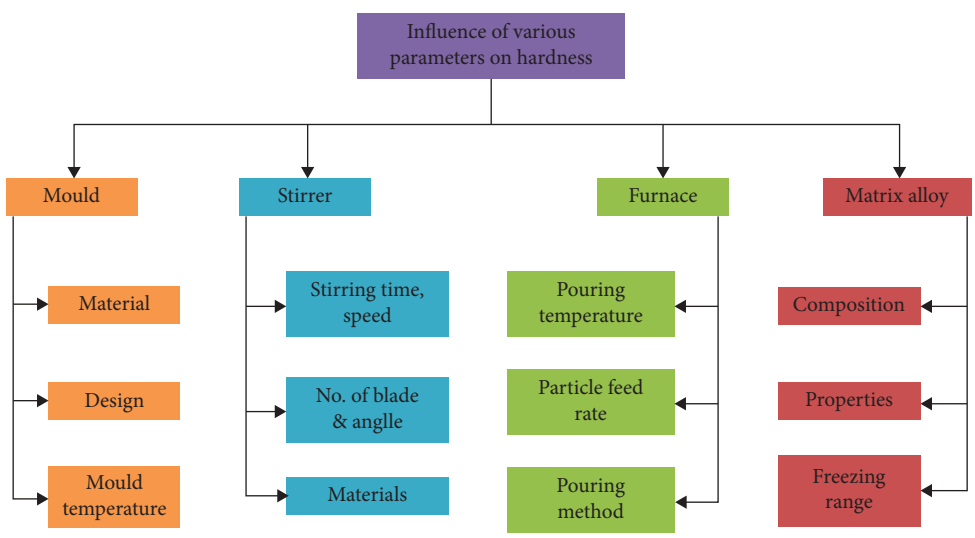

Figure 6: Influence of various parameters on hardness.

Table 1: Physical and mechanical properties of several ceramics reinforcements.

Sl. no	Properties	TiC	B_4C	ZrB_2	TiB_2
1	Melting point (°C)	2830	2780	3040	3225
2	Density (g cm^{-3})	4.77	2.52	6.08	4.52
3	Hardness (GPa)	22–24	18–20	35	25–35
4	Thermal conductivity ($Wm^{-1} K^{-1}$)	31.8	32.5	24.27	60–120
5	Molar mass (g/mol)	59.89	52.255	112.85	69.489
6	Crystal structure	Cubic	Rhombohedral	Hexagonal	Hexagonal
6	Elastic modulus (GPa)	450	472	451	560

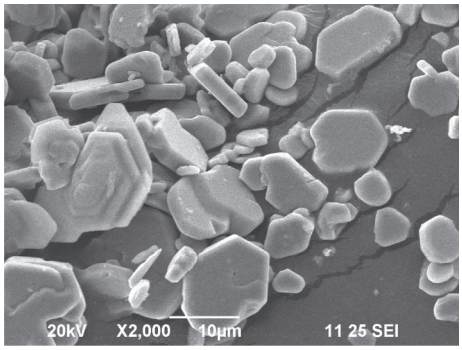

Figure 7: SEM image of TiB_2 particles.

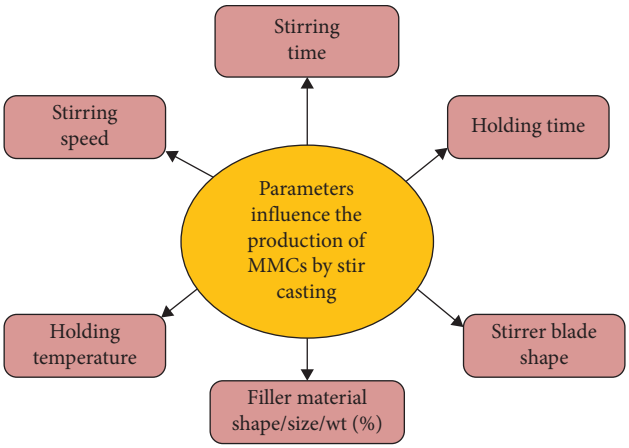

Figure 8: Process parameters influence the production of composites through the melt stirring route.

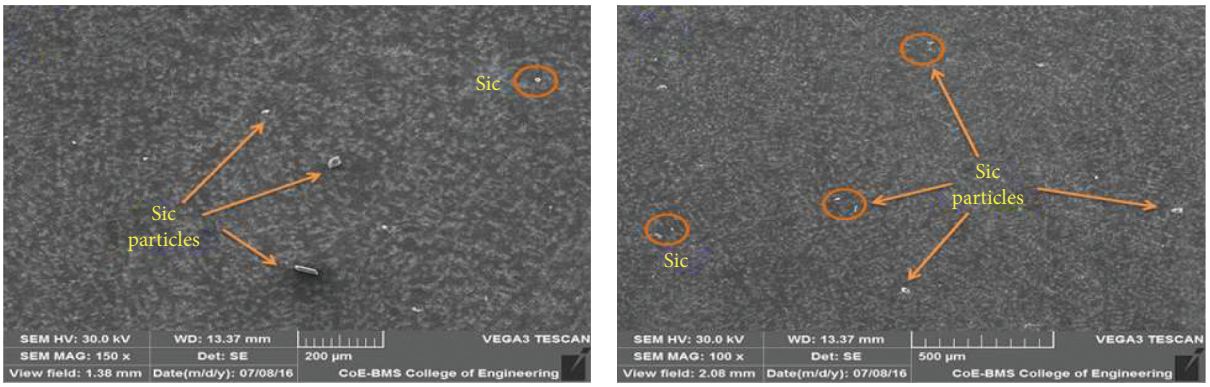

(a) (b)

Figure 9: Continued.

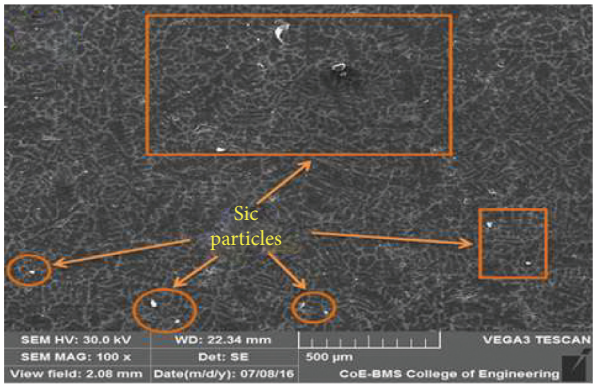

(c)

Figure 9: SEM images of (a) Al6351/4 wt% SiC AMCs, (b) Al6351/8 wt% SiC AMCs, and (c) Al6351/12 wt% SiC AMCs [18].

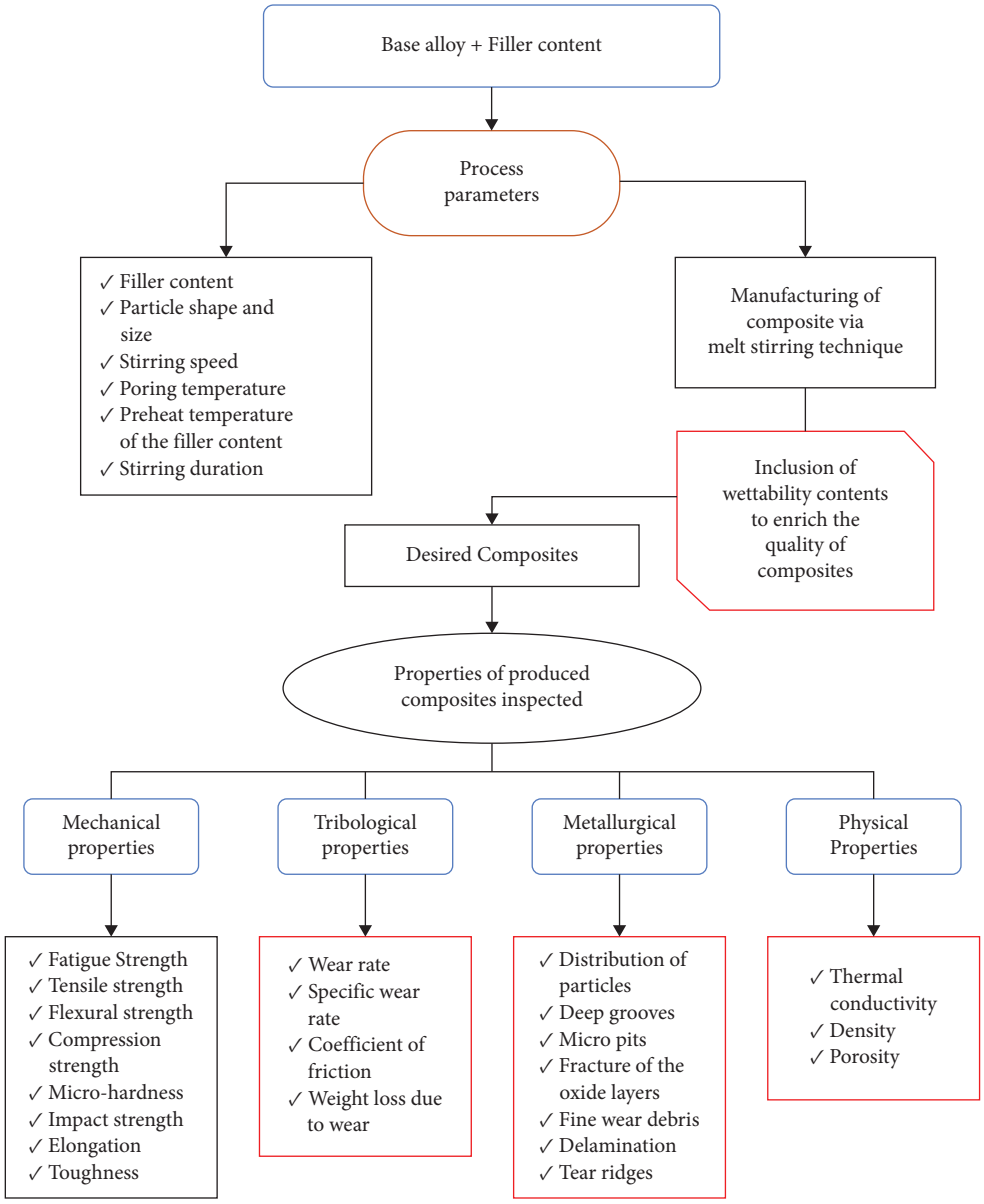

Figure 10: Experimental structure for the fabrication of composites through melt stirring route.

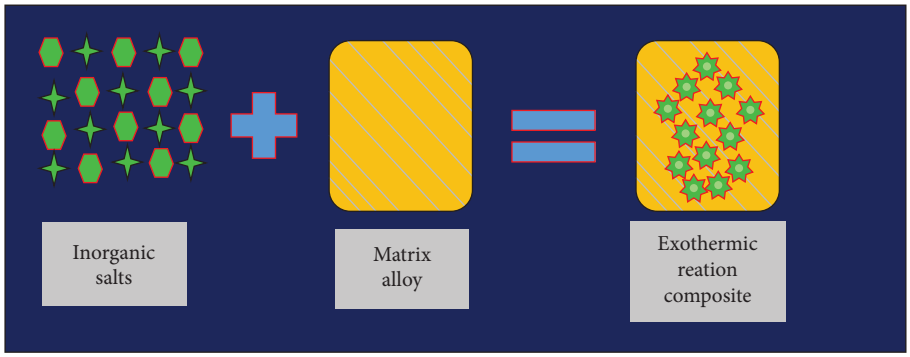

Figure 11: Manufacturing of in situ composite employing inorganic salts and aluminum matrix alloy.

is effortlessly accomplished without the need for incorporation of wetting agent. The in situ reactions, as provided in the following equations, resulted in the generation of TiB_2 particles. Consider the following:

$$\begin{aligned} K_2TiF_6 + \frac{13}{2}Al &\longrightarrow Al_3Ti + \frac{4}{3}AlF_3 + 2KF \\ 2KBF_4 + 3Al &\longrightarrow AlB_2 + 2AlF_3 + 2KF \\ Al_3Ti + AlB_2 &\longrightarrow TiB_2 + 4Al \end{aligned} \quad (1)$$

The formation pattern of TiB_2 can be classified as follows. (a) The incorporation of K_2TiF_6 (potassium hexafluorotitanate) and KBF_4 (potassium tetrafluoroborate) to molten aluminum generates intermetallic compounds, specifically Al_3Ti and AlB_2, which serve as for Ti and B atoms. (b) Boron atoms travel in the direction of particles from Al_3Ti. (c) The reaction occurred between atoms Ti and B in a gap from the surface of Al_3Ti to form TiB_2. (d) Boron atoms begin diffusing into TiB_2 particles because of the smaller scale. (e) Dissolution of Al_3Ti particle owing to normal cracking and fragmentation of Al_3Ti particles, which contribute to enriched TiB_2 generation rate. (f) Generation of TiB_2 particles, after the entire reaction. Moreover, the KBF_4 inorganic salt was incorporated slightly in excess of the stoichiometric ratio to avoid the formation of titanium trialuminide (Al_3Ti). Figure 11 reveals the manufacturing of in situ composite employing inorganic salts and aluminum matrix alloy.

In preparing AMCs, "in situ" techniques offer significant advantages over the conventional processing routes and in situ casting route is more economical. In situ type of processing is now in commercial use for TiB_2 particle reinforced aluminum matrix composites [21–23]. Moreover, the TiB_2 reinforcement particles in the composite inhibit dislocations, resulting in higher tensile strength. This interface allows for an efficient load transfer between the matrix alloy and the reinforcement. As the TiB_2 particle content increases, this composite has higher mechanical properties than pure aluminum alloy [22]. Figure 12 displays the experimental arrangement of in situ casting. In [23], the dry sliding wear parameters on LM4/TiB_2 composites were analyzed using the Taguchi method. Particulates reinforced

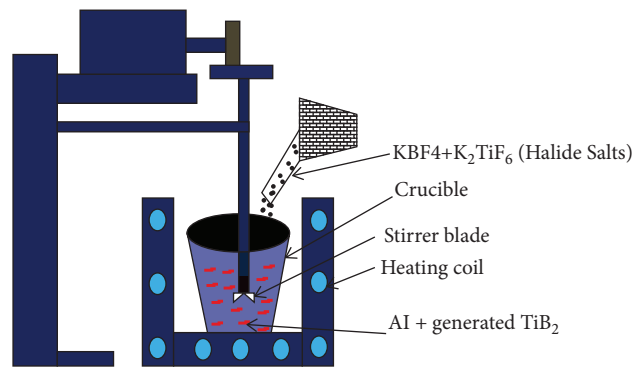

Figure 12: Experimental arrangement of Al-TiB_2 in situ composite.

aluminum matrix composite has better tribological properties compared to unreinforced aluminum matrix composite. Mohanavel et al. [21] employed in situ casting to manufacture AA6351/TiB_2 AMCs. Microhardness and strength increase with the enhancement of the weight percentages of TiB_2 particles. SEM micrographs of the resultant AA6351/TiB_2 AMCs comprising 0%, 4%, and 8% TiB_2, respectively, are revealed in Figures 13(a)–13(e). The SEM micrographs demonstrate a homogeneous dispersion of the TiB_2 in the AA6351 alloy.

3. Comparison of In Situ versus Stir Casting

Table 2 explicates results obtained by various researchers where TiB_2 is the reinforcement and the processes involved mostly are in situ and stir casting and the percentages at which superior mechanical properties emerge are spotted in Table 3. Both in situ and stir casting method can fabricate Al-TiB_2 composites with strong mechanical and wear properties. Most of the explorations have been done on titanium diboride filler particle for aluminum based in situ AMCs. Titanium diboride reinforced aluminum matrix composites are fabricated using halide salt reaction technique and it has proven to be cost effective [24]. Al-TiB_2 in situ composites are usually synthesized by the incorporation of inorganic salts like K_2TiF_6 and KBF_4 which react with molten aluminum and form TiB_2 in the Al melt [25–30]. The Al-TiB_2 in situ AMCs reveal superior mechanical and tribological

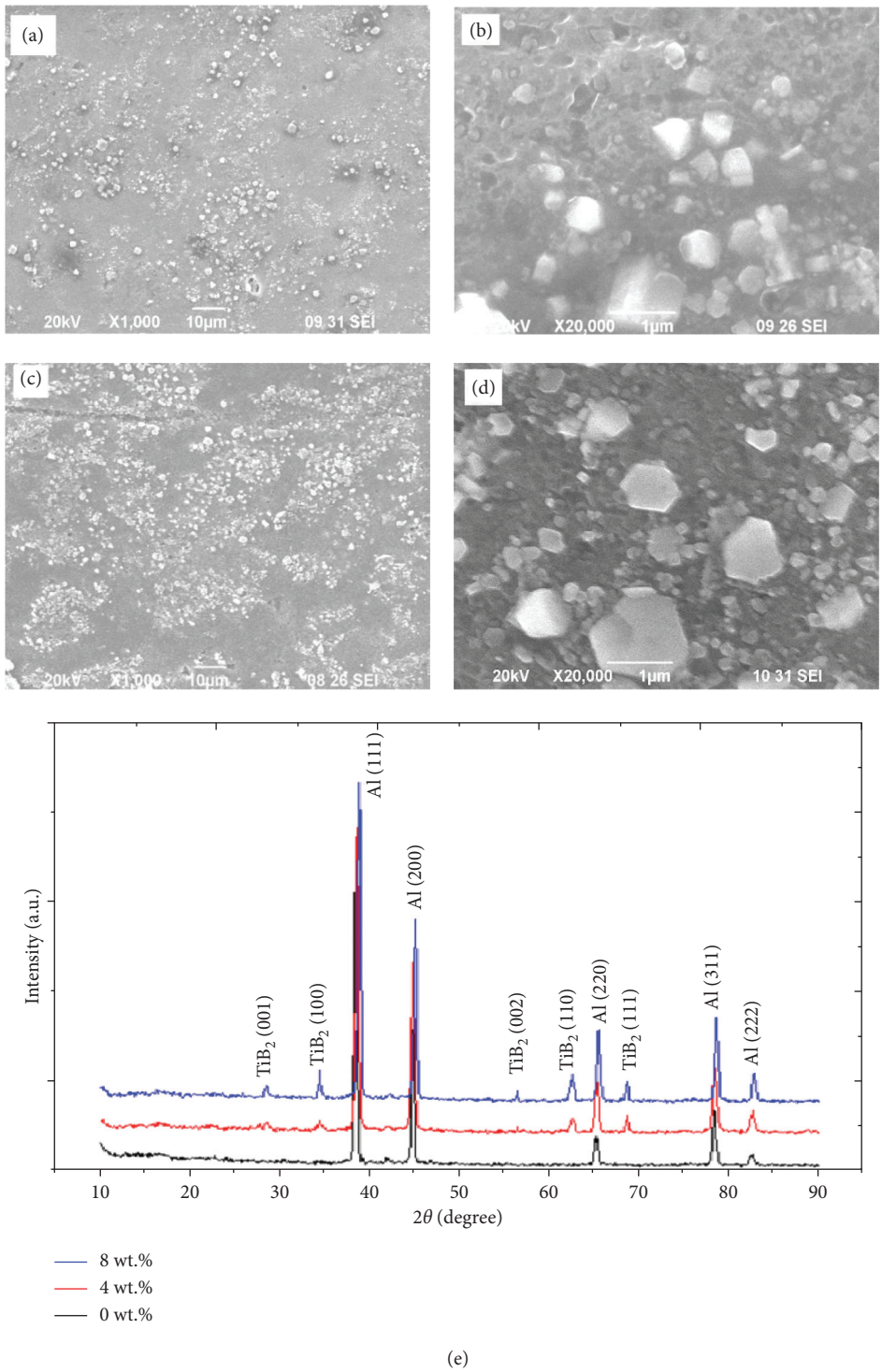

(e)

Figure 13: SEM micrograph of AA6351/TiB_2 AMCs containing: (a) 4% TiB_2, (b) 4% TiB_2, (c) 8% TiB_2, (d) 8% TiB_2, and (e) XRD patterns of AA6351/TiB_2 in situ composites [21].

properties compared with the base matrix alloy. In situ technique offers high mechanical bonding, homogeneous dissemination of small size of fillers in the matrix, thermodynamic stability, and clear interfacing between the solid and liquid in contrast to stir casting [31, 32]. TiB_2 involved composites have utilized stir casting, squeeze casting, centrifugal casting, and compocasting rarely. It is also more economical when compared to in situ casting. Mechanical and physical properties like density, porosity, flexural strength, and compression strength are analyzed by a few researchers only, where TiB_2 plays a vital role as reinforcement.

Table 2: Titanium diboride reinforced composites properties.

MMC within (wt %)	Manufacturing process	Mechanical properties	Remarks	Reference
Al 6061- TiB_2 (0, 4.98, 9.29, 13.62 wt %)	In situ casting	Microhardness, ultimate tensile strength	Hardness and tensile strength of the composite enhanced as compared to nonreinforced plain alloy matrix.	[33]
AA6061-TiB_2 (0, 12 wt %)	In situ casting	Brinell hardness, UTS, % elongation	All these mechanical characteristics of the AMCs were superior to those of pure Al matrix alloy. The incorporation of TiB_2 filler contents into the AA6061 alloy has diminished the elongation of the composite.	[34]
Al-TiB_2 (1, 4, 7 wt %)	Salt-metal reaction route	Hardness, UTS	All these mechanical properties of the AMCs were superior to those of plain aluminum.	[35]
A356-TiB_2 (0, 2.12, 4.66, 8.37 wt %)	In situ reaction process	UTS, YS, elongation	Mechanical behaviors of the AMCs were greater than those of plain alloy but superior testing results are obtained at 8.37 vol% of TiB_2 reinforced composites.	[36]
AA2219-TiB_2 (0, 5, 10 wt %)	In situ route	Hardness, UTS, YS, and elongation	Both hardness and UTS are being increased when the mass concentration of TiB_2 filler contents reached up to 10%. Addition of TiB_2 reduced the elongation of the plain matrix alloy.	[37]
Al 6063- TiB_2 (0, 4.29, 9.15, 13.12 wt %)	In situ casting	Hardness and tensile strength	Hardness and tensile strength properties are improved with the augmented content of hard titanium boride reinforcement.	[38]
Al 6061- TiB_2 (0, 2, 4, 6, 8, 10 wt %)	High energy metal stirring route	Hardness, UTS	Hardness and UTS of the developed AMCs were superior to those of base matrix but better results are obtained at the maximum percentage of TiB_2 reinforced composite.	[39]
AA7075-TiB_2 (0, 3, 6, 9 wt %)	Exothermic reaction process	Microhardness, UTS, % elongation	Both the UTS and the microhardness were enriched as compared to pure Al matrix. Incorporation of hard TiB_2 reduced the elongation of the base matrix.	[40]
Al 6063/TiB_2 (0, 5, 10 wt %)	Salt base exothermic reaction process	Microhardness	Microhardness of the produced composite increased steadily as hard TiB_2 reinforcement content increased.	[41]
A356-TiB_2 (0, 12.5 wt %)	In situ casting process	Ultimate tensile strength, yield strength.	Yield strength and tensile strength of the aluminum metal matrix composites were higher than those of unreinforced plain matrix alloy and then increased with the increase in the content of TiB_2 particle.	[42]
AA6061-TiB_2 (0, 4, 8, 12 wt %)	Stir casting	Hardness, tensile strength	The tensile strength and the microhardness of the prepared composite tend to increase with the increase in TiB_2 content.	[43]
Al-6Cu-0.2Mg-Mn-TiB_2 (0, 1, 3, 5 wt %)	In situ casting	Microhardness	Microhardness was greater than that of base matrix alloy. The variation in the presence of reinforcement particles is visible with increased content of TiB_2.	[44]
AA6061-TiB_2 (10 wt %)	Stir casting	Hardness and tensile strength	AA6061/10 wt%TiB_2 AMC exhibits 58HV of microhardness and 195 MPa of tensile strength. These AMCs are fabricated in liquid state by stir casting method.	[45]

Table 2: Continued.

MMC within (wt %)	Manufacturing process	Mechanical properties	Remarks	Reference
A390-TiB_2	In situ casting	Hardness, UTS, and % elongation	Ultimate tensile strength, ductility, and hardness of the produced composite were greater than those of nonreinforced matrix alloy but highest results are obtained at the largest percentage of TiB_2 reinforced composite.	[46]
AA2219/TiB_2 (0, 5, 10 wt %)	In situ reaction process	UTS, yield strength, ductility	Tensile and yield strength were greater than those of parent alloy and they raised with the raise in reinforcement, in all composites. Incorporation of TiB_2 reduced the elongation of the pure Al matrix.	[47]
LM 25/TiB_2 (0, 2.5, 5, 7.5)	Mixed salt method	UTS, yield strength, % elongation	UTS and yield strength were superior to those of base aluminum and they were enriched with the augmented mass proportion of reinforcement while the mechanical characteristics of the composite increases owing to the presence of TiB_2 filler materials.	[48]
Al/TiB_2 (0, 1.5, 2.5, 3.5, 5 and 10 wt % TiB_2)	Powder metallurgy	Compressive strength	Mechanical property was greater than that of basic alloy.	[49]
A356/TiB_2 (0, 0.5, 1.5, 3, and 5 vol %)	Stir casting	Hardness	Use of hard TiB_2 has a remarkable effect in increasing microhardness and UTS of the Al composite.	[50]
A356/TiB_2 (0, 3, 5.6, 7.8 vol%)	In situ casting	UTS, yield strength, and fracture toughness	The produced composite with 7.8 vol% TiB_2 shows the greatest improvement in mechanical performance when compared to the base metal.	[51]
AA6061/TiB_2 (0, 5, 7 wt%)	In situ casting	Microhardness, UTS, elongation	In all the composites microhardness and UTS were greater than those of unreinforced base matrix and they increased with increase in reinforcement content. The addition of TiB_2 particulates to the AA6061 matrix has led to reduced ductility of the AMC.	[52]
AA7075/TiB_2 (0, 5, 10 wt%)	In situ casting (mixing salt route)	Bending strength	Bending characteristics are enhanced with the increased content of filler materials.	[53]
AA6061- TiB_2 (0, 3, 6, 9 wt %)	In situ reaction process	Microhardness (HV)	Microhardness of the experimental AMCs was greater than that of plain alloy but highest results are achieved at the superior percentage of TiB_2 reinforced composite.	[54]
AA1100-TiB_2 (0, Al4.5%Cu-15 vol %TiB_2, Al4.5%Cu3 %C-15 vol% TiB_2)	In situ method	Tensile strength, elongation	Tensile strength of the composite was greater than that of unreinforced plain alloy and all these characteristics were enriched when augmented amount of filler content is found. Addition of TiB_2 reduced the ductility of the matrix alloy.	[55]
Commercial pure (CP) Al-TiB_2 (0, 5, 10, 15, 20 vol %)	Powder metallurgy	UTS, yield strength	UTS and yield strength were superior to those of base alloy in both processes and were enhanced with increase in filler material, in all composites.	[56]
LM 25-TiB_2 (0, 2.5, 5, 7.5 wt %)	In situ method	Brinell hardness, UTS, yield strength, elongation	The improved hardness and the reduction in the ductility of LM25-TiB_2 AMCs are observed when TiB_2 content is increased in the AMCs.	[57]

Table 2: Continued.

MMC within (wt %)	Manufacturing process	Mechanical properties	Remarks	Reference
Al-4Cu-TiB_2 (0, 2.5, 5, 7.5, 10 wt %)	In situ method	Hardness (HV)	The microhardness of the fabricated composite tends to augment with the rise in TiB_2 content.	[58]
Al-2.5% TiB_2 (25%, 120%, 140% KBF_4 excess than stoichiometry) 2.5% TiB_2	In situ method	Microhardness (HV)	Microhardness of the AMCs increased as compared to nonreinforced alloy matrix.	[59]
AA6061-TiB_2 (0, 3, 6, 9, 12 wt %)	Stir casting	Hardness, UTS, yield strength,	Yield strength, hardness, and tensile strength were superior to those of nonreinforced base matrix alloy.	[60]
AA6061-TiB_2 (0, 2, 4, 6, 8, 10, 12 wt %)	In situ and equal channel angular pressing (ECAP)	Hardness, UTS, elongation,	Both the tensile strength and the hardness were enhanced as compared to pure plain matrix alloy. The elongation of the AMCs was found to be somewhat lower than that of the base alloy.	[61]
Al-B_4C-TiB_2 (10, 20, 30, 40 wt % TiB_2)	Vacuum infiltration	Hardness (HRA) and flexural strength	The hardness and flexural strength of the specimens tend to decrease during the increment of the reinforcement content.	[62]
AA6061, AA6061-5 wt% TiB_2, AA7015, AA7015-5 wt% TiB_2	Hot extrusion	Hardness	Hardness of the AMCs was superior to that of plain alloy and it is enhanced with the rising content of hard TiB_2 reinforcement.	[63]
AA6061, AA6061-10% SiC- 2.5% TiB_2, 5% TiB_2	Stir casting	Hardness (HV)	Hardness of the Al-10%SiC-2.5%TiB_2 AMCs increased as compared to basic alloy matrix.	[64]
Al6061-TiB_2 (0, 6, 8, 10)	In situ casting route	Hardness, UTS, elongation	Hardness and UTS of the prepared AMCs were enriched linearly as TiB_2 content increased. The incorporation of hard TiB_2 filler materials into the AA6061 matrix has led to diminished elongation of the AMC.	[65]
Commercial pure aluminium (CP)-TiB_2 (0, 2.5, 5 wt% TiB_2)	In situ casting process	Hardness, UTS	Hardness, fracture, and tensile strength improved with enhanced titanium diboride particle content.	[66]
AA7178—0, 3, 6, 9 wt%TiB_2)	In situ casting method	Hardness, compression strength, and tensile strength	Microhardness, compression, and tensile strength are being improved when the weight fraction of TiB_2 particles reached up to 9%.	[67]
A1100-TiB_2, AlCu TiB_2 (15Vf% TiB_2)	Exothermic reaction process	UTS, yield strength	Mechanical properties of the AMMCs increased as compared to unreinforced plain matrix alloy.	[68]
Al-7Si/TiB_2 (0, 5, 10 wt% TiB_2)	In situ	Hardness, UTS, yield strength	Maximum hardness, yield, and tensile strength of the AMCs are obtained where the TiB_2 filler material reached 10%.	[69]
Al-4%Cu-TiB_2 (chemical reaction time-15, 25, 35 min)	In situ casting	Hardness, UTS, yield strength, elongation	Mechanical properties of the developed aluminum matrix AMCs were superior to those of unreinforced matrix.	[70]
A356-TiB_2 (0, 0.5, 1.5, 3.5-micron and nano TiB_2) (casting temperature 750, 800, 900°C)	Melt stirring casting	UTS and yield strength	Yield and tensile strength were augmented compared to those of basic alloy. A356-1.5 wt%TiB_2-900°C AMC exhibits higher mechanical properties.	[71]
AA6061/TiB_2/Gr 0%, 5%, 10%, 20%TiB_2 + 2%Gr, 5%, 10%, 20% TiB_2,	Melt stirring method	UTS and hardness	UTS and hardness of the AMCs were augmented compared to those of base alloy and were then boosted with the augmented content of filler material.	[72]

Table 2: Continued.

MMC within (wt %)	Manufacturing process	Mechanical properties	Remarks	Reference
AA6063/TiB_2 (0, 5, 10)	In situ	Hardness (HV)	Bulk hardness of the composite was superior to that of base alloy and it was enriched with the increasing content of filler material.	[73]
Al6063- TiB_2 (2.8, 6.7, 10 wt%)	In situ	Microhardness (HV)	Microhardness was 27.25% times superior to that of base aluminum while hardness increased with increased content of reinforcement.	[74]
A356- TiB_2 (2, 3, 4, 5, 6 wt% TiB_2) reaction time (20, 25, 30, 35, 40 min) temperature (800, 850, 900, 950, 1000°C)	In situ	Hardness (HV), UTS	Use of TiB_2 has a significant influence in enriching the hardness and tensile strength of the AMCs.	[75]
AA6061-10%SiC-(0, 2.5, 5 wt % TiB_2)	Stir casting	Hardness, tensile strength	Higher hardness was achieved at the percentage of Al-10%SiC-2.5TiB_2 AMC and maximum tensile strength obtained at the percentage of Al-10%SiC-0%TiB_2 AMC.	[76]
AA6061-5%, 10%TiB_2-1, 2, 3, 4% Gr	Stir casting	Hardness, compressive strength, tensile strength	Hardness and UTS of the aluminum composites were superior to those of parent matrix alloy and it is enriched by the increasing content of 10 wt%TiB_2 and 2 wt%Gr.	[77]
Al2014-TiB_2 (0, 5 wt% TiB_2 (5 wt% TiB_2 + 0.5% Ceo_2)	In situ casting	Hardness, tensile strength, yield strength	Hardness, yield, and tensile strength were superior to those of base alloy and they were enriched by augmenting the amount of filler content (TiB_2 + CeO_2).	[78]
AA2219-TiB_2/ZrB_2 (0, 3, 6%)	In situ casting	Microhardness (HV)	Microhardness of the composite was superior to that of basic alloy.	[79]
Commercial pure aluminum (CP)-TiB_2 (0, 5 vol% TiB_2, 5 vol% TiB_2 + 0.5 wt%CeO_2)	In situ casting	UTS, YS, elastic modulus	Mechanical properties of the experimental composites were superior to those of parent matrix alloy.	[80]
A356-TiB_2 (0, 2.5, 5, 7.5, 10%) At T6 treated	In situ composite	Vickers hardness (HV)	Microhardness was improved as compared to pure base matrix aluminum alloy.	[81]
Al-4 wt%Cu-5, 10, 15, 20%TiB_2)	Hot isostatic processing	Hardness, yield strength, UTS	All these properties of the composite were superior to those of base material.	[82]
Al6061-TiB_2 (10, 11, 12, 13, 14 wt% TiB_2)	In situ casting process	Hardness, UTS	Peak UTS and hardness of the produced AMCs are obtained where the TiB_2 content reached 14%.	[83]
A356-TiB_2 (0, 2.5, 5, 7.5, 10 wt %)	Salt metal reaction process	Hardness, UTS, % elongation	Mechanical behaviors of the produced aluminum-based metal matrix composites were superior to those of nonreinforced alloy.	[84]
AA7075-TiB_2 (0, 9 wt% TiB_2)	In situ method	Microhardness and tensile strength	UTS and hardness of the AA7075-9 wt % titanium boride AMCs increased as compared to nonreinforced alloy matrix.	[85]
AA2009-TiB_2 (8 wt% TiB_2) solution temperature (498, 508, 520, 530°C)	Exothermic reaction process	Hardness and UTS	The manufactured AMCs reveal the maximum hardness after solution was treated at 530°C and the superior tensile strength after solution was treated at 520°C.	[86]
AA2024-TiB_2 (0, 7 wt% TiB_2)	Stir casting	Microhardness	Microhardness of the developed composite was higher than that of unreinforced monolithic alloy.	[87]

Table 2: Continued.

MMC within (wt %)	Manufacturing process	Mechanical properties	Remarks	Reference
AA7075-TiB_2 (0, 6, 9, 12 wt% TiB_2)	In situ method	Microhardness and tensile strength	Mechanical properties of the manufactured composites were superior to those of monolithic alloy. Superior UTS and hardness of the proposed AMCs is achieved where the TiB_2 content reached 12%.	[88]

Table 3: Superior mechanical properties of titanium diboride based aluminum matrix composites.

MMCs	Manufacturing process	Macrohardness (BHN)	Microhardness (HV)	UTS (MPa)	YS (MPa)	Reference
AA7050/6 wt% TiB_2	In situ casting technique	—	—	746	701	[25]
AA6061/12 wt% TiB_2	Exothermic reaction process	88.6	—	173.6	94.2	[34]
Al/7 wt% TiB_2	Salt-metal reaction route	30	—	136.6	—	[35]
A356/8.37 vol% TiB_2	In situ reaction process	—	—	258.5	217.6	[36]
AA2219/10 wt% TiB_2	In situ casting technique	—	96	234	205	[37]
AA6063/13.12 wt% TiB_2	In situ casting	—	59.25	140.9	—	[38]
AA6061/10 wt% TiB_2	High energy stir casting	—	73.93	171	—	[39]
AA7075/9 wt% TiB_2	In situ method	—	128	285	—	[40, 85]
AA6063/10 wt% TiB_2	In situ casting route	—	110	—	—	[41, 73]
A356/12.5 wt% TiB_2	Exothermic reaction process	—	—	382	324	[42]
AA6061/12 wt% TiB_2	Stir casting	—	72.46	137.86	—	[43]
Al-6Cu-0.2Mg-1Mn/5 wt% TiB_2	In situ casting	—	84	—	—	[44]
AA6061/10 wt% TiB_2	Melt stirring process	—	58	195	—	[45]
AA2219/10 wt% TiB_2	In situ reaction method	—	—	426.97	301.75	[47]
LM/7.5 wt% TiB_2	Mixed salts method	—	—	202	164	[48]
A356/0.5 wt% TiB_2	Stir casting	—	118	—	—	[50]
AA356/7.8 vol% TiB_2	In situ casting	—	—	382	328	[51]
AA6061/7 wt% TiB_2	Mixed salt route	—	47	145	—	[52]
AA6061/9 wt% TiB_2	Exothermic reaction process	—	123	—	—	[54]
Al-4.5%Cu-3%C/15 vol% TiB_2	In situ method	—	—	257.6	—	[55]
Al(CP)/20 vol% TiB_2	Powder metallurgy	—-	—	191	115	[56]
LM25/7.5 wt% TiB_2	In situ reaction casting	81	—	202	164	[57]
Al-4Cu/10 wt% TiB_2	Liquid state in situ casting	—	138	—	—	[58]
AA6061/12 wt% TiB_2	Stir casting	—	77.93	140	—	[60]
AA6061/2.5 wt% TiB_2/10% SiC	Liquid state stir casting	—	71.46	—	—	[64]
AA6061/10 wt% TiB_2	In situ method	—	74.83	165.74	—	[65]
Al(CP)/wt% TiB_2	In situ method	—	—	180	96	[66]
AA7178/9 wt% TiB_2	In situ casting route	—	94	211	—	[67]
Al-7Si/13.12 wt% TiB_2	In situ reaction process	—	102	209	152	[69]
AA6061/20 wt% TiB_2/2Gr	Stir casting route	—	91.4	170	—	[72]
AA6061/2.5 wt% TiB_2/10 wt% SiC	Stir casting	—	75	—	—	[76]
AA6061/10 wt% TiB_2/2 wt% gr	Stir casting	—	79.04	—	—	[77]
AA2219—6 wt%TiB_2/ZrB_2	In situ casting	—	155.6	—	—	[79]
A356/2.5 wt% TiB_2	In situ technique	—	92	—	—	[81, 84]
AA6061/14 wt% TiB_2	In situ technique	—	128	334	—	[83]
AA2009/8 wt% TiB_2 (solution temperature 520°C)	In situ method	—	—	538	364	[86]
AA2024/7 wt% TiB_2	Stir casting	—	116	—	—	[87]
AA7075/12 wt% TiB_2	In situ technique	—	141	287.95	—	[88]

4. Conclusions

This review article examines the impact of titanium diboride (TiB_2) on aluminum matrix composites (AMCs). As seen in the previous section, various authors have discussed the mechanical properties of fabricated Al/TiB_2 composites, such as hardness, tensile strength, compressive strength, and yield strength. It shall be opined that the stir casting technique is the rare one in making Al-TiB_2 composite, whereas the in situ technique is the often-used technique due to its formation of more uniform TiB_2 particles in the matrix. The TiB_2 particles involved composites have rarely utilized squeeze casting, centrifugal casting, stir casting, and compocasting. Al alloys containing TiB_2 reinforcements are to reveal enriched mechanical properties compared to monolithic alloys. Reported works also indicate the linearly augmented mechanical properties with the incorporation of TiB_2. Several research works recommended that tensile strength and hardness of the AMCs were enriched with the inclusion of a rise in mass fraction of TiB_2 particle contents.

Data Availability

The data used to support the findings of this study are included within the article.

Conflicts of Interest

The authors declare that there are no conflicts of interest regarding the publication of this article.

References

[1] L. Li, Z. Han, M. Gao et al., "Microstructures, mechanical properties, and aging behavior of hybrid-sized TiB_2 particulate-reinforced 2219 aluminum matrix composites," *Materials Science and Engineering: A*, vol. 829, Article ID 142180, 2022.

[2] N. Saravanan, V. Yamunadevi, V. Mohanavel et al., "Effects of the interfacial bonding behavior on the mechanical properties of E-glass fiber/nanographite reinforced hybrid composites," *Advances in Polymer Technology*, vol. 2021, Article ID 6651896, 9 pages, 2021.

[3] V. Mohanavel, K. S. Ashraff Ali, S. Prasath, T. Sathish, and M. Ravichandran, "Microstructural and tribologi- cal characteristics of AA6351/Si_3N_4 composites manufactured by stir casting," *Journal of Materials Research and Technology*, vol. 9, no. 6, pp. 14662–14672, 2020.

[4] H. Abdizadeh and M. A. Baghchesara, "Investigation on mechanical properties and frac- ture behavior of A356 aluminum alloy based ZrO_2 particle reinforced metal-matrix composites," *Ceramics International*, vol. 39, no. 2, pp. 2045–2050, 2013.

[5] D. Dey, A. Bhowmik, and A. Biswas, "Influence of TiB_2 addition on friction and wear behavior of Al2024-TiB_2 ex-situ composites," *Trans Nonferrous Met Soc China*, vol. 31, pp. 1249–1261, 2021.

[6] H. Wang, H. Zhang, Z. Cui, Z. Chen, and D. Chen, "Compressive response and microstructural evolution of in-situ TiB_2 particle-reinforced 7075 aluminum matrix composites," *Trans Nonferrous Met Soc China*, vol. 31, pp. 1235–1248, 2021.

[7] A. Mohan Kumar, R. Rajasekar, P. Manoj Kumar, R. Parameshwaran, A. Karthick, and M. Muhibbullah, "Comparative analysis of drilling behaviour of synthetic and natural fiber-based composites," *Advances in Materials Science and Engineering*, vol. 2021, Article ID 9019334, 13 pages, 2021.

[8] P. Gurusamy, T. Sathish, V. Mohanavel et al., "Finite element analysis of temperature distribution and stress behavior of squeeze pressure composites," *Advances in Materials Science and Engineering*, vol. 2021, Article ID 8665674, 9 pages, 2021.

[9] R. Liu, W. Wang, H. Chen, and S. Wan, "Comparative study of recrystallization behavior and nanoindentation prop- erties of micro-/nano-bimodal size B4C particle-reinforced aluminium matrix composites under T6 and elec- tropulsing treatment," *Journal of Alloys and Compounds*, vol. 788, pp. 1056–1065, 2019.

[10] G. S. Guggari, S. Shivakumar, G. A. Manjunath et al., "Thermal and mechanical properties of vinyl ester hybrid composites with carbon black and glass reinforcement," *Advances in Materials Science and Engineering*, vol. 2021, Article ID 6030096, 7 pages, 2021.

[11] Z. Chen, T. Wang, Y. Zheng, and Y. Zhao, "Development of TiB2 reinforced aluminum foundry alloy based in situ composites - Part I: an improved halide salt route to fabricate Al-5wt%TiB2 master composite," *Mater Sci Eng A*, vol. 605, pp. 301–309, 2014.

[12] L. Zhenglong, B. Jiang, C. Yanbin, C. Xi, T. Ze, and Q. Xikun, "Effect of TiB_2 content on microstructural features and hardness of TiB_2/AA7075 composites manufactured by LMD," *Journal of Manufacturing Processes*, vol. 53, pp. 283–292, 2020.

[13] T. Sathish, S. Tharmalingam, V. Mohanavel et al., "Weldability investigation and optimization of process variables for TIG-welded aluminium alloy (AA 8006)," *Advances in Materials Science and Engineering*, vol. 2021, Article ID 2816338, 17 pages, 2021.

[14] K. Tian, Y. Zhao, L. Jiao, and S. Zhang, "Effects of in situ generated ZrB2 nano-particles on microstructure and tensile properties of 2024Al matrix composites," *Journal of Alloys and Compounds*, vol. 594, pp. 1–6, 2014.

[15] S. Ray, "Review synthesis of cast metal matrix particulate composites," *Journal of Materials Science*, vol. 28, pp. 5397–5413, 1993.

[16] R. Taherzadeh Mousavian, S. R. Damadi, R. Azari Khosroshahi, D. Brabazon, and M. Mohammadpour, "A comparison study of applying metallic coating on SiC particles for manufacturing of cast aluminum matrix composites," *International Journal of Advanced Manufacturing Technology*, vol. 81, no. 1-4, pp. 433–444, 2015.

[17] U. Muthuraman, R. Shankar, V. K. Nassa et al., "Energy and economic analysis of curved, straight, and spiral flow flat-plate solar water collector," *International Journal of Photoenergy*, 2021.

[18] V. Mohanavel, K. Rajan, S. Suresh Kumar, A. Chockalingam, A. Roy, and T. Adithiyaa, "Synthesis, mechanical and tribological characterization of stir-cast Al-SiCp composites," *Materials Today: Proceedings*, vol. 5, no. 1, pp. 1740–1746, 2018.

[19] H. Zhu, Bo Hua, T. Cui, and J. Huang, "Microwave combustion synthesis of in situ Al 2 O 3 and Al 3 Zr reinforced aluminum matrix composites," *Materials Research Bulletin*, vol. 68, pp. 283–288, 2015.

[20] Ö. Savas¸ and R. Kayikci, "Production and wear properties of metal matrix composites reinforced with boride particles," *Materials & Design*, vol. 51, pp. 641–647, 2013.

[21] V. Mohanavel, K. Rajan, S. Arul, and P. V. Senthil, "Production, Microstructure and Mechanical behavior of AA6351/TiB_2 composite synthesized by direct melt reaction method," *Materials Today: Proceedings*, vol. 4, no. 2, pp. 3315–3324, 2017.

[22] D. Dey, A. Bhowmik, and A. Biswas, "Charcaterization of Physical and mechanical properties of aluminium based composites reinforced with titanium diboride particulates," *Journal of Composite Materials*, vol. 55, no. 14, p. 2021, 1979–1991.

[23] D. Srinivasan, G. Veerappan, M. Ravichandran et al., "Investigation on electric erosion behavior of nickel-based super alloy (Waspaloy: Ni, Cr, Co, Mo, Ti, Al) using response surface methodology," *Surface Topography: Metrology and Properties*, vol. 9, no. 3, Article ID 035006, 2021.

[24] C. Mallikarjuna, S. M. Shashidhara, U. S. Mallik, and K. I. Parashivamurthy, "Grain refinement and wear properties evaluation of aluminum alloy 2014 matrix-TiB2 in-situ composites," *Materials & Design*, vol. 32, no. 6, pp. 3554–3559, 2011.

[25] Y. Ma, Z. Chen, M. Wang, D. Chen, N. Ma, and H. Wang, "High cycle fatigue behavior of the in-situ TiB2/7050 composite," *Mater Sci Eng A*, vol. 640, pp. 350–356, 2015.

[26] S. M. Ma, P. Zhang, G. Ji et al., "Microstructure and mechanical properties of friction stir processed Al–Mg–Si alloys dispersion-strengthened by nanosized TiB2 particles," *Journal of Alloys and Compounds*, vol. 616, pp. 128–136, 2014.

[27] J. Lei, Y. Zhao, Y. Wu, D. Chen, and X. Wang, "Microstructures of in-situ TiB2/7055Al composites by the ultrasonic and magnetic coupled field," *Rare Metal Materials and Engineering*, vol. 43, no. 1, pp. 6–10, 2014.

[28] T. Hong, X. Li, H. Wang, D. Chen, and K. Wang, "Effects of TiB2 particles on aging behavior of in-situ TiB2/Al- Cu-Mg composites," *Mater Sci Eng A*, vol. 624, pp. 110–117, 2015.

[29] K. Niranjan and P. R. Lakshminarayanan, "Dry sliding wear behaviour of in situ Al–TiB2 composites," *Materials & Design*, vol. 47, pp. 167–173, 2013.

[30] S. L. Zhang, X. W. Dong, Y. T. Zhao et al., "Preparation and wear properties of TiB2/Al-30Si composites via in- situ melt reactions under high-energy ultrasonic field," *Trans Nonferrous Met Soc China*, vol. 24, pp. 3894–3900, 2014.

[31] H. B. Michael Rajan, S. Ramabalan, I. Dinaharan, and S. J. Vijay, "Effect of TiB2 content and temperature on sliding wear behavior of AA7075/TiB2 in situ aluminum cast composites," *Archives of Civil and Mechanical Engineering*, vol. 14, no. 1, pp. 72–79, 2014.

[32] J. Sun, X. Zhang, Y. Zhang, N. Ma, and H. Wang, "Effects of alloy element on the morphology transformation of TiB2 particles in Al matrix," *Micron*, vol. 70, pp. 21–25, 2015.

[33] C. S. Ramesh, S. Pramod, and R. Keshavamurthy, "A study on microstructure and mechanical properties of Al 6061–TiB2 in-situ composites," *Materials Science and Engineering: A*, vol. 528, no. 12, pp. 4125–4132, 2011.

[34] T. V. Christy, N. Murugan, and S. Kumar, "A comparative study on the microstructures and mechanical properties of Al6061 alloy and the MMC Al6061/TiB2/12p," *Journal of Minerals and Materials Characterization and Engineering*, vol. 9, pp. 57–65, 2010.

[35] F. Chen, Z. Chen, F. Mao, T. M. Wang, and Z. Cao, "TiB2 reinforced aluminum based In-situ composites fabricated by stir casting," *Mater Sci Eng A*, vol. 625, pp. 357–368, 2015.

[36] M. Wang, D. Chen, Z. Chen, Y. W. Feifei, W. Naiheng, and H. Wang, "Mechanical properties of In-situ TiB2/A356 composites," *Mater Sci Eng A*, vol. 590, pp. 246–254, 2014.

[37] N. R. Rajasekaran and V. Sampath, "Effect of in situ TiB2 particle addition on the mechanical properties of AA2219 Al alloy composite," *Journal of Minerals and Materials Characterization and Engineering*, vol. 10, pp. 527–534, 2011.

[38] C. S. Ramesh, A. Ahamed, B. H. Channabasappa, and R. Keshavamurthy, "Development of Al 6063–TiB2 in situ composites," *Materials & Design*, vol. 31, no. 4, pp. 2230–2236, 2010.

[39] S. Suresh, N. Shenbaga Vinayaga Moorthi, S. C. Vettivel, and N. Selvakumar, "Mechanical behavior and wear prediction of stir cast Al–TiB2 composites using response surface methodology," *Materials & Design*, vol. 59, pp. 383–396, 2014.

[40] H. B. Michael Rajan, S. Ramabalan, I. Dinaharan, and S. J. Vijay, "Synthesis and characterization of in situ formed titanium diboride particulate reinforced AA7075 aluminum alloy cast composites," *Materials & Design*, vol. 44, pp. 438–445, 2013.

[41] S. Natarajan, R. Narayanasamy, S. P. Kumaresh Babu, G. Dinesh, B. Anil Kumar, and K. Sivaprasad, "Sliding wear behaviour of Al 6063/TiB2 in situ composites at elevated temperatures," *Materials & Design*, vol. 30, no. 7, pp. 2521–2531, 2009.

[42] F. Wang, J. Xu, J. Li, X. Li, and H. Wang, "Fatigue crack initiation and propagation in A356 alloy reinforced with In-situ TiB2 particles," *Mater Des*, vol. 33, pp. 236–241, 2012.

[43] S. Suresh and N. Shenbaga Vinayaga Moorthi, "Process development in stir casting and investigation on microstructures and wear behavior of TiB2 on Al6061 MMC," *Procedia Engineering*, vol. 64, pp. 1183–1190, 2013.

[44] F. Xie and Z. H. Xue, "Characterizing an in situ TiB2 particulates reinforced aluminium-based composite and its heat treatment," *Physics Procedia*, vol. 50, pp. 13–18, 2013.

[45] S. Johny James, K. Venkatesan, P. Kuppan, and R. Ramanujam, "Comparative study of composites reinforced with SiC and TiB2," *Procedia Engineering*, vol. 97, pp. 1012–1017, 2014.

[46] P. T. Li, Y. Li, Y. Wu, and Ma G. Liu, "Distribution of TiB2 particles and its effects on the mechanical properties of A390 alloy," *Mater Sci Eng A*, vol. 546, pp. 146–152, 2012.

[47] D. Chen, M. L. Wang, Y. J. Zhang, X. F. Li, Z. Chen, and N. H. Ma, "Microstructure and mechanical properties of TiB2/2219 composites," *Materials Research Innovations*, vol. 18, no. sup4, pp. 514–518, 2014.

[48] S. Madhavan and S. Balasivanandha Prabu, "Deformation behaviour and failure mechanisms of Al–TiB2in situcomposites," *Materials Science and Technology*, vol. 29, no. 3, pp. 268–272, 2013.

[49] P. Hosseini Vajargah, H. Abdizadeh, and M. A. Baghchesara, "Fabrication of TiB2 nanoparticulates-reinforced aluminum matrix composites by powder metallurgy route," *Journal of Composite Materials*, vol. 49, no. 25, pp. 3115–3125, 2015.

[50] M. Karbalaei Akbari, S. Rajabi, K. Shirvanimoghaddam, and H. R. Baharvandi, "Wear and friction behavior of nanosized TiB2 and TiO2 particle-reinforced casting A356 aluminum nanocomposites: a comparative study focusing on particle capture in matrix," *Journal of Composite Materials*, vol. 49, no. 29, pp. 3665–3681, 2015.

[51] F. Wang, J. Li, J. Xu, X. Li, Y. Zhang, and H. Wang, "Investigation on fracture toughness of aluminum matrix composites reinforced with In-situ titanium diboride particles," *Journal of Composite Materials*, vol. 46, pp. 2145–2150, 2011.

[52] V. Auradi, S. L. Biradar, S. M. Suresha, and S. A. Kori, "Microstructure and mechanical characterization of Al-Tib_2

in situ metal matrix composites produced via master alloy route," *Applied Mechanics and Materials*, vol. 592-594, pp. 494–498, 2014.

[53] D. Chen, Z. Chen, P. Zhang et al., "Bending properties of AA7075 aluminium alloy reinforced with in-situ TiB2 particles," *Advanced Materials Research*, pp. 1005–1010, 2012.

[54] V. Anandakrishnan and A. Mahamani, "Investigations of flank wear, cutting force, and surface roughness in the machining of Al-6061–TiB2 in situ metal matrix composites produced by flux-assisted synthesis," *International Journal of Advanced Manufacturing Technology*, vol. 55, no. 1-4, pp. 65–73, 2011.

[55] K. L. Tee, L. Lü, and M. O. Lai, "Improvement in mechanical properties of in-situ Al–TiB2 composite by incorporation of carbon," *Materials Science and Engineering: A*, vol. 339, no. 1-2, pp. 227–231, 2003.

[56] S. C. Tjong and K. F. Tam, "Mechanical and thermal expansion behavior of hipped aluminum–TiB2 com- posites," *Materials Chemistry and Physics*, vol. 97, no. 1, pp. 91–97, 2006.

[57] S. Madhavan, S. Balasivanandha Prabu, and K. A. Padmanabhan, "On the role of process parameters of aluminothermic reaction synthesis of in-situ Al-TiB2 composites: microstructure and mechanical proper- ties," *Letters on Materials*, vol. 4, no. 2, pp. 84–88, 2014.

[58] A. Mandal, M. Chakraborty, and B. S. Murty, "Effect of TiB2 particles on sliding wear behaviour of Al–4Cu alloy," *Wear*, vol. 262, no. 1-2, pp. 160–166, 2007.

[59] N. B. Dhokey, "Effect of KBF4 and K2TiF6 on precipitation kinetics of TiB2 in aluminium matrix composite," *Advanced Materials Letters*, vol. 2, no. 3, pp. 210–216, 2011.

[60] S. Suresh, N. Shenbaga Vinayaga Moorthi, and C. Emmy Prema, "Tribological and mechanical behav- ior study of Al6061-TiB_2 metal matrix composites using stir casting," *Advanced MateriAls Research*, vol. 984-985, pp. 200–206, 2014.

[61] R. Shobha, K. R. Suresh, and H. B. Niranjan, "Mechanical and microstructural evaluation of InsituAluminium titanium boride composite processed by severe plastic deformation," *Procedia Materials Science*, vol. 5, pp. 281–288, 2014.

[62] L. ü Peng, X. Yue, H. Ru, and Y. Liang, "Microstructure and mechanical properties of B4C- TiB2-Al composites fabricated by vacuum infiltration," *Rare Metals*, vol. 29, no. 1, pp. 92–97, 2010.

[63] J. Onora, "High-temperature mechanical properties of aluminium alloys reinforced with titanium diboride (TiB2) particles," *Rare Met*, vol. 30, pp. 200–205, 2011.

[64] G. Mahajan, N. Karve, U. Patil, P. Kuppan, and K. Venkatesan, "Analysis of microstructure, hard- ness and wear of Al-SiC-TiB_2 hybrid metal matrix composite," *Indian Journal of Science and Technology*, vol. 8, no. S2, p. 101, 2015.

[65] T. V. Christy, *Production, Characterization and Friction Stir Welding of Al-TiB2 Metal Matrix Composite*, Anna University, Chennai, 2010.

[66] N. B. Dhokey and K. K. Rane, "Wear behavior and its correlation with mechanical properties of TiB2Reinforced aluminium-based composites," *Advances in Tribology*, vol. 2011, Article ID 837469, 8 pages, 2011.

[67] V. Mohanavel, "Mechanical and microstructural characterization of AA7178-TiB2 composites," *Materials Testing*, vol. 62, no. 2, pp. 146–150, 2020.

[68] K. L Tee, L. Lu, and M. O Lai, "Synthesis of in situ Al–TiB2 composites using stir cast route," *Composite Structures*, vol. 47, no. 1-4, pp. 589–593, 1999.

[69] S. Kumar, M. Chakraborty, V. Subramanya Sarma, and B. S. Murty, "Tensile and wear behaviour of in situ Al–7Si/TiB2 particulate composites," *Wear*, vol. 265, no. 1-2, pp. 134–142, 2008.

[70] L. Lu, M. O. Lai, and F. L. Chen, "Al-4 wt% Cu Composite reinforced with in-situ TiB2 particles," *Acta Materialia*, vol. 45, no. 10, pp. 4297–4309, 1997.

[71] M. Karbalaei Akbari, H. R. Baharvandi, and K. Shirvanimoghaddam, "Tensile and fracture behavior of nano/micro TiB2 particle reinforced casting A356 aluminum alloy composites," *Materials & Design*, vol. 66, pp. 150–161, 2015.

[72] S. Suresh, N. Shenbaga Vinayaga Moorthi, S. C. Vettivel, N. Selvakumar, and G. R. Jinu, "Effect of graphite addition on mechanical behavior of Al6061/TiB2 hybrid composite using acoustic emission," *Materials Sci- ence and Engineering: A*, vol. 612, pp. 16–27, 2014.

[73] K. Sivaprasad, S. P. Kumaresh Babu, S. Natarajan, R. Narayanasamy, B. AnilKumar, and G. Dinesh, "Study on abrasive and erosive wear behaviour of Al 6063/TiB2 in situ composites," *Materials Science and Engineering: A*, vol. 498, no. 1-2, pp. 495–500, 2008.

[74] C. S. Ramesh and A. Ahamed, "Friction and wear behaviour of cast Al 6063 based in situ metal matrix composites," *Wear*, vol. 271, no. 9-10, pp. 1928–1939, 2011.

[75] K. Niranjan and P. R. Lakshminarayanan, "Optimization of process parameters for in situ casting of Al/TiB2 composites through response surface methodology," *Transactions of Nonferrous Metals Society of China*, vol. 23, no. 5, pp. 1269–1274, 2013.

[76] S. Johny James, K. Venkatesan, P. Kuppan, and R. Ramanujam, "Hybrid aluminium metal matrix composite reinforced with SiC and TiB2," *Procedia Engineering*, vol. 97, pp. 1018–1026, 2014.

[77] C. M. Anand Partheeban, M. Rajendran, S. C. Vettivel, S. Suresh, and N. S. V. Moorthi, "Mechanical behav- ior and failure analysis using online acoustic emission on nano-graphite reinforced Al6061–10TiB2 hybrid composite using powder metallurgy," *Materials Science and Engineering: A*, vol. 632, pp. 1–13, 2015.

[78] X. Jing, W. Jun, H. Y. Feng, C. Chong, and Sb Ole, "Behaviour of CeO2 additive in in-situ TiB2 particles reinforced Al alloy composite," *Trans Nonferrous Met Soc China*, vol. 22, pp. 1012–1017, 2014.

[79] A. Mahamani, A. Karthik, S. Karthikeyan, P. Kathiravan, and Y. P. Kumar, "Synthesis, Quantitative elemen- tal analysis, Microstructure characteristics and micro hardness analysis of AA2219 aluminium alloy matrix composite reinforced by In-situ TiB2 and sub-micron ZrB2 particles," in *Proceedings of the Frontiers in Automobile and Mechanical Engineering*, pp. 50–53, IEEE, Chennai,India, Nov 2010.

[80] J. Xue, J. Wang, Y. Han, L. Pan, and B. Sun, "Effects of CeO2 additive on the microstructure and mechanical properties of in situ TiB2/Al composite," *Journal of Alloys and Compounds*, vol. 509, no. 5, pp. 1573–1578, 2011.

[81] A. Mandal, B. S. Murty, and M. Chakraborty, "Sliding wear behaviour of T6 treated A356–TiB2 in-situ composites," *Wear*, vol. 266, no. 7-8, pp. 865–872, 2009.

[82] S. C Tjong and K. C Lau, "Properties and abrasive wear of TiB 2/Al-4%Cu composites produced by hot iso- static pressing," *Composites Science and Technology*, vol. 59, no. 13, pp. 2005–2013, 1999.

[83] S. J. Vijay, "Investigation on Al6061-TiB2 in-situ metal matrix composite," *Production, Friction Stir Welding and Characterization*, Anna University, Chennai, 2014.

[84] A. Mandal, M. Chakraborty, and B. S. Murty, "Ageing behaviour of A356 alloy reinforced with in-situ formed TiB2 particles," *Materials Science and Engineering: A*, vol. 489, no. 1-2, pp. 220–226, 2008.

[85] H. B. Michael Rajan, I. Dinaharan, S. Ramabalan, and E. T. Akinlabi, "Influence of friction stir processing on microstructure and properties of AA7075/TiB 2 in situ composite," *Journal of Alloys and Compounds*, vol. 657, pp. 250–260, 2016.

[86] T. Hong, X. Li, H. Wang, and D. Chen, "Influence of solution temperature on microstructure and properties of in-situ TiB2/2009 composites," *Mater Sci Eng A*, vol. 634, pp. 1–4, 2015.

[87] D. Dey, A. Bhowmik, and A. Biswas, "Wear behavior of stir casted aluminum-titanium diboride (Al2024-TiB2) composite," *Materials Today: Proceedings*, vol. 26, pp. 1203–1206, 2020.

[88] D. Sethi, S. Kumar, S. Choudhury, S. Shekhar, and B. S. Roy, "Synthe- sis and characterization of AA7075/TiB2 aluminum matrix composite formed through stir casting method," *Materials Today: Proceedings*, vol. 26, pp. 1908–1913, 2020.

Hindawi
Advances in Materials Science and Engineering
Volume 2021, Article ID 8273708, 10 pages
https://doi.org/10.1155/2021/8273708

Research Article

Characterization of TiZrN and TaZrN Nanocomposite Multilayer Coating Deposited via RF/DC Magnetron Sputtering on AISI4140 Steel

R. Hariharan,[1] **R. Raja**,[2] **R. J. Golden Renjith Nimal**,[3] **Mohamad Reda A. Refaai**,[4] **S Ravi**,[5] **and Haiter Lenin Allasi**[6]

[1]*Department of Mechanical Engineering, Bharath Institute of Higher Education and Research, Chennai-73, Tamilnadu, India*
[2]*VPMM Engineering College for Women, Srivilliputhur 626190, Tamilnadu, India*
[3]*Department of Mechanical Engineering, Jai Shriram Engineering College, Tirupur-638660, Tamilnadu, India*
[4]*Prince Sattam Bin Abdulaziz University, College of Engineering Department of Mechanical Engineering, Alkharj 16273, Saudi Arabia*
[5]*Centre for Materials Research, Chennai Institute of Technology, Chennai 600069, Tamilnadu, India*
[6]*Department of Mechanical Engineering, Wollo University Kombolcha Institute of Technology, Kombolcha, Ethiopia*

Correspondence should be addressed to R. Hariharan; hariharan.mech@bharathuniv.ac.in and Haiter Lenin Allasi; drahlenin@kiot.edu.et

Received 28 September 2021; Revised 4 November 2021; Accepted 13 November 2021; Published 22 December 2021

Academic Editor: P Ganeshan

In this present research work, TiZrN and TaZrN multilayer coating was deposited on 4140 steel by RF/DC magnetron sputtering for comparative work also prepared in single layer. The flow rate ratio of Ar/N2 was set to 15 : 3 sccm and the thin film was prepared by the PVD (physical vapor deposition) method by RF/DC magnetron using a Ti-Zr and Ta-Zr target with a purity of 99.99%. The crystal structure, surface morphology microstructure, and component arrangements were explored by X-ray diffraction (XRD), scanning electron microscope (SEM), and atomic force microscopy (AFM). It has been found that the crystal structure, surface morphology, microstructure, and elemental composition of the membrane are strongly dependent on deposition parameters. It is mechanically characterized by corrosion and Vickers hardness. In AFM measurements, coarse cluster particles with increasing Ti and Ta values not only increase the average roughness (Ra) by 2.341 nm (200°C) and 2.951 nm (400°C) but also have a continuous average thickness which was shown to increase by 1.504 nm and 781.75 nm. With the increase of hardness, the roughness decreases correspondingly. The TiZrN multilayer microhardness augmented to 314 GPa at 200°C and 371 GPa for TaZrN (400°C).

1. Introduction

There are various methods and processes for depositing TiZrN thin films, as most of them are made by a large applied arc current. However, the advantage of the deposition technology is that there is no additional request form, no polarized substrate, and a low temperature, which can reduce production time and thus manufacturing costs. The aim of this work was the deposition of nano structured thin TiZrN layers on unheated substrates without polarization of the substrate at different Ti sputtering currents with simultaneous asymmetrical DC magnetron sputtering [1–3]. The effect of the Ti sputtering current on the crystal structure morphology was analyzed.

Tantalum nitride is chemically inert, corrosion resistant, and hard. TaN thin films are thus gaining increasing attention for thin film resistors and diffusion barriers in the microelectronics industry. These films are known for their high temperature stability and their ability to resist oxidation up to 8000°C. TaZrN coatings can resist oxidation up to 13000°C [4, 5]. There have been investigations carried out on the mechanical properties of TaN films, which clearly

indicate their potential of being used as high hardness coatings. Some compounds present in TaN at high N_2 flow and higher substrate temperature, such as orthorhombic Ta4N and FCC TaN have theoretical hardness of 61 and 50 GPa, respectively, although other researchers have reported the FCC phase to have hardness around 20 GPa.

On the other hand, when we use these two high-k materials individually, there was a problem with the electronic instabilities of zirconium oxide on Si substrate [6]. Eventually, there would be an unstable interface at ZrO_2/Si stacks TiO_2/Si. Due to the very low offset of the conduction band, high leakage currents occur even at low temperatures. In order to accumulate the benefits of both oxide layers simultaneously in one device, we propose interface engineering that supports the chemical composition and physical structure of the titanium-doped zirconium oxide ($ZrTiO_2$) layer. Zr-doped TiO_2 thin films can be prepared by plasma-assisted pulsed laser deposited and atomic layer deposition, electron beam evaporation, DC magnetron sputtering, RF magnetron sputtering, and chemical deposition methods, namely, chemical bath deposition, chemical spray pyrolysis method, and sol-gel spin coating method.

2. Materials and Method

The TiZrN/TaZrN nanocomposite film is made by depositing titanium (Ti) and zirconium (Zr). The target and the tantalum (Ta) are each 99.99% pure. The initial pressure was reduced to 4×10^{-3} mbar and the target was presprayed for 5 minutes to remove contaminants from the target surface before injection. A high purity reactive gas (99.999%) is introduced into a vacuum chamber to form a thin TiZr/Ta–Zr film. Argon and nitrogen flow rates were adjusted to constant values throughout the investment. Table 1 shows the deposition parameters for the TiZrN coating [7]. Table 2 shows the chemical compositions of E19 steel.

3. Results and Discussion

3.1. Crystal Structure. Figures 1(a)–1(c) show the XRD shapes of samples S1 and S2 (TiZrN and TaZrN). The angle of incidence of X-rays was 0.5° and angle 2 was scanned from 20° to 59.983°. The 2 angles of the vertices were obtained by adjusting each vertex based on the Gaussian or Lorentz distribution hypothesis. The XRD models showed no additional phases not observed by the XRD. The crystalline level of TiZrN, i.e., (101), (101), (102), (103), and (200), was observed in the XRD pattern of sample S1 (Figure 1(a)). S2 sample models (Figure 1(b)) show that there were two phases in these bands, namely, TiZrN. As the current increased, the XRD intensity of level (101), (220), and (222) increased but decreased for level (200) [7]. The intensity of the plane (200) changed significantly, indicating a preferred orientation with maximum intensity. The development of the crystal structure is attributed to the additional energy of the deposition atoms on the substrate surface during the formation of the membrane, which leads to greater mobility of the Ad atom and therefore to greater crystalline of the membranes due to longer deposition time (60 minutes) [8–13]. In addition, the observation is that the XRD 2Θ peaks shift at lower Bragg angles than in the standard TiN refraction model, which shows the extraction of the lattice by replacing Zr atoms with Ti atoms in the TiN structure. Full width at half maximum (FWHM) is 0.4047 and I/Io is 143.31. Rp is the calculated model Rp = 72.4% and (200) the simple cubics present in the 45 present can have a base of multiple atoms. It has been found that the growth films consist of a simple cubic Ti–Zr–N structure. The crystal system is tetragonal, and the space group is I 4/mm (139). Cell characteristics were estimated using XRD analysis for the Ti–Zr–N structure and carried out using a wavelength of 1.541874 Å.

Table 1: Operating parameters for deposition of TiZrN/TaZrN thin film coating.

Parameters	TiZrN	TaZrN
Chamber base pressure	4×10^{-6} m bar	4×10^{-6} m bar
Deposition pressure	4×10^{-3} m bar	4×10^{-3} m bar
$Ar : N_2$ flow rate	15 : 3 sccm	15 : 3 sccm
Target distance	70 mm	70 mm
Substrate temperature	200°C and 400°C	200°C and 400°C
Interlayer	60 min	60 min
Ti (DC) and Ta (DC)	100 W	100 W
Zr (RF)	100 W	100 W

It can be easily confirmed by XRD data from TaZrN samples (Figure 1(c)). The full diffraction spectrum shows the typical plane distance of the TaZrN structure. Figure 1(c) shows the spectra of samples S1 and S2, which correspond to two extreme cases in terms of composition (Table 3). These data show clear directions (111) and (200), although other diffractions are also observed. A physical property of the cal. density is 13.434 g/cm^3 wave length 1.5309 Å to the FWHM 0.4047 and the 2θ is 41.81 (Sample S2 Figure 1(c)). The lack of separate diffraction groups for the two cubic grids indicates that the film studied is not an amphiphilic mixture of Ta and Zr due to the similarity between the two structural properties [14]. Figure 1(c) shows the grid parameters as a function. Tantalum material is represented by the composition Ta/(Zr + Ta), which clearly shows that the stored tape is a step. The data range is 20°–59.983°, and the wave length is 1.541874 Å [4]. Cubic cell parameters was taken at $a = 4.43400$ Å (sample S1 in Figure 1(c)).

4. Scanning Electron Microscope

Figures 2(a) and 2(b) show SEM cross-sectional images of the remaining samples at constant nitrogen and argon flow rates. Although the column is not visible in the sample remaining at 200°C, the structure becomes clearer as the flow rate increases. The thickness of the TiZrN tape ranges from 500 to 1000 nm and decreases with increasing temperature within a fixed storage time of 60 minutes [9]. The storage time is calculated by dividing the thickness by the storage time. The difference between the storage rate and the temperature ratio is shown in Figure 2. When the constant nitrogen flow rate increases, the decrease in the supply of Ti and Zr atoms decreases with increasing temperature so that the rate of precipitation decreases. In this process, the high

Table 2: Chemical compositions of E19 steel.

C (%)	S (%)	Si (%)	Cr (%)	Mn (%)	Mo (%)	P (%)
0.35 ~0.45	**≤ 0.050**	**0.10 ~0.35**	**0.90 ~1.50**	**0.50 ~0.80**	**0.20 ~0.40**	**≤0.035**

Bold shows % of chemical composition mixing in E19 steel.

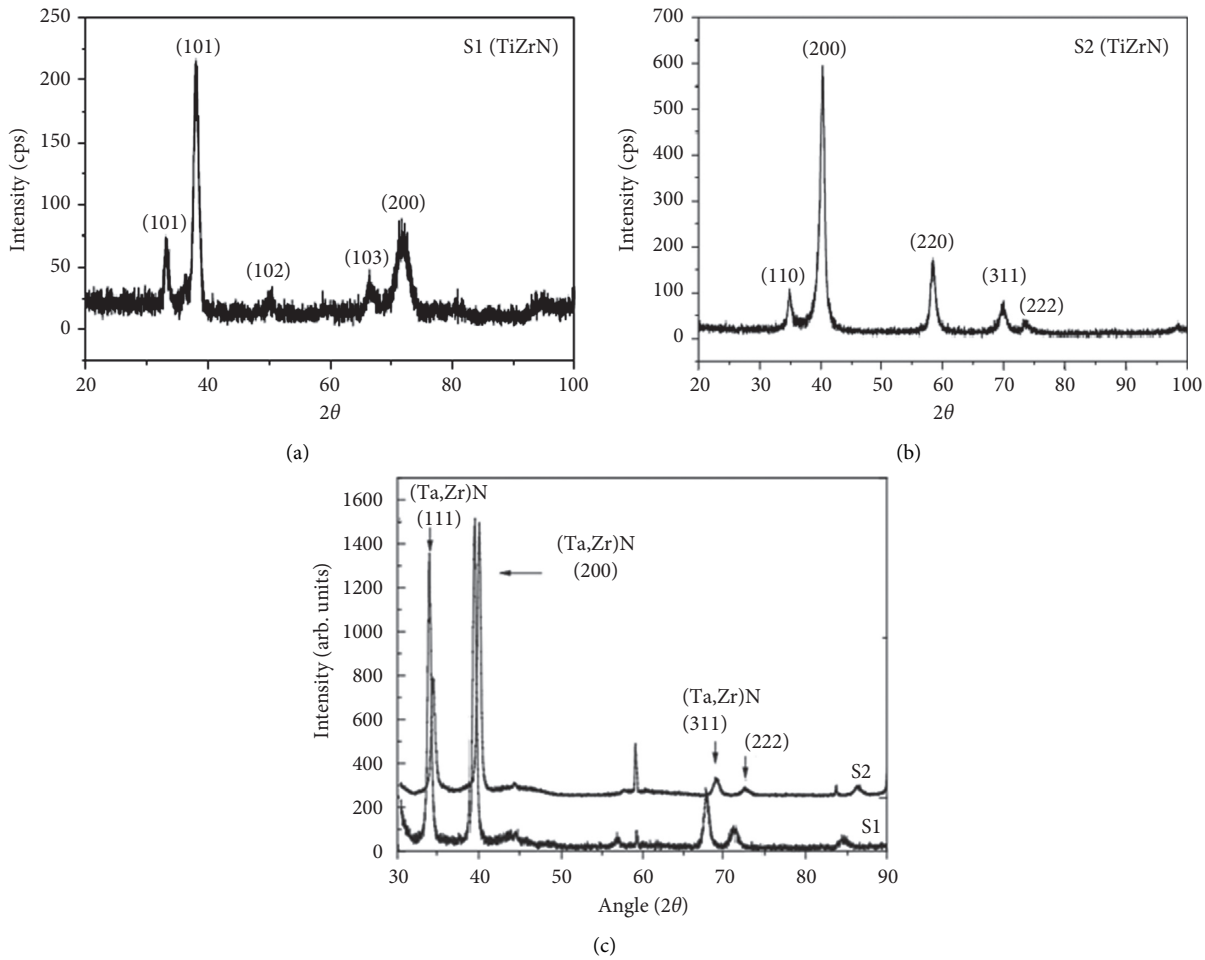

Figure 1: X-ray diffraction patterns of TiZrN/TaZrN films with different temperature contents.

Table 3: Surface roughness and hardness of coated material.

Coating type	Temperature (°C)	Hardness (GPa)	Surface roughness (Ra), nm	Root mean square (Rq), nm	Smooth Coefficient (Rku)	Sel. frequency (Hz)	Amplitude, nm	Scan rate (Hz)
TiZrN	200 (S1)	314	3.222	4.057	3.226	**287.523**	**30.9**	**0.5**
	400 (S2)	272.3	2.951	3.742	3.459			
TaZrN	200 (S1)	371.3	2.341	3.126	5.319			
	400 (S2)	286	2.359	3.186	6.040			

Bold values indicate that AFM was used to examine the surface roughness and hardness of two materials. The frequency, amplitude, and scan rate were all kept at the same value.

N_2 input reduces the concentration and energy of the Ar + ions in the plasma so that a lower Ta content is expected in the coating. Multilayer TaZrN coating is under various R/N_2 inputs [11]. There was an overlap of the columnar crystal structure and the μm residue formed under $R/N_2 = 15/3$ gave a smooth and abnormal image (see Figure 2(d)).

4.1. Atomic Force Microscope. The AFM images (auto probe NC microscope) in Figure 3 show a three-dimensional image of the morphology of the coated surface (5 μm piezoelectric scanner with up to 5 μm background scan area and up to 5 vertical scan area surface maps). Prepared sample temperatures were 200°C and 400°C (TiZrN/TaZrN). The scanning

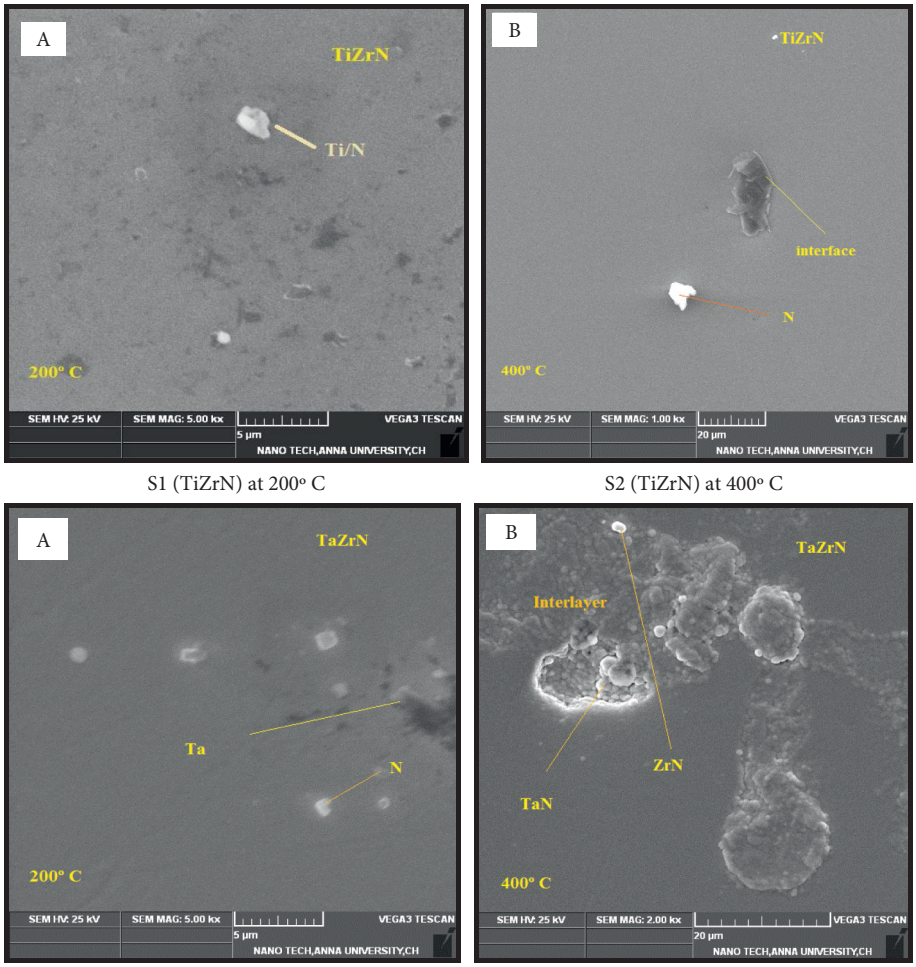

S1 (TiZrN) at 200° C S2 (TiZrN) at 400° C

S1 (TaZrN) at 200° C S1 (TaZrN) at 400° C

Figure 2: Cross-section SEM image of TiZrN/TaZrN films with different temperatures: (a) S1 (TiZrN) at 200°C, (b) S2 (TiZrN) at 400°C, (c) S1 (TaZrN) at 200°C, and (d) S1 (TaZrN) at 400°C.

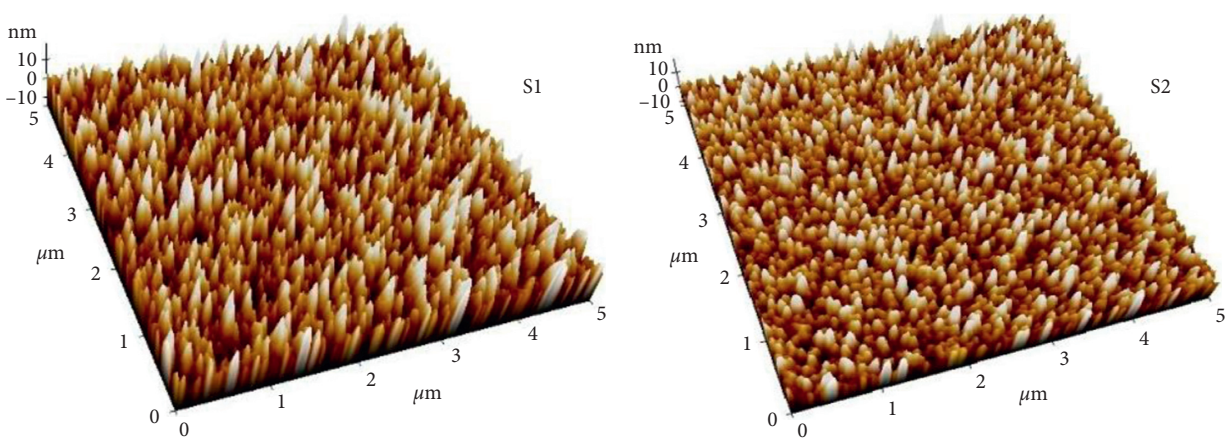

(a) (b)

Figure 3: Continued.

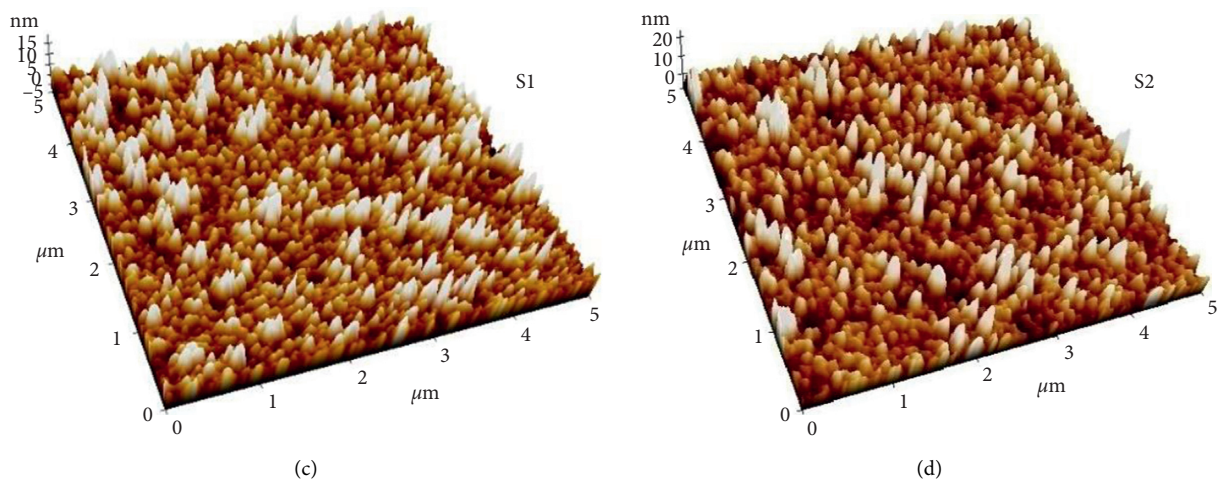

Figure 3: Surface morphology (3D view 5 × 5 μm) of TiZrN/TzZrN deposited at different temperatures: ((a), (c)) 200°C and ((b), (d)) 400°C.

rate, sel. frequency, and amplitude are commonly set by NC-AFM (0.5 Hz, 287.52E3 Hz, and 30.9 nm) Most grains of the same size and mixed grains are stored at 200°C. All grains at 400°C look large on the surface, elongated, and unfolded. Gradually, increase the number of seeds by filling most of the triangular shapes. Adjust the particle volume to form a larger triangle [15–19]. The valley theme and open superstructure are seen on TaZrN. The original root of the sample is Rq 4.057, 3.742 nm (TiZrN), and 3.126, 3.186 nm (TaZrN), respectively (refer Figure 4). AFM shows average thickness 3.222, 2.951 nm for TiZrN and increasing value at TaZrN from 2.341 and 2.359 nm by increasing the temperature (refer Table 3 and Figure 5). The results are related to increased atomic energy and increased temperatures of titanium and tantalum. The thickness of the film is more affected by the Ti and Ta particles coming out of the target. The smooth coefficient (Rku) value increased by corresponding temperature of the given sample. The values are 3.226 and 3.459 for Ti-based and 5.319 and 6.040 for Ta-based (refer Figure 4)

The Vickers hardness (Hv) followed to find the hardness in microscale of Hv0.1 for the test force $F = 0.9807$ N (Const. X test force/surface area of indentation). The hardness of TaZrN/TiZrN samples was measured at three diagonal widths between the grooves. Calculate the mean and standard deviation of hardness and modulus:

$$Hv = 0.102 \times \frac{2F\mathrm{Sin}136^{\circ}/2}{d^2}. \quad (1)$$

The concentration of titanium (isotope element) thermal expansion and electrical resistance is 8.6 μm/m.k at 25°C and 420 nΩm at 20°C, mechanical stability in that pure target was $\mu = 0.32$, $E = 116$ GPa, $\tau = 44$ GPa, and $\rho = 4.506$ g/cm^3. Tantalum has a low thermal and electrical resistance when compared to Ti because of its bcc and tetragonal structure (α-Ta, β-Ta). The mechanical characteristics of pure Ta are $= 0.34$, $E = 186$ GPa, $\tau = 186$ GPa, and $\rho = 16.69$ g/cm^3. Common layer of Zr (91.22 atomic mass unit)-based target has the density and melting point of $\rho = 16.49$ gms/cc and

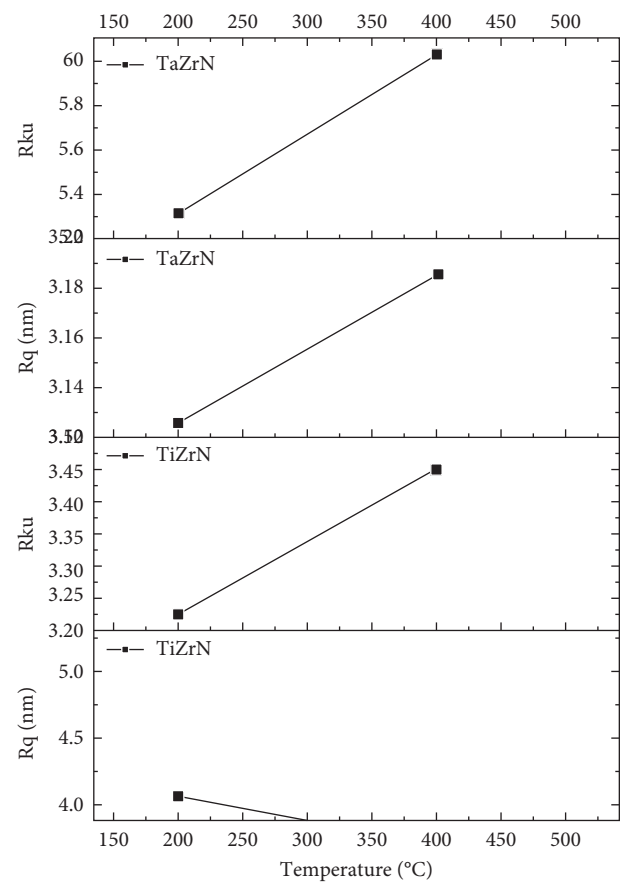

Figure 4: Temperature vs root mean square (Rq) and smooth coefficient (Rku).

1852°C. Multilayer coating hardness and modules are between single TaZrN/TiZrN layers. This means the law of mixing in mechanical behavior. The multilayered structure of this one-component zirconium nitride system helps improve hardness and modulus [20]. Figure 6 shows the hardness of the film and the relationship between tantalum and zirconium materials. The hardness of the film consisting

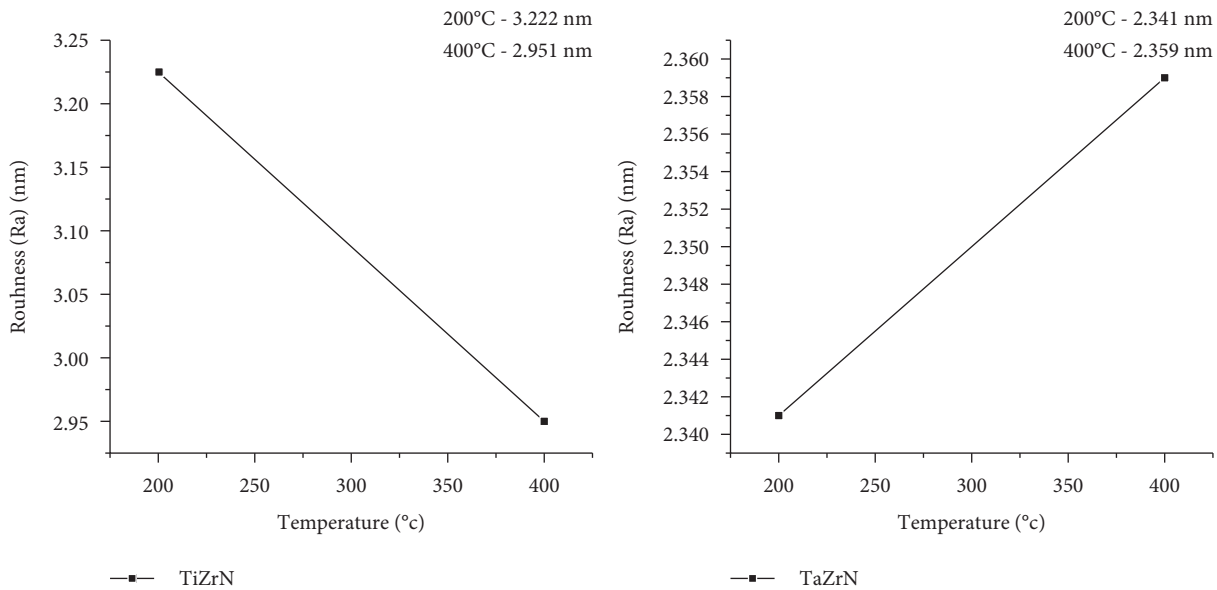

Figure 5: Temperature vs Avg. roughness (Ra).

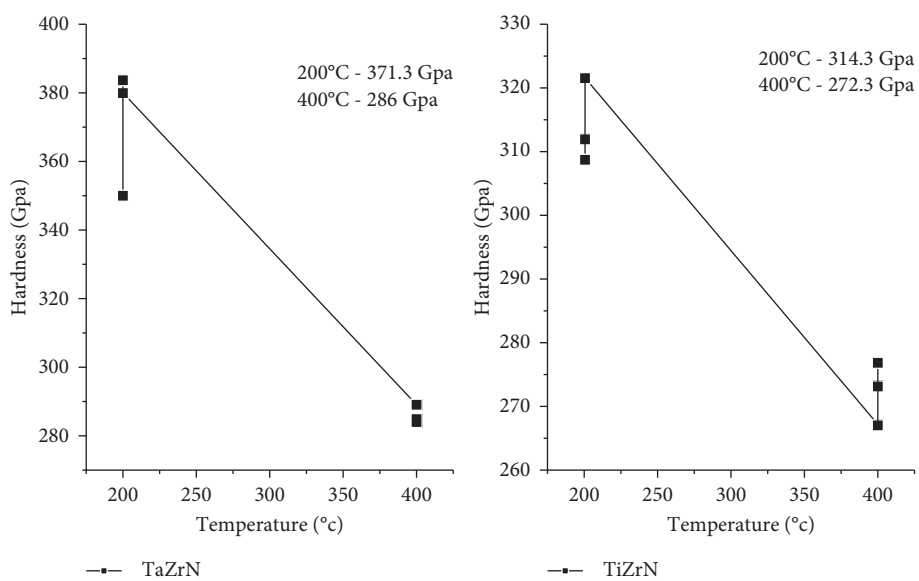

Figure 6: Temperature vs hardness (GPa).

Table 4: Details of testing parameters in constant humidity condensation atmosphere test (ref. 6270:2005 (E)).

Humidity	98% when measured with a hygrometer during a test
Temperature	35 to 45 degrees Celsius
Pr. of air for atomizing	Infinitely variable from 2 to 3 bar with pressure regulator
Mixed with brine (5% of sodium chloride, 1% of magnesium chloride, and deionized water 94%	For 1 liter of solution
pH of the solution	Maintained at 7.5 by the addition of a buffer solution
pH improvement	Measured every 8 hours
Some service providers	Tied with plastic wire and hanged on the hanger

Table 5: Important parameters evaluated from the coated samples of TiZrN/TaZrN tested in salt spray ASTM B-117 (ISO 9227:2017 (CASS TEST)).

pH	Samples	Temp. of solution	Concentration
3.13 to 3.18	TiZrN (200°C and 400°C) TaZrN (200°C and 400°C)	35.3°C ± 2°C	Sodium chloride (5.2% of NaCl + 0.26 g of CuCl2.2H_2O + acetic acid to maintain pH) – 52–53 g/l
6.7 to 7	TiZrN (200°C and 400°C) TaZrN (200°C and 400°C)	49.5°C ± 2°C	Pr. of compressed air 15 psi, collection of sol. Per hr 1.3–1.5 ml

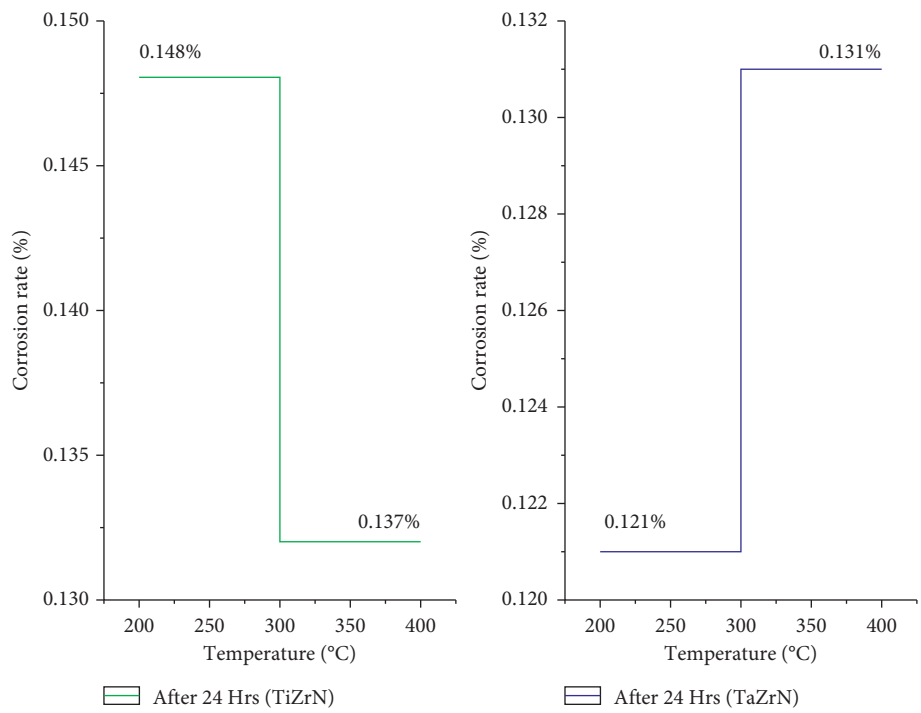

Figure 7: Temperature vs corrosion rate (%) for humidity test.

of Ta (Figure 6, TaZrN) gradually increases to 371.3 GPa. This is about 1.8 times the evenly collected diagonal length of ZrN in the same case. Due to the slight change in the load, the value of the hardness measured under the load has not changed [7, 21]. Due to the hard crystalline phase of TIN, the highest hardness and modulus of approximately 4,314.3 GPa were found in the C-type layer, respectively [11]. The hardness value decreased due to the temperature value increased for Ta and Ti-based and the highest value produced at 200°C in the density of 13.434 g/cm^3 for TaZrN and 6.82200 g/cm3 for TiZrN.

5. Corrosion Behavior

Salt spray technique and humidity fog test made it possible to investigate the corrosion behavior of the TiZrN/TaZrN coating on AISI 4140 steel [11]. This measurement initially initiated the investigation of corrosion behavior. The fog humidity test is shown in Table 4. Then, the salt spray samples were polarized in sodium chloride (5.2% of NaCl + 0.26 g of $CuCl_2.2H_2O$ + acetic acid to maintain pH) – 52–53 g/l, pressure of compressed air 15 psi, and collection of solution per hour 1.3–1.5 ml at air saturated at various pH 3.13 to 3.18 and 6.7 to 7 (Table 5). Effect of TiZrN/TaZrN coatings with anticorrosive behavior 7 shows the polarization curves for various temperature samples with the studied changes in surface roughness [22–28]. The important parameters estimated from the polarization curves are listed in Table 4. It is clear that the multilayer coating significantly affects the corrosion properties of AISI 4140 steel, in particular the corrosion current density (Icorr). In comparison with the corrosion rate of TiZrN/TaZrN samples, the corrosion rate significantly increases with surface roughness (Table 3 and Figure 7). The corrosion rate of humidity test carried temperature increases with increase in corrosion rate of 0.121–0.131% for TaZrN and surface roughness slightly affects the corrosion rate of 0.131–0.148% for TiZrN (Figure 7). This is because a high degree of irritation leads to

more defects in the coating, as well as a smaller sample with fuller coverage. Concentration in 5.2% of NaCl at air saturated at pH 7 exhibited better corrosion resistance. The result of a humidity test at 44°C ± 2°C with a pH of 7.5 was that no rust formed after 24 hours [14, 29–36].

6. Conclusion

Ti-Zr-N/TaZrN coating was synthesized by the method of RF/DC magnetron sputtering by 99.99% purity of targets. With increase of current, the XRD intensities of (101) plane (220) and (222) plane were increased. The Ti-Zr-N/TaZrN coating was done with an XRD intensity of 0.4047 at TiZrN (FWHM), space group I 4/mm (139), and a tetragonal crystal system with cell parameters of $a = 4.01900$ Å and $c = 9.57700$ Å. The data revealed strong (111) and (200) preferred orientations though other diffraction lines were also observed at TaZrN. A physical property of the cal. density is 13.434 g/cm^3 (FWHM) which is 0.4047 and the 2θ value is 59.30 (1.5571 Å) space group which is Fm-3m (225) and the crystal system is cubic [37–44]. The surface roughness of substrate of TiZrN/TaZrN film during corrosion testing is the corrosion rate increased with increasing surface roughness of substrate. Concentration in 5.2% of NaCl at air saturated at pH 7 exhibited better corrosion resistance. The corrosion rate of humidity test carried temperature increases with increase in corrosion rate of 0.121–0.131% for TaZrN and surface roughness slightly affects the corrosion rate of 0.131–0.148% for TiZrN (Figure 7). The hardness of the film (Figure 6, TaZrN) will gradually increase with the Ta value of 371.3 GPa. A highest hardness and modulus are around 314.3 GPa (Figure 6, TiZrN). The hardness value decreased due to the temperature value increased for Ta and Ti-based and the highest value produced at 200°C in the density of 13.434 g/cm^3 for TaZrN and 6.82200 g/cm^3 for TiZrN. AFM are 0.5 Hz, 287.52E3 Hz, and 30.9 nm. The compact morphology of 200°C-stored samples and 400°C-stored whole grains tends to be larger and longer and spread over the surface [37, 38, 45–51]. The particle size gradually increases in a triangular pattern. AFM shows that with increasing temperature, the average thickness continuously decreases from 3.222 to 2.951 nm for TiZrN and the value at TaZrN increases from 2.341 to 2.359 nm by increasing the temperature (see Table 3 and Figure 5). Interatomic energy and temperature of titanium and tantalum increased. It also affects the film thickness of some off-target Ti and Ta particles [4, 5, 39, 52–55]. The transported TiZr NSEM film thickness ranged from 500 to 1000 nm, which decreased with increasing temperature velocity over a 60-minute deposition time (Figure 2). This is probably due to the decrease in the number of Ti and Zr atoms with a constant increase in nitrogen flow. Precipitation decreases as the temperature rises. This will reduce the accumulation rate of Ar/$N = 15/3$ [42].

Data Availability

The data used to support the findings of this study are included within the article. Further data or information is available from the corresponding author upon request.

Conflicts of Interest

The authors declare that there are no conflicts of interest regarding the publication of this article.

Acknowledgments

This project was supported by the Deanship of Scientific Research at Prince Sattam Bin Abdulaziz University under the research project #2020/01/17093.

References

[1] S. M. Aouadi, P. Filip, and M. Debessai, "Characterization of tantalum zirconium nitride sputter-deposited nanocrystalline coatings," *Surface and Coatings Technology*, vol. 187, no. 2-3, pp. 177–184, 2004.

[2] J. A. Woollam, *Guide to Using WVASE32*, Woollam Company, Lincoln, NE, 1997.

[3] R. E. Hummel and P. Wißmann, *Handbook of Optical Properties, Optics of Small Particles, Interfaces, and Surfaces*, CRC Press, vol. 2, p. 164, New York, 1995.

[4] D. A. Jones, *Principles and Prevention of Corrosion*pp. 292–304, Prentice-Hall, London, 2nd ed. edition, 1996.

[5] C. Liu, A. Leyland, S. Lyon, A. Matthews, and A. Matthews, "An a.c. impedance study on PVD CrN-coated mild steel with different surface roughnesses," *Surface and Coatings Technology*, vol. 76-77, pp. 623–631, 1995.

[6] F. Wootten, *Optical Properties of Solids*, Academic Press, New York, 1972.

[7] R. Hariharan, R. Raja, and R. J. Golden RenjithNimal, "Investigation of mechanical and tribological properties of titanium nitride deposited on low carbon steel by RF magnetron sputtering," *Journal of Critical Reviews*, vol. 7, no. 04, pp. 324–328, 2020.

[8] P. Patsalas and S. Logothetidis, "Interface properties and structural evolution of TiN/Si and TiN/GaN heterostructures," *Journal of Applied Physics*, vol. 93, no. 2, pp. 989–998, 2003.

[9] C. Kittel, *Introduction to Solid State Physics*p. 159, 7th ed. edition, Wiley, New York, NY, 1996.

[10] D.-Y. Wang, C.-L. Chang, C.-H. Hsu, and H.-N. Lin, "Synthesis of (Ti, Zr)N hard coatings by unbalanced magnetron sputtering," *Surface and Coatings Technology*, vol. 130, no. 1, pp. 64–68, 2000.

[11] R. Hariharan, R. Raja, and S. Vasu, "Mechanical and tribologicalbehaviour of thin TaN coating produced on AISI 1018 substrate by DC magnetron sputtering," *IJRTE*, vol. 7, no. 6S2, pp. 591–598, 2019.

[12] J.-L. Ruan, J.-L. Huang, H.-H. Lu, J. S. Chen, and D.-F. Lii, "Effects of the Ta content on the microstructure and electrical property of reactively sputtered TaxZr1−xN thin films," *Thin Solid Films*, vol. 519, no. 15, pp. 4987–4991, 2011.

[13] L. Li, E. Niu, G. Lv et al., "Synthesis and electrochemical characteristics of Ta-N thin films fabricated by cathodic arc deposition," *Applied Surface Science*, vol. 253, no. 16, pp. 6811–6816, 2007.

[14] R. Hariharan, R. Raja, and R. J. Golden RenjithNimal, "Characteristic of h on mild steel/aln cermet selective surfaces deposited by Rf magnetron sputtering," *Journal of Critical Reviews*, vol. 7, no. 04, pp. 319–323, 2020.

[15] D. A. Neamen, *An Introduction to Semiconductor Devices*, McGraw-Hill, New York, 2006.

[16] M. Saib, J. C. Francois, P. Gravier, M. Sigrist, L. Argeme, and O. Cerclier, "Resistivity and hall effect of reactively zirconium nitride films," *Solid State Communications*, vol. 58, no. 6, pp. 385–388, 1986.

[17] L. E. Koutsokeras, N. Hastas, S. Kassavetis et al., "Electronic properties of binary and ternary, hard and refractory transition metal nitrides," *Surface and Coatings Technology*, vol. 204, no. 12-13, pp. 2038–2041, 2010.

[18] G. M. Matenoglou, L. E. Koutsokeras, and P. Patsalas, "Plasma energy and work function of conducting transition metal nitrides for electronic applications," *Applied Physics Letters*, vol. 94, no. 15, Article ID 152108, 2009.

[19] E. Guilmeau, D. Bérardan, C. Simon et al., "Tuning the transport and thermoelectric properties of In2O3 bulk ceramics through doping at In-site," *Journal of Applied Physics*, vol. 106, no. 5, Article ID 053715, 2009.

[20] T. Schuler and M. A. Aegerter, "Optical, electrical and structural properties of sol gel ZnO:Al coatings," *Thin Solid Films*, vol. 351, no. 1-2, pp. 125–131, 1999.

[21] K.-Y. Liu, J.-W. Lee, and F.-B. Wu, "Fabrication and tribological behavior of sputtering TaN coatings," *Surface and Coatings Technology*, vol. 259, pp. 123–128, 2014, SCT-19279.

[22] B. Bushan, B. K. Gupta, *Handbook of Tribology*, Vol. 57, McGraw-Hill, , New York, 1991.

[23] S. K. Kim and B. C. Cha, "Deposition of tantalum nitride thin films by D.C. magnetron sputtering," *Thin Solid Films*, vol. 475, no. 1-2, pp. 202–207, 2005.

[24] Y. X. Leng, H. Sun, P. Yang et al., "Biomedical properties of tantalum nitride films synthesized by reactive magnetron sputtering," *Thin Solid Films*, vol. 398-399, pp. 471–475, 2001.

[25] C.-S. Shin, Y.-W. Kim, D. Gall, J. E. Greene, and I. Petrov, "Phase composition and microstructure of polycrystalline and epitaxial TaNx layers grown on oxidized Si(001) and MgO(001) by reactive magnetron sputter deposition," *Thin Solid Films*, vol. 402, no. 1-2, pp. 172–182, 2002.

[26] G. R. Lee, H. Kim, H. S. Choi, and J. J. Lee, "Superhard tantalum-nitride films formed by inductively coupled plasma-assisted sputtering," *Surface and Coatings Technology*, vol. 201, no. 9-11, pp. 5207–5210, 2007.

[27] Y.-I. Chen, B.-L. Lin, Y.-C. Kuo, J.-C. Huang, L.-C. Chang, and Y.-T. Lin, "Preparation and annealing study of TaNx coatings on WC-Co substrates," *Applied Surface Science*, vol. 257, no. 15, pp. 6741–6749, 2011.

[28] Y. Kang, C. Lee, and J. Lee, "Effects of processing variables on the mechanical properties of Ta/TaN multilayer coatings," *Materials Science and Engineering: B*, vol. 75, no. 1, pp. 17–23, 2000.

[29] P.-L. Sun, C.-Y. Su, T.-P. Liou, C.-H. Hsu, and C.-K. Lin, "Mechanical behavior of TiN/CrN nano-multilayer thin film deposited by unbalanced magnetron sputter process," *Journal of Alloys and Compounds*, vol. 509, no. 6, pp. 3197–3201, 2011.

[30] Y.-W. Lin, C.-W. Lu, G.-P. Yu, and J.-H. Huang, "Structure and properties of nanocrystalline (TiZr)xN1−xThin films deposited by DC unbalanced magnetron sputtering," *Journal of Nanomaterials*, vol. 2016, pp. 1–12, Article ID 2982184, 2016.

[31] A. S. Korhonen, J. M. Molarius, I. Penttinen, and E. Harju, "Hard transition metal nitride films deposited by triode ion plating," *Materials Science and Engineering*, vol. 105-106, no. 2, pp. 497–501, 1988.

[32] L. P. Ward, K. N. Strafford, C. Subramanian, and T. P. Wilks, "Observations on the structure, hardness and adhesion properties of a selection of multicomponent refractory element nitride coatings," *Journal ofMaterials Processing Technology*, vol. 56, no. 1–4, pp. 375–384, 1996.

[33] L. A. Donohue, J. Cawley, and J. S. Brooks, "Deposition and characterisation of arc-bond sputter TixZryN coatings from pure metallic and segmented targets," *Surface and Coatings Technology*, vol. 72, no. 1-2, pp. 128–138, 1995.

[34] V. V. Uglov, V. M. Anishchik, V. V. Khodasevich et al., "Structural characterization and mechanical properties of Ti-Zr-N coatings, deposited by vacuum arc," *Surface and Coatings Technology*, vol. 180-181, pp. 519–525, 2004.

[35] P. J. Kelly and R. D. Arnell, "Magnetron sputtering: a review of recent developments and applications," *Vacuum*, vol. 56, no. 3, pp. 159–172, 2000.

[36] S. Chinsakolthanakorn, A. Buranawong, N. Witit-anun, S. Chaiyakun, and P. Limsuwan, "Characterization of nanostructured TiZrN thin films deposited by reactive DC magnetron Co-sputtering," *Procedia Engineering*, vol. 32, pp. 571–576, 2012.

[37] E. W. Niu, L. Li, G. H. Lv et al., "Characterization of Ti-Zr-N films deposited by cathodic vacuum arc with different substrate bias," *Applied Surface Science*, vol. 254, no. 13, pp. 3909–3914, 2008.

[38] D. Y. Wang, C. L. Chang, C. H. Hsu, and H. N. Lin, "Synthesis of (Ti,Zr)N hard coatings by unbalanced magnetron sputtering," *Surface and Coatings Technology*, vol. 130, pp. 64–68, 2000.

[39] C.-P. Liu and H.-G. Yang, "Systematic study of the evolution of texture and electrical properties of ZrNx thin films by reactive DC magnetron sputtering," *Thin Solid Films*, vol. 444, no. 1-2, pp. 111–119, 2003.

[40] P. W. Shum, W. C. Tam, K. Y. Li, Z. F. Zhou, and Y. G. Shen, "Mechanical and tribological properties of titanium-aluminium-nitride films deposited by reactive close-field unbalanced magnetron sputtering," *Wear*, vol. 257, no. 9-10, pp. 1030–1040, 2004.

[41] K. Singh, P. K. Limaye, N. L. Soni, A. K. Grover, R. G. Agrawal, and A. K. Suri, "Wear studies of (Ti-Al)N coatings deposited by reactive magnetron sputtering," *Wear*, vol. 258, no. 11-12, pp. 1813–1824, 2005.

[42] K. H. Chung, G. T. Liu, J. G. Duh, and J. H. Wang, "Biocompatibility of a titanium-aluminum nitride film coating on a dental alloy," *Surface and Coatings Technology*, vol. 188-189, pp. 745–749, 2004.

[43] E. Lugscheider, O. Knotek, C. Barimani, T. Leyendecker, O. Lemmer, and R. Wenke, "PVD hard coated reamers in lubricant-freecutting," *Surface and Coatings Technology*, vol. 112, pp. 146–151, 1999.

[44] J. V. Ramana, S. Kumar, C. David, and V. S. Raju, "Structure, composition and microhardness of (Ti,Zr)N and (Ti,Al)N coatings prepared by DC magnetron sputtering," *Materials Letters*, vol. 58, no. 20, pp. 2553–2558, 2004.

[45] V. V. Uglov, V. M. Anishchik, S. V. Zlotski, and G. Abadias, "The phase composition and stress development in ternary Ti-Zr-N coatings grown by vacuum arc with combining of plasma flow," *Surface and Coatings Technology*, vol. 200, pp. 6389–6394, 2006.

[46] M. B. Takeyama, T. Itoi, E. Aoyagi, and A. Noya, "Diffusion barrier properties of nano-crystalline TiZrN films in Cu/Si contact systems," *Applications of Surface Science*, vol. 216, pp. 181–186, 2003.

[47] J. A. Thornton, "Influence of apparatus geometry and deposition conditions on the structure and topography of thick sputtered coatings," *J VacSciTechnol*, vol. 11, pp. 666–670, 1974.

[48] C. Keawhan, P. Wongpanya, N. Witit-Anun, and P. Songsiriritthigul, "Corrosion behavior of AISI 4140 steel

surface coated by physical vapor deposition," *Journal of Metals, Materials and Minerals*, vol. 22, no. 1, pp. 69–76, 2012.

[49] S. D. Chyou and H. C. Shih, "The effect of nitrogen on the corrosion of plasma-n 4140 steel," *Corrosion*, vol. 47, no. 1, pp. 31–34, 1991.

[50] H. J. Grabke, "High nitrogen steels. The role of nitrogen in the corrosion of iron and steels," *ISIJ International*, vol. 36, no. 7, pp. 777–786, 1996.

[51] P. F. Hui, H. H. Cheng, K. L. Jung, and H. S. Yih, "Effects of PVD sputtered coating on the corrosion resistance of AISI304 stainless steel," *Materials Science and Engineering*, vol. 347, no. 1-2, pp. 123–129, 2003.

[52] R. Walter and M. B. Kannan, "Influence of surface roughness on the corrosion behaviour of magnesium alloy," *Materials & Design*, vol. 32, no. 4, pp. 2350–2354, 2011.

[53] S. H. Ahn, J. H. Yoo, Y. S. Choi, J. G. Kim, and J. G. Han, "Corrosion behavior of PVD-grown WC–(Ti1-x alx)N films in a 3.5 wt% NaCl solution," *Surface and Coatings Technology*, vol. 162, no. 2-3, pp. 212–221, 2003.

[54] Y.-W. Lin, J.-H. Huang, and G.-P. Yu, "Effect of nitrogen flow rate on properties of nanostructured TiZrN thin films produced by radio frequency magnetron sputtering," *Thin Solid Films*, vol. 518, no. 24, pp. 7308–7311, 2010.

[55] S. Hogmark, S. Jacobson, and M. Larsson, "Design and evaluation of tribological coatings," *Wear*, vol. 246, no. 1-2, pp. 20–33, 2000.

Hindawi
Advances in Materials Science and Engineering
Volume 2021, Article ID 5756563, 10 pages
https://doi.org/10.1155/2021/5756563

Review Article

3D Printing Manufacturing Techniques, Materials, and Applications: An Overview

D. Srinivasan,[1] M. Meignanamoorthy,[1] M. Ravichandran,[1] V. Mohanavel,[2] S. V. Alagarsamy,[3] C. Chanakyan,[4] S. Sakthivelu,[5] Alagar Karthick,[6] T. Ram Prabhu,[7] and S. Rajkumar[8]

[1]*Department of Mechanical Engineering, K.Ramakrishnan College of Engineering, Trichy 621112, Tamilnadu, India*
[2]*Centre for Materials Engineering and Regenerative Medicine, Bharath Institute of Higher Education and Research, Chennai 600073, Tamil Nadu, India*
[3]*Department of Mechanical Engineering, Mahath Amma Institute of Engineering and Technology, Pudukkottai 622101, Tamil Nadu, India*
[4]*Department of Mechanical Engineering, Government College of Engineering, Thanjavur 613402, Tamil Nadu, India*
[5]*Department of Mechanical Engineering, Mount Zion College of Engineering and Technology, Pudukkottai 622507, Tamil Nadu, India*
[6]*Renewable Energy Lab, Department of Electrical and Electronics Engineering, KPR Institute of Engineering and Technology, Coimbatore 641407, Tamil Nadu, India*
[7]*Centre for Military Airworthiness and Certification (CEMILAC), Defence Research and Development Organisation (DRDO), Bangalore 560075, Karnataka, India*
[8]*Department of Mechanical Engineering, Faculty of Manufacturing, Institute of Technology, Hawassa University, Awasa, Ethiopia*

Correspondence should be addressed to M. Ravichandran; smravichandran@hotmail.com and S. Rajkumar; rajkumar@hu.edu.et

Received 7 August 2021; Revised 4 September 2021; Accepted 9 November 2021; Published 10 December 2021

Academic Editor: Carlos R. Rambo

3D printing, also called additive manufacturing (AM), is a method of creating 3D solid parts from a digital document. By utilizing additive routes, the fabrication of 3D-printed objects can be made. These layers can be viewed as a gently cut level cross-area of the manifest object. 3D printing is somewhat in obstruction to subtractive manufacture, which is expelling/discharging out a touch of metal or plastic for the occurrence of a milling machine. 3D printing authorizes creating multifarious profiles employing fewer materials than conventional fabrication systems. This review article provides the general idea of 3D printing production techniques, materials used, and applications in the aircraft and automobile industry and biomedical fields.

1. Introduction

3D printing (or AM) is a procedure of linking materials to create parts from 3D model information, generally layer over layer. The component is designed using the CAD software, which is later sent out to a 3D printer. 3D printing gives a great deal of customization in component structure and could even print components, which cannot be produced by a few customary production methods. Difficult and complicated parts could be fabricated with a significant decrease in fabricating time, expenses, and material surplus [1]. 3D printing creates physical parts from a geometrical interpretation via advanced enlargement of materials. The 3D printing process is a quick developing process. Presently, 3D printing is generally utilized in the world. 3D printing process is more utilized for mass customization, making any sort of open-source plans in the farming, medicine, automobile, train, and flight sectors [2]. 3D printing or AM is a designing procedure utilized for delivering a 3D component layer over layer from a

computerized 3D model according to the prerequisite. AM is a quicker fabricating method. The developing interest for 3D printing is a direct result of its favorable circumstances like quick prototyping and creating adjustable parts. The technique has now become one of the conventional production methods. Several materials having a place with many groupings such as composites, polymers, and ceramics could be used in ventures such as automation, aviation, medical services and clinics, gadgets, food, and some more [3]. The 3D printing method presents a frontline innovation in the territory of prototyping and component improvement method in the present production drift. Further, to overcome the goals of Industry 4.0 upset, mutually in the academic and industrialized sector, the interest in 3D printing is developing dramatically to use the merits of the method. Utilizing 3D printing fabricating methods, it is currently conceivable to construct the geometry of the confounded structure, which was very monotonous in the subtractive production method. 3D printing is characterized as the method where the 3D CAD model is finished into the component via saving material layer over the other [4]. The 3D printing process was developed in the 1980s, commonly notorious as AM. 3D printing has quickly accumulated broad concentration and created as a developing production method. Thus, it was broadly embraced in different fields, such as design gems, polymer printed materials, applied autonomy and mechanization, tissue and frameworks, and gadgets items. 3D printing helped the application fields as indicated by its few qualities, for example, brief timeframe process, minimal effort, customization, and material decrease. Besides, the 3D printing process is in the dynamic phase of mechanical development, which could propel the production, creation method, and fabrication development as an insurgency method [5].

2. 3D Printing Production Techniques

Customary techniques for production want a serious extent of graceful supply chain management, need enormous work supremacy 3D printing process to be robotized, and depend on CAD programming to print items utilizing an assortment of materials, radically lessening the measure of supply chain management. When all is said in done, 3D printing does not utilize any expensive molds, nor does it need instruments, whichever for machining, structures, and punches, and it is an economical one. The 3D printing productions techniques are several depending on the sources. Based on the applications of the components, any one of the techniques can be selected. Figure 1 shows the classifications of 3D printing production techniques.

2.1. Powder-Based Systems. The powder-based system is one of the 3D printing production techniques. It uses regular and traditional inkjet print heads for the fabrication of components. Powder-based systems can be classified into four major categories: Laser Metal Deposition LMD, DMLS, SLM, and EBM.

2.2. Laser Metal Deposition (LMD). LMD is a 3D printing fabricating process that utilizes a laser beam to shape a pool of dissolved metal (a soften pool) outside a metallic substrate into which metal powder is infused utilizing a gas stream. Figure 2 shows the graphic illustration of the LMD method. The ingested metal powder makes a store on a superficial level. Regular applications incorporate the renovation of metallic parts, for example, form instruments, valves, worm screws. At first, the substrate is lighted by means of a laser beam, creating a liquefy puddle that catches and liquefies the powder elements passed up a nozzle. LMD uses different metals, and earthenware powder particles could be blended uniformly to get various composites ready through good properties. Then, powder particles are blended via fly of argon gases. By way of the laser source withdraws, the liquid pool hardens by means of warmth scattering via transmission, convection, and energy. The affidavit top, having the powder nozzle and optics for laser beam conveyance, goes beside the characterized way, thus framing a layer on the substrate. A short time later, the head passes up to the single-layer thickness for the deposition of the accompanying layer. In LMD, the principal layer is halfway reliquefied, filling in as another "substrate," subsequently assisting in the arrangement of the subsequent layer. A similar form of the 3D model is created in the CAD tool [6].

2.3. Direct Metal Laser Sintering (DMLS). DMLS is a method that permits the manufacture of difficult-formed objects from powder-based materials, as indicated via the 3D computer design. Figure 3 shows the graphic illustration of the DMLS method. DMLS is a laser-based 3D printing process, in which an entity is manufactured one layer over another utilizing powdered metal, radiant heaters, and a computer-operated laser. Fundamentally, the machine fabricates the entity on a transferable stage via smearing gradual layers of the design material. Intended for every layer, the machine sets out a film of powders, with a precise thickness (0.1 mm). At that point, a powerful laser beam is coordinated on a powder bed and modified to intertwine metal powders existing in its central region, as indicated by a computer-aided design document, in this manner producing a flimsy metal layer. The stage descends the prearranged layer thickness, a new film of powder is laid down, and the following deposit is softened with disclosure to the laser cause, so it adjusts to the past layer. Therefore, the procedure proceeds, one layer over another, till the component is manufactured [7].

2.4. Selective Laser Melting (SLM). SLM is a 3D printing method intended to utilize a high force thickness laser to liquefy and combine metallic powders. Figure 4 shows the graphic illustration of the SLM method. A part is worked by specifically dissolving and intertwining powders inside and amid layers. The SLM strategy is likewise generally called direct selective laser sintering, laser cussing, and direct metal laser sintering, and this method has been demonstrated to deliver close to the exact shape components up to 99.9%

Figure 1: Classifications of 3D printing production techniques.

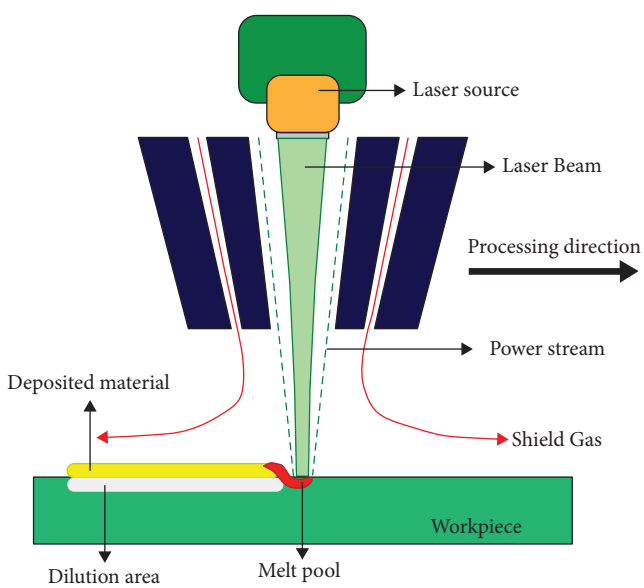

Figure 2: Graphic illustration of the LMD method.

relative thickness. This empowers the method to work close to complete thickness practical components and has reasonable monetary advantages [8].

2.5. Electron Beam Melting (EBM). EBM is another 3D printing fabrication process that is accepted to alter the production sector. Figure 5 shows the graphic illustration of the EBM method. The technique uses EB energy to liquefy the metal powder. The subsequent electron beam is utilized as the vital source of the whole procedure happens in a vacuum chamber. The vacuum guarantees extraordinary immaculateness by giving an oxygen-free condition and lessens the danger of hydrogen. When fabricating the component, a raised temperature of 700°C is kept up in the chamber to decrease leftover burdens and, consequently, twisting and warpage. The EB initially prewarms the powder layer through a greater sweep speed, tailed by liquefying the powder layer depending on the geometry characterized via CAD document. Each layer of a section is worked in dual steps in EBM. The external limit of the part is constructed first, which is alluded to as molding, and the powder inside the shape is dissolved along these lines to finish one layer. This method proceeds till the ideal 3D object is completely finished [9].

2.6. Solid-Based Systems. A solid-based system is a kind of 3D printing production process. Solid-based 3D printing methods use solids as the essential medium to make the component or model. They are totally diverse from the fluid-based photograph restoring process. They are likewise unique in relation to each other in that the essential type of strong materials in certain methods may come as fibers or wires, few as sheets or rolls, whereas others might be as pellets. An uncommon gathering of strong based 3D printing methods that utilize powder as the intermediate will be secured independently. The solid-based system can be classified into three major categories: Fused Deposition

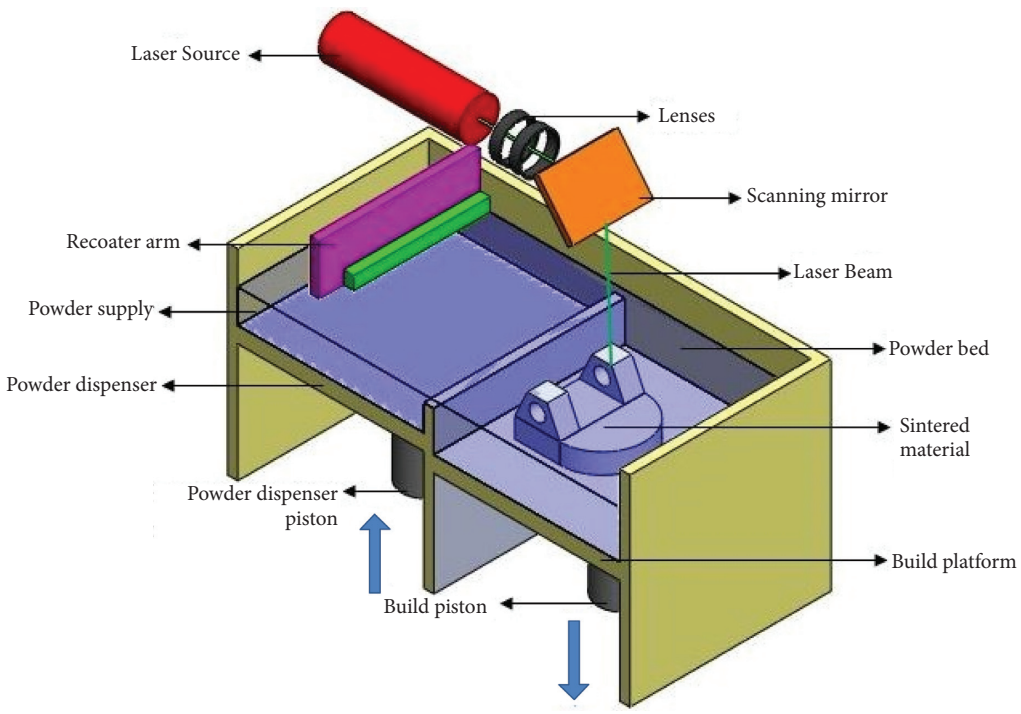

Figure 3: Graphic illustration of the DMLS method.

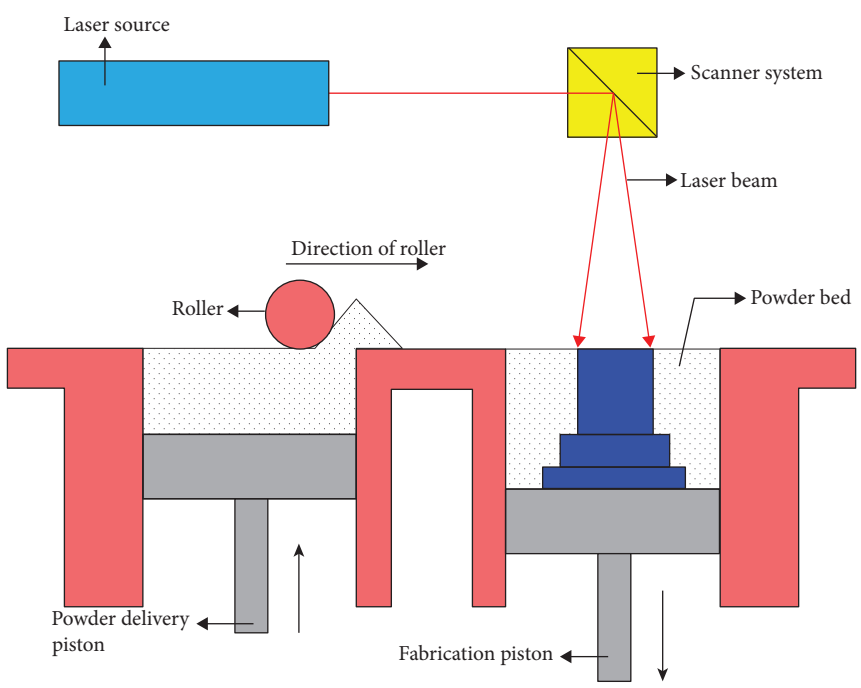

Figure 4: Graphic illustration of the SLM method.

Modeling (FDM), Electron Beam Freeform Fabrication (EBFF), and Wire Pulse Arc Additive Manufacturing (WPAAM).

2.7. Fused Deposition Modeling (FDM). A steady filament of a thermoplastic polymer is utilized to 3D print layers of materials in the FDM process. Figure 6 shows the graphic illustration of the FDM method. The fiber is heated by the sideways of the nozzle to show up at a semiliquid state and a short time later removed on the stage or on the head of late printed layers. The thermoplasticity of the polymer filament is a major property in this process, which permits the filament to consolidate in the course of printing and, a while later, to fix at room temperature in the rouse of printing. The deposit fatness, width and course of filament, and air

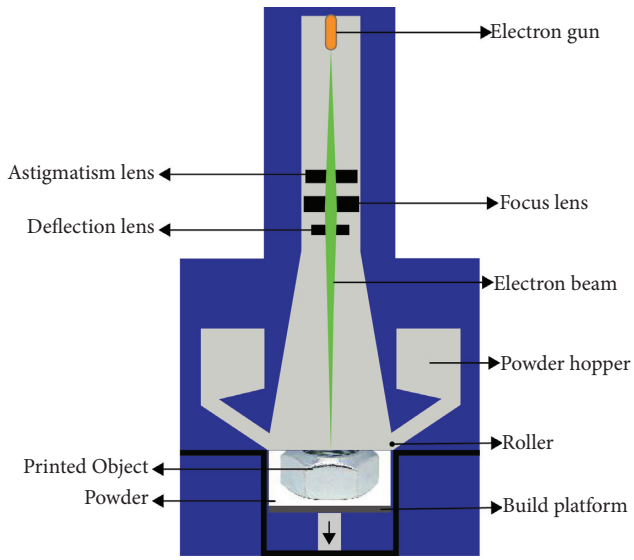

Figure 5: Graphic illustration of the EBM method.

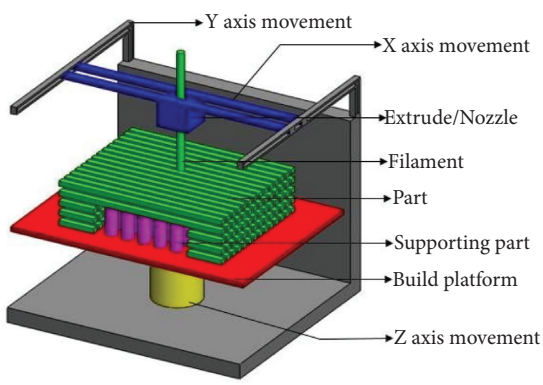

Figure 6: Graphic illustration of the FDM method.

opening are the essential getting ready limits that impact the mechanical properties of printed components. Amid layer meandering was viewed as the central driver of mechanical deficiency. Quick and ease operation techniques are the principal points of interest of FDM. In contrast, feeble-mechanical behaviors, layer by layer arrival, powerless surface quality, and a foreordained number of thermoplastic materials are the guideline weaknesses of FDM. The headway of fiber-strengthened composites making use of FDM has fortified the mechanical properties of 3D components [10].

2.8. Electron Beam Freeform Fabrication (EBFF). EBFF is a developing cross-cutting process for manufacturing structural metal components. Figure 7 shows the graphic illustration of the EBFF method. The method can be utilized to construct a difficult, combined component in a layer-added substance style, although the more prompt result is for usage as a production method for including subtleties to segments manufactured from improved castings and forgings or plate items. EBFF utilizes a powerful electron beam in a vacuum domain (1×10^{-4} torr or lower).

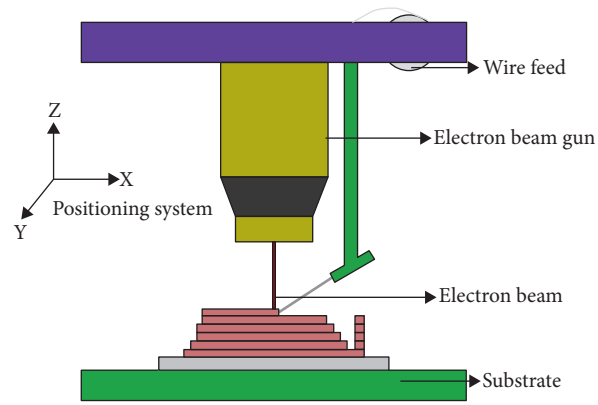

Figure 7: Graphic illustration of the EBFF method.

Wire feedstock is utilized because of troubles taking care of powder in a vacuum. In the meantime, the transporter gas utilized to help powder conveyance will be ionized in the electron beam. Activity in a vacuum guarantees a spotless procedure condition and disposes of the requirement for a consumable shield gas, as is normally utilized in laser affidavit methods.

The EBFF method is about 100% proficient in feedstock utilization and approaches 95% effectiveness in power use. The electron beam couples well with any electrically conductive material, containing profoundly intelligent composites, for example, aluminum and copper. An assortment of weldable composites can be prepared utilizing EBFF. Further improvement is required to decide whether nonweldable combinations can likewise be saved. Exhibited affidavit rates for EBFF are 330 to 2500 cm^3/hr (20 to 150 in^3/hr), with a lower goal in the capacity to assemble fine subtleties. Investigations are arranged with fine-width wires to endeavor to build fine subtleties and huge distance across wires to expand affidavit rate. EBFF offers suitable answers to issues of testimony rate, process effectiveness, and material similarity for inclusion into the creation condition [11].

2.9. Wire Pulse Arc Additive Manufacturing (WPAAM). Recently, WAAM methodology got a fascination of production ventures because of the capacity of fabricating perplexing and huge metal segments with a high affidavit rate with roughly 100% material use. Figure 8 shows the graphic illustration of the WPAAM method. WAAM is a method of affidavit of liquid metal in a layer over layer structure to accomplish the last item. This advancement is done with an electric curve as a warmth source to soften the metal wire because of expanding request in the present market to grow new structures with huge profitability with less material waste and low hardware cost [12]. The mix of filler wires are made of the metal to keep the frame surface as the warm, and it is called as the regular welding method. for example, gas metal bend welding. The process has uncovered numerous points of interest, for example, the better BTF proportion contrasted with traditional assembling forms, hypothetically no dimensional cutoff points for the segment

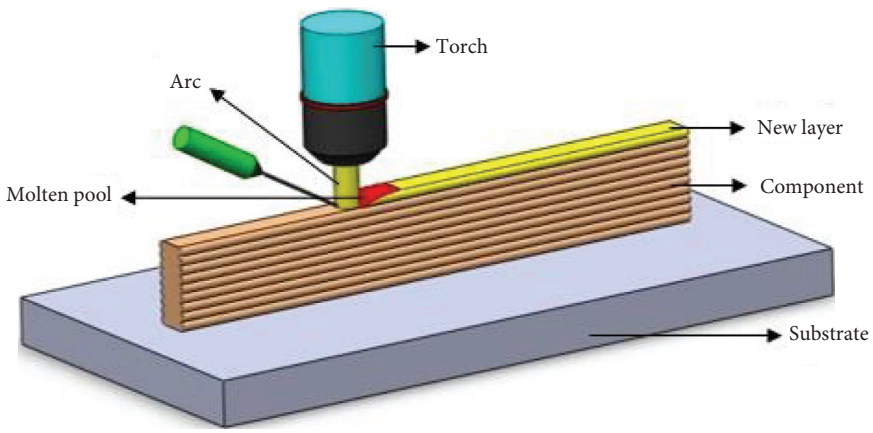

Figure 8: Graphic illustration of the WPAAM method.

producing and efficient method contrasted with powder-based methods when significant expense material is thought of [13].

2.10. Liquid-Based Systems. The liquid-based method involves diminishing or solidifying a photosensitive polymer when an impressive laser arrives at the tar. The principal classification of 3D printer makes object layers by specifically hardening a fluid sap known as photopolymer that solidifies when presented to laser or other light sources. Whatever photograph polymerization, 3D printers assembled object layers inside a tank of fluid. Then, others fly out a solitary layer of pitch and use ultraviolet light to set it strong before the following layer is added. A couple of 3D printers depend on the last-mentioned innovation and can blend a few distinctive photograph polymers in a similar print work, permitting them to yield objects produced using numerous materials. The liquid-based system can be classified into two major categories: stereolithography (SLA) and direct light processing (DLP) [14].

2.11. Stereolithography (SLA). Figure 9 shows the graphic illustration of the SLA method. The stereolithography technique was familiarized in the last part of the 1980s. Albeit numerous different methods have been created from that point forward, stereolithography stays the most impressive and adaptable method. It has the most noteworthy creation exactness, and an expanding number of materials that can be handled are opening up. Like most strong freestyle manufacture procedures, stereolithography is an added substance creation process that permits manufacturing parts from a PC helped plan (CAD) document. The production of 3D substances via stereolithography depends on the spatially controlled hardening of a fluid tar by photopolymerization. Employing a PC controlled laser beam or a computerized light projector with a PC driven structure stage, an example is lit up on the outside of a tar. Thus, the pitch in the example is cemented to a characterized profundity, making it hold fast to a help stage. After photographing polymerization of the principal layer, the stage is moved away from the surface and the assembled

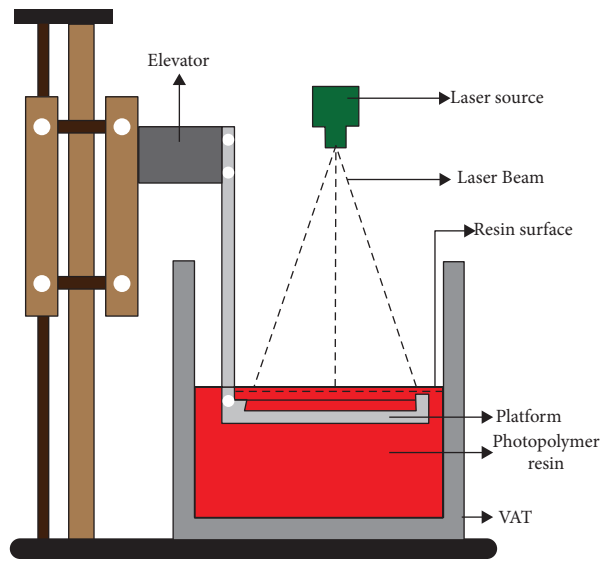

Figure 9: Graphic illustration of the SLA method.

layer is recoated with fluid tar. An example is then restored in this subsequent layer. As the profundity of restoring is marginally bigger than the stage step stature, greater adherence to the principal layer is guaranteed. These means are rehashed to develop a strong, three-dimensional article. In the wake of depleting and washing-off abundance pitch, an as-manufactured structure is got [15].

2.12. Direct Light Processing (DLP). Digital light processing (DLP) built 3D printing uses projection light to polymerize materials to acquire the preplanned structures. Figure 10 shows the graphic illustration of the DLP method. This method has critical focal points in printing goal, proficiency, and working conditions. Consequently, it can give numerous great highlights to the items. The DLP and laser helped printing strategies smear photopolymerization responses. These 3D printing stages have critical contrasts in printing instrument, speed, material determination, and goal. This strategy utilizes a lot of chipsets dependent on optical miniaturized scale electromechanical innovation to

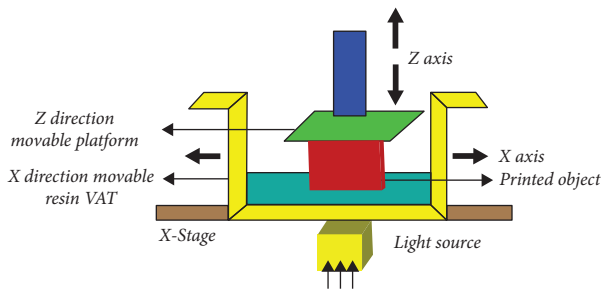

Figure 10: Graphic illustration of the DLP method.

the method employed light sources of photosensitive materials.

The fundamental utilitarian component is a computerized small scale reflect gadget (DMD), which comprises a gathering of micron-sized, controllable mirrors. The mirror turns to control the way of light and afterward venture it onto the photosensitive sap through working. The customary exhibits have an enormous number of mirrors, from almost a million mirrors to in excess of 2 million. Then again, the pixel dispersing of the miniaturized scale reflect is just a couple of microns or twelve microns. The goal of the DLP put together 3D printing based with respect to the projection plane balanced by DMD and focal point. Subsequently, the DLP printing procedure has a moderately high goal, for the most part at the micron scale [16].

3. Materials Used in 3D Printing

Each material plays a major role in different applications. Based on the applications of the components, any one of the suitable materials can be selected. Some of the materials utilized for numerous usages in 3D printing techniques are shown in Figure 11.

3.1. Metals Used in 3D Printing. Stainless steels are the most generally utilized metal in 3D printing. Stainless steels could have multiple uses for extraordinary strength and hardness circumstances, mainly for tools and molding uses. Stainless steels are predominantly complex to 3D printing parameters [10]. Gold is one of the rare metals utilized as raw material in selective laser melting. The major reason to choose gold as a raw material is its excellent thermal conductivity. The selective laser melting method uses gold as a raw material to manufacture jewels and ornaments. Silver is one of the metals utilized as raw material in the SLM method [17]. It permits the production of jewelry and ornaments with difficult designs, in any case not plausible with regular methods. In addition, it assists with diminishing the expense of creation by out-staging the utilization of costly shapes and bites the dust and by permitting unemployed powder to be recycled for the following group of fabrication [18]. Titanium is one of the major important raw materials used in the SLM and EBM methods. This material finds major applications in the biomedical field [19].

3.2. Ceramics Used in 3D Printing. Ceramics find extensive applications in aerospace, biomedical engineering, chemical industry, electronics, and machinery despite its outstanding mechanical, electrical, chemical, and thermal behaviors. Ceramics-based components can be fabricated via selective laser melting and fused deposition modeling techniques [20]. Ceramics such as Al_2O_3 [21], ZrO_2 [22], LiO_2 [23], SiO_2 [24], SiC [25], Si_3N_4 [26], and PZT [27] are used as raw materials to produce novel lightweight components such as turbine rotor, gear wheels, complex-shape parts, and different transducers.

3.3. Polymers Used in 3D Printing. Polymers find extensive applications in engineering industries despite their less weight and superior properties. Polymers-based parts can be manufactured easily via the fused deposition technique. Examples of polymers are nylon [28], resin [29], polylactic acid [30], polyethylene terephthalate [31], high impact polystyrene [32], and acrylonitrile.

Butadiene Styrene [33] finds numerous applications in 3D printing manufacturing industries. Polymer components such as crane hooks, gear wheels can be fabricated via 3D printing with desired properties.

3.4. Applications of 3D Printing in Engineering Industries. As the possible applications for 3D printing rise, engineering industries are starting to discover approaches to make new plans of action and openings with the methods. 3D printing technology possesses a major role in the major three engineering industries: aerospace, automotive, and biomedical. The demand for 3D printing technology in these three industries rapidly increases day by day because of its numerous advantages.

3.5. 3D Printing Applications in Aerospace Industry. 3D printing methods are perfect for manufacturing aerospace parts as they want little groups of parts, which have difficult geometries, vital for airflow and heat indulgence capacities. Besides, on-request and on-location fabricating should have been set up for space explorers to deliver parts for fixing or supporting space stations. Additionally, 3D printing is equipped for delivering leaves behind a low density-to-quality proportion, which is important for planes and space transports. Meanwhile, the materials utilized in the airplane business are costly, and 3D printing forms are identified as having the least waste material. 3D printing has become mainstream among makers in the aeronautic trade [34]. Aircraft parts should be lighter in weight and contemporary good strength and firmness-to-weight ratios to lessen expenditures and expulsions [10]. Aircraft have a long working presence of as long as 30 years. Possession of long-standing components acquires an eminent expense of stock. However, 3D printing is equipped for gathering components on request, along these lines reducing the upkeep time [35]. Nickel-based alloys and Ti–6Al–4V are materials utilized in aerospace components manufacturing. These materials possess superior tensile properties, hardness, destruction tolerance, and corrosion/

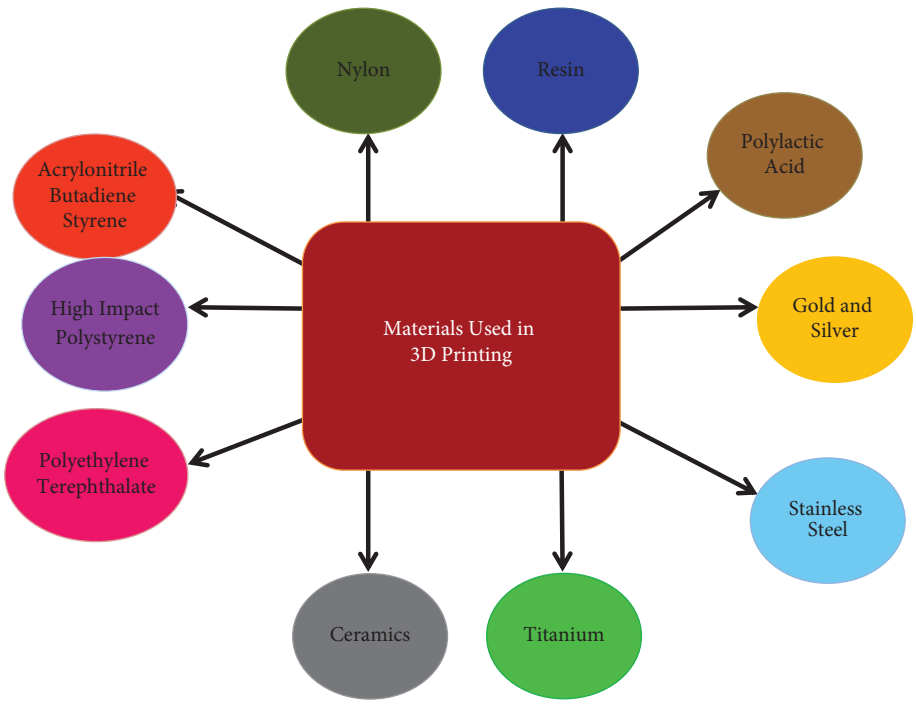

Figure 11: Types of materials used in 3D printing.

oxidation opposition [1]. Abrasive turbine blade tips can be manufactured via the SLM technique by using nickel-based superalloy as a raw material [36]. Airplanes fuel nozzles and brackets inside the traveler cabin can easily manufactured via 3D printing methods [37]. In aerospace productiveness, 3D printing method can possibly fabricate less weight components and enhance and intricate geometries, which could lessen energy necessity and resources.

At the same time, using the 3D printing method could speed fuel backup funds because it can reduce the material utilized to fabricate aerospace's components. Moreover, the 3D printing method has been broadly smeared to fabricate the additional pieces of a few aviation parts, such as engines. The engine components can be effectively impaired, which need normal replacement. Consequently, the 3D printing method is a virtuous key for acquiring such additional components [38]. Nonmetal 3D printing processes such as stereolithography and fused deposition modeling are utilized for the fast prototyping of components and producing installations and insides prepared via plastics, earthenware production, and composite materials. Together metallic and nonmetallic components for aviation applications can be produced or fixed utilizing 3D printing such as aero engine parts, turbine blades, and heat exchangers [39, 40].

3.6. 3D Printing Applications in Automotive Industry. Difficult and less weight-to-quality proportion is a need for components in the automobile. 3D printing is not just utilized for prototyping for automotive components; however, its favorable circumstances have likewise made it ready to be utilized for 3D printing of real parts and vehicles [41]. For Instance, optimize utilized LENS to decrease the material, time, and cost of fabricating red bull racing vehicle parts comprising drive shaft bugs and suspension mounting sections [42]. 3D printing methods in the automobile sector authorize the organization of effort dissimilar choices and stress straight in the enhancement phases, inciting perfect and successful automobile design [43]. Aluminum metal matrix composites (AMCs) have widespread 3D printing applications in the automotive sector because of their bitter properties. Using the selective laser melting method, automobile components can be fabricated easily with desired properties using AMCs as a raw material [44]. Multifaceted automobile components of different dimensions can be fabricated via the selective laser melting method using metals and alloys as raw materials [45]. Nowadays, using the 3D printing method, it is workable for vehicle fabricators to design and make one exclusive vehicle prototype that could fulfill the assorted perceptions and inclinations of clients in the marketplace. Likewise, the 3D printing method has prepared it workable for some vehicle fabricating companies to contend decently with their adversaries in the market. Besides, by utilizing the printing method to make vehicles, it has been workable for vehicle makers to spare generous expenses and work that would somehow be brought about when utilizing the conventional vehicle gets designs together [46]. Car roofs, fenders, and windshield frames can be manufactured using carbon fiber as a raw material. Using the selective laser melting methods, exhausts, emissions, pumps, valves within the fluid handling system, windbreakers, and bumpers could be manufactured easily [47].

3.7. 3D Printing Applications in Biomedical Field. Donor deficiencies for organ replacements are a significant clinical test around the world. Probable dangers that are definitely

experienced with conventional techniques incorporate intricacies, optional wounds, and constrained source donors. 3D printing method embraces the possibility to illuminate these impediments; it may be utilized to quickly produce customized tissue building frameworks, fix tissue surrenders in situ with cells, and even straightforwardly print tissue and organs [48]. Biomedical uses, such as tissues, frameworks, and obsession gadgets, have explicit manufacturing parts that ought to be thought of. For biomedical uses, utilizing these 3D printing techniques without inflexible help structures is firmly suggested [49]. Present progressions in tissue designing and recovery, remedial conveyance, clinical gadget manufacturing, employable administration, and arranging guarantee that 3D printing will keep on assuming an inexorably significant job later on for healthcare [50]. Medical 3D printing was previously an eager impractical imaginary. Period and endeavor make it unpretentious. At present, the 3D printing process expresses a foremost option to support pharmaceutical and clinical organizations with making more obvious medications, permitting a fast making of clinical embeds, and altering the mode that experts and specialists plan methodology. Patient precise 3D-printed anatomical replicas are rotating out to be gradually helpful devices in the current act of accurateness medication and for tailored medicines. Later on, 3D-printed implantable organs will be accessible, declining the holding up archives and intensifying the number of lives spared. Added substance production for human services is still predominantly in evolution. However, it is now applied from multiple points of view in the clinical field that previously reeling under tremendous tension concerning the ideal execution and decreased costs will raise extraordinary benefits from this great as-gold novelty [51].

4. Conclusions

Nowadays, the 3D printing method is one of the engineering industries. It offers numerous advantages to the industries. Along these lines, more data are predictable to advance the methods to improve the reception of 3D printing methods. More data about the 3D printing method will assist businesses with upgrading and improving the framework of 3D printing innovation. Thus, this article overviewed the types of 3D printing production methods, materials, and usages in various industries. This article will be helpful for academicians, researchers, and scientists to do much research on 3D printing production techniques and suitable materials for particular applications.

Data Availability

The data used to support the findings of this study are included in the article.

Conflicts of Interest

The authors declare that there are no conflicts of interest regarding the publication of this article.

References

[1] S. C. Joshi and A. A. Sheikh, "3D printing in aerospace and its long-term sustainability," *Virtual and Physical Prototyping*, vol. 10, no. 4, pp. 175–185, Article ID 1111519, 2015.

[2] N. Shahrubudin, T. C. Lee, and R. Ramlan, "An Overview on 3D printing technology: technological, materials, and applications," *Procedia Manufacturing*, vol. 35, pp. 1286–1296, 2019.

[3] T. Singh, S. Kumar, and S. Sehgal, "3D printing of engineering materials: a state of the art review," *Materials Today: Proceedings*, vol. 28, no. 3, pp. 1927–1931, 2020.

[4] K. M. Pradeep and P. Senthil, "Prediction of in-plane stiffness of multi-material 3D printed laminate parts fabri- cated by FDM process using CLT and its mechanical behaviour under tensile load," *MaterToday Comm*, vol. 23, Article ID 100955, 2020.

[5] M. Quanjin, M. R. M. Rejab, M. S. Idris, N. M. Kumar, M. H. Abdullah, and G. R. Reddy, "Recent 3D and 4D intelligent printing technologies: a comparative review and future perspective," *Procedia Computer Science*, vol. 167, pp. 1210–1219, 2020.

[6] M. A. Mahmood and C. Andrei, "Popescu and ion N. Mihailescu. "Metal matrix composites synthe- sized by laser-melting deposition: a review," *Materials*, vol. 13, no. 11, p. 2593, 2020.

[7] F. Mangano, L. Chambrone, C. Miller, V. R. Noort, P. Hatton, and C. Mangano, "Direct metal laser sintering titanium dental implants: a review of the current literature," *International Journal of Biology*, vol. 2014, Article ID 461534, 11 pages, 2014.

[8] C. Y. Yap, C. K. Chua, Z. L. Dong et al., "Review of selective laser melting: materials and applications," *Applied Physics Reviews*, vol. 2, no. 4, Article ID 041101, 2015.

[9] J. Sweels and F. E. Waiyy, "Laser and electron-beam powder-bed additive manufacturing of metal- lic implants: a review on processes. Mater and Desig," *Journal of Orthopaedic Research*, vol. 34, pp. 369–385, 2016.

[10] P. Gurusamy, T. Sathish, V. Mohanavel et al., "Finite element analysis of temperature distribution and stress behavior of squeeze pressure composites," *Advances in Materials Science and Engineering*, vol. 2021, Article ID 8665674, 9 pages, 2021.

[11] K. Taminger and R. Hafley, "Electron beam freeform fabrication: a rapid metal deposition process," in *Proceedings of the 3rd Annual Automotive Composites Conference*, pp. 1–6, Troy, MI, USA, September 2003.

[12] T. Kodati, Y. R. P. Subhashcvt, and K. L. Narayana, "Optimization of mechanical properties of wire arc additive manufactured specimens using grey-based taguchi method," *Journal of Critical Reviews*, vol. 7, no. 9, pp. 808–817, 2020.

[13] T. Sathish, S. Tharmalingam, V. Mohanavel et al., "Weldability investigation and optimization of process variables for TIG-welded aluminium alloy (AA 8006)," *Advances in Materials Science and Engineering*, vol. 2021, Article ID 2816338, 17 pages, 2021.

[14] A. Ramya and L. V. Sai, "3D printing technologies invarious applications," *International Journal of Mechanical Engineering & Technology*, vol. 7, no. 3, pp. 396–409, 2016.

[15] F. P. W. Melchels and D. W. Grijpma, "A review on stereolithography and its applications in biomedical engineering," *Biomaterials*, vol. 31, no. 24, pp. 6121–6130, 2010.

[16] J. Zhang, Q. Hu, S. Wang, J. Tao, and M. Gou, "Digital light processing based three- dimensional printing for medical applications," *International Journal of Bioprinting*, vol. 6, no. 1, 2019.

[17] J. Jhabvala, E. Boillat, and R. Glardon, "On the use of EBSD analysis to investigate the microstructure of gold samples built by selective laser melting," *Gold Bulletin*, vol. 44, no. 2, pp. 113–118, 2011.

[18] E. O. Olakanmi, R. F. Cochrane, and K. W. Dalgarno, "A review on selective laser sintering/melting (SLS/SLM) of aluminium alloy powders: processing, microstructure, and properties," *Progress in Materials Science*, vol. 74, pp. 401–477, 2015.

[19] J. NiH. Ling et al., "Three-dimensional printing of metals for biomedical applications," *Materials Today Bio*, vol. 3, Article ID 100024, 2019.

[20] Z. ChenZ. Li et al., "3D printing of ceramics: a review," *Journal of the European Ceramic Society*, vol. 39, no. 4, pp. 661–687, 2019.

[21] W. Jan, Y. C. Hagedorn, W. Meiners, and K. Wissenbach, "Additive manufac- turing of ZrO2-Al2O3ceramic components by selective laser melting," *Rapid Prototyping Journal*, vol. 19, no. 1, pp. 51–57, 2013.

[22] Y. C. Hagedorny, N. Balachandrann, W. Meinersw, and P. Wissenbachk, "SLM of net-shaped high strength ce- ramics: new opportunities for producing dental restorations," in *Proceedings of the Solid Freeform Fabrication Symposium*, pp. 8–10, Austin, Texas, August 2011.

[23] C. Steidle, D. Klosterman, R. Chartoff, G. Graves, and N. Osborne in *Proceedings of the 44th International SAMPE Symposium and Exhibition, Long Bach*, CA, USA, May 1999.

[24] M. Pfaffingerm and S. Gmeinerr, "Thermal debinding of ceramic-filled photopolymers," *Materials Science Forum Trans Tech Publication*, vol. 825-826, pp. 75–81, 2015.

[25] N. Travitzky, H. Windsheimer, and T. Fey, "Preceramic paper-derived ceramics," *Journal of the American Ceramic Society*, vol. 91, no. 11, pp. 3477–3492, 2008.

[26] N. Xu, X. Ye, D. Wei et al., "3D artificial bones for bone repair prepared by computed tomography-guided fused deposition modeling for bone repair," *ACS Applied Materials & Interfaces*, vol. 6, no. 17, Article ID 14963, 2014.

[27] M. Allahverdi, M. Jafari, A. Safari, and S. C. Danforth, "Processing of advanced electroceramic components by fused deposition technique," *Journal of the European Ceramic Society*, vol. 21, no. 10-11, pp. 1485–1490, 2001.

[28] X. Wang, M. Jiang, Z. Zhou, J. Gou, and D. Huic, "3D printing of polymer matrix composites: a review and prospective," *Composites Part B: Engineering*, vol. 110, pp. 442–458, 2017.

[29] H. Quan, T. Zhang, H. Xu, S. Luo, J. Nie, and X. Zhu, "Photocuring 3D printing technique and its challenges," *Bioact Mater*, vol. 5, no. 1, pp. 110–115, 2020.

[30] M. Caminero, J. Chacón, E. Núñe, J. Reverte, and J. Becar, "Additive manufacturing of PLA-based composites using fused filament fabrication: effect of gn reinforcement on mechanical properties, dimensional accuracy and texture," *Polymers*, vol. 11, no. 5, 2019.

[31] K. Tappa and U. Jammalamadaka, "Novel biomaterials used in medical 3D printing techniques," *Journal of Functional Biomaterials*, vol. 9, no. 1, 2018.

[32] D. Moises, B. Lopez, and R. Ahmad, "Tensile mechanical behaviour of multi-polymer sandwich structures via fused deposition modelling," *Polymers*, vol. 12, no. 3, 2020.

[33] M. M. Padzi, M. M. Bazin, and W. M. W. Muhamad, "Fatigue characteristics of 3D printed acrylonitrile Butadiene Styrene (ABS)," *IOP Conference Series: Materials Science and Engineering*, vol. 269, Article ID 012060, 2017.

[34] M. Mehrpouya and B. Fotovvati, D. Amir, V. Alireza, S. E. Sattar, and A. Gisario, "The potential of additive manufacturing in the smart factory," *Review. Applied Science*, vol. 9, no. 18, pp. 1–34, 2019.

[35] H. K. Siavash, P. Jouni, and H. Jan, "Additive manufacturing in the spare parts supply chain," *Computers in Industry*, vol. 65, no. 1, pp. 50–63, 2014.

[36] D. Suman, P. F. Timothy, D. Gregory, E. B. Lawrence, J. B. Joseph, and L. B. David, "Direct laser fabrication of superalloy cermet abrasive turbine blade tips," *Materials & Design*, vol. 21, no. 2, pp. 63–73, 2000.

[37] C. Buchanan, "Metal 3D printing in construction: a review of methods, research, applications, opportunities and challenges," *Engineering Structures*, vol. 180, pp. 332–348, 2019.

[38] Y. Cheng and Y. L. Tolyc, "Advanced 3D printing technologies for the aircraft industry: a fuzzy systematic approach for assessing the critical factors," *The International Journal of Advanced Manufacturing Technology*, vol. 105, pp. 4059–4069, 2019.

[39] L. Yin, X. Tian, and D. Li, "Design and characterization of radar absorbing structure based on gradient-refractive-index metamaterials," *Composites Part B: Engineering*, vol. 132, pp. 178–187, 2018.

[40] E. Turco, M. Golaszewski, I. Giorgio, and F. D'Annibale, "Pantographic lattices with non-orthogonal fibres: experiments and their numerical simulations," *Composites Part B: Engineering*, vol. 118, pp. 1–14, 2017.

[41] H. G. Kia, N. Huang, J. P. Spicer, and J. F. Arinez, "Additive Manufacturing of a Unibody Vehicle," *U.S. Patent No. 10,022,912*, Patent and Trademark Office, Washington, DC, USA, 2018.

[42] G. Nannan and C. L. Ming, "Additive manufacturing: technology, applications and research needs," *Front MechEngg*, vol. 8, pp. 215–243, 2013.

[43] R. Maghnani, "An exploratory study: the impact of additive manufacturing on the automobile industry," *J CurreEngg-Techn*, vol. 5, no. 1–4, 2015.

[44] S. Dadbakhsh, L. Hao, P. G. E. Jerrard, and D. Z. Zhang, "Experimental investigation on selective laser melting behaviour and processing windows of in situ reacted Al/Fe2O3 powder mixture," *Powder Technology*, vol. 231, pp. 112–121, 2012.

[45] M. A. Ryder, D. A. Lados, G. S. Iannacchione, and A. M. Peterson, "Fabrication and properties of novel polymer-metal composites using fused deposition modeling," *Composites Science and Technology*, vol. 158, no. 43–50, 2018.

[46] A. S. Elakkad, "3D technology in the automotive industry," *International Journal of Engineering Research*, vol. V8, no. 11, pp. 248–251, 2019.

[47] R. Manghnani, "An exploratory study: the impact of additive manufacturing on the automobile indus- try," *International Journal of Current Engineering and Technology*, vol. 5, no. 5, pp. 3407–3410, 2015.

[48] Q. Yan, H. Dong, J. Su, and J. Han, B. Song and Q. Wei, "A review of 3D printing technology for medical applications," *Engineering*, vol. 4, no. 5, pp. 729–742, 2018.

[49] F. S. S. Seyed, G. Samira, M. Mehdi et al., "A review on powder-based additive manufacturing for tissue engineering: selective laser sintering and inkjet 3D printing," *Science and Technology of Advanced Materials*, vol. 16, no. 3, Article ID 33502, 2015.

[50] P. Ahangar, M. E. Cooke, and M. H. Weber, "Current biomedical applications of 3D printing and additive manufacturing," *Applied Sciences*, vol. 9, no. 8, 2019.

[51] A. Aimar, P. Augusto, and B. Innocenti, "The Role of 3D printing in medical applications: a state of the art," *Journal of Healthcare Engineering*, vol. 2019, Article ID 5340616, 10 pages, 2019.

Hindawi
Advances in Materials Science and Engineering
Volume 2021, Article ID 7616666, 11 pages
https://doi.org/10.1155/2021/7616666

Research Article

The Investigation of Mixed Ferrofluids Containing Iron Oxide nanoparticles and Microspheres

Sharanabasava V. Ganachari,[1,2] Veerabhadragouda B. Patil,[3] Nagaraj R. Banapurmath,[2] Manzoore Elahi M. Soudagar,[4] Kiran Shahapurkar,[5] Ashraf Elfasakhany,[6] Mishal Alsehli,[6] Akshata Yavagal,[2] Pradyumna Mogre,[2] Vijayakumar M Hiremath,[7] and Shankar A. Hallad[2]

[1]*Department of Chemistry, School of Advanced Sciences, KLE Technological University BVB Campus Vidyanagar, Hubballi-80031, Karnataka, India*
[2]*Centre for Material Science, School of Mechanical Engineering, KLE Technological University BVB Campus Vidyanagar, Hubballi-80031, Karnataka, India*
[3]*Institute of Energetic Materials, Faculty of Chemical Technology, University of Pardubice, Studentska 95, Pardubice 53210, Czech Republic*
[4]*Department of Mechanical Engineering, School of Technology, Glocal University, Delhi-Yamunotri Marg, SH - 57, Mirzapur Pole, Saharanpur District, Uttar Pradesh-247121, India*
[5]*School of Mechanical, Chemical and Materials Engineering, Adama Science and Technology University, Adama 1888, Ethiopia*
[6]*Mechanical Engineering Department, College of Engineering, Taif University, P.O. Box 11099, Taif 21944, Saudi Arabia*
[7]*Centre for Nanotechnology, Department of Processing and Food Engineering, CAE, UAS, Raichur 584104, Karnataka, India*

Correspondence should be addressed to Kiran Shahapurkar; kiranhs1588@astu.edu.et

Received 19 September 2021; Revised 29 October 2021; Accepted 23 November 2021; Published 9 December 2021

Academic Editor: Ali Khorram

The aim of the present work is the synthesis and characterization of iron oxide (Fe_3O_4) nanoparticles. These nanoparticles are coated with oleic acid and polyvinyl butyral and mixed with microspheres and further developed ferrofluids with silicon oil. Studies of the performance of the nanoparticles in these ferrofluids with and without coating agents were carried out. The nanoparticles were synthesized using the chemical co-precipitation technique and coated with oleic acid and polyvinyl butyral, and it further mixed with microsphere ferrofluids and developed using silicon oil. The prepared Fe_3O_4 nanoparticles and their coated forms of oleic acid and polyvinyl butyral were mixed with microspheres; furthermore, ferrofluids were developed with silicon oil. All forms of these ferrofluids are characterized for morphology and phase purity (SEM, XRD, and FTIR). The iron oxide (Fe_3O_4) nanoparticles have shown different magnetic properties, differentiating macroscopic iron oxide in suspended particles. The ratio of surface to volume increases along with the decrease in atomic size, essential for assessing the surface morphological properties. The magneto-rheological (MR) fluids were determined, and shear stress of Expancel microsphere mixed iron oxide nanoparticle with and without them was found almost equal. However, the ferrofluid with PVB coated nanoparticles and microspheres emerged as a stable rheological ferrofluid, sustaining high shear stress and low viscosity with increasing shear rate. Also, shear rates up to 650 s^{-1} have been observed, showing very high shear stress withstanding capacity. The stability and performance of the magnetic colloidal ferrofluids depend on the thermal contribution and the balance between attractive/repulsive interactions.

1. Introduction

The rheological materials exhibit their properties instantly when subjected to variation of stimulus. These materials are electro-sensitive and magneto-sensitive, varying based on the materials state, whether solid, liquid, or gaseous. Researchers are working on modifications of magneto-rheological materials and their reactivity on the applied electric field [1–3]. These magneto-rheological materials are sensitive to small voltages and provide stimuli in the shortest

time. Usually, these materials exist in a suspension, mainly in watery fluid or oils with iron particles suspended in the media possessing an active magnetic nature [4, 5]. At the molecular level, the magnetic moment exists due to electrons partially filling/electron delocalization in the 3D [Fe] orbital. Researchers have predicted that a magnetic effect in materials such as iron aligns to an axis of the applied magnetic field vector. The magnetic effect changes the state of the nanoparticles by changing their entropy. The material attains a solid state after the molecules are aligned to post-magnetic field applications [6–8].

MR fluids are colloidal ferromagnetic (FM) particles with a size ranging from 1 to 20 μm in a transporter liquid, which does not show any characteristic magnetic properties. A portion of FM particles in an MR fluid ranges from 10 to 15% in quantity. These particles are generally synthesized from iron or iron oxides, cobalt, or nickel alloys [9–12]. The saturation magnetization of the material is around 2.2 T. The transporter liquid depends on the projecting application conditions of MR liquids (fluids). Most extensively used carrier fluids incorporate mineral or synthetic oils. Some of them are based on water, polyesters, or polyether. MR liquids may include adjuvants to prevent settling and assemblage of particles, increase their lubricity characteristics, and minimize these effects; SWCNT (single-walled carbon nanotubes) are incorporated in the CI-based MR fluid. There are some other combinations also available, primarily surfactants, which are added to increase fluid permanence. These incorporate polymers or carboxyl acids, and some with an inedible vegetable oil such as Honge (*Millettia* pinnata) oil as a transporter kind of liquids were used as fluid content, and only 25 kPa of yield stress has been generated [12–16]. The CI particles encapsulated with polymethyl methacrylate as core-shell designed particles enhanced the rinsing properties of the MR fluid. Wire-like iron nanostructures were applied to the standard MR fluid based on CI, and a form of dimorphous MR fluid was synthesized. For use in high-performance engineering, high yield stress and colloid distribution highly influence MR fluid performance. Among several magnetic materials, a primeval carbonyl iron (CI) has been extensively studied as an MR material for MR characteristics due to its high magnetic field strength properties. However, the CI-based MR suspensions have been identified to possess some disadvantages, for example, dispersion of sedimentation and nonuniformity of CI particles due to a significant difference in density [12–16]. However, to avoid this, dispersants in MR fluids were designed to increase dispersal constancy [17]. In other cases, magnetic particles coated with polymer cores or monodispersed polymer cores treated with magnetic particles enable a lower density of magnetic particles [18].

The iron nanoparticles have different magnetic properties, differentiating them from macroscopic iron in suspended particles. Their surface-to-volume ratio increases and reduces atomic size, so the surface properties are important for using any nanomaterial [19, 20]. It is also dependent on the ratio which is considered to be the function of size. Therefore, smaller size influences surface properties, interface properties, agglomeration of the particles, and physical properties of the material [21, 22]. For better consistency and longevity of the material, the nanosized iron is used to minimize the in-use thickening effect caused in macrosize particles [21]. The magnetic materials have been used in various applications in medical science, e.g., magnetic resonance imaging (MRI), sustained transfer of drugs to appropriate target organs/cells, cell isolation, biofluid detoxification, tissue repair, and hyperthermia. These magnetic nanoparticles show super paramagnetism phenomena and do not retain magnetism after the supply of the magnetic field, which offers the advantage of particle aggregation [18, 23–26]. The magnetic particles derived from magnetic transition metals (iron, nickel, and cobalt) are readily oxidized, whereas the iron oxide-like magnetite (Fe_3O_4) form is more stable against oxidation. These particles of nanomagnetite exhibit very strong ferri-magnetic behaviour and are less susceptible to oxidation. The iron oxide particles are highly condensed since they belong to nontoxic materials and are biologically consistent [27, 28].

Magnetic properties of the materials depend on the atomic radius of the nanoparticle synthesized along with the presence of ionic species with their ratios. The average diameter of the atoms ranges between 0.05 μM and 0.1 nM, which can be obtained by varying the experimental conditions (mainly environmental factors such as humidity, room temperature, and atmospheric pressures). However, the system is always polydispersed in size due to larger nanoparticles that grow at the cost of smaller nanoparticles [29]. Improvement in synthetic methods will obtain the size of the nanoparticles of the desired dimension. The uniform particles are typically prepared to separate nucleation and nuclei growth through a homogeneous precipitation reaction [30].

Synthesis and application of magneto-rheological fluid have been interesting studies from the past couple of decades [11, 25, 31, 32]. The main rise in this area is because of its impressive change in viscosity property under the applied magnetic field (Bingham plasticity). It has ability to turn a normal fluid-containing metal (iron) into a semisolid-like material, with various applications primarily in the automobile industry for the suspension system, braking system, etc. In the suspension system, the MR fluid is used to automatically adjust the stability of the car according to the road. Typically, MR fluid synthesis contains a 0.35–0.49 volume fraction of pure iron particles with nearly a spheroidal form, and size is usually of the range 1–8 nm. Also, the density has variations in the range 7–8 gm/cm^3. This property influences fair shear stress and a good off-state viscosity [19, 33–36].

As the magnetic field increases, viscosity changes along with yield strength but not to its full potential when it absorbs shock [37]. With iron being a dense particle, it easily agglomerates at the bottom, making it hard to redistribute. Many organic materials have been used before to protect the iron from rusting and avoid agglomeration [38]. A few study areas where advanced nanomaterials are critical include functionalized nanoparticles, polymers and nanocomposites, energetic materials and multifunctional materials, drug-delivery and tissue engineering, and bio-inspired and hybrid nanomaterials. [39–46].

The paper proposes numerous methods to obtain effective MR fluid for suspension purposes with higher damping properties for a longer period. The nanoiron is coated with surfactant PVB (polyvinyl butyral) and microsphere is added in the carrier fluid as a separate entity. The microspheres address increasing of the stress withstanding capacity of the MR fluids, whereas PVB avoids agglomeration and prevents rusting.

2. Materials

The primary materials, used along with the iron particles which also form aspects in deciding its efficiency, were polyvinyl butyral [$(C_8H_{14}O_2)_n$], microspheres DET, oleic acid, and silicon oil. All the materials were procured from Sigma Aldrich from a regional retailer.

2.1. Polyvinyl Butyral [$(C_8H_{14}O_2)_n$]. The polyvinyl butyral) (PVB) is consisting of reactive, markedly hydrophobic (water-hating), and hydrophilic (water-loving) polymer units. The hydrophobic group has good thermoplastic processability and solubility in the solvent. The hydrophilic group has high adhesion to inorganic material (in this case, iron particles).

2.2. Microspheres DET. Expancel microspheres 909 DET 80 d 40: its main property expands when external pressure is applied and returns to the original volume as the load is removed. The expanded microspheres are easy to compress, and it is made of 2 shells one covering the other; the inner shell can blow when pressure is applied.

3. Methods

The preparation is split into mainly three categories as preparation of nanoiron, coating with oleic acid as the surfactant, and coating with polymer PVB as the surfactant.

3.1. Preparation of Fe-Nanoparticle. Synthesis of nanoiron directly affects properties (magnetism, sedimentation, viscosity, etc., of the iron, in which the MR fluid comprising of Fe_3O_4 nanoparticles is developed by the chemical co-precipitation method used for the synthesis of iron Fe (III) (ferric) and iron Fe (II) (ferrous) salts in the alkaline medium which is known as Reimer's procedure. Preparation of Fe_3O_4 nanoparticles is done by adding two equivalents of $FeCl_2.4H_2O$ and three equivalents of, $FeCl_3.6H_2O$ in 500 ml of distilled waters; then, ammonium solution is added to it. The precipitate was filtered and then dried at 120°C, grinded by mortar-pestle, and characterized. The flow diagram of the chemical co-precipitation method is shown in Figure 1.

3.2. Fe_3O_4-Coated Nanoparticles with Oleic Acid. Prepared 10 gms of nanoiron was added to 100 ml diluted ammonium hydroxide such that pH 9 is obtained and 0.77% weight percentage of oleic acid solution is added to it; sonication is carried out at 353 K, after which dilute nitric acid is added dropwise so that pH 5 is obtained. The precipitate settles down; this residue was washed with water and acetone to remove the no-reacted oleic acid.

3.3. Fe_2O_3-Coated Nanoparticles with PVB. 5 g of PVB is dissolved in 100 ml of chloroform; in the other beaker, nanoiron 5 gm, SDS 2 gm, and 3 gm of a triblock copolymer were mixed into 400 ml of water. The whole was kept under 720 rpm for 4 hours and later for chloroform evaporation for two days. Subsequently, the precipitate was washed with distilled water and kept for drying. Table 1 shows the composition of the samples prepared.

For detailed understanding, the influence of each additive on the performance of ferrofluid composed mixtures for the study was prepared as mentioned in Table 1.

4. Characterizations

The characterization of the obtained samples was carried out using SEM coupled EDAX Model-JEOI-SEM 6360 with a high resolution of 3.0 nm at 30 kV and X-ray diffraction Phillips 3710 (wide angle powder X-ray diffractometer) in the 2θ range 10° to 100° using CuKα1 radiation source ($\lambda = 1.54056$ Å), at Shivaji University Kolhapur (SUK). FTIR spectrophotometer 4000 cm^{-1} to 450 cm^{-1} for spectral studies of the chemical bonds present in compounds was ascertained using Perkin Elmer spectrum one undertaken at Karnataka University, Dharwad (KUD). The analysis of the results is presented in the following section.

The rheological properties were ascertained at Indian Institute of Science (IISc), Bangalore. The discovery hybrid rheometer is a rotational shear rheometer with various measurement preferences that include viscosity, shear stress, storage and loss modulus, strain, and phase angle. The geometries available include a 40 mm parallel plate, 25 and 40 mm 2° angle, and cup rotor with options of a vaned and conical rotor. It has three heating system options, a Peltier plate, Peltier concentric cylinders, and an environmental test chamber. The viscosity, shear rate, and shear stress were ascertained here using the above-specified equation.

5. Results and Discussion

5.1. Scanning Electron Microscopy (SEM). There were large agglomerates formed and found in the sample of range 100 nm. It is seen from the images that range from Fe_3O_4 lied in between 10 and 75 nm Figure 2(a); oleic acid-coated nanoiron comes to be around 210 nm (Figure 2(b)); PVB coated image (Figure 2(c)) has maximum size which obtained 217 nm as per addition of less amount of PVB which was used for coating.

The nanoparticles in the sample have flakes-like structures, implying that the nanomaterial has characteristic properties of iron. Sample 1(b) containing oleic acid has obtained the striations at higher resolution, and sample 1(c) has obtained small thin-sized irregular-shaped particles, implying the copolymer present in the sample. Here, the agglomeration of particles was more widespread because of which the clusters of the compound are formed.

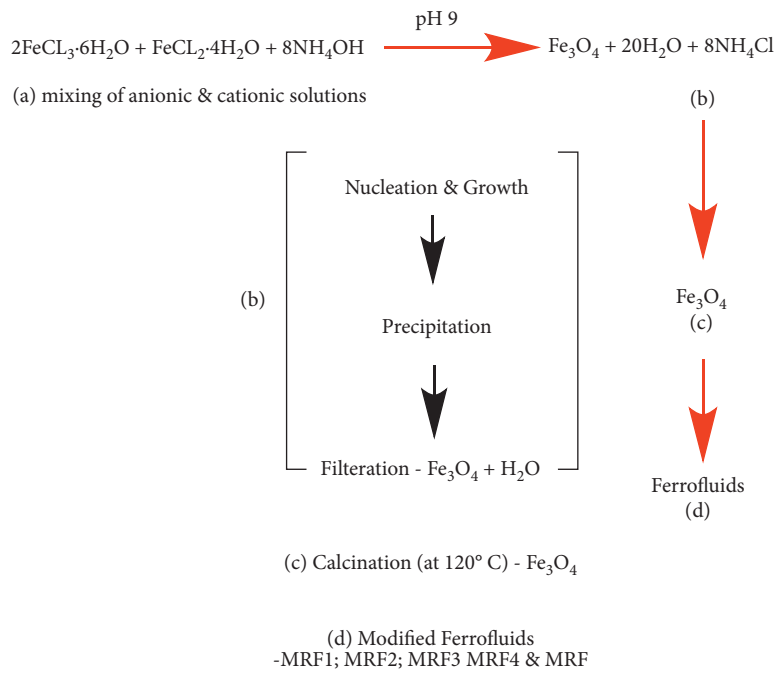

Figure 1: Flow diagram of the chemical co-precipitation method.

5.2. Fourier Transform Infrared Spectroscopy (FTIR). In the Fe_3O_4 graph, peaks around 600–400 cm^{-1} are assigned the Fe–O stretching; 516 cm^{-1}, 632 cm^{-1}, and 552 cm^{-1} show the presence of the Fe–O bond. The peak gets reduced for the coated nanoiron in spectra which confirm the presence of polymer at the surface and iron nanoparticles at core shell. In the spectrum of PVB + nano Fe_3O_4, O–H stretching is at 3437 cm^{-1} and also 1108 cm^{-1} peaks, which show C–O–C bond; stretching is more regarding PVB coated. The sample containing oleic acid has shown wavelengths of 750–800 cm^{-1}, which indicates the organic bonds, especially C=O bonds bending in the compound, i.e., ferric oxide coated with oleic acid particles and the composite of ferric oxide-PVB. In contrast with the pure ferric oxide particles, the distinctive vibrations of the ferric oxide coating are visible at the wavenumbers of about 700–500 cm^{-1} and 1060 cm^{-1} endorsed to C–O, C=O, and C–N bonds, respectively. The typical vibrations of PVB are detected at 1650 cm^{-1}, and series from approximately 1250 cm^{-1} to 700 cm^{-1} indicates the carbonyl groups and also C–H, C–C, and C–O bonds of the structure, respectively. At high wavenumbers (above 3400 cm ^{1}), the distinctive elongating from the hydroxyl groups are marginally observed.

With the interaction of the Fe_3O_4 coating with the PVB, the variances between the spectra are minor. A substantial lengthening is detected in 2600–3500 cm^{-1}. In this range, the specific stretching vibrations from the free hydroxyl groups are like what is visible in PVB, as it contains O–H groups. These interpretations could be suggestions of hydrogen bonding through the O–H groups from Figure 3.

5.3. Powder X-Ray Diffraction (XRD) Studies. The XRD patterns of the composite showed distinct peaks at 2θ values of 30.1, 34.5, 37.1, 57.1, and 62.6, which correspond to the characteristic peaks of Fe_3O_4 (JCPDS card number 19–0629) [18]. The results obtained for the ferric oxide are within its standard, and other compounds also tend to form the same. We can observe that the material in both ferric oxides with PVB and oleic acid tends to have disorders or the entropy change is similar due to the re-crystallization of the agglomerated particles. The improper re-crystallization is seen more in ferric oxide native form rather than as suspended particulate in other compounds. The improper re-crystallization tells us the state of the substance, as neither solid nor liquid it is analogous to jelly, but it is a suspension of magneto-rheological material.

The geometry of the material cannot be ascertained here in a distorted form of the state of the material. The size of the particles can be established with precision using Bragg's law, and the particle size ranges from 4 to 10 Å for the three samples for their corresponding peaks of the 2 θ shown in Figure 4.

5.4. Rheological Studies. The graphs in Figures 5 and 6 and Table 2 show the rheological parameters' variation of the samples prepared based on the indentation carried out. The samples were tested for five different current values for 310 seconds each, the stable one was extracted, and the shear rate vs. shear stress was plotted in Figure 5; similarly, viscosity vs. shear rate was also plotted in Figure 6. The graphs indicate the oleic acid does not significantly influence shear stress

Table 1: Composition and designation of samples.

Sl. No's	Codes	Components
1	MRF1	Silicon oil + oleic acid-coated iron oxide (Fe3O4) nanoparticles
2	MRF2	Silicon oil + oleic acid-coated iron oxide (Fe3O4) nanoparticles + microspheres
3	MRF3	Silicon oil + PVB coated iron oxide (Fe3O4) nanoparticles
4	MRF4	Silicon oil + PVB coated iron oxide (Fe3O4) nanoparticles microspheres
5	MRF5	Silicon oil + microsphere

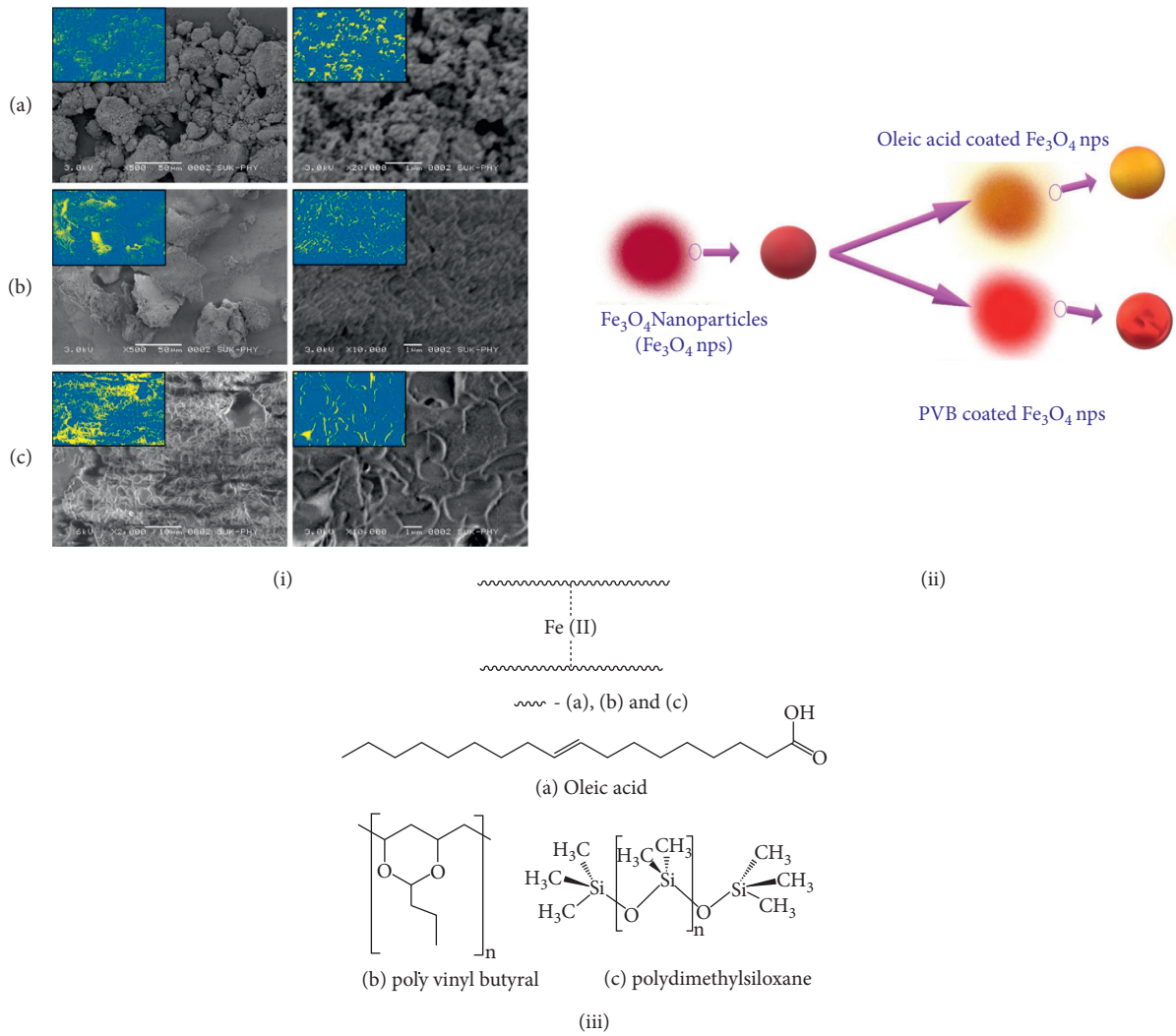

Figure 2: (a): SEM images of (A) iron oxide (Fe_3O_4) particles slightly agglomerated, (B) oleic acid-coated Fe_3O_4, and (C) PVB-coated Fe_3O_4 particles separated with gaining smoother surface. (b) Schematic representation of the coating with a zoomed view of a single particle. Oleic acid coating attains Fe nanoparticles to yellow-brownish coloration, whereas PVB gives glassy surface to the particles; it can be seen clearly in the SEM (C) images also. (c) Schematic representation of molecular interaction of Fe nanoparticles with a polymeric moiety.

compared to PVB. It looks like the shear stress of PVB coated nanoiron with microsphere is approximately the same as PVB coated nanoiron but showed very high shear stress withstanding capacity at 650 s^{-1} shear rates. However, the MRF4 showed a more linear stable and sustained shear strain compared to MRF3. It indicates that PVB and microspheres making iron nanoparticles maintain regular shear strain.

Similarly, in the case of viscosity variation to shear rate, MRF4 has a comparable viscosity to MRF3 but is very high compared to oleic acid coating. It indicates the significant influence of microspheres, and PVB makes easy flow by maintaining the high shear stress and decreasing viscosity with increasing shear rate. The microspheres have a very low density and do not settle down quickly. It clears that iron oxide nanoparticles' ferrofluid mixed with microspheres and

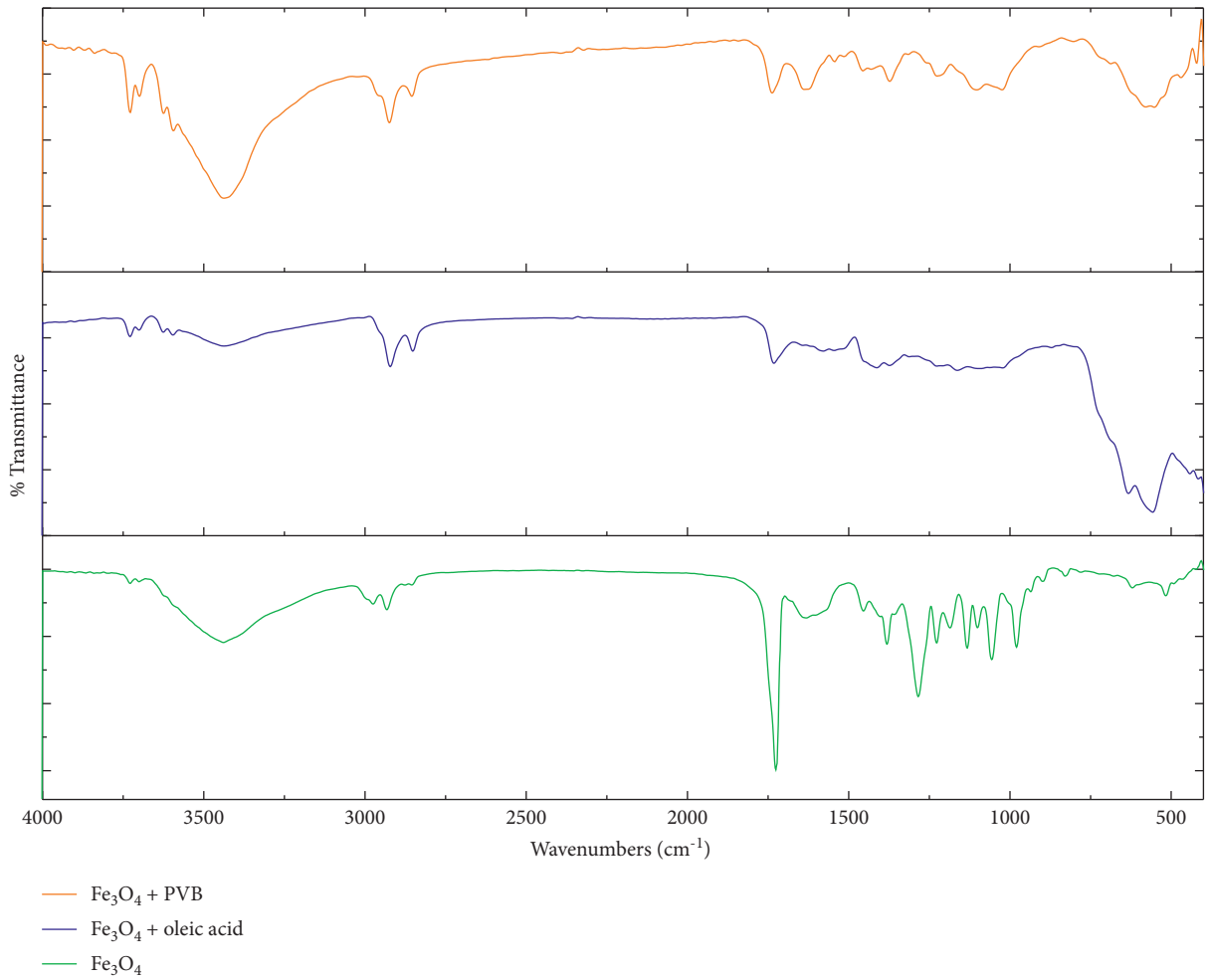

Figure 3: FTIR spectrum of all the forms of Fe_3O_4 nanoparticles.

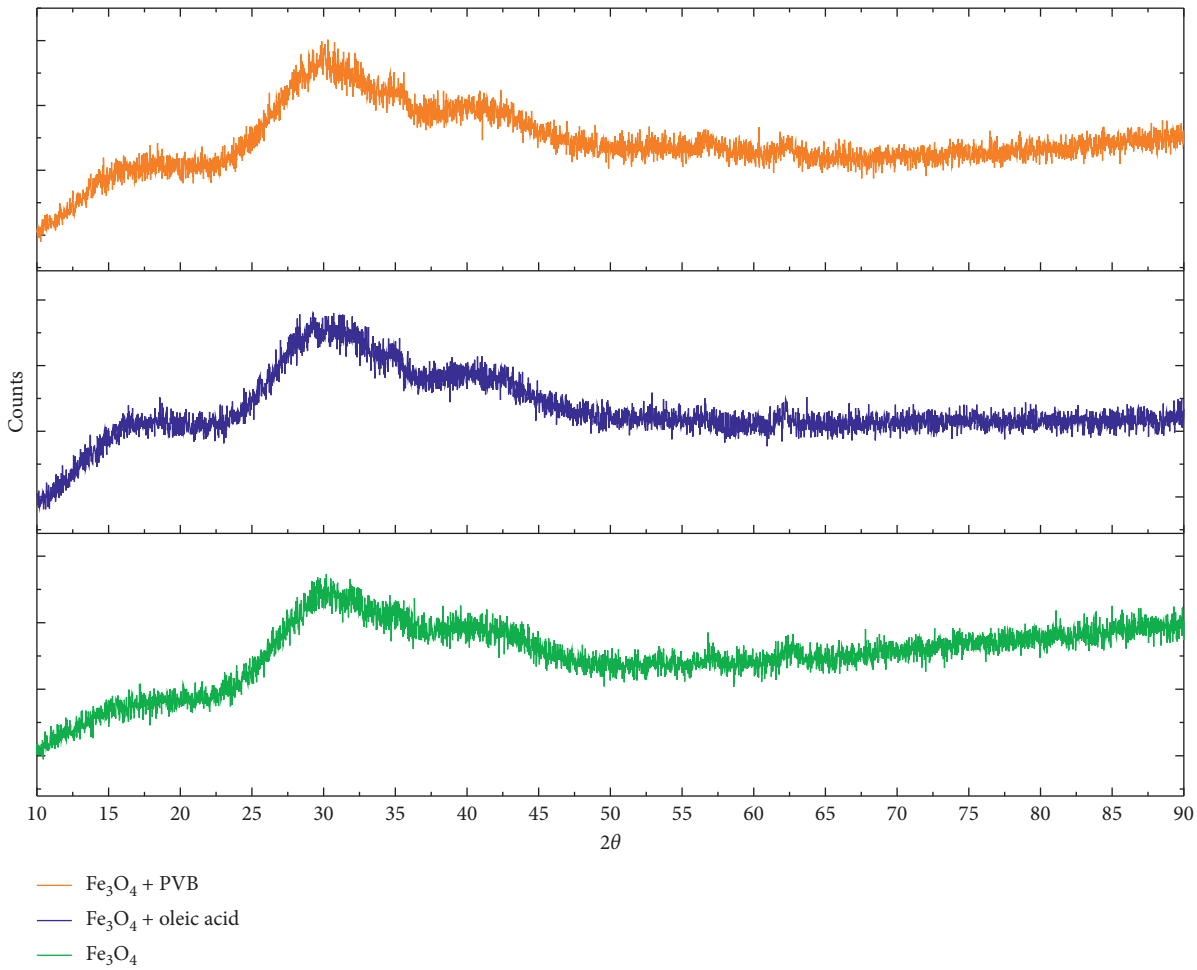

Figure 4: X-ray diffraction pattern of all the forms of Fe_3O_4 nanoparticles.

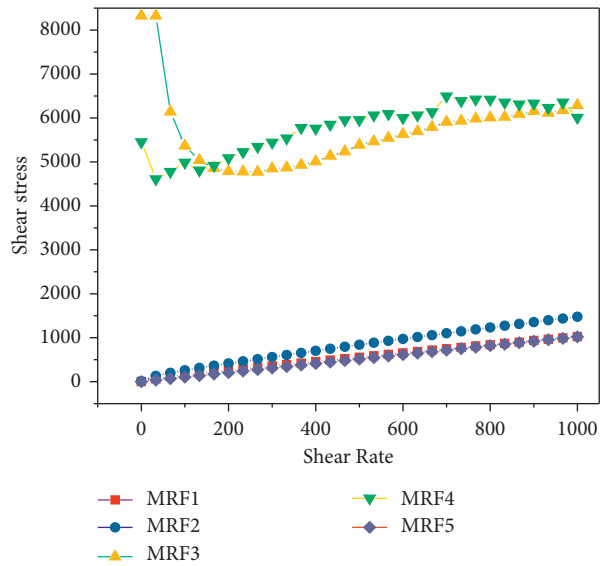

Figure 5: Shear rate vs. shear stress for MRFs.

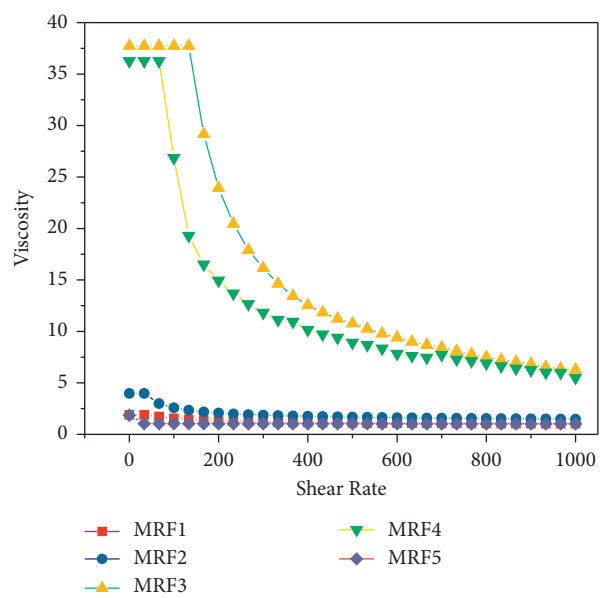

Figure 6: Shear rate vs. viscosity for MRFs.

Table 2: Rheological properties of synthesized ferrofluids.

Sl. No's	Code	Shear stress			Viscosity		
		At 0 shear rate	At 500 shear rate	At 1000 shear rate	At 0 shear rate	At 500 shear rate	At 1000 shear rate
1	MRF1	2.37	555.9	1026	1.888	1.112	1.026
2	MRF2	11.56	839.9	1476	3.97	1.68	1.476
3	MRF3	8326	5388	6292	37.74	10.77	6.286
4	MRF4	5453	5956	6009	36.26	8.913	5.505
5	MRF5	0.018	513.5	1020	1.862	1.027	1.02

PVB are very good for the application point of view, requiring stable shear strain and low viscosity.

6. Conclusion

The novel idea of adding the microsphere and coating polymer over the nanoiron in magneto-rheological fluids increases its load damping capacity and improves the life of nanoiron used. When scheming with new polymer nanocomposites, the following feature should be considered: size-dependent material characteristics of the nanoparticles used and the reproducibility of properties Particle conglomeration effect of adjuvants such as surfactants, plasticizing agents, and others on the composite characteristics. The highest approachable shear forces throughout compounding affect composite properties.

The precipitation technique used produced particle size maintaining in the nanorange to obtain the higher optimum values of iron in the material. PVB-coated iron shows similar magnetism when compared to normal oleic acid-coated molecules. The density of PVB is less, so they exhibit less agglomeration and help the iron from not getting oxidized under any other external environmental factors and enhance the rheological performance of ferrofluid. The stabilizers assist in maintaining the particles' colloidal in the liquid. When the magnetic particle is adsorbed on the outside to increase polarization, the surfactants activate the colloidal particles until the magnetic field requirement is met. The microsphere having the property of expansion and reduction of size is being used efficiently in the above-concluded experimentation. These ferrofluids can be used in futuristic applications such as rotating shaft motors and loudspeakers to dampen vibrations, etc. [47].

Data Availability

Data are available on request via mail to the corresponding author.

Conflicts of Interest

The authors declare no conflicts of interest.

Acknowledgments

The authors S. V. Ganachari and N. R. Banapurmath are thankful to KLE Society Belagavi and KLE Technological University (formerly known as B. V. Bhoomaraddi College of Engineering and Technology) for supporting this research. This research work was also supported by B. V. Bhoomaraddi College of Engineering and Technology under "Capacity Building Projects" (Principal Investigator Dr. Sharanabasava V. Ganachari). This work was supported by Taif University researchers supporting project number (TURSP-2020/205), Taif University, Taif, Saudi Arabia.

References

[1] J. Bajkowski, J. Nachman, M. Shillor, and M. Sofonea, "A model for a magnetorheological damper," *Mathematical and Computer Modelling*, vol. 48, no. 1-2, pp. 56–68, 2008.

[2] S. Odenbach, T. Rylewicz, and M. Heyen, "A rheometer dedicated for the investigation of viscoelastic effects in commercial magnetic fluids," *Journal of Magnetism and Magnetic Materials*, vol. 201, no. 1-3, pp. 155–158, 1999.

[3] K. Shahrivar, A. L. Ortiz, and J. De Vicente, "A comparative study of the tribological performance of ferrofluids and magnetorheological fluids within steel-steel point contacts," *Tribology International*, vol. 78, pp. 125–133, 2014.

[4] G. Bossis, S. Cutillas, E. Lemaire, A. Meunier, and O. Volkova, "Adaptative fluids: rheology and light transmission control," in *Proceedings of the 3rd International Conference on Intelligent Materials and 3rd European Conference on Smart Structures and Materials*, F.P. Gobin Pierre and J. Tatibouet, Eds., pp. 306–309, Lyon, France, June 1996.

[5] J. A. Miranda, R. M. Oliveira, and D. P. Jackson, "Adhesion phenomena in ferrofluids," *E Statistical Nonlinear Soft Matter Physics*, vol. 70, no. 3, pp. 036311–36410, 2004.

[6] J. Nowak and S. Odenbach, "A capillary viscometer designed for the characterization of biocompatible ferrofluids," *Journal of Magnetism and Magnetic Materials*, vol. 411, pp. 49–54, 2016.

[7] M. Martsenyuk, "A dissipative process in ferrofluid in non-homogeneous magnetic field," *IEEE Transactions on Magnetics*, vol. 16, no. 2, pp. 298–300, 1980.

[8] J. Nowak, D. Wolf, and S. Odenbach, "A rheological and microscopical characterization of biocompatible ferrofluids," *Journal of Magnetism and Magnetic Materials*, vol. 354, pp. 98–104, 2014.

[9] C. C. Ekwebelam and H. See, "Determining the flow curves for an inverse ferrofluid," *Korea-Australia Rheol. J*, vol. 20, no. 1, pp. 35–42, 2008.

[10] M. T. López-López, A. Gómez-Ramírez, L. Rodríguez-Arco, J. D. G. Durán, L. Iskakova, and A. Zubarev, "Colloids on the Frontier of ferrofluids. Rheological properties," *Langmuir*, vol. 28, no. 15, pp. 6232–6245, 2012.

[11] J. R. Morillas, E. Carreón-González, and J. De Vicente, "Effect of particle aspect ratio in magnetorheology," *Smart Material Structure*, vol. 24, no. 12, 2015.

[12] D. Susan-Resiga and L. Vékás, "Ferrofluid based composite fluids: magnetorheological properties correlated by Mason and Casson numbers," *Journal of Rheology*, vol. 61, no. 3, pp. 401–408, 2017.

[13] S. Masoud Hosseini, L. Vafajoo, E. Ghasemi, and B. H. Salman, "Experimental investigation the effect of nanoparticle concentration on the rheological behavior of paraffin-based nickel ferrofluid," *International Journal of Heat and Mass Transfer*, vol. 93, pp. 228–234, 2016.

[14] Y. Cheng, D. Li, and R. Dai, "Experimental analysis of starting torque of perfluoro polyethers-based magnetic fluid seal," *Harbin Gongcheng Daxue XuebaoJournal Harbin Eng Univ*, vol. 38, no. 8, pp. 1316–1321, 2017.

[15] K. Shahrivar and J. De Vicente, "Ferrofluid lubrication of compliant polymeric contacts: effect of non-homogeneous magnetic fields," *Tribology Letters*, vol. 56, no. 2, pp. 281–292, 2014.

[16] P. Ilg and S. Odenbach, *Ferrofluid structure and rheology*, Springer-Verlag, Berlin, Germany, 2009.

[17] Z. Laherisheth and R. V. Upadhyay, "Influence of particle shape on the magnetic and steady shear magneto-rheological properties of nanoparticle based MR fluids," *Smart Material Structures*, vol. 26, no. 5, 2017.

[18] R. Y. Hong, T. T. Pan, Y. P. Han, H. Z. Li, J. Ding, and S. Han, "Magnetic field synthesis of Fe3O4 nanoparticles used as a precursor of ferrofluids," *Journal of Magnetism and Magnetic Materials*, vol. 310, no. 1, pp. 37–47, 2007.

[19] G. Bossis and E. Lemaire, "Yield stresses in magnetic suspensions," *Journal of Rheology*, vol. 35, no. 7, pp. 1345–1354, 1991.

[20] A. Fazlali, S. Lashkarara, and A. H. Mohammadi, "Rheological properties of paraffin-based co3O4 nano-ferrofluid," *Adv Nanotechnol*, pp. 169–181, Nova Science Publishers, Inc., New York NY USA, 2014.

[21] L. M. Armijo, L. A. Ahuré-Powell, and N. M. Wereley, "Rheological characterization of a magneto-rheological ferrofluid using iron nitride nanoparticles," *Journal Applied Physics*, vol. 117, 2015.

[22] D. Borin, A. Zubarev, D. Chirikov, R. Müller, and S. Odenbach, "Ferrofluid with clustered iron nanoparticles: slow relaxation of rheological properties under joint action of shear flow and magnetic field," *Journal of Magnetism and Magnetic Materials*, vol. 323, no. 10, pp. 1273–1277, 2011.

[23] C. Rinaldi, A. Chaves, S. Elborai, X. He, and M. Zahn, "Magnetic fluid rheology and flows," *Current Opinion in Colloid & Interface Science*, vol. 10, no. 3-4, pp. 141–157, 2005.

[24] S. Thurm and S. Odenbach, "Magnetic separation of ferrofluids," *Journal of Magnetism and Magnetic Materials*, vol. 252, pp. 247–249, 2002.

[25] M. Timko, A. Zentko, M. Zentkova et al., "Magneto-rheological properties of some ferrofluids," *IEEE Transactions on Magnetics*, vol. 30, no. 2, pp. 1117–1119, 1994.

[26] C. Rinaldi, "Magneto-rheological measurements in suspensions of magnetic nanoparticles," in *Proceedings of the ASME 2005 International Mechanical Engineering Congress and Exposition*, vol. 1086, Orlando, FL, USA, November 2005.

[27] M. M. Rahman and A. Venkataraman, "Synthsesis of γ-Fe2O3 by thermal decomposition of ferrous gluconate dihydrate," *Journal of Thermal Analysis and Calorimetry*, vol. 68, no. 1, pp. 91–101, 2002.

[28] M. Nedyalkova, B. Donkova, J. Romanova, G. Tzvetkov, S. Madurga, and V. Simeonov, "Iron oxide nanoparticles - in vivo/in vitro biomedical applications and in silico studies," *Advances in Colloid and Interface Science*, vol. 249, pp. 192–212, 2017.

[29] C. N. R. Rao, "Raman spectra OF complex metal oxides," *Indian Journal Pure Applied Physics*, vol. 16, pp. 277–281, 1978.

[30] C. N. R. Rao, "Chemical approaches to the design of oxide materials," *Pure and Applied Chemistry*, vol. 66, no. 9, pp. 1765–1772, 1994.

[31] E. Ghasemi, A. Mirhabibi, and M. Edrissi, "Magnetoviscous effect in a maghemite ferrofluid," *Journal of Nanoscience and Nanotechnology*, vol. 11, no. 6, pp. 5285–5291, 2011.

[32] R. Mahesh, R. Mahendiran, A. K. Raychaudhuri, and C. N. R. Rao, "Effect of the internal pressure due to the A-site cations on the giant magnetoresistance and related properties of doped rare earth manganates, ln1-xAxMnO3 (ln = La, Nd, Gd, Y; A = Ca, Sr, Ba, Pb)," *Journal of Solid State Chemistry*, vol. 120, no. 1, pp. 204–207, 1995.

[33] K. Shah, S.-B. Choi, and H. Jin Choi, "Thermorheological properties of nano-magnetorheological fluid in dynamic mode: experimental investigation," *Smart Material. Structures*, vol. 24, 2015.

[34] C. C. Ekwebelam and H. See, "Using oscillatory shear to probe the effects of bidispersity in inverse ferrofluids," *Korea Aust. Rheol. J*, vol. 19, pp. 35–42, 2007.

[35] M. Chand, S. Kumar, A. Shankar, R. Porwal, and R. P. Pant, "The size induced effect on rheological properties of Co-ferrite based ferrofluid," *Journal of Non-crystalline Solids*, vol. 361, pp. 38–42, 2013.

[36] G. Bossis, E. Lemaire, O. Volkova, and H. Clercx, "Yield stress in magnetorheological and electrorheological fluids: a comparison between microscopic and macroscopic structural models," *Journal of Rheology*, vol. 41, no. 3, pp. 687–704, 1997.

[37] K. Vasu, H. S. S. R. Matte, S. N. Shirodkar et al., "Effect of high-temperature shock-wave compression on few-layer MoS2, WS2 and MoSe2," *Chemical Physics Letters*, vol. 582, pp. 105–109, 2013.

[38] S. V. Ganachari, V. K. Joshi, R. Bhat, R. Deshpande, B. Salimath, and N. V. S. Rao, "Large scale synthesis and characterization of γ-Fe2O3 nanoparticles by self-propagating low temperature combustion method," *International Journal Science Research*, vol. 1, no. 2, pp. 77–79, 2012.

[39] S. Sagar Iqbal, B. Ali, N. Hossain et al., "Synergetic influence of F-MWCNTS on polyvinylpyrrolidone sodium alginate composite membrane for reverse osmosis," *Journal of Environmental Chemical Engineering*, vol. 9, no. 5, Article ID 106085, 2021.

[40] S. V. Ganachari, L. R. Viannie, P. Mogre, R. P. Tapaskar, and J. S. Yaradoddi, L. Martínez, O. Kharissova, and B. Kharisov, "Conducting polymer composite-based sensors for flexible electronics," in *Handbook of Ecomaterials,* Springer, New York, NY, USA, 2019.

[41] S. Ali Mazari, N. Hossain, W. Jeffrey Basirun et al., "An overview of catalytic conversion of CO2 into fuels and chemicals using metal organic frameworks," *Process Safety and Environmental Protection*, vol. 149, pp. 67–92, 2021.

[42] S. A Mazari, R. Abro, and F. S. A. Khan, "Nanomaterials: Applications, waste-handling, environmental toxicities, and future challenges-a review," *Journal of Environmental Chemical Engineering*, vol. 9, no. Issue 2, Article ID 105028, 2021.

[43] K. R. Sanadi, P. D. Sanadi, M. L. Gaur, A. V. Mali, and G. S. Kamble, "Optical, electrical and morphological studies of βHgS thin film prepared by improved chemical bath deposition technique," *Bulletin of Materials Science*, vol. 44, no. 1, 42 pages, 2021.

[44] V. B. Patil, K. Zalewski, J. Schuster, P. Bělina, W. A. Trzciński, and S. Zeman, "A new insight into the energetic co-agglomerate structures of attractive nitramines," *Chemical Engineering Journal*, vol. 420, no. 3, Article ID 130472, 2021.

[45] K. C. Rathod, P. D. Kamble, K. R. Sanadi, G. S. Kamble, M. L. Guar, and K. M. Garadkar, "Photovoltaic application study of zinc telluride thin films grown by chemical bath deposition method," *Advances in Materials Physics and Chemistry*, vol. 11, no. 8, pp. 131–144, 2021.

[46] M. T. H. Siddiqui, H. Ahmed Baloch, S. Nizamuddin et al., "Synthesis and optimization of chitosan supported magnetic carbon bio-nanocomposites and bio-oil production by solvothermal carbonization co-precipitation for advanced

energy applications," *Renewable Energy*, vol. 178, pp. 587–599, 2021.

[47] V. Nimbagal, N. R. Banapurmath, A. M. Sajjan, A. Y. Patil, and S. V. Ganachari, "Studies on hybrid bio-nanocomposites for structural applications," *Journal of Materials Engineering and Performance*, vol. 30, no. 9, pp. 6461–6480, 2021.

Hindawi
Advances in Materials Science and Engineering
Volume 2021, Article ID 4933450, 10 pages
https://doi.org/10.1155/2021/4933450

Research Article

Exploration on Mechanical Behaviours of Hyacinth Fibre Particles Reinforced Polymer Matrix-Based Hybrid Composites for Electronic Applications

Pradeep Kumar Panda,[1] J. Jebastine,[2] Madhialagan Ramarao,[3] Shaik Fairooz,[4] Chirra Kesava Reddy,[5] Omaima Nasif,[6] Saleh Alfarraj,[7] Velu Manikandan,[8] and I. Jenish[9]

[1]*Department of Packaging, Yonsei University, Wonju-Si 26493, Gangwon-Do, Republic of Korea*
[2]*Department of Electronics and Communication Engineering, Jeppiaar Engineering College, Chennai 641407, Tamil Nadu, India*
[3]*Department of Mechanical Engineering, Bharath Institute of Higher Education and Research, Chennai 641407, Tamil Nadu, India*
[4]*Department of Electronics and Communication Engineering, Malla Reddy Engineering College, Secunderabad 500100, Telangana, India*
[5]*Department of Mechanical Engineering, Lincoln University College, Petaling Jaya, Selangor, Malaysia*
[6]*Department of Physiology, College of Medicine and King Khalid University Hospital, King Saud University, Medical City, P.O. Box-2925, Riyadh 11461, Saudi Arabia*
[7]*Zoology Department, College of Science King Saud University, Riyadh 11451, Saudi Arabia*
[8]*College of Environmental & Bioresource Sciences, Chonbuk National University, Iksan 570752, Republic of Korea*
[9]*Department of Mechanics, Seenu Atoll School, Hulhumeedhoo, Addu City 19060, Maldives*

Correspondence should be addressed to I. Jenish; jenish@satollschool.edu.mv

Received 16 August 2021; Accepted 25 October 2021; Published 6 December 2021

Academic Editor: P Ganeshan

Biocomposites with polylactic acid (PLA), nanosilica parts, and water hyacinth fibres have been developed in this experimental study. By changing the weight percentage of nanosilica particulate matter (0, 2, 4, 6, and 8 percent) with PLA and water hyacinth fibres, five composite mates were produced through a double screw extruder and compression moulding machine. According to the ASTM standards, the process to machine, the composite specimens have been adopted from the water jet machining process. The tensile, compression, flexural, impact, hardness, and water absorption tests were performed on the composite specimens to assess various mechanical properties and absorbance behaviour. The test findings reveal the significant improvement in the tensile and flexural properties of the composites. Composites contain 6 percent of the fine nanosilica particles by weight. Concerning adding the growing weight percentage (4 percent) of nanosilica particles to the composites, the water absorption properties of the composites have significantly improved. The tensile strength of 6% nanosilica mixed specimens showed the highest tensile stress rate as 36.93 MPa; the value was nearly 3.5% higher than the 4% nanosilica mixed composite specimens.

1. Introduction

Researchers have become particularly concerned with reducing their use of synthetic plastics because of environmental problems caused by plastic waste, not biodegradable. Synthetic mixing with biological (hybrid) materials and using fully biodegradable materials have been included in recent innovations. Bioplastics have been developing in the last ten years to replace synthetic plastics [1]. In most modern engineering fields, composites' most advanced physical features are more used against conventional metallic and alloying materials. Despite the high technical and physical features of the alloys, scientists are still trying to detect the new composite material due to its high strength to

rigidity ratio, resistance to corrosion, and cost factors. Consistent positive deterministic factors have also been found in the enhanced polymer materials (FRPs) [2], such as low weight, high stiffness-to-weight ratios, good chemical resistance, and corrosion resistance. Generally polymer matrix composites are widely used in aerospace, automobile, and electronic applications. The manufacture of printed circuit boards (PCBs) reached an all-time high of $51 billion in 2009, thanks to the rising demand for electronic devices. However, the PCB industry's rapid growth encourages it to focus on circuit innovation rather than the environmental impact of the materials used. It is necessary to take a fresh approach to the creation of more environmentally friendly foundation materials. Most commercial PCB materials are glass fibre cloth reinforced epoxy composites because they provide a suitable combination of mechanical and electrical qualities. Figure 1 reveals the schematic diagram of printed circuit boards.

Figure 2 reveals the types of fibre. Water hyacinth is a possible source of low-cost, nontoxic, and abundant natural fibre in Indonesia. The fibre content is comparable to that from other sources [3] and has approximately 40% cellulose content. The content of cellulose has a considerable impact on biocomposite properties. Like the previous study [4, 5], the high content of cellulose leads to better mechanical and thermal properties. The commonly used natural fibres are microfibers of a diameter of 1–1000 μm (micron metre) or nanofibers of a diameter of 1–100 nanometres [6, 7]. In previous research studies, microfibers from kenaf [8], water hyacinth [9, 10], ramie [11, 12], vacuous palm oil bunches [13], and microalgae's [14] were used. However, when dispersed in a stretch matrix, these microfibers usually form agglomerations or porosities, which produce low mechanical characteristics. Fibre must be nanosized to reduce agglomeration. Due to the high contact surface area, lower density, and good mechanical properties, smaller fibres result in better biocomposites [6, 15, 16]. Different cheap filler materials have been attempted in conjunction with these to reduce the cost to the total composite output to increase the strength of the FRPs. In most research publications [17, 18], silica has played a role in this sequence of filler materials such as calcium carbonate. A novel approach was to produce tough epoxy resin made from rice husk with a particle size distribution of 40–80 nm [19]. This study will discuss the Charpy impact comportment of composites based on WH fibre. This research shows that the impact strength of polymer composites is based on WH fibre compounds. It is sufficiently competitive compared to other composites based on natural fibre [20]. There was an increase in the tensile characteristics, impact strength, and fatigue life of reinforced glass-fiber composites by adding silica nanoparticles to the contents [21]. The incorporation of silica particles reveals a beneficial effect on the elasticity module, flexural modulus, and hardness of 2 wt% threshold value. However, silica's tensile and bending strength are reduced by a slightly higher bending strength than their tensile parts [22]. Increased interfacial bonding for Basalt fibre reinforced epoxy composite is added by adding SiO2 nanoparticles to the fibre surface [23]. Epoxy/silica/kenaf composites with different concentrations have been manufactured with silica particles. Untreated kenaf fibres with modified silica epoxy composites have increased their flexural and impact strength [24]. Aquatic plants like water hyacinth (*Eichhornia crassipes*) have a rapid growth rate, making them undesirable as garden plants. Water hyacinth's rapid growth has led to low levels of dissolved oxygen in the water, and it can spread across large areas. Water hyacinth is not all bad. It absorbs heavy metals and provides livestock feed, and its fibre can be used to make handicrafts [25, 26]. It is found that for water hyacinth-polypropylene composites, except traction strength, all mechanical properties are improved adequately. In the course of this study, water hyacinth fibre was chosen as a refurbishment, and nanosilica particles were chosen as the filler materials for polylactic acid (PLA). The execution methodology of this experimental research work is shown in Figure 3.

2. Materials and Methods

Matrix material, one of the reinforcement materials which is used in this experimental work, i.e., polylactic acid (PLA) and nanosilica powder, was purchased from Covai Seenu and Company Ltd, Coimbatore, Tamil Nadu, India. The green unit Coimbatore, Tamil Nadu, India, provides further reinforcing material, i.e., water hyacinth fibres. The nanoparticles known as silicon dioxide, also known as nanosilicas, are the base of a large degree of biomedical research due to their stability, low toxicity, and ability to operate with multiple molecules and polymers. Nanoparticles of silicon dioxide appear in white powder form. The physical properties of these nanoparticles are provided in the table below. Table 1 shows the various basic physical, chemical, and thermal properties of nanoparticles with silicon dioxide. P1 consists of pure PLA particulates of 100 wt percent. P2 is made of 80 wt% pure PLA particles, 0 wt% silica powder, and 20 wt% water hyacinth fibre. P3 contains 80 percent wt of pure PLA particles and 20 percent wt of powder of silica and 0 percent wt of powder of water hyacinth. P4 consists of 80% by weight of PLA pure, 2% by weight of silicon powder, and 18% by weight of hyacinth powder. P5 consists of pure PLA particles of 80% wt, silicone powder of 4% wt, and water hyacinth powder of 16% wt. P6 includes 80% wt of pure PLA, 60% wt of silica powder, and 14% wt of powder of hyacinth water. P7 comprises 80 wt% of the pure part of PLA, eight wt % of the silica, and 128 wt% of the water powder hyacinth.

The particle size of silica obtained at first does not match the size required. To comply with the requirement, silica powder was processed in a ball mill. The measured nanosilica particle diameter in the range of 75 to 100 nm was used as a reinforcement content. Before feeding these mixtures into the double screw extruder machine, PLA particles were heated above the melting temperature. Following heating, the PLA particles were transformed into a liquid stage. The weight percent of enhancement materials, i.e., nanosilica powder and short water hyacinth fibres, was added to liquid state PLA. After 45 minutes of adding filler and refill material to the fluid state PLA matrix, the entire mixture was thoroughly misled in one blender. The composite mix of the

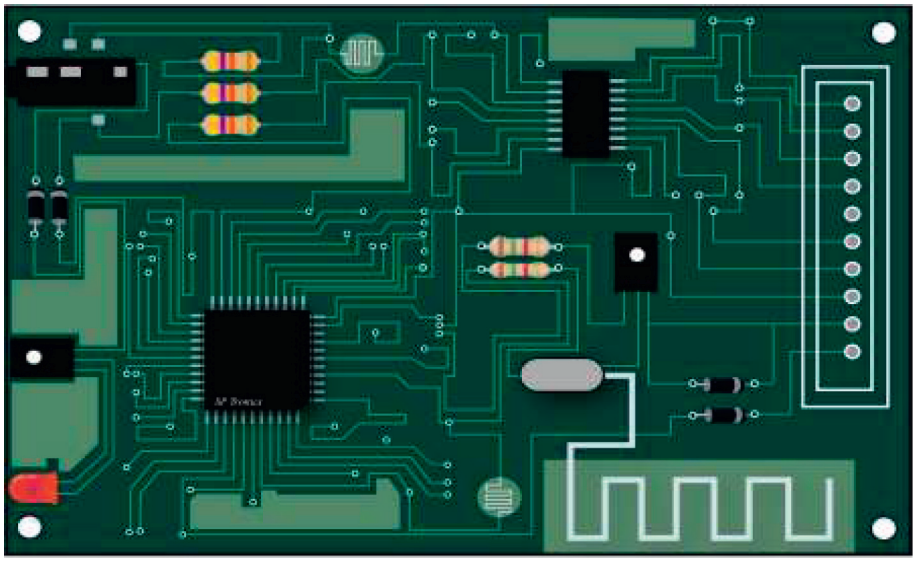

Figure 1: Schematic diagram of printed circuit boards.

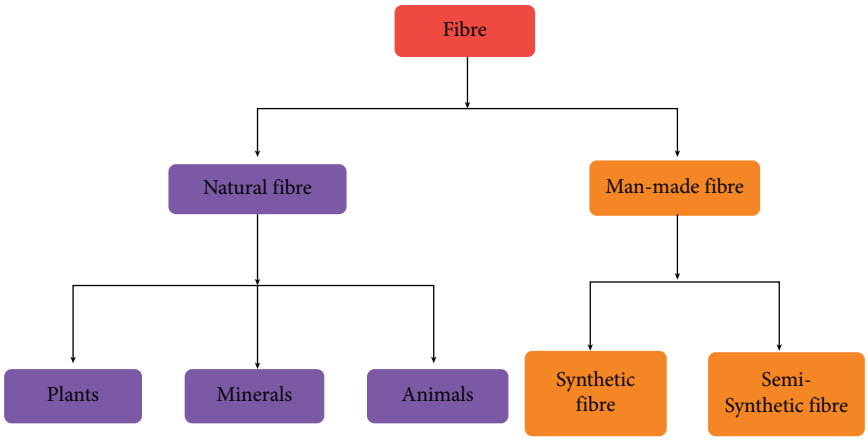

Figure 2: Types of fibre.

array and the reinforcing and the filler materials of smaller pieces (3 cm to 5 cm) in length was prepared by a double screw extruder. Figure 4 reveals the double screw extrusion process arrangement.

The composition of the rectangular bars from well-prepared, hybrid-based composite parts was prepared by a hydraulic injection moulding machine. The combined water hyacinth fibre, PLA, and silica particles had allowed the compression moulding machine to heat up to 100 °C at a specific hydraulic pressure for up to thirty minutes. The required composite plates had been collected and cooled at room temperature after the processing time of 30 minutes. Figure 5 reveals the advantages of injection moulding.

The composite plates were transferred after the cooling process to the water jet machining process, and the necessary composite components were separated from the composite compound according to ASTM standards. For the remaining compositions, the same process was repeated. Figure 6 reveals the tensile test sample. Tensile, flexural, and impact tests for establishing the mechanical properties of composites were permitted for the well-prepared composite specimens. The tensile test (ASTMD638), compression test (ASTM-D695 M), and flexural test (ASTMD790-10) of the composites at a load rating of 1 mm/min were used with a computerised 400 kN universal testing machine. Figure 7 reveals the universal testing machine. A Charpy impact test was also performed on the composite impact test specimens in the Impact Testing machine as defined by the ASTM D6110-97 standards. Figure 8 reveals the Impact Testing machine. A water absorption test was also performed in composite specimens of the water absorption test, according to the ASTM D5229 pure water standards. The tensile, compressive, bending, impact, toughness, and water absorption tests were given in different sample dimensions as given in Table 2.

The results of mechanical and water absorption tests, such as ultimate tensile strength, flexural strength, flexural strength, impact strength, and water absorption percentage, have been shown in the results and the discussions as a graphical colour plot.

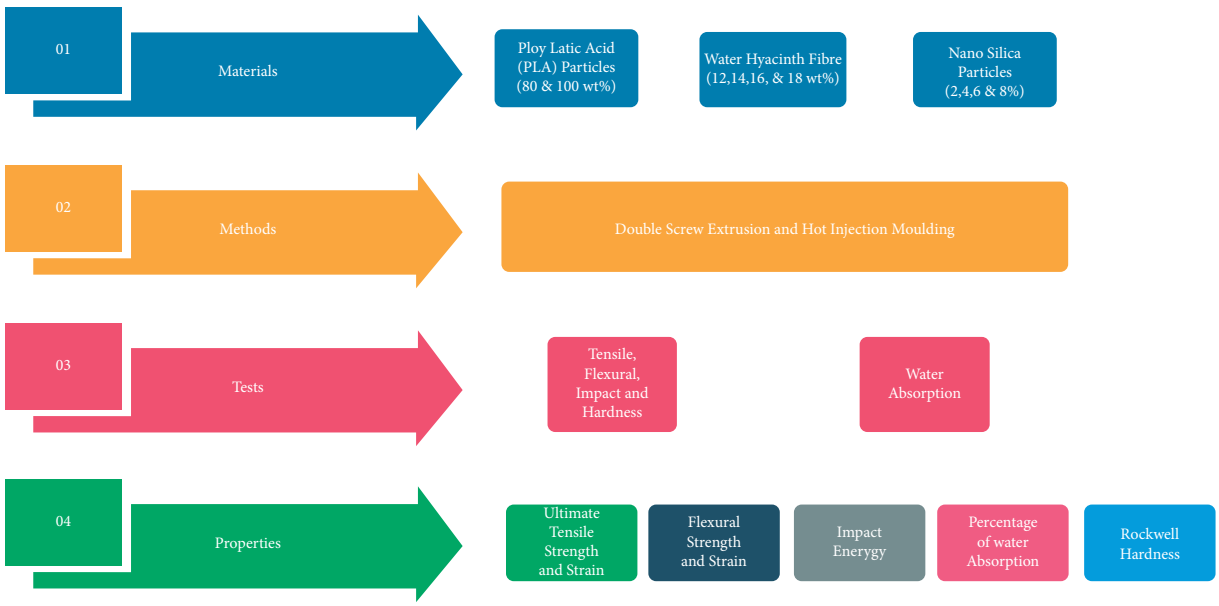

Figure 3: Execution methodology of this experimental research work.

Table 1: Physical, chemical, and thermal properties of silica.

Chemical composition	Silica 46.83% and oxygen 53.33%
Density	2.4 g/cm^3
Molar mass	59.96 g/mol
Melting point	1600°C
Boling point	2230°C

3. Results and Discussions

3.1. Tensile Test. Figure 9 illustrates the tensile strength and tensile behaviour of the water hyacinth reinforced PLA-filled particulate composites containing different ratios of loaded nanosilica and water hyacinth. Without any water hyacinth fibre or nanosilicone (P1 composite), the pure PLA composite showed a tensile strength of 31.45 MPa and the corresponding tensile strain rate was 0.34 percent. During the test, both ends were very strongly fixed on the grips of the universal test machine and the fracture test was performed with the gradual load at the speed of the crosshead to about 1 mm/min. The PLA matrix with 20 wt% nanosilica and 0 wt % water-enhanced fibre composite (P2 composites) had a tensile strength value of 32.95 MPa, and the respective stress rate was 0.35%. With a tensile strength value of 33.68 MPa and a tensile pressure rate of 0.36 percent, the PLA matrix with 0 wt percent nanosilica particles and 20 wt percent hyacinth water fibre enhanced composites (P3 composites).

After the test, the specimen was broken down at specimen length, and the fibre-pull-out fracture initially burns the load by fibre when it exceeds its load capacity, when the load was transferred to the matrix with the loss of interfacial strength from fibre to the matrix, thus losing the power interface between the fibre and the matrix. The addition of composites of 2 percent nanosilica particles (P4 composites) showed the tensile strength of 34.93 MPa; the tensile strength of the P1, P2, and P3 composites is almost 3.7, 6.09, and 11.06 percent higher. Its corresponding pressure rate was 0.32 percent higher than P1, P2, and P3 composites. The mixed specimens (P5 composites) of 4% nanosilica particles had shown a tensile stress value of 35.67 MPa, nearly 2.11% higher than the mixed specimens of 2% nanosilica (P4 composites). The tensile strength of 6% nanosilica mixed specimens (P6 composites) showed the highest tensile stress rate as 36.93 MPa; the value was nearly 3.5% higher than the 4% nanosilica mixed specimens (P5 composites), and the tensile pressure rate was 0.37%. The tensile strength of the 8% mixed specimens of nanosilica particles (P7 composites) has shown the stress value as 34.61 MPa; this value was almost 6.28% less than the 6% mixed particulate matter (P6 composites) for nanosilica, and the corresponding tensile strain rate was 0.35%. In addition, the 6% nanosilica particles, which had 14% water hyacinth in PLA composite samples, showed the highest pressure value for a tensile of 36.93 MPa, which was almost 12.07 higher than their corresponding strain rate which was respected to 0.39%. Similarly, given the tensile stress value of 4%, the jacinth was as high as the other five combinations, with the exception of P6 composite specimens. It is much higher than the other five. The combined or mixed cumulative tensile strength was also 36.30 MPa of 4% nanosilica particles and 6% water hyacinths higher. The respective strain rate was 0.38%, which was equally higher than all mixed proportions. Compared to the pure PLA composites, this experiment demonstrates the greater strength of the particulate composite. The stress rate also decreases in the case of the particulate addition to the matrix material. The stiffness increases so that the value of the tensile strength rises substantially.

3.2. Flexural Test. Figure 10 shows the flexural strength conduct of water hyacinth fibre reinforced PLA filling composites of nanosilica particles and water fibre loaded. First, the specimen was placed over two supports in the standard fixture

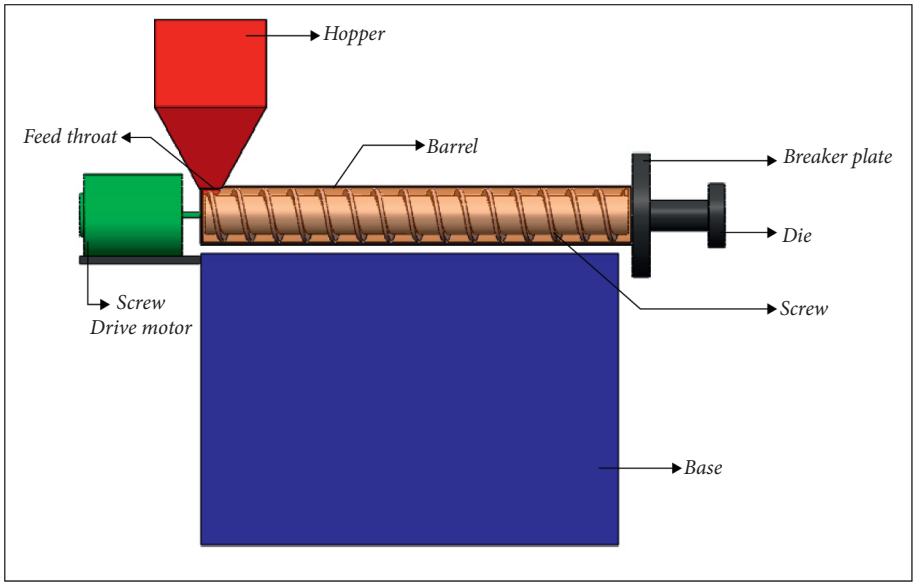

Figure 4: Double screw extrusion process arrangement.

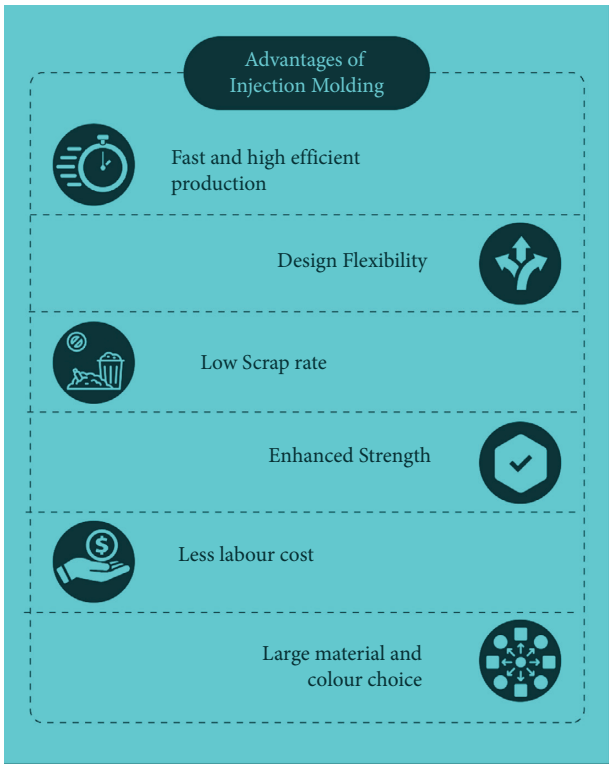

Figure 5: Advantages of injection moulding.

indicated by the standards. Then, using the universal test machine with standard crosshead speed, the centre of the specimen is permitted with the gradual load. With the aid of a digital device and a UTM device, the fracture load was noted.

As mentioned in the tensile strength analysis, the flexural strain value of 27.12 MPa for PLA pure composites (P1 composite) with a strain rate of 4.9 percent was given in bending strength. With a bending value of 26.72 MPa, the PLA matrix with 20 W/12% nanosilk particles and 0 W/8% water hyacinth fibre reinforced composites had a bending strength value of 4.3%. The PLA matrix had a flexural strength value of 28.97 MPa. The appropriate stress rate was distinguished by 3.2 percent, with 0 wt percent nanosilk particles and 20 wt percent water hyacinth fibre reinforced composite (P3 composites). The added 2 percent of nanosilica particles (P4 composites) showed that they have a Flexural Resistance value of 30.42 MPa; that value was nearly 12.17, 13.85, and 5 percent higher than the composites P1, P2, and P3, and their associated strain rate is 4.4

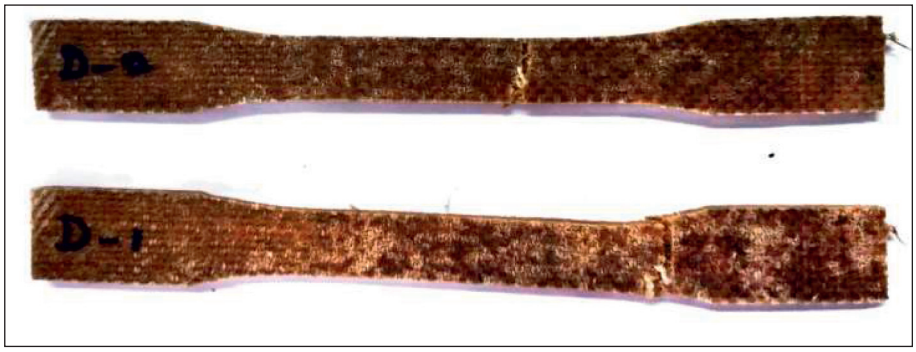

Figure 6: Tensile test sample.

Figure 7: universal testing machine.

percent, with a lower rate than the originally clean specimens. The loaded 4 percent (P5 composites) of nanosilica particles also showed a value of 31.82 MPa. That value was significantly higher than the remaining 4,6 percent set of values. The highest flexural strength was 32.53 MPa for 6 percent nanosilica particles (P6 composites) and was almost 19.95, 21.75, 12.30, and 6.98 and 2.23 percent above composites P2, P3, P4, and P5 and its corresponding strain rate is 5.3 percent. The 8% nanosilica composite (P7 composites) nanoparticles have shown a bending strength of 30.11 MPa, a value that was almost 7.44% lower than the P6 composites, and their corresponding stress rate was 4.7%. The values observed were 30.42, 31.82, 32.53, and 30.11 MPa for the 18, 16, 14, and 12 wt percent loaded water hyacinth as the value in nanosilica composites also demonstrated the spike in flexural stress. Whereas the 6% nanosilica particles and 14% hyacinths showed a tremendous increase in bending stress, the observed value is 32,53 MPa with a strain rate of 5.3%. All the observed results have demonstrated that the added particulate matter into the composites significantly increases the flexural stress value. Secondly, incorporating water hyacinth fibres maintains a higher bending strength while adding nanosilica particles to the matrix (6% nanosilica particles), reducing bending stress, and adding hyacinth again (14%) increase strength and further reduce bending stress appropriately.

Figure 8: Impact Testing machine.

Table 2: Composite specimen dimensions for mechanical and water absorption test.

Test	Dimensions in mm (length-width-thickness)
Tensile	$165 \times 12 \times 5$
Compressive	$150 \times 12 \times 5$
Flexural	$100 \times 12 \times 5$
Impact	$80 \times 12 \times 5$
Water absorption	$100 \times 100 \times 5$

4. Charpy

4.1. Impact Test. The impact strength of composites examined by the Charpy impact test is shown in Figure 11. The results demonstrated an additional 160.39, 46.21, 64.95, 24.77, and 10.88 percent in composites P2, P3, P4, and P5, respectively, and 6 wt percent of nanosilica particles in the composite P6. This is due to the fillers used by silica particles, which strengthened the PLA matrix less than 56 nm in the particle stage. The microparticle fillers (silica particles) helped increase the surface-to-volume ratio by providing a larger surface area. Thus, the stress transfer between the filler matrix was increased. In addition, the fillers showed good interfacial adhesion in the polymer matrix, which helped to increase stress transfer between the filler and the matrix.

Composite P6, compared with P1 composite ES, had a higher impact strength due to the presence of water hyacinth fibre and nanosilica particles that allowed greater power absorption in the event of an impact. Made of water hyacinth and nano silica are composites P4, P5, P6, and P7. The results enhance the impact strength of PLA from P4 to P6 composites. Compared to all other composites, pure PLA (P1 composites) also provided a small impact strength (P2 to P7). The highest impact strength of composite P6 was 9.27 kJ/m2, improving by 160.4% compared to pure PLA, because the water hyacinth and nanosilica continuous fibre provide additional energy absorption at impact. However, with the performance of the composite P2, impact to composites P3 to P7 was the lowest. The lack of water hyacinth fibre probably resulted. The result agreed with the finding from earlier studies of the subsequently reduced interaction among the fibres and the matrix by the formation of a crack and byproducts resulting from the reaction of nanosilica particles. Finally, because of the absence of reinforcement and filling materials in the PLA matrix, the impact properties of the composite material were reduced.

4.2. Rockwell Hardness. Hardness is a feature that measures the surface indentation and abrasion resistance of the material. Hardness is also a critical parameter that indicates the composite's durability and life span. The hardness of the various composition composites and PLA composite specimens is shown in Figure 12. All the composites produced were highly harder than the clean epoxy. This increased hardness was associated with the high rigidity and hardness of the distended stage parts, which can be reinforced due to their load carrying capacity. The results indicate that adding 6 wt% of nanosilica particles in the P6 composite improves hardness by 55.88, 43.24, 51.43, 17.78, and 8.16 percent, in P1, P2, P3, P4, and P5.

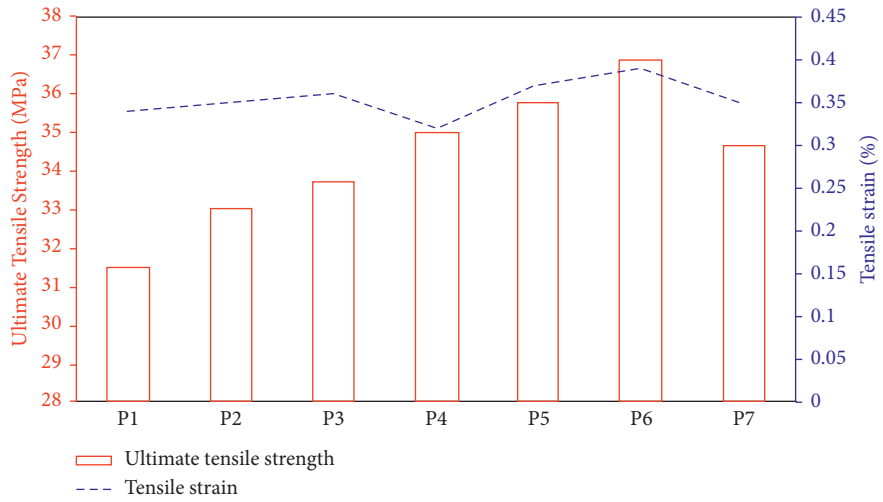

Figure 9: Ultimate tensile strength and strain analysis of composites.

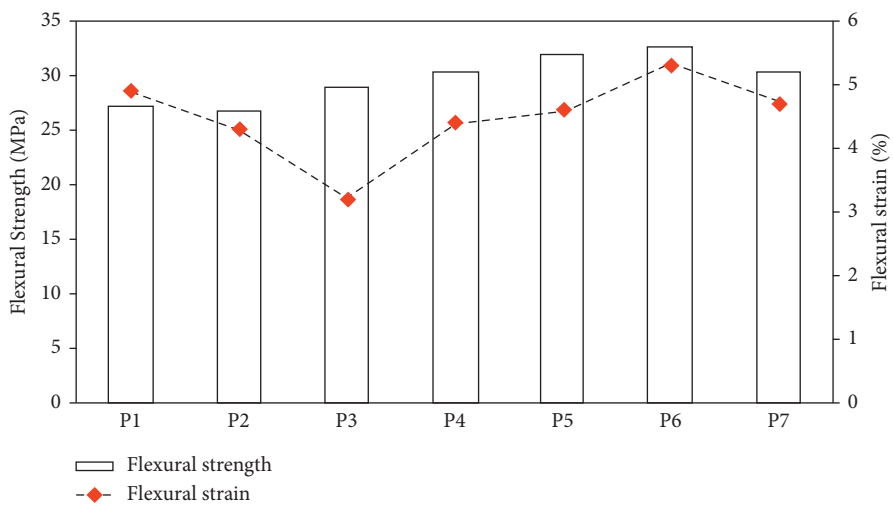

Figure 10: Variations on flexural strength and strain of nanosilica particles filled hybrid composites.

The plot observed that P6 composites have the highest hardness, 56% better than pure PLA composites (P1 composites). However, the hardness of a composite depends on the homogenous distribution of the reinforced particles and fibre into the matrix. Due to the increasing hardness of this composite, the silica content and water hyacinth fibres are increased by 6 wt%, but the loading of the particles increases slightly and gradually. The increase of the hardness value at lower particles charging can be attributed to the homogenous distribution of silica particles and water hyacinth fibre within the matrix, with a depreciation of the vacuums and a stronger interfacial adhesion between the matrix and the particles. It is worth noting that while silica has reduced the composition's tensile strength, it has increased the PLA matrix's hardness. The loading conditions are different. The low interfacial adhesion between both the tensile cargo conditions tends to cause the silica particles to debond from the PLA matrix. In the case of a hardness test, the composite is loaded vertically and downwards. This causes silica particles to be firmly pressed into the matrix. The pressure action causes a smooth transfer, although their interfacial adhesion has been poor, of the load from the matrix to the silica and water hyacinth. All of these lead to better composite hardness.

4.3. Water Absorption Properties. The durability of the water hyacinth fibre reinforced nanosilica particles filled PLA matrix biocomposites can be predicted through the water absorption tests. The weight of each specimen was measured before this test. Weight measured composite specimens are then immersed in normal water for 72 hours (three days). After this duration, the immersed specimens are taken away from the water container for the weight measuring purpose. Based on the weight of the specimen after the test, the percentage of water absorption has been calculated. The water absorption test results are illustrated in Figure 13 for all composite specimens.

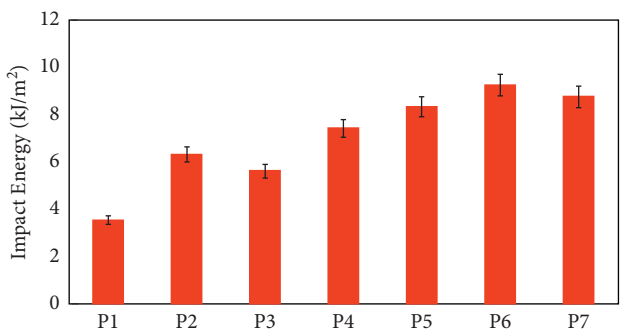

Figure 11: The impact energy of nanosilica particles filled hybrid composites.

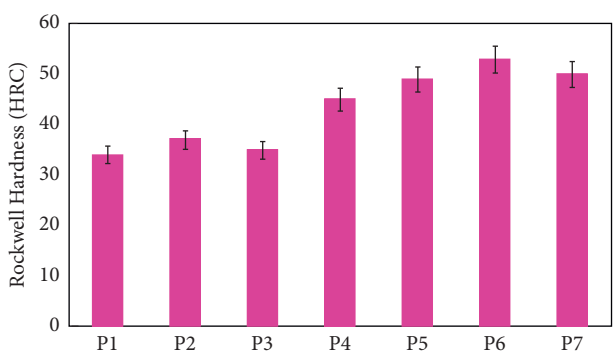

Figure 12: Rockwell hardness (HRC) values of the pure PLA and hybrid composite samples.

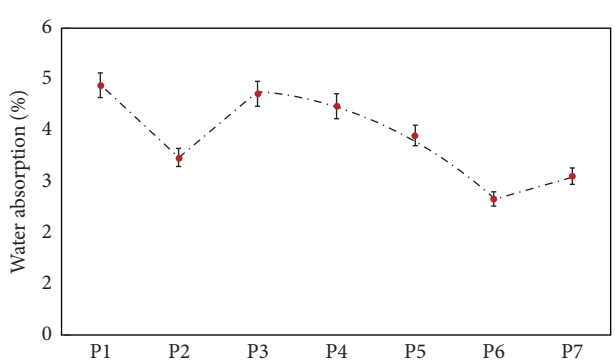

Figure 13: Water absorption test results of the composite specimens.

The percentage of water absorption has been calculated for all composites (P1 to P7 composite specimens) with a magnitude of 4.89, 3.48, 4.73, 4.51, 3.91, 2.67, and 3.12%, respectively. The maximum weight gained by the composite specimens after the water absorption test was found in pure PLA composites (P1 composites). The minimum weight gained by the composite specimens after the water absorption test was found in 6% nanosilica particles filled composites (P6 composites). The percentage of the water absorption has found a very lesser amount at 6% nanosilica particles weight percentage added to the composites. The maximum percentage of water absorption (4.89%) has been found at composites without the nanosilica particles and water hyacinth particles. The water absorption of the specimens has significantly reduced to increasing weight percentages of the nanosilica particles, which are added to the water hyacinth fibre PLA composites. Superior water absorption behaviour, due to removal of lignin, cellulose, and hemicellulose in the water hyacinth fibre, has been found in 14 wt% water hyacinth fibre enhanced composite specimens, and spaces may be made in the water hyacinth fibre molecules. The addition of limited filler content (6 wt percent), i.e., nanosilica particles in water hyacinth fibre voids, has been filled in and enhances the good quantity of water interface between water hyacinth fluid and PLA matrix.

5. Conclusions

Mechanical tests were carried out on the water hyacinth fibre which enhanced PLA matrix composites, nanosilica particles, and water hyacinth particulate matter. After the standard tests, the following observations are noted.

(1) The water hyacinth fibre enhanced epoxy composite is successfully produced by loading nanosilica particles with various proportions of hyacinth fibre particles.

(2) Tests such as tensile, bending, impact, hardness, and water absorption are conducted in different proportions. Based on tests, nanosilica particles and water hyacinth particles increase the specimens strengths considerably.

(3) The combinations of the two particles (6% nanosilica and 14% water hyacinth) nevertheless demonstrated their extraordinary efficiency in every test.

(4) It is suggested that both water hyacinth fibre and nanosilica particles reinforced PLA hybrid composites can be used as an alternate material for materials reinforced with natural fibre.

(5) Moreover, the most valuable aspect of this research is that water hyacinth, which is considered a waste and environmental pollutant, makes products that may replace high-cost glass fibre-based composites and help grow a healthier aquatic environment for the fishes and other aquatic plants.

Data Availability

The data used to support the findings of this study are included within the article.

Conflicts of Interest

The authors declare that there are no conflicts of interest regarding the publication of this article.

Acknowledgments

The authors appreciate the support from Seenu Atoll School, Maldives. The authors thank Bharath Institute of Higher

Education and Research, Chennai, and this project was supported by Researchers Supporting Project number (RSP-2021/257), King Saud University, Riyadh, Saudi Arabia.

References

[1] T. Ahmed, M. Shahid, F. Azeem et al., "Biodegradation of plastics: current scenario and future prospects for environmental safety," *Environmental Science and Pollution Research*, vol. 25, no. 8, pp. 7287–7298, 2018.

[2] V. Mohanavel, S. Suresh Kumar, J. Vairamuthu, P. Ganeshan, and B. NagarajaGanesh, "Influence of stacking sequence and fiber content on the mechanical properties of natural and synthetic fibers reinforced penta-layered hybrid composites," *Journal of Natural Fibers*, vol. 2021, Article ID 1875368, 13 pages, 2021.

[3] M. Asrofi, H. Abral, A. Kasim, and A. Pratoto, "XRD and FTIR studies of nanocrystalline cellulose from water hyacinth (eichornia crassipes) fiber," *Journal of Metastable and Nanocrystalline Materials*, vol. 29, pp. 9–16, 2017.

[4] H. Abral, M. H. Dalimunthe, J. Hartono et al., "Characterization of tapioca starch biopolymer composites reinforced with micro scale water hyacinth fibers," *Starch - Stärke*, vol. 70, no. 7-8, p. 1700287, Article ID 1700287, 2018.

[5] A. Komuraiah, N. S. Kumar, and B. D. Prasad, "Chemical composition of natural fibers and its influence on their mechanical properties," *Mechanics of Composite Materials*, vol. 50, no. 3, pp. 359–376, 2014.

[6] P. K. Panda, J.-M. Yang, Y.-H. Chang, and W.-W. Su, "Modification of different molecular weights of chitosan by p-Coumaric acid: preparation, characterization and effect of molecular weight on its water solubility and antioxidant property," *International Journal of Biological Macromolecules*, vol. 136, pp. 661–667, 2019.

[7] P. K. Panda, J. M. Yang, and Y. H Chang, "Water-induced shape memory behavior of poly (vinyl alcohol) and p-coumaric acid-modified water-soluble chitosan blended membrane," *Carbohydrate Polymers*, vol. 257, p. 117633, Article ID 117633, 2021.

[8] S. Karimi, A. Abdulkhani, P. M. Tahir, and A. Dufresne, "Effect of cellulosic fiber scale on linear and non-linear mechanical performance of starch-based composites," *International Journal of Biological Macromolecules*, vol. 91, pp. 1040–1044, 2016.

[9] M. Asrofi, H. Abral, Y. K. Putra, S. Sapuan, and H.-J. Kim, "Effect of duration of sonication during gelatinization on properties of tapioca starch water hyacinth fiber biocomposite," *International Journal of Biological Macromolecules*, vol. 108, pp. 167–176, 2018.

[10] H. Abral, G. J. Putra, M. Asrofi, J.-W. Park, and H.-J. Kim, "Effect of vibration duration of high ultrasound applied to bio-composite while gelatinized on its properties," *Ultrasonics Sonochemistry*, vol. 40, pp. 697–702, 2018.

[11] M. Asrofi, H. Abral, A. Kasim, and A. Pratoto, "Characterization of the microfibrillated cellulose from water hyacinth pulp after alkali treatment and wet blending," *IOP Conference Series: Materials Science and Engineering*, vol. 204, Article ID 012018, 2017.

[12] S. Wahono, A. Irwan, E. Syafri, and M. Asrofi, "Preparation and characterization of ramie cellulose nanofibers/CaCO3 unsaturated polyester resin composites," *ARPN J. Eng. Appl. Sci.*vol. 13, no. 2, pp. 746–751, 2018.

[13] E. Syafri, H. Abral, and A. Asben, "Effect of precipitated calcium carbonate on physical, mechanical and thermal properties of cassava starch bioplastic composites," *International Journal of Advanced Science, Engineering and Information Technology*, vol. 7, no. 5, pp. 1950–1956, 2017.

[14] M. J. Fabra, M. Martínez-Sanz, L. G. Gómez-Mascaraque, R. Gavara, and A. López-Rubio, "Structural and physicochemical characterization of thermoplastic corn starch films containing microalgae," *Carbohydrate Polymers*, vol. 186, pp. 184–191, 2018.

[15] A. M. Salaberria, J. Labidi, and S. C. M. Fernandes, "Chitin nanocrystals and nanofibers as nano-sized fillers into thermoplastic starch-based biocomposites processed by melt-mixing," *Chemical Engineering Journal*, vol. 256, pp. 356–364, 2014.

[16] H. P. S. Abdul Khalil, Y. Y. Tye, C. K. Saurabh et al., "Biodegradable polymer films from seaweed polysaccharides: a review on cellulose as a reinforcement material," *Express Polymer Letters*, vol. 11, no. 4, pp. 244–265, 2017.

[17] G. C. O. Isaac and O. Igwe, "Studies on properties of egg shell and fish bone powder filled polypropylene," *American Journal of Polymer Science*, vol. 2, no. 4, pp. 56–61, 2012.

[18] Y. N. P. Njogu, R. Kinyua, and P. Muthoni, "Biogas production using water hyacinth (eicchornia crassipes) for electricity generation in Kenya," *Energy and Power Engineering*, vol. 07, no. 5, pp. 209–216, 2015.

[19] T. D. Pham, C. M. Vu, and H. J. Choi, "Enhanced fracture toughness and mechanical properties of epoxy resin with rice husk-based nano-silica," *Polymer Science - Series A*, vol. 59, no. 3, pp. 437–444, 2017.

[20] M. Al Amin and M. Rafiquzzaman, "Charpy impact behavior of Water Hyacinth fiber based polymer composite," *J. Mater. Sci. Manuf. Technol.*vol. 2, no. 2, pp. 1–13, 2018, https://www.researchgate.net/publication/320700216%0ACharpy.

[21] M. Megahed, A. Megahed, and M. Agwa, "The influence of incorporation of silica and carbon nanoparticles on the mechanical properties of hybrid glass fiber reinforced epoxy," *Journal of Industrial Textiles*, vol. 49, no. 2, pp. 181–199, 2019.

[22] O. S. Akintayo, "Mechanical properties of epoxy matrix composites reinforced with green silica particles," *Annals of the Faculty of Engineering Hunedoara*, vol. 15, no. 4, pp. 167–174, 2017.

[23] K. L. Kuzmin, I. A. Timoshkin, S. I. Gutnikov, E. S. Zhukovskaya, Y. V. Lipatov, and B. I. Lazoryak, "Effect of silane/nano-silica on the mechanical properties of basalt fiber reinforced epoxy composites," *Composite Interfaces*, vol. 24, no. 1, pp. 13–34, 2017.

[24] C. N. A. Jaafar, M. A. M. Rizal, and I. Zainol, "Effect of kenaf alkalization treatment on morphological and mechanical properties of epoxy/silica/kenaf composite," *International Journal of Engineering & Technology*, vol. 7, no. 4, pp. 258–263, 2018.

[25] A. A. Hasibuan, R. Yuniati, and W. Wardhana, "The growth rate and chlorophyll content of water hyacinth under different type of water sources," *IOP Conference Series: Materials Science and Engineering*, vol. 902, Article ID 012064, 2020.

[26] O. P. Iio, M. D. Simatele, S. L. Nkomo, N. M. Mkhize, and N. G. Prabhu, "The benefits of water hyacinth (*Eichhornia crassipes*) for southern africa: a review," *Sustainability*, vol. 12, p. 9222, 2020.

Hindawi
Advances in Materials Science and Engineering
Volume 2021, Article ID 6843276, 20 pages
https://doi.org/10.1155/2021/6843276

Research Article

Statistical Modelling to Study the Implications of Coated Tools for Machining AA 2014 Using Grey Taguchi-Based Response Surface Methodology

Madhanagopal Manoharan,[1] Arul Kulandaivel,[2] Adinarayanan Arunagiri,[3] Mohamad Reda A. Refaai,[4] Simon Yishak,[5] and Gowthaman Buddharsamy[6]

[1]*Department of Mechanical Engineering, Indian Institute of Information Technology, Design and Manufacturing, Kancheepuram, Chennai 600127, India*
[2]*Department of Mechanical Engineering, Agni College of Technology, Thalambur, Chennai 600130, India*
[3]*Department of Mechanical Engineering, AMET University, Kanathur, Chennai 603112, India*
[4]*Prince Sattam bin Abdulaziz University, College of Engineering, Department of Mechanical Engineering, Alkharj 16273, Saudi Arabia*
[5]*College of Engineering and Argo-Industrial Technology, Sawla Campus, Arba Minch University, Addis Ababa, Ethiopia*
[6]*Department of Mechanical Engineering, Kings Engineering College, Sriperumbudur, Chennai 602117, India*

Correspondence should be addressed to Simon Yishak; simon.yishak@amu.edu.et

Received 4 October 2021; Accepted 2 November 2021; Published 30 November 2021

Academic Editor: P Ganeshan

Milling is the surface machining process by removing material from the raw stock using revolving cutters. This process accounts for a major stake in most of the Original Equipment Manufacturing (OEM) industries. This paper discusses optimizing process parameters for machining the AA 2014 T 651 using a vertical milling machine with coated cutting tools. The process parameters such as cutting speed, depth of cut, and type of the cutting tool with all its levels are identified from the previous literature study and several trial experiments. The Taguchi L_9 Orthogonal Array (OA) is used for the experimental order with the chosen input parameters. The commonly used cutting tools in the machining industry, such as High-Speed Steel (HSS) and its coated tools, are considered in this study. These tools are coated with Titanium Nitride (TiN) and Titanium Aluminum Nitride (TiAlN) by Physical Vapor Deposition (PVD) technique. The output responses such as cutting forces along the three-axis are measured using a milling tool dynamometer for the corresponding input factors. The input process parameters are optimized by considering the output responses such as MRR, machining torque, and thrust force. Grey Taguchi-based Response Surface Methodology (GTRSM) is used for multiobjective multiresponse optimization problems to find the optimum input process parameter combination for the desired response. Polynomial regression equations are generated to understand the mathematical relation between the input factor and output responses as well as Grey Relational Grade (GRG) values. The optimum process parameter combination from the desirability analysis is the HSS tool coated with TiAlN at a cutting speed of 270 rpm and a depth of cut value of 0.2 mm.

1. Introduction

Modern-day cutting tools used in the machining industry can be coated with combination of alloying elements, which provides a wide range of advantages in improving the tool life. These coated tools may reduce the manufacturing cost, and thereby the cost of the manufactured part is significantly reduced. The majority of modern machining is done using computer numerical control (CNC), which allows computers to control mills, lathes, and other cutting machines. Milling is a type of machining that removes material from a work piece by advancing rotary cutters in a direction that is at an angle to the tool's axis. From small individual pieces to huge, heavy-duty group milling processes, it encompasses a

wide range of procedures and machinery. It is one of the most widely utilized procedures for machining parts with sufficient precision and tolerance control in industry and machine shops today.

Milling operations performed using different milling cutters may be grouped as peripheral milling and face milling. The action of a milling cutter to generate a machined surface parallel to the cutter's axis is known as peripheral milling. This sort of milling is considered for study in this work. Commonly used milling cutters include end mill, ball nose cutter, slab mill, side and face cutter, hob, thread mill, face cutter, fly cutter, woodruff cutter, and hollow mill. Materials used in those cutters include High-Speed Steel (HSS), cemented carbides, tool steels, cast-tool material, plain carbon tool steel, and stellite. High-Speed Steel (HSS) mill tool is utilized in this work, which is widely used by several manufacturing industries for affordable metal cutting operations.

The coatings applicable for the HSS end mill cutter are Titanium Nitride (TiN), Titanium Aluminum Nitride (TiAlN), Titanium Carbo-Nitride (TiCN), Zirconium Nitride (ZrN), Diamond, and Black Oxide. TiN and TiAlN coating are used in this research to coat the HSS tool in these available coatings. Usually, these coatings can be provided on the cutting tool using Physical Vapor Deposition (PVD) or Chemical Vapor Deposition (CVD) techniques. In general, PVD coating is a cost-effective solution for sputtering applications. Hence, the PVD technique is used for coating the HSS tool cutters in this work. The TiN coating increases the hardness of the HSS cutting tool and can withstand higher oxidation temperature, while TiAlN coating provides more surface hardened tool than TiN. It is because of the presence of Al and Ti compositions. This TiAlN coated tool is a viable alternate option for high-speed machining and high-temperature machining applications. The formation of the aluminum oxide layer provides better tool life for high heat applications.

Aluminum Alloys are widely used in engineering structures, because they are of lightweight and better corrosion resistance [1]. The most common alloying elements for Aluminum Alloys is Copper (Cu), Magnesium (Mg), Manganese (Mn), Silicon (Si), Tin (Sn), and Zinc (Zn). Aluminum Alloy is the material of choice for several engineering applications, which has good aesthetic and high strength properties. These Aluminum alloys are available in several series such as 1xxx, 2xxx, 3xxx, 4xxx, 5xxx, 6xxx, and 7xxx series. This work uses AA 2014 as a working material for the milling process. AA 2014 is an Aluminum-Copper-based alloy widely used in aerospace, defense, and naval engineering applications. This AA 2014 is difficult to machine at particular tempers and has high strength next to Aluminum-Zinc alloys.

This work involves multiple input parameters and multiple-output responses. Some of the commonly applied methods for multiresponse optimization are Grey Relational Analysis (GRA), Artificial Neural Network (ANN), Convolutional Neural Network (CNN), Fuzzy logic, Principal Component Analysis (PCA), Simulated Annealing (SA), Bio-inspired algorithms, and Nelder–Mead Simplex method [2]. This sort of optimization study is used by researchers in various domains ranging from Civil Engineering [3] to advanced Additive Manufacturing techniques [4].

Recently, multiresponse optimization is a major interest for industries and academicians to find the optimum process parameters. Maiyar et al. used Grey Relational Analysis to explore the parameter optimization of end milling operation for Inconel 718 superalloy [5] using multiresponse criteria based on Taguchi L9 Orthogonal Array. The input parameters such as cutting speed, feed rate, and depth of cut are optimized by considering multiple output responses such as average surface roughness (R_a) and Material Removal Rate. Cutting velocity (75 m/min), feed rate (0.06 mm/tooth), and depth of cut were identified to be the best cutting parameters combination for machining by the authors (0.4 mm). The authors also observed that the Material Removal Rate (MRR) is increased by 64.8%, and surface roughness is decreased by 9.52%. Grey Relational Grade obtained is used for Analysis of Variance (ANOVA) calculations. Das et al. used an improved optimization approach by combining Taguchi L_{25} Orthogonal Array design and Grey-Fuzzy logic technique for optimizing machining parameters of the CNC milling of Al–4.5% Cu–TiC Metal Matrix Composites [6]. The optimum process parameter combination found in this study has a cutting speed (600 rpm), feed (40 mm/min), and depth of cut (0.30 mm) by considering the output responses such as cutting force (F_c), average surface roughness (R_a), and an average maximum height of the profile (R_z). The optimum process parameter combination has a high grey fuzzy reasoning grade (0.8191). Durakbasa et al. extended further study of the effect of coating on the tool and found that the coating in the cutting tool is the predominant factor affecting the surface quality of the machined parts [7]. The authors have coated the carbide tools with AlTiN, TiAlN, and ZrN to study the cutting parameter implications on machining AISI H13 hot work steel. Taguchi L_{27} Orthogonal Array is used to study the relationship between the input process parameter and output responses. Cutting tool tip radius and coating type are the significant input process parameters affecting the average surface roughness (R_a) of the machined surface besides feed rate, depth of cut, and cutting speed. Lu et al. used a hybrid approach by coupling the performance index Grey Relational Grade (GRG) with Principal Component Analysis (PCA). On the rough cutting of SKD61 tool steel, the authors discovered the optimal combination of cutting parameters such as milling type, spindle speed, feed per tooth, radial depth of cut, and axial depth of cut for high-speed end milling [8]. For high-speed milling of SKD61 tool steel, the down milling procedure with a spindle speed of 12000 rpm, feed rate of 0.04 mm/tooth, axial depth of cut (0.8 mm), and radial depth of cut (1 mm) is regarded the ideal cutting parameter combination.

The Response Surface Methodology (RSM) was used by Elsen et al. to study the end milling process parameters for multiobjective optimization [9]. The authors used stir cast Alumina reinforced Aluminum Metal Matrix Composites (AAMMC) and found that the cutting speed (1750 rev/min), feed rate (0.3 mm/rev), and depth of cut (0.2 mm) are the optimum parameters for end milling operations. Shaik and

Srinivas used the neural network-based RSM to find the optimum process parameter combination [10] for end milling operations in AA-6061 work material using a multiobjective approach. The authors found that the cutting speed of 1800.954 rpm, feed rate of 41.826 mm/min, and axial depth of 0.799 mm are the optimum combination for machining the AA-6061 material. Ren et al. presented a multiobjective optimization problem [11] using the Taguchi method for experimental design and Grey Relational Analysis to obtain the optimum process parameter combination in the end milling Ti–5Al–5Mo–5V–1Cr–1Fe titanium alloy. The authors considered multiresponse such as cutting forces, surface roughness, and acceleration on various tools with varying tool geometry. They found that the fluting rake angle of 4°, gash angle of 35° helix angle of 45°, gash rake angle of 2°, and pitch angle difference of 4° are the optimal controllable factors in the study. Adalarasan et al. considered the Taguchi L_{18} Orthogonal Array for designing the experimental order and extended RSM by using a hybrid approach such as Grey Taguchi based Response Surface Methodology (GT-RSM) for optimizing the process parameters [12]. The authors optimized the plasma arc cutting parameters such as arc current, torch stand-off, cutting speed, and gas pressure by considering the responses such as surface roughness and kerf width. The authors proposed that the optimized results provide better desirability for finding the optimum process parameters using GRG values. Similar multiobjective optimization to study the milling parameters for machining Ultrahigh-Strength Steel was introduced by Xu et al. using RSM equations. The authors used a Pareto-optimal solution to obtain the optimum process parameter combination using Non-Dominated Sorting Genetic Algorithm-II (NDSGA-II). The authors mentioned that the RSM could not deal with the multiresponse problem [13], and this sort of multiobjective optimization provides optimum process parameter combination. According to the literature review, more research into the influence of coated tools on milling AA 2014 is needed, taking into account the Material Removal Rate (MRR) and the impact of cutting pressures during the material removal process. As a result, the quality of the milled surface is explored experimentally in this paper in order to discover a relationship between the range of forces and Material Removal Rate (MRR) for the appropriate input process parameters.

2. Materials and Methods

Grey Relational Analysis provides a better solution for multiresponse optimization problems [14]. Engineering judgement, assignment of weight, Regression analysis, data envelopment based Ranking approach, fuzzy multiple attribute decision making, fuzzy logic, Grey Relational Analysis, Artificial Neural Networks, goal-programming approach, and desirability function analysis are the available methods for multiobjective multiresponse problems [15]. In this study, Grey Taguchi-based Response Surface Methodology (GT-RSM) is used to analyze the factor-response relationship. The full factorial Taguchi L_9 Orthogonal Array experimental design is selected to conduct the experiment in an organized manner. In the current study, the operating cutting speed considered in this study ranges from 90 to 450 rpm. The depth of cut varies from 0.2 mm to 0.6 mm, while the feed rate is kept constant at 40 mm/min. The work material is the Aluminum Alloy AA 2014 T 651 condition, a heat-treated solution, stress relieved by elongation, and artificial ageing. The chemical composition test is performed to confirm the presence of alloying in the right proportions and hardness tests to study the characteristics of the alloy. In addition, microstructural studies are carried out to visualize the AA 2014 microstructure using Optical Microscope. The cutting forces in three dimensions are measured using strain sensors placed on the work piece holding fixture using Milling Tool Dynamometer.

2.1. Material Selection. Aluminum Alloy AA 2014 can be easily machinable at a specific temperature, and it is one of the strongest available Aluminum Alloys with high hardness and better tensile properties. The density value of the chosen AA 2014 is 2.8 gm/cm^3.

2.1.1. Microstructure Characterisation. The AA 2014 specimens are polished using Silicon Carbide abrasive papers of various grid sizes (200#, 400#, 600#, 800#, 1000#, and 1200#) before microstructure characterization is shown in Figure 1. These specimens are then subjected to cloth polish using a diamond abrasive size 0.5 μm–1 μm to obtain mirror polish. The polished specimen surface is etched with Keller's reagent [16] of composition (1% HF + 1.5% HCl + 2.5% HNO_3 + 95% water). The surface has dispersed dots of particles (mostly copper), which shows a uniform distribution of alloying elements.

In addition to this microstructure analysis, chemical composition and hardness tests are also performed to examine the material property characteristics. The results are discussed in the upcoming sections.

2.1.2. Chemical Composition Analysis. The chemical composition test results of the purchased material are provided in Table 1. Copper is the primary alloying element in the AA 2XXX series.

Since there is a presence of 3.9 to 5% copper in this particular material, this indicates that it is Aluminum Alloy AA 2014 [17]. The purchased material is strengthened to get T651 condition by solution heat-treated, stress-relieved by stretching, and artificial ageing in controlled environmental conditions [18].

2.1.3. Hardness Test. The hardness of the AA 2014 material subjected to machining is tested using Brinell Hardness testing machine and Vickers microhardness tester.

(1) Brinell Hardness Test. The hardness of the AA 2014 work material is tested at various loads ranging from 1 kg to 3 kg using the Brinell scale, which is provided in Table 2. The details of the load application, diameter of impression, and specimen surface area are presented.

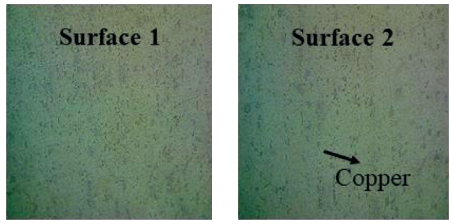

(a) (b)

Figure 1: Microstructure of the chosen AA 2014 (black dots represent copper).

Table 1: Percentage of elements distribution in the chosen AA 2014 material.

Type of element	Cr (%)	Cu	Fe (%)	Mg	Mn	Si	Ti (%)	Zn (%)	Al
% contribution	0.1	3.9%–5%	0.7	0.2%–0.8%	0.4%–1.2%	0.5%–1.2%	0.15	0.25	Rest

Table 2: Brinell hardness test on AA 2014 material.

Trial no.	Applied load (gm)	Diameter of impression (mm)		Specimen surface area (mm^2)	BHN
		D	d		
1	1000	10	3.2	8.26	121.06
2	2000	10	4.3	15.26	131.06
3	3000	10	5.0	21.04	142.58

In addition, a sample calculation is provided below to find BHN.

$$\text{Brinell Hardness Number (BHN)} = \frac{F}{A_s}, \quad (1)$$

where $A_s = \pi\ D(D - \sqrt{D^2 - d^2})/2$

The specimen surface area for the first trial is $A_s = \pi * 10(10 - \sqrt{10^2 - 3.2^2})/2$, where the value of specimen surface area is 8.26 mm^2. The BHN is the ratio of load applied to the calculated specimen surface area. The value of BHN for the first set is found to be 121.06.

(2) Vickers Microhardness Test. The Vickers microhardness test employs a square-shaped pyramid diamond indenter with a vertex angle of 136°, which is driven into the surface of the selected AA 2014 material at a predefined force, F. The initial application of force takes 2 to 8 seconds, and the force is sustained for 10 to 15 seconds during the test. The diagonal indentation lengths are measured when the applied force is removed to get the Vickers Hardness Number (VHN) with 1N application of force [19]. In the chosen AA 2014, the VHN on the Vickers scale is 158, 155, and 154.

2.2. Tool Selection. High-Speed Steel (HSS) tools are commonly used in medium scale and small scale industries. This affordable HSS tool can withstand more cutting force and better tool life compared to carbide tools. HSS material is widely used in various segments in the manufacturing industry as drill bits, reamer tools, side and face mill cutters, slab mills, end mills, and straddles milling cutters. In the current work, High-Speed Steel (HSS) tool and the HSS tool with coatings are used to study the milling operations. Table 3 shows the specifications of the HSS tool used in this study.

The manufacturer of the HSS mill tool is Sandvik Coromant, which is supplied by ProSol, Ambattur, Chennai, India. This HSS tool is highly suitable for intermittent cutting applications.

2.3. Coating Method. The tool's surface hardness will be increased by using coatings. These coatings will improve tool life and be enabled for faster cutting speeds and feeds [20]. This work uses two coating materials: Titanium Nitride (TiN) and Titanium Aluminum Nitride (TiAlN). The coating on the HSS tool was done at Oerlikon friction systems (India) Private Limited, Irungattukottai, Chennai, India. The coating of these tools is done based on the sputtering principle using the PVD technique.

3. Experimental Details and Data Analysis

All the experiments in this study are conducted in the vertical milling machine supplied by S. M. Engineering works, Punjab, India, shown in Figure 2. The HSS end mill tool with and without coating is used to machine the AA 2014 by performing experiments as per the experimental order in this machine.

The cutting forces acting in three dimensions are measured using Milling Tool Dynamometer (M/S Tamilnadu Engineering Instruments, Chennai, India). This device has four arms bounding strain gauge component bridge sensors to measure the three-dimensional axis forces. Three readings for each set of forces are calculated at the start of the cutting operation, half the cutting toolpath length, and near the end of the milling operation. The average of the three

Table 3: Tool description of the HSS mill tool.

Type of cutter	End mill cutter
Diameter of the cutting tool	10 mm
Length of the cutting tool	100 mm
Flute length	40 mm
Number of flutes	4

Type of cutting tool

Uncoated HSS tool (HSST)

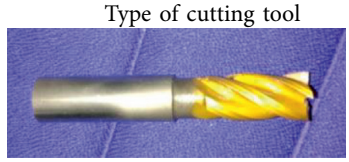

HSS tool - TiN coated (HSST-TiN)

HSS tool - TiAlN coated (HSST-TiAlN)

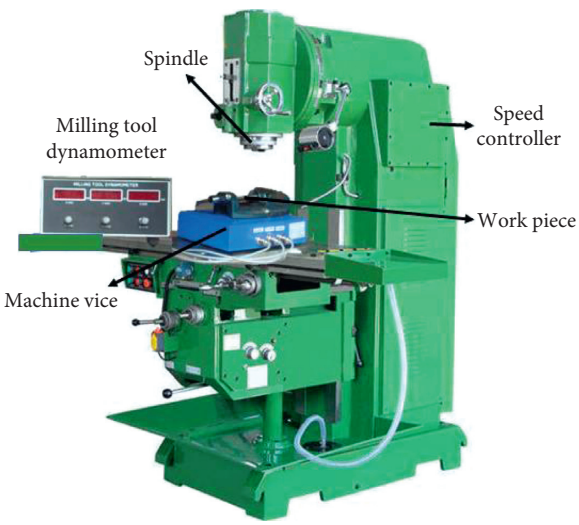

Figure 2: Vertical machining center used for experimentation in this research work.

readings for each measured force is used to calculate Torque and thrust force. Machining is carried out at various process parameter settings mentioned in Table 4. The notations of the end mill cutter tools are the High-Speed Steel tool (HSST), High-Speed Steel tool coated with Titanium Nitride (HSST-TiN) tool, and High-Speed Steel tool coated with Titanium Aluminum Nitride (HSST-TiAlN).

Several factors affect the production rate in the manufacturing industry. The major factors such as cutting speed, feed rate, and depth of cut are the predominant process parameters in any machining industry [21]. This study provides the influence of tool coating on the output responses such as Torque, thrust force, and Material Removal Rate. For improved visualization, response surface and contour graphs are supplied, which are also utilized to appropriately identify the input process parameters for the required output response.

3.1. Input Process Parameters and Their Levels. The number of experiments to identify the relationship between the input parameters and output responses is significantly reduced by implementing the Taguchi Orthogonal Array technique [22]. In this work, L_9 (3^3) Orthogonal Array design shown in Table 5 is used to find the influence of the input factors over the measured responses.

Table 4: Input parameters and their levels.

Input parameters	Level 1	Level 2	Level 3
Cutting speed (rpm)	90	270	450
Depth of cut (mm)	0.2	0.4	0.6
Type of cutting tool	HSST	HSST-TiN	HSST-TiAlN

Table 5: L_9 Orthogonal array for fitting the input process parameters.

Experimental order	Cutting speed (rpm)	Depth of cut (mm)	Type of cutting tool
1	90	0.2	HSST-TiAlN
2	90	0.4	HSST
3	90	0.6	HSST-TiN
4	270	0.2	HSST
5	270	0.4	HSST-TiN
6	270	0.6	HSST-TiAlN
7	450	0.2	HSST-TiN
8	450	0.4	HSST-TiAlN
9	450	0.6	HSST

The experimental machining is done on the AA 2014 material using individual blocks for each set as per the orthogonal array design. Figure 3 shows the images of the machined work pieces as per the experimental order.

All the work piece material used in this study has a standard size of 60 mm × 60 mm × 30 mm. The mill tool plunges in the work piece and performs machining for a length of 40 mm.

3.2. Output Measured Parameters. The Torque and MRR are calculated using the following measured forces and machining time in Table 6, where T_m represents the actual machining time.

A mill tool dynamometer is used to measure the forces operating on the work piece, and the machining time for each input process parameter combination is recorded.

4. Results and Discussion

The output response parameters considered in this study are the thrust force, Material Removal Rate (MRR), and Torque. Machining Torque is calculated with the help of cutting force and diameter of the tool, and Metal Removal Rate is calculated using the volume of material removed and

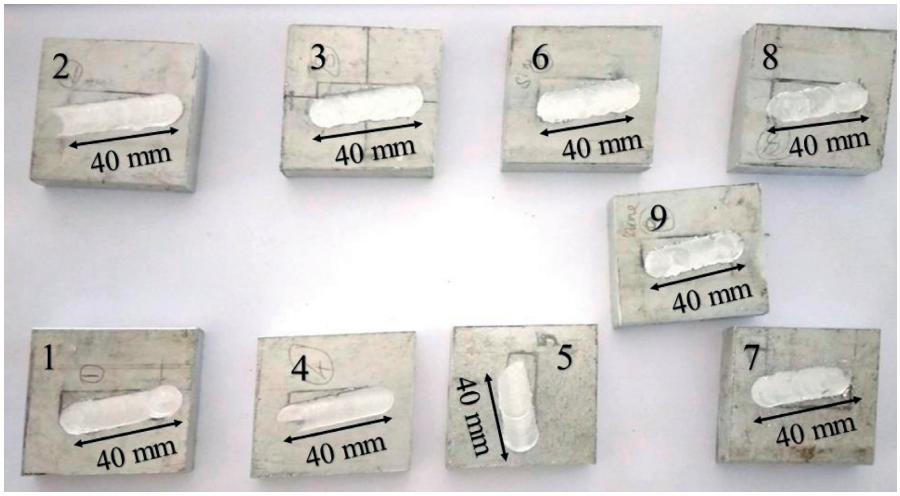

Figure 3: Machined work pieces of AA 2014 material.

Table 6: Measured response for the corresponding input process parameter set.

Exp. order	Cutting speed (rpm)	Depth of cut (mm)	Type of cutting tool	F_x (N)	F_y (N)	F_z (N)	T_m (sec)
1	90	0.2	HSST-TiAlN	78.48	93.2	117.72	127
2	90	0.4	HSST	58.86	78.48	78.48	165
3	90	0.6	HSST-TiN	73.58	103.005	88.29	151
4	270	0.2	HSST	68.67	88.29	39.24	98
5	270	0.4	HSST-TiN	83.39	78.48	125.57	82
6	270	0.6	HSST-TiAlN	88.29	122.63	78.48	56
7	450	0.2	HSST-TiN	107.91	117.72	103	43
8	450	0.4	HSST-TiAlN	117.72	176.58	264.87	38
9	450	0.6	HSST	80.44	127.53	147.15	45

machining time. For torque calculation, the following equation is used for the experimental order combination:

$$\text{Torque}\,(\text{Nm}) = \frac{\text{Cutting force}\,(\text{N}) \times \text{Dia. of mill tool}\,(\text{mm})}{2000}. \tag{2}$$

MRR is calculated by comparing the starting weight of the work piece before to machining with the final weight of the work piece after the material has been removed. Equation (3) provides the information to calculate the material removal rate in this experimental study:

$$\text{MRR}\left(\frac{\text{mm}^3}{\text{s}}\right) = \frac{(\text{Initial weight of workpiece}\,(\text{gm}) - \text{Final weight of workpiece}\,(\text{gm}))}{\text{Density}\left(\text{gm/mm}^3\right) \times \text{Machining time}\,(\text{sec})}. \tag{3}$$

The calculated MRR, torque, and thrust force are given in Table 7. These responses are used for the input for the Grey Relational Analysis.

To find the mathematical models link between the input process parameters and output response, second-order polynomial regression equations are produced. These equations are used to generate the response and contour plot for better visualization of the response-process parameter relationship and predict the proper set of the process parameter combination. All the regression analyses in this study are analyzed using Minitab software. The 3D response and 2D contour are plotted using MATLAB software from the equations obtained from regression analysis.

4.1. Second-Order Polynomial Regression Analysis for MRR. The second-order polynomial regression equation is generated for the MRR by varying the process factors such as cutting speed, cutting tool type, and depth of cut. In addition to these factors, several other process parameters affect the MRR, torque, and thrust force. It may differ by material, machine setting, and machining application. This regression

Table 7: MRR, Torque, and Thrust force values for the corresponding input factor.

Exp. order	Cutting speed (rpm)	Depth of cut (mm)	Type of cutting tool	MRR (mm^3/s)	Torque (nm)	Thrust force (N)
1	90	0.2	HSST-TiAlN	4.781	0.3924	93.2
2	90	0.4	HSST	5.628	0.2943	78.48
3	90	0.6	HSST-TiN	5.203	0.3679	103.005
4	270	0.2	HSST	9.111	0.3434	88.29
5	270	0.4	HSST-TiN	10.453	0.4170	78.48
6	270	0.6	HSST-TiAlN	12.755	0.4415	122.63
7	450	0.2	HSST-TiN	18.272	0.5396	117.72
8	450	0.4	HSST-TiAlN	19.737	0.5886	176.58
9	450	0.6	HSST	22.222	0.4022	127.53

equation is used to visualize the output response variation by plotting surface plots in three dimensions using response and contour surface plots by mapping the input process parameter information.

4.1.1. Regression Analysis for MRR (Cutting Speed vs. Depth of Cut). The second-order polynomial regression equation to find the MRR is shown in Table 8 by considering the effect of cutting speed and depth of cut. The value of R^2 represents the randomness in the generated statistical model. This R^2 value is around 0.9964, representing that the equation is statistically fit with the considered parameter levels of the cutting speed and depth of cut.

The three-dimensional response surface plot shown in Figure 4(a) represents the relation between the response such as MRR and the input process parameters (cutting speed, depth of cut). MRR value is more during machining the AA 2014 material at high cutting speed and depth of cut.

The variation and the values of the MRR are visualized in Figure 4(b). With an increase in cutting speed and depth of cut, the MRR rises steadily.

4.1.2. Regression Analysis for MRR (Cutting Speed vs. Type of Cutting Tool). The second-order polynomial regression value of MRR is given in Table 9. The R^2 value, in this case, is found to be 0.9656. This value represents a significant relation between the cutting speed and the cutting tool type impacting the MRR. The equation fits appropriately with the statistical model with a good variation of the output response for the given input process parameters.

The three-dimensional response surface plot shown in Figure 5(a) represents that the MRR increases steeply with the increase in the cutting speed. MRR is more for milling the AA 2014 material using the TiAlN cutting tool. Figure 5(b) shows the two-dimensional contour plot of MRR by varying the process parameters such as cutting speed and Type of cutting tool.

The MRR significantly determines the amount of material removed from the raw material during machining processes. In general, cutting speed has a significant relation in the calculation of MRR. And the results also proved that the MRR is directly proportional to the cutting speed.

4.1.3. Regression Analysis for MRR (Depth of Cut vs. Type of Cutting Tool). The relationship of MRR with the type of cutting tool and depth of cut is given in Table 10. The R^2 value of 0.8554 represents a less significant impact for milling AA 2014 using the depth of cut and type of cutting tool as the input parameters combination.

Table 8: Regression model and summary results for MRR.

Model	MRR = 4.19 + 0.00039 speed − 2.30 doc + 0.000058 speed * speed + 3.0 doc * doc + 0.02450 speed * doc	
Summary results	S value	R^2 value
	0.652535	0.9964

The three-dimensional surface plot and the two-dimensional contour plot are shown in Figures 6(a) and 6(b). There is an uneven variation of MRR by varying the depth of cut, and it exhibits more minor surface curve data variation. MRR is less affected by the depth of cut in this study.

The depth of cut results is not statistically significant, but those values significantly impact the machining materials. This process factor has less impact on the selected process parameter over machining AA 2014 material.

4.2. Second-Order Polynomial Regression Analysis for Torque. Torque plays a vital role to predict the power requirement for machining in an efficient manner. This section provides a detailed analysis of Torque based on the forces measured during milling AA 2014 with the coated cutting tools.

4.2.1. Regression Analysis for Torque (Cutting Speed vs. Depth of Cut). The following R^2 value of 0.8427 in Table 11 represents that the Torque has a moderate impact on the cutting speed and depth of cut.

The three-dimensional surface plot and two-dimensional contour plot are shown in Figures 7(a) and 7(b) respectively. The machining torque increases steeply with the increase in cutting speed. The results show that there is a surge of force at a higher cutting speed. The coating in the tool provides a better solution for milling the AA 2014 irrespective of controlling the depth of cut.

The contour graphs show that the cutting speed has a direct relation with the Torque. The parametric levels for depth of cut in this study are less adversely affecting the machining torque. The following section provides the detailed analysis of Torque by varying the cutting speed and type of coated cutting tools.

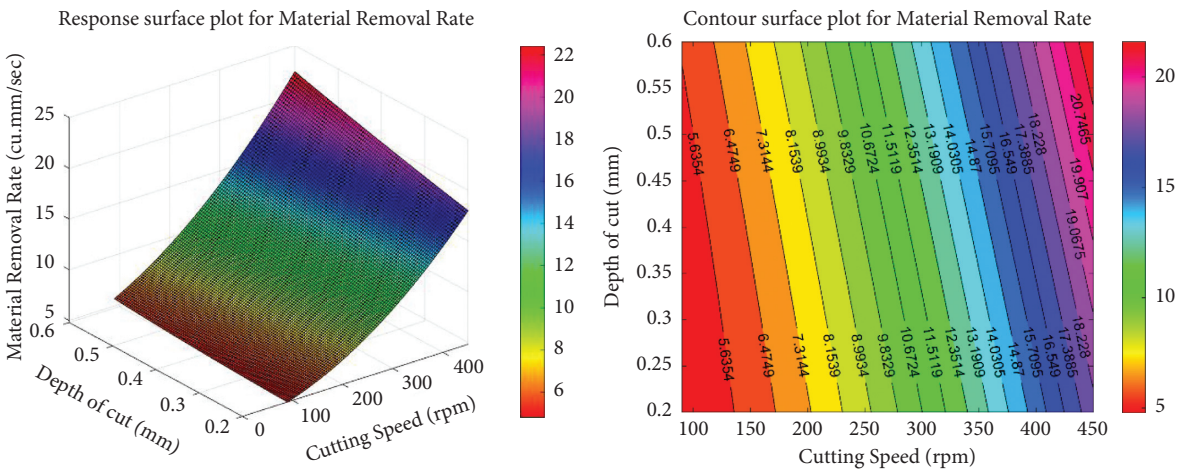

(a) (b)

Figure 4: (a)Response surface graph for MRR (cutting speed vs. depth of cut). (b)Contour surface plot for MRR (cutting speed vs. depth of cut).

Table 9: Regression model and summary results for MRR.

Model	MRR = 6.03 + 0.0147 speed − 3.59 tool + 0.000058 speed * speed + 1.06 tool * tool − 0.00228 speed * tool	
Summary results	S value 2.01489	R^2 value 0.9656

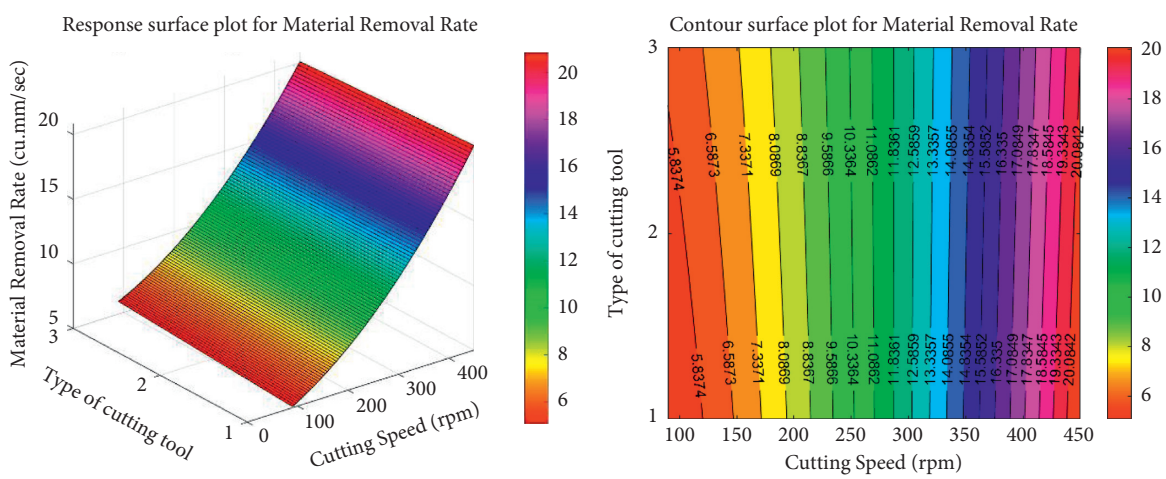

(a) (b)

Figure 5: (a)Response surface graph for MRR (cutting speed vs. type of cutting tool). (b)Contour surface plot for MRR (cutting speed vs. type of cutting tool).

Table 10: Regression model and summary results for MRR.

Model	MRR = 8.0 + 17 doc − 1.6 tool + 3 doc * doc + 1.06 tool * tool − 6.4 doc * tool	
Summary results	S value 4.5562	R^2 value 0.8554

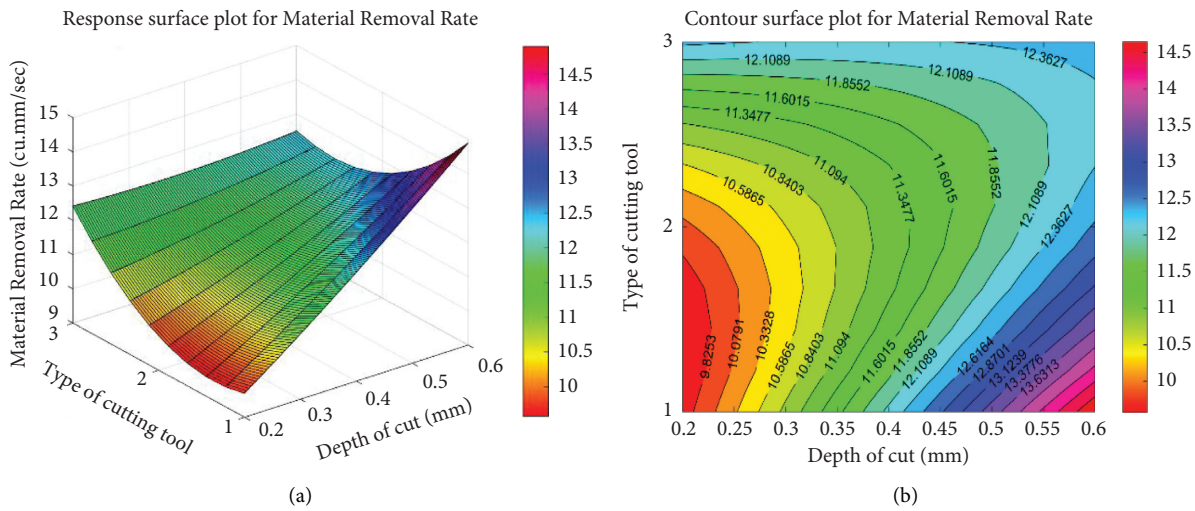

Figure 6: (a)Response surface graph for MRR (type of cutting tool vs. depth of cut). (b)Contour surface plot for MRR (type of cutting tool vs. depth of cut).

Table 11: Regression model and summary results for torque.

Model	Torque = 0.224 + 0.00025 speed + 0.53 doc + 0.000001 speed * speed − 0.47 doc * doc − 0.00078 speed * doc	
Summary results	S value 0.0904253	R^2 value 0.8427

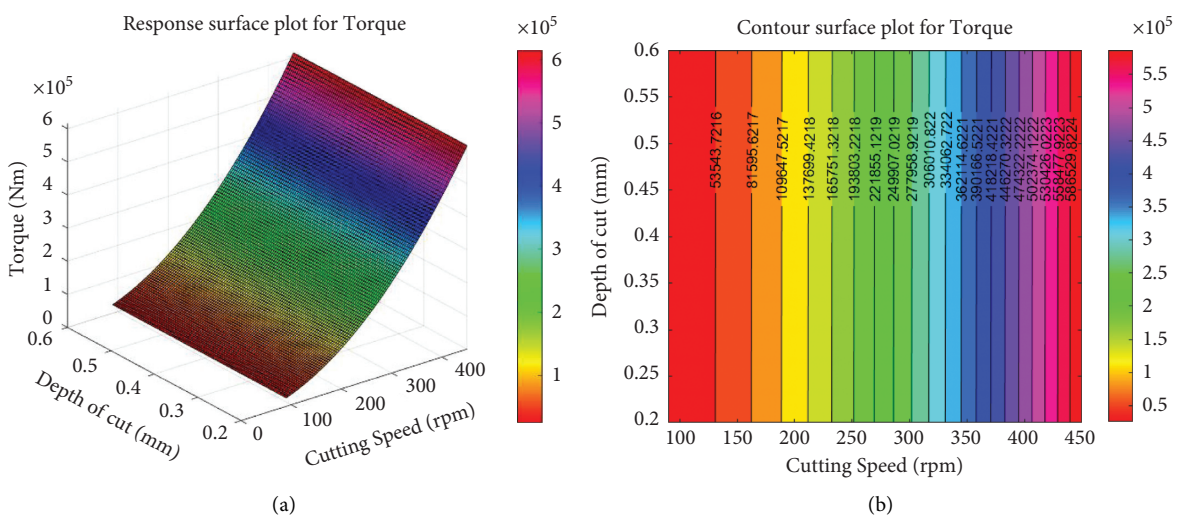

Figure 7: (a)Response surface graph for torque (cutting speed vs. depth of cut). (b)Contour surface plot for torque (cutting speed vs. depth of cut).

4.2.2. Regression Analysis for Torque (Cutting Speed vs. Type of Cutting Tool). The following R^2 value of 0.9880 in Table 12 represents that the torque impacts the cutting speed and type of cutting tool.

Figures 8(a) and 8(b) depict the three-dimensional surface plot and two-dimensional contour plot, respectively. It was discovered that when the cutting speed increases, the machining torque also increases. The type of cutting tool also plays a vital role in developing the machining torque. The torque value rises steeply for any cutting tool and attains a maximum value of 0.6 Nm at a cutting speed of 450 rpm using the TiAlN coated HSS cutting tool.

4.2.3. Regression Analysis for Torque (Type of Cutting Tool vs. Depth of Cut). The following R^2 value of 0.8040 in Table 13 represents that the Torque has a low impact on the type of cutting tool and depth of cut.

Table 12: Regression model and summary results for Torque.

Model	Torque = 0.1847 − 0.000308 speed + 0.1551 tool + 0.000001 speed; * speed − 0.0311 tool * tool + 0.000123 speed * tool	
Summary results	S value 0.0165464	R^2 value 0.9880

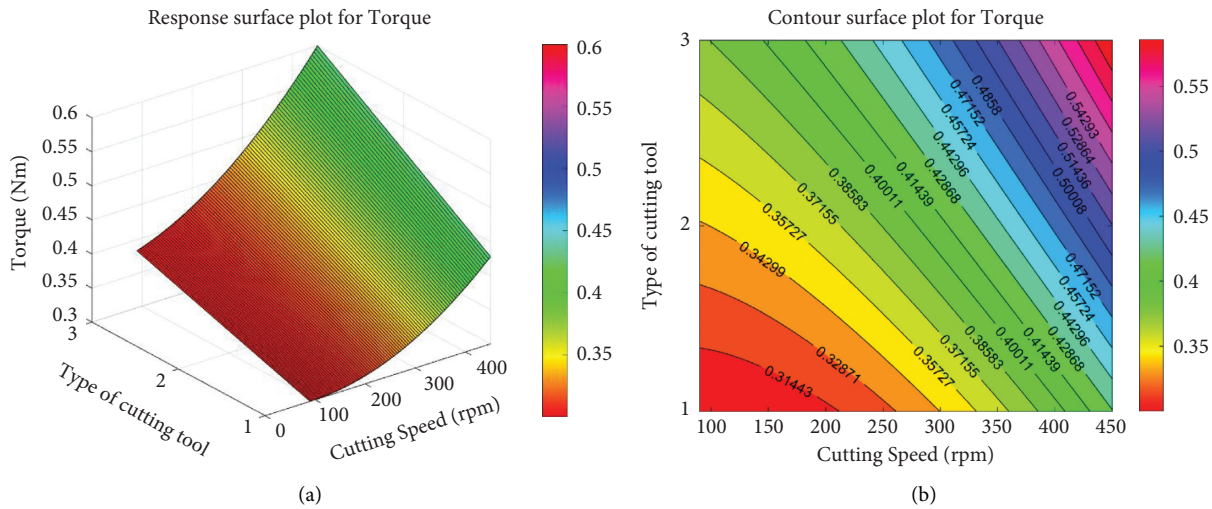

Figure 8: (a)Response surface graph for Torque (cutting Speed vs. type of cutting tool). (b)Contour surface plot for Torque (cutting Speed vs. type of cutting tool).

Table 13: Regression model and summary results for Torque.

Model	Torque = 0.138 + 0.35 doc + 0.193 tool − 0.47 doc * doc − 0.0311 tool * tool − 0.012 doc * tool	
Summary results	S value 0.116786	R^2 value 0.8040

The TiN coating enhances the machining torque irrespective of the depth of cut. But TiAlN coating still increases the machining torque resulting in a better milling process.

The response and contour graphs for machining torque by varying the input process parameters such as type of cutting tool and depth of cut are shown in Figures 9(a) and 9(b), respectively. Thrust force is also calculated in the study, and it is used for analyzing the impact of coated cutting tools at higher cutting speeds. The results of the thrust force are discussed in the next section.

4.3. Second-Order Polynomial Regression Analysis for Thrust Force. By managing the tool wear rate, the thrust force controls the tool life of the cutting tool under defined operating conditions. Hence, this response is considered in this study to understand its impact on the coated cutting tools.

4.3.1. Regression Analysis for Thrust Force (Cutting Speed vs. Depth of Cut). The following R^2 value of 0.8294 in Table 14 represents that the thrust force moderately impacts the cutting speed and depth of cut. Figures 10(a) and 10(b) show the three-dimensional response surface plot and two-dimensional contour plot, respectively.

It was discovered that as the cutting speed increases, the thrust force also increases. The thrust force increases as the cut depth increases. It was discovered that, with higher cutting speeds and deeper cuts, the maximal value of thrust force was recorded.

4.3.2. Regression Analysis for Thrust Force (Cutting Speed vs. Type of Cutting Tool). The following R^2 value of 0.8662 in Table 15 represents that the thrust force has a high impact on the cutting speed and cutting tool type.

It is evident from the response plots in Figures 11(a) and 11(b) that the maximum thrust force is obtained using TiAlN coated cutting tool at 450 rpm. The milling efficiency is higher, and the tool wear is lower at these controlled process parameters.

4.3.3. Regression Analysis for Thrust Force (Depth of Cut vs. Type of Cutting Tool). The depth of cut considered in this study has the least significant difference to impact the thrust force. The R^2 value of 0.8303 in Table 16 represents that there will be some additional factors or higher order levels of depth of cut to understand this process parameter study better.

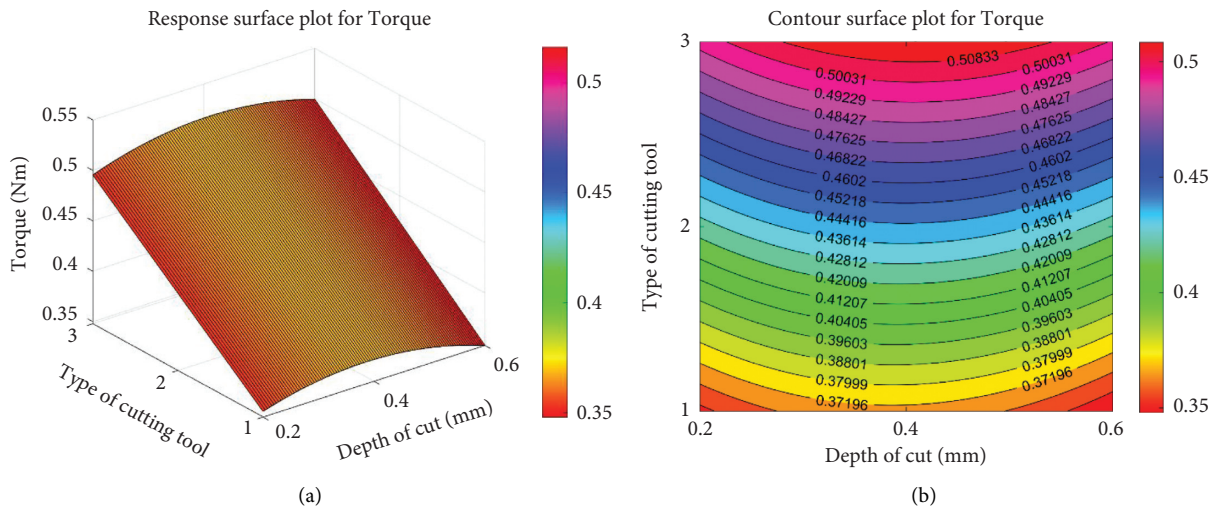

Figure 9: (a) Response surface graph for Torque (type of cutting tool vs. depth of cut). (b)Contour surface plot for Torque (type of cutting tool vs. depth of cut).

Table 14: Regression model and summary results for Thrust force.

Model	Thrust force = 77.7 − 0.191 Speed + 94 DOC + 0.000606 Speed * Speed − 61 DOC * DOC + 0.000 Speed * DOC	
Summary results	S value 30.9372	R^2 value 0.8294

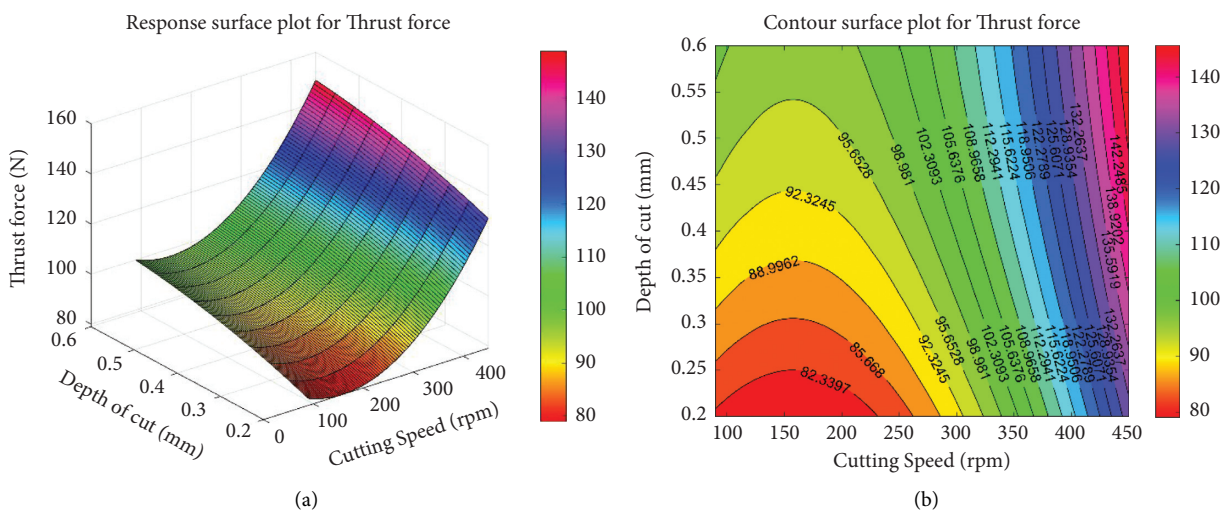

Figure 10: (a) Response surface graph for Thrust force (depth of cut vs. cutting speed). (b) Contour surface plot for Thrust force (depth of cut vs. cutting speed).

Table 15: Regression model and summary results for Thrust force.

Model	Thrust force = 145.9 − 0.286 Speed − 55.4 tool + 0.000606 Speed * Speed + 14.7 tool * tool + 0.0477 Speed * tool	
Summary results	S value 18.5875	R^2 value 0.8662

The response surface plot in Figure 12(a) is almost flat for the depth of cut axis. The thrust force values mentioned in Figure 12(b) show similar near-net values. Thus, there is a most negligible impact on the levels of depth of cut, and its contribution over the output responses is minimal in this study.

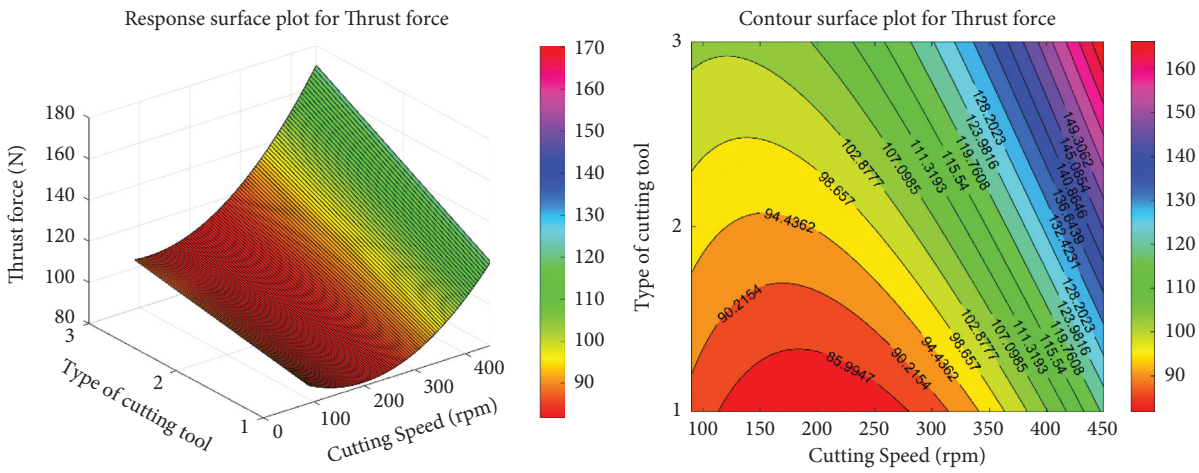

(a) (b)

Figure 11: (a) Response surface plot for Thrust force (cutting tool-type vs. cutting speed). (b) Contour surface plot for Thrust force (cutting tool-type vs. cutting speed).

Table 16: Regression model and summary results for Thrust force.

Model	Thrust force = 90 + 119 DOC − 38 tool − 61 DOC * DOC + 14.7 tool * tool − 12 DOC * tool	
Summary results	S value 41.5864	R^2 value 0.8303

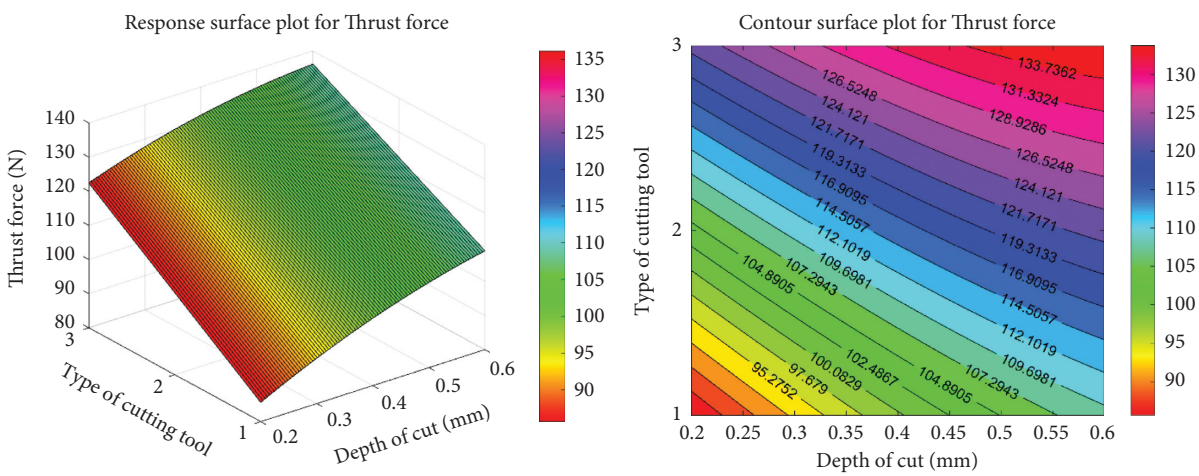

(a) (b)

Figure 12: (a) Response surface plot for Thrust force (depth of cut vs. cutting tool type). (b) Contour surface plot for Thrust force (depth of cut vs. cutting tool type).

4.4. Calculation of GRG Using Grey Relational Analysis. The Signal-to-Noise (S/N) ratio for MRR, Torque, and Thrust force is calculated using the *Larger the Better* characteristic. The formula to calculate the S/N ratio is given in equation (4) for the output responses.

$$\frac{S}{N}\text{ratio} = -10\log_{10}\left(\frac{1}{r}.\sum_{k=1}^{n}\left(\frac{1}{y_i}\right)_k^2\right), \quad (4)$$

where y_i is the measured output response; r represents the experiment replications; n is the number of output responses considered in this study; n is the maximum number of experiments carried out by varying the input process parameters; k is the experimental order value, which ranges from 1, 2, 3, . . .n.

The experimental trials' normalized S/N ratio (Zi) values modify the S/N ratio values restrained on a separate scale to a standard scale. The normalized S/N ratio values are fitted to a

scale ranging from 0 to 1. The normalized S/N ratio for the larger the better characteristic condition is calculated using

$$Z_i = \frac{y_i - \min(y_i, i = 1, 2, \ldots, n)}{\max(y_i, i = 1, 2, \ldots, n) - \min(y_i, i = 1, 2, \ldots, n)}. \quad (5)$$

These normalized S/N ratio values are used to find the relationship from the output responses by calculating the Grey Relational Coefficient (GRC) values, calculated using

$$\mathrm{GRC} = \frac{\Delta \min + \zeta \Delta \max}{\Delta(i) + \zeta \Delta \max}. \quad (6)$$

In the above relation, $\Delta \min$ and $\Delta \max$ represent the minimum and maximum of the normalized S/N ratio, respectively. Δi is the normalized S/N ratio for the ith experimental order in the set of executed experiments. The final step is calculating the Grey Relational Grade (GRG) by amalgamating the effect of all the individual measured responses (MRR, Torque, and Thrust force) into a single response. Equation (7) represents the formula to calculate the GRG for the set of experiments:

$$\mathrm{GRG}_i = \frac{1}{m} \sum_{i=1}^{m} \mathrm{GRC}_i, \quad (7)$$

where m is the total number of experiments.

The GRG results are used to construct the quadratic polynomial regression equation to map the relationship between the input process parameter and output response. The GRG values provide the quality characteristic for the multiresponse considered in this study. The higher value of GRG represents the experimental order offers more accurate and optimized results for the given input set of process parameters in this study. The calculated GRG values are shown in Table 17 for each set of the input process parameters in the experimental order. These numbers are examined to determine the best set of process parameter combinations for achieving the desired result.

These GRG values represent the output response such as MRR, Torque, and Thrust force into a single value. This data provides the relationship between all the responses over the input process parameter values. Table 18 provides the Analysis of Variance (ANOVA) results for the selected factors and their effect on the interaction between the process parameters combination. The normalized S/N ratio is calculated for the eta value of 0.8. The larger the better characteristic is considered for all output responses considered in this study.

Linear interaction, square interaction, and two-way interaction are considered in this study to understand the impact of the input process parameters over the desired output response. The percentage contribution of the model values for each input process parameter is given in Table 18. The individual factor contribution (linear model) accounts for 97.05%. The cutting speed variation significantly impacts the MRR, and a more significant amount of thrust force is needed to achieve the required machining torque. The coated cutting tool is the second predominant factor, contributing 13.99% in this process parameter optimization study. The depth of cut values are limited to a minimum value. This work can be extended to study the same milling process parameter setting at a higher depth of cut in the same AA 2014 material.

All the interaction terms (square and 2-way interaction) contribution is minimal, and the F-ratio value represents that these values are less significant in this study. The ANOVA table is calculated for 95% confidence interval and 5% significance level for the control factors over the GRG values calculated from the desired output responses. Figure 13 maps the percentage contribution of individual characteristics and their interaction values in the form of a three-dimensional pie-chart.

The variation of GRG values for the L_9 experimental matrix considered in this study for the corresponding process parameter setting is displayed in Figure 14. These means of the GRG values are analyzed further to find the optimum process parameter setting for milling AA 2014 material using the coated cutting tools.

4.5. Grey Taguchi-Based Response Surface Methodology. The second-order polynomial regression equation is derived to find the GRG values at a particular process parameter setting. Equation (8) shows the final derived result for the input process parameters:

$$\begin{aligned} \mathrm{GRG} = {} & 0.9702 - 0.001070\,\mathrm{Speed} + 0.618\,\mathrm{DOC} \\ & + 0.025\,\mathrm{Tool} - 0.00\,\mathrm{Speed} * \mathrm{Speed} \\ & - 1.225\,\mathrm{DOC} * \mathrm{DOC} - 0.0244\,\mathrm{Tool} * \mathrm{Tool} \\ & + 0.000756\,\mathrm{Speed} * \mathrm{DOC}. \end{aligned} \quad (8)$$

The formulated regression equation is statistically fitted with the measured experimental data values. The R^2 and adjusted R^2 values are calculated for this derived model to check the efficacy of the proposed GRG polynomial regression equation.

The R^2 value (0.9970) is of near unity in Table 19, for the predicted GRG model, representing no intervention of external factors in the fitted model. The adjusted R^2 value reasonably agrees with the predicted R^2 value, indicating that the experimental data fit adequately in the proposed second-order polynomial regression model.

4.5.1. Regression Analysis for GRG (Cutting Speed, Depth of Cut). The GRG model equation is derived for the cutting speed and depth of cut with an R^2 value of 0.8549. Table 20 depicts the regression model and the summary results for the input process parameter combination (Cutting speed and Depth of Cut).

This response and contour graph in Figures 15(a) and 15(b) represent the impact of cutting speed and depth of cut over the combined effect of all the measured output responses. Larger depth of cut and higher cutting speed need robust machine structure and holding fixture for proper machining accuracy and better surface finish in the machined parts. The mean range value of cutting speed

Table 17: Calculation of Grey Relational Grade (GRG) values.

Exp. order	S/N ratio			Normalized S/N ratio			GRC			GRG
	MRR	Torque	Thrust force	MRR	Torque	Thrust force	MRR	Torque	Thrust force	
1	13.5904	−8.1254	39.3883	0	0.415	0.2119	1	0.6584	0.7906	0.8163
2	15.0071	−10.624	37.8952	0.106	0	0	0.883	1	1	0.961
3	14.3251	−8.6854	40.2572	0.055	0.322	0.3353	0.9357	0.7129	0.7047	0.7844
4	19.1913	−9.2840	38.9182	0.4197	0.223	0.1452	0.6559	0.782	0.8464	0.7614
5	20.3848	−7.5973	37.8952	0.509	0.5028	0	0.6112	0.614	1	0.7417
6	22.1136	−7.1014	41.7719	0.639	0.585	0.5504	0.556	0.5776	0.5924	0.5753
7	25.2357	−5.3586	41.4170	0.873	0.875	0.5	0.4782	0.4776	0.6154	0.5237
8	25.9056	−4.6036	44.9388	0.923	1	1	0.4643	0.444	0.444	0.4508
9	26.9357	−7.9112	42.1122	1	0.4506	0.5987	0.444	0.6397	0.5720	0.5519
Min.	13.5904	−10.624	37.8952							
Max.	26.9357	−4.6036	44.9388							
Delta	13.3453	6.0206	7.0436							

*The larger the better–material removal rate, torque, and thrust force.

Table 18: ANOVA to investigate the input factor contribution for milling AA 2014.

Source	DF	Adj. SS	Adj. MS	*F*-value	*P*-value	% contribution	Remarks
Model	7	0.222295	0.031756	47.40	0.111		
Linear	3	0.215735	0.071912	107.34	0.071	97.05	Significant
Speed	1	0.178641	0.178641	266.66	0.039	80.36	Significant
DOC	1	0.006004	0.006004	8.96	0.205	2.70	Less significant
Tool	1	0.031090	0.031090	46.41	0.093	13.99	Significant
Square	3	0.005657	0.001886	2.81	0.407	2.54	Insignificant
Speed * Speed	1	0.000262	0.000262	0.39	0.644	0.118	Insignificant
DOC * DOC	1	0.004802	0.004802	7.17	0.228	2.16	Insignificant
Tool * Tool	1	0.000593	0.000593	0.89	0.519	0.267	Insignificant
2-Way Interaction	1	0.001480	0.001480	2.21	0.377	0.6658	Insignificant
Speed * DOC	1	0.001480	0.001480	2.21	0.377	0.6658	Insignificant
Error	1	0.000670	0.000670			0.3	Insignificant
Total	8	0.222965					

*DOC–depth of cut.

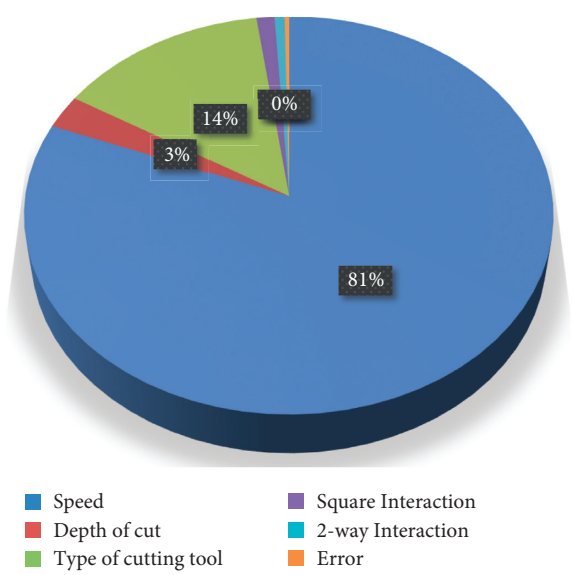

Figure 13: Percentage contribution of the input process parameters and their interactions.

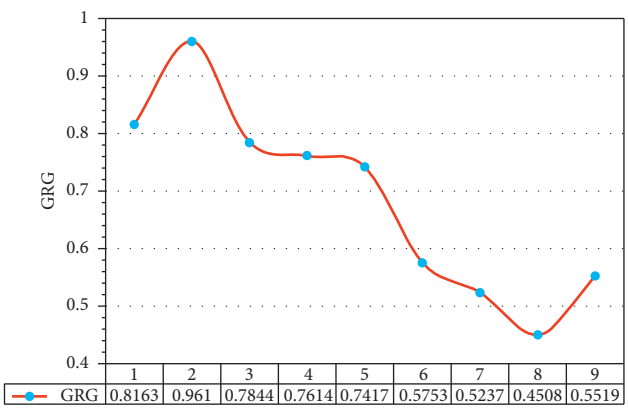

Figure 14: GRG values for the corresponding experimental order.

Table 19: Model summary result.

S value	R^2 value	R^2 value (adj.)
0.0258829	0.9970	0.9760

Table 20: Regression model and summary results for GRG.

Model	GRG = 0.871 − 0.00093 Speed + 0.71 DOC − 0.00 Speed * Speed − 1.22 DOC * DOC + 0.00042 Speed * DOC	
Summary results	S value 0.103847	R^2 value 0.8549

considered in this study will provide better results in the milled parts of AA 2014 material.

4.5.2. Regression Analysis for GRG (Cutting Speed, Type of Cutting Tool). The R^2 value (0.9440) is close to unity, which indicates that the cutting speed and the type of cutting tool have a more significant contribution to the output response than DOC values. Table 21 shows the regression model and the fit efficiency test results.

The three-dimensional plot in Figure 16(a) shows a flat plane, where there is a steep and unidirectional variation in the output response for the type of cutting tool and cutting speed. This process parameter combination holds the most significant stake in the output response value.

4.5.3. Regression Analysis for GRG (Type of Cutting Tool, Depth of Cut). The R^2 value of 0.8891 in Table 22 indicates that the model is statistically fit. There is a possibility that the inclusion of error terms in the model may increase the fit R^2 value. Since the Aluminum alloy AA 2014 is highly malleable, the cutting tool may plunge quickly into the material resulting in good machinability.

The coated cutting tool with different coating conditions is the second most dominant factor in milling AA 2014 material. The three-dimensional response surface and two-dimensional contour plots in Figures 17(a) and 17(b) show a limited variation of the GRG over the change in the DOC values. In addition to these significant parameters, the feed rate is also a parameter considered usually in the machining parameter optimization. This parameter is regarded as a constant in this study to better understand the implications of coated cutting tools. Similarly, there are a lot of external factors affecting the machining of AA 2014 material. Those parameters are considered as residuals or errors in the study. Residual analysis is discussed in the next section, providing a clear-cut idea of the influence of unconsidered process parameters in this experimental study.

4.6. Residual Analysis Study. The residual plots to analyze the error distribution [23] are plotted in Figure 18 as normal probability plot, error fit values, and histogram sorting for the corresponding experimental order considered in this study.

In the main effect plots of Figure 19, the maximum values for each input process parameter (cutting speed, depth of cut, and kind of coated cutting tool) imply a superior process parameter level setting for the relevant factor. But these parameters need to be optimized further by desirability analysis for better-optimized process parameter setting values.

The mean of GRG values is consistently increasing with the increase in the cutting speed, thereby better milling operation at 450 rpm in this study. But the vibration in the structure has a significant impact on the surface roughness in the machined surfaces. The mean GRG values for depth of cut has minor variation, because there is no significant impact at a considered depth of cut parameter level values. The TiAlN coating substantially impacts the considered output responses over the uncoated and TiN coated HSS end mill cutter. The TiAlN coated cutting tool, cutting speed of 450 rpm, and depth of cut of 0.6 mm have the higher mean of GRG values in this process parameter optimization study.

4.7. Predicted vs Actual GRG Values. The regression model is validated by plotting the actual and predicted GRG values using the Design-Expert software (version 13). The closeness in the values is observed at two locations in the graph, as shown in Figure 20. The predicted GRG values are obtained from the polynomial second-order regression equation.

4.8. Process Parameter Optimization Using Desirability Analysis. The desirability analysis test is carried out to predict the optimum input process parameters based on GRG values. Figure 21 shows the overall map of the input process parameter with the desirability and GRG values. The process capability index, C_{pk} function, is used for the predicted GRG values. The process parameter set containing the maximum desirability value is preferred to be the optimal process parameter setting values [24]. The variation of the input factors over the desirability function and predicted GRG values is represented in the form of line graphs.

The ramp function plot in Figure 22 shows the optimized process parameter setting value for the corresponding GRG desirability value. The blue dot in Figure 22 (use web

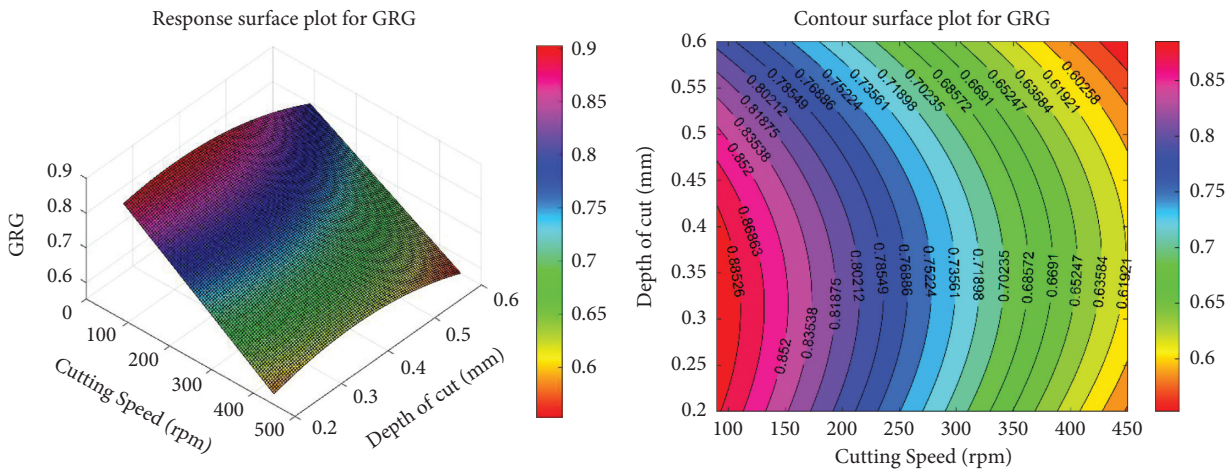

(a) (b)

Figure 15: (a) Response surface plot for GRG (cutting speed vs. depth of cut). (b)Contour surface plot for GRG (cutting speed vs. depth of cut).

Table 21: Regression model and summary results for GRG.

Model	GRG = 1.112 − 0.000889 Speed − 0.100 Tool − 0.00 Speed * speed + 0.0029 Tool * tool + 0.000061 Speed * Tool	
Summary results	S value 0.0644990	R^2 value 0.9440

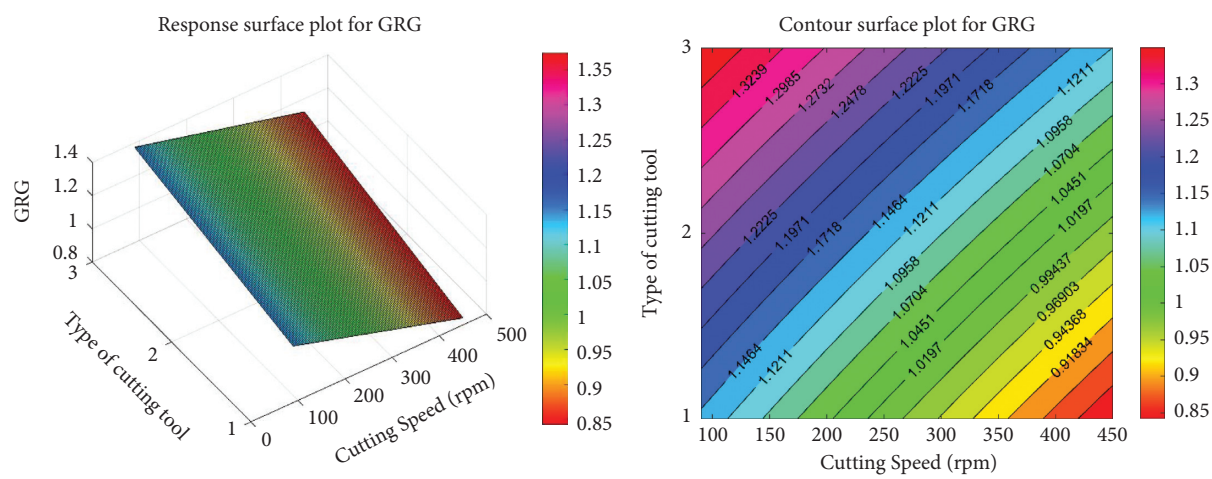

(a) (b)

Figure 16: (a) Response surface plot for GRG (cutting speed vs. type of cutting tool). (b) Contour surface plot for GRG (cutting speed vs. type of cutting tool).

Table 22: Regression model and summary results for GRG.

Model	GRG = 0.707 + 0.90 DOC − 0.068 Tool − 1.22 DOC * DOC + 0.003 Tool * Tool − 0.039 DOC * Tool	
Summary results	S value 0.245496	R^2 value 0.8891

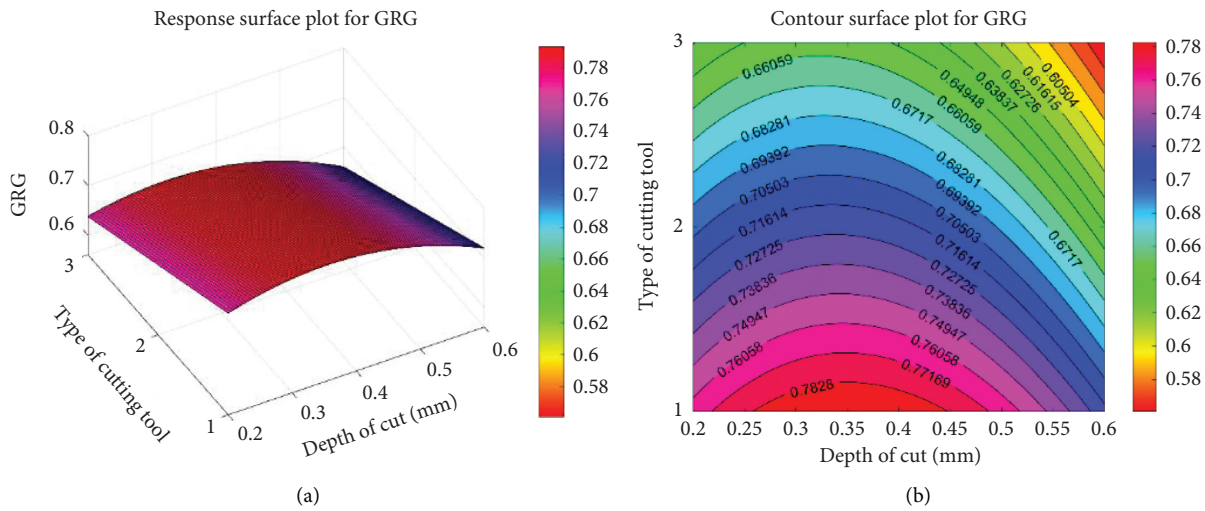

Figure 17: (a) Response surface plot for GRG (depth of cut vs. type of cutting tool). (b) Contour surface plot for GRG (depth of cut vs. type of cutting tool).

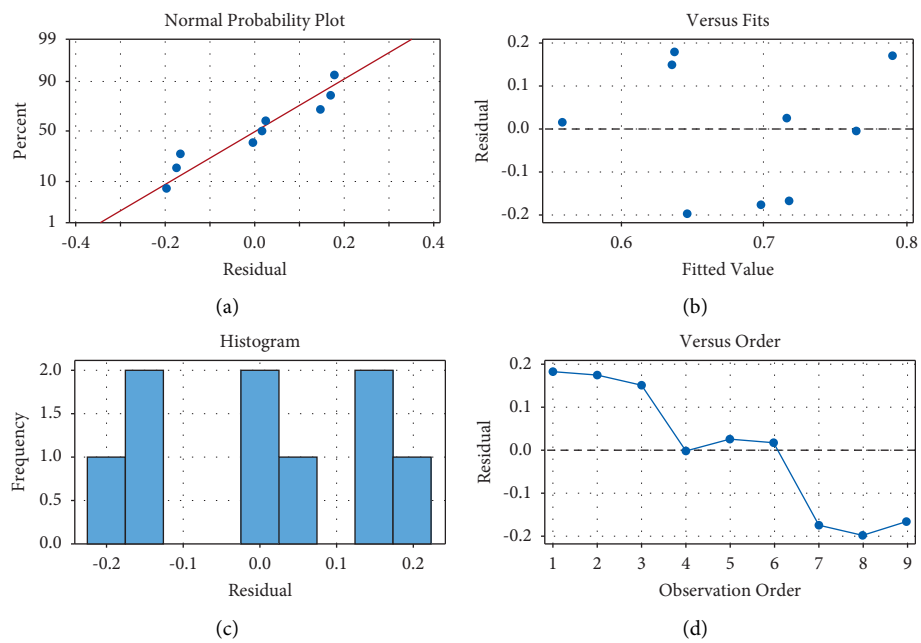

Figure 18: Residual plot analysis for milling AA 2014 material.

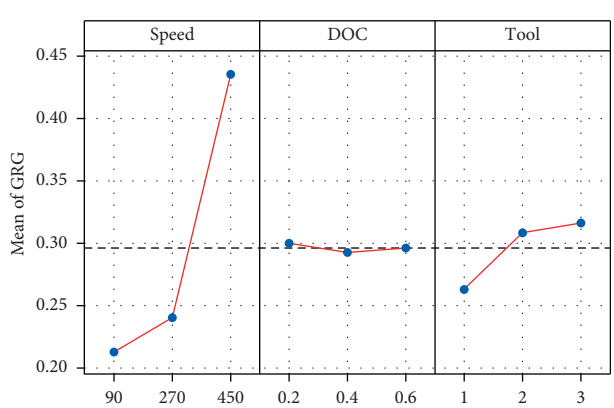

Figure 19: Main effect variation plot of GRG values for the process parameters.

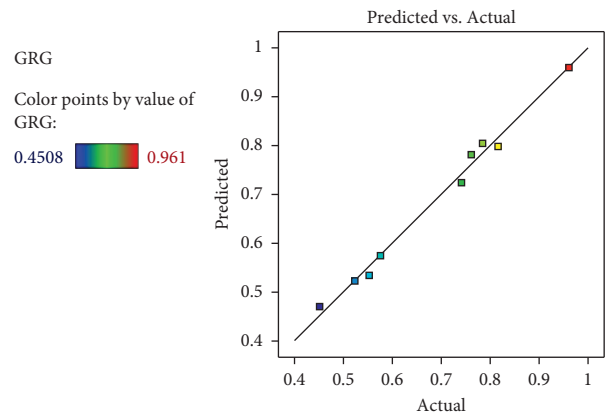

Figure 20: Predicted GRG data vs Actual GRG data.

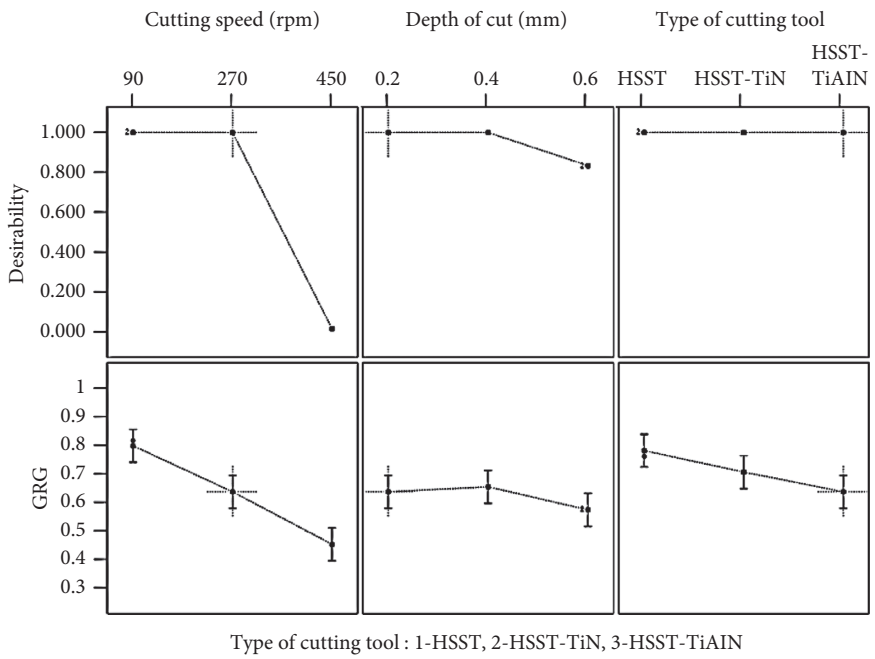

Figure 21: Desirability analysis result.

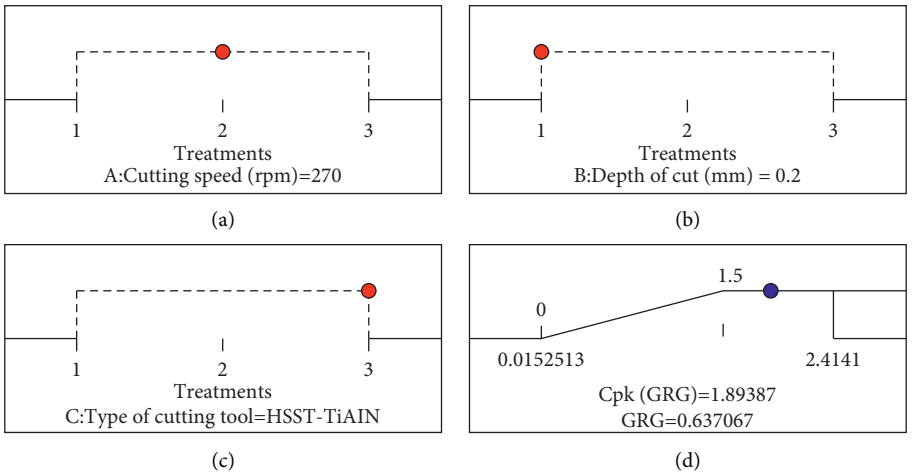

Figure 22: Ramp function graph for desirability analysis.

version) represents the desired process capability index value (1.89387) with its corresponding GRG value (0.637067).

In accordance with the index value, the optimized process parameters obtained in this study are cutting speed (270 rpm), depth of cut (0.2 mm), and HSS cutting tool coated with TiAlN material [25]. To validate the results, a confirmation experiment is carried out for this best process parameter combination.

5. Conclusion

The impact of TiN and TiAlN coating on the HSS tool was studied by analyzing output response parameters such as MRR, Torque, and Thrust force.

The ANOVA table results show that the cutting speed has 80.36% contribution, followed by the type of coated cutting tool with 13.99% contribution. The percentage contribution indicates that the input factor selection and level setting values are correctly designed in this experimental study.

The output response parameters are analyzed using Grey Relational Analysis, and the results are plotted in the form of response surface and contour surface graphs for better visualization.

The process factors such as cutting speed of 270 rpm, depth of cut of 0.2 mm, and TiAlN coated HSS cutting tool have the highest process capability index value of 1.89387 and desirability value of 0.637067. Hence, this process parameter setting is considered the optimized results for milling AA 2014 material in this study.

Data Availability

The data used to support the findings of this study are included in the article.

Conflicts of Interest

The authors declare that there are no conflicts of interest regarding the publication of this article.

Acknowledgments

The authors would like to thank Mr. Parthiban S and Mr. Sarath Kumar R of Saveetha Engineering College, Chennai, for their technical support towards data collection through experimentation. This project was supported by the Deanship of Scientific Research at Prince Sattam bin Abdulaziz University under the research project # 2020/01/17093.

References

[1] T. Kollapuri, M. Manoharan, R. B. Sadayan, and R. K. R. Sajja, "A study on the corrosion behaviour of aluminium alloy 2014 T-651 friction stir welds using stress corrosion cracking," *Volume 14: Emerging Technologies; Safety Engineering and Risk Analysis; Materials: Genetics to Structures*, vol. 14, pp. 1–9, 2015.

[2] Y. Lee, A. Resiga, S. Yi, and C. Wern, "The optimization of machining parameters for milling operations by using the Nelder-Mead Simplex method," *Journal of Manufacturing and Materials Processing*, vol. 4, no. 3, pp. 66–22, 2020.

[3] V. S. Devi, B. K. Gnanavel, P. Murthi, and M. Madhanagopal, "Investigation of novel sustainable concrete using optimization technique," *Advanced Materials Proceedings*, vol. 2, no. 2, pp. 86–92, 2017.

[4] K. Senthilkumaran, P. M. Pandey, and P. V. M. Rao, "Statistical modeling and minimization of form error in SLS prototyping," *Rapid Prototyping Journal*, vol. 18, no. 1, pp. 38–48, 2012.

[5] L. M. Maiyar, R. Ramanujam, K. Venkatesan, and J. Jerald, "Optimization of machining parameters for end milling of Inconel 718 super alloy using Taguchi based grey relational analysis," *Procedia Engineering*, vol. 64, pp. 1276–1282, 2013.

[6] B. Das, S. Roy, R. N. Rai, and S. C. Saha, "Application of grey fuzzy logic for the optimization of CNC milling parameters for Al–4.5%Cu–TiC MMCs with multi-performance characteristics," *Eng. Sci. Technol. an Int. J.*vol. 19, no. 2, pp. 857–865, 2016.

[7] M. N. Durakbasa, A. Akdogan, A. S. Vanli, and A. G. Bulutsuz, "Optimization of end milling parameters and determination of the effects of edge profile for high surface quality of AISI H13 steel by using precise and fast measurements," *Measurement*, vol. 68, pp. 92–99, 2015.

[8] H. S. Lu, C. K. Chang, N. C. Hwang, and C. T. Chung, "Grey relational analysis coupled with principal component analysis for optimization design of the cutting parameters in high-speed end milling," *Journal of Materials Processing Technology*, vol. 209, no. 8, pp. 3808–3817, 2009.

[9] S. R. Elsen, K. Dhamodaran, and J. R. Aseer, "Multi-objective optimization of end milling process parameter for stir casted alumina reinforced aluminium metal matrix composite using RSM," *IOP Conference Series: Materials Science and Engineering*, vol. 402, no. 1, Article ID 012193, 2018.

[10] J. H. Shaik and J. Srinivas, "Optimal selection of operating parameters in end milling of Al-6061 work materials using multi-objective approach," *Mech. Adv. Mater. Mod. Process.*vol. 3, no. 1, 2017.

[11] J. Ren, J. Zhou, and J. Wei, "Optimization of cutter geometric parameters in end milling of titanium alloy using the grey-taguchi method," *Advances in Mechanical Engineering*, vol. 7, no. 2, 2015.

[12] R. Adalarasan, M. Santhanakumar, and M. Rajmohan, "Application of Grey Taguchi-based response surface methodology (GT-RSM) for optimizing the plasma arc cutting parameters of 304L stainless steel," *International Journal of Advanced Manufacturing Technology*, vol. 78, no. 5–8, pp. 1161–1170, 2015.

[13] J. Xu, F. Yan, Y. Li, Z. Yang, and L. Li, "Multiobjective optimization of milling parameters for ultrahigh-strength steel AF1410 based on the NSGA-II method," *Annals of Materials Science & Engineering*, vol. 2020, Article ID 8796738, 11 pages, 2020.

[14] R. Adalarasan, M. Santhanakumar, and A. Shanmuga Sundaram, "Optimization of weld characteristics of friction welded AA 6061-AA 6351 joints using grey-principal component analysis (G-PCA)," *Journal of Mechanical Science and Technology*, vol. 28, no. 1, pp. 301–307, 2014.

[15] R. J. P. S. K. Krishnaiah, "Quality management research by considering multi-response problems in the Taguchi method – a review," *Journal of Advanced Manufacturing Technology*, vol. 26, pp. 1331–1337, 2005.

[16] A. Tamadon, D. J. Pons, K. Sued, and D. Clucas, "Development of metallographic etchants for the microstructure

evolution of A6082-t6 BFSW welds," *Metals*, vol. 7, p. 10, 2017.

[17] S. P. Dwivedi, S. Sharma, and R. K. Mishra, "Mechanical and metallurgical characterizations of AA2014/eggshells waste particulate metal matrix composite," *Int. J. Precis. Eng. Manuf. - Green Technol.*vol. 3, no. 3, pp. 281–288, 2016.

[18] S. R. K. Rao, G. M. Reddy, and K. P. Rao, "Effects of thermo-mechanical treatments on mechanical properties of AA2219 gas tungsten arc welds," *Journal of Materials Processing Technology*, vol. 202, no. 1–3, pp. 283–289, 2008.

[19] R. E. Smallman and A. H. W. Ngan, "Characterization and analysis," *Mod. Phys. Metall.*, pp. 159–250, 2014.

[20] A. Kulandaivel and S. K. Santhanam, "Experimental investigation on turning of monel K500 alloy using nano graphene cutting fluid under minimum quantity lubrication," in *Proceedings of the 2019 International Mechanical Engineering Congress and Exposition*, Nov 2019.

[21] A. Kulandaivel and S. Kumar, "Effect of magneto rheological minimum quantity lubrication on machinability, wettability and tribological behavior in turning of Monel K500 alloy," *Machining Science and Technology*, vol. 24, no. 5, pp. 810–836, 2020.

[22] Y. Sesharao, T. Sathish, P. Kumaran et al., "Optimization on operation parameters in reinforced metal matrix of AA6066 composite with HSS and Cu," *Annals of Materials Science & Engineering*, vol. 2021, Article ID 1609769, 12 pages, 2021.

[23] T. Sathish, S. Tharmalingam, V. Mohanavel et al., "Weldability investigation and optimization of process variables for TIG-welded aluminium alloy (AA 8006)," *Annals of Materials Science & Engineering*, vol. 2021, Article ID 2816338, 17 pages, 2021.

[24] S. Gopalakannan and T. Senthilvelan, "Application of response surface method on machining of Al-SiC nano-composites," *Meas. J. Int. Meas. Confed.*vol. 46, no. 8, pp. 2705–2715, 2013.

[25] K. Arul and S. Kumar, "Magnetorhelogical based minimum quantity lubrication (MR-MQL) with additive n-CuO," *Materials and Manufacturing Processes*, vol. 35, no. 4, pp. 404–414, 2020.

Hindawi
Advances in Materials Science and Engineering
Volume 2021, Article ID 2832149, 8 pages
https://doi.org/10.1155/2021/2832149

Research Article

Evaluation of Mechanical Properties of Sisal and Bamboo Fibres Reinforced with Polymer Matrix Composites Prepared by Compression Moulding Process

S. Krishna Mohan,[1] Arul Thayammal Ganesan,[2] M. Ramarao,[3] Amol L. Mangrulkar,[4] S. Rajesh,[5] Sami Al Obaid,[6] Saleh Alfarraj,[7] S. Sivakumar,[8] and Manikandan Ganesan[9]

[1]*Department of Mechanical Engineering, E.G.S. Pillay Engineering College, Nagapattinam 611002, Tamilnadu, India*
[2]*Department of Mechanical Engineering, St. Mary's Engineering College (SMEC), Hyderabad 686575, India*
[3]*Department of Mechanical Engineering, Bharath Institute of Higher Education and Research, Chennai 6000073, Tamilnadu, India*
[4]*Department of Mechanical Engineering, Rajiv Gandhi Institute of Technology, Mumbai 400053, India*
[5]*Department of Mechanical Engineering, Meenakshi College of Engineering, Chennai 6000078, Tamilnadu, India*
[6]*Department of Botany and Microbiology, College of Science, King Saud University, P.O. Box 2455, Riyadh 11451, Saudi Arabia*
[7]*Zoology Department, College of Science, King Saud University, Riyadh 11451, Saudi Arabia*
[8]*Department of Bioenvironmental Energy, College of Natural Resources & Life Science, Pusan National University, Miryang-si-50463, Republic of Korea*
[9]*Department of Electro-Mechanical Engineering, Faculty of Manufacturing, Institute of Technology, Hawassa University, Ethiopia*

Correspondence should be addressed to Manikandan Ganesan; mani301090@hu.edu.et

Received 9 September 2021; Accepted 26 October 2021; Published 29 November 2021

Academic Editor: P Ganeshan

Today's modern, dynamic world would be impossible to imagine without the concept of composite material advancement. Various studies are being conducted in this area in order to reach the desired level. In terms of compatibility, natural fibre reinforced polymer-based composites and synthetic fibre composites are very similar. Because they are lightweight, nontoxic, and nonabrasive, they are very popular with consumers. They are also readily available and affordable. Composite materials made from natural fibre have superior mechanical properties compared to those made from synthetic fibre. As part of this research, an epoxy-based composite with bamboo and sisal fibre reinforcement is examined. Reinforced with epoxy resin, bamboo fibre and sisal fibre are used to make composite materials. The effect of adding bamboo fibre and sisal fibre in various weight percentages on the mechanical behaviour of composites is investigated.

1. Introduction

Natural fibres are superior to artificial fibres because they are lighter, denser, and more environmentally friendly and have a higher specific strength. On the downside, they have a low gloss finish and are more prone to absorbing moisture [1]. There are also some quality variations. Automobile, packaging, aerospace, construction, and other industries commonly use natural fibre composites. So long as the fibre content does not reach an optimal level, the composites' tensile strength increases [2]. On account of environmental pollution and energy shortages, scientists and researchers began paying close attention to biomass composites in the early 21st century [3–7]. Plant fibres such as sisal, bamboo, bananas, and kenaf have been effectively employing them for reinforcement in addition to thermoplastic and thermoset matrixes. Natural fibres have a number of well-known advantages over synthetic fibres [8, 9]. Additionally, they have

high strength and elasticity modulus, as well as low price and low density. For example, sisal plant fibres have lower ultimate tensile strength than bamboo [10]. More than 500 bamboo species grow in China, which has a bamboo forest covering around 67,000 hectares, accounting for about one-fourth of the world's bamboo forests [11]. Bamboo is produced in China, which is the world's most famous bamboo-producing country. But only about 40% of the natural bamboo resources are currently being used [12]. Its low density, stiffness, and strength as well as its rapid growth have made bamboo popular [13, 14]. Scortechinii is abundant and has excellent mechanical properties. As a general rule, 3–5-year-old bamboo should be used in the construction industry [15]. Prior to the fibre's extraction, several treatments must be performed on the bamboo culms. Bamboo fibre extraction methods include retting, steam explosion, alkali treatment, degumming, grinding, and crushing [16–19]. The mechanical properties of a composite are improved when the fibres and matrices are well bonded at the interface. When the matrix becomes loaded, it will be transferred to the fibres [20]. According to some researchers, composites' mechanical properties are improved by interfacial strength [21, 22]. As a result of its versatility, bamboo is used in a variety of composite materials. Forms include short bamboo fibres, long bamboo strips, and the whole volume of bamboo. A growing number of researchers are interested in developing stronger bamboo fibre for use in industrial products [23]. Using vacuum-assisted resin transfer moulding, bamboo fibres and vinyl ester resins were combined to create environmentally friendly fibre reinforced composites. Using steam explosion, alkali extraction, and chemical extraction, bamboo fibre bundles were extracted prior to fabrication of green composites [24]. According to a comparison of the two materials, jute fibre reinforced epoxy composites had higher Young's modulus values than bamboo fibre reinforced epoxy composites [25]. Polymer composites may benefit from the addition of sisal fibre as a reinforcement. Sisal fibre has potential uses in the aircraft and automobile industries beyond traditional ones (such as ropes, carpets, and mats). Many factors influence how sisal fibre behaves physically and mechanically. These include the fibre's source, age, and location. By altering the surface of the hydrophilic sisal fibre, the hydrophobic polymer matrix has better interfacial adhesion with the hydrophilic fibre [26–28]. Bamboo fibre reinforced epoxy composites showed good longitudinal flexural strength. A number of studies have found that natural fibres such as jute and bamboo can affect the mechanical and physical strength of composites [29–31]. In order to replace conventional materials with natural fibre composites, hybrid combinations of natural fibres are preferred [32]. Because of its excellent mechanical properties, chemical resistance, and electrical insulation characteristics, polymer epoxy resin is used in the majority of bamboo fibre composite studies. The effects of various fibre volume fractions and fracture pattern morphology on bamboo fibre composites at room and elevated temperatures are described in detail. For the purpose of this study, we used varying amounts of bamboo and sisal fibres with epoxy resin to create hybrid composite specimens. Pure and hybrid composite specimens underwent tensile, flexural, compression, and impact tests to determine mechanical properties. Bamboo and sisal fibres were mixed with epoxy matrix to determine how much of each should be added to achieve desired strength of fibre in composites [7, 14, 33–36]. Bamboo and sisal fibre composites with different volume fractions were also evaluated for their mechanical properties.

2. Experimental Plans

2.1. Materials

2.1.1. Sisal Fibre and Its Extraction. A tropical or subtropical temperature is more conducive to sisal plant growth; it grows best above 30°C. Each plant produces 160 sword-shaped leaves over the course of its seven-year lifespan. Ropes, carpets, and so on are typically made from the 600–900 fibres found in the jute. They are removed when they reach an angle of greater than 40° with respect to their upright position. The leaves are then repeatedly beaten with rollers with rounded knife edges, a process called decortication. Squeezing the pulp from the leaf releases the fibres. In order to remove dust and other unwanted contents from the fibres, they are then exposed to the Sun for 4 to 5 days.

2.1.2. Bamboo Fibre and Its Extraction. The pseudo-stem of the bamboo plant is used to extract the bamboo fibres. This plant can reach a height of 15 to 20 feet, depending on the region and the climate. In addition to being 4 to 6 cm wide and 2 to 3 cm thick, the stalk's length is determined by the plant's height. The stalk's outer sheath contains fibres. 80 cm is cut off the plant's qualified stem, and the outer sheath is removed from it. It is then removed by crushing sections of the pulpy material between two roller drums and scraping them around the circumference of each drum. As the name suggests, tuxies is the term used to describe a process of removing fibres from the stalk. A thorough washing and drying operation in the sunlight for a few days is required to remove any remaining moisture.

2.1.3. Epoxy. Epoxy resin is an epoxy oligomer. Once the hardener or curing agent has been introduced into the mix, it takes on a three-dimensional structure. Epoxy resin properties can be altered by using different epoxy oligomers and curing agents. As matrix material, epoxy-LY556 with HY951 hardener is used. The resin-to-hardener weight-to-weight ratio is 10 : 1.

2.1.4. Composite Fabrication. In this case, the composite laminates used in this work were made by compression moulding (Figure 1). Bamboo and sisal fibres that have been exposed to the Sun are first separated and chopped. Epoxy resin, bamboo, and sisal fibre were combined in five different compositions (BS1—90, 10, and 0), (BS2—90, 10, and 10), (BS4—80, 12.5, and 7.5). (BS5—80, 17.5, and 2.5). Bamboo, sisal, bamboo-sisal fibres, and epoxy resin were used to create the composites, with the appropriate

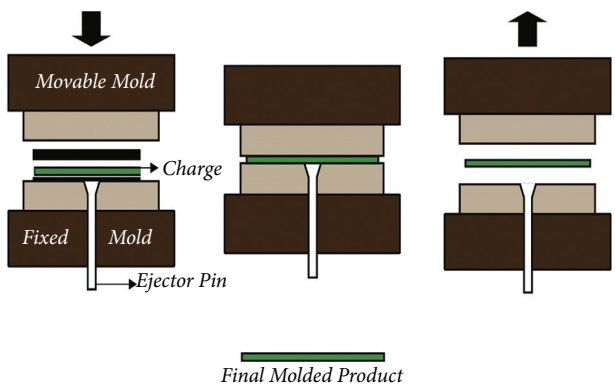

Figure 1: Schematic of compression moulding technique.

hardness selected. With a $250 \times 250 \times 20$ mm mould, the present work was created.

Epoxies are more resistant to water and heat than other polymeric matrices and have high corrosion resistance [37, 38]. In order to prevent resin from being deposited during the squeezing process, a polythene sheet was placed over the bottom jaw. Natural fibre premixed with epoxy resin was applied to the mould after the epoxy resin had been applied. Using a 150-ton hydraulic compression machine, the well-mixed compositions were compressed, and then the resin was applied to the top. For uniform resin distribution throughout the compositions, the pressure was gradually increased to remove trapped air. It took nearly 18 hours to cure the laminate under constant pressure. It was the same with other composite laminates. Table 1 shows the weight and volume percentages of bamboo fibre, sisal fibre, epoxy resin mixture, and laminate. In order to smooth the edges, burs were cut with a saw and rough edges were removed with emery sheets after the compressed laminate had been removed from the compression moulding machine. Most of the thermoset and thermoplastic polymer composites extensively use the compression moulding process. It is widely used in the high-volume production of composite components, like structural and automobile parts.

2.2. Specimen Preparation for Mechanical Test

2.2.1. Tensile Test. Tensile strength refers to a material's ability to stretch without snapping. ASTM D3039 was used to determine the laminate's tensile strength. The specimen needs to be checked to make sure that breaks occur where they should, and their necessity depends on where they occur. The specimen's ends were clamped in between the jaws of the clamp. In other words, the specimen is pulled taut by the jaw movement. This force was measured as a function of gauge length change. The test was performed on a Naveen Engineering universal testing machine with a maximum load capacity of 400 kN. Four millimetres per minute was used to load the samples. There were five samples per laminate for each of the three composite specimen types that were tensile tested. Figure 2 shows the tensile testing machine.

2.2.2. Flexural Test. During flexural testing, the specimen is subjected to tensile and compressive stresses, resulting in a shear stress along the specimen's centerline. The beam could only be bent by applying force. On the universal testing machine, with a load capacity of 400 kN, a flexural test was conducted. The ASTM D790 standard was used to measure the nominal specimen. Because of this, specimens were placed in the middle of two supports, 75 millimetres apart. 4 mm/min of load was applied to the specimen until it fractured and broke. According to Figure 3, this test involves flexural testing of a specimen. The flexural stress was calculated using the maximum load at failure.

2.2.3. Compression Test. Compressive strength refers to a material's ability to withstand a load without lateral deformation. In order to determine the laminate's tensile strength, ASTM D3410 was used. The specimen needs to be checked to make sure that breaks occur where they should, and their necessity depends on where they occur. The specimen's ends were clamped in between the jaws of the clamp. The specimen is compressed as the jaw moves. This force was measured as a function of gauge length change. A compression test was carried out on a Naveen Engineering universal testing machine with a maximum load capacity of 400 kN. The samples were loaded at a rate of 4 millimetres per minute. In order to obtain an average value, five samples from each of the five types of composite specimens were subjected to compression specimen.

2.2.4. Impact Test. Figure 4 shows the impact testing machine. This is the material's ability to withstand sudden application of load. Using the Izod impact test rig, we evaluated the laminates' impact resistance and abrasion resistance. This test method measured the kinetic energy required to initiate a fracture and continue it until the specimen breaks. ASTM D4812 is the standard measurement for the Izod test. An air pendulum blew kinetic energy onto a test specimen standing upright. Grippers were used to hold the test specimen vertically. During the toughness and ductility tests, a scale was used to measure how much energy was absorbed by the material before it broke apart. The specimen description for the Izod impact test is shown in Figure 5.

3. Results and Discussion

3.1. Tensile Strength. Nine different types of laminates are tested in the UTM to determine their tensile strength capabilities. Figure 6 shows the tensile strength of five composite specimens. Sisal is added to bamboo fibre to increase its tensile strength. Composite specimens with higher sisal fibre content in the skin layers stretch more at break than specimens made of bamboo fibre. Figure 6 shows that the tensile strength of the composite is directly related to the amount of bamboo and sisal fibre in it. The specimen fractures at 80 wt. percent epoxy resin, 17.5 wt. percent bamboo fibre, and 2.5 wt. percent sisal fibre reinforced composites. On the graph, the stress-strain values that

Table 1: Weight percentages of matrix and reinforcement materials.

Specimen description	Matrix material (epoxy resin)	Primary reinforcement (bamboo fibre)	Secondary reinforcement (sisal fibre)
B10/S0	90	10	0
B0/S10	90	0	10
B10/S10	80	10	10
B12.5/S7.5	80	12.5	7.5
B17.5/S2.5	80	17.5	2.5

Figure 2: Tensile test machine.

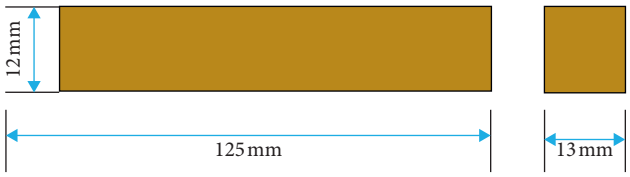

Figure 3: Specimen description for flexural test (ASTM D790 standard).

Figure 4: Impact test machine.

correspond to the tensile modulus of laminates can be measured. For all composite specimens, typical stress-strain curves were generated using the UTM. At its yield strength, the specimen begins to behave like brittle material and eventually breaks. UTM also provided a comparison plot of

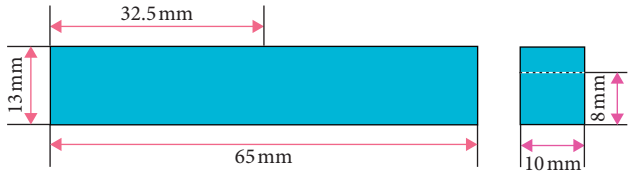

Figure 5: Specimen description for Izod impact test (ASTM D4812 standard).

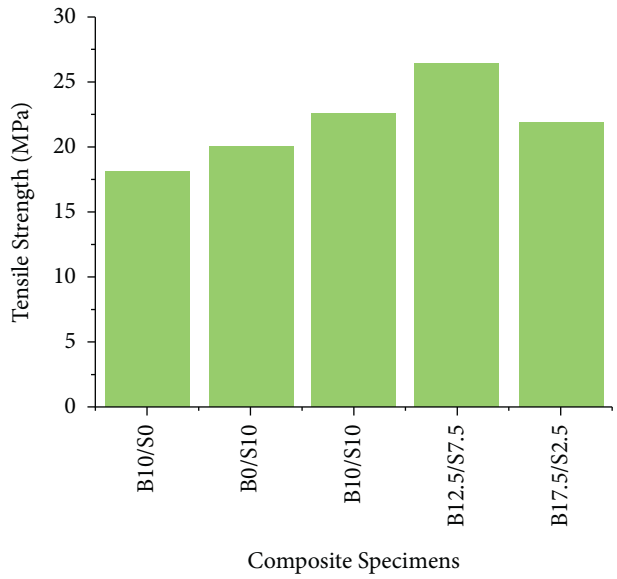

Figure 6: Tensile strength of the composite specimens.

load and displacement curves for each laminate during the tension test process. B0/S10 laminates with 100% sisal fibre have tensile strengths of 18.07 and 20.03 MPa, respectively, while B10/S10 composites with randomly mixed bamboo/sisal fibre have tensile strengths of 22.64, 26.41, and 21.82 MPa, respectively. Tensile properties of laminates are improved by 32% and 24% when bamboo fibre and sisal fibre are mixed together in higher weight percentages of bamboo fibre than sisal fibre. Naturally hybrid composite tensile strength increases with bamboo content. The tensile strength of bamboo fibre is increased by 32, 24, and 14%, respectively, by adding sisal fibre. There is no doubt that adding sisal fibre to bamboo fibre reinforced composite materials improves their strength, and that mixing bamboo fibre with sisal at higher weight ratios increases their resistance to tensile forces. Pure bamboo or sisal fibres cannot match the tensile strength of a hybrid bamboo-sisal fibre reinforced with

epoxy resin. It is also possible to compare maximum displacement and length of the various combination sets.

3.2. Flexural Strength. Figure 7 shows the flexural strength measured using the UTM. A sandwich material of bamboo and sisal fibre is found to be stronger than the other combinations. The load is evenly distributed between fibres and matrix in laminates that have been subjected to gradual loading before rupture. Cracks form and propagate along the laminate cross section due to poor adhesion between the fibre and matrix. 46.81 MPa is the higher flexural strength of the composites, attained at the combination of (B12.5/S7.5). There are almost no differences in strength between the bamboo and sisal fibre composite materials. It was found that the flexural strength increased by 13.45, 8.28, and 4.53% when sisal fibres were added to the bamboo fibre laminate and epoxy resin matrix, but it decreased by 3.54% when excess sisal fibre content was added. There is a maximum flexural strength of 46.81 MPa in composite specimens reinforced with 12.5 wt. percent of bamboo fibre and 7.5 wt. percent of sisal fibres (B12.5/S7.5). As shown in Figure 7, all composite specimens have similar flexural strengths. The hybrid bamboo-sisal fibre reinforced composite specimen outperforms the pure bamboo and sisal fibre reinforced composite specimens, and the properties seem to improve with the limited addition of sisal fibres, while the addition beyond a certain limit affects its strength-absorbing characteristics. With the 17.5 weight percent bamboo fibre and 2.5 weight percent sisal groupings, flexural properties improved less than with the 12.5 weight percent bamboo fibre and 7.5 weight percent sisal groupings, relative to each other. The distribution of reinforcement loads (compression and tension loads) and shearing forces in intermediate layers becomes less uniform as the number of layers increases.

3.2.1. Compressive Strength. Compressive strength was measured using the UTM as shown in Figure 8. It has been found that sandwich materials made from bamboo and sisal fibre are stronger than other combinations of these two materials. In laminates that have been subjected to gradual loading before rupture, the load is evenly distributed between fibres and matrix. Laminated cross sections crack due to poor adhesion between fibre and matrix. 26.92 MPa is the higher compression strength of the composites, attained at the combination of (B17.5/S2.5). There are almost no differences in strength between the bamboo and sisal fibre composite materials. However, the flexural strength is increased by 19.58, 11.52, 8.21, and 3.831% when sisal fibres are added in excess to the bamboo fibre laminate and epoxy resin matrix. There is a maximum flexural strength of 26.92 MPa observed in composite specimens reinforced with 17.5 wt. percent bamboo fibre and 2.5 wt. percent sisal fibre (B17.5/S2.5). A comparison of all composite specimens' compressive strength is depicted in Figure 8. In addition, the properties of the bamboo-sisal fibre reinforced hybrid composite specimen seem to improve with the addition of more sisal fibres, while adding more fibres beyond a certain point also improves its strength-absorbing characteristics.

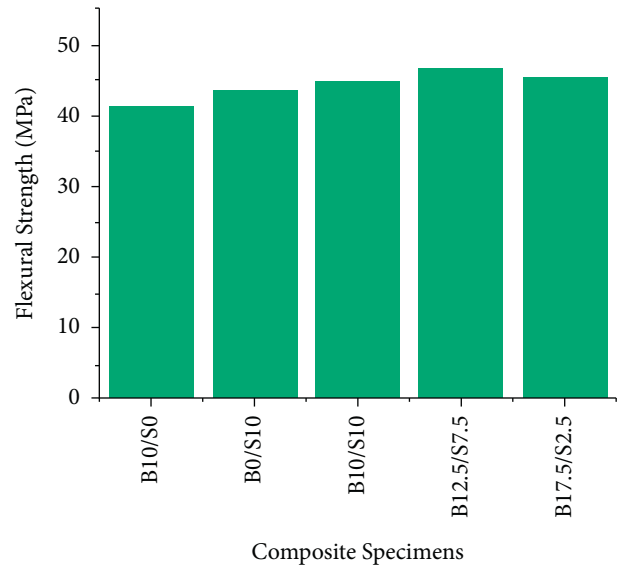

Figure 7: Flexural strength of the composite specimens.

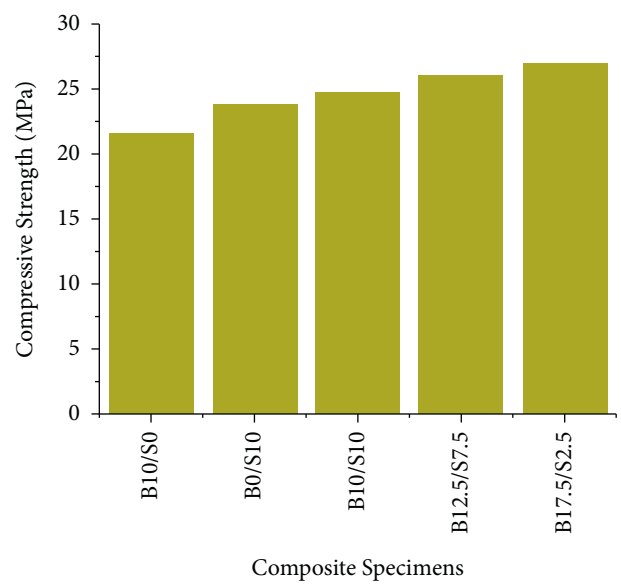

Figure 8: Compressive strength of the composite specimens.

17.5 wt. percent bamboo fibre groupings and 2.5 wt. percent sisal groupings show the greatest improvement in compressive properties, while 12.5 wt. percent bamboo fibre and 7.5 wt. percent sisal groupings show the least improvement. The distribution of reinforcement loads (compression and tension loads) and shearing forces in intermediate layers becomes less uniform as the number of layers increases.

3.2.2. Impact Energy. Five different compositions are tested for impact resistance. The Izod impact test machine is used to determine the energy lost during the impact process. Energy absorption by a specimen after it has been struck by an extremely heavy blow is shown in Figure 9. Hybrid fibre

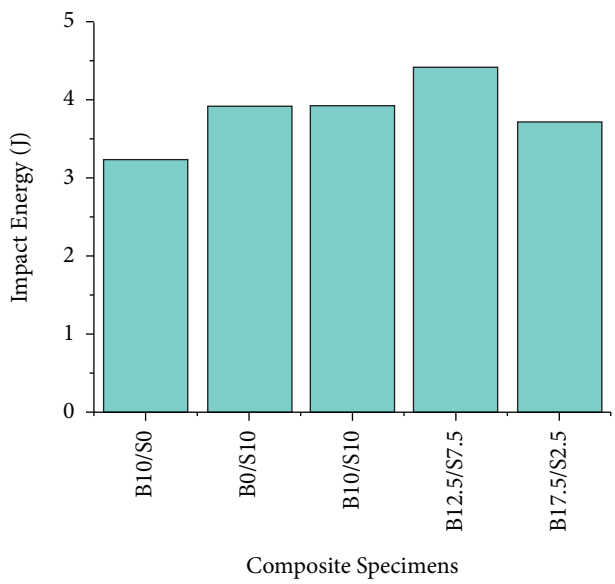

Figure 9: Impact energy of the composite specimens.

combinations with a higher proportion of bamboo fibre and a smaller proportion of sisal fibre outperform natural fibres. The crack propagates as a result of a loss of adhesion between the specimen's fibres and matrix. While the pure bamboo and sisal fibre reinforced composite specimen have impact energies of around 3.2 J and 3.9 J, the epoxy resin matrix with 12.5 wt. percent bamboo fibres and 7.5 wt. percent sisal fibres has an impact energy of 4.4 J. Researchers found that natural fibre laminates had lower impact energy than a bamboo-sisal hybrid composite, according to a study published in Nature Materials. Both the pure bamboo and sisal fibre composite specimens have a nearly identical impact energy as a result. Impact properties of bamboo fibre mat are dramatically improved when sisal fibres are added. Specimens made from composite materials with B10 and S10 content have impact performance improvements of 13% and 31%, respectively. B12.5/S7.5 composite specimen samples have the highest impact energy, which is 31% and 13% higher than pure bamboo and sisal fibre reinforced composite specimens, respectively. The glass fibres in hybrid composites absorb a large amount of energy because bamboo and sisal fibres alternate between layers. There is no positive trend in the impact performance of bamboo and sisal fibres when they are combined in equal weight ratios. As the load travels transversely, the impact properties of natural fibre layers become less effective. As shown in Figure 9, different composite specimens can be compared in terms of impact energy absorption.

4. Conclusions

The mechanical behaviour of bamboo fibre reinforced epoxy-based polymer composite was studied. This experimental investigation produced the following results.

(i) Bamboo and sisal fibre reinforced epoxy composite materials have been successfully fabricated.

(ii) Bamboo and sisal fibres have a significant influence on composite mechanical properties, including tensile strength, flexural strength, compressive strength, and impact energy.

(iii) A lack of proper bonding at the interface of bamboo and sisal fibres causes mechanical properties to degrade with the exception of compressive behaviour. Load transfer to bonding fibres is disrupted as a result. Bamboo and sisal fibres with higher compositions may have lower tensile strength, impact strength, and flexural strength because of this phenomenon.

(iv) The tensile strength of bamboo fibre is increased by 32, 24, and 14%, respectively, by adding sisal fibre. Composite specimens reinforced with 12.5 wt. percent bamboo fibre and 7.5 wt. percent sisal fibres had a maximum flexural strength of 46.81 MPa.

(v) In composite materials, bamboo (12.5 weight percent) and sisal fibre (7.5 weight percent) are added in order to increase tensile strength, flexibility, and impact resistance.

Data Availability

The data used to support the findings of this study are included within the article. Further data or information is available from the corresponding author upon request.

Conflicts of Interest

The authors declare that there are no conflicts of interest regarding the publication of this article.

Acknowledgments

The authors appreciate the support from Hawassa University, Ethiopia. The authors also thank Bharath Institute of Higher Education and Research, Chennai, and this project was supported by Researchers Supporting Project number (RSP-2021/315) King Saud University, Riyadh, Saudi Arabia.

References

[1] H. Ku, H. Wang, N. Pattarachaiyakoop, and M. Trada, "A review on the tensile properties of natural fiber reinforced polymer composites," *Composites Part B: Engineering*, vol. 42, no. 4, pp. 856–873, 2011.

[2] O. Faruk, A. K. Bledzki, H.-P. Fink, and M. Sain, "Progress report on natural fiber reinforced composites," *Macromolecular Materials and Engineering*, vol. 299, no. 1, pp. 9–26, 2014.

[3] R. Jeencham, N. Suppakarn, and K. Jarukumjorn, "Effect of flame retardants on flame retardant, mechanical, and thermal properties of sisal fiber/polypropylene composites," *Composites Part B: Engineering*, vol. 56, pp. 249–253, 2014.

[4] V. Mohanavel, T. Raja, A. Yadav, M. Ravichandran, and J. Winczek, "Evaluation of mechanical and thermal properties of jute and ramie reinforced epoxy-based hybrid composites," *Journal of Natural Fibers*, vol. 2021, Article ID 1958432, 11 pages, 2021.

[5] A. Alavudeen, N. Rajini, S. Karthikeyan, M. Thiruchitrambalam, and N. Venkateshwaren, "Mechanical properties of banana/kenaf fiber-reinforced hybrid polyester composites: effect of woven fabric and random orientation," *Materials & Design*, vol. 66, pp. 246–257, 2015.

[6] M. J. M. Ridzuan, M. S. A. Majid, M. Afendi, M. N. Mazlee, and A. G. Gibson, "Thermal behaviour and dynamic mechanical analysis of Pennisetum purpureum/glass-reinforced epoxy hybrid composites," *Composite Structures*, vol. 152, pp. 850–859, 2016.

[7] A. C. Manalo, E. Wani, N. A. Zukarnain, W. Karunasena, and K.-t. Lau, "Effects of alkali treatment and elevated temperature on the mechanical properties of bamboo fibre-polyester composites," *Composites Part B: Engineering*, vol. 80, pp. 73–83, 2015.

[8] X. Li, L. G. Tabil, and S. Panigrahi, "Chemical treatments of natural fiber for use in natural fiber-reinforced composites: a review," *Journal of Polymers and the Environment*, vol. 15, no. 1, pp. 25–33, 2007.

[9] S. V. Joshi, L. T. Drzal, A. K. Mohanty, and S. Arora, "Are natural fiber composites environmentally superior to glass fiber reinforced composites?" *Composites Part A: Applied Science and Manufacturing*, vol. 35, no. 3, pp. 371–376, 2004.

[10] A. V. R. Prasad and K. M. Rao, "Mechanical properties of natural fibre reinforced polyester composites: jowar, sisal and bamboo," *Materials & Design*, vol. 32, no. 8–9, pp. 4658–4663, 2011.

[11] X. Chen, X. Zhang, Y. Zhang, T. Booth, and X. He, "Changes of carbon stocks in bamboo stands in China during 100 years," *Forest Ecology and Management*, vol. 258, no. 7, pp. 1489–1496, 2009.

[12] J.-H. Chen, J.-K. Xu, P.-L. Huang, and R.-C. Sun, "Effect of alkaline pretreatment on the preparation of regenerated lignocellulose fibers from bamboo stem," *Cellulose*, vol. 23, no. 4, pp. 2727–2739, 2016.

[13] K. Okubo, T. Fujii, and E. T. Thostenson, "Multi-scale hybrid biocomposite: processing and mechanical characterization of bamboo fiber reinforced PLA with microfibrillated cellulose," *Composites Part A: Applied Science and Manufacturing*, vol. 40, no. 4, pp. 469–475, 2009.

[14] L. Osorio, E. Trujillo, A. W. Van Vuure, and I. Verpoest, "Morphological aspects and mechanical properties of single bamboo fibers and flexural characterization of bamboo/epoxy composites," *Journal of Reinforced Plastics and Composites*, vol. 30, no. 5, pp. 396–408, 2011.

[15] D. Ren, Z. Yu, X. Zhang, H. Wang, H. Wang, and Y. Yu, "Quantitative characterization of the interface between bamboo fiber and polypropylene with pull-out test and nanomechanical imaging," *Journal of Materials Science*, vol. 52, no. 3, pp. 1296–1307, 2017.

[16] P. Zakikhani, R. Zahari, M. T. H. Sultan, and D. L. Majid, "Extraction and preparation of bamboo fibre-reinforced composites," *Materials & Design*, vol. 63, pp. 820–828, 2014.

[17] K. M. M. Rao and K. M. Rao, "Extraction and tensile properties of natural fibers: vakka, date and bamboo," *Composite Structures*, vol. 77, no. 3, pp. 288–295, 2007.

[18] K. Okubo, T. Fujii, and Y. Yamamoto, "Development of bamboo-based polymer composites and their mechanical properties," *Composites Part A: Applied Science and Manufacturing*, vol. 35, no. 3, pp. 377–383, 2004.

[19] S. Biswas, Q. Ahsan, A. Cenna, M. Hasan, and A. Hassan, "Physical and mechanical properties of jute, bamboo and coir natural fiber," *Fibers and Polymers*, vol. 14, no. 10, pp. 1762–1767, 2013.

[20] B. Wang, S. Panigrahi, L. Tabil, and W. Crerar, "Pre-treatment of flax fibers for use in rotationally molded biocomposites," *Journal of Reinforced Plastics and Composites*, vol. 26, no. 5, pp. 447–463, 2007.

[21] E. S. Rodriguez, P. M. Stefani, and A. Vazquez, "Effects of fibers' alkali treatment on the resin transfer molding processing and mechanical properties of jute-vinylester composites," *Journal of Composite Materials*, vol. 41, no. 14, pp. 1729–1741, 2007.

[22] H.-S. Yang, H.-J. Kim, J. Son, H.-J. Park, B.-J. Lee, and T.-S. Hwang, "Rice-husk flour filled polypropylene composites; mechanical and morphological study," *Composite Structures*, vol. 63, no. 3–4, pp. 305–312, 2004.

[23] H.-S. Yang, H.-J. Kim, H.-J. Park, B.-J. Lee, and T.-S. Hwang, "Effect of compatibilizing agents on rice-husk flour reinforced polypropylene composites," *Composite Structures*, vol. 77, no. 1, pp. 45–55, 2007.

[24] H. Kim, K. Okubo, T. Fujii, and K. Takemura, "Influence of fiber extraction and surface modification on mechanical properties of green composites with bamboo fiber," *Journal of Adhesion Science and Technology*, vol. 27, no. 12, pp. 1348–1358, 2013.

[25] S. Biswas, S. Shahinur, M. Hasan, and Q. Ahsan, "Physical, mechanical and thermal properties of jute and bamboo fiber reinforced unidirectional epoxy composites," *Procedia Engineering*, vol. 105, pp. 933–939, 2015.

[26] R. V. Silva, D. Spinelli, W. W. Bose Filho, S. Claro Neto, G. O. Chierice, and J. R. Tarpani, "Fracture toughness of natural fibers/castor oil polyurethane composites," *Composites Science and Technology*, vol. 66, no. 10, pp. 1328–1335, 2006.

[27] S. Biswas, K. Debnath, and A. Patnaik, "Mechanical behaviour of short bamboo fiber reinforced epoxy composites filled with alumina particulate," 2012.

[28] L. A. Pothan, C. N. George, M. Jacob, and S. Thomas, "Effect of chemical modification on the mechanical and electrical properties of banana fiber polyester composites," *Journal of Composite Materials*, vol. 41, no. 19, pp. 2371–2386, 2007.

[29] K. Joseph, S. Thomas, and C. Pavithran, "Dynamic mechanical properties of short sisal fiber reinforced low density polyethylene composites," *Journal of Reinforced Plastics and Composites*, vol. 12, no. 2, pp. 139–155, 1993.

[30] T. W. Frederick and W. Norman, "Natural fibers plastics and composites," *EUA Kluwer Acad. Publ*, vol. 2, no. 3, 2004.

[31] X. Y. Liu and G. C. Dai, "Surface modification and micromechanical properties of jute fiber mat reinforced polypropylene composites," *Express Polymer Letters*, vol. 1, no. 5, pp. 299–307, 2007.

[32] M. Boopalan, M. Niranjanaa, and M. J. Umapathy, "Study on the mechanical properties and thermal properties of jute and banana fiber reinforced epoxy hybrid composites," *Composites Part B: Engineering*, vol. 51, pp. 54–57, 2013.

[33] J.-K. Huang and W.-B. Young, "The mechanical, hygral, and interfacial strength of continuous bamboo fiber reinforced epoxy composites," *Composites Part B: Engineering*, vol. 166, pp. 272–283, 2019.

[34] M. Yang, F. Wang, S. Zhou et al., "Thermal and mechanical performance of unidirectional composites from bamboo fibers with varying volume fractions," *Polymer Composites*, vol. 40, no. 10, pp. 3929–3937, 2019.

[35] S. S. Chee, M. Jawaid, M. T. H. Sultan, O. Y. Alothman, and L. C. Abdullah, "Thermomechanical and dynamic mechanical properties of bamboo/woven kenaf mat reinforced epoxy

hybrid composites," *Composites Part B: Engineering*, vol. 163, pp. 165–174, 2019.

[36] F. Wang, M. Yang, S. Zhou, S. Ran, and J. Zhang, "Effect of fiber volume fraction on the thermal and mechanical behavior of polylactide-based composites incorporating bamboo fibers," *Journal of Applied Polymer Science*, vol. 135, no. 15, Article ID 46148, 2018.

[37] V. Mohanavel, S. Suresh Kumar, J. Vairamuthu, P. Ganeshan, and B. NagarajaGanesh, "Influence of stacking sequence and fiber content on the mechanical properties of natural and synthetic fibers reinforced penta-layered hybrid composites," *Journal of Natural Fibers*, vol. 2021, p. 13, Article ID 1875368, 2021.

[38] V. Fiore, G. Di Bella, and A. Valenza, "The effect of alkaline treatment on mechanical properties of kenaf fibers and their epoxy composites," *Composites Part B: Engineering*, vol. 68, pp. 14–21, 2015.

Hindawi
Advances in Materials Science and Engineering
Volume 2021, Article ID 1934490, 10 pages
https://doi.org/10.1155/2021/1934490

Research Article

Liquid Crystal Display (LCD) and Organic Light Emitting Diode (OLED) Applications on Natural Fibre Reinforced Polymer Matrix Composites

V. Senthil Nayagam,[1] Anamika,[2] D. Gopinath,[3] K. Vetri Velmurugan,[4] Rani Fathima,[5] Mary Joy Kinol,[6] Prasath Alias Surendhar,[7] and David Christopher[8]

[1]*Department of Electrical and Electronics Engineering, Sathyabama Institute Science and Technology, Chennai 600119, Tamil Nadu, India*
[2]*Department of Electrical and Electronics Engineering, Galgotias College of Engineering and Technology, Greater Noida 201310, India*
[3]*Department of Mechatronics Engineering, SRM Institute of Science and Technology, Chennai 603203, Tamil Nadu, India*
[4]*Department of Mechanical Engineering, Sri Sairam Engineering College, Chennai 600044, Tamilnadu, India*
[5]*Department of Engineering, Electrical Section, University of Technology and Applied Sciences, Al Musanna, Oman*
[6]*Department of Electronics and Communication Engineering, Saveetha School of Engineering, SIMTAS, Saveetha University, Chennai, Tamil Nadu, India*
[7]*Department of Biomedical Engineering, Bharath Institute of Higher Education and Research, Chennai 600073, Tamilnadu, India*
[8]*Department of Mechanical Engineering, College of Engineering, Wolaita Sodo University, Wolaita Sodo, Ethiopia*

Correspondence should be addressed to David Christopher; david.santosh@wsu.edu.et

Received 8 September 2021; Accepted 28 October 2021; Published 26 November 2021

Academic Editor: P. Ganeshan

Natural materials are the alternative source for the manufacture of products due to environmental requirements. Hot injection moulding techniques make the composite product with fibreglass, granite waste filler, and polylactic acid (PLA). Five samples of each set and sampled with better hardness varied the volumetric percentage of glass fibre and the waste nanogranite particles. This effort is mainly concerned with evaluating the wear of dry sliding and friction of composites. Varying 15, 25, 35, and 45 N load, 750 and 1500 m sliding distance tested the composite materials, respectively. Parametric condition experiments were carried out at the stated process to record answers. Nanogranite composite materials are better than higher concentrations of glass fibre in PLA matrices composites, which are more resistant to wear and friction coefficients. The nanogranite powder is added with the filler element in the PLA matrix to provide a better coefficient of wear and rubbing. A high load of 45 N and a sliding distance of 1500 m were measured at low wear and low friction coefficients.

1. Introduction

Composite materials offer better performance, high specified strength and rigidity, excellent fatigue resistance, low weight, and low design flexibility than conventional structural materials. The winning alliance has become these properties, which leads to new space for fibrous composites. Reinforced plastic fibres and epoxy composites are used widely in automotive and aerospace industries, in addition to other orthodox engineering materials, given their enhanced properties. Researchers have extensively studied the incomparable performance of polymer matrix composite (PMC) materials. The compounds filled have scratch-resistance and can be found in automotive segments for piston blocks, cylinders, callipers, cylinder embedding rings, microwave channels, pulses, spatial structures, and vibrators

segment [1–7]. However, there is much information about composites of glass fibre epoxy [8]. The Glass fibre composite (GFC) exhibits increased resistance to indentation. The GFC exhibits increased resistance to indentation, and also, GFC has also widely employed several applications such as car bodies and brake sections, aircraft rates, and brake segments [9]. The GFC has increased resistance to indentation. Glass fibre reinforced plastics have a preferred density and excellent mechanical and thermal properties and also widely used in automobile and aerospace sectors [10]. E-glass fibre is of great importance between different glass fibres and study for its exceptional characteristics. E-glass is thermally resistant and resistant to corrosion and has good strength. In the electrical isolation industries and structural sectors, e-glass found helpful in cars [11].

Generally, PMCs are extensively utilized in aviation, automotive, and electronic applications. An electronic visual display serves as a video display for displaying images sent over the Internet. Televisions, computer monitors, cell phones, and other electronic visual displays are examples. Light-emitting diodes (LEDs) and liquid crystal displays (LCDs) are the two most common display systems. When triggered by applying an appropriate voltage, an LED is a two-lead semiconductor light source that generates light due to the electroluminescent effect. The energy bandgap of the semiconductor determines the hue of light. A liquid crystal display (LCD) makes use of features, including light modulation. LCDs have several advantages over LEDs, including lower power usage. Figure 1 reveals the structure of a typical LCD. A light-emitting diode (LED) with an organic emissive electroluminescent layer that produces light when an electric current is applied is known as an organic light-emitting diode (OLED). An organic materials layer is sandwiched between two electrodes in a conventional OLED (anode and cathode). All of the components are placed on a transparent electrically conductive substrate like ITO. Because of their outstanding performance, versatility, and ease of production, OLEDs have obtained a lot of interest as next-generation lighting and displays in recent years. Figure 2 reveals the typical construction of an OLED.

The sliding wear of fibre-reinforced composites is affected by the material durability [12]. The compound's load, sliding speed, and distance affect the friction and wear—excessive wear found in more excellent bags during the glass fibre epoxy composites wear test [13, 14]. The sliding wear distance limit significantly affects composite wear [15]. Studies examined for different fillers on cryogenic exposure and glass fibre epoxy composite [16]. The compression moulding technique helped develop polylactic acid matrix (PLA) composites reinforced with chitosan microparticles. The findings show that the mechanical and wear characteristic of the PLA matrix composites is improved positively. PLA has been used to develop food packaging, textiles, and, more recently, engineering polymers. Optimal chitosan reinforcement values for mechanical properties and wear resistance observed 6 wt. percent [17]. The most suitable biodegradable polymer is polylactic acid for wear study. Recent days have seen increased demand for the replacement of petroleum-based polymers [18]. Injection moulding goals include high productivity, design flexibility, low labor costs, and a low scrap rate. Figure 3 reveals the application of different manufacturing techniques in fabrication of structural components.

Since polymer materials are easy to fabricate, lightweight, cheap, and easy to make, they can manufacture a minor machine component. Also, a significant challenge for the existing situation is finding substitute materials with an equal force to the petroleum-based polymer. As PLA has enough mechanical properties as a renewable source polymer, it is used widely, such as packing, rolling, and biomedical applications. PLA's nature is very fragile and has low thermal conductivity, and therefore it is also essential to increase the strength of this polymer. Because of this, the use of PLA for machine components is more suitable in low load and low-speed applications [19, 20].

It is harder to analyse the usury thoroughly and frictional characteristics mixed with different materials and their synergism in the friction structure [21]: barium sulphate, caroline, and rubber filler like barium sulphate and cashew nut used. The filler component is used for design, cost reduction, and increase in manufacturability [22]. In brake pads with higher content, the filler used as Lignin decreased the execution of brake pads marginally. For brake pads, 10% lignin composite is chosen as the most suitable material because the general properties of the commercially available brake pads closely coordinated in its execution [23]. The excess assessment clearly shows that natural fibres in alternative materials are essential for formulating frictional materials with ideal binders and fillers. They consider that it is necessary to use natural binders and fillers connected with the supply and characterization of frozen material. Surprisingly, little research is conducted on composite fusions' tribological properties and available natural fibres [24]. Numerous studies on the tribological performance of composite reinforced fibre have reported before. Constant sliding distances of 300 metres and temperature 300°C are examined in applied loads (5 N, 10 N, 14 N, and 37 N) for mechanical and abrasive Nylon 6 and GFR Nylon 6 wearing at a varying content glass fibre (0–30 wt%). The findings have demonstrated the lowest specified wear rate of 30% of glass fibre content in Nylon 6 [25, 26]. The glass fibres in PEEK and PEEK composite were examined in 30 wt. per cent, and GF/PEEK found to be excellent in wear resistance than PEEK. The authors in [27] studied tribology performance of PEEE under dry and water-lubricated conditions of pure polyether ether ketone (PEEK) and 30 wt. percent fibreglass (GFR). The results indicated that when the pressure increased, a specific wear rate and the frictional coefficient for both composites increase slightly. The values of particular wear rates and rib coefficients were also less than the dry sliding condition in the water-lubricated condition. The GFR strengthened PEEK 30 wt. percent demonstrated strong wear resistance compared with pure PEEK [27]. The tribology of the glass epoxy composite composites with SiC and secondary filler in graphite particles was examined. SiC and graphite were

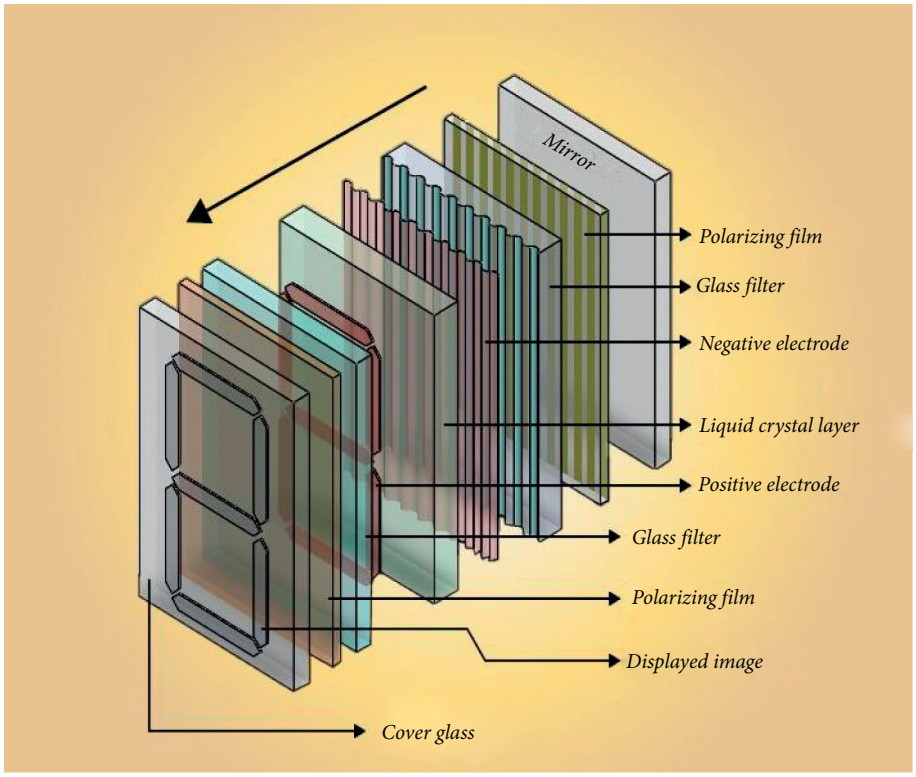

Figure 1: Structure of a typical LCD.

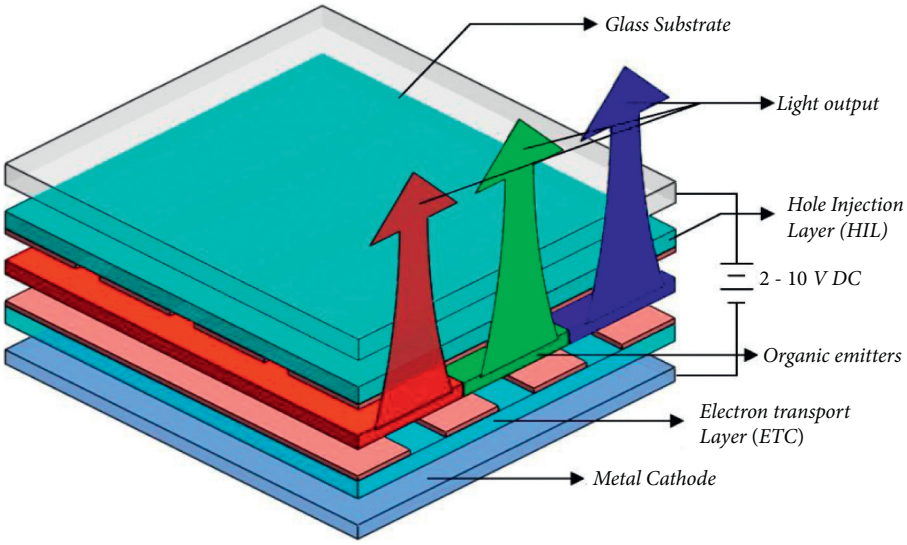

Figure 2: Typical construction of an OLED.

significantly improved in wear resistance properties as filler materials in glass/epoxy composites. In [28], three short E-glass fibre reinforced polyester abrasive wear behaviours were studied with and without filler material. They found that composite wear behaviour depends on different test parameters, including abrasive particle size, sliding speed, loading, and so on. It also observed that a higher fraction of the weight of polyester composites improves wear resistance. The current work focused on producing and investigating the tribological properties, of the different weight percentages of reinforced glass fibre, and PLA matrix with varying weight of waste granite powder. The overview of this experimental work is illustrated in Figure 4.

2. Experimental Plans

Polylactic acid is the most modified kind of phenol (PLA). It has the necessary phenolic characteristics that work as a suitable binder with high resistance to wear and tear.

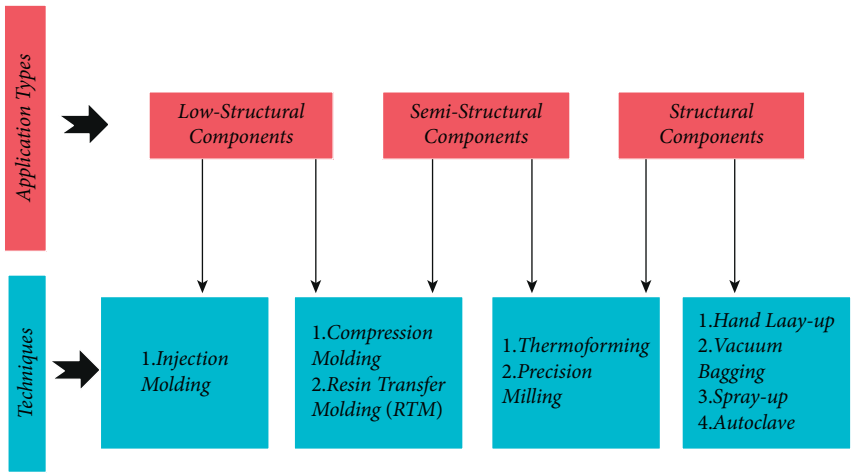

Figure 3: Application of different manufacturing techniques in fabrication of structural components.

Figure 4: Overview of this experimental work.

Flexibility, thermal stability, and impact resistance decrease the friction coefficient. In particular, for brake fitting, the thermosetting and binding properties are also combined. Freezes and increased fading strength, impact resistance, flexibility, rapid thermal disappearance, good noise resistance, wear resistance, improved reliability, heat resistance, and hygroscopic resistance have also reported. It is applicable in the polymers industry due to its polymerization versatility and low-cost modification of chemical products. The addition of nanogranite particles provides a better binding of glass fibre. PLA can be made the preferred initial adhesive by using its high extremity and innate PLA touchiness, and the ease with liquid is made solid. The added value of nanogranite particulate fillers in the samples improves wear and shear resistance in the counter-face zone to reduce the removal of the material.

Table 1: The different chemical compositions of glass fibre in wt. % (30).

SiO_2	Al_2O_3	TiO_2	B_2O_3	Cao	MgO	Na_2O	K_2O
55	14.00	0.2	7	0 22	0 1	0.5	0.3

Table 1 reveals the various chemical compositions of glass fibre. For this study, the main components of the study were the use of glass fibres with liquid PLA and nanogranite particles for the five combinations of samples with varying proportions. The PLA matrix added an adequate volume of 4, 6, 8, 10, and 12% nano granite, along with 4, 5, 6, 7, and 8% glass fibre. Glass fibres are shown in Table 2 for physical and mechanical properties. Figure 5 reveals the graphical representation of twin screw extrusion process for making hybrid composite pieces.

Table 2: Physical and mechanical properties of glass fibre (30).

Density (g/cm^3)	Tensile strength (GPa)	Young's modulus (GPa)	Elongation (%)	Coefficient of thermal expansion	Poison's ratio	Refractive index
2.58	3.445	72.3	4.8	54	0.2	1.558

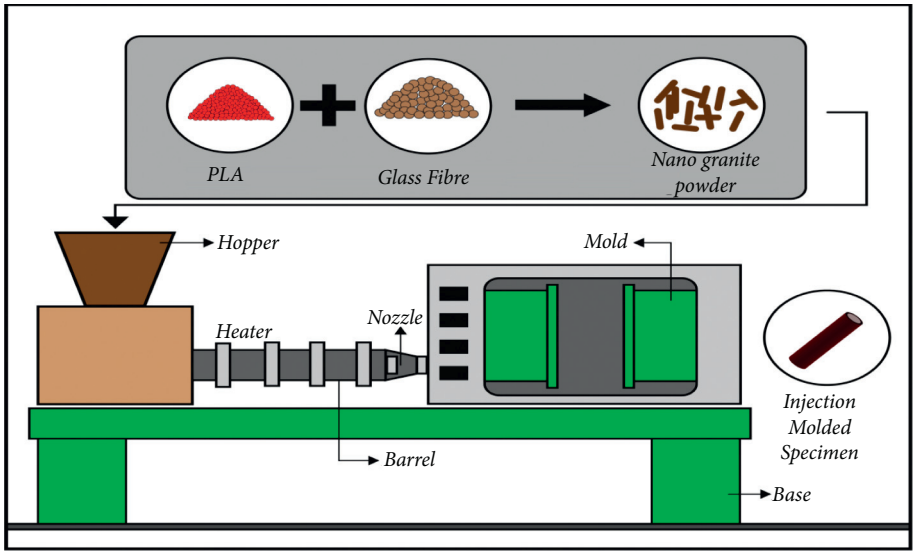

Figure 5: Twin screw extrusion process for making hybrid composite pieces.

The mixing is performed using a 500 rpm mechanical stirrer to make a compound uniform mix to avoid the accrual. Before pouring, it was possible to use a thin wax layer on the inner surface of the form for release and removal of the samples with too minor damage. The preheated mould cavity transferred from the prepared homogeneous mix to the preheated metal moulds of 13 mm diameter and 45 mm length. The bolted mould has been stored for approximately 4 hours in a hydraulic press at 130°C, guaranteeing complete consolidation and postcuring at 90°C in a heat air furnace.

Finally, for cylindrical expulsion, the compressive load of the prepared sample of size 13 mm × 45 mm has been released. For all four samples of PLA, different tribological tests have prepared in the next step of our proposed work according to our planned, designed matrix. The compositions of each prepared sample are shown in Table 3.

The composites of 12 mm and 45 mm diameter are processed and tested with a pin on the tribometer under dry sliding conditions. A PLA (W1, W2, W3, W4, and W5) performed a composite test. In describing the material for the braking system, this wear testing method is commercially used in different conditions (dry and wet), and all tests were conducted at room temperature.

The specimen keeps in contact with the holder of the model with the 62 HRC steel disc. The surface roughness of the sample and the steel disc is 0.9 μm and 1.6 μm, respectively. Different process parameters are used to test the tribometer, such as load 15, 25, 35, and 45 N, slope range 750 m, 1500 m, sliding runtime (15 min), and the track diameter 150 mm. The process parameters also adjusted accordingly. A suitable frozen surface layer has established before each test performed at a preliminary stage of 130 kPa. Each case before and after the trial examined the parallelism between the pin and the rotary disc. Before the test, acetone cleaned up the counter-face; SiC abrasive paper is used to polish the sample, and counter-face was correctly contacted. Figure 6 reveals the schematic diagram of pin on disc apparatus.

The nominal pin disc contact pressure was 13, 27, 42, and 53 KPa, and these steps are used in earlier studies. A 0.1 mg highly accurate digital weight indicator is used to calculate friction wear rate by measuring weight loss. The usage data are an average of four repeated tests in each particular sample. The researchers have used the same method of testing under appropriate standards. For all examples, tribological behaviours, like wear rate and friction coefficient, are taken, and values for further analysis are noted.

3. Results and Discussion

3.1. Wear Rate. Figures 7 and 8 interpret the sliding wear rate data of W1, W2, W3, W4, and W5 composites at a sliding distance of 750 m. The results of Figures 7 and 8 show that the nanogranite powder and glass fibre, which is PLA, are used as filler and reinforcements, and perform better against wear at different load conditions. The additional PLA and higher nanogranite powder reflect comparably less wear resistance to all stress conditions (15 N, 250 N, 35 N, and 45 N).

PLA is the most altered phenolic type. It includes essential elements that are straight phenolic and act as good wear resistance and an excellent tight binder. The addition of waste nanogranite powder is a better binding factor for glass fibres. PLA can be made the preferred initial adhesive using its high

Table 3: Compositions of each prepared sample.

Test specimen description	PLA (wt. %)	Glass fibre (wt. %)	Nanogranite powder (wt. %)
W1	93	3	4
W2	89	6	5
W3	85	9	6
W4	81	12	7
W5	77	15	8

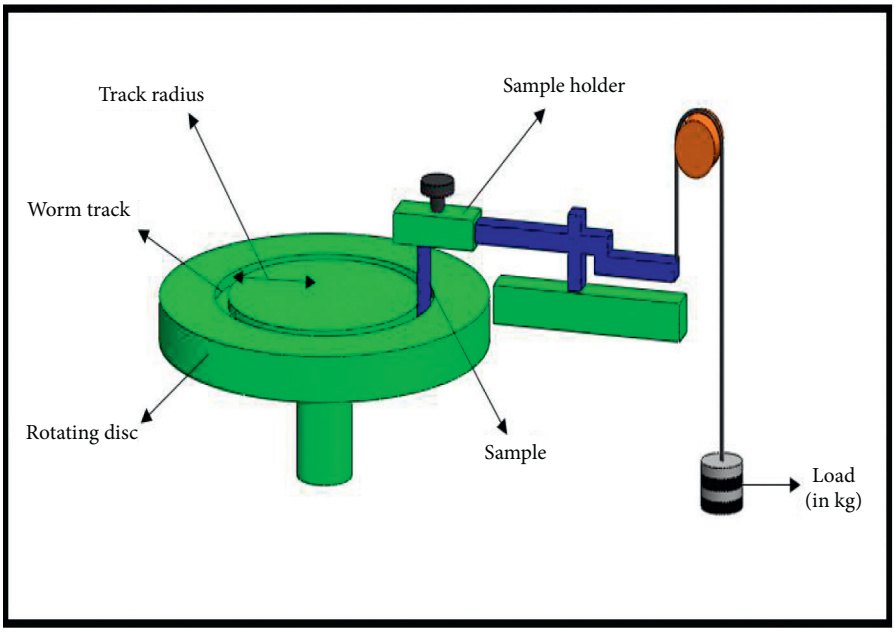

Figure 6: Schematic diagram of pin on disc apparatus.

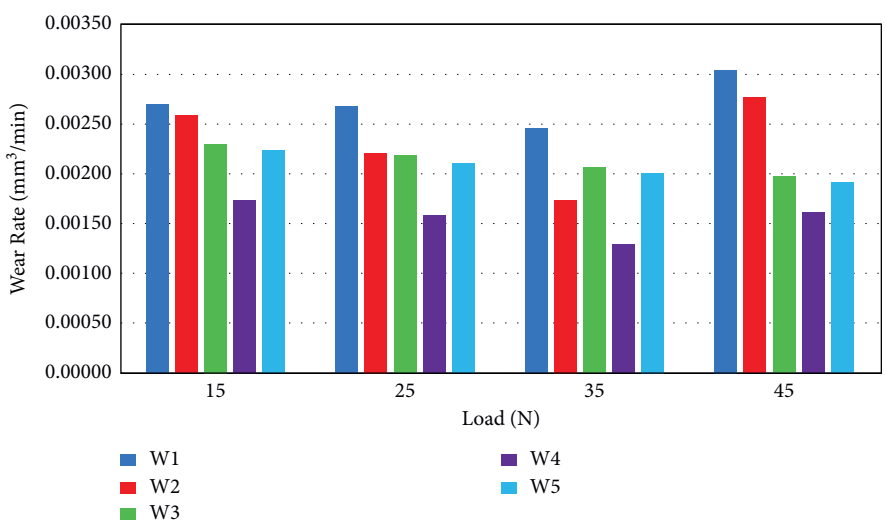

Figure 7: Variation on the wear rate of composites for 750 m sliding distance.

extremity and innate PLA touchiness and the ease with which liquid is made solid. The added value of the nanogranite powder filler waste in samples increases the wear strength and reduces the shear resistance in the rubbing zone against which the material evacuated. The unique wear behaviour of different charging composites is other matrix interfaces. Low load conditions reduce the pressure to cause the light waste material to be evacuated, which increases heavy explosions under high load conditions due to the rubbing effects of the disc and the composite material. The wear rate was higher at a low rotating distance, but the slide improved and became wearable, according to Figures 4 and 5.

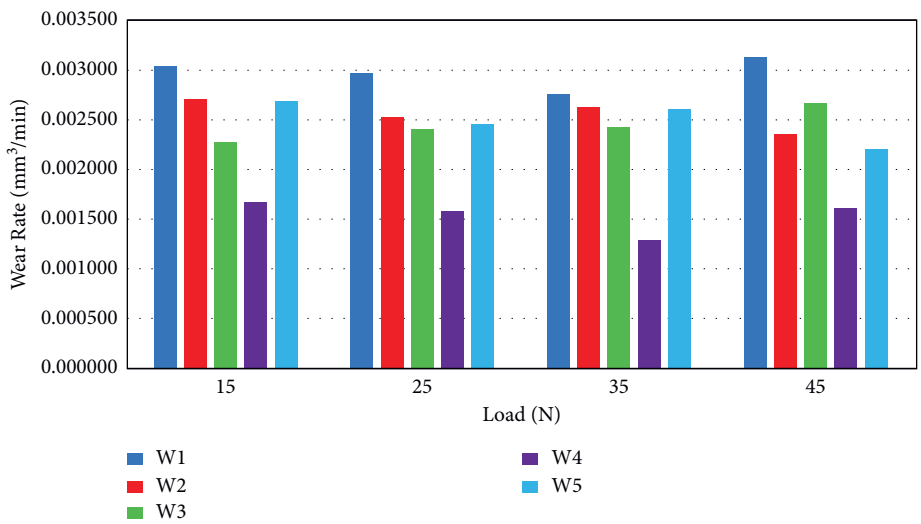

Figure 8: Variation on the wear rate of composites for 1500 m sliding distance.

Due to the application of stress, sliding length, and fillers exposed to opposition to wear, the pattern of wear rate in the specimen reduced in Figures 7 and 8. Initially, during exams, a large area was exhausted. The wear rate was higher. Later, wear debris dropped from the interface into the array, and plastic deformation formed the defensive layer over the fibre. The fillers and the PLA matrix area surface are also flushed, which led to a refusal of wear. The wear rate for W1 composites is high compared withPLA W4 composites, as shown in Figures 9 and 10 for sliding distances of 750 m and 1500 m. That is why the zero content of the waste granite powder fillet which usually less interfacially links filler-PLA matrix areas.

In the investigations, the surface area of the PLA matrix was in more significant contact with the rotary counter-face. Due to the low surface hardness, the material evacuation took place more in the PLA matrix area than the filler and PLA matrix. In turn, composite PLA W4 compared with other PLA samples tends to show a lower wear rate, which could occur because the actual contact area of the PLA matrix and the filling content of the frictional composition increased. In wear expulsion, the comprehensive filler content had a vital role to play. Wear out was gradually reduced by increasing the filling content and surface hardness and reducing the thermal and mechanical load. The required amount of fillers in the composition enhanced through homogeneously blending the stuffing with the PLA matrix with the help of an automatic mixer. The PLA sample W4 shows less wear resistance because the PLA matrix interaction range is higher, and the composites do not fill. Compared with all other samples, the PLA sample W4 shows a lesser wear rate. The high polarity and inherent tackiness of PLA and their wear on the PLA matrix and the containing fillers may be the reason for this.

If two bodies slide at a sliding distance, there is insufficient time for surface undulation to lock each other, thus decreasing the coefficient of friction. Wear rates are based on the coefficient of friction and, because of the increased sliding distance, the friction coefficient decreases. The interactive conditions of PLA and its counter-surface fillers play a significant role in cutting material expulsion. Lower wear rates with a high sliding distance observed and indicated that PLA is very resistant and can effectively prevent composite friction. However, when the sample is present with a continuous axial thrust, neither separation nor pull of fibre and PLA matrix occurs at maximum sliding with higher loads. The glass, granite, and PLA wastes in the W4 sample are perfect for interface adherence and bonding. Moreover, minor fibre fractures increased the load-carrying capabilities.

3.2. Coefficient of Friction (CoF). The force ratio between the application and the force defines the coefficient of friction. For braking conditions, a steady and higher coefficient of friction is needed. Figures 9 and 10 show corresponding friction coefficients compared with samples of sliding distance 750 and 1500 m for PLA matrix/fibre/waste nano-granite powder enhancing. The friction coefficient is high and reduced for load increase under lower load conditions.

The possible mechanism used in the sliding test reduces the frictional coefficient and increases the stress of the specimens. The bonding of the fibre matrix is weakened by heat stress at the interface. Due to the repeated pivotal thrust during high loads, the fibres tend to free and scar effectively. The nature of the coefficient friction depends on the interface between a fine polymer film and the type of fibre. When there is heavy loading of mixed waste, it deforms into a thin, cross section-sectional layer of polymers. This film reduces the friction factor due to its thin protective layer.

Presence of oxide decreases oxygen dissemination, increases load transport, and reduces the CoF through waste properties and contact temperature. The friction coefficients for sliding distance 750 metres are higher but decreased at various loads at a more excellent slip range of 1500 metres because of the greater resistance across the pin and sliding matter because the formation or destruction of the film is rapid. The constant surface smoothness at a high sliding

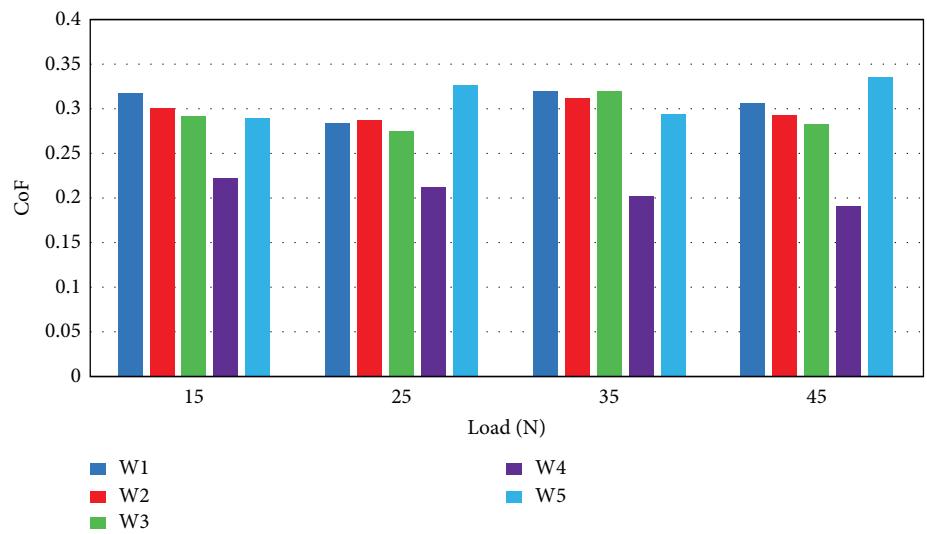

Figure 9: Variation on the coefficient of friction (CoF) of composites for 750 m sliding distance.

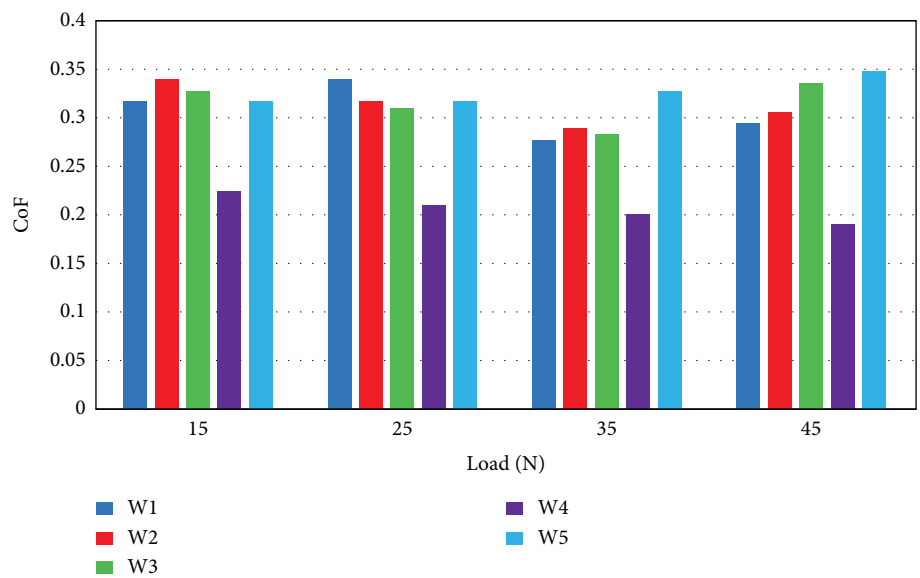

Figure 10: Variation on the coefficient of friction (CoF) of composites for 1500 m sliding distance.

distance also causes it to be determined, and the friction coefficient measures the interactions between the two surface bodies in contact. The presence of oxide reduces oxygen diffusion, increases load transport, and reduces CoF by waste characteristics and contact temperature. The friction coefficient is higher but decreased with various loads at a higher slip range of 1500 m because of the more excellent resistance between the pin and the sliding material since the transmission film is fastly formed and annihilated. The constant surface smoothness at a considerable slope distance also measures the surface interactions of contact between both bodies by the friction coefficient. The filler material ensures the necessary coefficient friction. The cassava shell expansion estimate of 10 per cent in the samples provides better wear resistance, with little shaking resistance, which reduces material removal in the counterfactual scouring zone. The added examples of PLA show a stable coefficient of friction at the increased load. The composite sample W4 has a lower friction coefficient than W1, W2, W3, and W5. The 12% filler W4 sample has a low wear ratio and the necessary friction value coefficient. The strength of the connection helps to reduce the material extraction volume. The PLA effectively provides this bonding strength between the fibres and the fillers, leading to the required friction coefficient value.

Therefore, it is apparent that the W4 composite sample has a good friction coefficient obtained from the other composite samples W1, W2, W3, and W5. The example gives you more excellent resistance to wear if PLA, fibre, and filler included in the necessary matrix. The PLA content ensures that the fibre and filler are binding and interfacially connected, making it better for the PLA to add sample W4 cashew.

4. Conclusions

Polylactic acid (PLA) polymer composites have been successfully manufactured using double-screw extrusion and a hot injection moulding technology in the glass fibre/nanogranite powder. The compound densities gradually increased as the powder of nanogranite and fibre strengthening increased by 3% to 15% wt of glass fibre and 4% to 8% wt of nanogranite powder. The results showed that PLA polymer composites wear behaviour reinforced with glass fibre/nanogranite powder improved by increasing the reinforcement percentage and increasing the reinforcement to a PLA matrix optimally. The lower wear rate and friction coefficient of four glass fibre/nanogranite reinforced powder polylactic acid polymer composite were 7 wt. percent nanogranite powder reinforcement and 12 wt. percent glass fibre reinforcement. There is an increase in wear and friction coefficients beyond the 7 wt. percent addition of nanogranite powder and 12 wt. percent of glass fibres. The wear test results indicate that the wear resistance of the PLA polymer composites specimens of granite powder has increased as reinforcement amounts have raised to an optimal addition of reinforcing materials to the PLA matrix. The most influential factor for specific wear and friction coefficients was found at a load of 45 N and 1500 m.

Data Availability

The data used to support the findings of this study are included within the article.

Conflicts of Interest

The authors declare that there are no conflicts of interest regarding the publication of this article.

Acknowledgments

The authors thank Sathyabama Institute Science and Technology, Chennai, and Sri Sairam Engineering College, Chennai, for providing facilities support to complete this research work.

References

[1] G. B. Veeresh Kumar, R. Mageshvar, R. Rejath, S. Karthik, R. Pramod, and C. S. P. Rao, "Characterization of glass fiber bituminous coal tar reinforced Polymer Matrix Composites for high performance applications," *Composites Part B: Engineering*, vol. 175, Article ID 107156, 2019.

[2] U. K. Annigeri and G. B. Veeresh Kumar, "Method of stir casting of Aluminum metal matrix Composites: a review," *Material Today Proceedings*, vol. 4, no. 2, pp. 1140–1146, 2017.

[3] A. Atiqah, M. Jawaid, S. M. Sapuan, M. R. Ishak, M. N. M. Ansari, and R. A. Ilyas, "Physical and thermal properties of treated sugar palm/glass fibre reinforced thermoplastic polyurethane hybrid composites," *Journal of Materials Research Technology*, vol. 8, no. 5, pp. 3726–3732, 2019.

[4] Z. Benzait and L. Trabzon, "A review of recent research on materials used in polymer–matrix composites for body armor application," *Journal of Composite Materials*, vol. 52, no. 23, pp. 3241–3263, 2018.

[5] J. Naveen, M. Jawaid, E. S. Zainudin, M. T. H. Sultan, and R. Yahaya, "Evaluation of Ballistic Performance of Hybrid Kevlar®/Cocos Nucifera Sheath Reinforced Epoxy Composites," *Journal of Textile Institute*, vol. 110, 2018.

[6] R. A. Ilyas, S. MohdSapuan, R. Ibrahim et al., "Sugar palm (Arenga pinnata (Wurmb.) Merr) cellulosic fibre hierarchy: a comprehensive approach from macro to nano scale," *Journal of Materials Research Technology*, vol. 8, no. 3, pp. 2753–2766, 2019.

[7] D. N. Saheb and J. P. Jog, "Natural fiber polymer composites: a review," *Adances in Polymer Technology. Journal of Polymer Processing Institute*, vol. 18, no. 4, pp. 351–363, 1999.

[8] S. K. Dey and M. Xanthos, "Glass fibers," *Funct. Fill. Plast*, vol. 21, pp. 141–162, 2010.

[9] F. Tanasa and M. Zanoaga, "Fiber-reinforced polymer composites as structural materials for aeronautics," *International Conference Science Paper AF ASES*, vol. 10, 2013.

[10] P. D. Mangalgiri, "Composite materials for aerospace applications," *Bulletin of Materials Science*, vol. 22, no. 3, pp. 657–664, 1999.

[11] R. Pramod and M. E. Shashi Kumar, "Evaluation of mechanical and insulation properties of nomex-T410 and HS glass polymer matrix composites," *Materials Today Proceeding*, vol. 4, no. 2, pp. 3233–3242, 2017.

[12] S. S. Mathapati and S. S. Mathapati, "Testing and analysis of mechanical properties of E- glass fiber reinforced epoxy polymer composites," *International Journal of Research and Innovations in Science and Technology*, vol. 2, no. 1, pp. 46–52, 2015.

[13] A. Arun and K. Kumar Singh, "Friction and wear behaviour of glass fibre reinforced polymer composite (GFRP) under dry and oil lubricated environmental conditions," *Materials Today Proceeding*, vol. 4, no. 8, pp. 7285–7292, 2017.

[14] S. Yadav, Z. Haque, and S. Kumar, "Mechanical and sliding wear behaviour of E-GLASS fiber reinforced with EPOXY composites," *International Research Journal of Engineering Technology*, vol. 3, no. 5, pp. 563–567, 2016.

[15] C. G. Basavarajappa S, "Wear studies on metal matrix composites Taguchi approach," *Journal of Materials Science & Technology*, vol. 21, no. 6, pp. 845–850, 2005.

[16] A. Vaidya and T. Rangaswamy, "A review on E-glass/epoxy composite combined with various filler materials and its mechanical behaviour under different thermal conditions," vol. 7, no. 4, pp. 83–90, 2017.

[17] O. O. Daramola, J. L. Olajide, I. O. Oladele et al., "Mechanical and wear behaviour of polylactic acid matrix composites reinforced with crab-shell synthesized chitosan microparticles," *Materials Today Proceedings*, vol. 38, pp. 999–1005, 2021.

[18] R. Girimurugan, N. Senniangiri, K. Adithya, and B. Velliyangiri, "Mechanical behaviour of coconut shell powder granule reinforced epoxy resin matrix bio composites," *Journal of Advanced Research Dynamical Control System*, vol. 10, no. 12, pp. 533–541, 2018.

[19] D. Robson, J. Hague, G. Newman, G. Jeronomidis, and M. Ansell, *Survey of Natural Materials for Use in Structural Composites as Reinforcement and Matrices*, Biocomposites Centre, Univ. Wales, Bangor, Wales, 1993.

[20] N. Peelman, P. Ragaert, B. Meulenaer et al., "Application of bioplastics for food packaging," *Trends in Food Science & Technology*, vol. 32, no. 2, pp. 128–141, 2013.

[21] P. Gopal, L. R. Dharani, and F. D. Blum, "Fade and wear characteristics of a glass-fiber-reinforced phenolic friction material," *Wear*, vol. 174, no. 1–2, pp. 119–127, 1994.

[22] S. H. R. Ali, B. S. N. Azzam, T. A. Osman, and A. M. Moustafa, "Experimental investigation and surface characterization of a developed frictional composite material for vehicle brakes," *SAE Technical Papers*, vol. 2017, pp. 2–7, 2017.

[23] J. Park, H. Hwang, J. Y. Kim, and J. W. Choi, "Applicability of lignin polymers for automobile brake pads as binder and filler materials and their performance characteristics," *Environmental Technology*, vol. 41, no. 4, pp. 488–497, 2020.

[24] R. Ranganathan, S. Gopal, T. Magudeeswaran, and R. Rangasamy, "Exploration of dry sliding wear behaviour of sisal fiber reinforced cashew nut shell liquid and epoxy polymer matrix composite as an alternative friction material in automobiles," *SAE Technical Papers*, vol. 28, no. 1, 2019.

[25] S. G. Bajwa, D. S. Bajwa, G. Holt, T. Coffelt, and F. Nakayama, "Properties of thermoplastic composites with cotton and guayule biomass residues as fiber fillers," *Industrial Crops and Products*, vol. 33, no. 3, pp. 747–755, 2011.

[26] K. R. N. R. K. Kishor Kumar and P. Ramesh Babu, "No title," *International Journal of Advanced Mechanical Engineering*, vol. 4, no. 1, pp. 371–380, 2014.

[27] K. Surendra and K. Venkateswara Rao, "No title," *International Journal of Engineering Trends and Technology*, vol. 2, pp. 116–120, 2015.

[28] T. P. Sathishkumar, S. Satheeshkumar, and J. Naveen, "Glass fiber-reinforced polymer composites - a review," *Journal of Reinforced Plastics and Composites*, vol. 33, no. 13, pp. 1258–1275, 2014.

Hindawi
Advances in Materials Science and Engineering
Volume 2021, Article ID 4594465, 7 pages
https://doi.org/10.1155/2021/4594465

Research Article

Influence of Flax Fibre Hybridization on Mechanical Behaviour of Sisal Fibre-Polypropylene Composites Prepared with an Injection Moulding Machine

J. Allen Jeffrey,[1] A. Sivakumar,[1] R. Naveen Kumar,[1] A. Anbazhagan,[1] G. Manojkumar,[2] Sami Al Obaid,[3] Saleh Alfarraj,[4] S. Sivakumar,[5] and S. Rajkumar[6]

[1]*Department of Mechanical Engineering, Loyola Institute of Technology, Chennai 600 123, Tamil Nadu, India*
[2]*Department of Mechanical Engineering, Arjun College of Technology, Coimbatore 642 120, Tamilnadu, India*
[3]*Department of Botany and Microbiology, College of Science, King Saud University, PO Box 2455, Riyadh -11451, Saudi Arabia*
[4]*Zoology Department, College of Science, King Saud University, Riyadh 11451, Saudi Arabia*
[5]*Department of Bioenvironmental Energy, College of Natural Resources & Life Science, Pusan National University, Miryang-si-50463, Republic of Korea*
[6]*Department of Mechanical Engineering, Faculty of Manufacturing, Institute of Technology, Hawassa University, Ethiopia*

Correspondence should be addressed to S. Rajkumar; rajkumar@hu.edu.et

Received 25 August 2021; Accepted 22 October 2021; Published 22 November 2021

Academic Editor: P Ganeshan

Due to their low weight, high specific strength, and low environmental impact, sisal fibre-polypropylene composites have gained popularity. However, the material has a low modulus and poor moisture resistance, among other shortcomings. This study investigated how flax fibre hybridization affects the physical parameters of sisal fibre-polypropylene composites. We used maleic anhydride-grafted polypropylene to improve compatibility between fibres and polypropylene. Adding flax fibres to polypropylene-silica composites resulted in increased tensile strength, flexibility, and impact strength, according to researchers. Water resistance was further improved by adding flax fibres. Tensile strength values of polypropylene-sisal fibre composites filled with 0, 5, 10, 15, and 20 wt% of flax fibres were 29.46, 30.56, 31.57, 33.12, and 34.64 MPa, respectively.

1. Introduction

In recent years, researchers have shifted their attention to developing pollution-free green composites that can replace polymer materials in commercial applications. In the development of natural composites, environmental resources have been used as reinforcement materials [1]. Organic fibre composite materials are used in the automobile and furniture industries. At present, coir, jute, and flax are the three most important organic fibres. They are also biodegradable [2]. Biodegradability and renewability of natural fibres make them effective reinforcement materials for composites [3]. Due to the availability of biocomposites, their use has skyrocketed across a variety of industries. Due to the scarcity of synthetic and traditional materials, most material science research focuses on biomaterials. Biocomposites have been studied by a number of academicians. These particles show superior hardness when mixed with epoxy resin matrix and banana fibre composites [4]. Due to their reduced compatibility with hydrophobic polymer matrixes, hydrophilicity is a disadvantage for natural fibres [5–9]. In composites with lignocellulosic fibres and polymeric matrix, such as polypropylene (PP), low levels of dispersion and adhesion occur [10]. Using acid compounds, organosilanes, or alkali treatments, fibre surfaces can be altered to adhere to each other. It has been demonstrated that the maleic anhydride-polypropylene copolymer is a very effective lignocellulosic fibre/PP composite compatibilizer [11–15]. In temperate and subtropical climates, flax fibres are formed in the inner bark of the stem. Flax fibre is a cellulosic, multicellular bast fibre

composed of natural materials like wood and cellulose. Flax fibres range from 10 to 100 centimetres in length. They have a 35–90 m diameter range. Because their polymers are almost perpendicular to the fibre axis, flax is more durable than cotton. Flax is an ancient textile material. Linen is the fabric name given to flax, the plant that is used to produce it. Several studies have compared the mechanical properties of natural fibre/organic matrix composites after similar treatments [16–19]. Fibre-reinforced composites made of natural fibres have a lower modulus and strength than those made of glass fibres and are less resistant to moisture. Two or more fibre types in a single matrix can improve a composite's mechanical performance [13, 15, 20]. Hybrid composites provide a wide range of material properties in the end. As a result, one type of fibre can compensate for the shortcomings of the other [21–25]. Using a combination of glass and natural fibres, we create hybrid composites that offer superior mechanical performance and environmental benefits. An effective material design could achieve a balance between performance and environmental benefits [26]. As a coupling agent, the maleic anhydride-polypropylene copolymer improved the mechanical properties of flax fibre-PP composites [27]. A flax-sisal fibre/polypropylene composite was examined for its mechanical properties. The mechanical and water absorption properties of these composite materials were compared with those of flax fibre-added composites [28–30]. In addition to impact strength, we compared sisal/flax blend strength, Young's modulus, flexural strength, and flexibility modulus. Flax fibre/polypropylene matrix composites and hybrid composites were also evaluated for their water absorption capacities. Figure 1 reveals the challenges and technical problems faced during fabrication of natural fibre composites.

2. Experimental Arrangements

2.1. Materials. Shine Polymers & Trading provided polypropylene. Crystal Fiber Products supplied the sisal fibres. Bharatiya Natural Fibres provided flax fibres in roving shape. The sisal and flax fibres had densities of 1.39 and 2.41 g/cm^3, respectively. Super Chemical Traders supplied polypropylene grafted with maleic anhydride, which was used as a compatibilizer.

2.2. Sisal Fibres. 1.45 grams per cubic centimetre of real density and 1.20 grams per cubic centimetre of apparent density have been observed in this material. At 65% relative humidity, moisture regain capacity is 11%, while at 100% RH, moisture regain capacity is 32%. The fibre has a moderate crystalline structure. Around the fibre axis, the spiral angle is 20–25°. 9.7% elastic strain is found in sisal fibres with a diameter of 21.5103 cm. Transverse compression of these fibres is higher than longitudinal compression. Lignin in sisal fibres causes them to fade rapidly when exposed to sunlight. The moisture reabsorption value of these fibres is affected by their swelling. Despite their low porosity, plant fibres with high moisture absorption swelling do not show much change in porosity. This indicates a less organised molecular arrangement in indirectly dried fibres. The chemical, physical, and mechanical composition of sisal fibres is shown in Table 1.

2.3. Flax Fibres. They range from 25 to 150"millimetres in length and have a diameter of 12 to 16"micrometres. Shorter tow fibres are used for coarser fabrics, while longer line fibres are used for refined fabrics. The flexibility and texture of the fabric are enhanced by flax fibre's "nodes." Flax fibres have irregular polygonal cross sections, which contribute to the fabric's abrasive surface. The chemical composition of flax fibres is given in Table 2.

2.4. Preparation of Fibres. Sisal and flax fibres of five millimetres were cut. A total of three hours of cooking in a methanol/benzene mixture was required to remove waxes and low-molecular-weight species from the fibres before further processing. Hemicellulose was removed from the fibres by soaking them in a 3% NaOH solution for three hours before washing. In the following days, we rinsed and dried the fibres at 90°C over the course of 24 hours.

2.5. Composite Preparation. In a vacuum oven set at 150°C for 14 hours, the fibres were dried before being mixed. Chemical treatments and compounding processes were used to determine the mechanical properties of flax and sisal fibre blends. Ingredients were mixed in an internal mixer and extruded using a twin screw extruder to create the final product. In the internal mixer, they were all mixed for 15 minutes at 60 rpm and 190°C after they were loaded. A speed of 60 rpm was set to run the twin screw extruder (rpm). The first zone was set at 170°C, the second at 180°C, the third at 185°C, and the fourth at 190°C (at die). Figure 2 depicts the twin screw extrusion process in schematic form.

A 12-hour vacuum oven at 120°C was used for both mixing procedures. Using an injection moulding machine, the pellets were injected in dry form. Plastic pellets were injected directly into the injection moulding machine as a comparison. As shown in Figure 3, the injection moulding process follows a flow chart. The ASTM D5943, ASTM D638, ASTM D256, and ASTM D570 standards were followed in the moulding of the samples. The true fibre content of composites was determined using xylene. In an oven, the recovered fibres were dried and weighed after the matrix had been dissolved and removed. Table 3 shows the different composite compositions and their descriptions.

2.6. Characterizations

2.6.1. Measurement of Fibre Length. The composites were heated in a furnace for 4 hours at 500°C to eliminate short glass fibres. The length of the fibres was determined using a reflectance light microscope on 200 samples.

2.6.2. Evaluation of Mechanical Properties. The speed of the Universal Testing Machine was set at five millimetres per second during the testing. ASTM D256-compliant impact

Figure 1: Challenges and technical problems faced during fabrication of natural fibre composites.

Table 1: Chemical, physical, and mechanical composition of sisal fibres.

Ingredients	Sisal fibres (%)
Cellulose	41.6–62.6
Hemicellulose	9.2–14.6
Lignin	11.4–19.5
Density (g/cm^3)	1.28–1.42
Tensile strength (MPa)	126–860
Tensile modulus (GPa)	4.6–16.8
Elongation (%)	1.54–3.85
Fibre diameter (μm)	145–440

Table 2: Chemical composition of flax fibres.

Ingredients	Raw flax%	Retted flax%
Cellulose	56.5	64.1
Hemicellulose	15.4	16.7
Pectin	3.8	1.8
Lignin	2.5	2.0
Fat and wax	1.3	1.5
Water solubility	10.5	3.9
Moisture regain capacity (water)	10.0	10.0
Total	100%	100%

tests were performed on Izods that had been notched. A hammer used to test the composite's impact characteristics weighed 25 kg. The crosshead speed on an ASTM D5943-compliant Universal Testing Machine was 5 mm/s. Figure 4 reveals the impact test specimen position.

2.7. Water Absorption Properties. According to ASTM D570, PP and fibre composites were tested for water absorption. During this experiment, five samples were submerged in distilled water (2 days). The water absorption rate formula is given as follows:

$$\text{percentage of water absorption} = \frac{(\text{SW2} - \text{SW1})}{\text{SW1}} \times 100, \quad (1)$$

where SW_1 = specimen weight before the test (grams) and SW_2 = specimen weight after the test (grams).

3. Results and Discussion

3.1. Mechanical Properties

3.1.1. Ultimate Tensile Strength and Young's Modulus. Composite materials, as shown in Figure 5, have high tensile strength and yield stress. When sisal fibres were added to polypropylene, Young's modulus increased. After flax fibres had been added to polypropylene/sisal fibre composites, tensile strength as well as Young's modulus increased. The interfacial adhesion of sisal-flax fibres and polypropylene matrix increased as a result of the composites' improved tensile properties. In comparison with polypropylene-sisal fibre composites, flax fibre-reinforced composites with a final tensile strength of 34.64 MPa have the best bonding and load-carrying capacity. Moreover, 0 wt% flax fibre-reinforced composites have a minimum tensile strength of 29.46 MPa. Tensile strength values of polypropylene-sisal fibre composites filled with 0, 5, 10, 15, and 20 wt% of flax fibres were 29.46, 30.56, 31.57, 33.12, and 34.64 MPa, respectively. Figure 6 illustrates how flax fibre content affects Young's modulus in pure and hybrid composites.

Using sisal fibre and polypropylene as a base, composites with a glass fibre content of 30 wt% were investigated to test the effects of glass fibre on composites. The 22.84 vol percent for sisal fibre and 14.23 vol percent for glass fibre are used to fabricate the composites. Adding glass fibres to the sisal fibre-polypropylene composite increased its strength slightly. Flax fibres, on the other hand, had no effect on Young's modulus and flexural modulus of polypropylene-silica fibre composites. Young's modulus and flexural modulus of polypropylene-sisal fibre composites were not significantly different when flax fibres were added. Flax fibre contents of 0, 5, 10, 15, and 20 wt% correspond to 3.89, 5.42, 6.44, 9.97, and 10.62 vol%, respectively. Sisal fibre-polypropylene composites were found to have little or no synergistic effect when flax fibres were added, according to the study.

3.1.2. Flexural Strength and Flexural Modulus. Bending the composite specimens in three directions results in a high degree of flexibility (see Figure 7). Due to the highest possible amount of flax fibre content present inside the composites, composite specimens reinforced with 20 wt% flax fibre had a better flexural strength of 71.38 MPa. The entire absence of flax fibre particles inside the composite specimens resulted in a minimum flexural strength of 67.01 MPa, that is, in 0 wt% flax fibre-polypropylene composites. The flexural strength ranged from 66.51 MPa to 71.38 MPa when polypropylene matrix-sisal fibre-reinforced composites were mixed with flax fibres at 0, 5, 10, 15, and 20 wt%. It was found that increasing the flax fibre content had

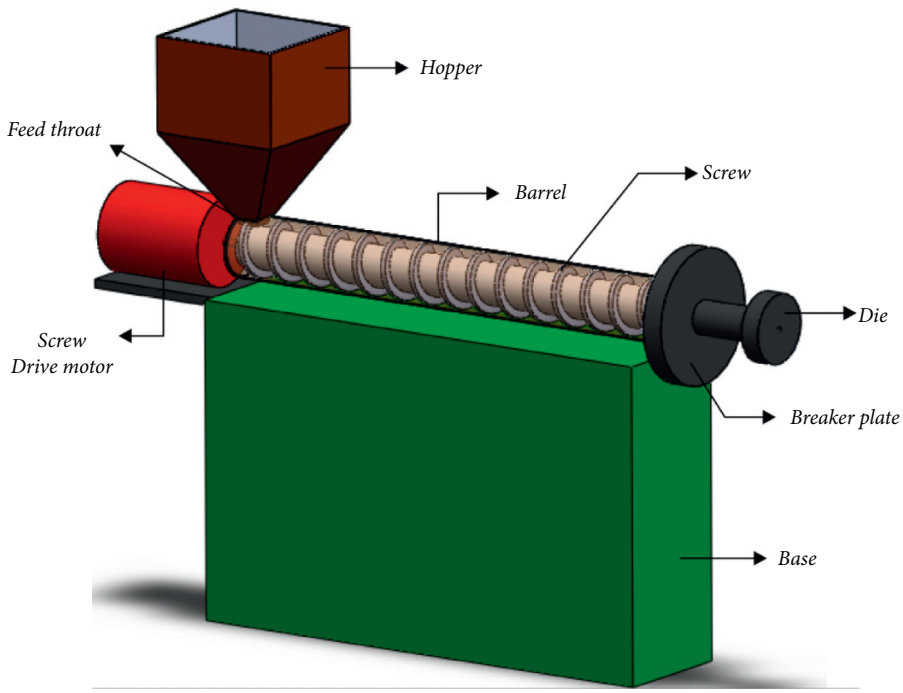

Figure 2: Schematic of the twin screw extrusion process.

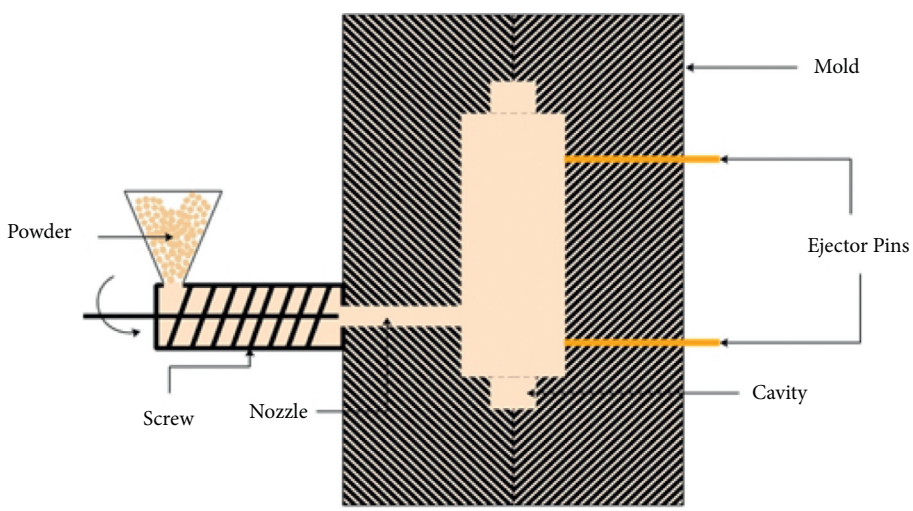

Figure 3: Schematic of the injection moulding process.

Table 3: Detailed description of the composite specimens and its compositions.

Description of the composite specimen	Polypropylene (PP) (wt%)	Sisal fibres (wt%)	Flax fibres (wt%)
PP	100	0	0
PP/SF	70	30	0
PP/FF	70	0	30
PP/25SF/5FF	70	25	05
PP/20SF/10FF	70	20	10
PP/15SF/15FF	70	15	15
PP/10SF/20FF	70	10	20

no significant impact on hybrid composites' flexural properties during the mixing process and the flax fibres were thoroughly mixed, as shown in Figure 8.

Flexural moduli of pure and hybrid composites were affected by flax fibre content, as shown in Figure 8. In polypropylene-sisal fibre composites reinforced with 0 wt%

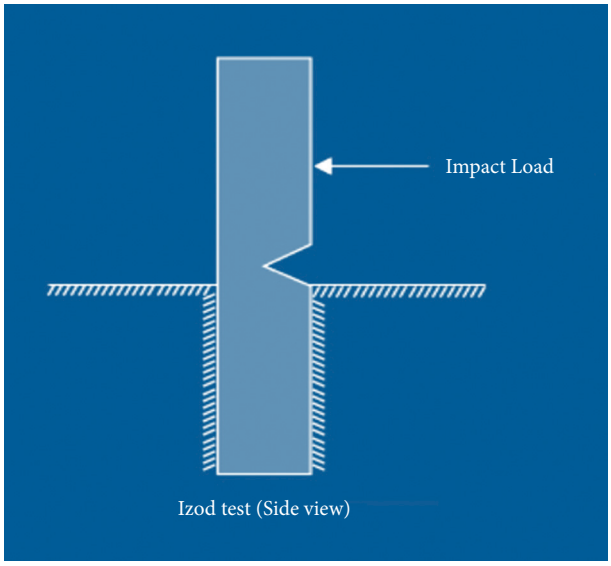

Figure 4: Impact test specimen position.

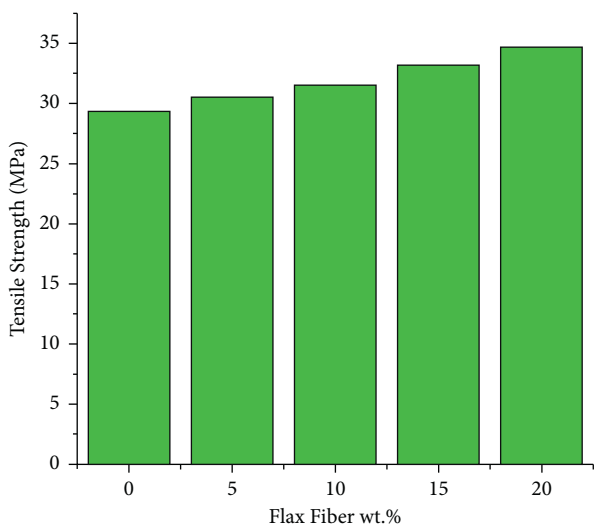

Figure 5: Effect of flax fibre content on tensile strength of pure and hybrid composites.

and 20 wt% of flax fibres, the maximum and minimum three-point bending test moduli were found to be 1.32 and 4.82 GPa, respectively. Composites reinforced with five, ten, fifteen, and twenty wt%. of fibres had flexural modulus values of 1.89, 3.97, 4.36, and 4.38 GPa, respectively. Flax fibres were added to epoxy polypropylene matrix-sisal fibre-reinforced composites to improve the flexural modulus.

3.1.3. Impact Strength. Adding flax fibres to natural fibre-polypropylene composites, on the other hand, was found to improve mechanical performance as per a number of researchers. Polypropylene's impact strength as a stress concentrator was lowered when sisal fibres were added. Impact strength of sisal-polypropylene composites was improved by adding flax fibres. The impact strength of composite specimens during the Izod impact test is shown in Figure 9. Flax

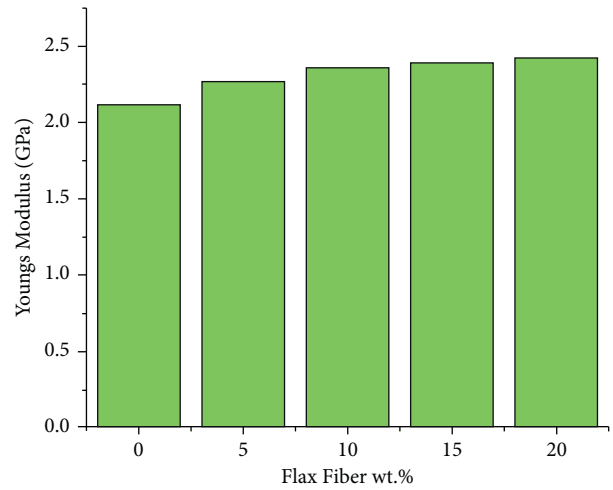

Figure 6: Effect of flax fibre content on Young's modulus of pure and hybrid composites.

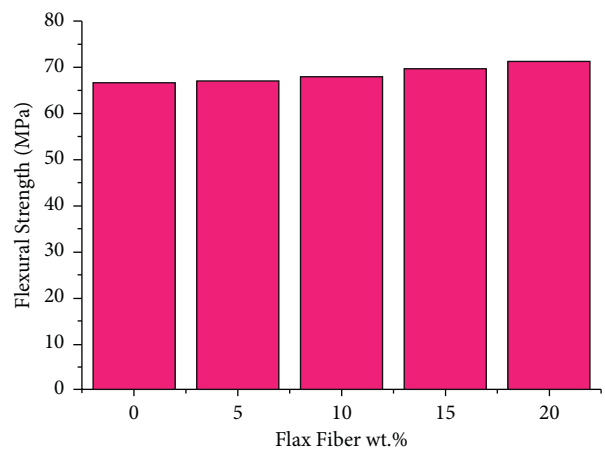

Figure 7: Effect of flax fibre content on flexural strength of pure and hybrid composites.

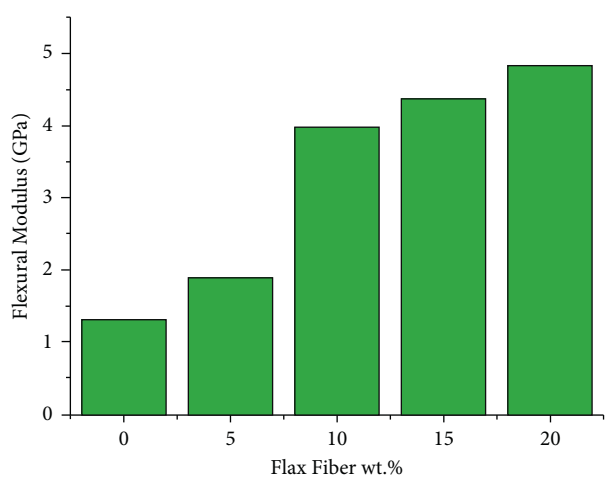

Figure 8: Effect of flax fibre content on flexural modulus of pure and hybrid composites.

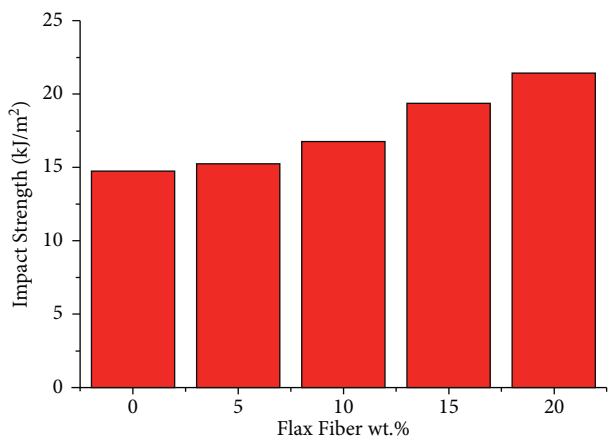

Figure 9: Effect of flax fibre content on impact strength of pure and hybrid composites.

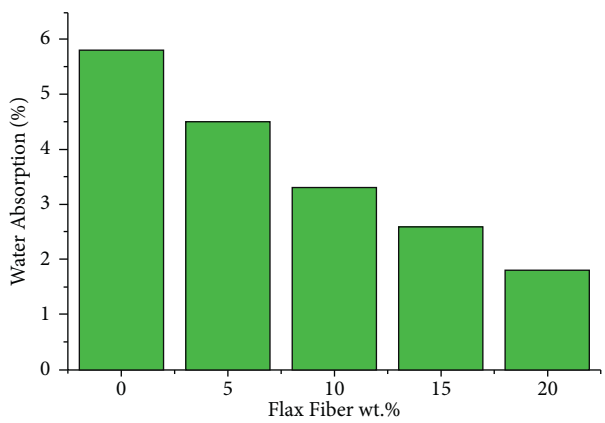

Figure 10: Water absorption of pure and hybrid composites during 48 hours of immersion in water.

fibre composites containing 0, 5, 10, 15, and 20% flax fibres had impact strengths of 14.78, 15.23, 16.86, 19.48, and 21.52 kJ/m^2. Surprisingly, as the weight percentage of flax fibres dispersed in the polypropylene-sisal fibre-reinforced composites increased, the specimens' impact strength improved. The highest impact strength of the 20 w% flax fibre-reinforced composites was 21.52 kJ/m^2, while the minimum impact strength of the 0 wt% flax fibre-reinforced composites was 14.78 kJ/m^2.

3.1.4. Water Absorption Behaviour. The water absorption behaviour of sisal-flax fibre-polypropylene composite is shown in Figure 10. Water absorption in sisal fibre-polypropylene composites was found to be reduced by flax fibres. In a polypropylene matrix containing flax and sisal fibres, researchers found that water absorption decreased.

4. Conclusions

A polypropylene matrix reinforced with sisal fibres was subjected to a flax fibre addition experiment to determine the mechanical properties of the composite. In addition to improving composite tensile, flexural, and impact properties, the compatibilizer improved interfacial adhesion. It was found that the fusion of flax fibres did not significantly improve the mechanical properties of composite materials. When compared to other weight percentages of flax fibres, composites comprising 20 wt% flax fibres, which were added into the polypropylene matrix-sisal fibre-reinforced biocomposites, demonstrated superior tensile and flexural behaviour. The water absorption of sisal-PP composites was reduced when they were hybridised with flax fibres. Flax fibre composites of 0, 5, 10, 15, and 20 wt% showed impact strengths of 14.78, 15.23, 16.86, 19.48, and 21.52 kJ/m^2.

Data Availability

The data used to support the findings of this study are included within the article. Further dataset or information is available from the corresponding author upon request.

Conflicts of Interest

The authors declare that there are no conflicts of interest regarding the publication of this article.

Acknowledgments

The authors appreciate the supports from Hawassa University, Ethiopia. The authors thank the Loyola Institute of Technology, Chennai, and Arjun College of Technology, Coimbatore, and this project was supported by researchers supporting project number (RSP-2021/315), King Saud University, Riyadh, Saudi Arabia.

References

[1] B. V. R. Girimurugan, N. Senniangiri, and K. Adithya, "Mechanical behaviour of coconut shell powder granule reinforced epoxy resin matrix bio composites," *J. Adv. Res. Dyn. Control Syst.*vol. 10, no. 12, pp. 531–544, 2018.

[2] R. G. C. Thiruvasagam, M. Selvaraj, S. Saravanan, and M. Vairavel, "Art of review - fiber reinforced polymer composites," *Journal of Information and Computing Science*, vol. 9, no. 11, pp. 461–468, 2019.

[3] G. Cantero, A. Arbelaiz, R. Llano-Ponte, and I. Mondragon, "Effects of fibre treatment on wettability and mechanical behaviour of flax/polypropylene composites," *Composites Science and Technology*, vol. 63, no. 9, pp. 1247–1254, 2003.

[4] R. Girimurugan, R. Pugazhenthi, P. Maheskumar, T. Suresh, and M. Vairavel, "Impact and hardness behaviour of epoxy resin matrix composites reinforced with banana fiber/camellia sinensis particles," *Materials Today: Proceedings*, vol. 39, pp. 373–377, 2021.

[5] P. Wambua, J. Ivens, and I. Verpoest, "Natural fibres: can they replace glass in fibre reinforced plastics?" *Composites Science and Technology*, vol. 63, no. 9, pp. 1259–1264, 2003.

[6] R. Gauthier, C. Joly, A. C. Coupas, H. Gauthier, and M. Escoubes, "Interfaces in polyolefin/cellulosic fiber composites: chemical coupling, morphology, correlation with adhesion and aging in moisture," *Polymer Composites*, vol. 19, no. 3, pp. 287–300, 1998.

[7] J. C. M. De Bruijn, "Natural fibre mat thermoplastic products from a processor's point of view," *Applied Composite Materials*, vol. 7, no. 5, pp. 415–420, 2000.

[8] W. D. Brouwer, "Natural fibre composites: where can flax compete with glass?" *SAMPE Journal*, vol. 36, no. 6, pp. 18–23, 2000.

[9] A. K. Mohanty, M. Misra, and G. Hinrichsen, "Biofibres, biodegradable polymers and biocomposites: an overview," *Macromolecular Materials and Engineering*, vol. 276-277, no. 1, pp. 1–24, 2000.

[10] M. C. Matias, M. U. De La Orden, C. G. Sánchez, and J. M. Urreaga, "Comparative spectroscopic study of the modification of cellulosic materials with different coupling agents," *Journal of Applied Polymer Science*, vol. 75, no. 2, pp. 256–266, 2000.

[11] N. E. Zafeiropoulos, D. R. Williams, C. A. Baillie, and F. L. Matthews, "Engineering and characterisation of the interface in flax fibre/polypropylene composite materials. Part I. Development and investigation of surface treatments," *Composites Part A: Applied Science and Manufacturing*, vol. 33, no. 8, pp. 1083–1093, 2002.

[12] N. E. Marcovich, M. a. M. Reboredo, and M. I. Aranguren, "Dependence of the mechanical properties of woodflour-polymer composites on the moisture content," *Journal of Applied Polymer Science*, vol. 68, no. 13, pp. 2069–2076, 1998.

[13] L. Y. Mwaikambo, E. Martuscelli, and M. Avella, "Kapok/cotton fabric-polypropylene composites," *Polymer Testing*, vol. 19, no. 8, pp. 905–918, 2000.

[14] M. Kazayawoko, J. J. Balatinecz, and R. T. Woodhams, "Diffuse reflectance Fourier transform infrared spectra of wood fibers treated with maleated polypropylenes," *Journal of Applied Polymer Science*, vol. 66, no. 6, pp. 1163–1173, 1997.

[15] K. Joseph, S. Thomas, and C. Pavithran, "Effect of chemical treatment on the tensile properties of short sisal fibre-reinforced polyethylene composites," *Polymer*, vol. 37, no. 23, pp. 5139–5149, 1996.

[16] R. Karnani, M. Krishnan, and R. Narayan, "Biofiber-reinforced polypropylene composites," *Polymer Engineering & Science*, vol. 37, no. 2, pp. 476–483, 1997.

[17] P. R. Hornsby, E. Hinrichsen, and K. Tarverdi, "Preparation and properties of polypropylene composites reinforced with wheat and flax straw fibres," *Journal of Materials Science*, vol. 32, no. 4, pp. 1009–1015, 1997.

[18] B. V. Kokta, R. G. Raj, and C. Daneault, "Use of wood flour as filler in polypropylene: studies on mechanical properties," *Polymer - Plastics Technology and Engineering*, vol. 28, no. 3, pp. 247–259, 1989.

[19] F. M. B. Coutinho, T. H. S. Costa, and D. L. Carvalho, "Polypropylene-wood fiber composites: effect of treatment and mixing conditions on mechanical properties," *Journal of Applied Polymer Science*, vol. 65, no. 6, pp. 1227–1235, 1997.

[20] T. H. D. Sydenstricker, S. Mochnaz, and S. C. Amico, "Pull-out and other evaluations in sisal-reinforced polyester biocomposites," *Polymer Testing*, vol. 22, no. 4, pp. 375–380, 2003.

[21] J. George, M. S. Sreekala, and S. Thomas, "A review on interface modification and characterization of natural fiber reinforced plastic composites," *Polymer Engineering & Science*, vol. 41, no. 9, pp. 1471–1485, 2001.

[22] A. C. Karmaker and J. A. Youngquist, "Injection molding of polypropylene reinforced with short jute fibers," *Journal of Applied Polymer Science*, vol. 62, no. 8, pp. 1147–1151, 1996.

[23] K. Oksman and C. Clemons, "Mechanical properties and morphology of impact modified polypropylene-wood flour composites," *Journal of Applied Polymer Science*, vol. 67, no. 9, pp. 1503–1513, 1998.

[24] J. M. Felix and P. Gatenholm, "The nature of adhesion in composites of modified cellulose fibers and polypropylene," *Journal of Applied Polymer Science*, vol. 42, no. 3, pp. 609–620, 1991.

[25] A. K. Rana, A. Mandal, B. C. Mitra, R. Jacobson, R. Rowell, and A. N. Banerjee, "Short jute fiber-reinforced polypropylene composites: effect of compatibilizer," *Journal of Applied Polymer Science*, vol. 69, no. 2, pp. 329–338, 1998.

[26] C. Chuai, K. Almdal, L. Poulsen, and D. Plackett, "Conifer fibers as reinforcing materials for polypropylene-based composites," *Journal of Applied Polymer Science*, vol. 80, no. 14, pp. 2833–2841, 2001.

[27] M. M. Thwe and K. Liao, "Durability of bamboo-glass fiber reinforced polymer matrix hybrid composites," *Composites Science and Technology*, vol. 63, no. 3–4, pp. 375–387, 2003.

[28] V. Mohanavel, S. Suresh Kumar, J. Vairamuthu, P. Ganeshan, and B. NagarajaGanesh, "Influence of stacking sequence and fiber content on the mechanical properties of natural and synthetic fibers reinforced penta-layered hybrid composites," *Journal of Natural Fibers*, vol. 2021, Article ID 1875368, 13 pages, 2021.

[29] Y. Li, Y.-W. Mai, and L. Ye, "Sisal fibre and its composites: a review of recent developments," *Composites Science and Technology*, vol. 60, no. 11, pp. 2037–2055, 2000.

[30] A. Arbelaiz, B. Fernández, J. A. Ramos, A. Retegi, R. Llano-Ponte, and I. Mondragon, "Mechanical properties of short flax fibre bundle/polypropylene composites: influence of matrix/fibre modification, fibre content, water uptake and recycling," *Composites Science and Technology*, vol. 65, no. 10, pp. 1582–1592, 2005.

Hindawi
Advances in Materials Science and Engineering
Volume 2021, Article ID 6450251, 15 pages
https://doi.org/10.1155/2021/6450251

Research Article

Optimization of FSP Process Parameters on AA5052 Employing the S/N Ratio and ANOVA Method

C. Chanakyan,[1] S. Sivasankar,[1] M. Meignanamoorthy,[2] M. Ravichandran,[2] V. Mohanavel,[3] Saleh Alfarraj,[4] Hesham S. Almoallim,[5] Velu Manikandan,[6] and J. Isaac JoshuaRamesh Lalvani[7]

[1]*Department of Mechanical Engineering, Government College of Engineering, Thanjavur, Tamilnadu, India*
[2]*Department of Mechanical Engineering, K. Ramakrishnan College of Engineering, Tiruchirappalli 621112, Tamilnadu, India*
[3]*Centre for Materials Engineering and Regenerative Medicine, Bharath Institute of Higher Education and Research, Selaiyur, Chennai 600073, Tamil Nadu, India*
[4]*Zoology Department, College of Science, King Saud University, Riyadh 11451, Saudi Arabia*
[5]*Department of Oral and Maxillofacial Surgery, College of Dentistry, King Saud University, PO Box-60169, Riyadh 11545, Saudi Arabia*
[6]*College of Environmental & Bioresource Sciences, Chonbuk National University, Iksan 570752, Republic of Korea*
[7]*Department of Mechanical Engineering, Faculty of Mechanical and Production Engineering, AMIT, Arbaminch University, Arba Minch, Ethiopia*

Correspondence should be addressed to J. Isaac JoshuaRamesh Lalvani; isaac.jrl@amu.edu.et

Received 3 August 2021; Accepted 7 September 2021; Published 11 October 2021

Academic Editor: P Ganeshan

AA5052 bead-on-plate processing has been achieved by the friction stir processing (FSP) technique to examine the manipulation of process parameters. It also improved the base metal surfaces to analyze the microstructure. The tool spinning speed, traverse speed, and axial load were preferred to investigate the effect of friction stir bead-on-plate processing on the tensile strength qualities and microhardness in AA5052. An optical microscope was used to dissect the fabricated processed zones of the microstructure. By using the design of the experiment, the orthogonal array of the L9 Taguchi method was used to construct the processing experiments. The analysis of variance and the signal-to-noise ratio methods were employed to identify the optimum unification of process parameters and the significant benefaction of a specific parameter on the responses. The outcomes showed that the tool spinning speed was the principal factor affecting the characteristics of tensile strength and microhardness, succeeded by the traverse speed and axial load. The intermetallic compound layer had formed during the processing under specified conditions. This examination revealed that the optimum parameters could intensify the mechanical behaviour of AA5052.

1. Introduction

Various materials of welding with appropriate mechanical finishing and high surface completion are essential for the processing of bead-on-plate welding. The properties of joints depend basically on the processing systems, base metal material properties, types of processed joints, the region of heat-influenced and metallurgical changes during bead-on-plate processing, and process parameters. The joining process is a secure-state method. It has different favourable circumstances over the standard fusion welding process, for example, excellent mechanical properties and comfort, no utilization of consumable material, and work in all positions. There have been numerous exploration projects with a broad scope, allowing for the benefits provided by FSP. Strengths of FSP and the impact of process parameters, namely, tool rotation speed, traverse speed, and axial load, are generally researched. Because of the motivation given by its application in the aviation, marine work, railroad, and transport industries, the FSP procedure is utilized in practically all mechanical segments. Investigational outcomes were measurably handled by analysis of variance (ANOVA) in the

Taguchi technique to forecast the optimized process parameters for friction stir processing (FSP). The results demonstrate that the rotational tool speed, traverse speed, and axial load process parameters have altogether influenced the tensile strength properties and microstructure of the bead-on-plate processed joints.

Cavaliere et al. examined the effect of FSW process parameters on tensile properties and the microstructure of joints of AA6056. Joints were created at the rotational speeds of 550, 850, and 1,050 rpm and traverse speeds of 44, 58, and 70 mm/min. According to the findings, the strongest material strengthening occurs at a traverse speed of 58 mm/min, and it decelerates at a rotating tool speed of 550 rpm. Additionally, it raises the rotational speed of the tool and welding speed and diminishes strength [1]. Minton et al. processed the aluminium composites of 6082-T6 with 6.5 and 4.5 mm thicknesses of welds with the assistance of a FSW milling machine with suitable clamping devices. The results revealed that the vertical milling machine has been equipped for processing the material. Microhardness of the processed joints changes in the range of 52 and 82% of the base material microhardness [2]. Elangovan et al. studied the traverse speed effect and FSW for AA2219 combination influenced by the tool pin profile. A different form of tool pin profiles (TPPs) like straight cylindrical-shaped, conical cylinder, threaded cylinder, triangular, and square is used to manufacture welding processing at various welding speeds of 0.36, 0.66, and 1.35 mm/sec. The results showed that the square tool pin profile had been formed mechanically and flaw-free welds contrasted with different tool pin profiles [3]. Jayaraman et al. studied the optimized parameters (axial load, welding, and rotational tool speed) of the FSW process for rigidity of aluminium 319 composites with the Taguchi technique. To combine the estimated tensile strength and process parameters, they created a numerical model by grey relational analysis. The ultimate tensile strength was found at 1200 rpm of rotational tool speed, 45 mm/min of traverse speed, and 4 kN of axial load [4]. Aydin et al. investigated the impact of elongation and tensile strength utilizing the Taguchi technique, and it was established by the grey relational analysis. Traverse speed, rotational speed, and tool shoulder diameter were used to analyze the FSW process in AA1050. They verified the possibility of using the Taguchi technique with the grey relational method for improving welding quality. The weight estimations were finished by using the analytical hierarchy process (AHP), and the loads were observed to be 0.30 and 0.70 N for tensile strength and elongation responses, respectively [5]. Lian et al. recommended a numerical technique empowered with grey relational analysis to construct a systematic method for investigating the concept of design evaluation. The results revealed that the proposed coarse grey relational investigation has a different option for evaluating the concept of design. The unclear primary information and design were displayed and investigated adequately and analytically [6]. Chi-hui et al. enhanced friction stir processing on AA5083 composites by utilizing the GRA technique with the Taguchi design. The process parameters were pin profile length, rotational speed, tilt angle, and traverse speed. The natural factors are the extreme tensile strength and elongation for the processed material. An outcome with 1800 rpm rotational speed and 180 mm/min welding speed at 180 mm/min, 10° tilt angle of the tool, and 2.5 mm pin length was optimum for finishing quality with minimum expense [7]. Mithra et al. used the Taguchi strategy with the grey relational method to decide various characteristics of drilling quality in the laser process. They showed the possibility of using the grey-Taguchi method for constant enhancement of the quality of fabricated products. The final results showed that the development of a tapered hole is 16.30 and 8.78 percent from the start to the optimal location [8]. Karun Kumar et al. analyzed the solid-state welding process using AA5052. Pentagonal and square pin profiles were used for welding the two pieces of the base plate. Aluminium alloy (AA) 5052 is broadly used in sheet metal work, gas-in-fuel tankers, ships, and aircraft. The parameters, such as axial load, welding speed, tool pin profiles, and tool rotation speed, play a significant role in friction stir processing of AA5052. During this investigation, the use of pentagonal pin profiles in the friction stir welding obtained excellent welds compared to the square pin profile. Three various traverse speeds of 40, 60, and 80 mm/min were considered. The enhancement in mechanical properties was identified while using the pentagon pin profile at 60 mm/min traverse speed [9]. Shanavas et al. addressed the prediction of weld quality in AA5052 with significant parameters of friction stir welding. They developed a regression and a fuzzy logic model for improving the quality of tensile strength and % elongation. The central composite design was used to perform the welding in AA5052 to obtain the maximum tensile stability of welded joints and its outcomes compared with the statistical method. The developed model demonstrated the confidence level at 95% efficiently. The fuzzy model was predicted and used to obtain an acceptable output with minor errors compared to the statistical method [10]. Venkateshkannan et al. compared the distinctive tool pin profiles such as cylindrical threaded, squared, cylindrical, step, and tapered. Dissimilar friction stir welding was executed on AA2024 and AA5052. The SEM and microstructure analysis obtained the mechanical characteristics. Among the different pin profiles, tapered and cylindrical pins exhibited the minor level of discontinuities in macrograph outputs. They determined the optimal parameters of 1000 rpm of tool spinning speed and 40 mm/min of feed. Using step pin profiles achieved the highest tensile strength (297 MPa) on dissimilarly welded base plates [11].

Friction stir processing is a method for processing different alloy components. In this investigation, the bead-on-plate processing method is a preprocessing technique to develop the properties of base metal surface [12]. A spinning tool is infused into the base metal plate surfaces and passed through the length of the plate for processing. Frictional heat produced by the tool spinning against the workpiece makes it delicate and plastically deformed. Rotational and traverse developments of the tool pin strengthen the processing of the base material. The Taguchi method recognizes the optimum level of process parameters for the mechanical characteristics of the bead-on-plate specimen. Besides, the ANOVA found the percentage contribution of the processed

parameters. An optical microscope was able to investigate the microstructure as fine as the processed surfaces of the fabricated bead-on-plate processing.

2. Experimental Procedure

2.1. Materials and Processing. For this experiment, aluminium alloy (AA) 5052 was selected for friction stir bead-on-plate processing. The excellent formability and good weldability were of concern in the base material. AA5052 is composed of basically a superplastic material and is easily made from ultra-refinement structures during the friction stir processing. In the present day, the base material is used in aircraft, marine, and vehicle industries for structural applications. The mechanical properties of AA5052 are 251.34 MPa tensile strength, 19% elongation, and 70 Hv microhardness, and its chemical composition is presented in Table 1. In this study, FIE (from India) (tensile strength testing machine) with the standard of ASTM E9 and Shimadzu HMV-G (microhardness tester) with the standard of ASTM B724 were utilized to conduct the mechanical test. In this investigation, the normal hardness test does not attain the strength of the processed specimens due to low weight being added during the test. But, the FSPed specimen surface was covered by the onion ring structure. It is revealed that microhardness was a key factor to measure the strength with the maximum load capacity of the processed specimen. The base materials prepared have the dimensions of 100 mm × 100 mm × 6 mm. In this study, high carbon high chromium die steel (HCHCr) was utilized as a tool material for the bead-on-plate friction stir processing due to its high toughness and wear-resistant property. Normally, HCHCr is ceramic-based tool material, and it possesses microhardness 10 times higher than of the base material to enhance the material properties. The pentagonal tool pin profile was obtained by surface grinding and CNC. The dimension of the pentagonal tool pin profile was 5.7 mm pin length and 18 mm shoulder diameter [13]. Figures 1(a) and 1(b) show the tool pin profile and friction stir processing. The required size of the base metal marked with a centre line, and the influence of the pentagonal pin profile produced the onion ring structure on the surface of the material to manipulate the characteristics [14]. Figures 2(a) and 2(b) show the friction stir processed image and the prepared tensile specimens, respectively.

2.2. Method of Process Parameters. The optimization of friction stir bead-on-plate process parameters was designed by the Taguchi technique and used to form the orthogonal arrays, which consider a smaller amount of experimentation among a large number of decision variables. Signal-to-noise proportions were used to measure and predict the quality of the responses. Lowest and moderate improvement costs can be achieved by this efficient process. Transformation of the experimental data into the required decision was performed by the analysis of variance (ANOVA). The Taguchi technique was used to prefer the most reasonable orthogonal array to design the experiments and to consign process parameters [15]. Various researchers found the optimal specimens below the specified parameters within the limit. Based on the literature review, the parameters of friction stir bead-on-plate processing were preferred, and the level of each bead-on-plate process parameters for the three factors is presented in Tables 2 and 3, individually. During the hardness test, each plate has 20 values that are marked in the mid-section of the processed plates. In the current study, the percentage contribution of processed parameters to the mechanical properties was determined and successfully implemented by ANOVA. By using the statistical software of MINITAB, the investigational responses were modified into the S/N ratio. Table 4 describes the estimated S/N ratio values.

3. Results and Discussion

3.1. Influence of Process Parameters on the Tensile Strength. Table 5 presents the response table for tensile strength and S/N ratio. From the response table, tool spinning speed is the most significant influencing factor on the tensile strength, accompanied by traverse speed and axial load. Accordingly, an increase in tool spinning speed to advance the maximum friction occurs between the tool and the base material 5052 aluminium alloy, thus delivering high temperatures at the interface of the processed specimen, which helps in increasing the tensile strength. Similarly, increasing the traverse speed increases the tensile strength. Figures 3(a)–3(c) exhibit the graph of mean of S/N ratios for tensile strength versus process parameters such as tool spinning speed, traverse speed, and axial load. It is exposed that the maximum tensile strength attained by the optimum level of process parameter unifications is $A_2B_3C_2$, which shows the tool spinning speed at level 2 (1000 rpm), traverse speed at level 3 (30 mm/min), and axial load at level 2 (5 kN). Table 6 displays the ANOVA outcomes for tensile strength. It is validated that the tool spinning speed is the most significant process parameter with a 91.8% contribution, succeeded by an axial load of 5.04%. The traverse speed is a less significant process parameter with a 3.09% contribution. The 99.79% *R*-Sq value of tensile strength conceded that the model is capable of predicting the response with greater efficiency [16].

The interaction influence of process parameters, such as tool spinning speed, traverse speed, and axial load, on the tensile strength is displayed in Figures 4(a)–4(c). From the interaction graph, the parallel line and nonparallel line show no interaction and significant interaction of the process parameters on the tensile strength, respectively. In Figure 4(a), the interactions of the tool spinning speed with traverse speed were significant at the tool spinning speed of 1000 rpm. Therefore, it is clearly explained that the increase in the tool spinning speed increases the tensile strength. Figure 4(b) shows the interactions between the tool spinning speed and axial load. It is revealed that increasing the tool spinning speed led to increase in the tensile strength at 1000 rpm. The interaction of traverse speed with tool spinning speed is significant at 1000 rpm tool spinning speed and 20 mm/min traverse speed, due to the reason that lower

Table 1: Chemical composition of the AA5052 base plate.

Components	Mg	Fe	Cr	Mn	Si	Cu	Zn	Al
Weight in %	2.5	0.3	0.2	0.1	0.1	0.1	0.1	Bal

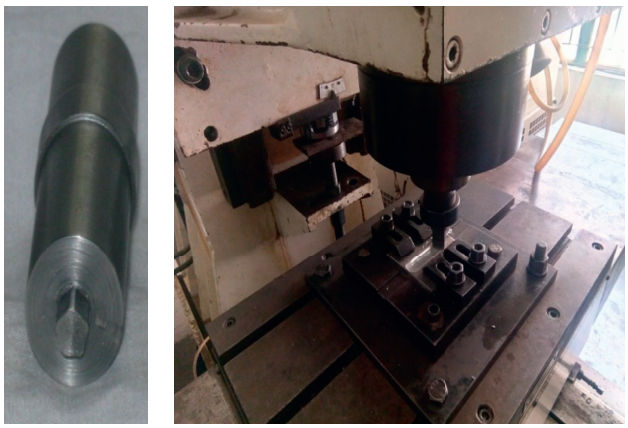

(a) (b)

Figure 1: (a) Pentagonal tool pin profile and (b) friction stir processing.

(a) (b)

Figure 2: (a) Friction stir processed image and (b) prepared tensile specimens.

traverse speed increases the tensile strength for the entire tool spinning speed as shown in Figure 4(c). Consequently, the tensile strength of the AA5052 processed specimen decreased for the high axial load (7 kN) if tool spinning speed (1200 rpm) and traverse speed (20 mm/min) were high, although moderate tool spinning speed (1000 rpm), low traverse speed (20 mm/min), and the medium level of axial load (5 kN) produced higher tensile strength [17].

The contour plots for the tensile strength for inconstant process parameters are demonstrated in Figures 5(a)–5(c). Figure 5(a) exhibits the influence of the tool spinning speed and axial load on the tensile strength. It is revealed that the tensile strength increases with the increase in tool spinning speed at any axial load. Still, at the lower tool spinning speed, the axial load caused the increase in the tensile strength to be less in the processed specimen. It is explained that the maximum tensile strength (215 MPa) was obtained at the medium level of axial load and the moderate level of tool spinning speed. The influence of traverse speed and axial load on the tensile strength is demonstrated in Figure 5(b). It is perceived that the moderate level of axial load and lower level of traverse speed achieved better tensile strength (209 MPa) due to sufficient heat produced in the nugget region. The higher level of axial load and traverse speed achieved the poor tensile strength due to insufficient heat between the tool and specimen. Figure 5(c) displays the influence of the tool spinning speed and traverse speed on the tensile strength. It is revealed that the maximum tensile strength was achieved at the moderate level of tool spinning speed (1000 rpm) and a lower level of traverse speed (20 mm/min).

Table 2: FSP parameters and factor levels.

Bead-on-plate process parameters	Notation	Factor levels		
		1	2	3
Tool spinning speed (rpm)	TSS (A)	800	1000	1200
Traverse speed (mm/min)	TS (B)	20	25	30
Axial load (kN)	Al (C)	3	5	7

Table 3: Design of the experimentation by using the L9 orthogonal array.

Runs	TSS (rpm)	TS (mm/min)	AL (kN)
1	800	20	3
2	800	25	5
3	800	30	7
4	1000	20	5
5	1000	25	7
6	1000	30	3
7	1200	20	7
8	1200	25	3
9	1200	30	5

3.2. Influence of Process Parameters on the Microhardness. Table 7 presents the response table for microhardness means and S/N ratio. From the response table, tool spinning speed is the most significant influencing factor on the microhardness, accompanied by traverse speed and axial load. Accordingly, an increase in tool spinning speed to advance the maximum friction occurs between the tool and the base material 5052 aluminium alloy, thus delivering high temperatures at the interface of the processed specimen, which helps in increasing the microhardness. Similarly, increasing the traverse speed led to increase in the microhardness. Figures 6(a)–6(c) exhibit the graph of mean of S/N ratios for microhardness with respect to process parameters such as tool spinning speed, traverse speed, and axial load. It is exposed that the maximum microhardness attained by the optimum level of process parameter unifications is $A_2B_3C_2$, which shows the tool spinning speed at level 2 (1000 rpm), traverse speed at level 3 (30 mm/min), and axial load at level 2 (5 kN). Table 8 displays the ANOVA outcomes for microhardness. It is validated that the tool spinning speed is the most significant process parameter with a 60.8% contribution, succeeded by an axial load of 29.66%. The traverse speed is a less significant process parameter with a 9.48% contribution. The 99.70% *R*-Sq value of tensile strength conceded that the model is capable of predicting the response with greater efficiency [18].

The interaction influence of process parameters, such as tool spinning speed, traverse speed, and axial load, on the microhardness is exhibited in Figures 7(a)–7(c). From the interaction graph, the parallel line and nonparallel line show no interaction and significant interaction of the process parameters on the tensile strength, respectively. Figure 7(a) shows that the interactions of tool spinning speed with traverse speed were significant at the tool spinning speed of 1000 rpm. Therefore, it is clearly explained that the increase in the tool spinning speed increases the microhardness value. Figure 7(b) shows the interactions between the tool spinning speed and axial load. It is revealed that increasing the tool spinning speed led to the increase in microhardness at 1000 rpm. The interaction of traverse speed with tool spinning speed is significant at a tool spinning speed of 1000 rpm and traverse speed of 20 mm/min, due to the reason that lower traverse speed increases the microhardness for the tool spinning speed as shown in in Figure 7(c). Therefore, the microhardness of the AA5052 processed specimen decreased for the high axial load (7 kN) if tool spinning speed (1200 rpm) and traverse speed (20 mm/min) were high, although moderate tool spinning speed of 1000 rpm, low traverse speed of 20 mm/min, and the medium level of axial load of 5 kN produced higher microhardness.

The contour plots for the microhardness for variable process parameters are established in Figures 8(a)–8(c). Figure 8(a) displays the influence of the tool spinning speed and axial load on the microhardness. It is exposed that the microhardness value increases with increase in tool spinning speed at an axial load of 5 kN. However, at the lower tool spinning speed, the axial load caused the decrease in the microhardness in the processed specimen. It is explained that the maximum microhardness (69 Hv) was obtained at the medium level of axial load and the moderate level of tool spinning speed. The influence of traverse speed and axial load on the microhardness is demonstrated in Figure 8(b). It is perceived that the moderate level of axial load and lower level of traverse speed achieved better microhardness (68 Hv). The higher level of axial load and traverse speed achieved less microhardness value due to insufficient heat produced between the tool and specimen. Figure 8(c) displays the influence of the tool spinning speed and traverse speed on the microhardness. It is revealed that the maximum microhardness was achieved at the moderate tool spinning speed (1000 rpm) and a lower traverse speed (20 mm/min).

3.3. Regression Equation of Tensile Strength and Microhardness. The regression equation is refined based on the investigational output responses. It establishes the

Table 4: Estimated S/N ratio values.

Runs	Parameters			Response of the output		S/N ratio of the output	
	TSS (rpm)	TS (mm/min)	AL (kN)	Tensile strength (MPa)	Microhardness	Tensile strength (MPa)	Microhardness
1	800	20	3	173	61	44.7609	35.70
2	800	25	5	184	66	45.2964	36.40
3	800	30	7	183	64	45.2490	36.12
4	1000	20	5	215	69	46.6488	36.78
5	1000	25	7	213	68	46.5676	36.65
6	1000	30	3	212	67	46.5267	36.52
7	1200	20	7	169	61	44.5577	36.71
8	1200	25	3	170	62	44.6090	35.85
9	1200	30	5	185	66	45.3434	36.39

Table 5: Response table for tensile strength.

Level	TSS (A)	TS (B)	AL (C)
S/N ratio of tensile strength			
1	45.10	45.32	45.30
2	46.58	45.49	45.76
3	44.84	45.71	45.46
Delta	1.74	0.38	0.46
Rank	1	3	2
Mean of tensile strength			
1	180.0	185.7	185.0
2	213.3	189.0	194.7
3	174.7	193.3	188.3
Delta	38.7	7.7	9.7
Rank	1	3	2

equivalence between the input process parameters for friction stir processing. Regression equations (1) and (2) provide the equivalence between the measured process parameters to produce the maximum tensile strength and microhardness [19]. Figures 9(a) and 9(b) exhibit the comparison plots for investigational and regression-predicted values of tensile strength and microhardness:

$$\text{tensile strength (MPa)} = 179.3 - 0.0133\,\text{tool spinning speed (rpm)} + 0.77\,\text{traverse speed (mm/min)} + 0.83\,\text{axial load } (k\text{N}), \tag{1}$$

$$\text{microhardness (Hv)} = 60.3 - 0.0167\,\text{tool spinning speed (rpm)} + 0.200\,\text{traverse speed (mm/min)} + 0.250\,\text{axial load (kN)}. \tag{2}$$

3.4. Microstructure Analysis. In the friction stir bead-on-plate processing of AA5052, a diversity of microstructure is captured in different zones using an optical microscope (Dewinter Inverted Trinocular). The microstructure outcomes showed the structure of grain refinement in the various zones (nugget zone, thermomechanically affected zone, and heat-affected zone) of the processed aluminium alloy 5052. The shape and size of the nugget zone for optimal processed samples were realized depending on the bead-on-plate process parameters and the interaction of the base material with the pentagonal pin profile tool and its shoulder. The microscopic picture showed reflection of the optimal value of the input factors with output response of tensile strength [20]. The microstructure image was captured within the limitation of 100x and 100 μm. Figure 10(a) shows the AA5052 base metal of the microstructure. Figures 10(b)–10(d) exhibit the cross section of the bead-on-plate processing, processed at 1000 rpm, 20 mm/min, and 5 kN, besides with different zones identified. The thermomechanically affected zone surrounded the nugget regions. The NZ (nugget zone) changes in the fine-grained morphological structure. The main inference behind the microstructure reformation is due to the accomplished thermal cycle during the processing phase. The interface of the nugget zone was characterized by the direction of tool spinning speed and traverse speed. The heat-affected zone (HAZ) enveloped the thermomechanically affected zone (TMAZ). In HAZ, the grain formation does not refine any plastic deformation. The microstructural region was slightly modified in the heat-affected zone [21]. Figures 11(a)–11(c) and Figures 12(a)–12(c) expose the blemish-free processed samples obtained by friction stir bead-on-plate processing at 1200 rpm,

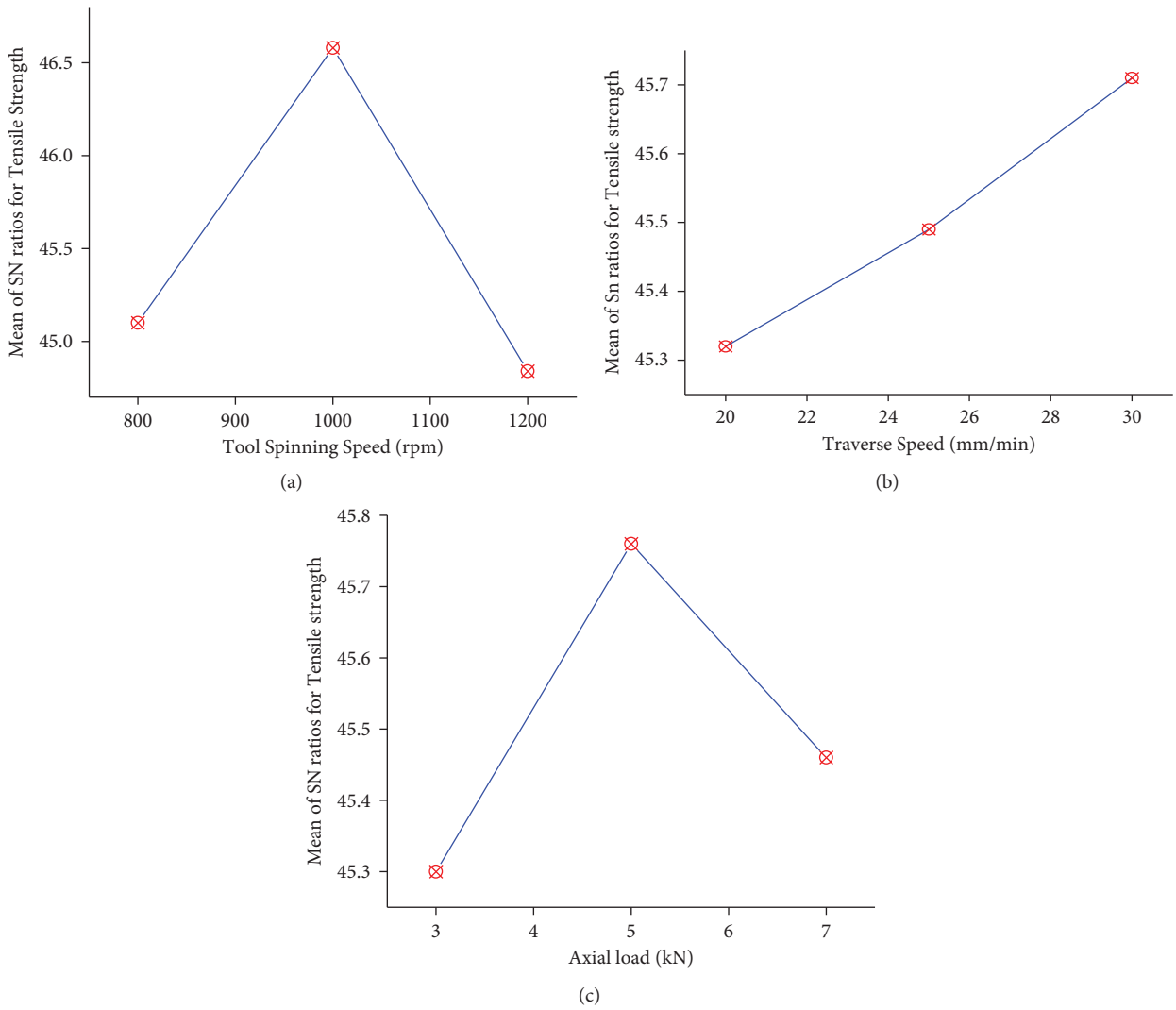

Figure 3: Mean of S/N ratios for (a) tensile strength versus tool spinning speed, (b) tensile strength versus traverse speed, and (c) tensile strength versus axial load.

Table 6: ANOVA outcomes for tensile strength.

Process parameters	DF	% contribution	Adj SS	Adj MS	F ratio	*P* value
TSS	2	91.8	2634.67	1317.33	439.11	0.002
TS	2	3.09	88.67	44.33	14.78	0.063
AL	2	5.04	144.67	72.33	24.11	0.040
Residual error	2	0.07	6.00	3.00		
Total	8	100	2874.00			

$S = 1.7321$; R-Sq = 99.79%; R-Sq (adj) = 99.61.

30 mm/min, and 5 kN and 1200 rpm, 20 mm/min, and 7 kN—the sound of defect-free processed AA 5052 specimens. The natural bond interface and the interblended structure were composed between the top and bottom of the processed specimens. The characteristic microstructural regions, such as the nugget zone, thermomechanically affected zone, heat-affected zone, and the base metal, were examined. Due to the effect of the thermal cycle and plastic deformation generated by the tool spinning speed, the dynamic recrystallization transpired in the nugget zone. The various the locations of the nugget zone, the different the forms of fine equiaxed grains formed. The coarse grain structure occurred in the different locations of TMAZ as shown in Figures 11(b) and 12(b), respectively [22].

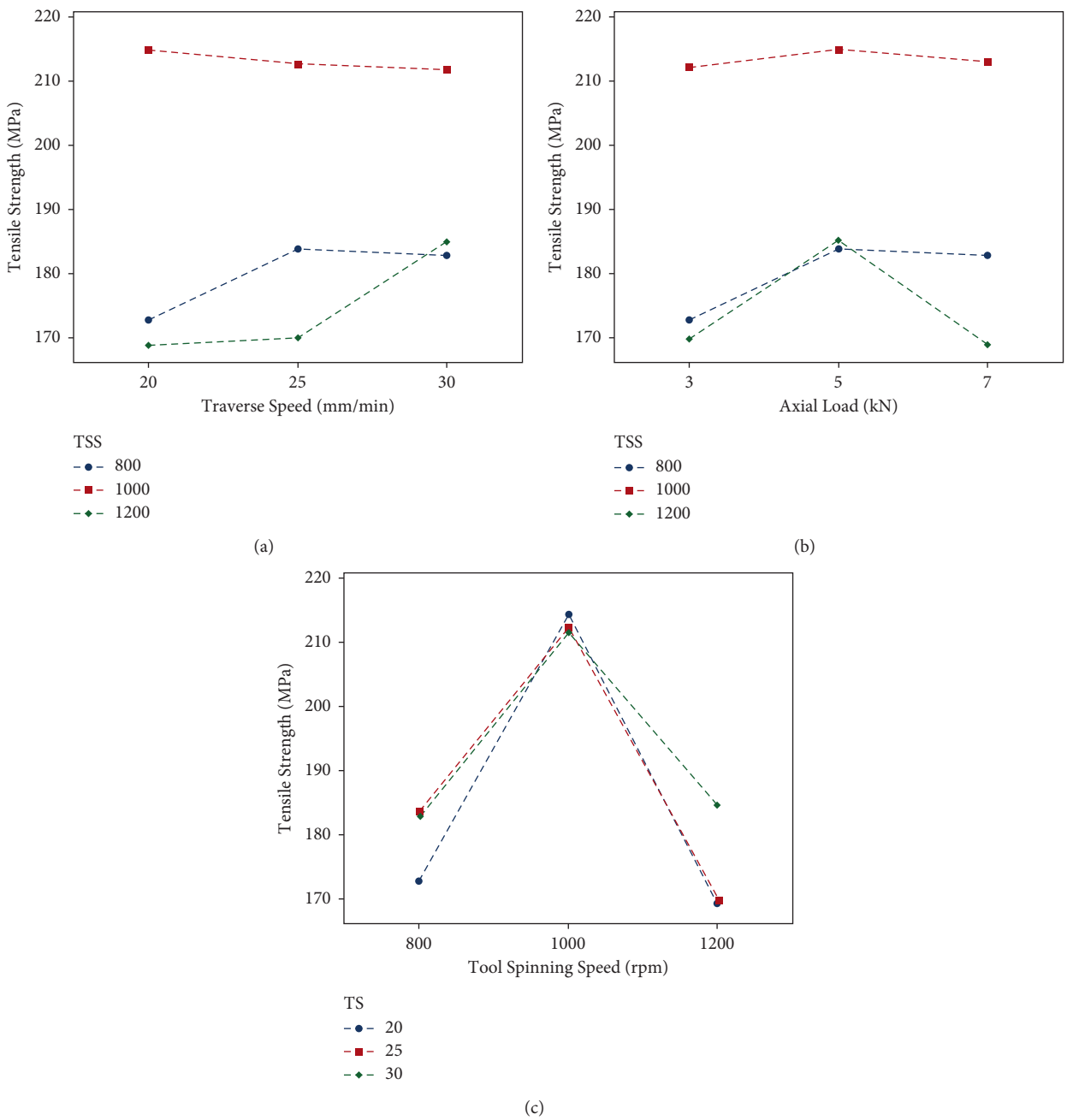

Figure 4: Interaction plots of tensile strength for (a) tool spinning speed versus traverse speed, (b) tool spinning speed versus axial load, and (c) traverse speed versus tool spinning speed.

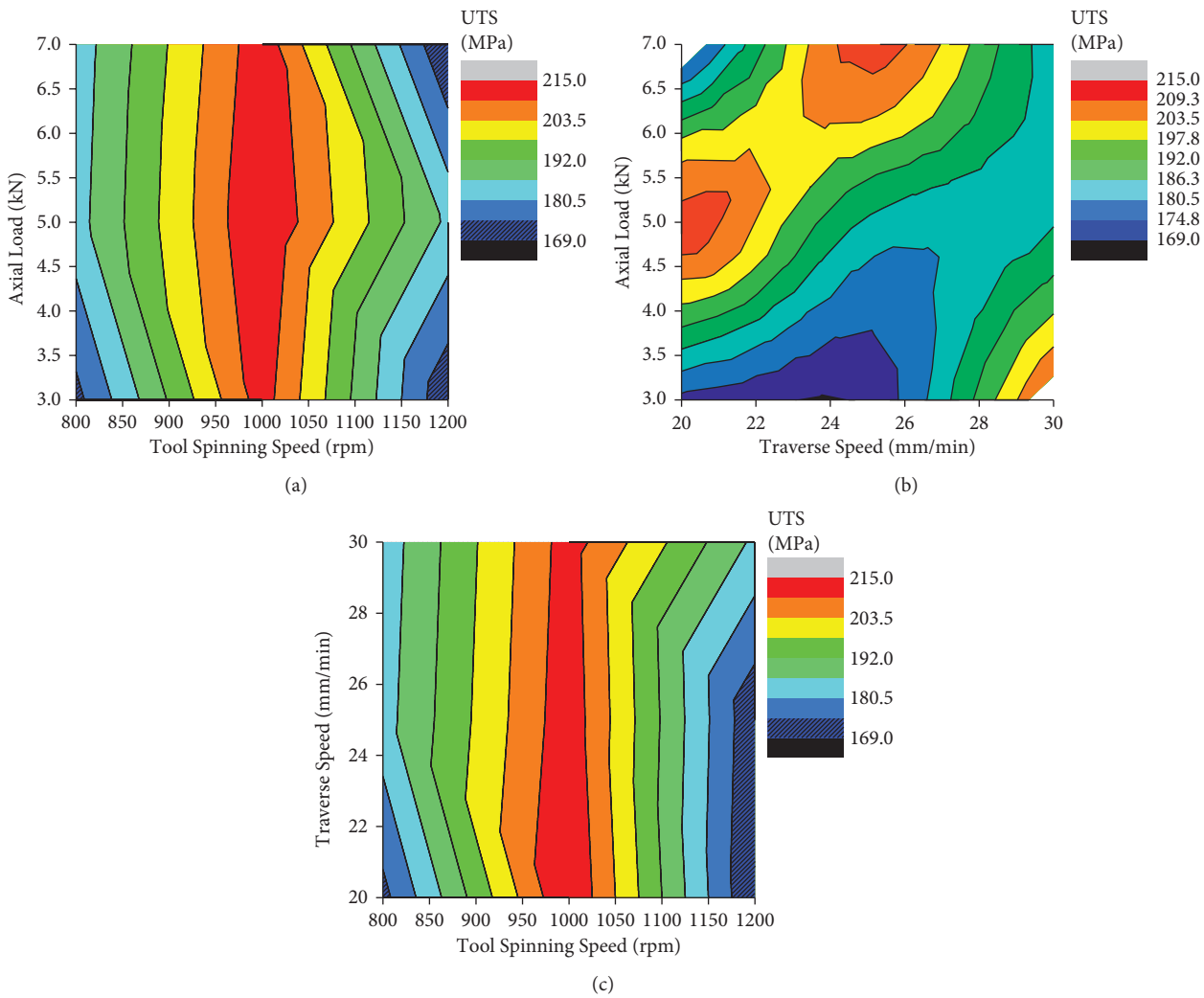

Figure 5: Contour plot of tensile strength for (a) tool spinning speed versus axial load, (b) traverse speed versus axial load, and (c) tool spinning speed versus traverse speed.

Table 7: Response table for microhardness.

Level	TSS (A)	TS (B)	AL (C)
S/N ratio of microhardness			
1	36.07	36.06	36.03
2	36.65	36.03	36.52
3	35.98	36.35	36.16
Delta	0.67	0.28	0.49
Rank	1	3	2
Mean of microhardness			
1	63.67	63.67	63.33
2	68.00	65.33	67.00
3	63.00	65.67	64.33
Delta	5.00	2.00	3.67
Rank	1	3	2

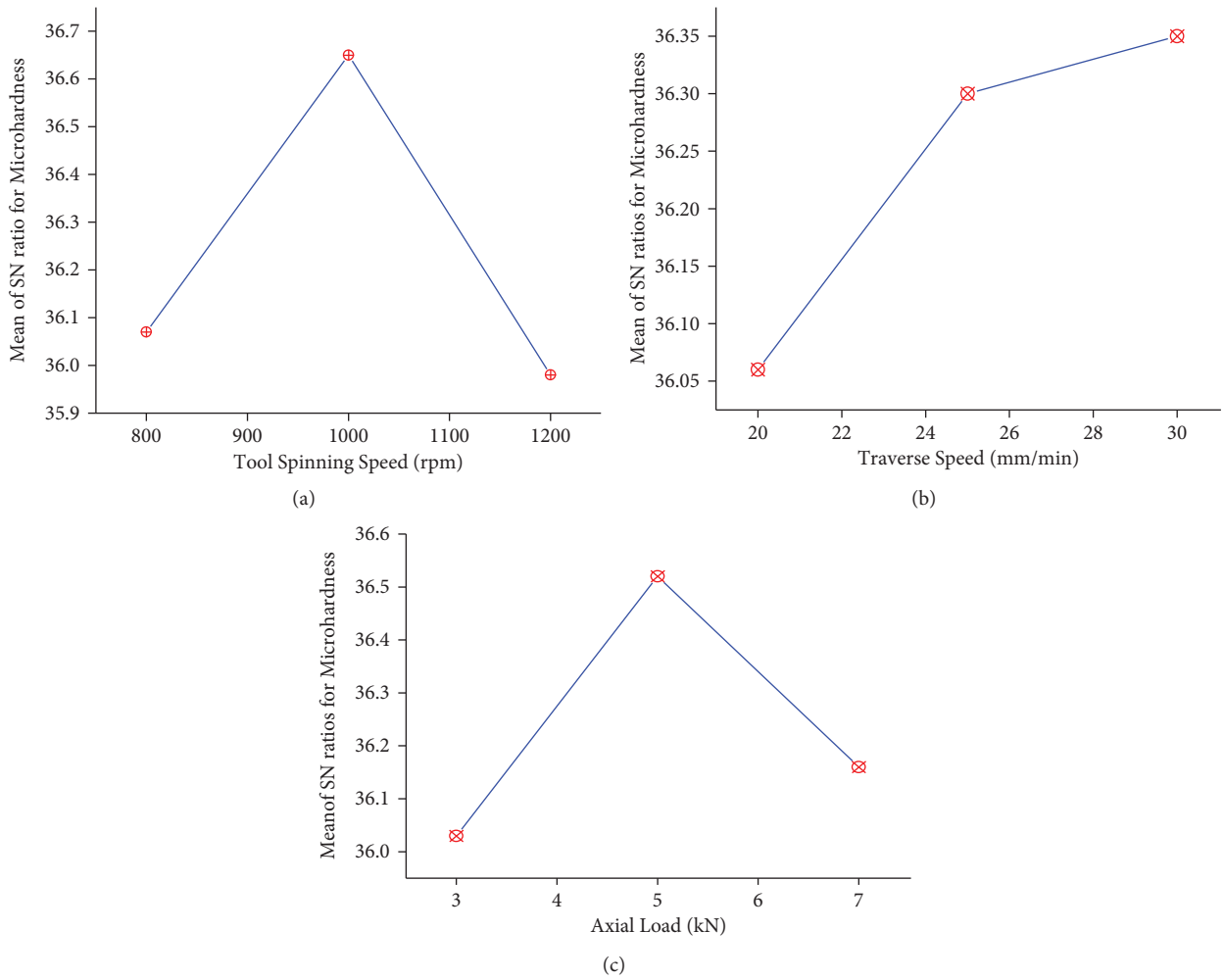

Figure 6: Mean of S/N ratios for (a) microhardness versus tool spinning speed, (b) microhardness versus traverse speed, and (c) microhardness versus axial load.

Table 8: ANOVA outcomes for microhardness.

Process parameters	DF	% contribution	Adj SS	Adj MS	F ratio	P value
TSS	2	60.8	44.2222	22.1111	199.00	0.005
TS	2	9.48	6.8889	3.4444	31.00	0.031
AL	2	29.66	21.5556	10.7778	97.00	0.010
Residual error	2	0.06	0.2222	0.1111		
Total	8					

$S = 0.3333$; R-Sq = 99.70%; R-Sq (adj) = 98.78.

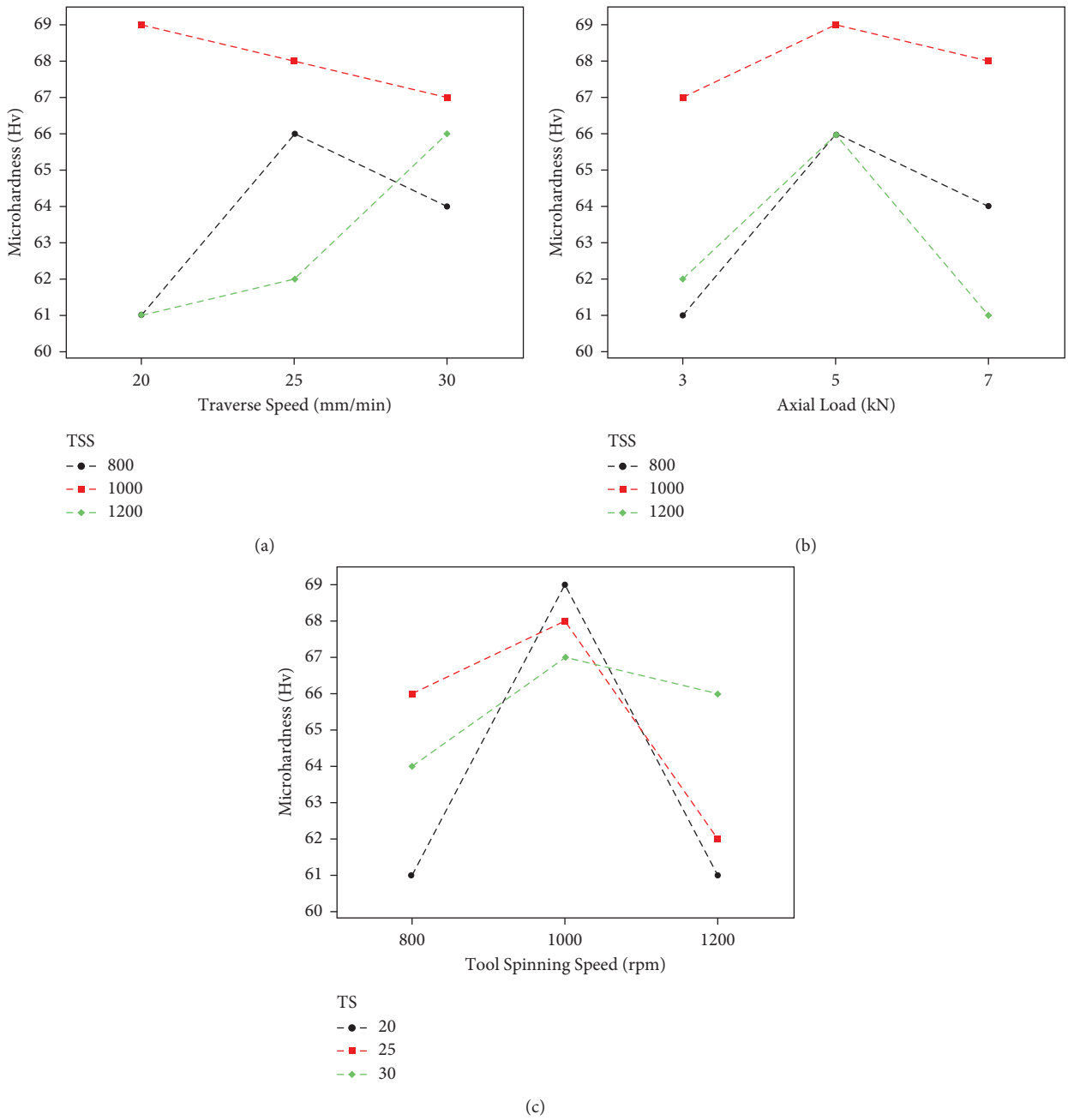

Figure 7: Interaction plots of microhardness for (a) tool spinning speed versus traverse speed, (b) tool spinning speed versus axial load, and (c) traverse speed versus tool spinning speed.

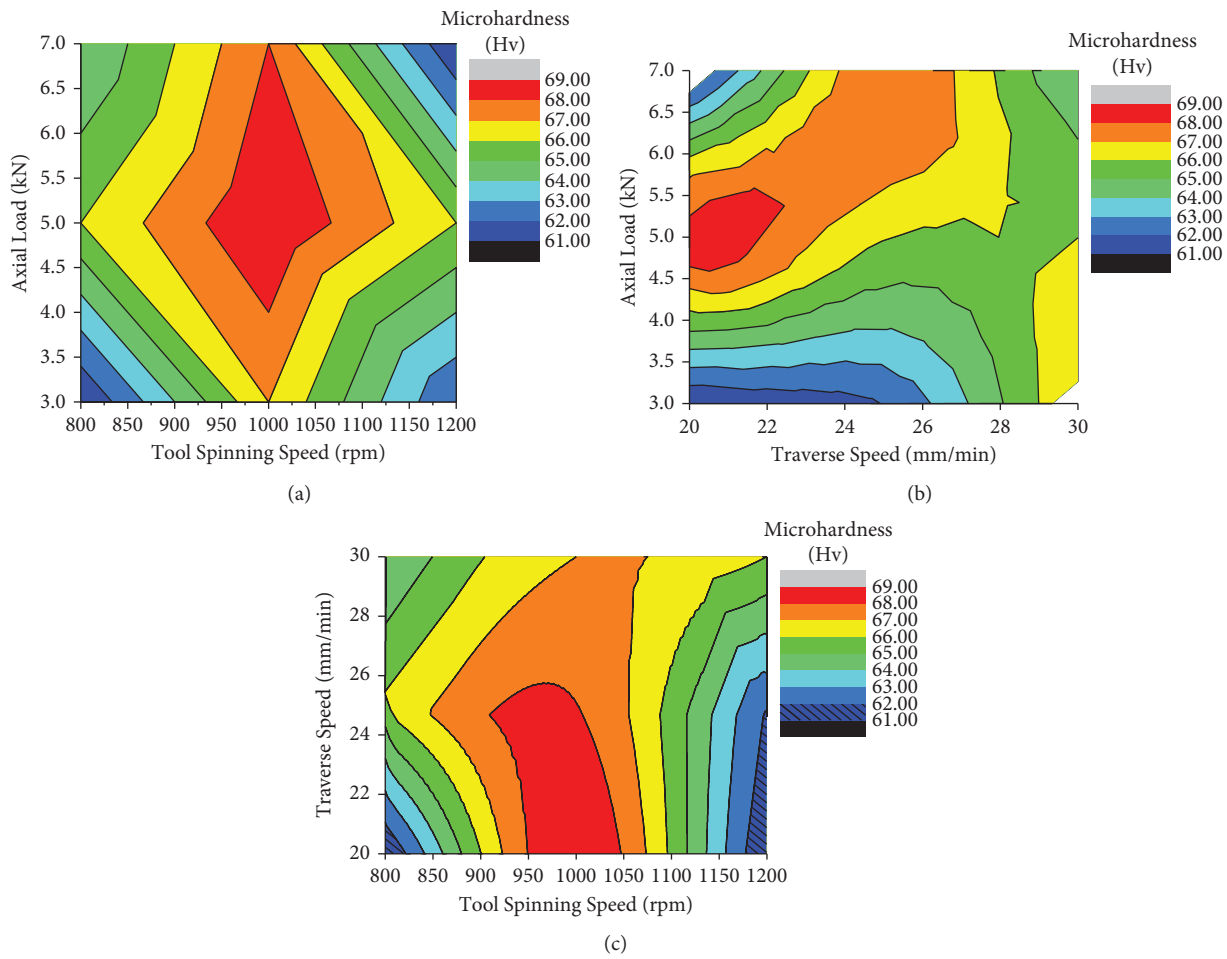

Figure 8: Contour plots of microhardness for (a) tool spinning speed versus axial load, (b) traverse speed versus axial load, and (c) tool spinning speed versus traverse speed.

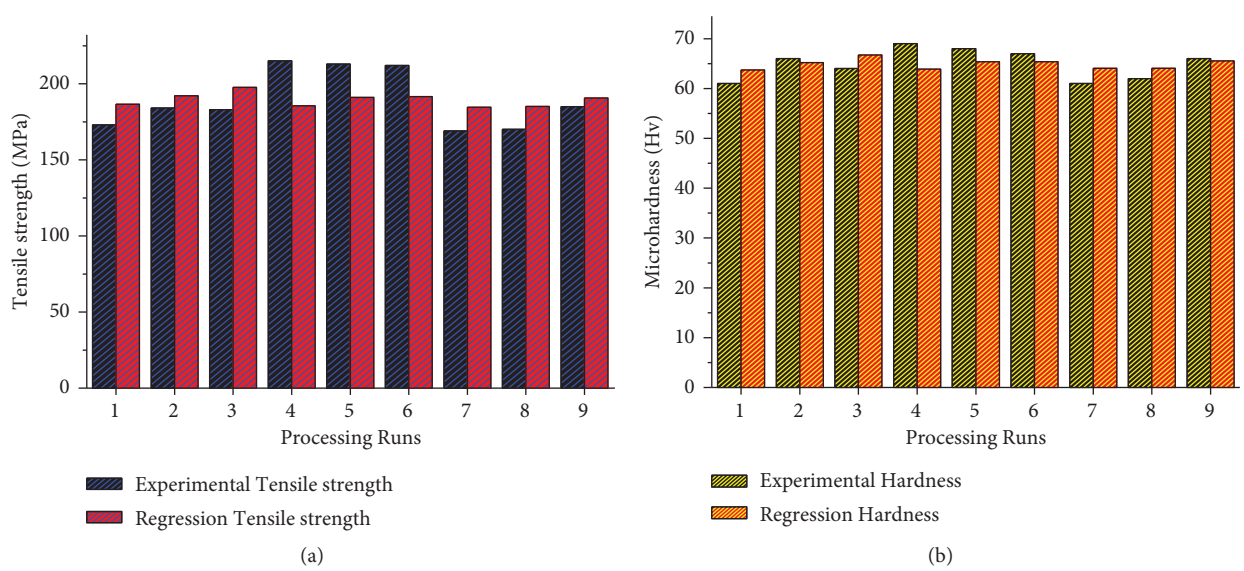

Figure 9: Experimental and regression values of (a) tensile strength and (b) microhardness.

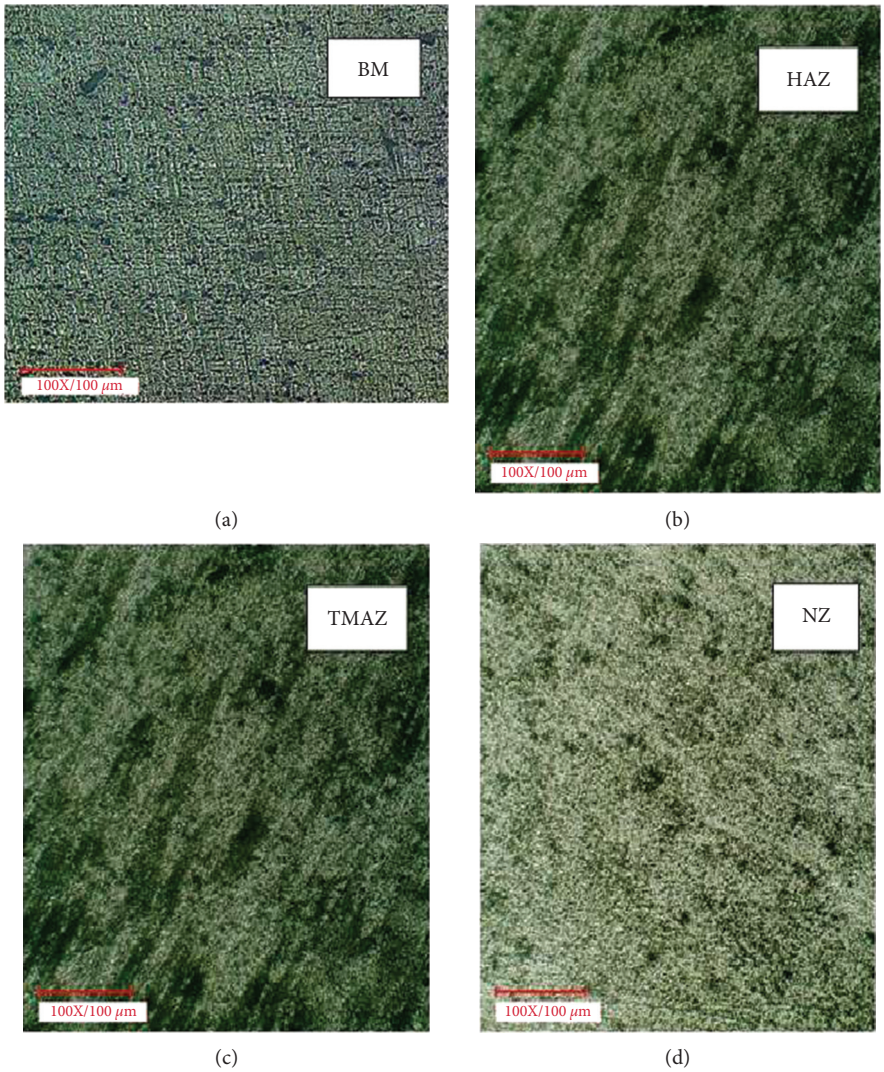

Figure 10: (a) Microstructure of the base metal of AA5052 and (b–d) cross section of the bead-on-plate processed specimen at a tool spinning speed of 1000 rpm, traverse speed of 20 mm/min, and axial load of 5 kN.

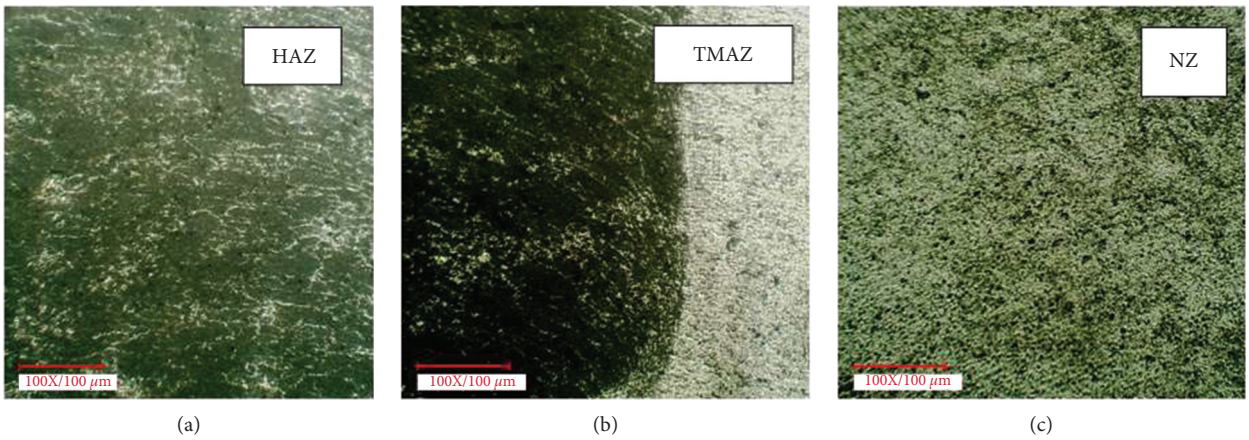

Figure 11: (a–c) Microstructure of cross section of bead-on-plate processed specimen at a tool spinning speed of 1200 rpm, traverse speed of 30 mm/min, and axial load of 5 kN.

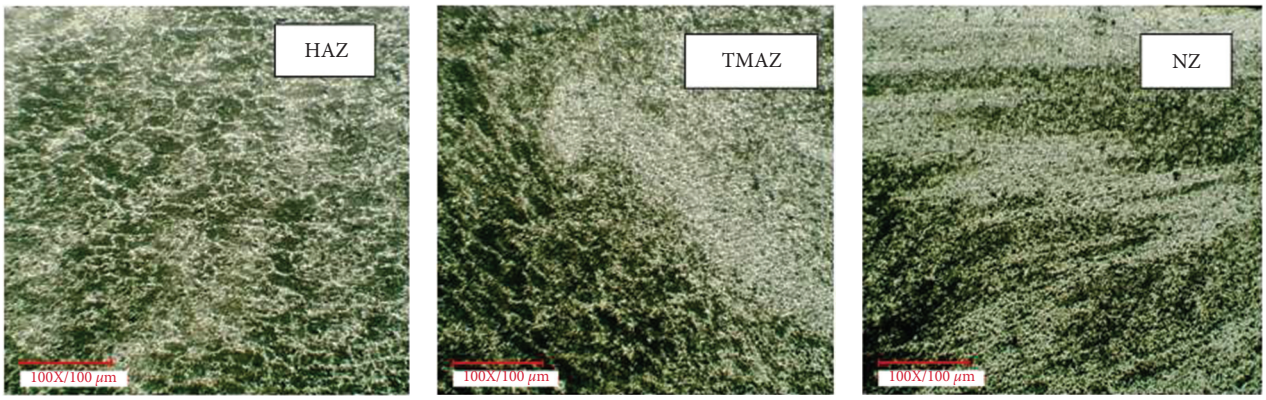

(a) (b) (c)

Figure 12: (a–c) Microstructure of cross section of bead-on-plate processed specimen at a tool spinning speed of 1200 rpm, traverse speed of 20 mm/min, and axial load of 7 kN.

4. Conclusions

This work aimed to examine the effect of friction stir process parameters such as tool spinning speed, traverse speed, and axial load on the tensile strength and microhardness during friction stir bead-on-plate processing. The following conclusions are composed:

(1) The bead-on-plate processing of AA5052 was completed through the friction stir processing technique. The optical micrograph shows the uniform equiaxed grain distributions in the nugget zones of FSPed aluminium alloy 5052.

(2) The S/N ratio of Taguchi technique identifies the optimal process parameters for the friction stir processing of AA5052 to minimize the tensile strength and microhardness, to predict the FSP responses by the developed regression equations.

(3) The optimal process parameters for maximum tensile strength and microhardness were obtained at the tool spinning speed of 1000 rpm, traverse speed of 30 mm/min, and axial load of 5 kN.

(4) The ANOVA outcomes revealed that the tool spinning speed has the most influence as the process parameter on the mechanical properties of the processed specimen, followed by the axial load. The increase in tool spinning speed and axial load leads to an increase in tensile strength.

(5) The microstructure of optimal process parameter limitations displayed the fine grain structure in nugget zones on the surface of the specimen.

(6) The other optimization techniques, such as genetic algorithm and principal component analysis, can be used in the future to optimize the process parameters for enhancing the mechanical properties.

Data Availability

The data used to support the findings of this study are included within the article.

Conflicts of Interest

The authors declare that there are no conflicts of interest regarding the publication of this article.

Acknowledgments

The authors thank the Bharath Institute of Higher Education and Research, Chennai, and this project was supported by researchers supporting project number: RSP-2021/283, King Saud University, Riyadh, Saudi Arabia.

References

[1] P. Cavaliere, G. Campanile, F. Panella, and A. Squillace, "Effect of welding parameters on mechanical and microstructural properties of AA6056 joints produced by friction stir welding," *Journal of Materials Processing Technology*, vol. 180, no. 1–3, pp. 263–270, 2006.

[2] T. Minton and D. J. Mynors, "Utilisation of engineering workshop equipment for friction stir welding," *Journal of Materials Processing Technology*, vol. 177, no. 1–3, pp. 336–339, 2006.

[3] K. Elangovan and V. Balasubramanian, "Influences of tool pin profile and welding speed on the formation of friction stir processing zone in AA2219 aluminium alloy," *Journal of Materials Processing Technology*, vol. 200, no. 1–3, pp. 163–175, 2008.

[4] M. Jayaraman, R. Sivasubramanian, V. Balasubramanian, and A. K. Lakshminarayan, "Optimization of process parameters for friction stir welding of cast aluminium alloy A319 by Taguchi method," *Journal of scientific Industrial Research*, vol. 68, pp. 36–43, 2009.

[5] H. Aydin, B. Ali, U. Esme, Y. Kazancoglu, and O. Guven, "Application of grey relation analysis and Taguchi method for the parametric optimization of friction stir welding process," *Material Technology*, vol. 44, pp. 205–211, 2010.

[6] Z. Lian-Yin, K. Li-Pheng, and Z. Zhao-Wei, "Design concept evaluation in product development using rough sets and grey relation analysis," *Expert Systems with Applications*, vol. 36, no. 3, pp. 7072–7079, 2009.

[7] C. Chi-Hui and L. Wei-Bang, "Thaiping C 2011 Optimal FSW process parameters for aluminum alloys AA5083," *Journal of*

the Chinese Institute of Engineers, vol. 34, no. 1, pp. 99–105, 2011.

[8] S. Mitra, D. Ganguly, B. Acherjee, and A. S. Kuar, "Hole characteristics optimization in Nd:YAG laser micro-drilling of zirconium oxide by grey relation analysis," *International Journal of Advanced Manufacturing Technology*, vol. 610, pp. 1255–1262, 2012.

[9] K. Karun kumar, A. Kumar Kaviti, and N. Kiran Kumar, "Experimental investigation of friction stir welded AA5052 using square and pentagonal tool pins," *Materials Today: Proceedings*, vol. 5, no. 9, pp. 18230–18237, 2018.

[10] S. Shanavas and J. E. R. Dhas, "Quality prediction of friction stir weld joints on AA 5052 H32 aluminium alloy using fuzzy logic technique," *Materials Today: Proceedings*, vol. 5, no. 5, pp. 12124–12132, 2018.

[11] M. Venkateshkannan, V. Rajkumar, P. sadeesh, N. Arivazhagan, S. Narayanan, and K. D. Ramkumar, "Influences of tool geometry on metallurgical and mechanical properties of friction stir welded dissimilar AA 2024 and AA 5052," *Procedia Engineering*, vol. 75, pp. 154–158, 2014.

[12] R. Bharathikanna and G. Elatharasan, "An investigation on microstructures and mechanical properties of AA1050 in friction stir processing technique," *Advance in Natural Applied Science*, vol. 8, pp. 316–321, 2017.

[13] C. Chanakyan and S. Sivasankar, "Parametric advancement of numerical model to predict the mechanical properties of friction stir processed AA5052," *International Journal of Rapid Manufacturing*, vol. 8, no. 1/2, pp. 147–160, 2019.

[14] K. Elangovan, V. Balasubramanian, and M. Valliappan, "Influences of tool pin profile and axial force on the formation of friction stir processing zone in AA6061 aluminium alloy," *International Journal of Advanced Manufacturing Technology*, vol. 38, no. 3-4, pp. 285–295, 2008.

[15] M. Shunmugasundaram, A. Praveen Kumar, L. Ponraj Sankar, and S. Sivasankar, "Optimization of process parameters of friction stir welded dissimilar AA6063 and AA5052 aluminum alloys by Taguchi technique," *Materials Today Proceedings*, vol. 27, 2020.

[16] M. Koilraj, V. Sundareswaran, S. Vijayan, and S. R. Koteswara Rao, "Friction stir welding of dissimilar aluminum alloys AA2219 to AA5083-optimization of process parameters using Taguchi technique," *Materials & Design*, vol. 42, no. 1, 7 pages, 2012.

[17] M. Habibnia, M. Shakeri, S. Nourouzi, and M. K. B. Givi, "Microstructural and mechanical properties of friction stir welded 5050 Al alloy and 304 stainless steel plates," *International Journal of Advanced Manufacturing Technology*, vol. 76, no. 5–8, pp. 819–829, 2015.

[18] G. Ugrasen, G. Bharath, G. K. Kumar, R. Sagar, P. R. Shivu, and R. Keshavamurthy, "Optimization of process parameters for Al6061-Al7075 alloys in friction stir welding using taguchi's technique," *Materials Today: Proceedings*, vol. 5, no. 1, pp. 3027–3035, 2018.

[19] C. Chanakyan, S. Sivasankar, M. Meignanamoorthy, M. Ravichandran, and T. Muralidharan, "Experimental investigation on influence of process parameter on friction stir processing of AA6082 using response surface methodology," *Materials Today: Proceedings*, vol. 21, pp. 231–236, 2020.

[20] C. Chanakyan, P. Dinesh babu, and J. Janarthanan, "An experimental investigation on mechanical properties and microstructure of friction stir welding of AA5052," *Applied Mechanics and Materials*, vol. 48–52, pp. 592–594, 2014.

[21] H. Fujii, L. Cui, M. Maeda, and K. Nogi, "Effect of tool shape on mechanical properties and microstructure of friction stir welded aluminum alloys," *Materials Science and Engineering A*, vol. 419, no. 1-2, pp. 25–31, 2006.

[22] P. L. Threadgill, "Terminology in friction stir welding," *Science and Technology of Welding & Joining*, vol. 12, no. 4, pp. 357–360, 2007.

Hindawi
Advances in Materials Science and Engineering
Volume 2021, Article ID 1539230, 9 pages
https://doi.org/10.1155/2021/1539230

Research Article

Preparation of Polymeric Nanomaterials Using Emulsion Polymerization

Satyajeet Sahoo,[1] **Anitha Gopalan**,[2] **S. Ramesh**,[3] **P. Nirmala**,[2] **G. Ramkumar**,[2] **S. Agnes Shifani**,[4] **Ram Subbiah**,[5] **and J. Isaac JoshuaRamesh Lalvani**[6]

[1]*Department of Electronics and Communication Engineering, Vignan's Foundation for Science,Technology and Research (Deemed to be University), Vadlamudi, Guntur, Andra Pradesh 522213, India*
[2]*Department of Electronics and Communication Engineering, Saveetha School of Engineering, SIMATS, Chennai 602105, Tamil Nadu, India*
[3]*Department of Electronics and Communication Engineering, Sri Shakthi Institute of Engineering and Technology, Coimbatore 641062, Tamilnadu, India*
[4]*Department of Electronics and Communication Engineering, Jeppiaar Maamallan Engineering College, Chennai, Tamilnadu, India*
[5]*Department of Mechanical Engineering, Gokaraju Rangaraju Institute of Engineering and Technology, Nizampet, Hyderabad, India*
[6]*Department of Mechanical Engineering, Faculty of Mechanical and Production Engineering, AMIT, Arba Minch University, Arba Minch, Ethiopia*

Correspondence should be addressed to Satyajeet Sahoo; satyajeetsahoo.eltc@gmail.com and J. Isaac JoshuaRamesh Lalvani; isaac.jrl@amu.edu.et

Received 24 August 2021; Accepted 23 September 2021; Published 8 October 2021

Academic Editor: P Ganeshan

Nanoparticles are said to be active particles which are entrapped in the surface of the polymeric core. Since nanoparticles were used in medical and biotechnological fields, there is a great demand in the preparation of nanoparticles. Nanoparticles are prepared from different substances; mainly, polymer material is used in the field of preparing nanomaterials. There are different methods involved in the preparation of nanoparticles from the polymer. Various experiments and research studies were carried out on the basic preparation of nanoparticles. Emulsion polymerization could be used to make polymeric nanoparticles with a high solid concentration without the need of surfactants. To make carboxylate polystyrene beads or amidine polystyrene nanoparticles, polymeric nanocolloids containing surface functional groups were produced. In this research, the preparation of nanoparticles from emulsion polymerization is represented along with the size and distribution material.

1. Introduction

To achieve the challenges in drug delivery, polymer nanotechnology is considered as one of the promising systems. This involves drug targeting as well as delivering undelivered compounds such as oligonucleotides. The important challenges in nanotechnology are the preparation of nanoparticles, with suitable properties of nanoparticles, and this confirms proper drug transporting and pointing [1]. Various grades of poly and copolymers are used to prepare the nanoparticles in a wide range. The ability to synthesize polymers with well-controlled structures and conformation also paves the way for nanoparticles with precisely tuned characteristics, which are needed to meet drug targeting goals. This enthusiasm stems from the belief that nanoparticles with sizes ranging

from 10 nanometers to more than 100 nanometers improved chemical, physical, or biological capabilities while developing specifically for certain applications [2].

Water-in-oil (W/O) or reverse emulsion polymerization is a suitable and well-studied technique for the generation of water-soluble nanopolymer particles with high molecular weight and low viscosity. The important parameter for the inverse emulsion polymerization process is established by the originated type and amount and the emulsifier type. Various solvents were utilized as a continuous phase, reaction locus, and monomeric reservoir in the reverse emulsion polymerization of acrylamide. The effect of the process parameter is determined, and hydrophilic equilibrium, emulsifier type and concentration, initiator, and reaction temperature are just some of the questions that have been investigated.

Microfluidics capacity to quickly mix chemicals, produce the homogeneous reaction, continually modify reaction environments, and introduce chemical components at exact time intervals during reaction advancement has made it popular knowledge for a wide range of applications; reagents are utilized in very modest concentrations [3]. By allowing the fabrication of the inorganic nanoparticle, the combination of the microfluid and particle technology is obtained. The inorganic nanoparticle is about 4–9 nm and the microparticle is 10 nm, facing a significant issue for its maximum exploitation in certain circumstances with narrow size dispersal or different morphologies. This is especially relevant because the bulk mixing and nanoprecipitation of medicines and biodegradable polymeric predecessors used to make biodegradable polymeric nanoparticles often gets out of control, which can affect the characteristics of resultant nanoparticles. Microfluidics with quick and customizable mixing allows for greater control of the nanoprecipitation procedure as well as screening of diverse preparation circumstances on a single platform by altering parameters such as precursor composition, flow rates, and mixing time [4].

Polymerization can be used to produce live block copolymers separately or in combination with the stage of micelle formation. The thermodynamic properties of these polymer/solvent devices allow the development of nanoparticles of different shapes such as spheres and cords. Additional steps can be performed during block copolymer synthesis or in one or more posttreatment procedures performed on the nanoparticles produced to introduce special properties such as functional groups and water generation. At least two alternative approaches can be used in the manufacture of polymeric nucleus nanoparticles: one involves the consecutive mixture of the nucleus and hull structure, and the other involves the self-assembling of block copolymers.

2. Related Works

Industrial production can be scaled using macromolecular self-assembly techniques in determining the transformation of unique polymer core-shell nanoparticles. The characterization, application, and synthesis of polymeric nanoparticles were proposed by Wang et al. [5]. This work describes the methods of assembly and algorithms that regulate the proposal of mechanical properties required for favorable use, such as improving the performance of the extract in elastic vulcanization and improving the performance of rubber configurations. The nanoparticles were made by polymerizing block copolymers and allowing them to self-assemble into micelles in solvents, followed by core cross-linking to stabilize their structure. A range of core-shell nanoparticles of various forms are produced which are dependent on the kind and macrostructure of the block copolymers, the concentration, the solvent, and other progression factors. The majority of the nanoparticles had a solid, elastomeric, and deeply cross-linked core shell. The progression and structure of nanoparticles have been studied and characterized throughout different phases of the process.

PNPs are particle dispersions or solid particles ranging in size from 10 to 1000 nanometers. The use of particle delivery schemes as carriers for small and large molecules has flashed a lot of investigations in the field of medicine delivery. Nagavarma et al. [6] proposed a review on different methods utilized in the polymeric nanoparticles' preparations. Particulate systems, such as nanoparticles, have been used to modify and enhance the pharmacokinetics and pharmacodynamics of many medicinal compounds. Several approaches for generating polymeric nanoparticles have been established, and these methods are categorized based on the particle production which involves a reaction in polymerization or whether the nanoparticles form directly from a macromolecule or premade polymer. Many strategies for preparing polymeric nanoparticles are explained in this review.

A review on the drug-laden polymer nanoparticle is done based on the strategies employed in modern medicine. The method was proposed by Castro et al. [7], formulation capable of delivering medication in a regulated and precise manner at a given location. In this situation, stimulus-reactive nanoparticles are identified because they have lengthy circulation durations, can reach the illness site, and can optimize intracellular medicine administration. As a result, this review focused on current trends in drug delivery techniques as well as the impact of external and internal stimulus causes on stimulus-reactive nanocarriers. In addition, both traditional and novel approaches for the manufacture of polymer nanomaterials were examined.

The polymeric nanoparticles were produced as aqueous distributions using an emulsion that included a salting step to remove surfactants and chlorinated solvents. The preparation of the aqueous polymeric nanodispersion method was proposed by Allémann et al. [8]; this was done by a changeable salting-out procedure, and the particle size was influenced by this process. A salting-out technique prevents acetone from combining with water in the saturated aqueous solution. Following the production of emulsion of oil-in-water, an adequate amount of water is added to allow complete acetone dispersal into the aqueous phase, resulting in the development of nanospheres. During the production process, the stirring rate, internal/external phase ratio,

polymer absorption in the acetone phase, electrolyte type, and attentiveness and type of PVAL in the aqueous stage were all modified.

3. Methodology

For the production of numerous and different molecular designs, the polymer is found to be a convenient material. These molecular designs could be integrated into an inimitable nanoparticle, and they are used to design different medical applications. For the preparation of polymeric nanoparticles, more than a few methods were developed during the last two decades. Based on their information, the design procedure of the PNP can be classified, and this includes the reaction of polymerization or formation of the nanoparticle from the macromolecule, and the ionic gelation method is also included [9]. Based on the preparation of the nanoparticle, nanocapsules or nanospheres are obtained. Figure 1 shows the difference in the nanosphere and nanocapsule. The drugs confined in the cavity are defined as nanocapsules, and the cavity is enclosed by an inimitable polymer membrane; on the contrary, the atmosphere system in which the drug is substantially and unvaryingly dispersed is termed as the nanosphere. Polymer nanoparticles play an important role in the field of electronics, conducting materials, photonics, medicine, environmental technology of the sensor system, and pollution control.

4. Nanoparticle Preparation and the Polymer

The polymers should be adaptable (nontoxic) and antigenicity-free, as well as biodegradable and biocompatible with the human body. The natural polymer and the synthetic polymer used in the preparation of polymeric nanoparticles are given in Table 1.

Depending on the particular application, the assets of the polymer nanoparticle could be optimized. The method on the preparation plays a dynamic role in achieving properties of the PNP. As a result, having preparation methods to create PNPs with the appropriate characteristics for a certain application is quite beneficial. Polymerization, ionic gelation, and premade polymers are among the procedures employed [10]. Appropriate polymer nanoparticle is designed based on the desired properties for specific applications, and this can be done during the preparation of the polymerization of monomers. In this research, two important methods were discussed based on the preparation of polymeric nanoparticles. They are emulsion polymerization and salting out [11].

4.1. Method Used in Polymeric Nanoparticle Preparation. There are different methods used in the polymeric nanoparticle preparation, and they are expressed in Figure 2(a) which shows the dispersion of the performed polymer, and Figure 2(b) shows the polymerization of monomers. At first, the preparation of the nanoparticle from the dispersion of the performed polymer is presented, and then the nanoparticle preparation from the polymerization of monomers is expressed [12].

5. Preparation of the Nanoparticle from the Polymerization of the Monomer

5.1. Emulsion Polymerization. The fastest method of polymeric nanoparticle preparation is the emulsion polymerization method, and it is readily ascendable. Based on the organic or aqueous phase, the following method is divided into two categories. The dispersion of the monomer into an emulsion is involved in the continuous organic phase; this can also be defined as the inverse microemulsion or nonsolvent monomers [13]. To avoid aggregation at the beginning of polymerization, protective or surface-active soluble polymers were used as a method of producing the nanoparticle. Due to its requirements, this method is said to be of low impact; the requirements include the organic toxic solvent, monomers, mediators, and surfactants. These parameters are neglected from the nanoparticles prepared [14]. The alternative method provides more interest when the preparation process becomes difficult to handle, and as a result, the nature of the polymer becomes nonbiodegradable. By the dispersion process, nanoparticles such as polymethyl methacrylate, poly-ethyl cyanoacrylate, and polybutyl cyanoacrylate were prepared, and in this process, the organic phase used solvents such as cyclohexane, pentane, and toluene. In the aqueous continuous phase, emulsifier or surfactants are not essential since in the continuous phase situation, the monomers dissolved, and this is commonly used as an aqueous solution.

Figure 3 illustrates the emulsification process. In different mechanism processes, the polymerization process could be originated. When the monomer molecule gets dissolved in the continuous phase, the initiator molecule strikes with it. The originator molecule may be ions or radicals. The monomer molecule gets transformed into originating radicals by the high-energy radiation system, and this includes g-radiation or UV rays and strong visible light [15]. A mechanism of anionic polymerization causes monomeric ions or monomeric radicals to collide with other monomeric molecules, causing the chain to develop. Stage parting and the creation of solid particles may occur before or after the completion of the polymerization reaction.

5.2. Miniemulsion Polymerization. In recent years, the number of articles published on polymerization based on miniemulsion and the creation of a wide range of useful polymer materials has improved substantially. Stabilizers, water, monomer blends, surfactants, and initiators are common ingredients in miniemulsion polymerization formulations. The common parameters of the polymerization in miniemulsion are monomer mixture, water, stabilizer, and originator; these were used based on the formulization. The use of a molecule with a low molecular mass as a costabilizer [16], as well as the use of a high-shear device, distinguishes polymerization emulsion from polymerization miniemulsion. Lot of interfacial tension was produced in the miniemulsion process, and to attain the steady-state condition, a great shear is required, and the miniemulsion is critically stabilized.

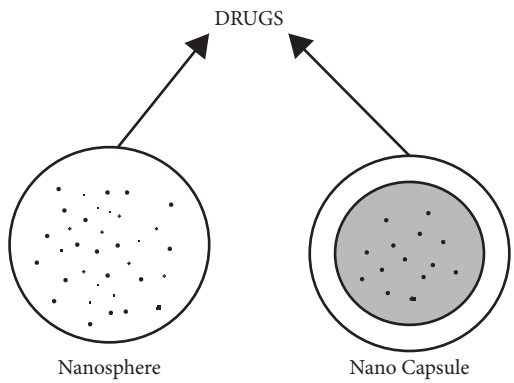

Figure 1: Difference in the nanosphere and nanocapsule.

Table 1: Classification of polymers.

No.	Natural polymer	Synthetic polymer
1	Chitosan	Polylactides
2	Gelatin	Polyglycolides
3	Sodium alginate	PLGA (polylactide-co-glycolide)
4	Albumin	Polyanhydrides

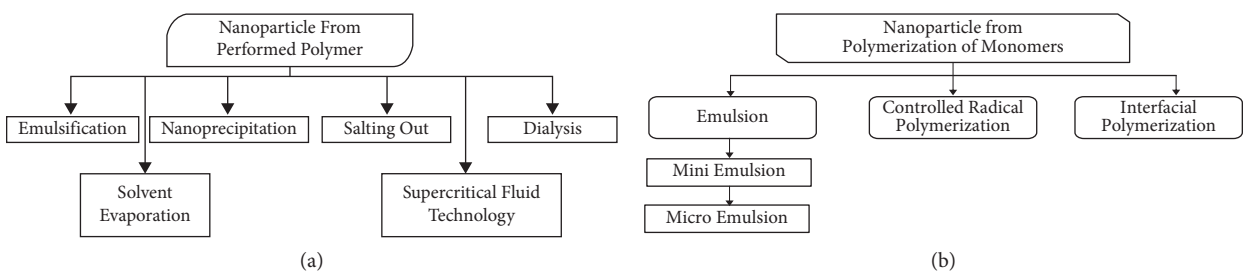

Figure 2: Polymerization of monomers.

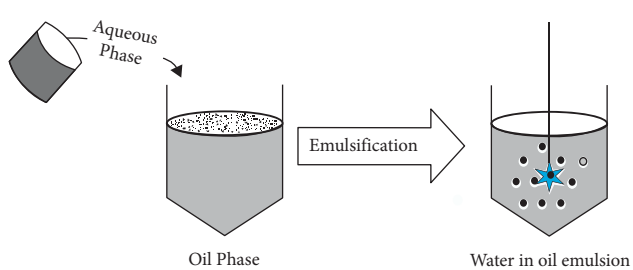

Figure 3: Emulsification process.

5.3. Microemulsion Polymerization. Microemulsion polymerization is a successful method to produce nanosized polymer particles which has received much attention. In spite of the fact that emulsion and polymerization by microemulsion can form colloidal polymer particles with a large molar mass, they are completely different kinetically. The particle size and average number of strings per particle are substantially smaller in microemulsion polymerization. An initiator, often water soluble, is added to the aqueous phase of a stable thermodynamic microemulsion containing inflated micelle in microemulsion polymerization. The polymerization process begins with this steady, spontaneously generated thermodynamic state and is based on large quantities of surfactants with low interfacial tension at the oil/water interface. Furthermore, due to the application of a large quantity of the surfactant, the particles are completely coated with the surfactant. Subsequently, the osmotic and elastic impact of the chains destabilized fragile microemulsions, causing particles to grow, empty micelles to form, and secondary nucleation. Some of the critical elements

determining microemulsion polymerization kinetics and PNP characteristics include the initiator type and concentration, surfactants, monomer, and reaction temperature.

5.4. Determining the Molecular Weight and Intrinsic Viscosity of the Polymeric Nanoparticle. By using the Ubbelohde capillary viscometry method, the molecular weights of the final polymers could be determined. Equation (1) determines that the polyacrylamide nanoparticle at 25°C is dissolved in water.

$$(\zeta)_{\text{intrinsic}}\left(\frac{\text{ml}}{\text{g}}\right) = 6.31 \times 10^{-3} M_w^{0.8}\left(\frac{\text{g}}{\text{mol}}\right). \quad (1)$$

Excess of acetone (1 : 6) was used to precipitate a piece of each final emulsion, which was then washed multiple times with acetone. The precipitates were then dried for 48 hours at 60°C. Under stirring, 200 milligrams of pure polymer powder were dissolved in 100 milliliters of deionized water. The produced solution (0.2 g of polymer per 100 mL) was diluted to provide concentrations of 0.18, 0.14, 0.10, and 0.06 g of the polymer per 100 mL deionized water. A capillary viscometer (constant factor = 0.01026 mm^2/s) was used to measure the viscosity of each solution three times. The intrinsic viscosity is calculated from the intercept value of a linear regression, and this has a link with the specific viscosity and polymer content. The molecular weight of the finished polymer is determined using the DLS method.

5.5. Measurement of Monomer Conversion. 15 g of dispersion (n_1) was removed from the reaction vessel at various time intervals to determine AM conversion as a function of time. To stop the polymerization process, each sample was given a 0.10 wt% hydroquinone aqueous solution. To achieve constant weights, samples were precipitated with excess of acetone (1 : 8) and dried in a freeze dryer at 50°C for 48 hours (n_2). Finally, equation (2) was used to compute the conversion of PAM nanoparticles.

$$y\% = \frac{n_2 - \text{hydroquinone weight}}{\text{primary monomer weight/weight of the particle based on the parameter}} \times 100\%. \quad (2)$$

5.6. Size and Distribution of the Emulsion Particle. By using the Malvern Zetasizer Nano series, the *Z*-average diameter of the polyacrylamide nanoparticle is determined, and the distribution is measured. Under the scattering angle of 90°, the light source with a wavelength of 645 nm is measured, and this has an ambient temperature of 30°C. After vigorous mixing, the emulsions were injected into 10% Span 80 in cyclohexane solution (10,000 rpm). A field emission scanning electron microscope is used to measure particle size. On the sample holder, one drop of the finished emulsion was deposited without any treatment and then spin-coated to remove water. It is worth noting that the *Z*-average employed an intensity-based estimated value of particle size which is the optimum value to provide for particle size in the face of even modest changes in the sample in dynamic light scattering studies.

6. Results and Discussion

There are various methods involved in the preparation of nanoparticles, and different technologies have been evolved for the preparation of the nanoparticle from the polymeric material. To prepare the nanoparticle from the polymeric material, a simple, safe, and reproducible method has been adapted; now, this type of method is used in the preparation of the drug-loaded nanosphere and nanocapsules [17]. Various polymeric nanoparticle preparation processes are available. It is discovered that formulating PNPs is a cutting-edge skill that necessitates the selection of an appropriate procedure from a variety of options. Three characteristics distinguish nanoparticle preparation methods: (1) reagents that are less hazardous are required, (2) procedure simplification to allow for cost-effective scale-up, and (3) to improve the yield and entrapment efficiency by optimization. The general advantage and disadvantage about the preparation of nanoparticles are defined [18]. Polymeric nanoparticles design experiment is represented in Table 2. These values ensure that the results were consistent. Experimental errors for monomer conversion, intrinsic viscosity and particle size, molecular weight and distribution, and second virial coefficient were found to be 0.2%, 1%, 1.5%, and 3%, respectively.

Figure 4 shows the polymeric nanoparticle design experiment which is illustrated based on Table 2. The graph is plotted for the water and oil ratio, HLB, water, and CH at wbt%. From the graph, it can be verified that the level of water and CH get increased after a constant range and again maintained a constant range.

6.1. Temperature and Reaction Time Effects. Table 3 represents the full conversion of monomers. When a portion of the emulsion was taken from the reaction vessel at different time intervals, six reactions were evaluated: 20 minutes, 125 minutes, and 210 minutes. After 120 minutes, the results were stable, revealing the time required for nearly full monomer conversion. In the subsequent runs, a polymerization time of 120 minutes was employed. The droplet phase increased the radical desorption rate of initiator-derived radicals (as the water-soluble APS initiator was used) due to the reduced average number of radicals per particle (the expected value for the examined system at 60°C is substantially below 0.5), and the resulting polymers will have a higher molecular weight and intrinsic viscosity.

Table 2: Polymeric nanoparticle design experiment.

Run	Initiator	W/O ratio	HLB	Water (wbt%)	CH (wbt%)	T (°C)	N (rpm)
1	APS	0.1	6.8	5.2	89.9	65	550
2	APS	0.2	6.8	11.4	81.8	65	550
3	APS	0.3	6.8	15.0	76.2	65	550
4	APS	0.5	6.8	34.9	76.2	65	550
5	APS	0.4	6.8	16.5	76.2	65	550
6	APS	0.4	6.8	16.5	76.2	65	550
7	APS	0.4	6.8	16.5	76.5	65	550
8	APS	0.4	6.8	16.5	76.8	65	550
9	APS	0.4	6.8	16.5	76.2	65	550
10	APS	0.4	6.8	16.5	76.9	65	550
11	APS	0.4	6.8	16.5	76.7	65	550

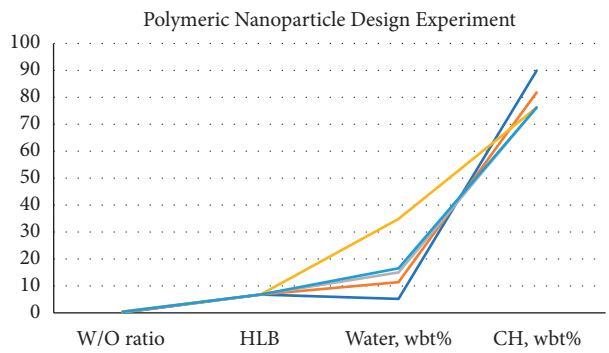

Figure 4: Polymeric nanoparticle design experiment.

Table 3: Effect of time and temperature.

Run	Time	Temperature	Technique of dynamic light scattering				Capillary viscometer technique		M_w^{VDif}	Y%
			D (nm)	PSD	M_w^{DL} (MDA)	A (mL mol)	$[\zeta]$ (mL/g)	M_w^{VS}		
3′	25	60	65	64–165	0.88	$+0.205E-5$	345	0.85	3.46	68.0
3	125	0	60	50–180	6.55	$+0.670E-4$	1675	6.05	7.88	99.2
3″	250	0	61	28–160	6.55	$+0.655E-5$	1678	6.04	7.25	99.9
6	125	55	65	45–189	5.15	$+0.685E-4$	1470	5.15	1.05	85.8
5	125	45	65	50–220	4.05	$+0.680E-4$	1210	4.00	0.30	59.5

As a result, as the temperature rises, the ratio of propagation to termination constant will rise, as will the length of polymer chains and their intrinsic thicknesses, under the investigated conditions (Table 3). The reaction temperature had no effect on the stability of the latex dispersions because the A_2 coefficients were not significantly different.

Figure 5 shows the variation of monomers which is represented in a graphical form. It is obvious that increasing the reaction temperature increased polymerization rate, resulting in a significant increase in conversion over the entire reaction time, with nearly full conversion reached in only 125 minutes in the reaction done at 65°C. As a result, the polymer chains' length and their inherent viscosities will grow under the examined conditions, as would the ratio of propagation to termination constant at improved temperature.

Figure 6 shows the W/O reaction, which depicts the kinetics of inverse emulsion polymerization of AM using various initiators. The reaction rate for the system begun using APS is clearly higher than that for the system initiated with AIBN.

Figure 7 represents different initiator types where PSD and SEM pictures of nanoparticles generated at various agitation rates are displayed. As the initiator concentration is increased, the molecular weight of the resultant polymer drops because of higher number of initiators produced radicals inside similar size particles.

The effect of the polymer in nanoparticles on loading and entrapment efficiency is given in Table 4, and it is illustrated in Figure 8. The values of loading efficiency are in the range of 7.95–16.8%, and the values of entrapment efficiency are about 56.7–74.8%. It is predicted that entrapment efficiency is high for the formulation of polymer nanoparticles. The loading efficiency is improved by improving the polymer ratio so that the adequate quantity of the polymer will be available to entrap the drug present

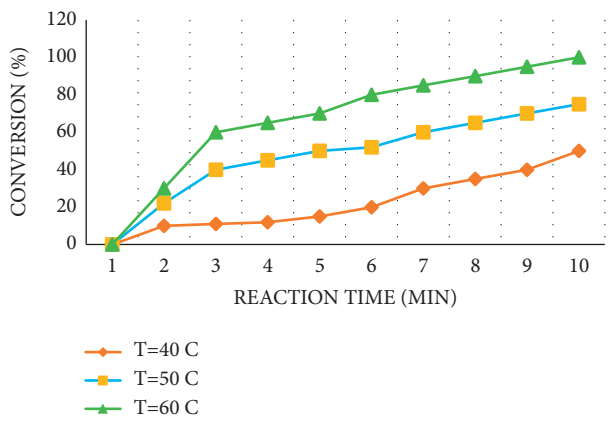

Figure 5: Variation of monomers.

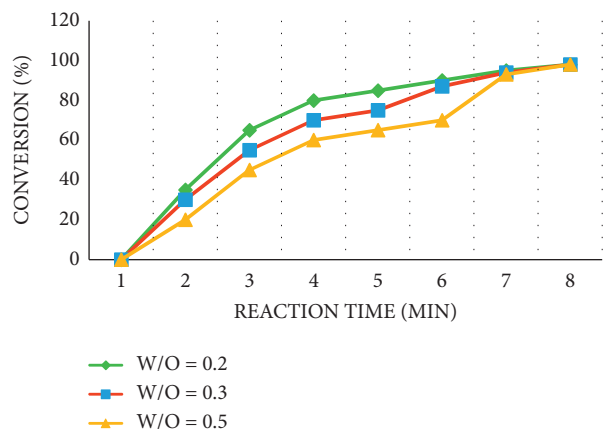

Figure 6: W/O reaction.

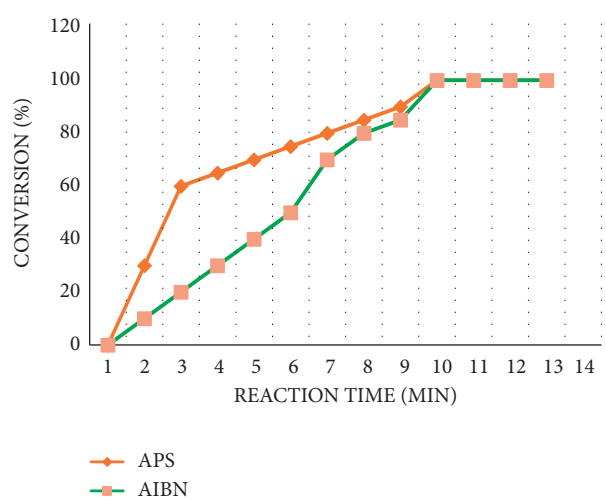

Figure 7: Different initiator types.

Table 4: Loading and entrapment efficiency.

Sl. no.	Formulation code	Loading efficiency	Entrapment efficiency
1	PNP 1	12.32	56.7
2	PNP 2	16.8	72.7
3	PNP 3	7.95	74.8

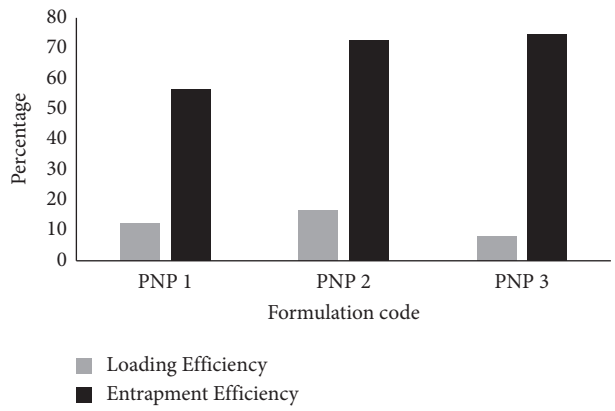

Figure 8: Effect on the loading and entrapment efficiency of the polymer.

in the solution. The polymer may be labeled or grafted onto the polymer by integrating it during the manufacturing process of nanoparticles made from pre-made polymers. PCL and PLA, for example, can determine the concentration after using a fast technique that occurs in organic resolution at low temperatures and may be used on polymers with high molecular weight.

7. Conclusion

The research was designed to provide the details about the preparation of nanoparticles. There are different methods used in preparing the polymeric nanoparticles. Polymerases, which can be found in the field of polymer colloids, are new structures awaiting to join the family of nanoparticulate drug delivery devices. Most of the polymeric nanoparticles are used mainly in the preparation of the drugs in the medical field such as nanospheres and nanocapsules. To describe the relation to nanospheres, different types of drugs are associated. These drugs may dissolve within the polymeric matrix or get absorbed by the polymer. The effect of nanoparticles based on the temperature and time is discussed in the result section. The research expresses the details about the preparation of polymeric nanoparticles from different polymerization methods. Salting-out and emulsification methods are expressed with the diagrammatic representation, and finally, the advantages and drawbacks about the nanoparticle preparation method are tabulated. Thus, the novel approach for the preparation of polymer nanoparticles is presented.

Data Availability

The data used to support the findings of this study are included within the article.

Conflicts of Interest

The authors declare that there are no conflicts of interest regarding the publication of this article.

Acknowledgments

The authors would like to express their gratitude towards Vignan's Foundation for Science, Technology and Research (Deemed to be University) for providing the necessary infrastructure to carry out this work successfully.

References

[1] S. Sahoo, "Conduction and switching behavior of e-beam deposited polycrystalline Nb_2O_5 based nano-ionic memristor for non-volatile memory applications," *Journal of Alloys and Compounds*, vol. 866, Article ID 158394, 2021.

[2] M. Joshi and U. Chatterjee, "Polymer nanocomposite," in *Advanced Composite Materials for Aerospace Engineering*Elsevier, Amsterdam, Netherlands, 2016.

[3] S. Sahoo, P. Manoravi, and S. R. S. Prabaharan, "Titania based nano-ionic memristive crossbar arrays: fabrication and resistive switching characteristics," *Nanoscience and Nanotechnology-Asia*, vol. 9, no. 4, pp. 486–493, 2019.

[4] E. M. Pridgen, F. Alexis, and O. C. Farokhzad, "Polymeric nanoparticle drug delivery technologies for oral delivery applications," *Expert Opinion on Drug Delivery*, vol. 12, no. 9, pp. 1459–1473, 2015.

[5] X. Wang, J. E. Hall, S. Warren et al., "Synthesis, characterization, and application of novel polymeric nanoparticles," *Macromolecules*, vol. 40, no. 3, pp. 499–508, 2007.

[6] B. Nagavarma, H. K. Yadav, A. Ayaz, L. Vasudha, and H. Shivakumar, "Different techniques for preparation of polymeric nanoparticles-a review," *Asian Journal of Pharmaceutical and Clinical Research*, vol. 5, no. 3, pp. 16–23, 2012.

[7] K. C. d. Castro, J. M. Costa, and M. G. N. Campos, "Drug-loaded polymeric nanoparticles: a review," *International*

Journal of Polymeric Materials and Polymeric Biomaterials, vol. 2020, Article ID 1798436, 13 pages, 2020.

[8] E. Allémann, R. Gurny, and E. Doelker, "Preparation of aqueous polymeric nanodispersions by a reversible salting-out process: influence of process parameters on particle size," *International Journal of Pharmaceutics*, vol. 87, no. 1–3, pp. 247–253, 1992.

[9] S. Moein Moghimi, "Recent developments in polymeric nanoparticle engineering and their applications in experimental and clinical oncology," *Anti-Cancer Agents in Medicinal Chemistry*, vol. 6, no. 6, pp. 553–561, 2006.

[10] V. Vijayan, K. R. Reddy, S. Sakthivel, and C. Swetha, "Optimization and charaterization of repaglinide biodegradable polymeric nanoparticle loaded transdermal patchs: in vitro and in vivo studies," *Colloids and Surfaces B: Biointerfaces*, vol. 111, pp. 150–155, 2013.

[11] S. Mallakpour and V. Behranvand, "Polymeric nanoparticles: recent development in synthesis and application," *Express Polymer Letters*, vol. 10, no. 11, pp. 895–913, 2016.

[12] J. Liu, Z. Qiu, S. Wang, L. Zhou, and S. Zhang, "A modified double-emulsion method for the preparation of daunorubicin-loaded polymeric nanoparticle with enhanced in vitro anti-tumor activity," *Biomedical Materials*, vol. 5, no. 6, Article ID 065002, 2010.

[13] C. Vauthier and K. Bouchemal, "Methods for the preparation and manufacture of polymeric nanoparticles," *Pharmaceutical Research*, vol. 26, no. 5, pp. 1025–1058, 2009.

[14] C. Zhao and X. Li, "Synthesis of high solid content (ST/BA/AA) emulsion, particle size and its distribution," *Polymeric Materials: Science and Engineering*, vol. 2, 2005.

[15] C. Pinto Reis, R. J. Neufeld, A. J. Ribeiro, and F. Veiga, "Nanoencapsulation I: methods for preparation of drug-loaded polymeric nanoparticles," *Nanomedicine: Nanotechnology, Biology and Medicine*, vol. 2, no. 1, pp. 8–21, 2006.

[16] A. J. Ribeiro, "Chapter 7: preparation of drug-loaded polymeric nanoparticles," in *Nanomedicine in Cancer*, pp. 171–214, Jenny Stanford Publishing, Dubai, UAE, 2017.

[17] B. N. Ganguly, *Nanomaterials in Bio-Medical Applications: A Novel Approach*, Materials Research Foundations, Millersville, PA, USA, 2018.

[18] R. Karnik, F. Gu, P. Basto et al., "Microfluidic platform for controlled synthesis of polymeric nanoparticles," *Nano Letters*, vol. 8, no. 9, pp. 2906–2912, 2008.

Hindawi
Advances in Materials Science and Engineering
Volume 2021, Article ID 7663348, 10 pages
https://doi.org/10.1155/2021/7663348

Research Article

Artificial Intelligence to Analyze the Performance of the Ceramic-Coated Diesel Engine Using Digital Filter Optimization

P. Nirmala,[1] **G. Ramkumar**,[1] **Satyajeet Sahoo**,[2] **G. Anitha**,[1] **S. Ramesh**,[3] **S. Agnes Shifani**,[4] **and Agegnehu Shara Shata**[5]

[1]*Department of Electronics and Communication Engineering, Saveetha School of Engineering, SIMATS, Chennai 602 105, Tamil Nadu, India*
[2]*Department of Electronics and Communication Engineering, Vignan's Foundation for Science, Technology and Research (Deemed to be University), Vadlamudi Guntur, Andra Pradesh-522213, India*
[3]*Department of Electronics and Communication Engineering, Sri Shakthi Institute of Engineering and Technology, Coimbatore-641062, Tamilnadu, India*
[4]*Department of Electronics and Communication Engineering, Jeppiaar Maamallan Engineering College, Chennai, Tamilnadu, India*
[5]*Faculty of Mechanical Engineering, Arba Minch Institute of Technology, Arba Minch, Ethiopia*

Correspondence should be addressed to P. Nirmala; nirmalajai@gmail.com and Agegnehu Shara Shata; agegnehu.shara@amu.edu.et

Received 6 August 2021; Accepted 31 August 2021; Published 9 September 2021

Academic Editor: P Ganeshan

The completeness of oil goods activates the barriers of lack of goods, inequality in the society, and surroundings impoverishment. Avoiding their use overnight and switching to clean electric motors are a challenge. Under all these conditions, researchers can launch their research on alternative fuels for a preeminent solution. Oxygenated fuel additives and thermal barrier coating (TBC) applications are essential to decrease the emission levels of exhaust and improve the performance of the vehicle. The main objective of this research is to analyze the performance of the ceramic-coated diesel engine. The ceramic particles use polymer coating to enhance the functionality and durability. Optimum outcomes are determined using Taguchi method. The impacts of various casting parameters of composites have been examined in detail. PSO-GA (Particle Swarm Optimization and Genetic Algorithm) is utilized to analyze the performance. Using an artificial neural network (ANN), the performance of diesel engine is examined to reduce time, cost, and experimental repetition. Thus, by using the artificial intelligence, the performance of the ceramic-coated diesel engine is analyzed and the polymeric substance and condition in coating ceramic engine is discussed.

1. Introduction

An enormous opening up of trade abroad and, on the other hand, the increase in emissions towards the impoverishment of the environment has brought attention to the replacement of diesel and gasoline. Oil provides energy for around 90% of transportation and transport, and mandate is growing gradually, particularly in developing countries such as India and China [1]. Our country's home oil stock accounts for only a quarter of total demand, with the remaining demands being satisfied with petroleum products imported from other nations. As a result, the essential steps have been taken to reduce the country's reliance on crude oil imports from other countries. The blends of biofuel are made from fats of veggies and animals and the fatty methyl acid is prepared from biomass. Biofuel is a biodegradable, recreate able fuel that may be used in fuel engines. Despite the fact that biofuel has the ability to reduce net CO_2 emissions, there are two barriers to its widespread adoption as a fossil fuel diesel substitute. As a result, the biofuel adoption strategy is to mix biofuel with fossil fuel diesel fuels, with permissible limits of diesel-biofuel blend compositions determined to safely use biofuel without harming diesel engines and to reduce NOx emissions.

Pores are frequently avoided in ceramic components due to their brittle nature, unlike porous metal and polymer constructions. However, in current decades, the number of submissions needing porous ceramics has been increased, particularly in situations including high temperatures, extensive wear, and corrosive fluids. After drying and pyrolyzing the polymeric model covered in ceramic, it is carefully heated between 3001 and 8001 degrees Celsius. To allow for progressive disintegration and diffusion of the polymeric material, heating rates of less than 11 C/min are required at this step [2]. Allowing pressure to build up in coated spacers is not a good idea. To provide ceramic coatings strong enough to prevent spacer cracking during pyrolysis, binders and plasticizers are added to the initial suspension. Some of the most commonly used binders include colloidal aluminum orthophosphate, potassium and sodium silicates, magnesium orthoborate, hydratable alumina, colloidal silica, polyvinyl butyral with polyethylene glycol as a plasticizer, and polymerizable monomers. The ceramic covering is densified after the polymer plate is removed by sintering in a suitable environment at temperatures ranging from 11001 to 11000 degrees Fahrenheit, depending on the material [3].

Plasma polymerization has been utilized to increase the corrosion and photodegradation resistance of items in a variety of industrial applications. Surface activation in a plasma environment through particle impact or photon radiation enhances monomer molecule deposition and polymerization on the substrate surface, providing a benefit not seen in nonplasma methods [4]. In reciprocating and rotary engines for transportation and stationary power, ceramic coatings have a considerable impact on reducing wear and abrasion failure. When operating temperatures are pushed higher to improve efficiency in these engines, the wear/abrasion problem gets more challenging, because lubrication in high temperature regions becomes increasingly problematic [5].

In automobiles, the IC engine is the major source of power. The piston, cylinder head, and cylinder block are among the many components that make up the engine. The most important components of an IC engine are piston and cylinder head, which is situated between the cylinder head's bottom and the piston. Pollutants are created as a result of combustion [6]. Combustion is the process of burning fuel in the presence of air. Diesel engines are used as the preferred engines for heavy-duty vehicles because of their high performance and low specific fuel consumption. Their use in light-duty vehicles has also increased over the last couple of years. In view of the strict legislation on emission control, statutory limits have become even more stringent. The major pollutants are fumigated, HC, NOx, and the material involved. However, diesel engines became more popular than other engines due to better torque characteristics and fuel economy [7].

2. Related Works

The literature review section of the paper includes the work proposed previously for analyzing the performance of ceramic coating diesel engine.

In the presence of thick layer polymer, acidic solutes have strong relation with zirconia surface [8]. The phosphate in the phase of mobile can reduce these interactions, making the polymer-coated zirconia's small solute retention qualities equivalent to alkyl silane-derivatized silica-based reversed-phase supports. With crude vegetable oil and different injector opening pressures, [9] examined the performance of a diesel engine with a ceramic-coated cylinder head. The performance parameters of the ceramic-coated combustion chamber were measured at various brake mean effective pressures and associated to neat operation of diesel on a conventional engine (CE) and vegetable oil operation at similar operating conditions.

The authors in [10] described that the ethanol can be made by fermenting and distilling biomasses, and it can thus be called a renewable fuel. Using the ethanol fuel CI engine as a Low-Heat-Rejection Engine is one method to improve its efficiency (LHR). The thermal efficiency of the CI engine can be improved in the LHR engine by limiting heat loss to the environment through coolant and exhaust gas. Heat transmission can be reduced by insulating the piston and cylinder walls, as well as covering the piston and cylinder walls with ceramics that can tolerate high temperatures. The low thermal conductivity of the coating materials reduces the heat flow into the piston and hence the heat transfers to the coolant.

Reference [1] discovered that using correlation coefficients, the ANN model can accurately estimate engine exhaust emissions with very low root mean square errors. The ANN method may be utilized precisely to anticipate the performance and internal combustion engines emission as an alternative to traditional modelling techniques, according to this study. The thickness of ceramic material which is about 200 m topcoat has been applied to the piston. Blends have been evaluated at their rated compression ratio under a variety of operational stresses. According to a comparison of engine parameters driven by diesel, mechanical competence progressively increases with a percentile increment of n-butanol in the mix. Using a backpropagation learning approach, the ability of an artificial neural network model to forecast specific fuel consumption and exhaust temperature of a Diesel engine for various injection timings is examined. The results of the experiment and the network were found to be consistent, with a mean absolute relative error of less than 2%. A well-trained neural network model is thought to produce quick and reliable findings, making it a simple tool to utilize in preliminary research for such thermal engineering challenges.

The chemistry of the surface polymer phase differs significantly from that of bulk polymers. The ease with which polymer coatings can be distributed and handled is one of their most appealing features. They can be applied as liquids, similar to paints, and other additives can be added to improve their qualities [6]. The polymer was identified using infrared, Raman spectroscopy, scanning and transmittance electron microscopy, and a dispersibility test. A uniform core-shell structure and a substantial number of acidic sites characterize the manufactured catalysts. More phosphor tungstic acid can be spread on the polymer's surface thanks to the presence of vinyl benzyl chloride in the polymer [11].

3. Methodology

This study investigates the performance of polymer-coated composite diesel engine. The robust Taguchi method and Minitab-16 software were also used in the experiment. Finally, the prediction of tensile strength and hardness of the composites was performed using ANN.

The performance of and emissions characteristics such as load and speed were changed using diesel, cotton seed oil blended with diesel fuel at a ratio of 10% to 20%, and the engine was tested using diesel, cotton seed oil blended with diesel fuel at a ratio of 10% to 20% [12]. The tests make use of Taguchi orthogonal arrays (OA). The OA was selected with the statistical software Minitab'16. OA is used to create the design of experiments (DOE).

In Figure 1, at first, the engine to be analyzed is selected and then the material to be applied is selected. These two are one of the important processes in investigation process. Continuing to this processing, the engine coating is done and after the completion of coating process, the experimental analysis is done and then continuing to this prediction of ANN result is given.

The tests are carried out in a 150 cc Kirloskar multi-fuel driven diesel engine equipped with an eddy current dynamometer and a gas analyzer. The system provides for the measurement of coated engine emission characteristics K. R. Patil and colleagues investigated diesel engine emissions and tested their performance using ISO 8178-C1 and ISO 8178-D2 protocols. CO is detected using a nondispersive infrared (NDIR) sensor, HC is detected using a flame ionization detector (FID), and NOx is detected using a chemiluminescent analyzer. Zircon is usually used to make zirconia ($ZrSiO_4$). Properties of cotton seed oil as shown in Table 1.

The zircon must be treated with NaOH and HCl to convert it to zirconyl chloride, which is then used to make zirconia. The cylinder head and valve surfaces will be coated with the PSZ powder that is currently available. The following procedures are carried out in this. (1) Rust, scale, sand, paint, and other contaminants are removed from the cylinder head and valve surfaces during precleaning and premachining. (2) Using the polymer spraying technique, apply the PSZ powder to the component surfaces up to the appropriate thickness [13]. Grinding, lapping, polishing, and cleaning are examples of final finishing procedures. It is best for internal combustion engines and has excellent corrosion resistance.

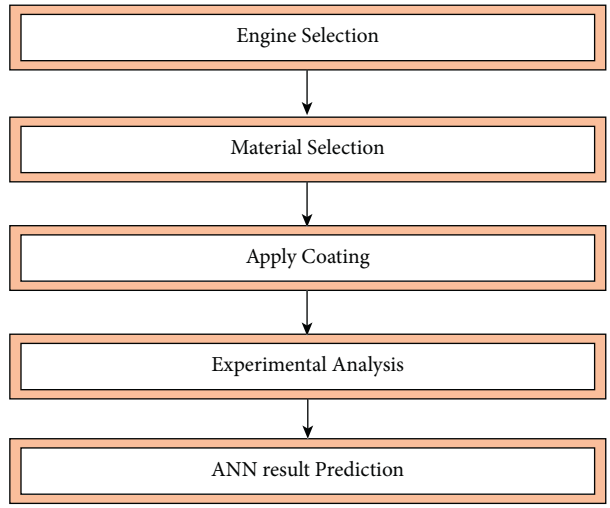

Figure 1: Step-by-step process of investigation process.

Table 1: Properties of cotton seed oil.

S. no.	Parameters	Values
1	Thickness	857 kg/m^3
2	Flash point	198°C
3	Fire point	225°C
4	Greasy value	35 MJ/kg
5	Cetane number	38

4. Polymer Coating

Plasma polymerization has been used to enhance hydrophily or hydrophobicity, erosion or oxidation resistance, and photodegradation resistance in a range of industrial applications. When the surface of a plasma is stimulated by particle impact or photon radiation, deposition and polymerization are accelerated. Monomeric molecules on the surface of the substrate indicate a benefit not seen in loss-free methods. To change the properties of films surface and powder particles, several types of imbalanced cold plasma have been introduced. Using the atmospheric microwave plasma CF_4/Ar or O_2/Ar , contact angle of the polypropylene film was checked. Hydrophobicity is enhanced by polymerization of tetrafluoroethylene on the surface of silica particles in luminescent dielectric barrier discharges.

The plasma processing sample is made up of zirconium ceramic powders with an average particle diameter of 130 nm. Figure 2, plasma Reactor Schematic A quartz jar with an interior diameter of about 80 mm, and a length of about 200 mm makes up the reactor chamber. A 27 MHz RF power supply drives a five-revolutions-per-minute RF antenna [7] that bypasses the chamber to accomplish a decent sign of at least 60% of the Fresnel zone. In numerous down-to-earth settings, transceivers might work with a lower radio wire stature, yet the higher the better. There is additionally a compromise between the receiving wire stature and the measure of RF link expected to range the handset to the radio wire. The sample holder and zirconia powders are dispersed throughout the center of the substrate surface; hence, a glass substrate is used in the chamber. After being fully blended, nitrogen-diluted ethylene is fed into the reactor chamber. With a mass flow control, the mixture ratio is changed by altering the flow rate of each gas. An empty pressure gauge is used to check the overall gas pressure [14]. Inductively coupled C_2H_4/N_2 discharges deposit a narrow polymer coating on the surface of ceramic nano-zirconia particles. Transmission electron microscopy was used to evaluate plasma-treated specimens (TEM). This means that zirconium nanoparticles cover the whole surface of a 5 nm thick polymer film. The film presents the chemical structure of a long chain of quasi-polyethylene hydrocarbons

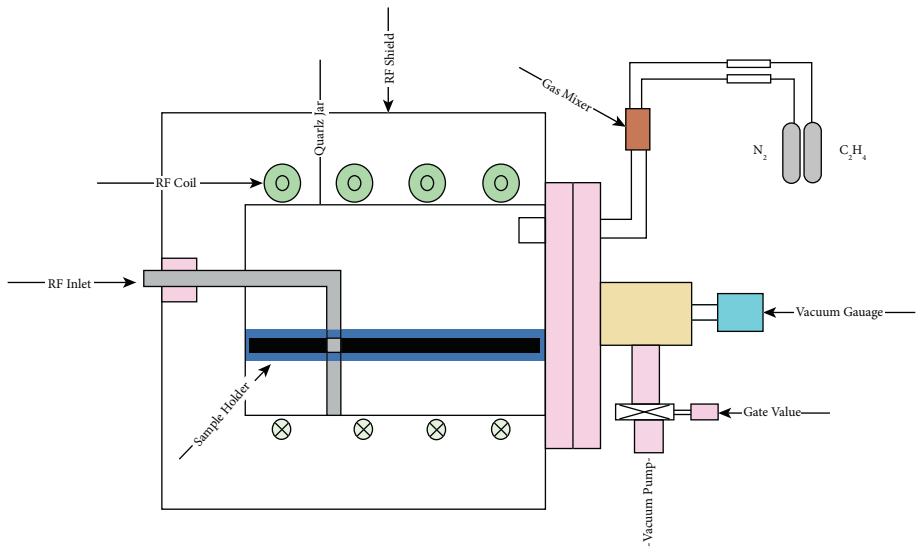

Figure 2: Schematic plasma reactor.

examined by X-ray photoelectric spectroscopy (XPS). This low-temperature dry surface treatment approach for ceramic nano particles is combined with fluidized bed technology. Plasma polymerization could be improved to aid in the synthesis of novel ceramics and improve the technological process [14].

As a plasma processing sample, zirconium ceramic powders with an average particle diameter of 130 nm were used. Figure 2 depicts the plasma reactor schematic. A quartz jar with an interior diameter of roughly 80 mm and a length of 200 mm makes up the reactor chamber [15]. A 27 MHz RF power supply drives a turn 5 RF coil that bypasses the chamber. A glass substrate is used as the specimen holder in the chamber, with zirconia powders scattered in the middle of the surface. After being fully blended, nitrogen-diluted ethylene is fed into the reactor slot. With a mass flow regulator, the blending rate is changed by altering the flow rate of each gas. A vacuum pressure gauge regulates the total pressure of the gas. After plasma treatment, the layer of powders that is the furthest from thin is taken as a sample. TEM (Hitachi, H-800) and XPS are used to analyze the shape and content of the polymeric covering (Perkin-Elmer, PHI-5300 ESCA). Within the XPS system, the radiation source is the Al Ka s1486.6 eVd line. The reading acquisition's passing energy is 100 eV, while the detail acquisition's is 25 eV, with resolutions of 2 and 0.5 eV, respectively.

4.1. Polymer-Coated Zirconia Preparation. Stable zirconia-based reversed phases were generated by depositing and crosslinking polymers on the zirconia surface. Reverse phase is generated by depositing stable zirconia and polymers crosslinked on the zirconia surface. Properties of polymer zirconium material are listed in Table 2.

Aside from stability, polymer-coated reversed phases have the advantage of being able to create materials with a wide range of carbon loading, regardless of the inhabitants of sensitive sites on the external or the firmness of surface bonds. By varying the amount of polybutadiene applied to the support, the quantity of carbon on the support surface can be changed by an order of magnitude [16]. When looking at the carbon analysis, it is critical to examine the surface area of the zirconia supports. When standardized to the support surface area, these values cover a wide range of carbon loads, including typical commercial salivated carbon loads. The carbon analysis data obtained on dissimilar zirconia with the same amount of polybutadiene agrees, indicating that the modification process is repeatable under the conditions stated above, as evidenced by the carbon analysis data obtained.

Table 2: Properties of polymer zirconium material.

S. no.	Parameters	Values
1	Tensile strength	225–540 N/mm^2
2	0.2% proof strength	100–440 N/mm^2
3	Elongation	5–35%
4	Hardness (HV)	55–175
5	Electrical conductivity	80% IAC
6	Thermal conductivity	300 W/moK
7	Melting point	1080°C

5. Coated Piston

The design for heat distribution for the thermal inquiry in steady state was simulated using ANSYS. An uncoated piston (without alteration) was found to have a temperature range of 350°C to 313.97°C, with a high of 352°C and a low of 313.96°C. The temperature 355°C and 323.85°C were discovered to be the maximum and lowest temperatures for an altered piston (at top surface of ceramic coat). The heat flow of uncoated and coated pistons may also be seen. Based on the aforementioned steady-state thermal investigation, the plasma spray technique was chosen as a thermal spray coating technique to apply the ceramic coating to the piston with a thickness of 200 m topcoat. The medium coated is heated to a molten state,

causing it to strike the membrane surface and instantly cool, forming a coating. This study proposes a ceramic-coated piston for testing biofuels in order to decrease the essential amount of gas pollution emitted by the engine.

Transesterification has been chosen as a filtration strategy for the production of pure biofuel, which should be followed by the esterification procedure. In this case, the oils of *Pongamia pinnata* and *Calophyllum inophyllum* contain a lot of free lipids. The raw sample was heated and then stirred with the addition of NaOH as a methanol and base catalyst. After a chemical reaction and isolation by water washing, the gravitational technique has traditionally been used to isolate the glycerol content of biofuel. These methyl esters were combined with pure diesel in various volume proportions (P10, P20, C10, and C20) with a magnetic agitator for biodiesel preparation procedure as shown in Figure 3.

These samples are blended with an additive (butyl alcohol) in various probabilities ranging from 6% to 12% in volume terms with a 6% interval once more. Because its high burn rates, n-butanol was used as an addition (oxygenate) in this investigation and can rapidly react with diesel. As a result, it appears to be able to sustain combustion in the presence of sufficient oxygen [16]. Before engine testing, the parameters of all mixes are measured with various equipment and are listed in Table 3.

The experiment is carried out on a single cylinder that has been cooled with water four times and injected directly. To apply the load, the CI motor has a ceramic-coated plunger with an eddy current dynamometer. An upper layer of 200 m of alumina was used as a ceramic substance to coat the piston. A low-heat-emitting engine is a compression-ignition (IC) engine having its piston covered in any ceramic material, resulting in minimal heat loss. This redesigned engine is gaining important in today's globe due to growing fuel prices and environmental devastation because it releases fewer emissions [17]. It had a lot of features, including the ability to measure combustion pressure and crank angle. There is a place where you can measure airflow and fuel flow, as well as temperatures and other things. The calorimeter's water flow and the cooling water flow are both measured using Rotameters. To evaluate computerized performance, a flexible set of motors has been added. In computerized mode, a layout allows for the measurement of fuel injection pressure at the nozzle.

6. PSO-GA Algorithm

When PSO and GA are combined, the exploring powers of GA are combined with the exploitation abilities of PSO. In this study, a novel combination of PSO and GA was applied, in which PSO and GA were run in order at each iteration with a small population. PSO for N probable solutions is used at the start of each iteration. Following PSO, the best n solutions are given to a GA procedure, which is based on fitness value. The GA operator pairs these solutions at random while simultaneously applying a mutation to a randomly chosen offspring, which is then brought back to PSO in the following iteration. To reduce dynamometer time, a small population N is desired. In order to reduce time to convergence in conventional benchmark testing, the optimal population size was found to be 8 in the interval [18]. For the sake of simplicity, N and n are both set to 4. The GA mutation rate, as well as the PSO constants C1 and C2, can be found. An objective function was constructed to evaluate each trial's fitness based on the cumulative fitness of five variables in order to optimize several objectives at once for both PSO-GA and ABC. CO, HC, NOx, and PM emissions specific to brakes (g/kW-h) were fed into the objective function and fuel consumption.

7. Taguchi Orthogonal Design

Taguchi method has been effectively employed among the optimization techniques for optimizing the process parameter for a simple and robust procedure. There are three alternative average square deviations estimated for the signal-to-noise ratio according to Taguchi's design objectives: better-the-nominal, better-the-large, and better-the-small. The goal of the study is to reduce warpage and shrinkage. The minimum rate of shrinkage and warpage must be achieved; therefore, the S/N ratio of the smaller-the-better formula must be chosen for optimizing the parameter rate, and so the combination is attained. Orthogonal array design of experiment with various types of fuels is listed in Table 4.

8. Artificial Neural Network

An ANN model can oblige different information factors to anticipate numerous yield factors. It contrasts from ordinary displaying approaches in capacity to find out about the framework can be demonstrated without earlier information on the cycle connections. The forecast by an all-around prepared ANN is typically a lot quicker than the ordinary reproduction programs or numerical models as no extensive iterative computations are expected to address differential conditions utilizing mathematical techniques, yet the determination of a fitting neural organization geography is significant as far as model exactness and model straightforwardness [18]. Notwithstanding the dynamic exportation of oil, the public authority actually needs to import an enormous measure of raw petroleum to satisfy neighborhood interest. A temperamental uncontrolled oil value prompts high government consumption in the spending plan, because of the strategy of exceptionally financed fuel for the neighborhood market later on.

The ANN model is shown in Figure 4. The back-propagation (BP) learning technique is used in this work among the several types of ANN algorithms available. In order to train and evaluate neural networks, the target and input data patterns are required. The existing dataset was separated into two sets while creating an ANN model [19], one for training the network and the other for testing the network's generalization capabilities. The user does not need to know any technical specifics of neural networks because they operate in a "black box" fashion. They are capable of determining the relationship between the input and output. Weights are adjusted to reduce the discrepancy among the network output and the real value, and the network is given

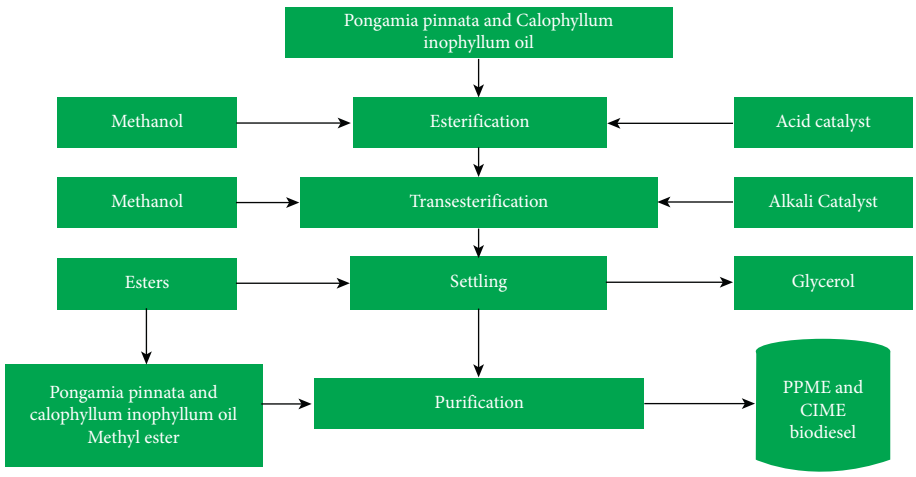

Figure 3: Procedure of biodiesel preparation.

Table 3: Tested sample fuel properties.

Model	Density (kg/m^3)	Gaudy point (°C)	Heating point (°C)	Thickness (cSt)	Calorific value (kJ/Kg)
D100	831	57	65	3.22	42505
P100	899.7	166	180	2.48	35667
C100	897.8	157	166	2.83	35088
P1B6	850	60	69	3.12	41252
P10B12	853	61	71	3.16	40699
P20B6	857	63	74	3.21	40616
P20B12	859	57	75	3.23	40098
C10B6	850	59	78	3.03	41014
C10B12	851	60	67	3.12	40426
C20B6	853	63	69	3.14	40132
C20B12	855	64	72	3.19	39718

Table 4: Orthogonal array design of experiment.

Exp. no.	Fuel	Load (%)	Speed (rpm)
1	Diesel type	0	1360
2	Diesel type	50	1380
3	Diesel type	100	1400
4	B10 type	0	1380
5	B10 type	50	1400
6	B10 type	100	1360
7	B20 type	0	1400
8	B20 type	50	1360
9	B20 type	100	1380

input–output pairs to operate with. Predictions can be made using the previously trained network on a new batch of data once the network has been trained. The input is break mean effective pressure (BMEP), injection timing, and engine speed (n), and exhaust temperature and brake specific fuel consumption (BSFC) are the outputs. The input and output values of a neural network must be between 0.1 and 0.9.

9. Result and Discussions

9.1. Analysis of Deposits on Polymer Surface. Biofuel fuel oxidation produces hydroperoxides, which break down and form low molecular weight compounds. Polymerization of tiny units produces heavy entities as well. A thin layer of residue forms on the polymer surface as a result of the breakdown and polymerization processes. The layer that forms is too thin and barely adheres to the surface, yet a soluble solvent dissolves it. After separating the solvent, the layer that can be easily studied. Ethanol and toluene are employed separately for various samples; there is no discernible difference between them, although the residues are sufficiently soluble in both.

9.2. Taguchi Optimization. The MINITAB-16 program was used to optimize the composite for optimal tensile strength and hardness. The results were obtained from the Taguchi orthogonal array studies on several materials by altering the reinforcement percentage, stirring speed, time, and temperature according to the Taguchi method. Figure 5 shows experiment versus hardness ratio which is illustrated in graphical representation and the values are listed in Table 5.

In Figure 6, experimental versus S/N ratio is illustrated in graphical representation. The comparison is done between experimental result and S/N ratio. The tensile strength (SN) and the hardness of the experimental and S/N ratio are compared. In experimental result, the tensile strength value is high compared to the S/N ratio, while in the other hand, the hardness is slightly variable in two processes. Hence, from the figure, we state that the tensile strength and the hardness are high in experimental value compared to the S/N ratio.

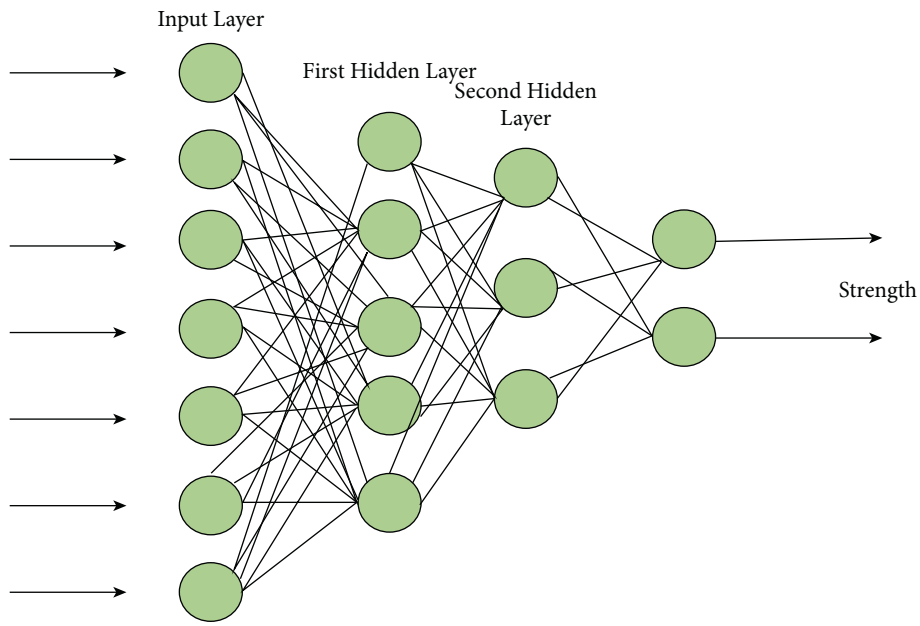

Figure 4: Model of ANN.

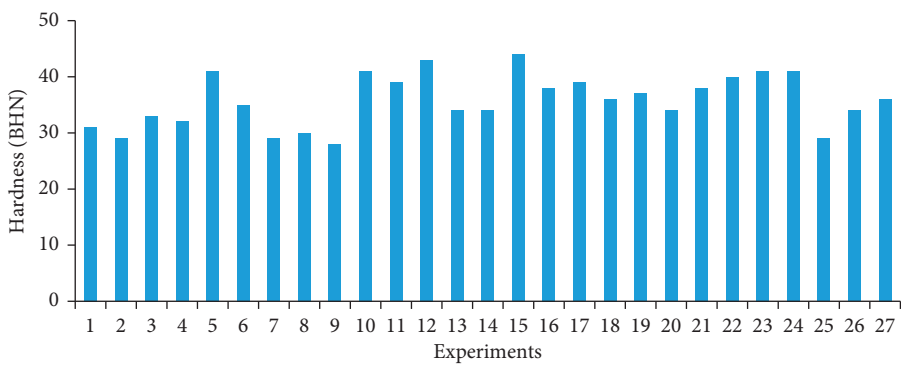

Figure 5: Taguchi optimization.

Table 5: Experimental and S/N ratio results.

Ex	TS (MPa)	Hardness (BHN)	S/N of tensile strength	S/N of hardness
1	71	30	37.7419	29.8272
2	72	29	37.1665	29.2480
3	79	33	38.1525	30.3703
4	76	32	37.6163	30.1030
5	77	41	37.3846	32.2557
6	74	35	37.3846	30.8814
7	74	29	37.5012	29.2480
8	73	30	37.2665	29.5424

10. Comparison between NO_x and Load for PPME Samples

Based on the tested fuel properties, the comparison between NO_x and load for PPME sample is calculated, and the graphical representation is given in the following.

In Figure 7, there is a comparison between the No_x and load for PMME; the graph is plotted against load and NOx in PPM; the load is literally high in 3rd stage when comparing to the other stages and only slight difference is found between each sample of PMME.

In Figure 8, there is a comparison between the No_x and load for CIME. The graph is plotted against load and NOx in PPM; the load is literally high in 3rd stage when comparing to the other stages, and only slight difference is found between each sample of CIME.

Figure 9 illustrates CO versus load for PPME samples. It is done at three stages and compared to one another. At first

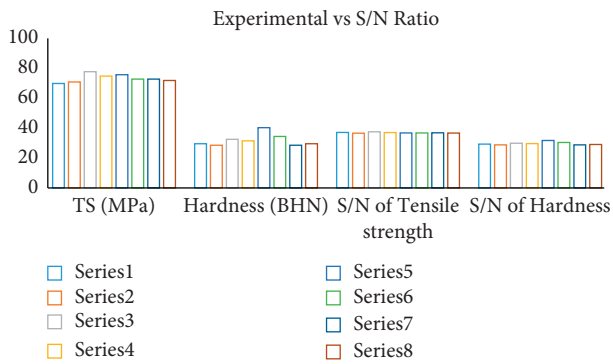

Figure 6: Experimental versus S/N ratio.

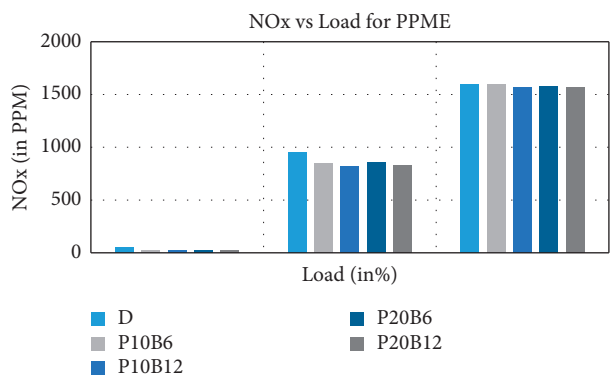

Figure 7: NOx versus load for PMME.

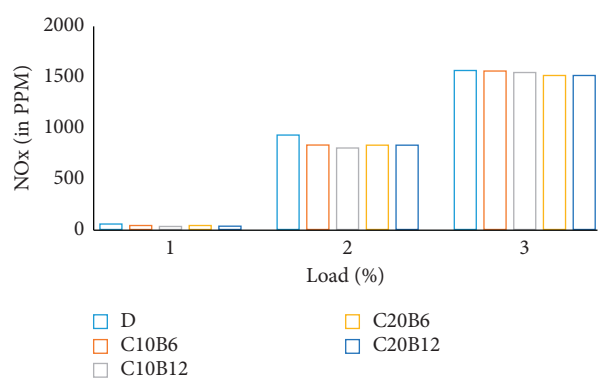

Figure 8: NOx versus load for CIME.

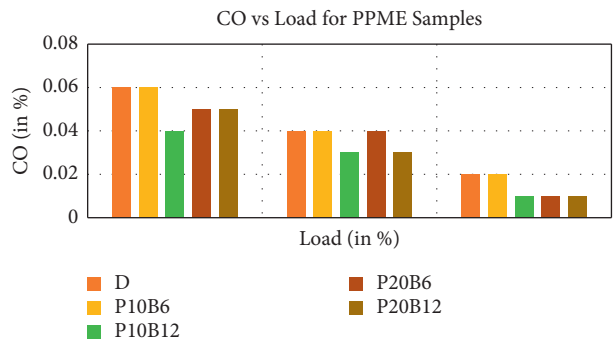

Figure 9: CO versus load for PPME Samples.

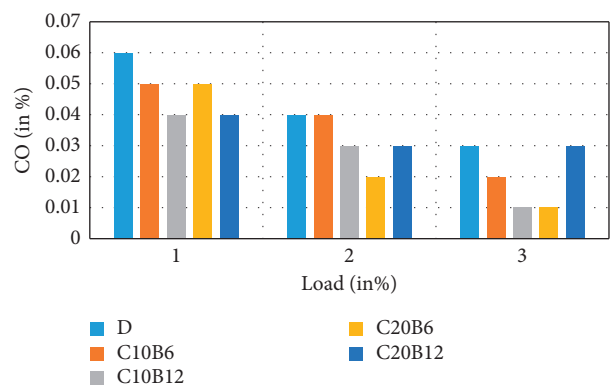

Figure 10: CO versus load for CIME samples.

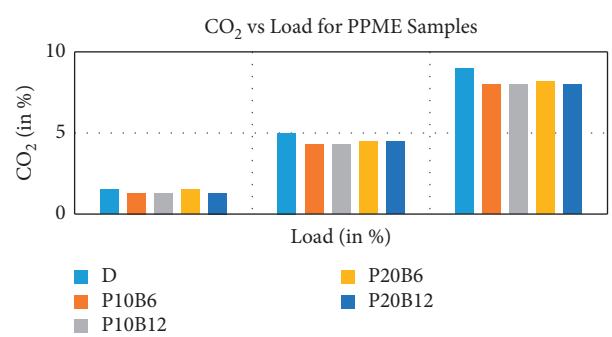

Figure 11: CO_2 versus load for PPME samples.

stage, *D* and P10B6 are high, compared to the other models, and in the second stage, *D*, P10B6, and P20B6 are equally high when compared to P20B12 and P10B12. In the final stage, *D* and P10B6 are equal, and P20B6, P10B12, and P20B12 are equal.

The CO versus load for CIME samples is illustrated in Figure 10; at the first stage, *D* is high when compared to other models. In the second stage, *D* and C10B6 are equal. In the final stage, when comparing to the other models, *D* and C20B12 are equal.

The CO_2 versus load for PPME samples is presented in Figure 11. At the first stage, all models or trails maintain an equal loading, and in the second stage, *D* is higher than the other models. In the final stage, *D* is high and the other models maintained an equal loading.

The CO_2 versus load for CIME samples is presented in Figure 12. At the first stage, all models or trails maintain a slight difference in loading, and in the second stage, C20B12 is higher than the other models. In the final stage,

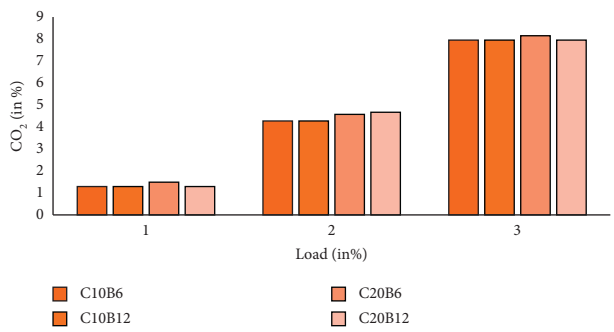

Figure 12: CO_2 versus load for CIME samples.

C20B6 is high, and the other models maintained an equal loading.

11. Conclusion

An artificial neural network architecture was constructed for predicting particular fuel consumption and exhaust temperature in a diesel engine. The effects of various composite casting parameters have been thoroughly investigated. Aside from stability, another advantage of polymer-coated reversed phases is the possibility to construct materials with a wide range of carbon loading. By combining evolutionary theory and natural swarm intelligence behaviors, hybrid PSO-GA algorithms create effective and usable data in less time than a thorough parametric investigation. Saving time lowers costs, making it easier to take advantage of innovative and proven techniques for improving engine performance. The performance of a diesel engine can be improved by using an artificial neural network (ANN), which saves time, money, and experimental repetition, due to the accuracy and the possibility of studying indiscriminately problems that will be solved by statistical and traditional ways by employing ANN. Even though it provides high accuracy, more time was taken for training purpose. This should be overcome in the future research.

Data Availability

The data used to support the findings of this study are included within the article.

Conflicts of Interest

The authors declare that there are no conflicts of interest regarding the publication of this article.

Acknowledgments

The authors would like to express their gratitude towards Saveetha School of Engineering, Saveetha Institute of Medical and Technical Sciences (formerly known as Saveetha University), for providing the necessary infrastructure to carry out this work successfully.

References

[1] T. K. Kotteda, R. B. R. Chekuri, B. Naga Raju, P. R. Kantheti, and S. Balakumar, "Analysis on emissions and performance of ceramic coated diesel engine fueled with novel blends using artificial Intelligence," *Advances in Materials Science and Engineering*, vol. 2021, Article ID 7954488, 13 pages, 2021.

[2] A. R. Studart, U. T. Gonzenbach, E. Tervoort, and L. J. Gauckler, "Processing routes to macroporous ceramics: A review," *Journal of the American Ceramic Society*, vol. 89, no. 6, pp. 1771–1789, 2006.

[3] R. M. Spriggs, "Applications and prospective markets for advanced technical ceramics," *Key Engineering Materials*, vol. 56-57, pp. 1–12, 1991.

[4] M. H. Ali, M. Rasul, M. Khan, N. Ashwath, and T. Rufford, "Emission characteristics of polymer additive mixed diesel-sunflower biodiesel fuel," *Energy Procedia*, vol. 156, pp. 59–64, 2019.

[5] I. Taymaz, K. Çakır, and A. Mimaroglu, "Experimental study of effective efficiency in a ceramic coated diesel engine," *Surface and Coatings Technology*, vol. 200, no. 1–4, pp. 1182–1185, 2005.

[6] M. M. K. Bhuiya, M. G. Rasul, M. M. K. Khan, N. Ashwath, A. K. Azad, and M. A. Hazrat, "Prospects of 2nd generation biodiesel as a sustainable fuel - Part 2: properties, performance and emission characteristics," *Renewable and Sustainable Energy Reviews*, vol. 55, pp. 1129–1146, 2016.

[7] A. Parlak, Y. Islamoglu, H. Yasar, and A. Egrisogut, "Application of artificial neural network to predict specific fuel consumption and exhaust temperature for a diesel engine," *Applied Thermal Engineering*, vol. 26, no. 8–9, pp. 824–828, 2006.

[8] M. P. Rigney, T. P. Weber, and P. W. Carr, "Preparation and evaluation of a polymer-coated zirconia reversed-phase chromatographic support," *Journal of Chromatography A*, vol. 484, pp. 273–291, 1989.

[9] M. V. S. M. Krishna, T. O. Prakash, P. Ushasri, N. Janardhan, and P. V. K. Murthy, "Experimental investigations on direct injection diesel engine with ceramic coated combustion chamber with carbureted alcohols and crude jatropha oil," *Renewable and Sustainable Energy Reviews*, vol. 53, pp. 606–628, 2016.

[10] T. H. Prasad, K. Hema Chandra Reddy, and M. M. Rao, "Performance and exhaust emissions analysis of a diesel engine using methyl esters of fish oil with artificial neural network aid," *International Journal of Engineering and Technology*, vol. 2, no. 1, pp. 23–27, 2010.

[11] N. A. Negm, M. A. Betiha, M. S. Alhumaimess, H. M. A. Hassan, and A. M. Rabie, "Clean transesterification process for biodiesel production using heterogeneous polymer-heteropoly acid nanocatalyst," *Journal of Cleaner Production*, vol. 238, Article ID 117854, 2019.

[12] H. Wang, S. Morando, A. Gaillard, and D. Hissel, "Sensor development and optimization for a proton exchange membrane fuel cell system in automotive applications," *Journal of Power Sources*, vol. 487, Article ID 229415, 2021.

[13] Y. Ö. Özgören, S. Çetinkaya, S. Sarıdemir, A. Çiçek, and F. Kara, "Artificial neural network based modelling of performance of a beta-type Stirling engine," *Proceedings of the Institution of Mechanical Engineers-Part E: Journal of Process Mechanical Engineering*, vol. 227, no. 3, pp. 166–177, 2013.

[14] T. W. Simpson, T. M. Mauery, J. Korte, and F. Mistree, "Kriging models for global approximation in simulation-

based multidisciplinary design optimization," *AIAA Journal*, vol. 39, no. 12, pp. 2233–2241, 2001.

[15] D. Wen and Y. Ding, "Effective thermal conductivity of aqueous suspensions of carbon nanotubes (carbon nanotube nanofluids)," *Journal of Thermophysics and Heat Transfer*, vol. 18, no. 4, pp. 481–485, 2004.

[16] K. Viswanathan, W. Wu, M. I. Taipabu, and W. Chandra-Ambhorn, "Effects of antioxidant and ceramic coating on performance enhancement and emission reduction of a diesel engine fueled by Annona oil biodiesel," *Journal of the Taiwan Institute of Chemical Engineers*, vol. 125, pp. 243–256, 2021.

[17] J. Sharaf, "Exhaust emissions and its control technology for an internal combustion engine," *International Journal of Engineering Research and Applications*, vol. 3, no. 4, p. 14, 2013.

[18] L. Dobrzański, M. Staszuk, and R. Honysz, "Application of artificial intelligence methods in PVD and CVD coatings properties modelling," *Archives of Materials Science and Engineering*, vol. 58, no. 2, pp. 152–157, 2012.

[19] S. Fidan, H. Oktay, S. Polat, and S. Ozturk, "An artificial neural network model to predict the thermal properties of concrete using different neurons and activation functions," *Advances in Materials Science and Engineering*, vol. 201913 pages, 2019.